19th

ISOT

CANCÚN · 2018 · MÉXICO

International Symposium on Optomechatronic Technology

EXTENDED ABSTRACT · BOOK ·

Table of Contents

Welcome from ISOT 2018 Conference Chairs	2
Greeting Message from ISOM President	3
Venue	5
Topics	8
Symposium Committees	9
Program at a Glance	11
Plenary Speakers	12
Extended Abstracts by Topic	
3D processing 3D fabrication and 3D printer	23
Biomedical applications	36
Material laser processing	45
Micro optoelectro mechanical systems	50
Optical imaging interferometry	59
Optical inspection for industry	80
Optical manipulation and tweezers and their applications	93
Optical metrology	96
Optical sensors on robotics autonomous vehicles and other applications	132
Optomechatronics for sensing and imaging	143
Solar cell	158
Thin film technology	163
Vision based monitoring and control / Visual motion tracking and control	166
Special Session 1: Polarization technology	179
Special Session 2: Sensors based on the use of lasers and fiber optics	192
Others	220
Local Information	242
Author Index	243

Welcome

On behalf of International Society for Optomechatronics, ISOM, and the Optical Research Center (Centro de Investigaciones en Óptica), CIO, we would like to welcome you to the 19th International Symposium on Optomechatronic Technology, ISOT 2018, in Cancún, Quintana Roo, México.

We would like to thank the participation of ten distinguished plenary speakers whose abstracts are included at the beginning of the program guide.

A total of 100 papers were accepted through a review process and will be presented at the Symposium; out of these papers, twenty were selected as invited.

Participants of the ISOT 2018 came from around the globe and included 15 countries: 6 from Canada, 4 from China, 2 from France, 3 from Germany, 2 from India, 1 from Italy, 1 from Iran, 8 from Japan, 72 from Mexico, 1 from Singapore, 1 from South Korea, 1 from Spain, 5 from Taiwan, 1 from United Kingdom and 2 from United States of America.

The proceedings book "Progress in Optomechatronic Technologies: ISOT 2018" will be published by Springer under the book series "Springer Proceedings in Physics".

We are happy and proud to have welcomed in Cancún well-known experts who came to discuss current and future challenges related to relevant topics in the tracks included in the program of the Symposium. Please enjoy the Symposium and the beautiful and peaceful beaches of Cancún.

Thank you so much for participating!!

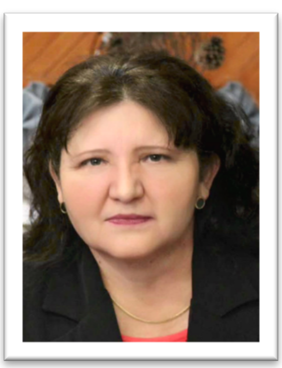

Amalia Martínez-García
ISOT 2018 General Chair
Centro de Investigaciones en Óptica, México

Indrani Bhattacharya
ISOT 2018 General Co-Chair
University of Calcutta, India

***In memoriam* of Prof. Joel Kubby, who was Steering Committee Member of ISOT.**

Welcome Address by the President of ISOM

A warm welcome to the 19th International Symposium on Optomechatronic Technologies, ISOT. Over the years this special conference has established itself as a meeting point of a growing community of scientists working in the interdisciplinary field of optomechatronics. This covers a variety of topics that range from microelectromechanical sensors to astronomical telescopes, from medical instruments to computer and telecommunication equipment and from machines for nanolithography to industrial robots. Beside the annual ISOT symposia the open access, peer-reviewed International Journal of Optomechatronics IJO is a communication platform of the community. Furthermore the International Society for Optomechatronics ISOM was founded to promote research and activities in this field. You may find more information about ISOM on the webpage www.optomechatronics.org. Looking back, each ISOT had different topical foci, depending on recent developments and on the core research areas of the respective organizers. Now for the first time ISOT takes place in Mexico. Universities and research institutions in Mexico have an excellent reputation in optical metrology and therefore ISOT 2018 has an emphasis on optical sensing, optical metrology and optical inspection. But you will find contributions on robotics, autonomous vehicles, optical tweezers or 3D printing as well. The proceedings book “Progress in Optomechatronic Technologies: ISOT 2018” will be published by Springer under the series “Springer Proceedings in Physics” which will be indexed in ISTP (Conference Proceedings Citation Index).

In addition to regular and invited oral presentations and posters there will be ten plenary talks, presented by well-respected international experts. Thanks to the tremendous effort of Amalia Martínez García (General Chair), Indrani Bhattachariya (Co-chair), the International Program Committee, the Local Organizing Committee and the Technical Committee you will get information about latest research results, get the opportunity to meet colleagues from all over the world and enjoy the hospitality of an exciting country. You are heartily invited to attend ISOT 2018 in Cancún, México!

Rainer Tutsch
TU Braunschweig, Germany
President of ISOM

Hosted by Centro de Investigaciones en Óptica, CIO

In CIO we do basic and applied research that contributes to the knowledge generation as well as innovation in the optics and photonics field strengthening technological leadership in the country and promoting new enterprises based on knowledge. We offer the best graduate program in optics and photonics and contribute in the development of a technological and scientific culture.

Centro de Investigaciones en Óptica is located in the city of León, Guanajuato, México, in the middle of the country. More information in https://www.cio.mx/en/

Venue

Symposium will take place at the Krystal Hotel & Resort Cancún.

Cancun is located on the north east coast of the state of Quintana Roo, in the south east of Mexico, at a distance of 1,700 km from Mexico City.

Cancun is a cosmopolitan city in the Mexican Caribbean with world class tourism development certified by the World Tourism Organization (WTO). Its relatively recent creation and its growing development have brought together an interesting mixture of inhabitants from different regions of Mexico and other countries, thanks to numerous job opportunities offered by the tourism sector. Furthermore, as result of its regional location, Cancun is renowned for its folk gastronomy and customs from the neighbouring state of Yucatan, and of course, the great Mayan Culture.

The Mexican Caribbean is a unique corner of the world with a harmonious combination of natural beauties; 25% of its total area is considered to be an ecological reserve, and it has the second largest reef system in the world, making it a paradise.

Krystal Hotel & Resort Cancún

Located: 23.2 km from Cancún International Airport

Address: Boulevard Kukulcán, km 9, Zona Hotelera, 77500 Cancún, Quintana Roo, Mexico

Phone: (998) 848 9800

https://www.krystalhotels.com.mx/cancun

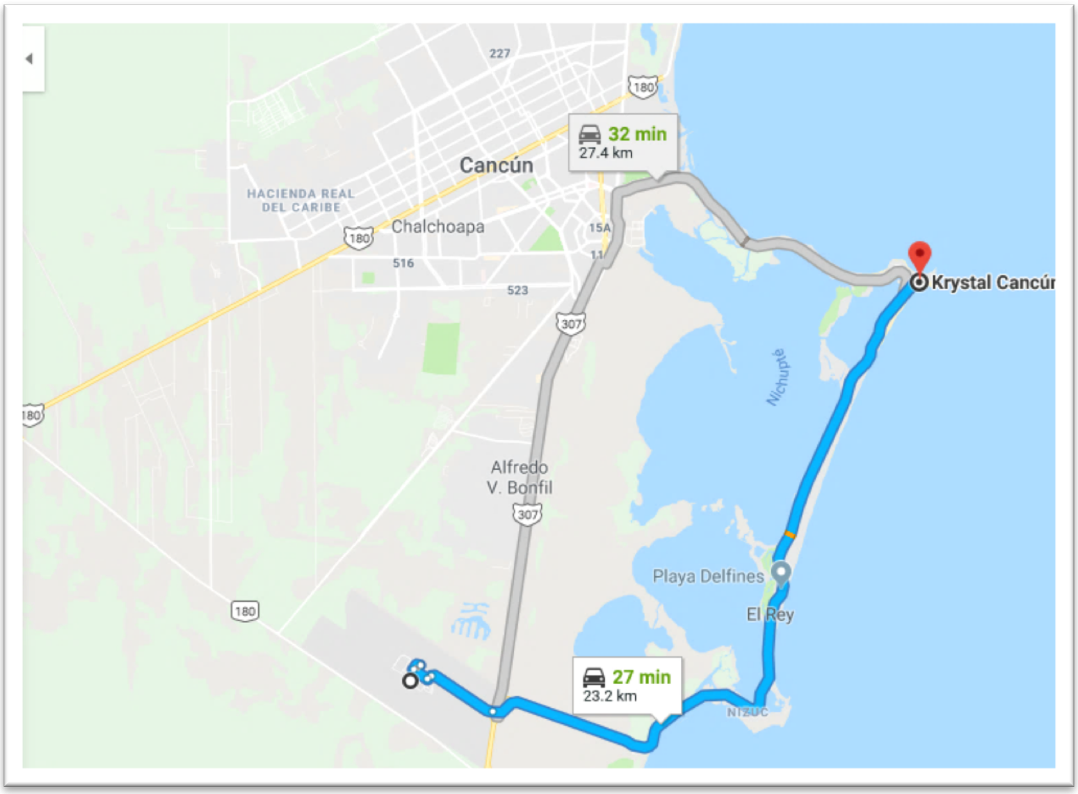

Its Surroundings

* Krystal Cancun, with a privileged location in the heart of the Hotel Zone of Cancun.

* Close to the area of the most famous nightclubs and discos.

* Very close to the Convention Center.

* 15 minutes from downtown.

* 5 minutes from La Isla Shopping Village.

* 11 km from Plaza Las Americas.

* 5 minutes from Plaza Kukulcán.

* 1 block from Plaza Forum.

* 13 km from the Nizuc Park.

* 20 minutes from the Cancun International Airport.

Rooms Map
Krystal Hotel & Resort Cancún

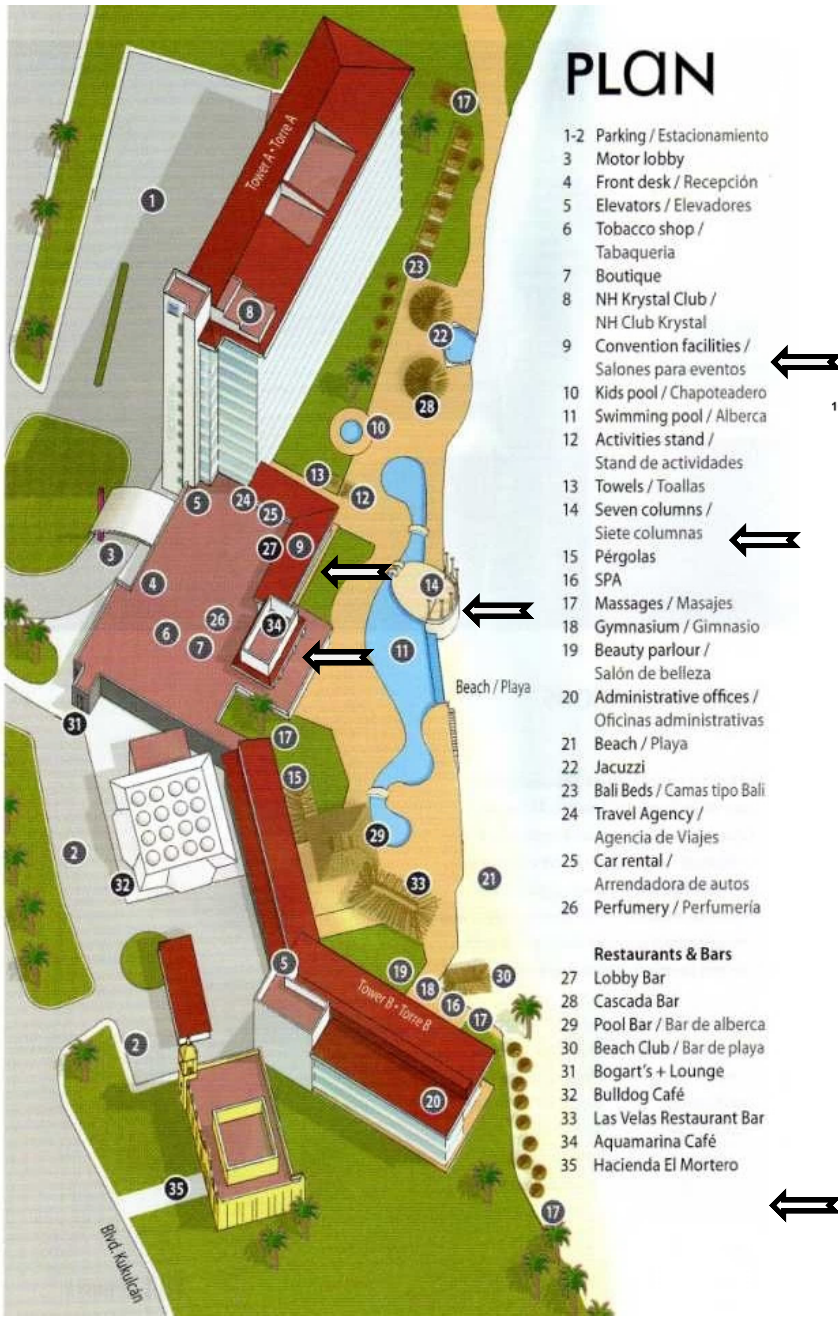

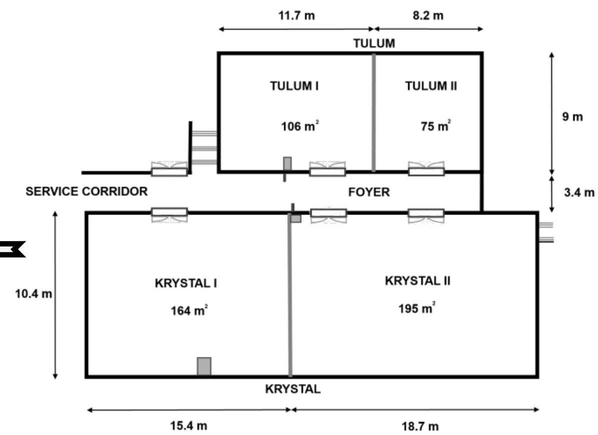

Topics

International Symposium on Optomechatronic Technology: ISOT, the world premium annual meeting for connectivity between optics, electronics and mechanical technologies since 2000.

The program of the Symposium will include, but will not be limited to, the following areas:

Optical metrology
Optical imaging/interferometry
Optical fiber sensors
Polarization sensing and imaging
Laser-based sensors
Optical sensors on robotics autonomous vehicles and other applications
Optofluidics
Optomechatronics for sensing and imaging
Micro optoelectro mechanical systems
Optical inspection for industry
Adaptive optics
Visual motion tracking and control
Biomedical applications
Vision-based monitoring and control
Optical manipulation and tweezers and their applications
Material laser processing
Actuators based on optics and optomechatronics
3D processing, 3D fabrication and 3D printer
Thin film technology
Solar cell
Special Session 1: Polarization technology
Special Session 2: Sensors based on the use of lasers and fiber optics

Symposium Committees

Conference General Chair

Amalia Martínez-García, Centro de Investigaciones en Óptica, México

General Co-Chair

Indrani Bhattacharya, University of Calcutta, India

Honorary Chairs

- Hyung Suck Cho, Professor Emeritus, KAIST, Korea
- Toru Yoshizawa, Director, Non-Profit Organization "3D Associates", Japan
  Professor Emeritus, Tokyo University of Agriculture & Technology
  Former professor, Saitama Medical University and Yamanashi University
- George K. Knopf, Professor, Department of Mechanical & Materials Engineering, Faculty of Engineering, The University of Western Ontario, Canada

Steering Committee Members

Yukitoshi Otani (JP)
Wei-Chih Wang (TW)
Lionel Watkins (NZ)
Toru Yoshizawa (JP)
Foued Ben-Amara (CA)
Hyungsuck Cho (KR)
Sergej Fatikow (DE)
Youngjune Cho (KR)
Yoshio Hayasaki (JP)
Farrokh Janabi-Sharifi (CA)
Shun'ichi Kaneko (JP)
Claudio Perez (CL)
Okyay Kaynak (TR)
Philippe Lutz (FR)
George K. Knopf (CA)
Yves Bellouard (NL)
Jonathan Kofman (CA)
Yeung Yam (HK)
Kee S. Moon (US)
Yu-Lung Lo (TW)
Rainer Tutsch (DE)
Indrani Bhattacharya (IN)
Ulrike Wallrabe (DE)
Chen, Shih-Chi (HK/CN)
Amalia Martínez-García (MX)

Program Committee Members

Yukitoshi Otani, Chair, (JP)
Wei-Chih Wang, Co-Chair (TW)
Cheng-Mu Tsai (TW)
Chia-Yuan Chen (TW)
Chien-Hung Liu (TW)
Claudio Pérez (CL)
Psang-Dain Lin (TW)
Rainer Tutsch (DE)
Ryoichi Kuwano (JP)
Satoshi Hasegawa (JP)
Sergej Fatikow (DE)
Sheng-Lung Huang (TW)

Farrokh Janabi-Sharifi (CA)
Foued Ben-Amara (CA)
George K. Knopf (CA)
Han-Sheng Chuang (TW)
Hyungsuck Cho (KR)
Jonathan Kofman (CA)
Kee S. Moon (US)
Liang-Chia Chen (TW)
Lionel Watkins (NZ)
Masaki Michihata (JP)
Marenori Kawamura (JP)
Ming Chang (TW)
Okyay Kaynak (TR)
Philippe Lutz (FR)
Shien-Kuei Liaw (TW)
Shun´ichi Kaneko (JP)
Terry Yuan-Fang Chen (TW)
Toru Yoshizawa (JP)
Wei-Chung Wang (TW)
Yasuhiro Mizutani (JP)
Yeung Yam (HK)
Yi-Chin Fang (TW)
Yoshio Hayasaki (JP)
Youngjune Cho (KR)
Yu-Lung Lo (TW)
Yun-Jiang Rao (CN)
Yves Bellouard (NL)

Local General Chair

Gonzalo Páez Padilla, Acting Director at Centro de Investigaciones en Óptica, Chair.

Baldemar Ibarra Escamilla, President of Mexican Academy of Optics, Co-Chair.

Local Organizing Committee

Francisco Cuevas de la Rosa
Gabriel Ramos Ortiz
Gerardo Ramón Flores Colunga
Juan Antonio Rayas Álvarez
Jorge Mauricio Flores Moreno
Manuel Ignacio Peña Cruz
María del Socorro Hernández Montes
Rodolfo Martínez Manuel
Cruz Meneses Fabián
David Ignacio Serrano García
Diana Tentori
Eduardo Tepichín Rodríguez
Geliztle Alejandra Parra Escamilla
Héctor Cerecedo Nuñez
Jorge Ramón Parra Michel
María Auxiliadora Araiza
Miguel León Rodríguez
Noel Iván Toto Arellano
Patricia Padilla Sosa
Rosario Porras Aguilar (US)
Rufino Díaz Uribe
Víctor Hugo Flores Muñoz

Technical Committee

Annette Torres-Toledo, Technical Secretary
Francisco-Javier Omedes-Alrich
Lucero Alvarado-Ramírez
José-Ignacio Diego-Manrique
Guadalupe López-Hernández

19th ISOT 2018 Program at a glance

Hotel Krystal

November 5-7, 2018. Cancún, México

<u>Sunday 4</u>: Registration 15:00-19:00, Executive Office
Welcoming reception: 19:00-20:30, Seven Columns

Time	Monday 5	Tuesday 6	Wednesday 7
8:00-17:30	Registration (closed from 13:00-14:30)	Registration (closed from 13:00-14:30)	Registration (closed from 13:00-14:30)
8:30-9:00	Opening Ceremony		
9:00-10:00	**Plenary Talk 1:** Emergence and Development of New Generation of Compact Photonic Sensors B. M. Azizur Rahman City, University of London, United Kingdom	**Plenary Talk 4:** Review of techniques to measure the cornea of the human eye Daniel Malacara Hernández Centro de Investigaciones en Óptica, México	**Plenary Talk 7:** Problem-specific optical methods with application in biomechanics Katia Genovese Università degli Studi della Basilicata, Italy
10:00-11:00	**Plenary Talk 2:** Polarization remote sensing of the atmosphere Joseph A. Shaw Optical Technology Center, Montana State University, USA	**Plenary Talk 5:** Optical fiber interferometers for precision sensing Joel Villatoro University of the Basque Country UPV/EHU and IKERBASQUE – Basque Foundation for Science. Bilbao, Spain	**Plenary Talk 8:** Quantitative birefringence microscopy using a rotating polarizer Kallol Bhattacharya Department of Applied Optics and Photonics, University of Calcutta, India
11:00-11:30	**Exhibit Hall Opening and Coffee Break**		
11:30-13:10	Research Parallel Session Invited Talks & Oral Contributions	Research Parallel Session Invited Talks & Oral Contributions	Research Parallel Session Invited Talks & Oral Contributions
13:10-14:30	Lunch Restaurant Aquamarina	Lunch (on your own)	Lunch (on your own)
14:30-15:30	**Plenary Talk 3:** Collimation testing procedures using interferometry and moiré phenomenon Rajpal Singh Sirohi Physics Department, Alabama A&M University, USA	**Plenary Talk 6:** Advances in Biomedical Image Processing of OCT images Vasudevan Lakshminarayanan University of Waterloo, Canada	**Plenary Talk 9:** Interferometric micro- & and nanoscale patterning and its industrial applications Murukeshan Vadakke Matham Nanyang Technological University, Singapore
15:30-16:30	Posters Session Exhibit Hall Opening	Posters Session Exhibit Hall Opening	**Plenary Talk 10:** Some recent advances in digital image correlation Bing Pan Institute of Solid Mechanics, Beihang University, Beijing, China
16:30-17:50	Research Parallel Session Invited Talks & Oral Contributions	Research Parallel Session Invited Talks & Oral Contributions	**Closing Ceremony**
17:50-	Photo		
20:00-		Conference Banquet Room Krystal I	

PLENARY SPEAKERS

Speaker Biography

Prof. B. M. Azizur Rahman received the B. Sc. Eng and M. Sc. Eng. degrees in Electrical Engineering with distinctions from Bangladesh University of Engineering and Technology (BUET), Dhaka, Bangladesh, in 1976 and 1979, respectively. He also received two gold medals for being the best undergraduate and graduate students of the university in 1976 and 1979, respectively. In 1979, he was awarded with a Commonwealth Scholarship to study for a PhD degree in the UK and subsequently in 1982 received his PhD degree in Electronics from University College London.

In 1988, he joined City University, London, as a lecturer, where became a full Professor in 2000. At City University, he leads the research group on Photonics Modelling, specialised in the development and use of rigorous and full-vectorial numerical approaches to design, analyse and optimise a wide range of photonic devices. He has published more than 550 journal and conference papers, and his journal papers have been cited more than 4600 times with an h-index of 33. He has supervised 29 students to complete their PhD degrees as their first supervisor and received more than £11 M in research grants. Prof. Rahman is Fellow of the IEEE, Optical Society of America and the SPIE.

Emergence and Development of New Generation of Compact Photonic Sensors

Souvik Ghosh and B M A Rahman
City, University of London, Northampton Square, London EC1V 0HB, UK
Email: b.m.a.rahman@city.ac.uk

ABSTRACT

Although fibre based optical sensors are now sufficiently mature and well established in the market, however, designs based on more exotic tapered nanowires and photonic crystal fibres are becoming increasingly important and showing much improved sensitivity by accessing a larger evanescent field. Similarly, novel planar Integrated Optic design concepts, such as the silicon slot guide-based design is showing even greater promise, allowing the exploitation of well-developed CMOS fabrication technologies for potentially low-cost sensor elements. Micro-resonators supporting whispering gallery modes, plasmonic slots, and ring resonators are also emerging as novel photonic sensors by exploiting strong light-matter interactions. The designs and optimizations of a suite of novel optical sensors will be presented, showing the need and value of using rigorous full-vectorial numerical approaches.

Speaker Biography

Prof. Joseph Shaw

He is the Director of the Optical Technology Center, Professor of Optics and Photonics, and Professor of Electrical Engineering at Montana State University in Bozeman, Montana, USA. Dr. Shaw develops optical remote sensing instruments for applications ranging from laser detection of fish from airplanes to measuring clouds for climate science. He also is a passionate photographer and loves to use his pictures to teach about optics in nature. He is the author of the 2017 book, Optics in the Air, which shows and explains numerous photographs of beautiful optical phenomena that can be seen in nature. Recognition for Dr. Shaw's contributions to optics research and education include the Presidential Early Career Award for Scientists and Engineers, the Vaisala Award from the World Meteorological Organization, and the Award for Excellence in Talent Development from the University Economic Development Association. He has just been announced as the recipient of the 2019 G. G. Stokes Award from SPIE for outstanding contributions to optical polarization. Dr. Shaw is a Fellow of both the Optical Society of America (OSA) and the International Society for Optics and Photonics (SPIE).

Polarization remote sensing of the atmosphere

Joseph A. Shaw, Laura M. Eshelman, Martin Jan Tauc, Wataru Nakagawa
Optical Technology Center, Montana State University, Bozeman, Montana, USA
E-mail: joseph.shaw@montana.edu

ABSTRACT

The blue light we see in the sky is a result of molecular scattering ("Rayleigh scattering"), which also leads to strongly polarized light in a region located approximately 90 degrees from the Sun. At Montana State University we designed and built several all-sky polarization imagers to study the spatial, temporal, and spectral distribution of skylight polarization. We also are designing nano-engineered optical devices that can be used to build an imaging system with pixels that simultaneously filter the incident light by wavelength and polarization state. These devices will operate at wavelengths in the range of 1500-1800 nm for remote sensing of cloud thermodynamic phase (i.e., to determine if the clouds contain ice or liquid water). This talk will describe and show all-sky polarization images under different conditions that include clear and cloudy skies in day and night - as well as a clear sky during the total solar eclipse of 21 August 2017 - and will briefly describe the nano-engineered optical elements and their intended use for cloud phase remote sensing.

Speaker Biography

Prof. R.S. Sirohi had been deeply engaged in academic administration and research since 2000 as Director IIT Delhi (Dec. 2000- April 2005), Vice-Chancellor Barkatullah University, Bhopal (April 2005-Sept. 2007), Vice-Chancellor of Shobhit University, Meerut (Oct. 2007-March 2008) and Vice-Chancellor of Amity University Rajasthan, Jaipur (March 2008-Oct.2009). Prof. Sirohi did his Masters in Physics in 1964 from Agra University and Post M.Sc. in Applied Optics and Ph. D. in Physics, both from Indian Institute of Technology, New Delhi in 1965 and 1970 respectively. Prof. Sirohi was Assistant Professor in Mechanical Engineering Department at Indian Institute of Technology Madras during 1971-1979. He became Professor in the Physics Department of the same Institute in 1979.

Prof. Sirohi worked as Humboldt Fellow at Physikalische - Technische Bundesanstalt Braunschweig, Germany (1974-75). He was a Senior Research Associate at Case Western Reserve University Cleveland, USA (1979-80). Prof. Sirohi was an Associate Professor at Rose Hulman Institute of Technology, Terre Haute, USA (1985-86). He was ICTP (International Center for Theoretical Physics, Trieste Italy) Consultant to Institute for Advanced Studies, University of Malaya, Malaysia and ICTP Visiting Scientist to the University of Namibia. He was Visiting Professor at the National University of Singapore (1996-97) and Humboldt awardee at the University of Oldenburg, Germany (1997-98). During September 2011 and May 2013, he was Distinguished Scholar in the Department of Physics and Optical Engineering, Rose-Hulman Institute of Technology, Terre Haute, IN (USA). During August 2013 and October 2016, he was Chair Professor at Tezpur University, Assam (India). **Currently he is serving as faculty member in the department of Physics at Alabama A&M University, Huntsville (USA).**

Prof. Sirohi is Fellow of several important academies/ societies in India and abroad including Indian National Academy of Engineering; National Academy of Sciences, Optical Society of America; Optical Society of India; SPIE (The International Society for Optical Engineering) and honorary fellow of ISTE and Metrology Society of India. He is member of several other scientific societies, and founding member of India Laser Association. Prof. Sirohi was also the Chair for SPIE-INDIA Chapter, which he established with co-operation from SPIE in 1995 at IIT Madras. He was invited as JSPS Fellow and JITA Fellow to Japan. He was a member of the Education Committee of SPIE.
Some selected awards (out of 21) received by Prof. Sirohi are:

- Humboldt Research Award (1995) by Alexander von Humboldt Foundation, Germany
- Galileo Galilei Award of International Commission for Optics (1995)
- Padma Shri, a national Civilian Award (2004)
- Holo-Knight, inducted into Order of Holo-Knights during the International Conference-Fringe 05-held at Stuttgart, Germany (2005)
- Life-Time Achievement Award by Optical Society of India (2007)
- Gabor Award 2009 by SPIE (The International Society for Optical Engineering) USA (2009)
- Distinguished Alumni Award by Indian Institute of Technology Delhi (2013)
- Vikram Award 2014 by SPIE (International Society for Optical Engineering) USA (received 2015)

Prof. Sirohi is a member on several Boards and Committees in India. He was the President of the Optical Society of India during 1994-1996. He has been President of Instrument Society of India for three terms. He was on the International Advisory Board of the Journal of Modern Optics, UK and on the editorial Boards of the Journal of Optics (India), Optik, Indian Journal of Pure and Applied Physics. He was Guest Editor to the Journals "Optics and Lasers in Engineering" and "Optical Engineering". Currently he is Senior Editor of the International Journal “Optical Engineering”, USA and Series editor of series on Optics, Photonics and Optoelectronics published by Institute of Physics, UK.

Prof. Sirohi has published 245 papers in national and international journals, 72 papers in Proceedings of the conferences/symposia and has authored/co-authored/edited thirteen books including five milestones for SPIE. He has participated in numerous international and national conferences and presented 166 papers. He has delivered 56 invited talks in various national and international conferences/symposia. He was Principal Co-ordinator for 26 projects sponsored by Government Funding Agencies and Industries. He has supervised 25 Ph.D. theses, 7 M.S. theses and numerous B.Tech., M.Sc. and M.Tech. theses.

Prof. Sirohi's research areas are Optical Metrology, Optical Instrumentation, Laser Instrumentation, Holography and Speckle Phenomenon.

Collimation testing procedures using interferometry and moiré phenomenon

Rajpal Singh Sirohi
Physics Department, Alabama A&M University, Huntsville AL-35763, USA
E-mail: rs_sirohi@yahoo.co.in

ABSTRACT

Laser beam is highly directional and diffraction limited. For many applications the beam is expanded using an inverted telescopic system. Degree of collimation of such a beam is to be checked. Collimation of beam is essential in long path interferometry otherwise significant error may be introduced in the measurement. A number of methods have been devised over the years and this paper presents some of these methods.

These methods can be grouped under two major heads; those based on interferometry and those based on moiré phenomenon. Plane parallel plate is the most commonly used element for collimation testing. Due to its inherent shortcomings, a wedge plate replaces it. The wedge plate also has some shortcomings and hence a wedge-plate pair, which provide self-referencing and double the sensitivity, has been proposed. There are several modifications of this in which dual field is provided. Multiple-beam interferometry with a coated wedge plate has also been used for collimation tesing. Also some methods are demonstrated which use phase conjugation as well for collimation testing.

Linear grating when illuminated with a collimated beam, self-images: the transverse periodicity gets manifested into the longitudinal periodicity. However when the beam is either convergent or divergent, self-imaging still takes places but self-image planes are not equidistant and self-images are as if grating is projected. Location of self-image planes and pitch of the grating in the self-image planes is obtained using moiré phenomenon. A linear grating along with self-imaging has been used for collimation testing. However, it requires a reference line like in wedge plate shear interferometry. Using a double-grating (two gratings enclosing an acute angle or obtuse angle) provides self referencing and double the sensitivity for collimation testing. We then proceed to study self-imaging with a triangle grating, a square grating and so on until it generates into a circular grating in the limit and examine their applications for collimation testing.

- Rajpal S. Sirohi and Mahendra P. Kothiyal, Double wedge plate shearing interferometer for collimation test, Appl. Opt., 26, 4054-56 (1987)
- Mahendra P. Kothiyal and Rajpal S. Sirohi, Improved collimation testing using Talbot interferometry, Appl. Opt., 26, 4056-57 (1987)
- K. V. Sriram, M. P. Kothiyal and R. S. Sirohi, Self referencing collimation testing techniques, Opt. Eng., 32, 94-100 (1993).
- K. V. Sriram, P. Senthilkumaran, M. P. Kothiyal and R. S. Sirohi, Double wedge plate interferometer for collimation testing - new configurations, Appl. Opt., 32, 4199-4203 (1993).
- K. V. Sriram, M. P. Kothiyal and R. S. Sirohi, Collimation testing with linear dual-field, spiral and evolute gratings: A comparative study, Appl. Opt., 33, 7258-7260 (1994).
- P. Senthilkumaran, K. V. Sriram, M. P. Kothiyal and R. S. Sirohi, Multiple beam wedge plate shear interferometer for collimation testing, Appl. Opt., 34, 1197-1202 (1995)

Speaker Biography

Prof. Daniel Malacara obtained his B. Sc. in Physics in 1961 from the National University of Mexico, his M. Sc. in Optics in 1963 from the University of Rochester, and his Ph. D. in Optics in 1965 from the University of Rochester. In 1965, he joined the Institute of Astronomy of the National University of México. In 1972 he collaborated with Dr. Guillermo Haro in the creation of the Instituto Nacional de Astrofísica, Óptica y Electrónica in Tonantzintla, Pue., México.
In 1979 he returned to the National University of México, to work as the leader in a project for the establishment of the Centro de Investigaciones en Óptica at León, Gto. He was its first General Director.

He has been author and/or editor of several books in optics, were the most well-known is the book Optical Shop Testing, for which he was the editor, and the author of several chapters. This book has been translated into Russian and Chinese and Japanese.

His scientific production includes more than one hundred and fifty refereed papers. His publications and books had been cited in the scientific literature more than six thousand times.
He is a Fellow member, both of the Optical Society of America and The International Society for Optical Engineering (SPIE).

In 1989 he was granted the Rudolf and Hilda Kingslake Chair in Optical Engineering, at the Institute of Optics of the University of Rochester.

He received in 1994 the A. E. Conrady Award for Scientific Achievement by SPIE.- International Society for Optical Engineers and in 1996 the Galileo Galilei Award, by the International Commission for Optics, and the Joseph Fraunhofer Award.-Robert M. Burley, from the Optical Society of America in 2002. In 2012 he received the Gold Medal Award by SPIE.- International Society for Optical Engineers.

Review of techniques to measure the cornea of the human eye

Daniel Malacara Hernández
Centro de Investigaciones en Óptica, México
E-mail: dmalacara@cio.mx

ABSTRACT

In this presentation a review of the main techniques used to measure the radius of the curvature of the eye as well as its topography will be described. The advantages and disadvantages of each method will be considered.

Speaker Biography

Prof. Joel Villatoro received the M.Sc. and Ph.D. degrees in optics from the National Institute for Astrophysics, Optics, and Electronics, Puebla, Mexico, in 1995 and 1999, respectively. He is currently Ikerbasque Research Professor at the University of the Basque Country (UPV/EHU). Prior to his current position, Joel was a research fellow in industrial photonics at Aston Institute of Photonic Technologies, Birmingham, U.K., and Ramon y Cajal researcher at the prestigious Institute of Photonic Sciences (ICFO), Barcelona, Spain. He has also held research posts at the Centro de Investigaciones en Optica A. C., Leon, Mexico, the University of Valencia, Spain, and the Case Western Reserve University, Cleveland, Ohio, USA. Joel is the author of more than 115 scientific publications and 6 patents. He is internationally recognized for his seminal contributions to the fundamentals and technology of interferometric optical fiber sensors. To date, he has more than 3000 citations and h-factor of 31. He has given around 26 invited talks at international events. Joel's research interests include interferometric sensors based on standard, multicore and photonic-crystal fibers, applications of sensors in real-world environments, and development of micro- and nano-sensors for biomedical applications.

Optical fiber interferometers for precision sensing

Joel Villatoro
Ikerbasque Research Professor
University of the Basque Country UPV/EHU and IKERBASQUE –Basque Foundation for Science. Bilbao, Spain.
E-mail: agustinjoel.villatoro@ehu.es

ABSTRACT

Interferometry in one of the most sensitive optical detection methods; it is widely used in high-resolution metrology. With optical fibers and associated fiber-optic devices, robust and versatile interferometers can be implemented. Such all-fiber interferometers have made possible the measurements of many variables in challenging conditions. In this talk, the research, advances, and novel applications of interferometric optical fiber sensors will be discussed. Instead of implementing all-optical-fiber versions of conventional interferometers, we have focused our research on new concepts and approaches to develop highly compact interferometers with specialty optical fibers. In most cases, we exploit the phase difference between two modes in photonic-crystal fibers, or between two supermodes in strongly coupled multi-core optical fibers. Microscopic interferometers built with polymer micro-cavities deposited onto the facet of a conventional telecommunications optical fiber will also be discussed. An important advantage of our interferometers is the fact that they operate at well-established telecommunications wavelengths and their interrogation can be carried out with battery-operated LEDs and inexpensive handheld spectrometers. Our efforts to develop devices that outperform state-of-the-art optical sensors in both sensitivity and functionality will be discussed. Some examples of interferometric sensors that the capability of sensing multiple parameters and that operate in real-world environments will be given.

Speaker Biography

Vasudevan Lakshminarayanan (Vengu) is a professor of vision science, physics, electrical and computer engineering and systems design engineering at the University of Waterloo. He was a "KITP Scholar" at the Kavli Institute for Theoretical Physics at UC Santa Barbara, an associate of the Michigan Center for Theoretical Physics and has held research and teaching positions at UC Irvine, UC Berkeley, University of Michigan and the University of Missouri amongst others. He is also an adjunct professor of Electrical and Computer Engineering at Ryerson University, Toronto. He has been a visiting professor at various universities worldwide. He also served on both of UNESCO's International Year of Light and International Day of Light planning committees and is , a founding member of the UNESCO ALOP Program . He is on the optics advisory board of the International Center for Theoretical Physics at Trieste, iIaly since 2003, a consultant to the medical devices group of the US FDA (since 2011), has represented the United States at two IUPAP general assemblies, was chair of the US advisory committee for the International Commission on Optics, chair of the committee on international scientific affairs of the APS, a AAAS Science and technology policy fellow, a director of the OSA, etc. He is a fellow of a number of professional societies including the American Physical Society, AAAS, Optical Society of America, SPIE-the International Society for Optical Engineering, Institute of Physics, etc. He has published widely in a number of areas ranging from quantum physics and spectroscopy, to bioengineering, mathematical optics, optical physics and engineering, image processing, optometry, ophthalmology, applied mathematics and cognitive neuroscience. He is the recipient of a number of Awards including the SPIE Optics educator award (2011) and the Esther Beller Hoffman medal of OSA (2013). He has been/or is technical editor/associate editor for a number of journals, including Optics Letters and Journal of Modern Optics and serves on a number of NIH study sections (including those on bioengineering, neurotechologies, etc.) as well as other international funding agencies.

Advances in Biomedical Image Processing of OCT images

Vasudevan Lakshminarayanan
University of Waterloo, Ontario, Canada
E-mail: vengumo@gmail.com

ABSTRACT

In this talk I will review the application of new computational methods for processing of Optical Coherence Tomography images for automated diagnosis of retinal diseases such as glaucoma, retinal detachment and macular holes, three major blinding diseases. There segmentation methods include graph theoretical methods, texture based methods, active contour with dynamic programming techniques, denoising methods as well as applications of deep learning techniques.

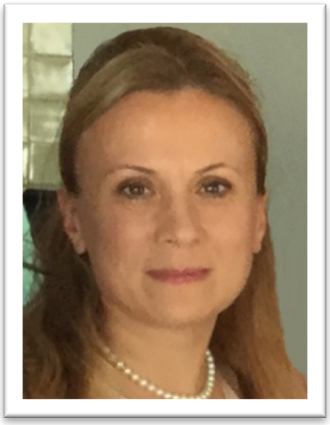

Speaker Biography

Prof. Katia Genovese received M.Sc. in Mechanical Engineering at Polytechnic of Bari, Italy, and Ph.D. in Experimental Mechanics at University 'Federico II' in Naples (2002). Worked as research scientist at Laser Research Centre - Italy and as visiting scholar at Nottingham University - UK, Union College - USA, Centro de Investigacíones en Óptica - Mexico, Ecole Nationale Supérieure des Mines - France, Texas A&M University - USA, Yale University - USA, University of Arizona - USA, Benemerita Universitad Autonoma de Puebla - Mexico, Universidade Federal de Santa Catarina - Brazil. From 2002 to 2015, she joined the Mechanical Engineering Dept. at the University of Basilicata (Potenza, Italy), as Assistant Professor in Machine Design. Authored 40 journal papers, and over 60 papers on International Conference Proceedings. Research areas concern optical methods for shape and deformation measurement (Moiré, Electronic Speckle Pattern Interferometry, Fringe Projection, Digital Image Correlation) and hybrid experimental/numerical methods for material characterization. She is currently Associate Professor in Machine Design and Head of the Experimental Mechanics Laboratory of the School of Engineering at University of Basilicata, Italy.

Problem-specific optical methods with application in biomechanics

Katia Genovese
School of Engineering, University of Basilicata, Italy
E-mail: katia.genovese@unibas.it

ABSTRACT

The non-contact full-field capabilities of optical methods make their use particularly suitable for shape and deformation measurements for biomedical applications. Currently, in fact, optical methods are successfully used to map the regional varying material properties of biological structures thus allowing to gain an important insight into the mechanics of healthy and diseased tissues and organs. Nevertheless, the full potential of optical methods is still limited by the inherent complexity in terms of shape and material composition/distribution of most biological structures. To perform an accurate inverse mechanical characterization, in fact, it is of foremost importance to test the biological structure in its native shape under reproduced physiological load/boundary conditions. This requirement introduces a series of challenges that fail to be treated with traditional approaches and push towards the development of specially-designed measurement methods.

A first problem occurs whenever the measurement involves largely deformed images such as those obtained from two angled-views of complex-shaped parts (e.g. in lower limbs studies) or from an inadequate temporal sampling of fast- or slow-evolving phenomena (e.g. in growth and remodeling studies) over a large range of deformation. A further frequent issue is represented by the need to get time-resolved information over the full 360° surface of complex-shaped parts and/or to process sets of images obtained from different video-systems at different time and under different experimental conditions.

This talk aims to give an overview on problem-specific experimental protocols based on Fringe Projection (FP) and Digital Image Correlation (DIC) that have been recently developed to collect dense sets of 3D shape and deformation data on complex biological parts. Illustrative examples of application to the in-vitro testing of natural and synthetic structures of biomedical interest are given presenting experimental data collected with standard stereo-DIC, hybrid DIC-FP methods, multi-camera and panoramic DIC systems.

Speaker Biography

Prof. Kallol Bhattacharya

Affiliation:
Professor Department of Applied Optics and Photonics, University of Calcutta
Educational Qualifications:
B. Sc. (Physics Hons.) from Calcutta University 1985
M. Sc. (Tech.), Dept. of Applied Physics, Univ. of Calcutta, 1988
Ph. D. (Tech.), Dept. of Applied Physics, Univ. of Calcutta 1996
Past Affiliations:
1992-1994: Lecturer, Instrumentation Engineering Department, Jadavpur University
1994-2001: Scientist D, Saha Institute of Nuclear Physics, Kolkata
2001-2009: Associate Professor, Calcutta University
2009-present: Professor, Calcutta University
Fellowships/ Awards:
1996: Japanese Government (Monbusho) Fellowship
2006: Research Award from Mitutoyo Association of Science and Technology (MAST), Japan
Research Interests:
Optical Metrology, Polarization Interferometry, Birefringence measurements, Nonlinear Optics, Optical Coherence Tomography
Publications: ~60 in archival journal

Quantitative birefringence microscopy using a rotating polarizer

Kallol Bhattacharya
Department of Applied Optics and Photonics, University of Calcutta
E-mail: kbaop@caluniv.ac.in

ABSTRACT

It has been widely recognized that the phenomenon birefringence can act as an effective marker for various diseases including a variety of cancer types where loss of birefringence in normal tissues as in cervical cancer or the formation of birefringence structures surrounding accompanying inflammatory reaction as thyroid cancer has been established and well documented However, microscopes for complete and quantitative estimation of birefringence are not easily available as most of the proposed prototypes are complex in terms of their optical configuration and data acquisition. A simple hardware configuration whereby a standard light microscope may be converted to a birefringence microscope capable of quantitative analysis of birefringence is therefore the key to the use of birefringence for diagnostic purposes. The present work specifically addresses this problem. In a typical bio sample under test, both the magnitude of retardation and its direction are in general space varying parameters. It will be shown that if the bio specimen is illuminated by linearly polarized light it is possible to evaluate both of these parameters over the sample zone by combining a series of images captured as the polarizer rotates in steps from 0 to 180 degrees. The technique is refined further by using interpolation techniques whereby it is possible to decode the entire birefringence information accurately by using only five image frames at five different orientations of the output polarizer. Results in terms of the normalized Stokes parameter and degree of polarization images for several samples including nerve tissues, malignant breast tissues and botanical specimens will be presented.

Speaker Biography

Prof. Murukeshan Vadakke Matham carried out his Ph. D at the Indian Institute of Technology, Madras in and at the University of Oldenburg, Germany under the DAAD Fellowship and was awarded Ph. D in 1997 from IIT Madras (INDIA). Since 1997 he is with Nanyang Technological University (NTU), Singapore as a faculty. He has 25+ years of research experience, and 20 plus years of teaching experience. He is a Life member of Optical Society of India (OSI), and regular member of Optical Society of America (OSA) and Senior Member of SPIE. He is also a Fellow of the Institute of Physics, UK. He has given more than 25 invited, 12 plenary/Keynote talks and over 5 pedagogical lectures at major Conferences in the field of Biomedical Optics, Nanoscale Optics and Applied Optics for metrology. He has given many visiting lectures at optics chapters of SPIE through VLP programmes. Further, he is very actively engaging and coordinating optics outreach programs with local schools in Singapore and around through the Center for Optical and Laser Engineering (COLE). He has given many short term courses to engineers/practitioners in the industries and academia to update them about the latest in optical engineering through continuing education programs. He is currently serving as the Associate Editor of Optical Engineering and International journal of Optomechatronics (IJO). He is also in the member, editorial team of Scientific Reports (Nature publishing group journal). He is also a regular reviewer in leading Nature journals, optics journals that includes many SPIE and OSA journals. He has authored/co-authored over 170 international journal papers (which include five papers published in nature publication group journals, top impact biomedical and nanoscale optics journals), over 140 international conference proceedings papers/presentations and 6 book chapters (three on biomedical Optics and three on nanoscale optics and fabrication). He is also inventor/Co-inventor of 14 patents (Filed /Awarded) and 11 innovation disclosures He is serving as the Director of Centre for Optical & Laser Engineering (COLE), and as the deputy director of The Photonics Institute(TPI), NTU Singapore

Interferometric micro- & and nanoscale patterning and its industrial applications

Murukeshan Vadakke Matham
Centre for Optical & Laser Engineering, Nanyang Technological University, Singapore
Email: MMurukeshan@ntu.edu.sg

ABSTRACT

Optics technology that focuses on semiconductor, biomedical, and energy sectors in the recent past has seen the impact of nanoscale patterning, a challenging trend to achieve smaller features or devices with micro- or nano-scale features. This demanded automatically the need for achieving much smaller features beyond the forecasted sub- 30nm fabrication methodologies. Hence, there is significant push for smaller dimension recently that has posed many challenges. In this context, a new branch of conventional and nearfield optical concepts, such as evanescent wave and plasmonics, for improving patterning resolution has started developing. These approaches have been receiving considerable attention for its ability to produce high-density sub-wavelength features at the micro- and nano-scale levels. This plenary talk will be covering the above mentioned aspects focussing on the in house developed concepts and technologies in the related areas by the author's group. The talk will initially details the need for using visible or near UV wavelengths for patterning and explore how interferometric concepts can enable such approaches. It will then details the development and instrumentation details of a multi-beam laser interferometric lithography system for conventional and near field optics assisted patterning at the micro- and nanoscale. These patterned structures are then demonstrated for semiconductor applications detailing the challenges faced in meeting the forecasted technology nodes of sub-30nm features by 2020. A configuration of layered plasmonic and gap mode assisted structures for improved broadband absorption in thin film Si solar cells will then be discussed followed by novel nanoscale patterning approaches using random optics such as the recently proposed and innovative speckle lithography. This has proven to make reliable hydrophobic, hydrophilic surfaces, and black or white silicon structures for potential industrial applications. The talk will conclude by highlighting the current and future research challenges using periodic and aperiodic patterns obtained by interferometric approaches for high resolution imaging.,The conference travel and researches presented in this talk were supported through NTU, Singapore, COLE-EDB Funding and Ministry of Education (AcRF Tier 1), Singapore.

Speaker Biography

Dr. Bing Pan is a full professor in School of Aerospace Science & Engineering at Beihang University (BUAA), China. He received his Ph.D degree in Mechanical Engineering from Tsinghua University in 2008. After working with Professor Anand Asundi in Nanyang Technological University (Singapore) as a postdoctor, he joined Institute of Solid Mechanics, BUAA in 2009. His current research interests mainly focus on advanced optical techniques and their applications in experimental mechanics, especially the digital image/volume correlation techniques for surface/internal deformation measurement of solid materials and structures, as well as new experimental techniques for characterizing thermo-mechanical behavior of hypersonic materials and structures. He has published more than 100 peer-reviewed articles in international journals, including 8 review papers, 7 ESI highly cited papers and 4 cover stories. All the publications more than 6300 times according to Google Scholar. Dr. Pan was selected for Youth Changjiang Scholars (Minitstry of Education, China) in 2016, and won the National Natural Science Funds for Excellent Young Scholar of NSFC in 2013

Some recent advances in digital image correlation

Bing Pan
Institute of Solid Mechanics, Beihang University, Beijing, 100191, China
Email: panb@buaa.edu.cn

ABSTRACT

Digital image correlation techniques have been widely accepted as a versatile and powerful tool for full-field surface motion and deformation measurements of solid materials, components and structures. These outstanding advantages of DIC techniques (e.g., simple and inexpensive experimental setup, easy implementation, wide applicability with adjustable spatial and temporal resolutions, and strong robustness against ambient vibrations) not only have led to the dominance of DIC techniques in the experimental mechanics community over other competing interferometric optical techniques, but also engender their prevalence in new areas of application, such as material science, biomechanics, civil engineering, geotechnical engineering, and aerospace engineering.

In this talk, we report the following important advances recently made in digital image correlation (DIC), which have enabled more accurate, more convenient and better DIC measurements to be made. First, we developed a fast, robust and accurate DIC algorithm without redundant calculations, which combines a robust reliability-guided displacement tracking strategy with an efficient and accurate inverse-compositional Gauss-Newton algorithm. This advanced DIC algorithm outperforms existing one based on the classic Newton-Raphson algorithm in terms of efficiency, accuracy and noise-proof performance. Second, we comprehensively investigated the error sources involved in single-camera 2D-DIC and stereo-DIC systems due to imperfect and unstable imaging, and presented a novel reference sample compensation method for accurate DIC measurements. Based on the thorough understanding of these error sources, we established three kinds of single-camera video extensometer, which can deliver real-time, accurate strain measurement in material testing. In addition, we developed a novel mirror-assisted panoramic DIC system for full-surface 360-deg profile reconstruction and deformation measurement in material testing. Third, we reviewed existing single-camera stereo-DIC techniques, and proposed a novel and elegant color stereo-DIC technique using a single color 3CCD or CMOS camera. Typical applications of the newly-developed color stereo-DIC are also demonstrated.

Extended Abstracts

Session
3D PROCESSING, 3D FABRICATION AND 3D PRINTER

Pg.

Using Deep Learning to Estimate User Impressions of Designs for 3D Fabrication 24
Koichi Taguchi, Manabu Hashimoto, Kensuke Tobitani, Noriko Nagata

Development and implementation of a 3D platform for micro-structure printing by laser ablation process and LOPA photolithography 26
Camarena-Chávez Victor, Castro-Beltrán Rigoberto, Gutiérrez Juárez Gerardo, Álvarez-Valtierra Leonardo, Ramos-Ortiz Gabriel

Theoretical and experimental study Of colloidal transport in microfluidic geometries 28
María Eugenia Soto Alcaraz, Ramón Castañeda-Priego, R. Castro-Beltrán and Marco Laurati,

Selective Electron Beam Melting Model of Titanium Alloy 30
Trong-Nhan Le, Yu-Lung Lo and Hong-Chuong Tran

Rapid prototyping of microfluidic devices by SLA 3D printing and biocompatibility study for cell culturing 32
S. Marquez, V. Piazza and D. Hernández-Velázquez

Construction and characterization of a laser doppler velocimeter printed in 3D. 34
H. Méndez-Dzul, M. Pérez-Cortés, M. Ortíz-Gutiérrez, M. de Coss-Gómez, J. Lugo-Jiménez, C. Vinajera

Using Deep Learning to Estimate User Impressions of Designs for 3D Fabrication

Koichi TAGUCHI†, Manabu HASHIMOTO†, Kensuke TOBITANI††, Noriko NAGATA††

†: Chukyo University, 101-2 Yagoto Honmachi, Showa-ku, Nagoya-shi, AICHI (Japan) 466-8666

††: Kwansei Gakuin University, 2-1 Gakuen, Sanda-shi, HYOGO (Japan) 669-1337

†: {taguchi, mana}@isl.sist.chukyo-u.ac.jp, ††: {tobitani, nagata}@kwansei.ac.jp

Abstract: In this paper, we propose a method for reflecting human impressions directly into product designs, for use in fabrication of products using 3D printers. The method automatically estimates human impressions of the shape of an item by analyzing the 3D shape in terms of three representative sensibilities: “hard-soft”, “sober-flashy”, and “unstable-stable”. This technique can be used for new 3D fabrication processes that reflect the designer’s intentions directly into the shapes of products. To estimate impressions of the shape of an object, we need to draw strong correlations between impressions, which are psychological factors, and aspects of the shape of the object, which are physical factors. The proposed method uses Deep Learning effectively to address this issue. The object being evaluated is first converted to a set of images by photographing it from 20 surrounding directions. This image set is used as input data for Deep Learning, with parameters of human impressions of the object as a supervisory signal. In experiments, we used many 3D objects with assigned impressions that had been quantified using the semantic differential (SD) method. Experimental results show that the correlation coefficients between impressions estimated using the proposed method were 0.23 for “hard-soft”, 0.30 for “sober-flashy”, and 0.22 for “unstable-stable”, respectively. These values indicate that our deep learning-based method improved the performance by 0.02 for “sober-flashy” and “unstable-stable” compared with previous method.

1. Introduction

Fabrication equipment such as 3D printers has become increasingly common recently. With this change, fabrication processes are expected to transition in the future, from mass production (large volumes in a factory) to personal fabrication (by individuals). To realize this, each individual will need to have technology to create 3D data for 3D printers (“modeling technology”), but this is not a type of technology that everyone typically has. As such, we propose a method for estimating human impressions of an object, to be used to support such modeling technologies. Normally, we would consider that impressions of an object would be determined holistically based on shape, color and material, but for this research, we have assumed that shape is the dominant factor determining impressions of objects, based on a method from Tobitani et al. [1]. We also defined three types of impressions of objects as particularly important: “hard-soft”, “fancy-simple”, and “stable-volatile”.

2. Previous research

In previous research, Taguchi et al. [2] treated 3D models as point sets, proposed feature that focused on localized roundedness in the shape, and estimated human impressions of objects by analyzing with multiple linear regression. However, it was difficult to compute appropriate feature and discriminators for each impression with this method, and they were only able to apply it for the “hard-soft” impression. In contrast, this research uses a Deep Learning approach that can estimate typical impressions of the shapes of objects with one method that covers everything from selection of feature through to discrimination.

3. Impression estimation method

Our method uses a Deep Learning convolutional network with multi-viewpoint images to estimate impressions. We began by using the semantic differential (SD) method [3] to estimate values for impressions of each object, and we used these values as a supervisory signal. Input data for the network consisted of a set of images of the object taken from 20 directions spaced equally surrounding the object. Impression estimation was realized by using this image set as input for Deep Learning, and training to minimize the difference between the estimated result and the supervisory signal. Our method consisted of a first stage with five convolutional layers and three pooling layers, and a second stage with a view-pooling layer, which integrated the multi-viewpoint image, and three fully connected layers. The error function used was least-squares error, and the optimization method used was Adam [4].

4. Impression estimation experimental results

In our experiments, we used the SD method [3] to associate a supervisory signal to 3D objects. For 3D objects, we used bottle models. This models were made by us. Each 3D object was evaluated by 11 people, and the average response was used as the supervisory signal. In the experiments, the method by Taguchi et al.[2] and the proposed method were evaluated using correlation coefficients. The experimental data set was evaluated using cross validation. Figure 1 shows two distributions of relationships between the estimated results and the supervisory signal. Blue dots means results by previous method, and red dots means results by our new method. Also table 1 shows the estimation results and correlation coefficients with the supervisory signal.

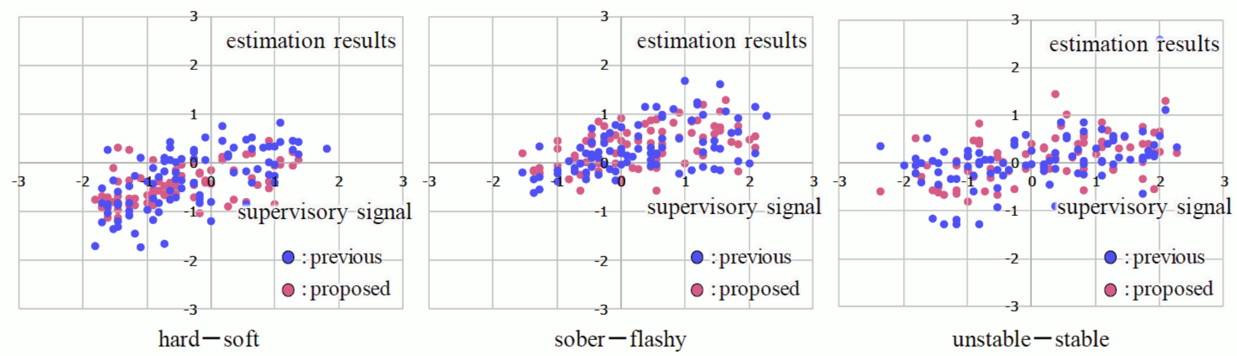

Figure 1 Relationships between the estimated results and supervisory signal.

Table 1 Correlation coefficients between estimation results and supervisory signal

Method	Correlation coefficients for impressions		
	hard-soft	sober-flashy	unstable-stable
Our previous method[2]	0.41	0.28	0.20
Proposed method	0.23	0.30	0.22

Correlation coefficients between impression values estimated by the proposed method and the supervisory signal were 0.23 for “hard-soft”, 0.30 for “sober-flashy”, and 0.22 for “unstable-stable”. As for “sober-flashy” and “unstable-stable”, these results are 0.02 higher than results compared with our previous method which uses special features designed by humans [2].

5. Acknowledgements

This research is partially supported by the Center of Innovation Program from Japan Science and Technology Agency, JST.

References

[1] K. Tobitani, S. Akizuki, K. Katahira, M. Hashimoto, and N. Nagata, “A Comparison Study on 3D Features in Terms of Effective Representation for Impression of Shape,” The 2nd International Conference on Digital Fabrication, No. 22, (2016).
[2] K. Taguchi, K. Sasaki, M. Hashimoto, K. Tobitani, N. Nagata, “A proposal of 3D local feature for estimating human’s impression factor to shape of object,” International Workshop on Advanced Image Technology (2017).
[3] Osgood, C. E., Suci, G. J., & Tannenbaum, P. H., The measurement of meaning (1957). Oxford, England, University of Illinois Press.
[4] Diederik P. Kingma, “Adam: A Method for Stochastic Optimization,” International Conference on Learning Representations (2015).

Development and implementation of a 3D platform for micro-structure printing by laser ablation process and LOPA photolithography

Camarena-Chávez Victor, Castro-Beltrán Rigoberto, Gutiérrez Juárez Gerardo, Álvarez-Valtierra Leonardo, Ramos-Ortiz Gabriel*
Universidad de Guanajuato, División de Ciencias e Ingenierías, Loma del Bosque 103, Lomas del Campestre CP. 37150, León, Guanajuato., México
Centro de Investigaciones en Óptica, Loma del Bosque 105, Lomas del Campestre, CP. 37150, León, Guanajuato, México*
camarenacv2013@licifug.ugto.mx

Abstract: There has been a recent interest in the creation and implementation of micro-devices for example in fields of Optics for photonic crystals [1,2], Materials Processing for developing hydrophobic surfaces [3]. For the development of this structures multiple techniques have been used, one of most common is Direct Laser Writing (DLW) that basically consists in the use of the properties of laser radiation to induce a permanent change in a material structure. For manipulating the sample through the laser beam a platform that enables movement of sample and beam manipulation becomes a first necessity for this technique. In this work the development and characterization of a 3D platform programmed using open source software (Python and Arduino) for creation of microchannel systems and surface processing is presented.

A 3D platform developed from scratch and programmed using open source code like Arduino for controling the steppers that move the sample and change where the laser spot is focused and a Graphical User Interface created using Python was first characterized for printing different patterns by DLW in distinct materials through laser ablation and Low One Photon Absorption (LOPA). Since the physical processes are completely different, disctint optimal parameters like scan speed, laser intensity, minimal effective spot size should be find to get the best results using the platform created.

The principal characteristics of the platform are minimal resolution in each axis of 20 micrometers, maximal speed of 322 $\mu m/s$, minimal speed of 94 $\mu m/s$, using a microscope objective LMH-5X-532 of Thorlabs the effective focused spot size was about 60 µm.

For the laser ablation process a Nd:YAG pulsed laser double in frequency, wavelenght centered at 532 nm, pulse duration of 5 nanoseconds, repetition frequency of 10 Hz was used. The laser ablation was performed in soda lime glass sustrates printing microchannels in the surface. A whole methodology was determined from sustrate cleaning to post-ablation treatment. It was found that the optimal scan speed is 94 $\mu m/s$ and laser average intensity of 8 mW.

The following images show some of the best results obtained by the laser ablation process.

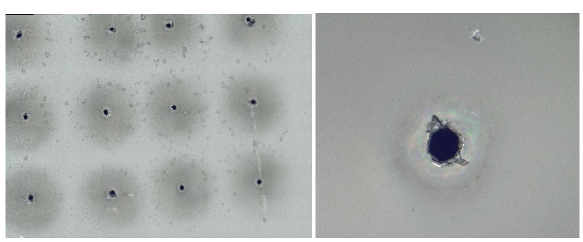

Fig. 1 Holes grid produced by laser ablation (left) and hole from grid in more detailed (right).

In Fig.1 each hole was created by letting the laser hit that spot for 40 seconds. The average separation between each hole is around 1100 µm. The average diameter of each hole is 60 µm.

The next image shows a microchannel with a 1 cm lenght, 300 µm wide and average depth of 155 µm.

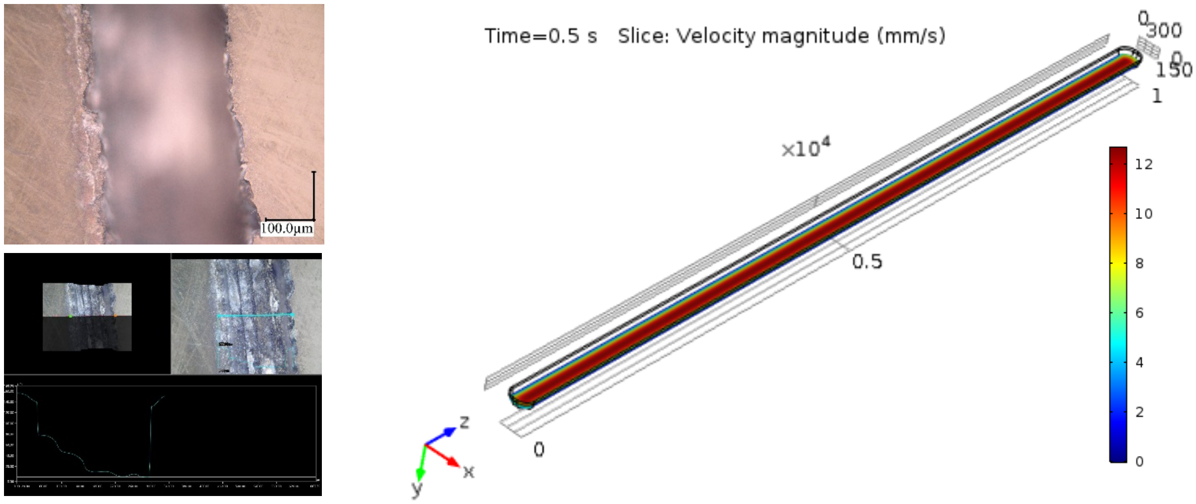

Fig 2. Section of the microchannel mentioned aboved (left), graph of depth obtained with Keyence VH-5000X microscope (left) and simulation of speed flow inside the channel made in Comsol.

It can be observed in Fig. 2 that the borders of the microchannel are homogeneous and smooth. A simulation in Comsol was created to see how flow will behave inside the channel. As expected at the center we find maximum speed and near the borders speed becomes almost zero.

For LOPA photolithography a Millenia Pro 5W continuum laser was used, with wavelenght centered at 532 nm. A SU-8 2050 film was deposited in soda lime glass sustrate by spin-coating. It was find that optimal scan speed is 320 $\mu m/s$ and laser intensity of 50 mW.

One of the most important results in this case was the fabrication of a diffraction grating with average sepration of 100 µm, show in the image below.

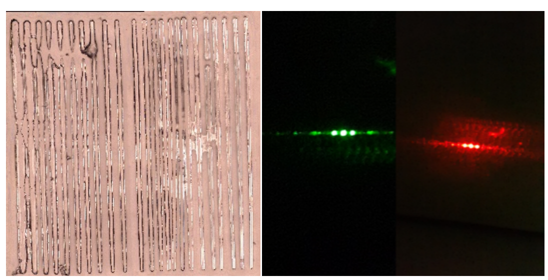

Fig. 3 Diffraction grating (left) and diffraction patterin obtained (right).

References

[1] Q. Li, "Optimization of point spread function of a high numerical aperture objective lens: Application to high resolution optical imaging and fabrication", Ph.D. dissertation, ECOLE NORMALE SUPERIEURE DE CACHAN, 2014.

[2] M. T. Do, "Fabrication of submicrometer 3d structures by one-photon absorption direct laser writing and applications," Ph.D. dissertation, ECOLE NORMALE SUPERIEURE DE CACHAN, 2015.

[3] R. Jagdheesh, J. García-Ballesteros, and J. Ocaña, "One-step fabrication of near superhydrophobic aluminum surface by nanosecond laser ablation," Applied Surface Science, vol. 374, pp. 2–11, 2016.

Theoretical and experimental study of colloidal transport in microfluidic geometries

María Eugenia Soto Alcaraz[1], Ramón Castañeda-Priego[1], R. Castro-Beltrán[1] and Marco Laurati[1]
[1]División de Ciencias e Ingenierías, Universidad de Guanajuato, Loma del Bosque #103, Lomas del Campestre, C.P. 37150. León Gto., México.
me.sotoalcaraz@ugto.mx

Abstract: In this work different geometries are produced by laser ablation in a soda-lime glass substrate of 0.160 mm by using a nanosecond pulsed laser 532 nm wavelength. These geometries as micro channels and micro cylinders are patterns where colloidal suspensions are deposited in order to study the behavior of the hard spheres when they are influenced by confinement of nearby walls so they can be analyzed by confocal microscopy. Simulations in software as COMSOL and C++ programming are also considered to compare the experimental results with the theoretical ones.

1. Introduction.

Microfluidics has become relevant in many fields of research today. Microchannels can be used for high-throughput sorting of cancer cells and healthy blood cells in a blood sample; lab on a chip devices are also examples of the increasing interest in the development of microfluidics field [1]. Colloidal suspensions need to be studied to understand how new medicaments will behave in human blood flow in narrow tubes or in order to understand the process of crystallization or sedimentation when only a gravitational force is acting. These examples consider that particles have a defined initial distribution and tend to distribute them in certain trajectories in the fluid when external forces act on the particles, such as electric or magnetic forces [2].

Colloidal suspension hard spheres have been widely studied in bulked fluids when it comes to Brownian motion related. The aim of this work is to study the behavior of these hard spheres when they are in the presence of confined walls as diffusion coefficients and flow of the particles. Most of the well known behavior of the colloids is in the diluted limit, but our particular interest is to work with more concentrated suspensions where the interactions between the hard spheres become more important [3].

2. Our project.

In order to achieve our goals we first have to develop a method to identify the particle trajectories of a colloidal suspension. These concentrated suspensions are deposited in micro cylinders and micro channels which are produced by laser ablation on glass substrates approximately of 0.160 mm width. We are working with a neodymium YAG pulsed laser of 532 nm that through a lenses arrangement provides from 6 to 8 mW to produce the geometries mentioned before.

Once suspensions are put in these configurations we are able to collect images from a confocal microscope, which will be analyzed by IDL (Interactive Data Language) Workbench software. The analysis of these images will provide the hard spheres trajectories through a frame time previously determined well, the radial distribution function and the MSD (mean squared displacement). High concentrated polimetylmetacrilate (PMMA) particles confined in large cylinders, figure 1, were used in the very first analysis with IDL workbench to obtain the radial distribution function, figure 2.

An algorithm developed in C++ language reproduces statistical methods such as Monte Carlo and Brownian dynamics. From theoretical assumptions we will be able to provide certain information to the algorithm and obtain information from the colloidal systems as radial distribution of the particles and other macroscopic properties. [4-5]. Particle tracing module in COMSOL Multiphysics software is another tool we are using to simulate the Brownian motion of the colloidal particles in the different geometries to compare the images obtained from the confocal microscope.

We are expecting to obtain similar results from the experiments and the simulations to have a better understanding of how the hard spheres react when confined in different geometries in concentrated suspensions.

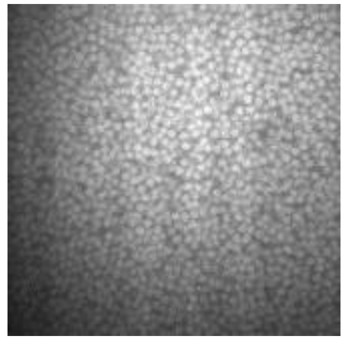

Fig. 1. PMMA particles seen from a confocal microscope.

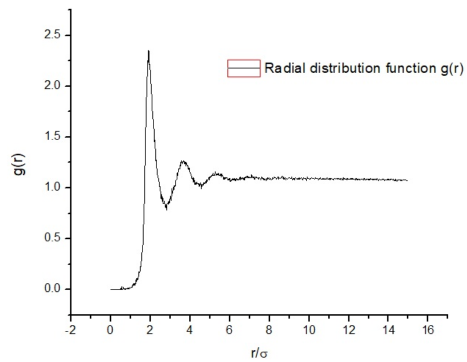

Fig. 2. Radial distribution function g(r) from PMMA particles.

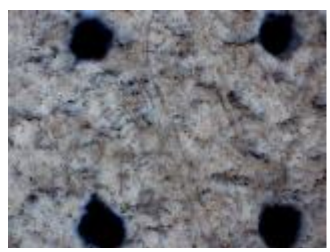

Fig. 3. Micro cylinders in a 0.160 mm glass substrate.

References

[1] C. Liu, C. Xue, J. Sun, and G. Hu, "A generalized formula for inertial lift on a sphere in microchannels," Lab on a Chip, vol. 16, no. 5, pp. 884–892, 2016.

[2] HampusSöderqvist, "Modeling and simulation of particle dynamics in microfluidic channels", Master's thesis Department of Physics, Umeå University, pp. 1-2, 2017.

[3] Somnath Ghosh, "Colloidal dynamics in flow and confinement", ISBN: 978-90-365-4022-3, 2015.

[4] Salvador Herrera-Velarde, Ramón Castañeda-Priego, "Structure and dynamics of interacting Brownian particles in one-dimensional periodic substrates", Journal of Physics, Condensed Matter 19 (22), 226215, 2007.

[5] Ronja F. Capellmann, Néstor E. Valadez-Pérez, Benedikt Simon, Stefan U. Egelhaaf, Marco Laurati, Ramón Castañeda-Priego, "Structure of colloidal gels at intermediate concentrations: the role of competing interactions", Soft Matter, 2016, 12, 9303-9313, 2016.

Selective Electron Beam Melting Model of Titanium Alloy

Trong-Nhan Le, Yu-Lung Lo* and Hong-Chuong Tran
Department of Mechanical Engineering, National Cheng Kung University, Tainan, Taiwan
*Corresponding author: loyl@mail.ncku.edu.tw (Yu-Lung Lo)

Abstract: Selective Electron Beam Melting (SEBM) is emerging as one of the most developed metal powder-based Additive Manufacturing (AM) technologies, however, SEBM process parameters control and optimization are still the toughest challenge in maximizing the quality of the manufactured parts. A multi-scale simulation framework is proposed to study the SEBM process parameters in Ti6Al4V titanium alloy fabrication. Utilizing Monte Carlo ray-tracing simulations at the micro-scale for electron-atom interactions and at the meso-scale for electron beam-powder interactions, we proposed a new volumetric heat source considering the effects of the powder bed. For investigating the melt pool dimensions and temperature distribution of the process, the new volumetric heat source is used in a 3-dimensional finite element heat transfer simulations. It is proven that the numerical results are in good agreement with published experimental data.

Keywords: Selective electron beam melting, Ray tracing, Volumetric heat source, Melt pool

1. Introduction

Together with others Additive Manufacturing technologies, including Direct Energy Deposition (DED) or Laser Engineer Net Shaping (LENS), powder-based systems such as Selective Electron Beam Melting (SEBM), Selective Laser Sintering (SLS), Selective Laser Melting (SLM), SEBM is one of the few technologies having the capability of fabricating full-density operational metallic components [1]. However, process parameters play a crucial role in the quality of the fabricated metal parts. Hence, investigating the influence of SEBM process parameters on melt pool geometries and thermal distribution through numerical simulation is extremely necessary and much more efficient compare to the conventional trial-error approach [2]. Moreover, the fidelity of numerical calculations is strongly dependent on the modeling of the heat source. Accordingly, the present research introduces a new volumetric heat source and a multi-scale simulation framework for the SEBM process constructed based on Monte Carlo ray-tracing simulations in both atomic level and powder-scale level.

2. New volumetric heat source for powder-bed SEBM process

Initially, ray-tracing simulations are performed in a micro-scale level to investigate the interactions between electrons and bulk material atoms of Ti6Al4V. Final results of the micro-scale simulation is the absorption characteristics of electron energy as a function of impinge angle. The absorptivity is then applied as input to Monte Carlo ray-tracing simulations conducted at the powder particle level (meso-scale) in order to obtain the absorption profile of the electron beam energy along the depth of the powder layer constructed with a known powder size distribution [3]. Lastly, a derivation of a new volumetric heat source is proposed and utilized as the input to COMSOL Multiphysics® finite element (FE) simulations to study the molten pool geometries and temperature distribution as a function of the process parameters (beam current, beam diameter and scanning speed). As a result of the meso-scale simulation, the absorption profile along the depth of the powder layer of Ti6Al4V can be obtained, hence, the volumetric heat source can be derived as follows:

$$q(x,y,z,t) = \frac{2Q}{\pi R_b^2} exp\left\{-\frac{2[(x-vt)^2+y^2]}{R_b^2}\right\}\frac{dA}{dz} \tag{1}$$

where Q is the electron power, R_b is the beam radius and the absorption profile through the depth of the powder bed is described by a derivative term dA/dz [3].

3. Model validation and discussions

The fidelity of the proposed numerical framework was evaluated by conducting comparison between the numerically calculated melt pool dimensions with a corresponding thermal profile along a single scan and the experimental results published by Price et al.[4]. The simulations commenced by studying the influence of the electron beam current on the molten pool geometries and thermal distribution. For the consideration of beam current effects, two different beam currents were studied, namely 4.8 mA and 7.7 mA. The scanning speed of 506 mm/s and beam diameter of 0.65 mm were kept constant in all of the simulations. For both cases of beam current, a rise in both melt pool length (see Figure

1 (a)) and melt pool width (see Figure 1 (b)) with an increasing beam current as a result of the higher thermal energy input to the powder bed during the single scan. Figures 1 (c) represents the calculated thermal distribution along the scanning direction in comparison with the experimental data for beam currents of 4.8 mA and 7.7 mA in [4]. It is observed that the current simulation case reached a maximum temperature approximately 200 K and 500 K higher than the experimental value for a beam current of 4.2 mA and 7.7 mA, respectively. However, the overall trends of thermal distributions in both simulation cases are in good qualitative agreement with the experimental profiles obtained by Price et al. [4].

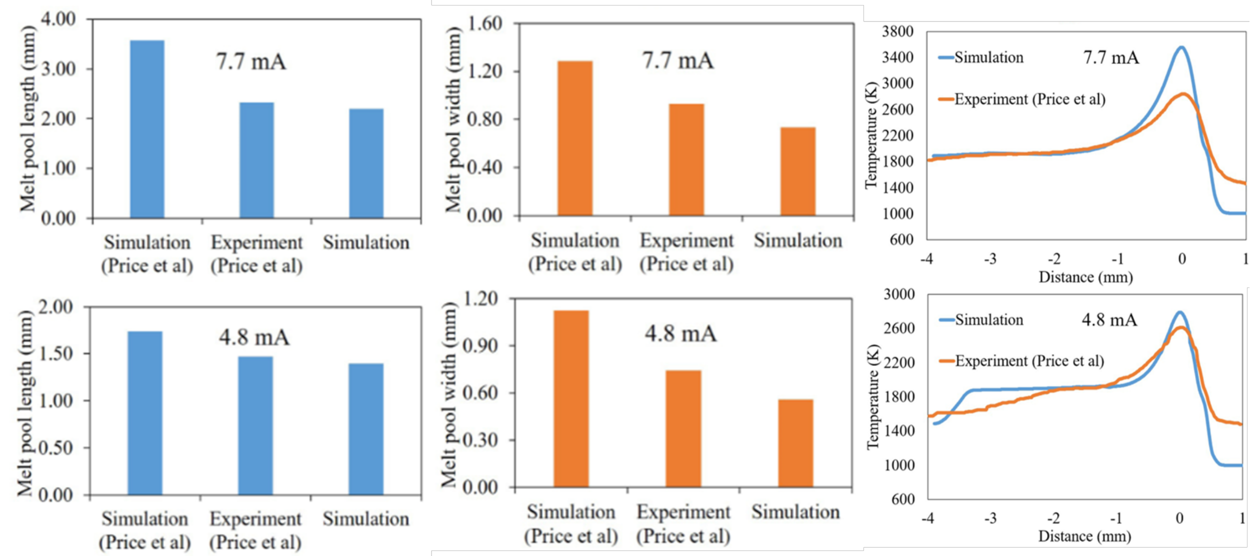

(a) (b) (c)

Fig. 1. Effects of SEBM beam current on melt pool dimensions. (a) Melt pool length, and (b) melt pool width. (Note that the present simulation results are compared with the experimental and simulation results reported in [4]). (c) Comparison of simulated and experimental temperature profiles along single scan track given electron beam currents

Melt pool dimensions and thermal profile along the scan track obtained by the FE heat transfer simulation in pure-thermal conduction mode are both in good agreement with the experimental results recorded by Price et al.[4], hence, the accuracy of the numerical modeling framework is confirmed.

Acknowledgements

The authors gratefully acknowledge the financial support provided to this study by the Ministry of Science and Technology of Taiwan under Grant No. MOST 105-2218-E-006-015. The research was also supported in part by the Ministry of Education, Taiwan, under funding provided to the Headquarters of University Advancement to the Intelligent Manufacturing Research Center (iMRC), National Cheng Kung University (NCKU).

References

[1] X. Gong, T. Anderson, and K. Chou, "Review on powder-based electron beam additive manufacturing technology," ASME/ISCIE 2012 international symposium on flexible automation, pp. 507-515, 2012.
[2] H. C. Tran and Y. L. Lo, "Heat transfer simulations of selective laser melting process based on volumetric heat source with powder size consideration," *J. Mater. Process. Technol.*, vol. 255, pp. 411–425, 2018.
[3] H. C. Tran, Y. L. Lo, and M. H. Huang, "Analysis of Scattering and Absorption Characteristics of Metal Powder Layer for Selective Laser Sintering," vol. 22, no. 4, pp. 1807–1817, 2017.
[4] S. Price, B. Cheng, J. Lydon, K. Cooper, and K. Chou, "On Process Temperature in Powder-Bed Electron Beam Additive Manufacturing: Process Parameter Effects," *J. Manuf. Sci. Eng.*, vol. 136, no. 6, pp. 061019, 2014.

Rapid prototyping of microfluidic devices by SLA 3D printing and biocompatibility study for cell culturing

[1]S. Marquez, [1]V. Piazza and [2]D. Hernández-Velázquez
[1]Research Center in Optics A.C., Loma del Bosque 115, Lomas del Campestre, Leon Guanajuato 37150, Mexico
[2]University of Guanajuato, Division of Sciences and Engineering, Department of Chemical, Electronic and Biomedical Engineering, Loma del Bosque 103, Leon Guanajuato 37150, Mexico
smarquez@cio.mx

Abstract: In this work, we demonstrate the feasibility to create microfluidic devices using Stereolithography (SLA) 3D printing as a simple and low-cost methodology compared to conventional soft-lithography carried on at cleanroom facilities. SLA printing has gaining much interest for rapid prototyping of designs in the fields of jewelry, dentistry and materials engineering. Therefore, we explode this potential in microfluidics for creating biocompatible platforms. Reproducibility of devices using this fabrication strategy was achieved for a minimum feature size of 750 µm. Moreover, we have qualitatively proven the biocompatibility of the microfluidic devices for culturing of HeLa cells by following a simple surface functionalization strategy. This study opens up a pathway for fabricating low-cost, portable and biocompatible microfluidic devices subject to the imagination of the designer to create new biosensing platforms.

1. Fabrication of 3D printed microfluidic devices

Computer-aided design (CAD) of microfluidic devices was done in Autodesk Inventor (Education stand-alone license). Two configurations of SLA printed parts were designed: devices used as master molds for replica of soft polymers, and microfluidic devices made entirely of photoresin. Printing of designs was done in a desktop SLA 3D printer (Form 2, USA) using two types of resins: standard clear and dental LT (Formlabs, USA). The procedure for printing the microfluidic devices can be found in [1]. The first step consisted of studying the minimum resolvable size (MRS) of printable microfluidic devices in the X, Y and Z axes. According to the manufacturer, the theoretical MRS of the SLA printer is 150 µm for X and Y axes, and 25 µm for Z axis. Therefore, microchannels with rectangular and circular cross-section dimensions from 25 µm to 1500 µm were printed, see Fig. 1-(1).

For devices used as master molds, a subsequent step was followed to replicate soft polymer microfluidic devices. Polydimethylsiloxane (PDMS Sylgard 184, Dow Corning Corp) was prepared at a mixing ratio of 1:15. A degassing step was done using a desiccator and a vacuum pump for 30 min. Then, PDMS was gently poured into the master molds followed by a second degassing step. PDMS was cured for 4 h using a hotplate at 40°C. The replica microfluidic devices were unmolded at room temperature. Inlet reservoirs for injection of liquids were done using a 3 mm in diameter punching tool. Finally, sealing of the PDMS microfluidic devices was done by using an oxygen plasma treatment (15 s at 20 sccm of O_2) for permanent bonding of the devices with previously cleaned glass slides, see Fig. 1-(3).

2. Characterization of 3D printed microfluidic devices

The topography of printed devices used as master molds was characterized using a profilometer (KLA Tencor D-600) to resolve for the MRS of the X, Y and Z axes. For 3D microfluidic devices printed directly on standard clear and dental LT resins, simple visual inspection was carried out to verify the openings of the microchannels, see Fig. 1-(1b). Filling of the microchannels was done by injecting a mixture of ethanol and blue ink using an ultra-fine insulin syringe (6 mm x 31G, BD Veo) affixed to each inlet reservoir, see Fig. 1-(2a).

3. Biocompatibility of 3D printed parts

Biocompatibility of the 3D printed parts was qualitatively studied by culturing HeLa cells. Two methodologies were studied: 1) Direct culturing of HeLa cells on devices made of biocompatible Dental LT resin, and 2) HeLa cell culturing on devices made of standard clear resin using a surface pretreatment with Poly-D-Lysine similar to [2] but with a simpler methodology. An 8-well support was designed and printed with wells of 6.25 mm in diameter and different heights for volumes in the range of 20 to 50 µL, see Fig. 1-(4).

Sample pretreatment. The entire 8-well support was washed using ethanol (70% ethanol in water (v/v)) and let it dry at room temperature. The part was then sterilized using UV light for 15 min in a laminar flow hood. Any residual ethanol was removed by rinsing the support with 3 mL of PBS (pH 7.4) in three subsequent steps. As follows, the 8-

well support was filled with poly-D-lysine (hydrobromide [2 mg/mL]) and incubated at 37°C for 1 h. Thereafter, any excess of poly-D-lysine was removed by rinsing three times with PBS.

Cell culturing. HeLa cells were grown in a 25 cm^2 flask up to 90% confluency and passed according to conventional protocols. The cells were resuspended in 4 mL of culture medium and the wells of the support were filled with the correspondent volume of cell resuspension. The support was then incubated for 2 days at 37ºC.

Cell observation and survival study. After 2 days of incubation, 1 mL of PBS was added to the culture dish and the support was turned upside-down for observation, avoiding bubble formation in the wells. Images of adherent cell at the bottom of the wells were taken using an inverted microscope (Zeiss Axon integrated with a pixel-linked camera (PL-B959U)). For determining cell survival, a Trypan Blue Stain for live-dead cells was employed. In this methodology, all cells are detached from the support, get resuspended in PBS and, after incubation with Trypan Blue and rinsing, dead cells display cytoplasmic incorporation of the blue dye, see Fig. 1-(6).

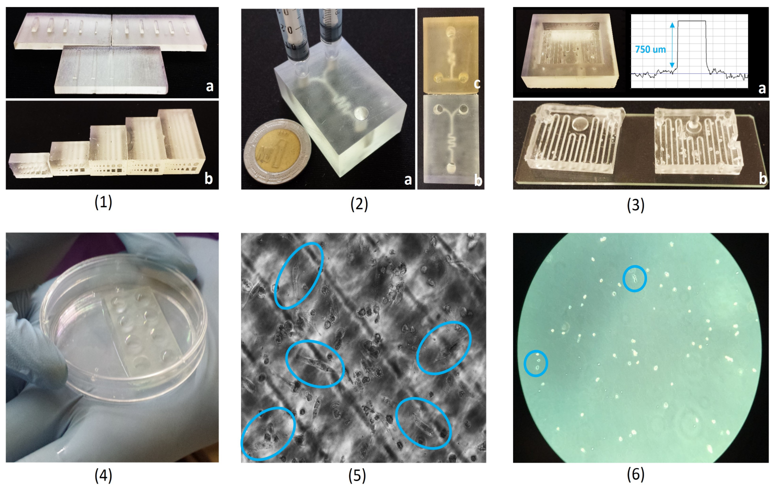

Fig. 1. Schematic showing SLA printed microfluidic devices. (1) Master molds (a), and microchannels (b). (2) 3D printed microfluidic devices (a) using clear (b) and dental LT (c) resin, respectively. (3) Master mold of serpentine microchannel and cross-sectional profile (a), PDMS replica with and without embedded air bubbles (b). (4) 8-well support surface pretreatment with Poly-D-Lysine. (5) HeLa cells attached to the bottom of a well. (6) Cell survival showing death cells with blue color inside

4. Results and discussion

In regard to 3D printed master molds, topographical measurements showed that reproducible devices were obtained for dimensions above 750 µm and 1000 µm (with a 5% error) for the standard clear and dental LT resin, respectively, see Fig. 1-(1,3). We noticed that replicated PDMS microfluidic devices from master molds cured with UV sunlight had embedded air bubbles after curing the PDMS in the hotplate at temperatures above 40°C, see Fig. 1-(3b). We assume that air filtrated through small pores of the cured photoresin. To circumvent this issue, we used a 365 nm UV light for 20 min using a commercial nail-curer device (54 W), which combines UV light and temperature increase to improve the post-curing of the printed parts.

With respect to the microfluidic devices printed by SLA, also the minimum resolvable size was 750 µm, see Fig. 1-(1b). We assume that clogging of microchannels with features below 750 µm occurs due to the high viscosity of the uncured resin that is trapped inside the microchannels while printing the parts. Filling of 3D printed microfluidic devices was successfully proven without any clogging of the microchannels, see Fig. 1-(2).

The biocompatibility of the devices was qualitatively demonstrated using the surface functionalization pretreatment with poly-D-Lysine for culturing of HeLa cells, see Fig. 1-(4). Attached cells at the bottom of the 8-well support with the proper morphology were observed and the staining methodology showed the presence of live cells, Fig. 1 – (5,6). One drawback that needs to be addressed is the poor transparency of the printed devices which made challenging the visualization of cells in the inverted microscope. We also discarded the directly use of Dental LT as a biocompatible resin for HeLa cell culturing owing that the cells died during the procedure.

References

[1] Formlabs, “The Ultimate Guide to SLA 3D printing,” (2018) https://formlabs.com/blog/ultimate-guide-to-stereolithography-sla-3d-printing/#printing-process

[2] S. Sivashankar, S. Agambayev, K. Alamoudi, U. Buttner, N. Khashab, y K. N. Salama, "Compatibility analysis of 3D printer resin for biological applications", *IET Micro Nano Lett.*, vol. 11, n. 10, pp. 654-659 (2016).

Construction and characterization of a laser doppler velocimeter printed in 3D.

H. Méndez-Dzul[1], M. Pérez-Cortés[2], M. Ortíz-Gutiérrez[3], M. de Coss-Gómez[2], J. Lugo-Jiménez[2], C. Vinajera[2].
1 Instituto Nacional de Astrofísica, Óptica y Electrónica. Luis Enrrique Erro #1, Tonantzintla, Pue. 72000
2 Universidad Autónoma de Yucatán. Av. Industrias no Contaminantes s/n. Mérida, Yucatán. 97200.
3 Universidad Michoacana de San Nicolás de Hidalgo. Morelia, Mich.
og.heck.5500@gmail.com, mperez.cortes@correo.uady.mx, mortizg@yahoo.com, dcgomez@correo.uady.mx

Abstract: This work shows the application of an optical system built in a 3D printer. Its operation and characteristics are shown.

Introduction.

An optical system is a set of mechanical and optical elements placed in an aligned and systematized form, their objective is to make a measurement that is recorded through a natural or artificial sensor [1,2].

The interest of this work was to realize through a 3D printer the construction of a mechanical system, and implement an optical system adjusted to our possibilities, as well as adjust a hamamatsu avalanche sensor.

A small experiment was carried out to show the functioning of our system built with an adaptation with some mechanical elements [3-6].

We present in this work the measurement of a pair of experiments for the characterization of the optical 3D-PLA system, these experiments consisted in measuring the speed of a chopper, and the water velocity of a small source system.

As an example, Fig. 1 shows the assembly of the experiment with a chopper and its frequency to determine the speed [7,8]:

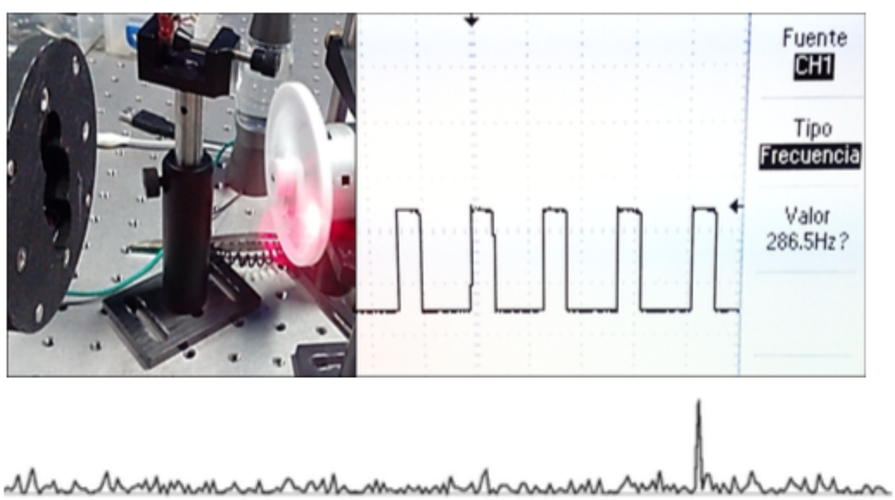

Fig. 1. Operation of the laser doppler velocimeter system.

The determination of the speed of the chopper is made for some loops of the experiment, obtaining the results shown in the Table 1 shown below:

Table 1

Frecuencia leida (hz)	$v_c(cm/seg)$	$\bar{v}$ (cm/seg)	Q (cm^3/seg)	$t_{llenado}$ (seg)
46985	6.95	3.47	77.62	40.67
47541	7.03	3.51	78.54	40.20
47578	7.04	3.52	78.60	40.17
47878	7.08	3.54	79.10	39.91
47876	7.08	3.54	79.10	39.91
40358	5.97	2.98	66.68	47.35
47880	7.08	3.54	79.11	39.91

Where the average central speed recorded in this experiment is 6.81cm / sec.

Through the construction of this prototype, and its evaluation in the previous experiments, the utility was demonstrated in applications where it is necessary to measure the speed in a non-invasive way. It is planned to continue with the research of the system, as well as to make improvements in the proposed design.

1. Improvement of the optical system: perform the design and construction of an objective system with variable focal distance, and present corrections of the spherical aberration, to be able to make measurements in positions further away from the anemometer.
2. Perform fiber optic application, to decrease the physical size of the system.
3. Improvement of the light source: implement a spatial filtering on the source, as well as the lens of collimation and concentration.
4. Improvements on the data acquisition system: design and implement a system that performs the analog-digital conversion, dimensioned to a specific band. Implement wireless communication from the acquisition system to the processing system.
5. Improvements on the software: make the program through the Python language, and implement it on Android.

References

[1] Hecht, E. (2001). *Optics* 4th edition AddisonWesley Publishing Company 2001 (Vol. 1). Addison Wesley.
[2] Menn, N. (2004). *Practical optics* (first edit). Elsevier.
[3] Albrecht, H.-E., Borys, M., Damaschke, N., and Tropea, C. (2003). *Laser Doppler and phase Doppler measurement techniques*. Cryogenics (Vol. 43).
[4] Cengel, Y. A. (2006). *Mecánica de fluidos*. McGraw-Hill (Vol. 1).
[5] Coupland, J. (2000). *Laser Doppler and pulsed laser velocimetry in fluid mechanics*. Photo- mechanics, 412, 373–412.
[6] Donald, O. (1985). *Elements of modern optical design* (first). Atlanta: John wiley and Sons. Durst, F., Melling, A., Whitelaw, J. H., and Wang, C. P. (1977). *Principles and Practice of Laser-Doppler Anemometry*. Journal of Applied Mechanics.
[7] Fredriksson, I., Fors, C., and Johansson, J. (2007). *Laser Doppler Flowmetry - a Theoretical Framework*. Measurement, 1–22.
[8] Fredriksson, I., Larsson, M., and Strömberg, T. (2009). *Measurement depth and volume in laser Doppler flowmetry*. Microvascular Research, 78(1), 4–13.

Extended Abstracts

Session
BIOMEDICAL APPLICATIONS

	Pg.
Research of Testing Technique of Internal Deformation of Materials Combined with Optical Coherence Tomography and Digital Volume Correlation Cuiru Sun, Fanchao Meng, Cheng Chen	37
Ultrasonic waves generated in pure water by cavitation produced by a low power, CW thulium laser N. Korneev, and P. Rodríguez-Montero	39
A bioimpedance sensor based on a spectral enrichmentwith a Howland source L. G. Martínez-Ramirez, J. M. Sierra-Hernandez, A. A. Fernandez-Jaramillo	41
Glucose concentration measurement of a transparent sample by using a Gaussian probe beam with high spherical aberration. Etna Yáñez, Moisés Cywiak, Juan Manuel Franco S	43

Research of Testing Technique of Internal Deformation of Materials Combined with Optical Coherence Tomography and Digital Volume Correlation

Cuiru Sun*, Fanchao Meng, Cheng Chen
Department of Mechanics, Tianjin University, Tianjin, China
Tianjin Key Laboratory of Modern Engineering Mechanics, Tianjin University, Tianjin, China
*carry_sun@tju.edu.cn

Abstract: The mechanical properties of biological tissues have great significance for researching, diagnosis and therapy of diseases. However, the structure of biological tissues is relative complicated, and it is very difficult to testing the internal full-field mechanical properties. An experimental system which is adapting to testing the static compression of biological tissues has been integrated combined with a high-accuracy loading equipment and an existing optical coherence tomography (OCT) system in the laboratory. The sensitivity of the test system based on digital volume correlation (DVC) method and the OCT system is 0.3 μm for displacement tests and is 9×10-4 for strain tests according to the stationary tests. The accuracy of the test system is 3.4% for displacement tests according to the test of rigid body displacements and is 9.7% for strain tests according to the compressive tests. Furthermore, the elastic modulus of a homogenous material was acquired (Young's modulus is 1486.0 kPa which matches perfectly with the tensile test result and Poisson's ratio is 0.477) by the virtual fields method (VFM). Finally, the internal full-field deformation and elastic modulus of a double layer phantom were acquired by the DVC method based on OCT and the VFM. The research results not only enriched the new technology of experimental mechanics but also provided a new testing method for biomechanical tests.

1. Introduction

The mechanical properties of biological tissues have great significance for diagnosis and therapy of diseases. However, the structure of biological tissues are relative complicated and it is very difficult to testing the internal full-field mechanical properties. Digital volume correlation (DVC) method depends on 3D imaging technique and can make the non-contacting internal full-field displacement and strain testing come true. Optical coherence tomography (OCT) is a high-resolution 3D imaging technique. If it is combined with DVC technique, it will realize the high-resolution full-field three-dimensional testing for internal mechanical properties of biological tissues.

As OCT provides good contrast for soft tissue images and high resolution, DVC method is applicable to OCT 3D reconstructions. Fu et al applied DVC on OCT reconstructed volumes to derive volume strain data for the first time [1]. However, the FFT based algorithm induces aliasing fringes in the displacement and strain fields, which brought serious interruption to the measuring results, especially to the strain field. In the same year, Nahas et al combined full field OCT with DVC to measure the static strain map in micron scale [2]. They have verified their method through comparing the ratio of the average values of strain in two different layers with the ratio of the Young's modulus of the two layers. However, the accuracy for strain and displacement distribution was not verified and the accurate values of the Young's modulus were not acquired. Hence, the properties of composite materials have not been revealed using OCT and DVC method in biomechanics.

An experimental system has been integrated combined with a high-accuracy loading equipment and an existing OCT system. And then, the sensitivity and accuracy of the test system based on OCT system and DVC method have been verified by experiments. Furthermore, Young's modulus of a homogenous material was acquired with high accuracy combined with the virtual fields method (VFM). Finally, the internal full-field deformation and elastic modulus of a double layer phantom were acquired by the DVC method based on OCT and the VFM.

2. Methods

For the DVC method, lately Pan et al proposed a 3D inverse compositional Gauss–Newton (IC-GN) method, which has good ability of noise resistance and high speed [3]. The iterative scheme can be written as follow:

$$\Delta\mathbf{p} = -\mathbf{H}^{-1}\cdot\sum\nolimits_{\boldsymbol{\xi}}\left\{\left(\nabla f\cdot\frac{\partial\mathbf{W}}{\partial\mathbf{p}}\right)^{T}\cdot\left[\left(f(\mathbf{x}+\boldsymbol{\xi})-f_m\right)-\frac{\Delta f}{\Delta g}\left(g\left(\mathbf{x}+\mathbf{W}(\boldsymbol{\xi};\mathbf{p})\right)-g_m\right)\right]\right\} \tag{1}$$

Where $f(\mathbf{x})$ and $g(\mathbf{x})$ are gray functions of reference and target sub-volumes; $\boldsymbol{\xi}$ is local coordinates in the sub-volume; f_m and g_m are the mean intensity values; Δf and Δg are the standard deviations of gray functions; ∇f is the gradient of the reference sub-volume; $\mathbf{H}$ is the Hessian matrix; $\boldsymbol{W}$ is the linear displacement mapping function; $\mathbf{p}$ is the precomputed deformation parameter vector; $\Delta\mathbf{p}$ is the incremental deformation parameter vector. Update the warping function during each iteration as $\mathbf{W}(\boldsymbol{\xi};\mathbf{p}^{(n+1)}) = \mathbf{W}(\boldsymbol{\xi};\mathbf{p}^{(n)}) \cdot \mathbf{W}^{-1}(\boldsymbol{\xi};\Delta\mathbf{p}^{(n+1)})$, where the superscript (n) represents the n^{th} iteration. Hence, $\Delta\mathbf{p}$ can be solved with reasonable condition of convergence.

For the VFM, according to the principle of virtual work and assumption that the material is compressed statically and the body forces can be neglected and the material is homogenous, the linear equations can be derived as follow:

$$Q_{ij}\int_V \varepsilon_j\varepsilon_i^* dV = \int_{S_f} \overline{\mathbf{T}}\cdot\mathbf{u}^*\, dS \tag{2}$$

Where Q_{ij} is elastic constant; ε^* is the virtual strain tensor; ε is the real stress tensor; $\mathbf{u}^*$ is the virtual displacement vector; $\overline{\mathbf{T}}$ is the external force vector on the surface of S_f, so Q_{ij} can be solved [4].

3. Results

Above all, the sensitivity of the system has been tested according to stationary experiments. To research the influence of the contrast and correlation, different scanning numbers of A and B are chosen. Here, let the number of A-scans equals to B-scans. The best choice of the number of transverse scans is 214 for small errors, relative robust data and high correlation coefficient. Meanwhile the sensitivities of the system are tested. They are 0.3 μm for displacement and 9×10^{-4} for strain. Furthermore, the accuracy of the system has also been tested. In the rigid body displacements tests, the imposed displacements are 30 μm and 60 μm in two different directions and the matching results are 30.8 μm and 57.9 μm. Hence, the relative errors are 2.6% and 3.4% respectively. In the compressive tests, the imposed strain is -0.0031 in depth direction while the mean value of the strain of the matching result is -0.0034. Therefore, the relative error is 9.6%. Moreover, the Young's modulus and Poisson's ratio were acquired by the VFM. They are 1486.0 kPa and 0.477 respectively. The Young's modulus matches perfectly with the tensile test result (1471.3 kPa) and the relative error is 1.0%. Finally, the internal full-field deformation and elastic modulus of a double layer phantom were acquired. Fig. 1. shows the displacement fields after compression in three directions. The 3D strain fields have also been tested which are not shown because the page is limited. What's more, the constitutive parameters of the two layers were obtained. For the lower layer, the Young's modulus and Poisson's ratio are 339.5kPa and 0.436; they are 182.7 kPa and 0.334 for the top layer. The relative errors of the Young's modulus for the two different types of layers are 26.2% and 51.2% respectively compared with the tensile results (462.1 kPa and 120.8 kPa), which are larger than the compressive test of the homogeneous material. The mainly reason is the degradation of the images' qualities caused by the deformation.

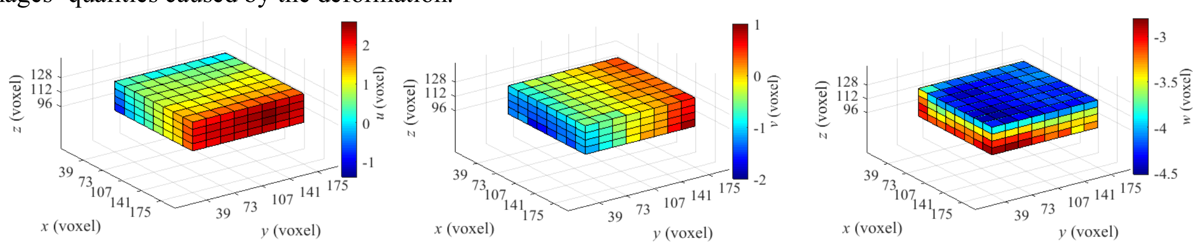

Fig. 1. The displacement fields after compression

4. Conclusion

An experimental system based on the DVC method and VFM that can test the internal full-field deformation and constitutive parameters was designed. Experimental results demonstrated the feasibility of this method for the internal deformation and the elastic modulus measurement of materials. The better results will be obtained with further data analysis in the following studies. These research results not only enriched the new technology of experimental mechanics but also provided a new testing method for biomechanical tests.

References

[1] J. W. Fu, F. Pierron, and P. D. Ruiz, "Elastic stiffness characterization using three-dimensional full-field deformation obtained with optical coherence tomography and digital volume correlation," Journal of Biomedical Optics, 18, (2013).

[2] A. Nahas, M. Bauer, S. Roux, and A. C. Boccara, "3D static elastography at the micrometer scale using Full Field OCT," Biomedical Optics Express, **4**, 2138-2149 (2013).

[3] B. Pan, B. Wang, D. F. Wu, and G. Lubineau, "An efficient and accurate 3D displacements tracking strategy for digital volume correlation," Optics and Lasers in Engineering, **58**, 126-135 (2014).

[4] Pierron F and Grédiac M. *The Virtual Fields Method* (Springer New York, 2012), Part 1. Chap. 3.

Ultrasonic waves generated in pure water by cavitation produced by a low power, CW thulium laser

N. Korneev, and P. Rodríguez-Montero
Instituto Nacional de Astrofísica, Óptica y Electrónica
Luis Enrique Erro 1, Tonantzintla, Pue. 72840
ponciano@inaoep.mx

Abstract: We experimentally studied the ultrasound wave generated by the cavitation bubble produced when the light of a low power, CW thulium doped laser with a wavelength emission around 1950 nm is focused in pure water.

1. Introduction

Cavitation in water generated by high power pulsed laser has been extensively studied [1]. However, cavitation can be induced also with low power, CW lasers (~100-1000 mW) in strongly absorbing liquids [2]. The mechanism in this latter technique is the thermoactivation, i.e., a small volume of water is overheated, and the nucleation event results in the formation of a cavitation bubble and a subsequent collapse. On the collapse, a strong ultrasound pulse is generated.

The first demonstrative experiments using low power, CW lasers were performed using toxic or corrosive dyes, which are not suitable for biomedical applications. For biomedical applications it is important to produce the thermoactivation directly in water. The high absorption (necessary for the thermoactivation mechanism) in pure water is close to 1950 nm, which is within the tuning range of the thulium doped lasers.

Here, we report the experimental study of thermoactivated cavitation in pure water induced by a low power, CW thulium doped laser.

2. Experimental setup

Figure 1 shows the experimental setup. A home-made tunable thulium doped fiber laser (TDFL) with a maximum power of 750 mW, was used to generate laser emission near of one the absorption peaks of pure water (~ 1950 nm). The output beam was collimated and focused inside a cell filled with deionized water. The focusing lens was mounted on an axial translational stage. Due to the high absorption of the water in the emission range of the thulium laser, the formation of cavitation bubbles occurs in the vicinity of the input window. The cavitation events produce ultrasound shock waves which are detected by a simple optical system based on the measurement of the deflection that the shock wave induces on a focused probe laser beam (a DPSS laser with emission at 532 nm). The beam deflection was monitored by a position detector and the signals were stored and displayed with a digital oscilloscope.

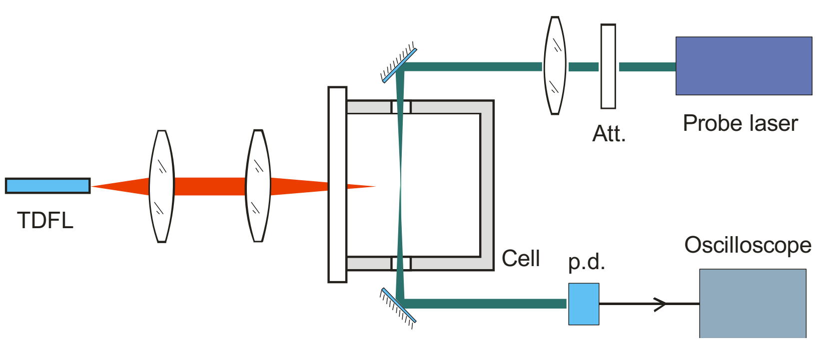

Fig. 1. Optical setup employed to study the ultrasonic waves induced by cavitation upon illumination of a low power, CW thulium-doped fiber laser (TDFL). Att.: attenuator, p.d. photodiode.

3. Experimental results

Figure 2 shows a typical ultrasonic trace displayed by the oscilloscope. It was obtained near the position of the smallest spot size (which is obtained by the axial movement of the focusing lens). The spike due to the first arrival of the shock wave is clearly observed at $t = 0$. Some rebounds from the input window surface, water-air interface and cell walls are also observed.

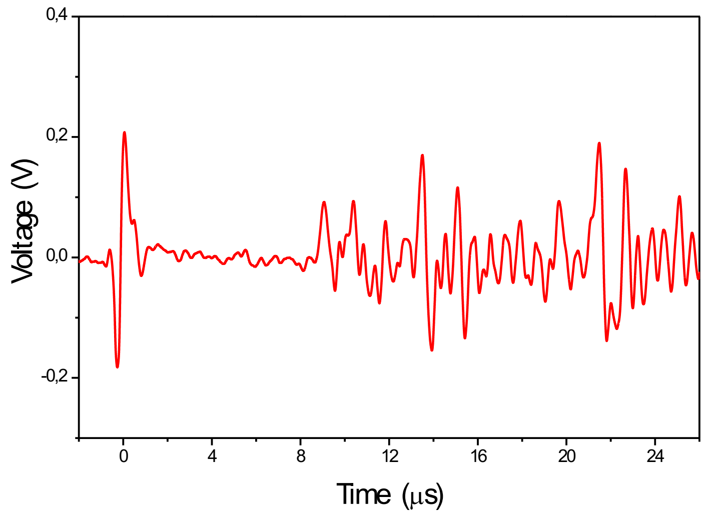

Fig. 2. Oscilloscope trace of an ultrasonic signal produced by cavitation. The wavelength of the incident light was 1932 nm with a power of 220 mW. The oscilloscope triggering is done by the first spike arrival.

Similar to the experiments performed using saturated copper nitrate saline solutions [3], it was observed that the pulse repetition frequency is maximal for the exact position of the focus, and it diminishes when the laser spot becomes bigger; but the pulse amplitude, on the contrary, is higher for bigger laser spots.

For our wavelength tuning range (1914-1949 nm), the absorption length varies less than 10% and it is approximately 0.09 mm at 1950 nm [4]. Thus, not much variation in signal is observed in function of wavelength.

In conclusion, we have demonstrated that cavitation can be produced in water using low power, CW lasers with a wavelength close to 1950 nm. High amplitude of the ultrasonic wave with high spatial resolution obtained without the use of bulky pulsed lasers makes of the proposed technique a very attractive source of medical ultrasound.

References

[1] K.-T. Byun, H.-Y. Kwak, and S. W. Karng, "Bubble evolution and radiation mechanism for laser-induced collapsing bubble in water," Japanese Journal of Applied Physics **43**(9A), 6364-6379 (2004).
[2] S. Rastopov and A. Sukhodol'sky, "Cluster nucleation in the process of cw laser induced thermocavitation," Physics Letters A **149**(4), 229– 232 (1990).
[3] J. Ramirez-San-Juan, E. Rodriguez-Aboytes, A. Martinez-Canton, O. Baldovino-Pantaleon, A. Robledo-Martinez, N. Korneev, and R. RamosGarcia, "Time-resolved analysis of cavitation induced by cw lasers in absorbing liquids," Optics Express **18**(9), 8735–8742 (2010).
[4] Joseph A. Curcio and Charles C. Petty, "The Near Infrared Absorption Spectrum of Liquid Water", Journal of the Optical Society of America **41**(5), 302-304 (1951

A bioimpedance sensor based on a spectral enrichment with a Howland source

L. G. Martínez-Ramirez[1*], J. M. Sierra-Hernandez[1], A. A. Fernandez-Jaramillo[2] D. Jauregui-Vazquez[1], J. C. Hernandez-Garcia[1], J. M. Estudillo-Ayala[1], L. M. Contreras-Medina[3], and R. Rojas-Laguna[1]

[1]Departamento de Ingenieria Elctronica, División de Ingenierías, Campus Irapuato-Salamanca, Universidad de Guanajuato, Carretera Salamanca-Valle de Santiago km 3.5+1.8, Comunidad de Palo Blanco, Salamanca, Gto., C.P. 36885, México.

[2]Unidad Academica de Ingenieria Biomedica, Universidad Politecnica de Sinaloa, Carretera Municipal Libre Mazatlan Higueras km 3, Col. Genaro Estrada, Mazatlan, Sin., C.P. 82199, México.

[3]Departamento de Ingenieria Biomedica, Facultad de Ingenierias, Universidad Autonoma de Queretaro, Cerro de las Campanas S/N, Santiago de Queretaro, Qro., C.P. 76010, México.

**lg.martinezramirez@ugto.mx*

Abstract: In this work, an intelligent bioimpedance sensor with spectral enrichment using the Howland source was implemented. The experimental results shown that, the greatest discrimination between water and the concentration of magnesium nitrate 40g, calcium nitrate 40g and potassium Nitrate 20g within the range in a bandwidth of 300 to 400 Hz.

1. Introduction

In recent years different types of biosensors have been proposed for sensing biological and chemical parameters such as; various carcinoembryonic antigen, label-free analysis at cell scale, DNA and endocrine-disrupting chemicals (EDC), norfluoxetine and BDE-47. Many of these are based on impedance method [1-3]. Because, it has a simple optical configuration, low cost, high sensitivity and compact size. For this reason, several bioimpedance sensors have been implemented by using different fabrication techniques, applying an alternating current signal with constant amplitude and current through two electrodes that would be in contact with the tissue, causing a potential difference that is closely related to the resistive value of the tissue. There are different configurations to generate it, such as the Howland source and its multiple improved modifications.

2. Principle of operation of the bioimpedance sensor

One of the main contributions in the work is the implementation of waveforms. For this it is necessary to focus first on the implementation of the Digital Signal Synthesis. Due to the characteristic of personalizing the signals, it must be implemented from scratch on a selected digital platform. Afterwards, a program based on metaprogramming will be developed to implement the different signals through a high-level language, such as the one used in Matlab. The aforementioned, with the purpose that through a function described in the program, an implementation of a so-called "look up table" with the discrete values of the function can be generated. With the objective of; if necessary, stimulate with different specific frequencies, a single signal could be generated with the sum of the frequencies necessary for its excitation, and thus increase the capabilities of the bioimpedance meter. The system is essential that has a DAC (digital-analog conversion) for the generation of analog signal. Subsequently, the generated signal has to maintain a constant current for a correct measurement. There are different configurations to generate it, such as the Howland source. In addition to the above, the interface will be designed to integrate the sample for analysis and their respective electrodes for the application of the different signals. Finally, the ADC (analog-digital conversion) that will acquire the signal for its storage will be instrumented. With the above, it will be possible to generate a database with samples measured with different waveforms for later analysis. The Schematic diagram of the system is shown in figure 1. The technique currently proposed gives us the possibility to personalize the source of excitation of the proposed system. The above in order to exert a spectral enrichment within the sample to be analyzed. On the other hand, if the sample is excited with different waveforms with greater spectral complexity, more information can be injected into the sample and thus have a more complete response; This means that, through a triangular signal, saw teeth or square, there are high-frequency components coupled with their fundamental component. With the spectral enrichment technique, more complex signals will be available with more response information, giving the possibility to implement digital signal processing techniques in order to distinguish deformations, attenuations or Amplifications within it, and so relate are deformations with phenomena that are sought to investigate. In order to attend to the aforementioned, in the case of simply seeing the changes in the spectral content of the signal obtained from the sample, it is possible to apply techniques such as fast Fourier transform.

3. Results and discussion

To carry out the experimental experiments, the concentration samples were used different salt concentrations, which were of magnesium nitrate, potassium nitrate and calcium nitrate at 20, 40 and 60g. After applying the proposed measurement technique, the response spectrum was observed. However, it is necessary to identify the frequency bands where a greater discrimination can be made between said solutions at the mentioned concentration. The greatest discrimination was observed between water and the concentration of magnesium nitrate 40g in a bandwidth of 378 to 382 Hz as shown in figure 2, also between water and calcium nitrate 40g specifically in the 355 Hz is the point higher with a significant difference as shown in figure 3. This type of circuit allows us to develop an implementation that has a customizable source capable of generating a spectral enrichment when making bioimpedance measurements. For experimental development, integrating solutions with different types of salts and concentrations contained in biological samples were identified and discriminated through the proposed system. The above was achieved with the help of digital signal processing techniques, which, together with the source with spectral enrichment, provided enough information to be processed, analyzed, and thus achieves satisfactory measurements. The implementation of the techniques previously described opens the possibility of further research and characterization of components and controlled compounds under different waveforms, and frequency sweeps, giving the possibility to characterize them accurately. And thus, move to more complex biological samples, such as saliva, blood, skin, in order to make biosensors capable of detecting anomalies and pathologies in them.

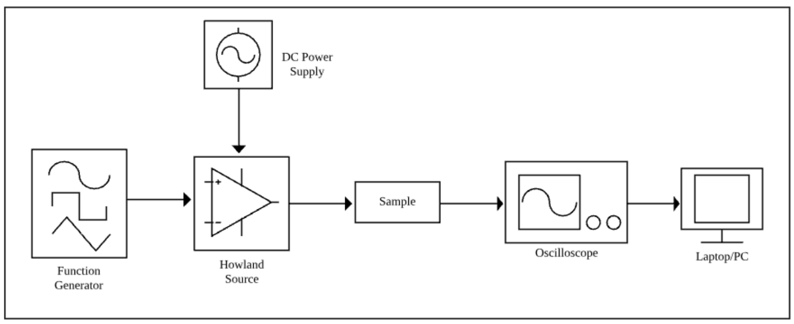

Fig. 1. Schematic diagram of the system

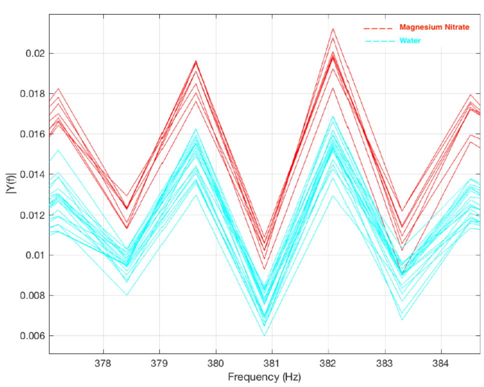

Fig. 2. Response spectrum of water and magnesium nitrate 40g.

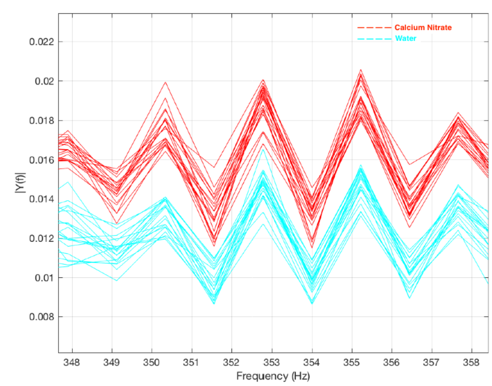

Fig. 3. Response spectrum of water and calcium nitrate 40g.

References

[1] Rajeswaran Radhakrishnan,Ian I. Suni, Candace S. Bever, and Bruce D. Hammock, "Impedance Biosensors: Applications to Sustainability and Remaining Technical Challenges",2014.

[2] Hanbin Ma, Richard W. R. Wallbank, Reza Chaji, Jiahao Li, Yuji Suzuki, Chris Jiggins& Arokia Nathan, "An impedance-based integrated biosensor for suspended DNA characterization",2013.

[3] C. Dalmay, M. Cheray, A.Pothier, F. Lalloué, M. O. Jauberteau, P. Blondy "Ultra sensitive biosensor based on impedance spectroscopy at microwave frequencies for cell scale analysis",2010.

Glucose concentration measurement of a transparent sample by using a Gaussian probe beam with high spherical aberration.

Etna Yáñez[1], Moisés Cywiak [1], Juan Manuel Franco S.[1]
[1]Centro de Investigaciones en Óptica A.C. Loma del Bosque No. 115 León Gto., México.
etnay@cio.mx, moi@cio.mx, franco@cio.mx .

Abstract: We present results of our technique previously reported for glucose concentration measurements on a transparent sample. The technique is based on an optical probe beam with high spherical aberration. We have reported that it is possible to attain better sensitivity compared to a system that uses a probe beam free of aberrations under similar conditions.

1. Introduction

Many diseases are associated to abnormal glucose concentration in blood, increasing the importance of better glucose measurement systems. For improving the accuracy of these measurements, several techniques have been developed; however, in general, these techniques rely on low signal-to-noise ratios [1, 2], making it necessary to conduct further research on this subject. In a previous report, we have presented a technique based on the diffractive properties of a transmitted Gaussian probe beam with high spherical aberration that propagates through a transparent sample under inspection [3].The advantage of this technique is that it does not depend on the amplitude of a single weak signal as it is based on the profile of the probe beam that propagates through the sample. Thus, this technique is in principle immune to noise, making it more reliable.

2. Experimental Setup

The optical setup is depicted in figure 1.

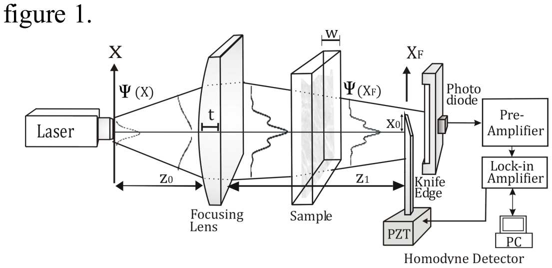

Figure 1. The vertex of a singlet focusing lens with central thickness t is placed at a distance z_0 from the waist-plane with coordinate x of a laser Gaussian beam with amplitude distribution $\Psi(x)$. The observation plane with coordinate x_F is located at a distance z_1 from the back surface of the lens. A transparent sample with width w is placed between the lens and the observation plane. The intensity distribution $\Psi(x_F)$is acquired by a Homodyne detector. (We have reported a similar figure in [3]).

3. Results of Measurements

In figures 2(a - d) it is depicted how at a near vicinity of the back focal plane of a focusing singlet, spherical aberrations of an illuminating commercially available He-Ne laser beam with a Gaussian intensity profile are developed as the distance between the laser and the focusing singlet (z_0) increases.

In a previous report [3] we demonstrated that the Gaussian probe free of aberrations is less sensitive to glucose concentration changes compared with the one obtained with a Gaussian probe beam with spherical aberrations.

It can be appreciated from figures 3(a, b) how the primary side-lobes heights increase while the index of refraction of the sample under inspection increases. The system is adjusted by setting the height of the primary side-lobes to a vertical height of 60% when the sample under inspection is filled with tri-distilled water which corresponds to a concentration of C_A=0 mg/dl. Then, we measure different known glucose concentrations to calibrate the system, figures 4(a, b). Once the system has been calibrated it can be used in a simple manner as it exhibits a linear response.

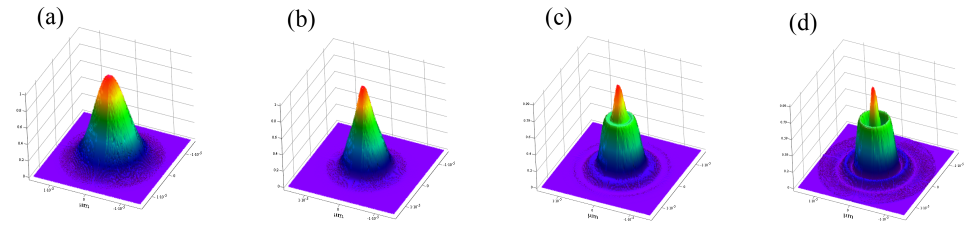

z_0 =100 cm z_0 =300 cm z_0 =500 cm z_0 =700 cm

Figure 2. Development of spherical aberrations at a vicinity of the back focal plane of a focusing singlet, illuminated by a commercially available laser beam with a Gaussian intensity profile as the distance (z_0) increases.

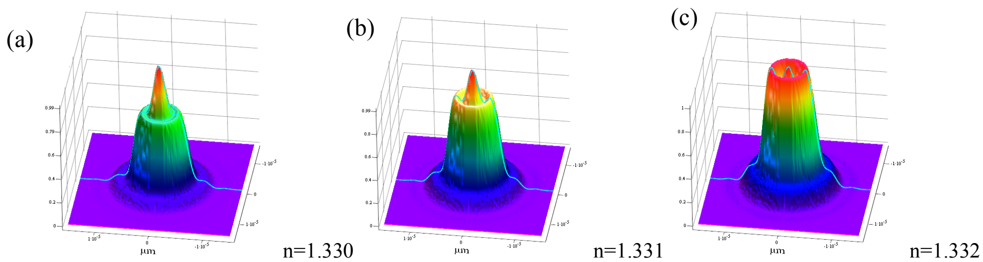

Figure 3. Increasing of the heights of the primary side-lobes of the detected probe beam as the glucose concentration increases in the sample under inspection. z_0 =500 cm, Δn = 0.001, which corresponds to approximately changes of 500 mg/dl between samples (the concentration changes are exaggerated for visualization purposes).

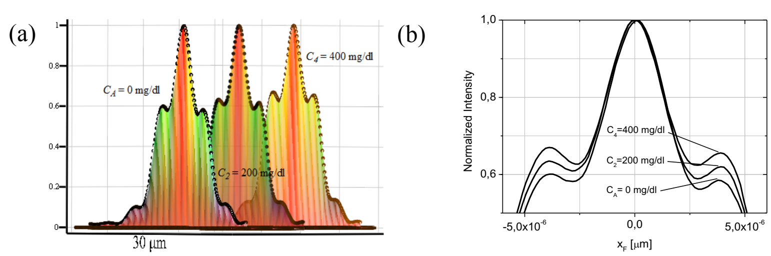

Figure 4. (a) Normalized experimental intensity profiles for three different sample concentrations C_A=0 mg/dl, C_2=200 mg/dl, and C_4=400 mg/dl. (b) corresponds to a zoom of (a).

4. Conclusions

We demonstrated analytical and experimentally that a Gaussian probe beam with high spherical aberration is more sensitive than a Gaussian probe beam free of aberrations for glucose concentration measurements. We demonstrated experimentally that the system has a linear response in a range of interest with high repeatability and stability, making this system feasible for glucose concentration measurements in transparent liquid media. As the system exhibits a linear response an additional advantage is that the system is still reliable even over slightly misalignments.

References

[1] McNichols, R. J., & Coté, G. L. (2000). Optical glucose sensing in biological fluids: an overview. Journal of biomedical optics, 5(1), 5-16.
[2] So, C. F., Choi, K. S., Wong, T. K., & Chung, J. W. (2012). Recent advances in noninvasive glucose monitoring. Medical Devices (Auckland, NZ), 5, 45.
[3] Yáñez, E., Cywiak, M., & Franco, S. J. M. (2018). Gaussian probe beam with high spherical aberration for glucose concentration measurement. Applied optics, 57(15), 4153-4157.

Extended Abstracts

Session
MATERIAL LASER PROCESSING

	Pg.
Using Convolution Mathematical Method for explanation on nonlocality in Kerr-Type medium with arbitrary degree of Nonlocality Majid Hesami, Mahrokh Avazpour, Marcela. Maribel Méndez Otero, J. Jesús Arriaga Rodríguez, Marcelo David Iturbe Castillo	46
Design and implementation of modal dissipator in high power fiber lasers Septien Olmos, Eduardo; Guerrero Viramontes, J. Ascención; Martinez Rios, Alejandro; Toral, Daniel.	48

Using Convolution Mathematical Method for explanation on nonlocality in Kerr-Type medium with arbitrary degree of Nonlocality

Majid Hesami[1*], Mahrokh Avazpour[2], Marcela. Maribel Méndez Otero[2], J.Jesús Arriaga Rodríguez[1], Marcelo David Iturbe Castillo[3]
1-Instituto de Física"Ing. Luis Rivera Terrazas" Av. San Claudia Y BLVD. 18 Sur, Col. San Manuel, C.P. 72570, Puebla, Puebla, México
2- Facultad de Ciencias Físico-Matemáticas, Benemérita Universidad Autónoma de Puebla, Av. San Claudio y 18 Sur. Col San Manuel, C.P. 72570, Puebla, Puebla, México
3- Instituto Nacional de Astrofísica, Óptica y Electrónica, Luis Enrique Erro # 1, C.P. 72840 Tonantzintla, Puebla, México.
*hesamistudent@gmail.com

Abstract: At the first we demonstrated that it is possible to define the effect of nonlocality in Non-Linear-Schrodinger-Equation (NLSE) with mathematical method of integration that is called Convolution. And by changing one factor on Nonlocal-Response-function of medium we can control the degree of nonlocality. So that we made it easy to study the way that standard soliton behaves during propagation, and finally by iteration algorithm over width of initial beam it is presented that is possible to have Bright spatial optical soliton with some oscillation that is called Quasi-Soliton. All the calculation and graphs are done by numerical method with the Matlab software.

1. Introduction

One purpose of modern nonlinear optics is to accelerate transferring data in the best way and avoid losing energy of beam due to diffraction with the help of compensation of diffraction effect and self-focusing that requires employing optical spatial solitons which keeps constant transversal area of beam. In this case wave induces a waveguide, so that light can guide light with fundamental concept of soliton propagation in Kerr medium [1]. In Kerr medium, refractive index has intensity dependency. When intensity response in medium solely is measured at exact point of medium, we have Local medium, however for other type of medium, intensity response of medium has dependency over neighborhood points (Nonlocal medium)[2]. So that for solving NLSE that includes nonlocality, we are going to solve it numerically by usage of convolution code in Matlab software. We are doing iteration over width of initial spatial soliton function for obtaining best spatial soliton width.

2. Experimental Methodology

In the Local case that refractive index has the form of $n(I) = n_0 + n_2 I$, that n_0 is linear refractive index and n_2 is Kerr-coefficient, and our NLSE has the form of equation (1).

$$\frac{\partial^2 A(x,z)}{\partial x^2} + 2in_0k_0\frac{\partial A(x,z)}{\partial z} + (n^2(I) - n_0^2)k_0^2 A(x,z) = 0 \tag{1}$$

After normalization process in equations (2), such that $X = \frac{x}{\omega_0}, Z = \frac{z}{Z_R}, Z_R = \frac{n_0 \pi \omega_0^2}{\lambda_0}, A(x,z) = \sqrt{I_m}q(x,z)$, we have normalized NLSE (2). ω_0 is initial width of beam in z=0, and Z_R is Rayleigh range, L_{NL} is Self-focusing distance, and I_m is maximum intensity.

$$-\frac{i\partial q(x,z)}{\partial Z} = \frac{1}{4}\frac{\partial^2 q(x,z)}{\partial x^2} + \eta |q(x,z)|^2 q(x,z) \ , \qquad \eta = \frac{Z_R}{L_{NL}} = 1 \tag{2}$$

The relation $Z_R = L_{NL}$ has to be valid for compensating effect of diffraction with self-focusing. The equation (2) is NLSE for local medium. And one of its answers is Bright spatial soliton $q(X,Z) = Sech\left(\sqrt{2}\,X\right) * \exp\left(\frac{iZ}{2}\right)$. However for nonlocal medium the response function R(X) as a Gaussian function with some normalization characteristics[3], is employed as written in equation (3). Then Nonlocal NLSE (4) is obtained.

$$R(X) = \frac{1}{\alpha\sqrt{\pi}}\exp\left(-\left(\frac{X}{\alpha}\right)^2\right) \quad , \quad \int_{-\infty}^{+\infty} R(X)dX = 1 \tag{3}$$

$$-\frac{i\partial q(X,Z)}{\partial Z} = \frac{1}{4}\frac{\partial^2 q(X,Z)}{\partial X^2} + \eta\, q(X,Z)\int_{-\infty}^{+\infty} R(X-X')q(X',Z)dX' \tag{4}$$

Convolution code in Matlab is used to calculate the integral part of equation (4). Value of α is defining the degree of nonlocality. When it is less than 1, we have locality, and by increasing its value, nonlocality also increase. Here $\alpha = 10$ is demonstrating the highly nonlocal. In below figures secant hyperbolic function is used by equation (5).

$$q(X,Z) = 1 * Sech\left(\frac{X}{b}\right) \tag{5}$$

In local case, value of b in equation (5) is $b = \frac{1}{\sqrt{2}} = 0.7071$. Here in Fig.1 and Fig.2 we keep this width.

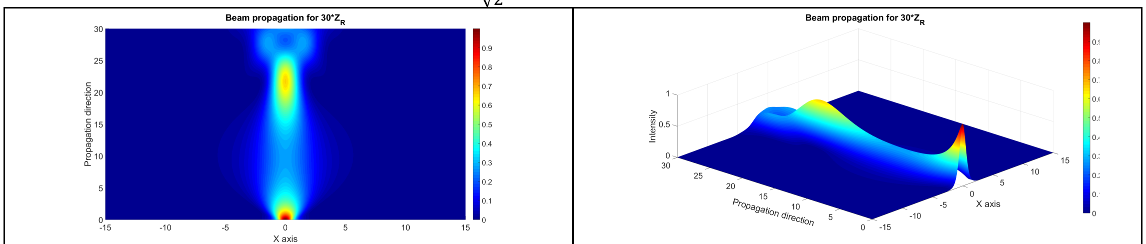

Fig. 1. $\alpha = 5$, $b = 0.7071$

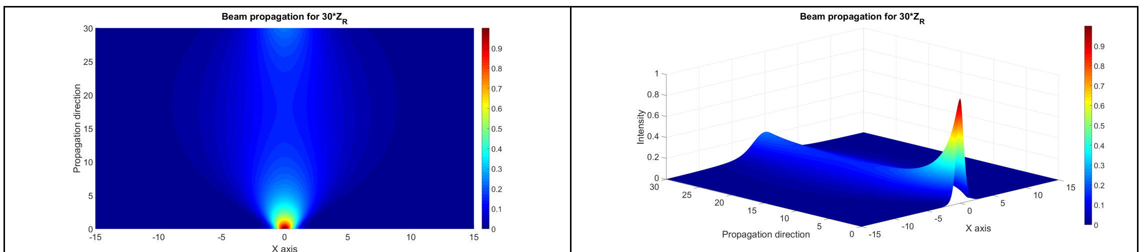

Fig. 2. $\alpha = 10, b = 0.7071$

By iteration over width (b) of initial secant hyperbolic beam we can obtain the best width for having quasi-soliton .

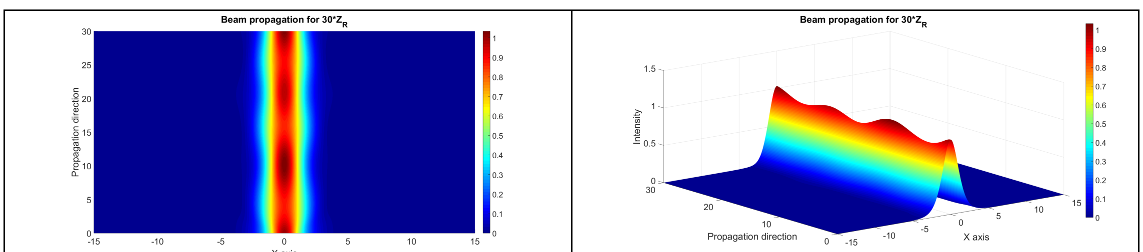

Fig. 3. $\alpha = 5,\ b = 1.4$

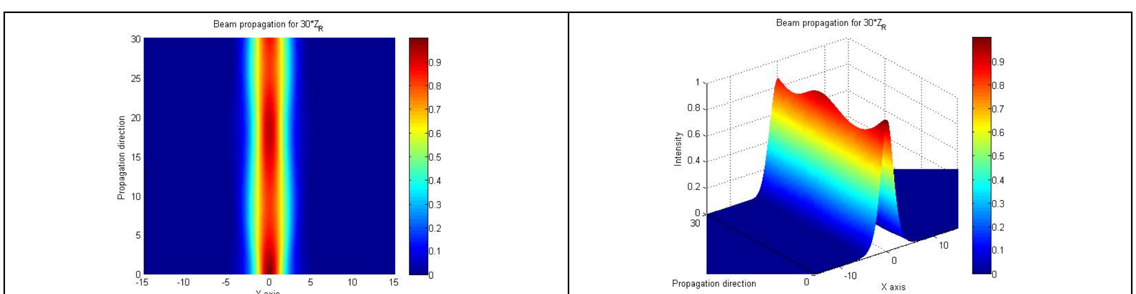

Fig. 4. $\alpha = 10,\ b = 1.8$

3. References

[1] Kivshar Y S and Stegeman G I, Solitons Guiding Light for Future Technologies Opt. Photonics News 59–63(2002)

[2] Królikowski W and Bang O, Solitons in nonlocal nonlinear media: Exact solutions Phys. Rev. E - Stat. Nonlinear, Soft Matter Phys. **63** 1–6(2001)

[3] Shi X, Guo Q and Hu W, Propagation properties of spatial optical solitons in different nonlocal nonlinear media with arbitrary degrees of nonlocality Optik (Stuttg). **119** 503–10, (2008)

Design and implementation of modal dissipator in high power fiber lasers

Eduardo Septien Olmos[1], J. Ascención Guerrero Viramontes[1], Alejandro Martinez Rios[2], Daniel Toral[2]

[1]TecNM/Instituto Tecnológico de Aguascalientes. Adolfo López Mateos Ote. No. 1801, Fracc. Bona Gens, 20256 s
[2]Centro de Investigaciones en Óptica A.C. Lomas del Bosque 115, Campestre, 37150 León, Gto

Abstract: The work seeks to find a suitable method for the elimination of the unwanted light in the cladding in the fibers for high power lasers, performing in the first instance the modification of the structure of the coating using a femtosecond laser associated to a device of micro machining. In the second instance, it is sought to coat the treated area with soft metals such as aluminum (Al), tin (Sn), Gold (Au) and Indian (In) as the studies show that the soft metals are suitable in the extraction of unwanted light in cladding for high-power fiber lasers [1]. Also, the experiments show that the contact area must be optimized to obtain the highest attenuation and thermal load in the high power fiber lasers and to avoid localized heating.

1. Theoretical Considerations

A Modal Heatsink (Pump Power Stripper), is an ideal device to eliminate the residual power of pumping, the ASE and the modes of escape of the core of the inner lining of the fibers of double coating, preserving at the same time a minimum degradation of the power of the signal and beam quality (M2). Reflected The strength of the signal in the inner cladding can also be eliminated with this method. The ability to handle release power is up to 800W or even higher. [2]

2. Objective

Perform methods to modify the physical structure of the coating that allows the modal dissipation in a high power laser and efficiently eliminate the associated generated heat.

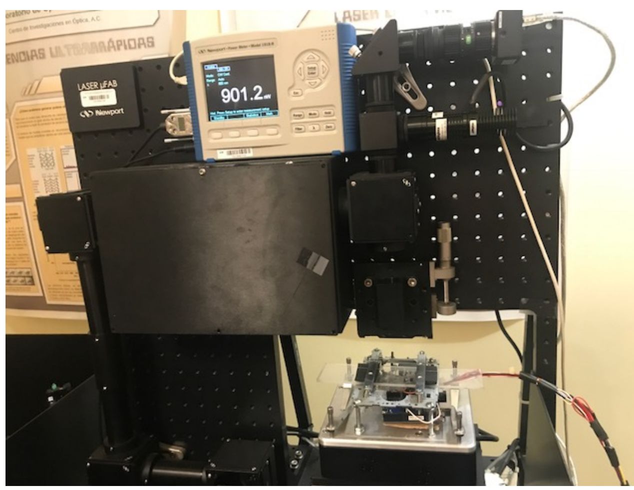

Fig. 1 Newport µfab laser machining center where the modification of the laser fiber coating is performed. With the device to rotate the fiber in the coating.

3. Materials and methods

The work sought to find a suitable method for the elimination of unwanted light in the cladding in the fibers for high power lasers, performing in the first instance the modification of the structure of the coating using a femtosecond laser associated with a device of micro machining.

For the modification of the optical fiber coating, a microfabricated microtitre center from Newport was used, which receives a source of a femtosecond laser with a pulse of 50 fs., Coherent pound HE to perform the laser machining. Because the micromachining center has three degrees of freedom, displacements in x, y and z. It became necessary to design a mechanism that would allow the fiber to rotate and create another degree of freedom so that the laser power modifies the entire perimeter of the fiber. The main difficulty is to rotate the fiber in a constant way and without exerting too much pressure on the fastening points. And that at the same time this mechanism does not interfere with the focus lens of the laser, as it is a microscope objective, the spot is very close to the lens, the proposed solution is a traction mechanism that converts a linear movement into one of rotation with which we are allowed to make the first machinations to different types of fiber.

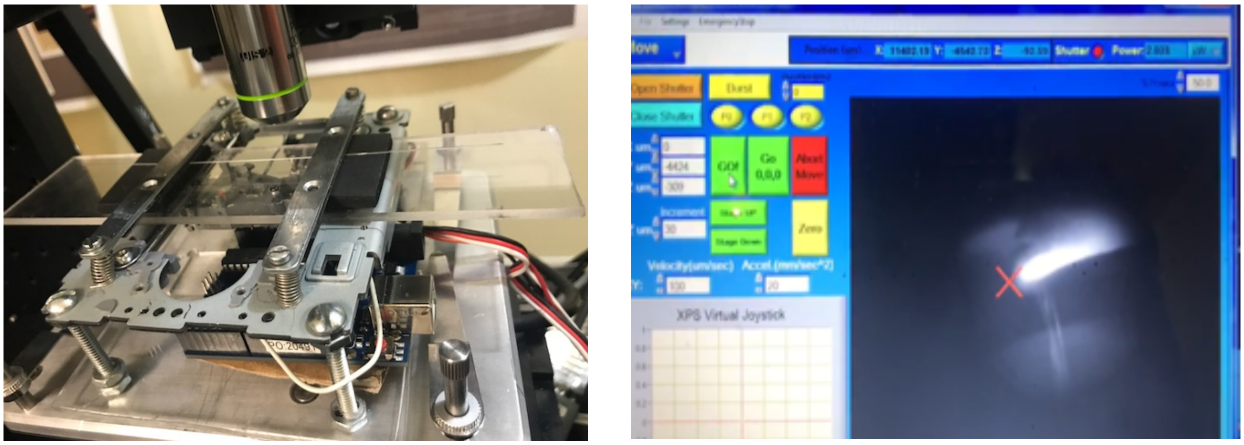

Fig. 2 Mechanism of rotation for the fiber on the table of translation of the center of micro machining (A); laser modifying the cladding structure of the fiber (B).

4. Results

It has managed to create a mechanism that allows rotating the optical fiber in the center of micro machining, so micro-machining tests are carried out on fibers of different thicknesses in which they are going to perform light tests where they will be analyzed the power input and output in the core, and a second analyzing the input and output of light throughout the fiber.

If the tests come out satisfactorily, the modified area will be covered with different types of soft metal such as gold (Au), tin (Sn), or Indian (In), seeking to create the best contact area between the metal and fiber, perform the characterization of the modified fibers and compare the results obtained between the modified cladding with laser without and with coating to look for the most economical and efficient option for the modal dissipation.

References

[1] Amin Babazadeh, Et all., “Robust cladding light stripper for high-power fiber lasers using soft metals”. Iranian National Center for Laser Science and Technology, Tehran, Iran. published 15 April 2014

[2] Jon Martínez De Mendivil Varas, “Láseres integrados en dobles tungstatos y niobato de litio basados en guías de onda”. Tesis Doctoral, Universidad Autónoma De Madrid, Facultad De Ciencias Departamento De Física DE Materiales, Madrid, 2015

Extended Abstracts

Session
MICRO OPTOELECTRO MECHANICAL SYSTEMS

Pg.

Photonic microsystem made by dynamic micro-assembly 51
N. Courjal, A. Caspar, C. Eustache, F. Behague, M. Suarez, R. Salut, J.-Y. Rauch, O. Lehmann, V. Calero, C. Clevy, P. Lutz, M-P. Bernal

Instrumented Nano-Tweezer based on Opto-Mechatronic approach 53
César Martinez Mozo, Cédric Clévy, Houari Bettahar, Djaffar Belharet, Nadège Courjal and Philippe Lutz

Piezo-actuated Adaptive Prisms for Optical Scanning 55
Florian Lemke, Pascal M Weber, Ulrike Wallrabe, Matthias C Wapler

Fabrication of an Adaptive Micro Fresnel Mirror Array 57
Binal P Bruno, Ruediger Grunwald, Ulrike Wallrabe

Photonic microsystem made by dynamic micro-assembly

N. Courjal *, A. Caspar, C. Eustache, F. Behague, M. Suarez, R. Salut, J.-Y. Rauch, O. Lehmann, V. Calero, C. Clevy, P. Lutz, M-P. Bernal
FEMTO-ST institute, Université de Bourgogne-Franche-Comté 15B avenue des Monboucons, 25030 Besançon, FRANCE
nadege.courjal@femto-st.fr

Abstract: We report on the production of hybrid photonic microsystem made by the dynamic structuration and assembly of photonic building blocks in F.I.B. (Focused Ion Beam) environment. More particularly, we show how to produce a low-loss integrated $LiNbO_3$ resonator composed of a free-suspended microguide and a microdisk, which shows great potential for electro-optic sensors or comb generators. The method opens the way toward new 3D electro-optical or mechanical hybrid photonic micro and nanosystems.

1. Introduction

While photonics is emerging as an attractive alternative to electronics in high-bit-rate telecommunication systems, sensors or signal processing devices, there is a need of specific 3D photonic architectures that cannot be easily engineered by clean-room processes. As an example there is a great interest in developing lithium niobate ($LiNbO_3$) integrated microresonators for applications as varied as integrated gyrometers, sensors, spectrometers, dynamic filters or modulators. However, the low-loss integration of $LiNbO_3$ micrometer scale resonators with an input/output waveguide is still a critical issue. A tapered fiber coupled with a microdisk [1] is too fragile to be envisioned as a commercial solution. The monolithic integration, where both the waveguide and the microresonator are produced on the same wafer by clean room processes, can lead to high quality factors (> 10^5) and low propagation losses (< 1 dB/cm) [2-5], but the insertion losses are usually higher than 10 dB due to the large mode mismatch between the fibers and the confined microguides. Here we propose to reduce significantly the coupling losses by dynamically structuring and assembling a pigtailed low-loss microguide [6] and a $LiNbO_3$ microdisk. The proposed method can advantageously be extrapolated to 3D electro-optical or mechanical photonic microsystems.

2. Model, fabrication and preliminary results

The proposed hybrid microsystem is depicted in Fig. 1(a). It is made of a locally thinned $LiNbO_3$ waveguide coupled with a microdisk. In the free-standing-section, the waveguide has a thickness of 2 µm. The waveguide is surrounded by electrodes allowing an electro-optic control of the operating point. A local etching is performed on both sides of the waveguide to confine the light laterally (see bottom of Fig. 1(b)), while measuring simultaneously the optical transmission. This approach allows to preserve low insertion losses, and to prepare a strong coupling with a photonic element placed at te top of the ridge. A microdisk is fabricated separately and is assembled dynamically at the waveguide top. Hence, the insertion losses and the microdisk coupling are optimized separately.

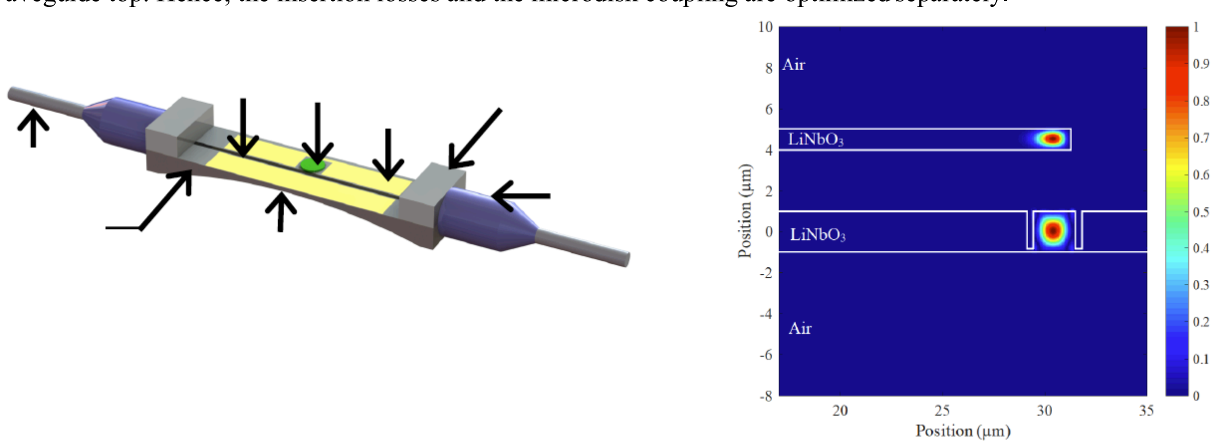

(a) (b)

Figure 1: pictures of the proposed component. (a) Schematic diagram of the pigtailed $LiNbO_3$ microdisk. (b) Cross section of the electric fields in the disk (top) and in the suspended ridge (bottom). The calcultation are performed by finite element method (F.E.M.), COMSOL®.

F.E.M. based numeric calculations were performed for different photonic architectures. An overview of the calculated modes is seen in Fig. 1(b) for a 2 μm-thick waveguide and a 1 μm-thick microdisk. Noteworthy, a ridge configuration (see Fig. 1(b)) increases the coupling efficiency. Calculations also show that the coupling is optimal when the disk is positioned at the waveguide top.

Firstly, the microguide was fabricated through standard techniques (lithography, Ti-diffusion, deposition of electrodes), and then the substrate was locally thinned down to 2 μm by precise dicing as described in [6]. The tapers were obtained by lifting the blade before the end of the waveguide. The free-suspended waveguide was pigtailed to two SMF28 fibers, as represented in Fig. 1(a). The measured propagation losses are of 0.2 dB/cm for both propagating polarization, and the insertion losses are lower than 3 dB. Noteworthy, a high index UV-adhesive was used for pigtailing, so as to limit the Fabry-Perot effect between the input and output of the waveguide.

The micodisk was produced through precise dicing followed by Focused Ion Beam (FIB) milling, as seen in Fig. 2. Finally, the pigtailed waveguide and the microdisk were assembled in the FIB environment. A lateral etching was performed on both sides of the waveguide by FIB milling, leading to a local ridge surrounded with tapers in the suspended section. A microgriper was used to grip the disk and to place it accurately at the top of the waveguide. The precise assembly can be optimized by measuring the transmitted response through the guide simultaneously with the positioning. This method has been validated for 1 μm to 4 μm-thick midrodisks, with diameters ranging from 50 μm to 300 μm. Preliminary results show a quality factor of 3887.

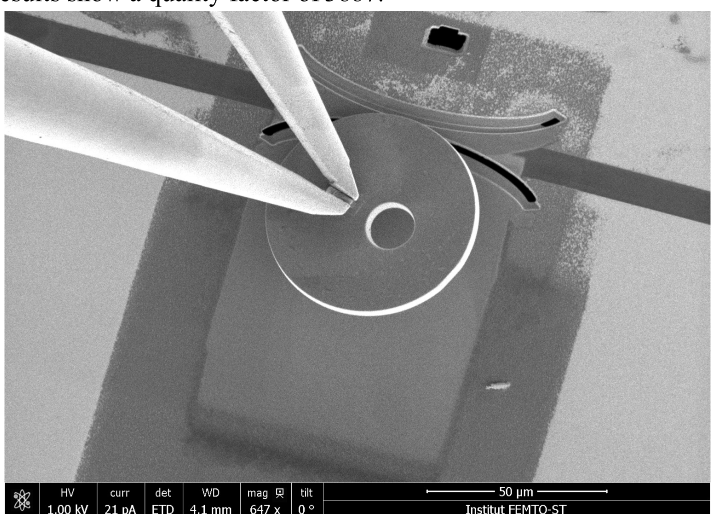

Figure 2: SEM image of a microdisk in a membrane before being micromanipulated with a needle.

3. Conclusion

We propose a micromanipulation-based technique to produce low-loss 3D photonic microsystems. In particular, a low-loss integrated $LiNbO_3$ microresonator is demonstrated, opening the way toward new 3D photonic architecture with dynamically optimized photonic responses.

References

[1] M. Wang, F. Bo, S. Wan, W. Li, F. Gao, J. Li, G. Zhang, and J. Xu, “ On-chip electro-optic tuning of a lithium niobate microresonator with integrated inplane microelectrodes », Opt. Express **23**, 23072-23078 (2015).

[2] C. Wang, M. Zhang, B. Stern, M. Lipson, and M. Lončar, "Nanophotonic lithium niobate electro-optic modulators," Opt. Express **26**, 1547-1555 (2018).

[3] I. Krasnokutska, J.-L. J. Tambasco, X. Li, and A. Peruzzo, "Ultra-low loss photonic circuits in lithium niobate on insulator," Opt. Express **26**, 897-904 (2018)

[4] A. Rao and S. Fathpour, “Compact electro-optic modulators”, IEEE Journal of Selected Topics in Quantum Electronics **4,** 1-14 (2018).

[5] M. Zhang, C. Wang, R. Cheng, A. Shams-Ansari, and M. Lončar, "Monolithic ultra-high-Q lithium niobate microring resonator," Optica **4**, 1536-1537 (2017).

[6] N. Courjal, A. Caspar, V. Calero, G. Ulliac, M. Suarez, C. Guyot, and M.-P. Bernal, "Simple production of membrane-based $LiNbO_3$ micro-modulators with integrated tapers," Opt. Lett. **41**, 5110-5113 (2016)1

Instrumented Nano-Tweezer based on Opto-Mechatronic approach

César Martinez Mozo, Cédric Clévy, Houari Bettahar, Djaffar Belharet, Nadège Courjal and Philippe Lutz
FEMTO-ST Institute, CNRS, Univ. Bourgogne Franche-Comté, UFC, ENSMM 24 rue Savary 25000 Besançon, FRANCE
cedric.clevy@femto-st.fr

Abstract: This paper presents the design and development of a robotic tweezer for nanomanipulation purpose that can meet together high positioning accuracy and manipulation abilities. Indeed, the gripper combines an innovative actuation principle based on smart materials (thick piezoelectric films) and integrated optical fibers (using Fabry-Perot interferometry) that enables online position measurement and gripping force estimation. The paper introduces the general principle of the gripper, its design and first experimental characteristics that validate the proposed working principle and demonstrates the very high potential of the nano-tweezer for many tasks at the micro and nanoscales.

1. Introduction

Robotics pays a very high and again growing interest to investigate micro and nanoscales especially robotic gripping approaches that enables to achieve complex tasks with a high versatility and dexterity [9][10]. The capabilities and performances of microgrippers directly influence the task to be done, reason why many micro and nanogrippers have been proposed [6][7]. In terms of actuation, widespread approaches relies on smart materials due to their capability to achieve high resolution motions in very confined spaces. Scaling down issues fully change the paradigm of motion generation especially when targeting nanomanipulation tasks. Electrothermal actuation notably enables to generate very large motions within very small volumes [4][5] but whose control to achieve tasks with high accuracy still appears as a challenge. Alternatively, piezoelectric actuation that is extensively used for microscale purposes shows much less interest for nanoscale application due to too high stiffness intrinsinc to bulk materials used. To meet high performances and small free space together, an emerging solution consisting in using thick piezoelectric films is employed in our works [1][12]. Also, despite well known and modelled behavior, the open loop control of piezoelectric actuators still appears limited to the micrometer range [3]. Targeting nanomanpulation thus requires closed loop control [8][11]. Among existing approaches we chose to use an integrated optical principle consisting in using an optical fiber and the Fabry-Perot interferometric principle to estimate the displacement of the tweezers tips.

2. Working principle

The gripper includes two beams made of piezoelectric thick films. They are 4mm long and built along a monomorph architecture combining a piezolayer of 21 μm thickness and a passive layer made of Nickel with 7 μm thickness. This architecture enables to have high electric fields and low stiffness of the beams resulting in very large deformations for low voltages. Typically, voltages less than 10 volts induce displacement of 120 μm at the end ofthe beam.

This tweezer has been instrumented using optical fibers (monomode with λ=1550 nm wavelength) and small reflective mirrors integrated onto every tweezer jaw. Between them an optical cavity exists where the Fabry Perot interference happens, this optical signal is then used as reported in [2]. The resulting optical signal induces fringes such as shown in Fig. 2 (left-bottom) that enables to estimate the displacement of the tip of every tweezer jaw considering that every fringe induces a displacement of $\lambda/2$. A force estimator has also been proposed based on Ballas modelling to derive the force estimation based on the known voltage input and the measured displacement. Fig. 1 highlights the general principle of the gripper and a picture of its realization as well as a picture of the experimental bench that has been developed for its characterization.

3. Experimental validation of the approach

The proposed instrumented smart nano-tweezer has been characterized using the experimental bench displayed in Fig. 2 (b). A keyence laser is notably used as reference displacement sensor. Also a force sensor from the TEI company is used as reference force sensor. A ramp input voltage is applied to the tweezer beam as displayed in Fig 2 (top left). The initial conditions make that the beam has no contact, as a consequence the beam starts bending (named free displacement) step. After 20 seconds, the tip of the beam comes into contact with the external/reference force sensor, this step is named “constraint displacement”. Fig. 2 left bottom shows the optical signal including the interferences fringes. Fig 2 right displays the measured displacement and estimated force based on this optical signal that are in good adequation with expected behavior but that also show the capability to combine simultaneously position measurement and force estimation at high resolution in a extremely integrated manner. These results validate the proposed approach and clearly state the interest for instrumented nanotweezers combining thick piezoelectric films and displacement measurement/force estimation based on optical Fabry Perot interferometry principle.

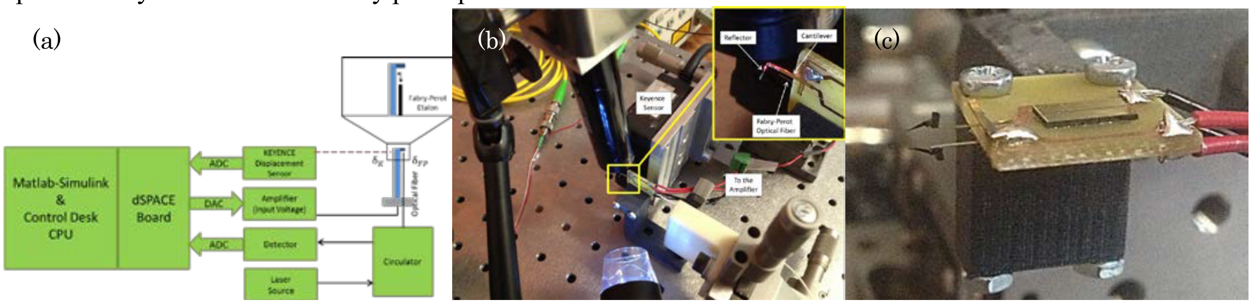

Fig. 1: (a) Principle scheme of one tweezer finger (b) experimental set-up for the characterization of microgrippers fingers (c) instrumented tweezer including piezoelectric beams, passive gripping tools and optical components.

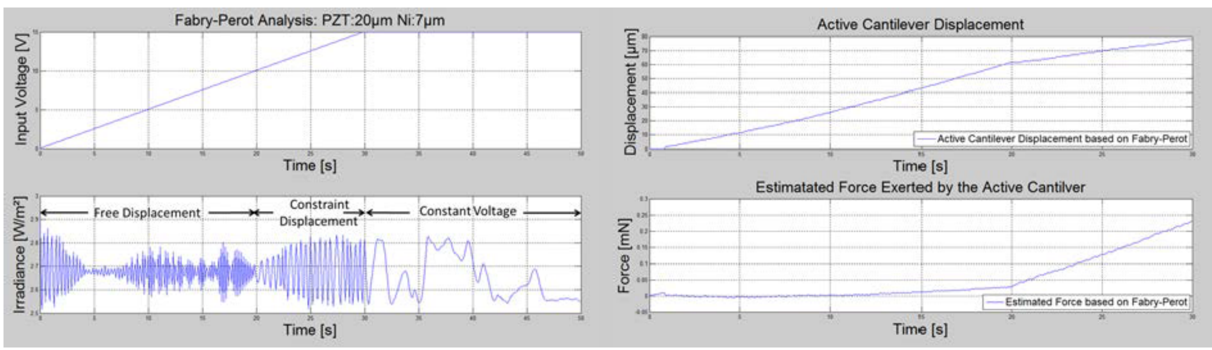

Fig. 2: Experimental results of the instrumented microgrippers fingers showing the voltage/displacement/force behaviors, displacement and force being estimated using voltage input and optical irradiance measurement.

References

[1] A. Bienaimé, V. Chalvet, C. Clevy, T. Baron L. Gauthier-Manuel, and M. Rakotondrabe. Static/dynamic trade off performance of pzt thick film micro actuators. Journal of Micromechanics and Microengineering, 2015.

[2] H. Bettahar, A. Caspar, C. Clevy, N. Courjal and P. Lutz. Photo-Robotic Positioning for Integrated Optics. IEEE Robotics and Automation Letters, Vol. 2, No.1, January 2017.

[3] M. Rakotondrabe, Y. Haddab and P. Lutz. Nonlinear modeling and estimation of force in a piezoelectric cantilever. IEEE/ASME - AIM, (International Conference on Advanced Intelligent Mechatronics), Zurich Switzerland, Sept 2007.

[4] N. Chronis and L. P. Lee. Electrothermally Activated SU-8 Microgripper for Single Cell Manipulation in Solution. Journal of Microelectromechanical Systems.

[5] K. Kim, X. Liu, Y. Zhang and Y. Sun. Nanonewton force-controlled manipulation of biological cells using a monolithic MEMS microgripper with two-axis force feedback. Journal of Micromechanics and Microengineering. 2008.

[6] F. Beyeler, A. Neild, S. Oberti, D. Bell, Y. Sun, J. Dual, B. Nelson. Monolithically Fabricated Microgripper With Integrated Force Sensor for Manipulating Microobjects and Biological Cells Aligned in an Ultrasonic Field. Journal of Microelectromechanical Systems. 2007.

[7] Y. Haddab, N. Chaillet, A. Bourjault. A Microgripper Using Smart Piezoelectric Actuators. Proceedings of the 2000 IEEE/RSJ International Conference on Intelligent Robots and Systems. 2000.

[8] Micky Rakotondrabe and Ioan Alexandru Ivan. Development and Force/Position Control of a New Hybrid Thermo-Piezoelectric MicroGripper Dedicated to Micromanipulation Tasks. IEEE Transactions on Automation Science and Engineering. 2011.

[9] J. E. Jang, S.N. Cha, Y. Choi, D. J. Kang, D. G. Hasko, J. E. Jung, J. M. Kim and G. Amaratunga. A Nanogripper Employing Aligned Multiwall Carbon Nanotubes. IEEE Transactions on Nanotechnology. 2008.

[10] S. Akita and Y. Nakayama. Manipulation of Nanomaterial by Carbon Nanotube Nanotweezers in Scanning Probe Microscope. The Japan Society of Applied Physics. 2002.

[11] M. Rakotondrabe, Y. Haddab and P. Lutz. Nonlinear modeling and estimation of force in a piezoelectric cantilever. IEEE/ASME - AIM, (International Conference on Advanced Intelligent Mechatronics), Zurich Switzerland, Sept 2007.

[12] A. Benouhiba, D. Belharet, A. Bienaimé, V. Chalvet, M. Rakotondrabe & C. Clévy, Development and characterization of thinned PZT bulk technology based actuators devoted to a 6-DOF micropositioning platform, Microelectronic Engineering, May 2018.

Piezo-actuated Adaptive Prisms for Optical Scanning

Florian Lemke, Pascal M Weber, Ulrike Wallrabe, Matthias C Wapler
Department of Microsystems Engineering – IMTEK, Laboratory for Microactuators, University of Freiburg, Georges-Koehler-Allee 102, 79110 Freiburg, Germany florian.lemke@imtek.uni-freiburg.de

Abstract: We present two different piezo-actuated adaptive prisms with apertures ≥8 mm based on a tiltable glass window on top of an optical fluid. In the first prism, we realized a simple monoaxial scanner based on a lever principle. In our second design, we extended the scanning to two axes using three individually controllable piezo cantilevers. We were able to prove the concept of our continuously variable prisms and achieved tilt angles up to ±3.7° with response times of 36 ms.

1. Introduction

While novel microscopes use focal power adaptive lenses for focusing and aberration correction along the z-axis [1, 2], scanning perpendicular to the beam path requires 1d- or 2d-scanners [3]. These scanners normally work with tilting mirrors, leading to a complex beam path and a bulky setup. Furthermore, most of the scanners operate in resonance, which enables high scanning rates and enhanced deflection angles, but does not allow for a continuous measurement at a static position. Existing transmissive prism concepts, based on liquid crystals [4] or electro-wetting [5], provide only monoaxial scanning or a non-continuous scanning in steps for two dimensions.

For continuous actuation, to enable static measurements and to reduce the beam path complexity using a transmissive instead of a reflective scanner, we developed and characterized two different adaptive prisms. The basic concept is based on a tiltable rigid glass substrate that is located on top of a flexible chamber filled with an optical fluid and is actuated using piezo bimorph bending beams (fig. 1). The two different configurations (fig. 2) provide mono- or biaxial scanning ability and will have different scanning speeds and scanning angles.

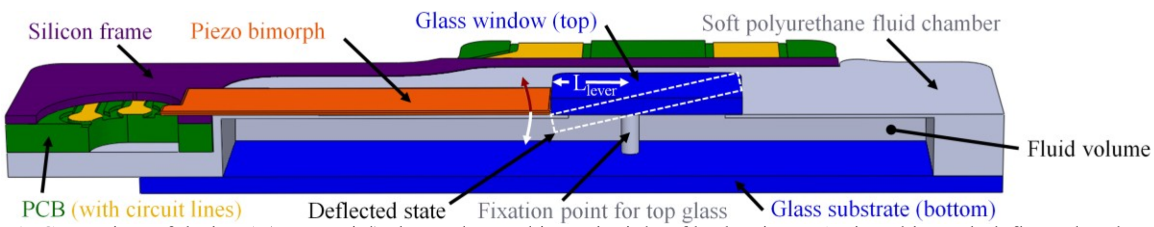

Figure 1: Cross view of design 1 (monoaxial) shows the working principle of both prisms: A piezo bimorph deflects the glass window, what leads to a tilt. An incident light beam refracts according to Snell's law, when the chamber contains a fluid (n ≠ 1).

2. Design

The first design is a monoaxial prism with a lever actuation principle (fig. 1, 2a) that we actuate using a piezo-bimorph actuator with a length L_{piezo}=21 mm and a rather large width W_{piezo}=10 mm. For a given piezo thickness t_{piezo}=120 µm, a piezoelectric coefficient d_{31} and an applied symmetric voltage V, we can approximate the deflection D at the tip of the beam (neglecting forces) and the corresponding tilt angle α:

$$D \approx \frac{L_{piezo}^2 d_{31} V}{{t_{piezo}}^2}, \qquad \alpha \approx \arcsin\left(\frac{D}{L_{lever}}\right) \quad . \quad (1)$$

The lever in combination with the high force of the rather wide beam leads to a high deflection angle, with the drawback that it provides only monoaxial scanning. We choose L_{lever}=4.5 mm for our prototype with a glass window of 11mm, but this can be changed to adjust the maximum deflection angle.

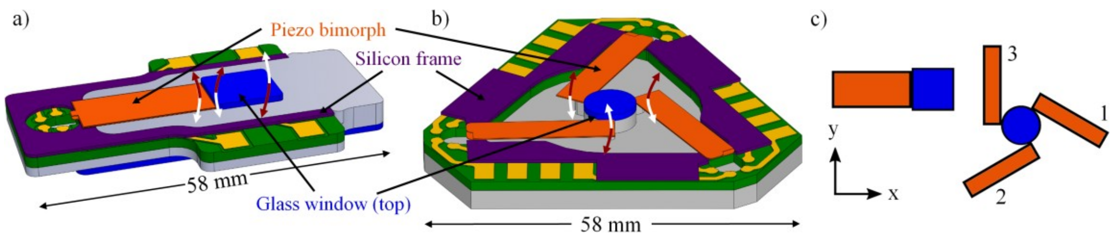

Figure 2: a) Monoaxial prism and b) biaxial prism: Direction of positive/negative bending movement indicated by red/white arrows for tilt in one example direction. c) Alignment of prisms for measurement with beam numbers.

Our second design (fig. 2b), uses three piezo bimorph beams with L_{piezo}=21 mm and W_{piezo}=5 mm, enabling biaxial scanning. The beams tilt three points along the circumference of a circular glass window (diameter d= 9mm) using elastic hinges that are integrated into the fluid chamber. The top glass now tilts approximately around the center point, reducing the mass of the displaced fluid and setting L_{lever} essentially to half of the aperture.

3. Fabrication

We first detach piezos sheets from sound buzzers (Ekulit) with an exceptionally high d_{31}=487 pm/V [6] and laser structure them. Then, we glue these to bimorph bending beams, using hard polyurethane (shore hardness 80D). Then, we glue these parts to the silicon frame and to the molded fluid chamber, made from soft polyurethane (shore hardness 50A). Subsequently, we close the chamber with a glass substrate from the bottom and we add the upper glass window. Finally, we inject the optical fluid (paraffin oil, n=1.48) into the chamber using syringes.

4. Measurement & Evaluation

We measure the deflection of the top glass by scanning with a confocal distance sensor to obtain the tilt and actuation speed. To determine the maximum deflection angle, we use a quasi-static sinusoidal actuation to avoid the creeping effects of the piezos. For both prisms, we apply voltages with a phase delay of 180° to the upper and lower piezo to bend the beams, limited between V_{min}=-50 V and V_{max}=150 V to avoid depolarization and electrical breakdown. Fig. 3 shows that the lever prism tilts as expected only along the X-axis with an approximately linear voltage dependence and a total tilt angle of 7.4°. For the biaxial prism, we postulated a voltage trajectory that outlines the working range by bending the beams up (150V/-50V), neutral (0V/0V) or down (-50V/150V) in all possible combinations. The results in figure 4 show, that the minimum working range is 2.0° in the directions between the beams and the maximum range is 2.6° along the tilt directions of the beams. There appears a small misalignment of the axes by 8.8° and beam 2 achieves 16.2% less displacement than the other beams. The dashed line shows a circular rotation applying sinusoidal voltages with phase shifts of 120° to all beams. In fig. 3c we find a the response time from 0 to 90% of the maximum deflection is 36 ms for the monoaxial prism and for the biaxial prism 59 ms for a tilt along the X-axis actuating beams 1,2 and 3 and 82 ms along the Y-axis actuating beams 1 and 2. (fig. 3c); the drop times are similar.

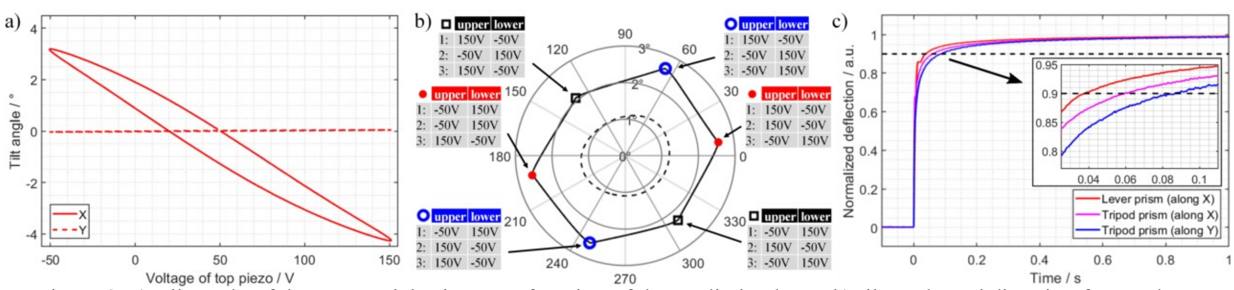

Figure 3: a) Tilt angle of the monoaxial prism as a function of the applied voltage, b) tilt angle and direction for a voltage trajectory outlining the operating region of the biaxial prism (solid, beam numbers see fig. 2c)) and circular voltage trajectory (dashed), c) normalized deflection for a voltage step from minimal to maximal deflection (step applied at time t=0 s)

5. Conclusion and outlook

We successfully demonstrated the proof of concept for two continuously adjustable adaptive prisms with one- and two-dimensional scanning ability with apertures of 11 mm and 9 mm, respectively. We found, that the monoaxial prism achieved the highest scanning angle of 7.4° and gave the shortest response time of 36ms. By adjusting the critical dimensions of the different designs, e.g. the lever length L_{lever} or the width of the fixation point to lower counteracting forces, we can improve both prisms towards higher tilt angles or speed in the future.

[1] MC Wapler et al., "A Compact, Large-Aperture Tunable Lens with Adaptive Spherical Correction," in International Symposium on Optomechatronic Technologies, (Seattle, WA, 2014), pp. 130-133.
[2] K Philipp et al., "Axial scanning and spherical aberration correction in confocal microscopy employing an adaptive lens," in Optics, Photonics, and Digital Technologies for Imaging Applications, pp. 10679-10685 (2018)
[3] AJ Nichols et al., "Video-rate Scanning Confocal Microscopy and Microendoscopy, " *J. Vis. Exp.* 56, e3252 (2011)
[4] GD Love et al., "Liquid-crystal prisms for tip-tilt adaptive optics," Opt. Lett. 19, pp. 1170-1172 (1994)
[5] D Kopp et al., "Tubular optofluidics as a versatile optical toolbox," in 19th International Conference on Solid-State Sensors, Actuators and Microsystems (TRANSDUCERS), (Kaohsiung, 2017), pp. 866-869.
[6] BP Bruno et al., "Properties of piezoceramic materials in high electric field actuator applications," arXiv:1804.00192 [physics.app-ph].

Fabrication of an Adaptive Micro Fresnel Mirror Array

Binal P Bruno[1], Ruediger Grunwald[2], Ulrike Wallrabe[1]
[1]Laboratory for Microactuators, Department of Microsystems Engineering, University of Freiburg, Germany
[2]Max-Born-Institute for Nonlinear Optics and Short Pulse Spectroscopy, Berlin, Germany
binal.bruno@imtek.uni-freiburg.de

Abstract: In this paper, we present the fabrication of a miniaturized array of piezoelectrically tunable Fresnel mirrors, which can be used to generate propagation invariant and self-healing interference patterns. The widths of the interference patterns can be tuned by changing the tilting angles of the mirrors, which are actuated using a circular piezoelectric actuator. The array consists of four Fresnel mirrors arranged in 2x2 configuration with each mirror having an area of 2x2 mm^2. The achievable mirror angle ranges from -10 to +10 mrad.

1. Introduction

A Fresnel mirror consists of two mirror segments, inclined at a small angle to each other. The tilt of the mirrors generates a propagation-invariant, and self-healing interference pattern when illuminated with coherent light [1], the spatial frequency and extension of which depend on the wavelength and the tilt angle between the mirrors. Adaptive Fresnel mirrors were applied to adaptive pulse autocorrelation [2] and to generate laser-induced periodic surface structures [3]. In this paper, we present a further development of the first tunable Fresnel mirror designed by Brunne et al. [4] by reducing the size of the mirror from 5 mm to 2 mm in diameter and by fabricating a 2x2 array of them.

2. Design and simulation

Two movable mirror segments that meet at the center line of the device are made from a silicon wafer, coated with aluminum as a reflective layer, and are fixed on a soft silicone (PDMS) layer. The mirrors are actuated by a piezoelectric bimorph bending disc attached to the PDMS layer (figure 1 (a) & (b)). Upon actuation, the piezo discs undergo a spherical deflection, which acts as a pressure load on the PDMS layer. As a result, the two mirrors are pulled downwards as shown in figure 1 (c) thus changing the tilting angle. The maximum achievable mirror angle depends on the thickness of the silicon wafer, the piezoelectric material used, the geometry of the hinge, the thickness of the PDMS base layer and Young's moduli of the PDMS at the hinges and base layer.
For simplicity, a single Fresnel mirror was simulated in *COMSOL Multiphysics* with quarter symmetry. The diameter of the individual actuators and the thickness and stiffness of the PDMS layers were determined using a parametric sweep with a trade-off between the achievable mirror angle and the pitch of the array. With the optimal parameters, the simulated maximum achievable mirror angle is in the range of ±12 mrad.

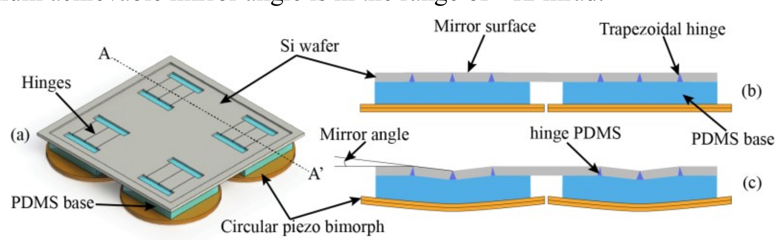

Figure 1: (a) 3D model of the 2x2 array of Fresnel mirrors each having an area of 2x2 mm^2. The actuation principle of the Fresnel mirror at cross-section (A-A') of the mirrors is sketched in (b) at 0 V and (c) at 200 V.

3. Fabrication

The fabrication of the mirror arrays starts with the etching of the mirror hinges by KOH on a 200 µm thick Si wafer. The mask opening for the etching is created by traditional photolithography methods. A 300 nm thick aluminum layer is evaporated on the front side of the wafer to get a reflective optical surface. The piezo bimorph actuator is fabricated from two 120 µm thick sheets of PZT from *Ekulit GmbH* which are glued together using high-temperature epoxy (figure 2 (a) & (b)). The PDMS base layer, with Young's modulus of 600 kPa, is fabricated directly on the bimorphs using a negative mold (figure 2 (c)). Individual 2x2 Fresnel mirror arrays are separated from the wafer by using a UV laser. The backside of the hinges is treated with an adhesion promoter, and hinges are filled with PDMS with a Young's modulus of 1.5 MPa. The piezo bimorph actuator with the silicone base layer is aligned and attached to the backside of the mirror while PDMS is being cured (figure 2 (d)). After curing, the piezo bimorph is laser structured from the back side to separate and de-couple the individual actuators for each mirror, and the mirrors are made free to move around the hinges by separating those from the front side (figure 2 (e)). The finished device is glued to a laser structured FR4 PCB-substrate (figure 2 (f)) for easier handling and providing electrical connections.

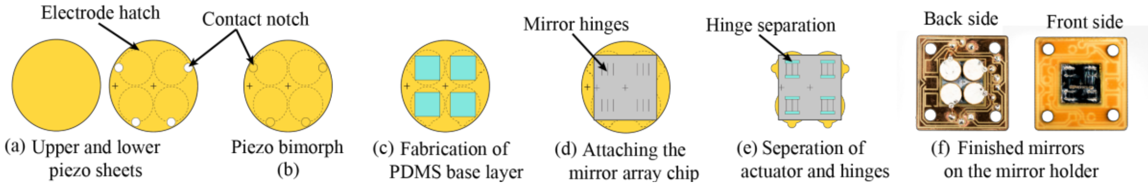

Figure 2: Process steps in the fabrication of Fresnel mirror array. The laser structured piezo sheets (a) which are glued to form a bimorph (b). Fabrication of PDMS base layer on the bimorph (c). Attaching the mirror chip (d) and separating the hinges and the individual actuators (e). Mirror holder with the contact pads for the housing (f).

4. Mechanical Characterization

The device is mounted on a custom mount, which also contains an electrical protection circuit that prevents the depolarization of the piezo sheets by limiting the voltage against the direction of polarization to 33% of the coercive field strength [5]. The mirror deflection is measured by a profilometer equipped with a confocal distance sensor while actuating at 1 Hz sinusoidal signal. The angle between the device plane and the mirror plane is evaluated for each applied electric field from the measured surface profile. The tilt angles as a function of the electric field are shown in figure 3 (a). A negative tilt angle denotes the mirrors deflecting downwards. The deflection range reaches 22 mrad, which is close to simulated results. However, each mirror shows a different, undesired pre-deflection. Typically, only negative angles are required for application, which reduces the deflection range in the symmetric case by 50%. To overcome this problem, the pre-deflection can be defined by depolarizing the piezo sheets before gluing and finally re-polarizing. The effect of this remanent strain in the piezo bimorphs is shown in figure 3 (b). The range of usable angles was increased from 10 mrad to 15 mrad.

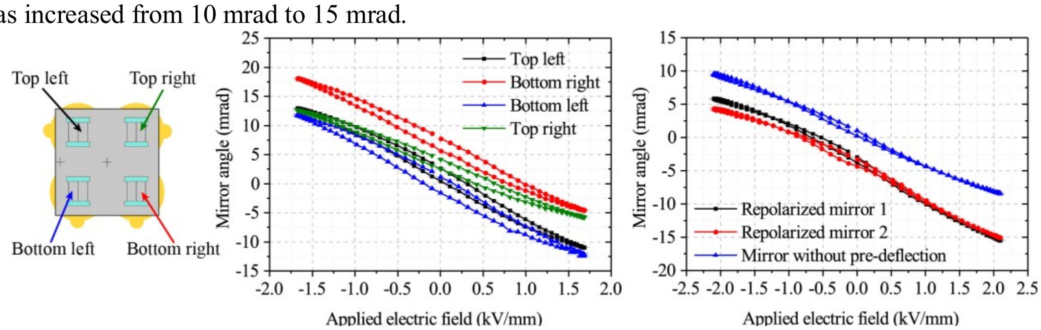

Figure 3: (a) The mirror angle as a function of the applied electric field for all mirrors in the array. (b) The defined pre-deflection in the mirror angle generated by depolarization and repolarization of the piezo bimorph actuator.

5. Summary and outlook

A Fresnel mirror array was designed and optimized using FEM simulations, which showed a maximum achievable mirror deflection of ±12 mrad, and the mechanical characterization of the fabricated device yielded similar results. However, the mirrors showed different pre-deflections among the mirrors of the same array, which is undesired as the mirrors need to be actuated synchronously. This can be reduced by introducing a defined pre-deflection by the depolarization and re-polarization of the piezo actuators. The maximum deflection range can be increased further by increasing the electric field against the polarization from 33% to 85% [6]. Further measurements such as mechanical cross talk, frequency response, and optical characteristics are needed to fully characterize the device.

[1] Fresnel A, “Theorie de la lumiere, Ouevres completes d’Augustin Fresnel, Tome II” Paris: Imperial, p 55 (1868).
[2] A. Treffer, J. Brunne, M. Bock, S. König, U. Wallrabe, and R. Grunwald, “Adaptive non-collinear autocorrelation of few-cycle pulses with an angular tunable bi-mirror, ” Appl. Phys. Lett. 108, 051103 (2016).
[3] Brunne J, Treffer A, Block M, Grunwald R and Wallrabe U, “Fast optical line shaper for ultrashort-pulse laser nanomachining” Proc. IEEE Opt. MEMS and Nanophotonics (Istanbul), pp 5-6 (2011).
[4] Brunne J, Wapler M C, Grunwald R, and Wallrabe U, “A tunable piezoelectric Fresnel mirror for high-speed lineshaping” J. Micromech. and Microeng. 23, 115002 (9pp) (2013).
[5] Ruschmeyer K, “Piezokeramik. Grundlagen, Werkstoffe, Applikationen” Renningen-Malmsheim: Expert-Verlag, p 155, (1995).
[6] Bruno B P, Fahmy A R, Stürmer M, Wallrabe U and Wapler M C, “Properties of piezoceramic materials in high electric field actuator applications” arXiv:1804.00192 [physics.app-ph] (2018).

Extended Abstracts

Session
OPTICAL IMAGING INTERFEROMETRY

	Pg.
Azimuthal Walsh filter: An interesting tool to produce 2D and 3D light structures Indrani Bhattacharya, Lakshminarayan Hazra	60
Interferometer with remote phase control module for high precision measurements of thickness and parallelism of mechanical parts Shyh-Tsong Lin, Xin-Yu Liu, Jing-Yao Lin	62
Six-degree-of-freedom interferometer for detecting geometric errors of precision stages Shyh-Tsong Lin, Chao-Ting Ma, Hong-Yu Huang, Po-Chen Lin and Yu-Hsin Lin	64
Nano-antennas excitation through visible light and response observation in the THz range with a Confocal Microscope Daniel Luis Noriega, Fernando Mendoza Santoyo, Jorge Mauricio Flores Moreno, Javier Méndez-Lozoya, Francisco Javier González	66
First Order Filtering Least-Squares Method for Phase-Shifting Interferometry O. Medina-Cázares, M. Leon-Rodríguez, A. Barrientos-García, J. Guel-Tapia	68
Measurement of the Out-of-plane Displacement Field of non-Flat Surfaces Juan Antonio Rayas, Amalia Martínez-García, Miguel León-Rodríguez	70
First photon ghost imaging by single photon counting Yasuhiro Mizutani, Hiroki Taguchi and Yasuhiro Takaya	72
Evaluating Modified-SIFs of Vibrating Composite Plates with Clamped-End Crack by Amplitude-Fluctuation ESPI Chi-Hung Hwang, Wei-Chung Wang	74
Comparison of nulling interferometry and rotational shearing interferometry for detection of extra-solar planets Beethoven Bravo-Medina, Marija Strojnik	76
Review on the Analytical Wavefront Representation by Means of Polynomials Daniel Malacara-Doblado, Francisco Javier Gantes Nuñez	78

Azimuthal Walsh filter: An interesting tool to produce 2D and 3D light structures

Indrani Bhattacharya[1], Lakshminarayan Hazra[2]
[1]Research Scholar, Department of Applied Optics and Photonics, University of Calcutta, JD-2, Sector-III, Kolkata 700106, India
[2]Emeritus Professor, Department of Applied Optics and Photonics, University of Calcutta, JD-2, Sector-III, Kolkata 700106, India
[1]bindrani03@gmail.com, [2] lakshminarayanhazra@gmail.com

Abstract: Azimuthal Walsh filters derived from radially invariant polar Walsh functions can be used as an effective tool for producing 2D and 3D light structures near the focal plane of a rotationally symmetric imaging system by manipulating far-field diffraction characteristics when used as pupil filters. Starting with the definition of azimuthal Walsh filters, this research work reports the possibility of modifying the beam structure around far-field plane by the diffraction characteristics of azimuthal Walsh filters placed at exit pupil plane when computed analytically. The asymmetrical beam produced due to the phase asymmetries introduced by azimuthal Walsh filters can be used to form gradient force trap for optical tweezers for manipulating objects of size comparable to a single atom to 100μm without mechanical contact, is also proposed in this paper.

1. Introduction

The possibility of using azimuthal Walsh filters, derived from the orthogonal set of azimuthal Walsh functions, as base functions has been proposed to manipulate the far-field diffraction patterns of imaging systems. Starting with the definition of Walsh functions, this research work reports diffraction characteristics of azimuthal Walsh filters placed at exit pupil plane has been computed analytically for far-field plane. The transverse intensity distributions along the far-field plane shows asymmetrical patterns due to the phase asymmetries introduced by them. Azimuthal Walsh filters may be used as unique pupil plane filters for tailoring 2D and 3D transverse intensity distributions near the focal plane of a rotationally symmetric imaging system.

2. Walsh functions and Azimuthal Walsh functions

Walsh functions [1] form a complete set of normal orthogonal functions [2] over a given finite interval and take the values of either +1 or -1 within the pre-specified domain except at finite points of discontinuity where the value is zero. The order of the Walsh function is equal to the number of zero crossings or phase transitions within the specified domain. Walsh functions have the interesting property that an approximation of a continuous function over a finite interval by a finite number of base functions of this set leads to a piecewise constant approximation to the function [3]. Walsh filters of various orders may be obtained from the corresponding Walsh functions by realizing values of +1 or -1 with 0 or π phase respectively.

Azimuthal Walsh function $W_v(\theta)$ of index $v \geq 0$ and argument θ over a sector bounded by 0 and 1 as inner and outer radii respectively, is defined as,

$$W_v(\theta) = \prod_{m=0}^{\alpha-1} \mathrm{sgn}\left[\cos\left(v_m 2^m \frac{\theta}{2}\right)\right] \tag{1}$$

where the integer ν can be expressed in the form,

$$v = \sum_{m=0}^{\alpha-1} v_m 2^m \tag{2}$$

where v_m are the bits, 0 or 1 of the binary numeral for ν, and 2^α is the largest power of 2 that just exceeds ν. The orthogonality condition implies:

$$\int_0^{2\pi} W_v(\theta) W_£(\theta) d\theta = \frac{1}{2}\delta_{v£} \tag{3}$$

where $\delta_{v£}$ is the Krönecker delta defined as,

$$\delta_{v£} = \begin{cases} 0, & v \neq £ \\ 1, & v = £ \end{cases} \tag{4}$$

Manipulating the values of v_m, azimuthal Walsh functions of different orders namely, zero and above can be generated.

Each azimuthal Walsh function, $W\nu$ (θ), ν = 1, 2, 3,... may be considered to be consisted of 2^N no. of sectors where the value of N depends on the order ν. For example, for W_0, W_1, W_2 and W_2, N = 4. Value of transmission T in each of the four sectors is either +1 or -1, depending upon the order of the Walsh function. Far-field amplitude distribution for each of these Walsh functions, Wν (θ) can be calculated as [4-6]:

$$A(p,\zeta) = \sum_{s=0}^{N} T_s\,[C_s(p,\zeta;\theta) - iS_s(p,\zeta;\theta)] \qquad (5)$$

where $C_s(p,\zeta;\theta)$ and $S_s(p,\zeta;\theta)$ are the real and imaginary parts of $A(p,\zeta)$ at the far-field plane and T_S the transmission factor of the pupil function given by:

$$T_s = \sum_{s=0}^{N} e^{-ik\psi_s} \qquad (6)$$

The normalized intensity point spread function at the far-field plane, $I_N(p,\zeta)$is given by:

$$I_N(p,\zeta) = I(p,\zeta)/I(0,0) \qquad (7)$$

where $I(0,0)$ is the intensity distribution at the origin of the far-field plane where p = 0, ζ = 0

The azimuthal Walsh filter W_ν (θ) of order ν = 1, 2, 3,... is placed on the exit pupil of a rotationally symmetric imaging system (Fig. 1) and the complex amplitude distribution and 2D IPSF on a transverse plane in the far-field of azimuthal Walsh filters are computed from equations (5) and (7). 3D IPSF corresponding to 2D has been generated to synthesize the asymmetrical beam pattern [7] for different orders of W_ν (θ).

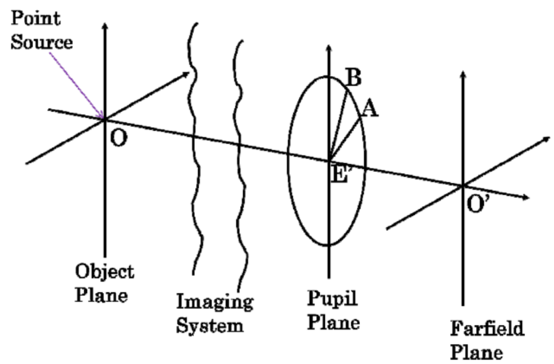

Fig. 1 Schematic diagram of a rotationally symmetric imaging system.

We have used MATLAB 2017a platform for the advance level computation and generate high-quality graphics for the study of the far-field diffraction pattern for different orders of azimuthal Walsh filters. Practical implementation of these filters can be achievable by the availability of high-speed Spatial Light modulators [7] where the in-situ generation of different orders of azimuthal Walsh filters are possible and combinations of lower order filters to achieve higher orders may be explored. Further scope of research includes efficient using azimuthal Walsh filters can be used very efficiently near the focus of an imaging system to cater the needs of complex imaging in advanced microscopy, 3D imaging, lithography, optical superresolution, optical tomography including optical micro- and nano-manipulation.

References

[1] J. L. Walsh, "A closed set of normal orthogonal functions", Am. J. Math., vol. 45, no. 1, 5 - 24, (1923).

[2] H. F. Harmuth, "Transmission of Information by Orthogonal Functions", Springer-Verlag, Berlin, pp. 31, (1972).

[3] L. N. Hazra, "Walsh filters in tailoring of resolution in microscopic imaging", Micron, vol. 38, Issue 2, 129 - 135, (2007).

[4] A. I. Mahan, C. V. Bitterli and S.M. Cannon, "Far-field diffraction patterns of Single and Multiple Apertures bounded by arcs and radii of concentric circles", J. Opt. Soc. Am.A, vol. 54, no.6, 721 - 732, (1964).

[5] R. A. Lessard and S. C. Som, "Imaging properties of Sector-shaped Apertures", App. Opt., vol. II, no. 4, 811 - 817, (1972).

[6] T. Vierke and Jürgen Jahns, "Diffraction theory for azimuthally structured Fresnel zone plate", J. Opt. Soc. Am. A, vol. 31, no. 2, 363 - 372, (2014).

[7] I. Bhattacharya, A. Saha and L.N.Hazra, "Asymmetrical PSF by Azimuthal Walsh Filters", in Advances in Optical Science and Engineering Silicon Photonics II: Proceedings of 2015 Second International Conference on Opto-Electronics and Applied Optics, Vasudevan Lakshminarayanan and Indrani Bhattacharya, Eds, IEEE Xplore Digital Library, at University of British Columbia, Vancouver, Canada, (2015).

[8] S. Mukhopadhyay, S. Sarkar, K. Bhattacharya and L. N. Hazra, "Polarisation phase shifting interferometric technique for phase calibration of a reflective phase spatial light modulator", Opt. Eng., 52, 3, 035602-1- 035602-6 (2013).

Interferometer with remote phase control module for high precision measurements of thickness and parallelism of mechanical parts

Shyh-Tsong Lin*, Xin-Yu Liu, Jing-Yao Lin
Department of Electro-optical Engineering, National Taipei University of Technology, 1, Sec.3, Chung-Hsiao East Road, Taipei 10608, Taiwan.
*Corresponding author e-mail address:f10402@ntut.edu.tw

Abstract: An innovative interferometer composed of a white light laser, phase control module (PCM), plastic fibre, and interferometric module (IM) is proposed for high precision measurements of mechanical parts in this research; where the PCM converts the beam from the laser into two co-axial beams having a direction toward the entrance of the fibre; the fibre delivers the incoming beams for a distance to the IM; and the IM, which is of the common-path apparatus, exports an interference pattern whose phase is relative to the contours of the sample and can be remotely shifted using the PCM. The proposed interferometer can therefore examine the thickness and parallelism of the sample using phase-scanning and phase-shifting techniques, respectively, while perturbations around the IM are effectively resisted. This paper discusses the configuration, measurement theory, and experimental results of the proposed interferometer. The results verify the operational concept and applicability of the interferometer.

1. Introduction

With the ongoing development of automatic fabrication in industry, optical instruments for measuring the fabricated components become popular since they are with the abilities of full-field, non-contact, and high-precision inspection. Among which, the phase-shifting interferometers [1-4], multi-wavelength interferometers [5-7], and scanning white-light interferometers [8-12] are particularly useful for thickness [5-12], flatness [1-4], and parallelism examinations [5-12]. However, they are inapplicable to in-situ measurements since their double-path configuration makes them be highly sensitive to perturbations propagating from environment.

To surmount this drawback, we developed an innovative interferometer, which contains two important features: common-path apparatus and remote phase control module and two measurement modes: phase-shifting and phase-scanning, capable of in-situ measurements of thickness and parallelism of mechanical parts. The configuration, measurement theory, and experimental results of this interferometer are demonstrated in the following sections.

2. Configuration and theory

Figure 1 (a) presents a schematic diagram of the proposed interferometer. It is composed of a white light laser, phase control module (PCM), plastic fibre, and interferometric module (IM).

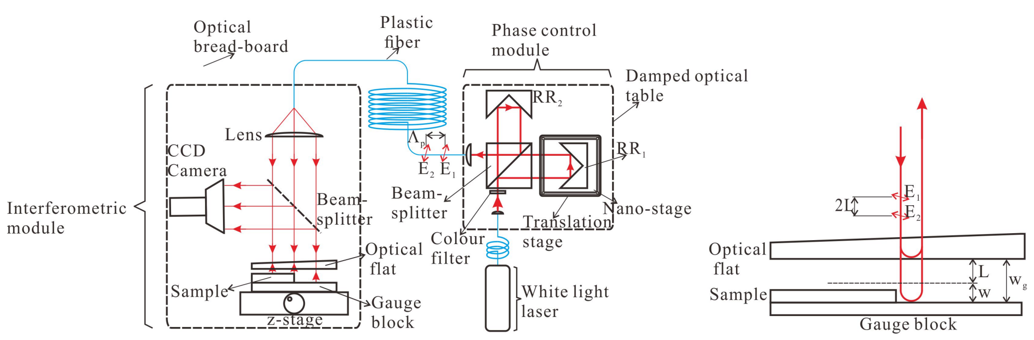

Fig. 1 (a) Schematic of the proposed interferometer; (b)magnification of the optical flat, sample, and gauge block.

The white light laser emits a low-coherent beam to the PCM. The PCM, which comprises a colour filter, two retro-reflectors (RR_1 and RR_2), a beam-splitter, and a compound stage (i.e. a stage assembled by mounting a nano-stage on the platform of a translation stage) on which RR_1 is fixed, converts the incoming beam into two co-axial beams having a direction toward the entrance of the plastic fibre. The plastic fibre delivers the incoming beams for a distance to the IM. The IM includes a lens, a beam-splitter, an optical flat, a gauge block, the sample wrung on the gauge block, a z-stage on which the optical flat, sample, and gauge block are placed, and a CCD camera; wherein the lens expands and collimates the beams from the plastic fibre to illuminate the optical flat, sample, and gauge block simultaneously, and the optical flat, sample, and gauge block reflect the incoming beams to the CCD camera to generate an interference pattern having an intensity of

$$\mathbf{I = I_0[1 - \gamma \cos\frac{4\pi}{\lambda}(w_g - L)] = I_0(1 - \gamma \cos\frac{4\pi}{\lambda} w)}; \quad (1)$$

of which $\boldsymbol{\lambda}$ denotes the central wavelength of the source, $\boldsymbol{\gamma}$ is an envelope function, and $\mathbf{w_g}$, $\mathbf{L}$ and $\mathbf{w}$ represent the gap between the sample (or gauge block) and optical flat, the amount by which the distance between RR_1 and the beam-splitter exceeds that between RR_2 and the beam-splitter, and contour height of the sample (or gauge block), respectively. Further demonstration about $\mathbf{w_g}$, $\mathbf{L}$ and $\mathbf{w}$ is given by Fig. 1(b).

According to Eq. (1), the interferometer is capable of inspecting the sample using two measurement modes: phase-shifting and phase-scanning. The former is when the band-width of the source is narrow, and it examines the parallelism of the opposite surfaces of the sample using phase-shifting technique. The latter is when the band-width of the source is broad (i.e. the colour filter in Fig 1(a) is withdrawn), and it retrieves the thickness of the sample using phase-scanning technique (i.e. optical coherence tomography).

Note the interferometer is designed to install the PCM in an independent space isolating environmental perturbations and the IM in a workspace. The interferometer can therefore implement the measurements while the phase is remotely modulated using the PCM and the environmental perturbations around the IM are resisted due to the nature of common-path design of the IM.

3. Experiments and results

To implement the proposed interferometer, a setup composed of the interferometer and an image processing system was constructed and conducted to measure three gauge blocks. The measurement results are shown in Table 1, which validate the feasibility of the proposed interferometer.

Table 1 Specs of the samples and measured results of these samples

Nominal thickness (μm)	Limit of thickness deviation (μm)	Tolerance of parallelism (μm)	Measured thickness (μm)	Measured parallelism (μm)
1005	<0.12	<0.10	1005.84	0.19
1080	<0.12	<0.10	1080.17	0.05
1200	<0.12	<0.10	1200.13	0.10

References

1. https://www.zygo.com/?/met/interferometers/
2. D. Malacara, Optical Shop Testing, 3rd Ed., Wiley, New York, 2007.
3. M. Vannonia and R. Bertozzi, "Parallelism error characterization with mechanical and interferometric methods," Opt. & Lasers Eng. 45, 719–722(2007).
4. X. Y. Yao, "Analysis of optical flat flatness measuring method with phase-shifting laser interferometer," Proc. SPIE 9677, 96771Y (2015).
5. P. de Groot, "Three-color laser-diode interferometer," Appl. Opt. **30,** 3612–3616 (1991).
6. Y. Bitou, A. Hirai, H. Yoshimori, F. Hong, Y. Zhang, A. Onae, and K. Seta, "Gauge block interferometer using three frequency-stabilized lasers," Proc. SPIE 4401, 288–297 (2001).
7. A. J. Lewis, Absolute length measurement using multiple-wavelength phase-stepping interferometry, PhD Thesis, University of London (1993).
8. P. de Groot and L. Deck, "Surface profiling by analysis of white-light interferograms in the spatial frequency domain," J. Mod. Opt. **42,** 389–401(1995).
9. C. Poilâne and P. Sandoz, "Thickness measurement of nontransparent free films by double-side white-light interferometry: Calibration and experiments," Rev. Sci. Instrum. 77, 055102(2006).
10. A. Winarno, S. Takahashi, A. Hirai, K. Takamasu, and H. Matsumoto, "Absolute measurement of gauge block without wringing using tandem low-coherence interferometry," Meas. Sci. Technol. 23, 125001 (8pp) (2012).
11. Y. Zhao, G. Schmidt, D. T. Moore, and J. D. Ellis, "Absolute thickness metrology with submicrometer accuracy using a low-coherence distance measuring interferometer," Appl. Opt. 54, 7693-7700 (2015).
12. W. J. Walecki, K. Lai, A. Pravdivtsev, V. Souchkov, P. Van, T. Azfar, T. Wong, S. H. Lau, and A. Koo, "Low-coherence interferometric absolute distance gauge for study of MEMs structures," Proc. SPIE 5716, 182-188 (2005).

Six-degree-of-freedom interferometer for detecting geometric errors of precision stages

Shyh-Tsong Lin,[1*] Chao-Ting Ma,[1] Hong-Yu Huang,[1] Po-Chen Lin[2] and Yu-Hsin Lin[3]
[1]Department of Electro Optical Engineering, National Taipei University of Technology, 1, Sec.3, Chung-Hsiao East Road, Taipei 10608, Taiwan.
[2]Department of Automation Technology, National Taipei University of Technology, 1, Sec.3, Chung-Hsiao East Road, Taipei 10608, Taiwan.
[3]Shuztung Machinery Industrial Co.,Ltd, 30, Houke S. Rd., Houli Dist., Taichung City 421, Taiwan.
*Corresponding author e-mail address:f10402@ntut.edu.tw

Abstract: An interferometer, composed of a dual-frequency laser and six interference modules, capable of inspecting precision stages was proposed in this research, where the interference modules retrieve six displacements, two along x-axis, three along y-axis, and one along z-axis, of the examined stage, which are then used to figure out the stage's six-degree-of-freedom geometric errors. This paper introduces the interferometer in detail, it then presents the experimental results from the use of the interferometer. The results confirm the applicability of the proposed interferometer.

1. Introduction

Precision linear stages are now the key components of machine tools, computer numerical control machine centers, LCD inspecting machines, coordinate measuring machines, etc. Ideally, a precision linear stage travels along a straight line without positioning error; however, fabrication errors, installation errors, and environmental perturbations make the movement be with errors in six-degrees-of-freedom (6-DOF), one positioning error (i.e. $\boldsymbol{\varepsilon}_{\mathbf{x}}$), two straightness errors ($\boldsymbol{\varepsilon}_{\mathbf{y}}$ and $\boldsymbol{\varepsilon}_{\mathbf{z}}$), and three rotation errors (α,β, and γ), which largely influence the performance of the stage. To realize how large the 6-DOF errors are, the laser calibration systems have been developed [1-3]; however, their measurements are time-consuming and incapable of retrieving α-error, where the time-consuming is because of the required procedures of measuring the other errors one by one.

To surmount the drawbacks of the commercialized laser calibration systems, many optical instruments are proposed; some of them are based on the theories of interferometer and position sensing detector [4-8], some on interferometer and grating [9], and some on interferometer, position sensing detector, and auto-collimator [10]. However, some of them use specific components that make the duplication of the them difficult, and some of them are with low measurement resolution in some components of the errors.

2. The proposed interferometer

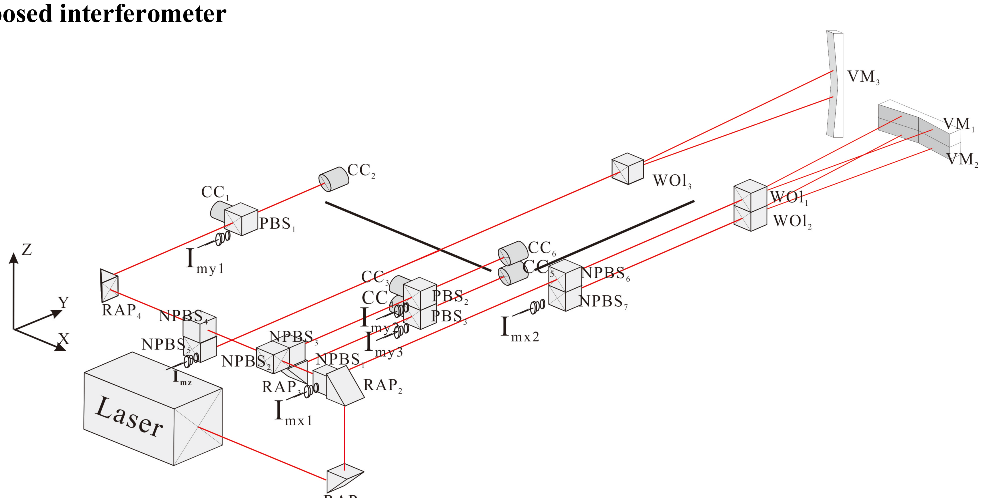

Fig. 1 Configuration of the proposed 6-degrees-of-freedom interferometer

An interferometer, shown in Fig. 1, composed of a laser and Y_1, Y_2, Y_3, X_1, X_2, and Z interference modules is therefore proposed; where the laser emits a dual-frequency laser beam to the interference modules and exports a reference beat-frequency signal; the Y_1, Y_2, Y_3, X_1, X_2, and Z interference modules, assemblies of PBS_1, CC_1, CC_2, and D_{my1}, PBS_2,

CC_3, CC_6, and D_{my2}, PBS_3, CC_4, CC_5, and D_{my3}, $NPBS_6$, WOl_1, VM_1, and D_{mx1}, $NPBS_7$, WOl_2, VM_2, and D_{mx2}, and $NPBS_5$, WOl_3, VM_3, and D_{mz}, respectively, output beat-frequency signals of I_{my1}, I_{my2}, I_{my3}, I_{mx1}, I_{mx2}, and I_z, respectively; the interferometer extracts the displacements of v_1, v_2, v_3, u_1, u_2, and w of the examined stage by comparing the phase of the reference beat-frequency signal with the phases of I_{my1}, I_{my2}, I_{my3}, I_{mx1}, I_{mx2}, and I_z, respectively; and the interferometer determines the 6-DOF geometric errors of the examined stages by $\varepsilon_x = u_1$, $\varepsilon_y = (v_1 + v_2)/2 - v_c$, $\varepsilon_z = w$, $\alpha = (v_3 - v_2)/d$, $\beta = (u_1 - u_2)/h$, and $\gamma = (v_2 - v_1)/l$. Here v_c denotes the command displacement of the stage; d, h and l are distances between Y_2 and Y_3, X_1 and X_2, and Y_1 and Y_2, respectively.

3. Experiments and results

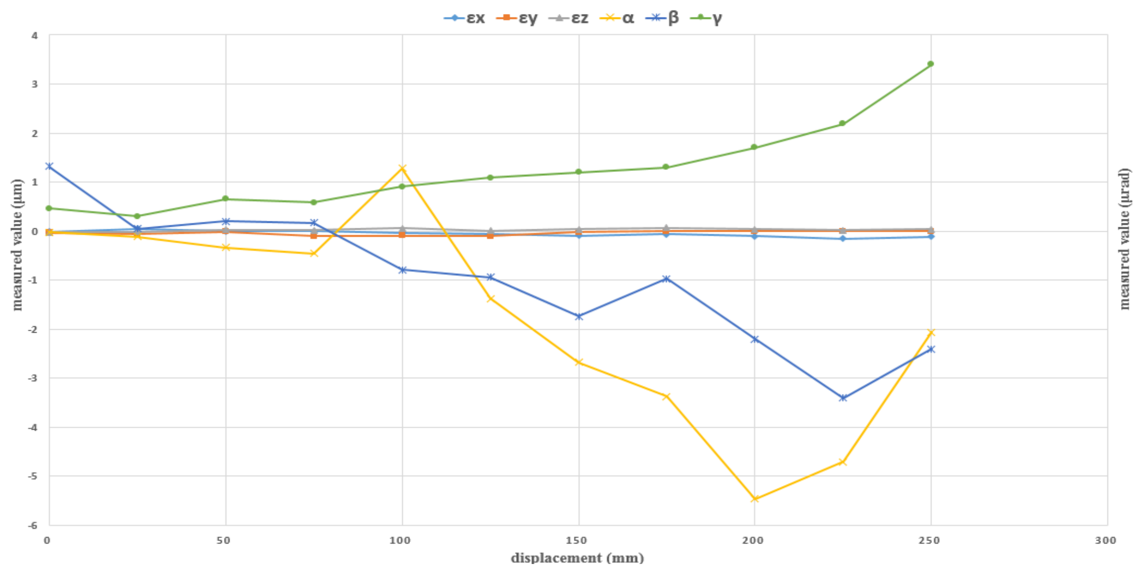

Fig.2 Measured results

The interferometer was installed and conducted to examined the 6-DOF geometric errors of a stage with two air-bearing linear guides, parallel to Y_1 and Y_2, respectively, and a travel range of 250mm. The results are shown in Fig.2, they validate the feasibility of the proposed interferometer.

Reference

1. http://www.renishaw.com/en/xl-80-laser-system--8268.
2. http://literature.cdn.keysight.com/litweb/pdf/5989-9354EN.pdf.
3. https://www.zygo.com/?%2Fmet%2Fmarkets%2Fstageposition%2Fzmi%2F.
4. S.W. Lee, R. Mayor, and J. Ni, "Development of a six-degree-of-freedom geometric error measurement system for a meso-scale machine tool," J. Manuf. Sci. Eng. **127**, 857-865(2005).
5. H. Y. Wang, B. H. Liao, M. J. Chou, Y. Y. Tseng, and K. C. Fan, "Development of a miniature multidegree-of-freedom measurement system for ultra precision stages," Proc. of SPIE 8916, 89160A(2013).
6. B. Chen, B. Xu, L. Yan, E. Zhang, and Y. Liu, "Laser straightness interferometer system with rotational error compensation and simultaneous measurement of six degrees of freedom error parameters," Opt. Exp. **23**, 9052-9073, (2015).
7. Y. Lou, L. Yan, B. Chen, and S. Zhang, "Laser homodyne straightness interferometer with simultaneous measurement of six degrees of freedom motion errors for precision linear stage metrology," Opt. Exp. 25, 6805-6821(2017).
8. Y. T. Chen, W. C. Lin, C. S. Liu, "Design and experimental verification of novel six-degree-of freedom geometric error measurement system for linear stage," Opt. & Lasers Eng. 92, 94–104(2017).
9. H. L. Hsieh, and S. W. Pan, "Development of a grating-based interferometer for six-degree-of-freedom displacement and angle measurements," Opt. Exp. **23**, 2451-2465(2015).
10. F. Qibo, Z. Bin, C. Cunxing, K. Cuifang, Z. Yusheng, and Y. Fenglin, "Development of a simple system for simultaneously measuring 6DOF geometric motion errors of a linear guide," Opt. Exp. **21**, 25805-25819(2013).

Nano-antennas excitation through visible light and response observation in the THz range with a Confocal Microscope

Daniel Luis Noriega[1,*], Fernando Mendoza Santoyo[1], Jorge Mauricio Flores Moreno[1], Javier Méndez-Lozoya[2], Francisco Javier González[2]
[1]Centro de Investigaciones en Óptica A.C., Lomas del Bosque 115, Col, Lomas del Campestre, León Guanajuato, 37150, México
[2]Universidad Autónoma de San Luis Potosi, Alvaro Obregon 64, Centro, San Luis Potosi, SLP, 78000, México
*dluis@cio.mx

Abstract: The experimental results from a cluster of nano-antennas excited with visible light are presented. A confocal microscope was used to observe the electromagnetic field produced, shown by the dynamic behavior of iron oxide nanoparticles previously deposited over the cluster.

1. Introduction

Antennas have been used since as long as a century to control the emission and capture of radiation and microwaves. The reescalation of said antennas to smaller sizes have gave birth to things like the optic nano-antennas, whom can focus farther than the diffraction limit, which allows to highlight for the better some optic process like high harmonic generation [1], fluorescence [2,3], Raman scattering [4,5] and infrared absorption [6,7].

It is well known that the metallic particles sustain resonance plasmonic modes in visible wavelengths, making them natural optic antennas [1,8].

The objective is to characterize qualitatively the dynamic behavior of nanoparticles super paramagnetic by exposing them to an electromagnetic field generated by excited nano-antennas type bowtie.

2. Methodology

We used iron oxide Fe_3O_4 nanoparticles (Np) with a size of 50-100 nm previously scattered in an immersion fluid (no polar fluid) with the help of an ultrasonic bath.

Then, 20 μl of dispersed Np were deposited over the substratum of THz nano-antennas (Na). Then, the Np were forced to get close to the substratum with two neodymium magnets. After the magnets were retired, the substratum was irradiated with two wavelengths, one for observation (λ_o of 543 nm) and one for excitation (λ_e of 1 μm).

3. Results

In the Fig.1, we present a series of images with a field of view of 21x23 μm in which the concentration of Np was the 0.42 g/l. The images were taken along an interval of 20 minutes.

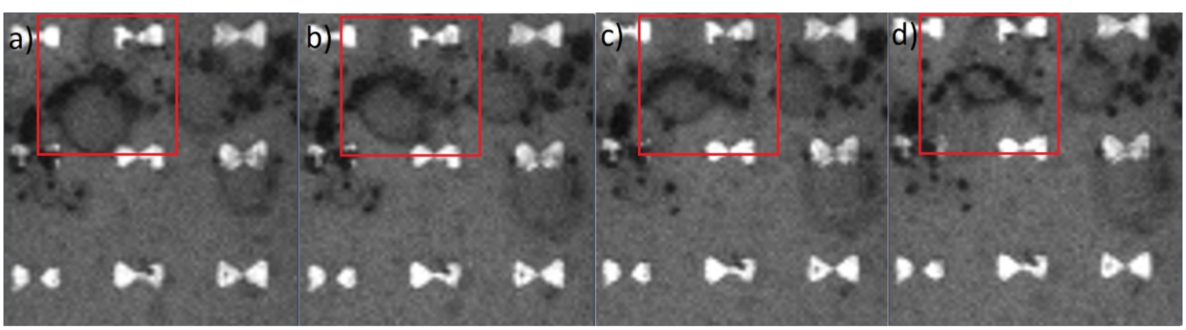

Fig. 1. Images of substratum being irradiated by both λ_e and λ_o in a time of: a) $t{\sim}0$ min. b) $t{\sim}7$ min. c) $t{\sim}14$ min. d) $t{\sim}20$ min. Inside the red zone we can observe the formation and dispersion of circles.

In the Fig.2 we show the same area over the substratum, with the same Np, but now we turn off the λ_e, so now we put the Np through a period of relaxation of ~20 min to check if the behavior observed in the Fig.1 is caused solely by the λ_e and not the λ_o. As you can see in the Fig.2, there isn't an observable phenomenon along this period, other than the slight fading of circles.

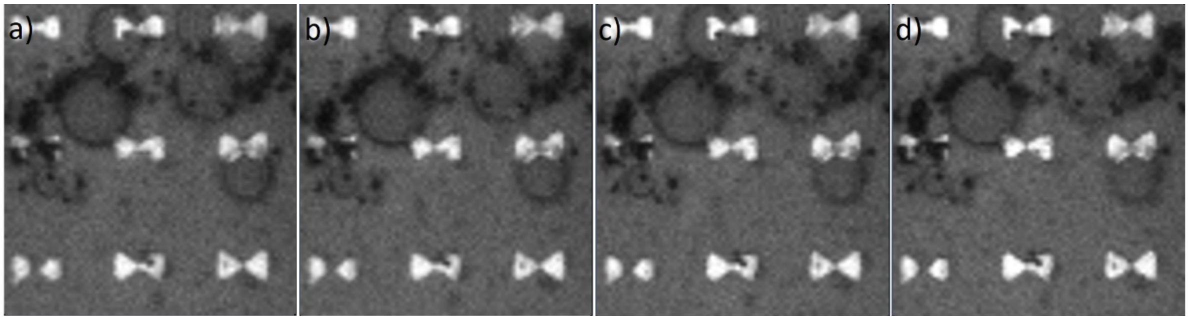

Fig. 2. Substratum without λ_e at a time: a) t~0 min. b) t~7 min. c) t~14 min. d) t~20 min.

4. Conclusions

We observed a rearrangement of the Np when the substratum was irradiated with the λ_e, but the same phenomenon did not repeat when the λ_e was absent, which make us think that the λ_o by itself is not enough to excite the Na. The observable response of the Np to the electromagnetic field produced by the Na is slow and not always the same to the presented here.

5. Future work

Improve the experimental methodology until the dynamic phenomenon is faithfully repeatable. Characterize the dynamic of the Np resulted from the electromagnetic field of excited Na.

Acknowledgement

F. J. González would like to acknowledge support from Project 32 of "Centro Mexicano de Innovación en Energía Solar" and by the National Laboratory Program from CONACYT through the Terahertz Science and Technology National Lab (LANCYTT).

References

[1] T. H. Taminiau, F. D. Stefani, F. B. Segerink, and N. F. van Hulst, "Optical antennas direct single-molecule emission," Nat. Photonics 2(4), 234–237 (2008).
[2] S. Kim, J. Jin, Y.-J. Kim, I.-Y. Park, Y. Kim, and S.-W. Kim, "High-harmonic generation by resonant Plasmon field enhancement," Nature 453(7196), 757–760 (2008).
[3] R. M. Bakker, V. P. Drachev, Z. Liu, H.-K. Yuan, R. H. Pedersen, A. Boltasseva, J. Chen, J. Irudayaraj, A. V. Kildishev, and V. M. Shalaev, "Nanoantenna array-induced fluorescence enhancement and reduced lifetimes," New J. Phys. 10(12), 125022 (2008).
[4] P. Anger, P. Bharadwaj, and L. Novotny, "Enhancement and quenching of single-molecule fluorescence," Phys.Rev. Lett. 96(11), 113002 (2006).
[5] K. Kneipp, Y. Wang, H. Kneipp, L. T. Perelman, I. Itzkan, R. R. Dasari, and M. S. Feld, "Single molecule detection using surface-enhanced Raman scattering (SERS)," Phys. Rev. Lett. 78(9), 1667–1670 (1997).
[6] G. Das, F. Mecarini, F. Gentile, F. De Angelis, H. Mohan Kumar, P. Candeloro, C. Liberale, G. Cuda, and E. Di Fabrizio, "Nano-patterned SERS substrate: application for protein analysis vs. temperature," Biosens. Bioelectron. 24(6), 1693–1699 (2009).
[7] F. Neubrech, A. Pucci, T. W. Cornelius, S. Karim, A. García-Etxarri, and J. Aizpurua, "Resonant plasmonic and vibrational coupling in a tailored nanoantenna for infrared detection," Phys. Rev. Lett. 101(15), 157403 (2008).
[8] E. R. Encina and E. A. Coronado, "Plasmonic nanoantennas: Angular scattering properties of multipole resonances in noble metal nanorods," J. Phys. Chem. C 112(26), 9586–9594 (2008).

First Order Filtering Least-Squares Method for Phase-Shifting Interferometry

O. Medina-Cázares[1*], M. Leon-Rodríguez[1], A. Barrientos-García[1], J. Guel-Tapia[1]
Universidad Politecnica de Guanajuato,
Av. Universidad Sur 101, Comunidad Juan Alonso. Cortazar, Guanajuato, México. CP 38483.
ommedina@upgto.edu.mx[*]

Abstract: In this work, we develop an iterative first order filtering method to demodulate a Phase-Shifting Interferogram (PSI) sequence. This algorithm is based on the minimization of a Regularized Least-Squares (RLS) functional. This demodulation method is linear and provides stable convergence. Furthermore, it is able to obtain a phase without noise and uses at least three interferograms.

1. Introduction

The main difference between the demodulation method presented here and the ones reported in [1-3] is that our demodulation method is based on the least-squares (LS) method [4]. Therefore, the energy cost function is linear, while in works [1-3] the proposed cost function are non-linear.

2. Objective: Least Squares Method

In general, an interferogram sequence for PSI can be modeled as:

$$I^k_{x,y} = a_{x,y} + b_{x,y}\cos\left(\phi_{x,y} + \alpha k\right), \quad k = 0, 1, 2, \dots, L-1, \tag{1}$$

where $I^k_{x,y}$ is the intensity at the site x, y of the k-interferogram in a sequence of L interferograms, being $a_{x,y}$ its background illumination, $b_{x,y}$ its contrast, $\phi_{x,y}$ the modulating phase under test and αk the phase-shift of the k-interferogram. Defining a new set of variables from Eq. (1) as $\varphi_{x,y} = b_{x,y}\cos\left(\phi_{x,y}\right)$, $\psi_{x,y} = b_{x,y}\sin\left(\phi_{x,y}\right)$, $C_k = \cos\left(\alpha k\right)$, $S_k = \sin\left(\alpha k\right)$, we can rewrite Eq. (1) as

$$I^k_{x,y} = a_{x,y} + \varphi_{x,y}C_k - \psi_{x,y}S_k, \quad k = 0, 1, 2, \dots, L-1, \tag{2}$$

if we know αk, we have a system of 3×3 unknowns for each pixel. These unknowns can be solved using the least-squares method. An energy cost function that describe Eq. (2) can be written as

$$U_{x,y}\left(a_{x,y}, \varphi_{x.y}, \psi_{x,y}\right) = \sum_{k=0}^{L-1}\left[a_{x,y} + \varphi_{x.y}C_k - \psi_{x,y}S_k - I'_{x,y,k}\right]^2 \tag{3}$$

where $I'_{x,y,k}$ is the k-th experimentally measured intensity of the interferogram sequence. Knowing the steps αk, the LS criteria require to make zero the gradient of Eq. (3) as: $\nabla U\left(a_{x,y}, \varphi_{x,y}, \psi_{x,y}\right) = 0$. This functional gradient yields $\vec{x} = A^{-1}\vec{b}$, where $\vec{x} = \left[a_{x,y} \quad \varphi_{x,y} \quad \psi_{x,y}\right]^T$, A is a 3×3 matrix that is composed of the coefficients of C_k and S_k and $\vec{b} = \left[\sum I'_{x,y,k} \quad \sum I'_{x,y,k}C_k \quad \sum I'_{x,y,k}S_k\right]^T$. To ensure that A is nonsingular, Eq. (3) requires at least three different phase-steps. Therefore, the phase ϕ at point x, y can be determined from $\phi_{x,y} = \arctan\left(-\psi_{x,y} / \varphi_{x,y}\right)$. Note that the inverse of A is performed only once because its components depend only on the αk steps.

3. Experimental Methodology: Regularized Least Square

In order to regularize the LS functional Eq. (3) we propose the following cost function:

$$U_{x,y}\left(a_{x,y},\varphi_{x,y},\psi_{x,y}\right)=\sum_{k=0}^{L-1}\left[a_{x,y}+\varphi_{x,y}C_k-\psi_{x,y}S_k-I'_{x,y,k}\right]^2+\lambda\nabla\left[a_{x,y}\right]^2+\mu\nabla\left[\psi_{x,y}\right]^2+\mu\nabla\left[\varphi_{x,y}\right]^2, \tag{4}$$

where λ and μ are the regularization parameters that control the smoothness of $a_{x,y}$, $\psi_{x,y}$ and $\varphi_{x,y}$. Operator $\nabla[*]$ takes the first order differences along the x and y directions as follows: $\nabla\left[f_{x,y}\right]=\left[f_{x,y}-f_{x-1,y}, f_{x,y}-f_{x,y-1}\right]^T$. To find our unknown phase map we need to minimize the cost functional in Eq. (4). Equating the partial gradient to zero and solving, we can obtain a direct solution for each pixel as in LS for the background illumination a and the phase map ϕ.

4. Results: Experimental Test

Now, we are going to show the performance of our method with experimentally obtained interferograms. The interferogram sequence was generated using an electronic speckle pattern interferometry technique, and the wave-front under test was modified by applying pressure. For the phase step, a phase-shift of $\pi/2$ radians was introduced. The object under test was a circular metal plate with circular perforations all along its edge. Figure 1 a) shows the first experimental phase-shifting interferogram of a four samples sequence. In Fig. 1 b), we show the wrapped phase estimation of the classic least-squares method, whereas in Fig. 1 c), we see the wrapped phase estimation of the RLS method proposed here. Another significant feature of this algorithm is that in sections where there is no information, such as black circles and scratches, the algorithm was able to fill-up the empty spaces satisfactorily; this is because it takes into account the neighboring pixel information and the regularization terms.

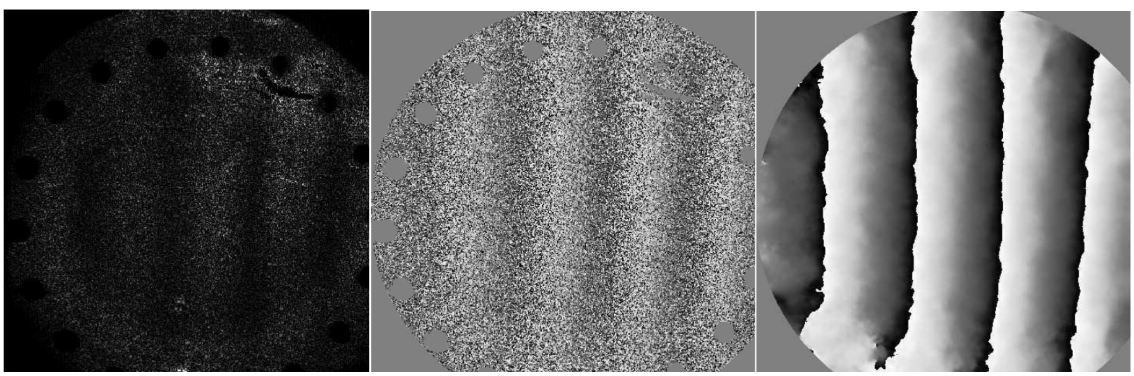

a) Interferogram b) LS Phase c) RLS Phase

Fig. 1. Experimental results. a) One of the four experimental interferogram sequences, b) Recovered phase map using classic LS, c) Recovered phase map using our proposed RLS method.

5. Conclusions

We have presented a RLS phase-shifting demodulation method for noisy interferograms sequences. As shown in the results, our demodulation method is able to recover the modulating phase without noise. Given the linearity of the proposed functional, the demodulation method presented here provides stable convergence, recovers the modulated phase and removes noise with as few as three interferograms. In addition, the presented algorithm is capable of interpolating small empty spaces of missing data, since it takes into account the temporal and spatial information.

References

[1] Marroquin, J., Figueroa, J., & Servin, M. "Robust quadrature filters". J. Opt. Soc. Am. A, 14, pp.779-791 (1997).
[2] Marroquin, J., Servin, M., & Rodriguez-Vera, R. "Adaptive quadrature filters and the recovery of phase from fringe pattern images". J. Opt. Soc. Am. A, 14, pp.1742-1753 (1997).
[3] Marroquin, J., Servin, M., & Rodriguez-Vera, R. (1998). "Adaptive quadrature filters for multiple phase-stepping images". Opt. Lett., 23, pp.238-240 (1998).
[4] Kong, I. "General algorithm of phase-shifting interferometry by iterative least-squares fitting". Opt. Eng., 34, p.183 (1995).

Measurement of the Out-of-plane Displacement Field of non-Flat Surfaces

Juan Antonio Rayas[1], Amalia Martínez-García[1], Miguel León-Rodríguez[2]
1 Centro de Investigaciones en Óptica. Loma del Bosque 115, León, Gto. México.
2 Universidad Politécnica de Guanajuato. Av. Universidad Sur 1001, Cortazar, Gto. México
e-mail address: jrayas@cio.mx

Abstract: Measurements of the displacement field by optical interferometry depend on the induced phase difference and on the interferometer's sensitivity vector; the latter depends in turn on the positions of the illuminating source and the observation (case of out-of-plane interferometer), and on the topography of the analyzed sample. The aim of this study is the quantification of the out-of-plane displacement field of a car fender which is subjected to mechanical loading. Special attention was paid to evaluating contributions to the displacement when the fender shape is considered. The displacement field is evaluated by using an electronic speckle pattern interferometer and the topography is obtained by a fringe projection technique.

1. Introduction

Electronic Speckle Pattern Interferometry (ESPI) is an optical technique which enables interferometric measurements of surface displacements in almost any material. The non-contact and full-field measurement allow the calculation of the three-dimensional distribution of the displacements and strains of the object under test as a response to a mechanical or thermal loading. ESPI has successfully been applied in many fields, including automotive, aerospace, electronics and materials research, for the study of material properties, fracture mechanics, fatigue testing, NDT and dynamic behavior of a variety of components [1]. Displacements measurements depend on the induced phase difference and on the interferometer´s sensitivity vector [2]. In this work we describe the dependence of the sensitivity vector on the shape of the object.

2. Sensitivity vector

The general relationship between the measured phase difference $\varphi(P)$ and the displacement vector $d = d(u, v, w)$ at a point $P = P(x, y, z)$ in an ESPI interferometer is given by [2]:

$$\varphi(P) = s(P) \cdot d(P), \tag{1}$$

where $s = \frac{2\pi}{\lambda}(k_o - k_l)$ is the sensitivity vector, λ is the employed laser light wavelength and k_o, k_l are the unit vectors in the observation and illumination direction, respectively. The components of the sensitivity vector s can be written as

$$s_x(x,y,z) = \frac{2\pi}{\lambda}\left(\frac{x_0 - x}{l_0} - \frac{x - x_l}{l_l}\right), \qquad s_y(x,y,z) = \frac{2\pi}{\lambda}\left(\frac{y_0 - y}{l_0} - \frac{y - y_l}{l_l}\right), \qquad s_z(x,y,z) = \frac{2\pi}{\lambda}\left(\frac{z_0 - z}{l_0} - \frac{z - zl}{l_l}\right), \tag{2}$$

where (x_o, y_o, z_o) is the observation point (entrance pupil position of the CCD camera), (x_l, y_l, z_l) is the object illumination light source position and l_0, l_l are the distances between the observation point and P to the illumination light source, respectively. The l_o and l_l can be written as

$$l_o = \sqrt{(x - x_o)^2 + (y - y_o)^2 + (z - z_o)^2}, \qquad l_l = \sqrt{(x - x_l)^2 + (y - y_l)^2 + (z - z_l)^2}. \tag{3}$$

The coordinate z is associated to topography of the object at the point (x, y).

3. Experimental results

Figure 1 shows the 3D shape of a car fender retrieved by the fringe projection technique. This shape has been corrected by the iterative method proposed in [3]. Using a Verdi laser whose wavelength is 532 nm, a phase map of interference fringe pattern is obtained by ESPI system with *out-of-plane* sensitivity; Figure 2 shows the phase field $\varphi(x, y)$ evaluated after applying mechanical load. To evaluate the sensitivity vector components [Eqs. (2)] we considered the following coordinates: $(x_o, y_o, z_o) = (0\,mm, 0\,mm, 1250\,mm)$ and $(x_l, y_l, z_l) = (63.5\,mm, 0\,mm, 1250\,mm)$ which are associated to position of the CCD and illumination source respectively. Figure 3 shows the component s_z of the sensitivity vector to a) a flat surface and b) the fender topography. Figure 4 shows the relative error associated to displacements measurement when a flat surface is considered instead of the object shape.

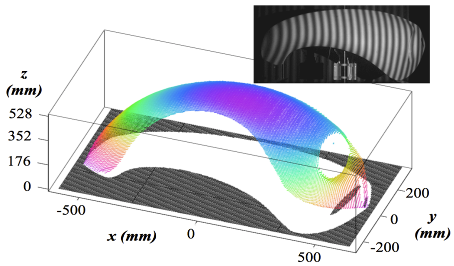

Fig. 1. 3D shape of the car fender retrieved with fringe projection technique.

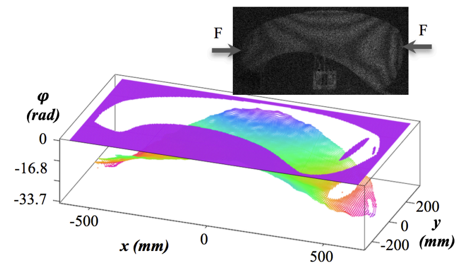

Fig. 2. Phase map for the applied mechanical load.

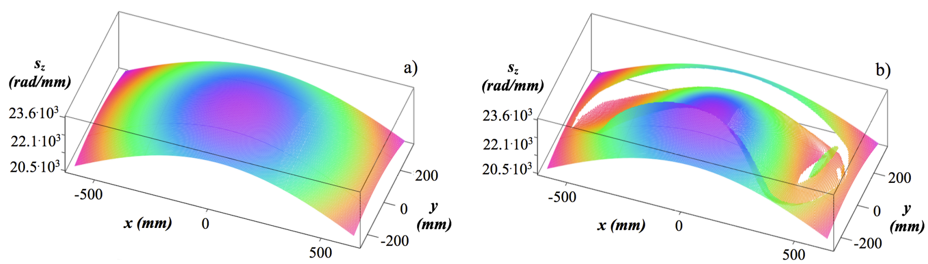

Fig. 3. Sensitivity vector a) assuming a flat shape and b) considering the actual shape of the object.

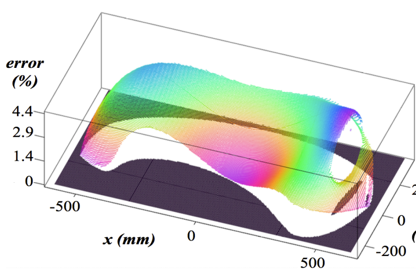

Fig. 4. Relative error due to the topography of the object when is supposed flat surface.

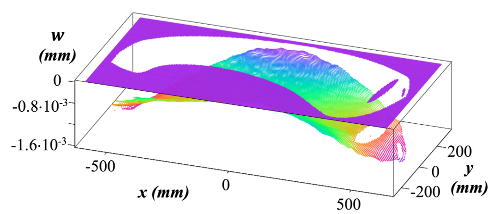

Fig. 5. Displacement field $w(x, y)$ calculated assuming a flat shape.

4. Conclusions

The displacement field $w(x, y)$ was calculated considering the shape of the object and assuming a flat shape (see Figure 5). The maximum error associated to this assuming is of the 4 %. We have shown the relative error increases to large surface shape.

References

[1] R.S. Sirohi and F.S. Chau, Optical Methods of Measurement: Whole Field Techniques (Marcel Dekker, New York, 1999), Chap. 6.

[2] A. Martínez, J.A. Rayas, R. Rodríguez-Vera, and H.J. Puga, "Three- dimensional deformation measurement from the combination of in-plane and out-of-plane electronic speckle pattern interferometers" Applied Optics. **43**, 24, 4652-4658 (2004).

[3] A. Martínez, J.A. Rayas, H.J. Puga, Katia Genovese, "Iterative estimation of the topography measurement by fringe-projection method with divergent illumination by considering the pitch variation along the x and z directions" Optics and lasers in engineering. **48,** 877-881 (2010).

First photon ghost imaging by single photon counting

Yasuhiro Mizutani, Hiroki Taguchi and Yasuhiro Takaya
Department of Mechanical engineering, Osaka University, 2-1 Yamadaoka, Suita, Osaka 565-0871 Japan
mizutani@mech.eng.osaka-u.ac.jp

Abstract: We describe a new method for a photon-counting imaging by a ghost imaging (GI) for realizing a high sensitivity imaging. The GI is one of the single pixel imaging and an imaging technique based on a correlation method. Because of a correlation method, the GI has an advantage of a signal-to-noise ratio. For using illumination with lower intensity, we focused on an arrival time of a photon from a sample to a detector. By calculate spatial dispersion of correlation efficiency between illumination patterns and an arrival time of the photons, we have obtained fluorescence images using several hundred photons.

1. Introduction

A Ghost imaging (GI) is one of a single pixel imaging and a correlation-based imaging method between illumination patterns and detected intensity from a sample [1]. The Gi has an advantage for a signal-to-noise ratio, because the correlation-based technique can reduce non-correlated noise. In the view point of sensitivity, our previous paper led to have an advantage of sensitivity by comparison between a normal imaging with CCD camera and the GI with patterned illuminations [2]. The GI would offer advantage for an imaging with lower intensity of illumination. We feel that this advantage particularly attractive for a photon imaging. In an attempt to advance of the advantage, instead of light intensity for correlation, we have used an arrival time of the photon "first photon detection time (FPDT)" from a sample to a detector. We first give a brief description of a principle and an experimental setup and then show images by several hundred photons.

2. Principle of the first photon detection ghost imaging (FPDGI)

The Ghost imaging is a correlation-based technique between illumination patterns and detected light intensities. Our method used an FPDT from a sample to a detector by using a photon counting technique instead of light intensity for imaging with lower intensity. The FPDT can be used for the GI because it is proportional to light intensity.

Figures 1 shows a principle of the FPDGI. As shown in fig.1 (a), a patterned illumination coded by a PC $I_n(x,y)$ was projected onto a fluorescence sample by a DMD projector. Then, an FPDT of the fluorescent photon t_n was measured by a photo multiplier tube (PMT) and a photon counting device. The ghost image $G(x,y)$ is a spatial dispersion of a correlation efficiency. Figure 1 (b) shows a timing sequence of the FPDGI. All devices were synchronized with a trigger signal from the DMD device. The trigger signal was generated with a pattern illumination. Then a counter of the photon counting device started by the trigger signal and measured the first signal of the photon. In the case of the high intensity, the detected signal means a photon density. However, in the lower case, the detected signal was discrete and means a probability of the arrival photon. In other words, the FPDGI was the correlation method between illumination patterns and probabilities of the photons.

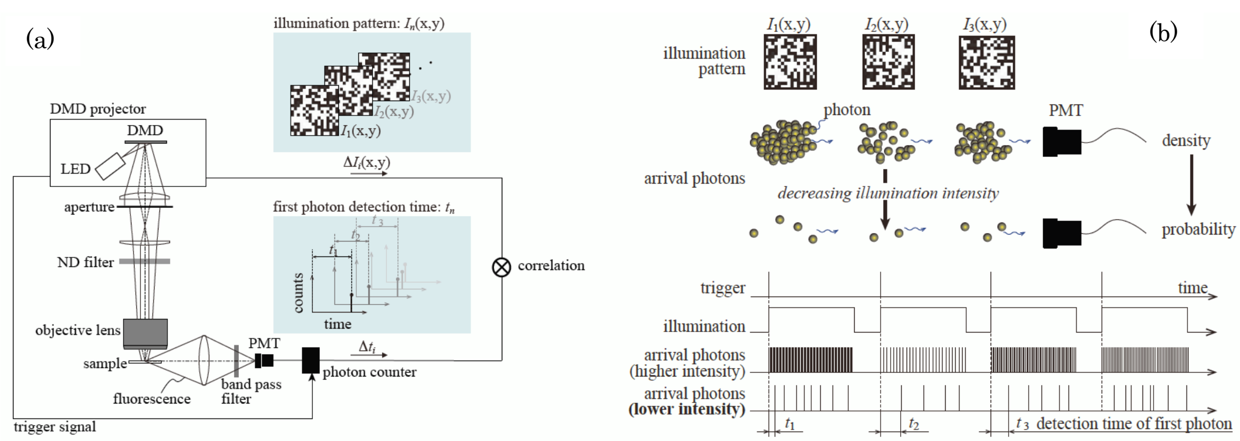

Fig. 1 Principle of the first photon detection ghost imaging by single photon counting. (a) optical setup and (b) timing sequence of intensity detection by the first detection time of the single photon.

3. Experimental results and discussion

The FPDGI is based on an imaging using discreate signals of detected photons and considers light intensity. Possibility of detecting the lower intensity was confirmed by measuring FPDT depended on a photon rate. Filtered light at 532 nm which intensity was controlled by ND filter was irradiated on a fluorescence bead and then a fluorescence photon was detected by the PMT. Figures 2 show experimental results of detected signals. As shown in fig.2 (a), the detected signals were discreated. Photon rate has a profound effect on an arrival time and decreasing photon rate tends to increase the FPDT. The dependence of the FPDT on a photon rate is shown in fig. 2 (b). In the range of lower photon rate, experimental values agree well with theoretical values. This experiment yielded $ct_a \leqq 1$ for the FPDGI.

(a) (b)

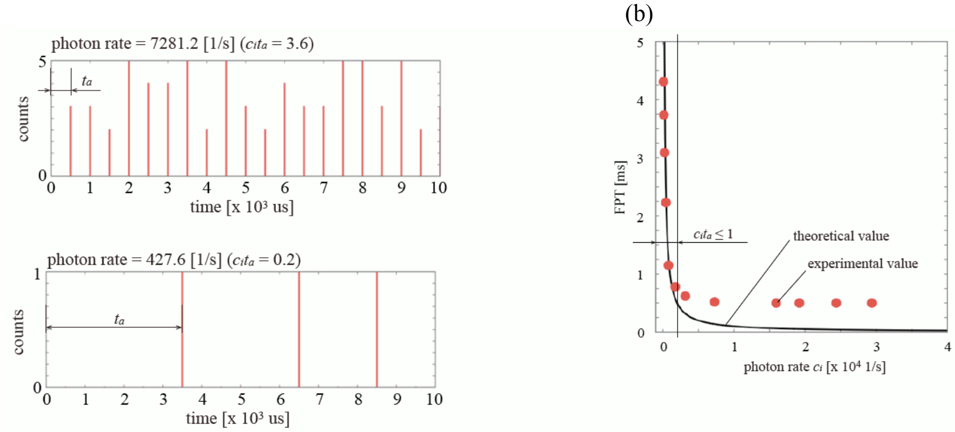

Fig. 2 Experimental results of detected FPDT t_a. (a) variation of time dependent signals of photon with a photon rate, (b) dependence of FPDT on photon rate c.

Figures 3 shows experimental results of obtained images and its ability for damage-less imaging of fluorescence samples. As shown in fig.3 (a), the image detected by the FPDGI has the highest quality of images detected by other proposed technique. We show in fig.3 (b), the dependence of a photon rate on imaging numbers. The FPDT decreased with increasing an imaging number slower than that measured by the proposed GI. The FPDT plays an important role in increasing the image quality as well as decreasing sample damage.

(a) (b)

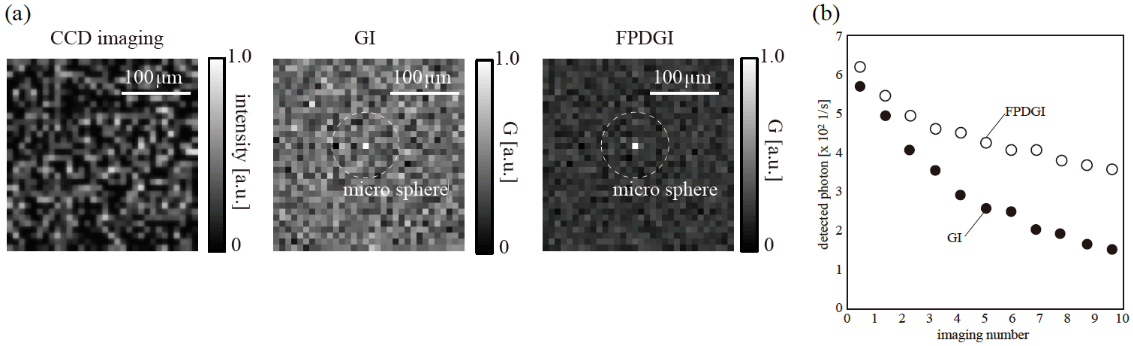

Fig. 3 Experimental results of obtained images. (a) image comparison FPDGI with CCD imaging and proposed GI, (b) comparison of sample damage by photo bleaching.

4. Conclusions

The fluorescence microscope using the GI by a probability of photon detection has been proposed. Firstly, we confirmed properties of a probability of photon detection. The results indicate the FPDGI possible to obtain an image by a correlation calculation. For a fluorescence imaging by using a probability of photon detection, the FPDGI has an advantage to obtain a high contrast image compared with other proposed imaging.

References

[1] R.S. Bennink, S.J. Bentley, R.W. Boyd, ''Two-photon coincidence imaging with a classical source," Phys. Rev. Lett. **89**, 113601 (2002).

[2] K. Shibuya, K. Nakae, Y. Mizutani, T. Iwata, "Comparison of reconstructed images between ghost imaging and Hadamard transform imaging," Opt. Rev. **22**, 897 (2015).

Evaluating Modified-SIFs of Vibrating Composite Plates with Clamped-End Crack by Amplitude-Fluctuation ESPI

Chi-Hung Hwang[1], Wei-Chung Wang[2]
[1]Instrument Technology Research Center, NARLabs, Hsinchu, Taiwan
[2]Department of Power Mechanical Engineering, National Tsing Hua University, Hsinchu, Taiwan
Author e-mail address: chhwang@itrc.narl.org.tw

Abstract: In this paper, an optical interferometery method named as amplitude fluctuation (AF) electronic speckle pattern interferometry (ESPI), a kind of time-averaged ESPI method, was implemented to perform the measurement of dynamic properties of a crack existed cantilever composite plate. The crack was manufactured perpendicular to the vertical edge of the composite plate and then clamped by a vise to simulate a crack generated along the clamped edge where the geometric defect is most likely introduced by bending moment. The modified-SIF can be evaluated by Δw-$\sqrt{r}$ plot which concludes that if a crack exists in the structure, the stress failure criterion must also be considered, especially for higher frequency vibration.

1. Background

When composite structures are in service, occasionally, cracks might be introduced due to accidental impact or degraded due to sever operational conditions. Therefore, dynamic properties of composite structures may be changed. Modal modes different from those generated by defect-free composite structures and stress intensity factors (SIFs) induced by vibration are produced. Structures may then be failed because of the large displacement introduced by additional free surface or crack prorogation. Many experimental methods can be applied for measuring vibration parameters, such as holography, modal testing method, shadow moiré method, laser Doppler vibrometer, shearography, electronic speckle pattern interferometry (ESPI), etc. In this paper, the modified STFs were evaluated by following the proposed experimental method proposed by Wang etc. [1], therefore, the crack opening displacement (COD) would be first determined; after that, by implementing COD-SIF relationship, the modified KIII values of different resonant frequencies were evaluated. As indicated by previous study performed by Wang etc. [1], to evaluate crack introduced stress intensity factors of the cracked composite plates by COD approach, more stable fringe patterns and higher measurement sensitivity were required. Therefore, the amplitude fluctuation (AF) ESPI method was proposed by the Wang etc. [2] was adopted.

2. Experimental Setups and Specimens

In this paper, an optical interferometery method named as amplitude fluctuation (AF) electronic speckle pattern interferometry (ESPI), as shown in Fig. 1, which is a kind of time-averaged ESPI based on the fluctuation of vibration driving force, was implemented to perform the measurement of dynamic properties of a crack existed cantilever composite plate. The crack was manufactured perpendicular to the vertical edge of the composite plate and then clamped by a vise to simulate a crack generated along the clamped edge where the geometric defect is most likely introduced by bending moment.

Two composite plates with $[0]_{16}$ stacking sequence but different crack lengths were used for the study. The crack was created and clamped as mentioned to simulate the crack locates along the clamped edge. Two crack lengths were selected, i.e. 20 mm and 40 mm. The composite plate was produced from the 250 mm x 250 mm unidirectional CFRP prepreg and then cured by the vacuum bag method. The cured CFRP plate was cut into several 190 mm x 90 mm sheets, as shown in Fig.2, by using a diamond wheel. To produce the crack, a screw slotting cutter of 0.35 mm thick was used.

3. Results and Discussions

In this paper, the mode shapes and the modified SIFs are two vibration characteristics for discussions. The composite plate was excited by a shaker at different frequencies. Thanks to the whole field measurement capability of the AF ESPI method, the vibration modes at different resonant frequencies can be determined. A typical AF ESPI fringe pattern is shown in Fig. 3. The displacement across the crack at different resonant frequencies was determined by interpreting the fringe order with fringe formula. In this study, sub-fringe order on the crack was evaluated by linear interpolation between adjacent fringes to provide better resolution. Then based on the relationship between the crack opening displacement (COD) and the stress intensity factor (SIF), the modified-SIF values of different resonant frequencies of the crack-contained composite plate were evaluated. Different from the conclusions of early numerical and theoretical studies on crack subjected to the dynamic periodic loads, the values of the modified SIFs are upper-bound values instead of becoming infinite in spite of the crack contained plate is subjected to resonant vibration force.

4. Conclusions

In this study, while the cracked structure subjected to a resonant loading, two failure criteria need to be evaluated to investigate the reliability of the structure. They are the displacement criterion and the stress criterion. Different from the traditional dynamic structure design, particular a defect-free structure, large displacement instead of stress is always first considered to dominant the structural failure. In this study, the modified SIFs of the first six modes were determined by the displacement on the upper surface of the crack. Based on Δw-$\sqrt{r}$ plot, the magnitude of modified SIFs can be then be compared, where Δw is the displacement difference between crack surfaces and r is the radial distance from the crack tip. The plot provides very important results that if there is a crack exists in the structure, the stress failure criterion must also be considered, especially for higher frequency vibration.

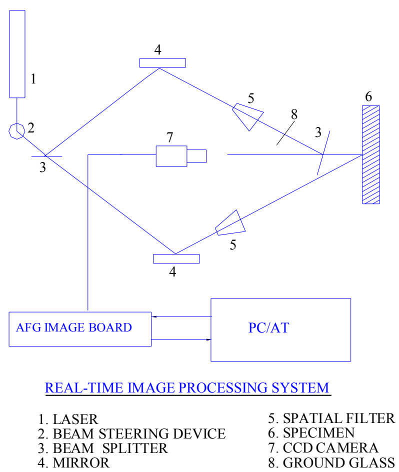

Fig. 1 Schematic of the assembled experimental setup

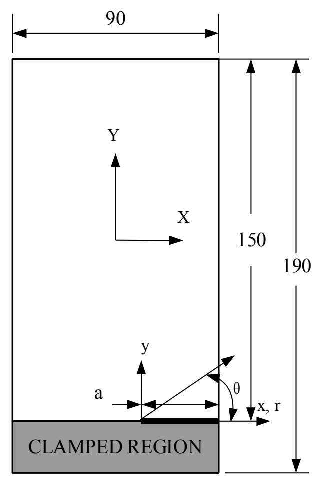

Fig. 2 The edge cracked specimen with $[0]_{16}$ stacking sequence

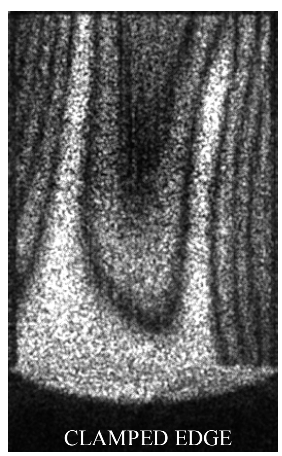

Fig. 3 Typical ESPI fringe pattern of a $[0]_{16}$ composite plate with 20mm crack length on the clamped edge

References

[1] W. C. Wang and C. H. Hwang, “Experimental analysis of vibration characteristics of an edge-cracked composite plate by ESPI method” Int. Journal of Fracture Mechanics, 91(4), 311-321(1998).
[2] W. C. Wang, C. H. Hwang, S. Y. Lin, "Vibration Measurement by the Time-Averaged Electronic-Speckle- Pattern-Interferometry Methods", Applied Optics, 35(22), 4502-4509(1996).

Comparison of nulling interferometry and rotational shearing interferometry for detection of extra-solar planets

Beethoven Bravo-Medina*, Marija Strojnik
Centro de Investigaciones en Óptica, Apdo Postal 1-948, 37000, León, México
*beethoven@cio.mx, marias@cio.mx

Abstract: In the last few years, the extra-solar planet detection has been an important science topic. An overwhelming number of the current detections were accomplished using indirect methods. In order to achieve direct detections of planets, a number of interferometric techniques have been proposed. Among those some already implemented in terrestrial observatories. The most published of these techniques is the nulling interferometry. We are working on a derivative interferometric technique, referred to as rotational shearing interferometry. We perform a comparison between these techniques and report on the status of their development.

1. Challenges of detecting an extra-solar planet

The interest of the scientific community and general population about the planets outside our Solar system has been increased during the last thirty years. The number of confirmed extra-solar planets has increased only in the latest decade, from 427 in 2011 to over 2900 in 2018. The main detection techniques used in these observations are transit and radial velocity. Unfortunately, these techniques are indirect techniques; they provide indirect and limited data. Therefore, a direct detection technique is necessary to validate the current observations [1].

The main challenge in the extra-solar planet detection lies in the very large distance of the nearest stars to the Earth. This distance implies two resolution problems: the radiometric and the spatial one. The radiometric resolution is the minimum irradiance change that may be detectable by the sensor. The radiation ratio between the planet and the star is at least 10^{-6} in the visible region. The spatial resolution is the minimum angular separation that allows us to distinguish between two point sources. For a planet with an orbit similar to that of the Earth that orbits a star at ten parsecs from the observatory, the angular separation between the planet and the star is 0.1 arcsec.

Additionally, the stars are surrounded by the exo-zodiacal dust. This dust is located in the habitable zone of the planetary systems, meaning where the planets are likely to be located. Its presence obstructs the detection of exo-planets acting as veil [2]. In order to decrease these resolution challenges and the effect of exo-zodiacal dust, several interferometric techniques have been proposed. The most highly-developed of these techniques is the nulling interferometry. We are pursuing an alternate interferometric technique, the rotational shearing interferometry where we already demonstrated some initial promising results [3].

In this work, we compare the nulling interferometry and the rotational shearing interferometry for exo-planet detection. In Sec. 2, we describe the operating principle of each technique. Then, we present the state of development and implementation of each technique in Sec. 3. Finally, we present the summary in Sec. 5.

2. Analysis

Due to the large distance between the star-planet system and the Earth, it is necessary to model the star and the planet as point sources. Additionally, their wave fronts may be modeled as planar. If the star is aligned with the optical axis, its wave front is perpendicular to the optical axis and the planet wave front is slightly tilted as illustrated in Fig. 1.

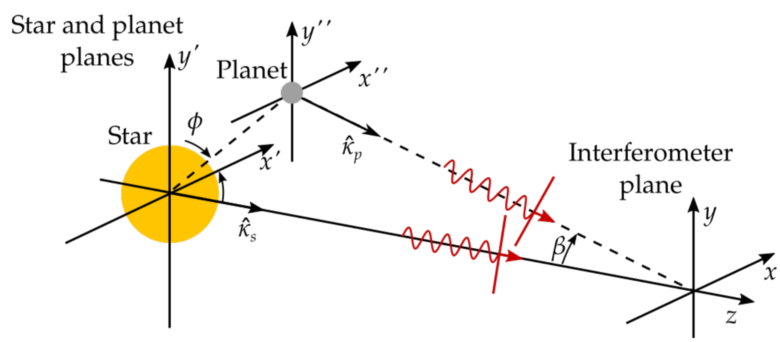

Fig. 1. Star-planet system viewed from the interferometer. The star is aligned with the interferometer optical axis.

The nulling interferometry technique interferes the star wave front with itself. The star wave front through two interferometer paths may be canceled because the incorporation of beam splitters under ideal condition. Due to planet-wave-front tilt, its wave front propagates by a slightly different optical path and avoids the cancellation. The result of the star's self-interference is an uniform irradiance level without fringes. This irradiance level depends of the angular separation between the planet and the star, and the optical path difference (OPD) of the interferometer. This technique allows the radiometric-resolution improvement.

The rotational shearing interferometer (RSI) interferes the wave front with a rotated version of itself. The RSI is insensitive to rotationally-invariant wave fronts. When the rotationally-symmetric star wave front interferes with its rotated version, the resultant interference pattern has uniformly irradiance with a single fringe, characterized by a uniform field. Furthermore, the star irradiance may be canceled when the interferometer OPD has adjusted to $\lambda/2$. This adjust may be performed with a wedge prism [4] or a Risley prism [5]. The planet wave front is rotationally asymmetric because it is tilted with respect to the optical axis. Therefore, the interferometric pattern generated in the RSI of the planet wave front consists of straight fringes. The fringe density and orientation depend on the shearing angle [6]. This technique allows the improvement of radiometric and spatial resolution. Finally, the RSI may be used to cancel symmetric rings of exo-zodiacal dust.

3. Implementation

Since the first proposal in 1979, several projects to implement nulling interferometry in exo-planets detection have been proposed. The most important of these projects is the Darwing / TPF project [7]. This project contemplates a spatial nulling-interferometer, whose deployment is planned for about 2030. There are additional subprojects that involve nulling interferometry. Two of these subprojects are the Keck Nuller Interferometer (KNI) [8] and the large binocular telescope interferometer (LBTI) [9]. The initial objective of these interferometers is the characterization of the exo-zodiacal dust. The first detection of warm dust with the LBTI around the star η Crv was reported in 2015.

Meanwhile, the RSI has been proposed to be implemented in an observatory at the moon.

4. Summary and future work

Both, the nulling interferometry and the Rotational Shearing Interferometry have been proposed and studied for the exo-planet detection. Both techniques may be used to enhance the radiometric resolution of a stellar observatory. However, only the RSI allows the enhancement of the spatial resolution. The search for direct detection of extra-solar planets is a long-term project. We continue demonstrating RSI features in laboratory experiments. Its current capabilities include the cancelation or at least attenuation of rotationally-symmetrical structures of exo-zodiacal dust.

References

[1] Strojnik, M., Bravo-Medina B., et al., "Optimal band for extra solar planet detection: Sub-millimeter spectral region." in Infrared, Millimeter, and Terahertz Waves (IRMMW-THz), (2017).

[2] Strojnik, M., "Rotationally shearing interferometer for extra-solar planet detection," in SPIE Proc.10762-12, Infrared Remote Sensing and Instrumentation XXVI, (2018).

[3] Strojnik, M., "Extra-solar planet detection methods," in SPIE Proc.10762-2, Infrared Remote Sensing and Instrumentation XXVI, (2018).

[4] Bravo-Medina, B., et al., "Shearing interferometer with adjustable optical path difference for exoplanet detection." in SPIE Proc. 9973 Infrared Remote Sensing and Instrumentation XXIV, (2016).

[5] Bravo-Medina, B., Strojnik, M., et al., "Error compensation in a pointing system based on Risley prisms." Applied optics **56.8,** 2209-2216 (2017).

[6] Strojnik, M. and Baltazar-Barron R., "Detection of planet in nearby solar system with rotational shearing interferometer: concept demonstration," in Latin America Optics & Photonics Conference, (2014).

[7] Fridlund, C. V. M., "Darwin-the infrared space interferometry mission." ESA bulletin. **103.3**, 20-25 (2000).

[8] Serabyn, E., et al., "The Keck interferometer nuller." The Astrophysical Journal **748.1,** 55 (2012).

[9] Defrere, D., et al., "First-light LBT nulling interferometric observations: warm exozodiacal dust resolved within a few AU of η Crv." The Astrophysical Journal **799.1,** 42 (2015).

Review on the Analytical Wavefront Representation by Means of Polynomials

Daniel Malacara-Doblado, Francisco Javier Gantes Nuñez and Daniel Malacara-Hernández
Centro de Investigaciones en Óptica, AC. León, Gto.
dmalacdo@cio.mx

Abstract: A tutorial review on the several methods for the analytical representation of wavefront aberrations and the topography of optical surfaces is described.

1. Introduction to the style guide, formatting of main text, and page layout

Ideally, a wavefront should either have a flat or spherical shape in the absence of any aberrations. The on-axis wavefront aberrations of a centered optical system with perfectly coaxial surfaces with rotational symmetry also have rotational symmetry about the optical axis. The off-axis aberrations of this perfect centered optical system do not in general have rotational symmetry, but they are laterally symmetric about the meridional plane. These are the so called primary and high order Seidel aberrations [1]. However, if the optical system has tilted or, decentered optical surfaces, without rotational symmetry or with local deformations, the wavefront aberrations have deformations without any kind of symmetry.

2. Wavefront Representation with a Linear Combination of Polynomials, Orthogonal in a Discrete Base

When performing a least squares fitting of a polynomial of degree K to a set of measured data points, it is well known that in the process a set of K + 1 linear simultaneous equations with K + 1 unknowns appear. It is also known that the matrix of this system has a matrix that it is symmetric, all elements in a minor diagonal are equal and it is nearly singular. In other words, its determinant has a small numerical value. This makes the matrix difficult to invert, mainly if K is large. The alternative procedure is to express the wavefront deformations as a linear combination of orthogonal polynomials, as it will be explained here.

$$W(x,y)=\sum_{j=1}^{L}\alpha_j G_j(x,y) \\ =\alpha_1G_1+\alpha_2G_2+\alpha_3G_3+\alpha_4G_4+\alpha_5G_5+\alpha_6G_6+\alpha_7G_7+.... \tag{1}$$

with an orthogonality condition, similar to the scalar product of vectors:

$$\sum_{n=1}^{N}G_i(x_n,y_n)G_j(x_n,y_n)=0 \qquad \text{if} \quad i\neq j \tag{2}$$

and the points (x_i, y_i) with i = 1, 2, 3,…N are the points in the pupil where the wavefront is measured. As in a system of orthogonal vectors, we say that a system of functions $G_i(x,y)$ are orthogonal to each other, in a certain domain, if none of the functions could be expresses in terms of the other functions. This set of functions is complete if any other possible function can be expressed as a linear combination of the functions, members of the set. For this reason we say that the polynomials are orthogonal in a discrete base. A least squares fitting to the measured $W'(x_n, y_n)$ values of the wavefront is done with:

$$\varepsilon=\sum_{n=1}^{N}\left[W(x_n,y_n)-W'(x_n,y_n)\right]^2 \\ \varepsilon=\sum_{n=1}^{N}(\alpha_1G_1+\alpha_2G_2+\alpha_3G_3+\alpha_4G_4+\alpha_5G_5+..-W')^2 \\ \frac{\partial\varepsilon}{\partial\alpha_j}=2\sum_{n=1}^{N}(\alpha_1G_1+\alpha_2G_2+\alpha_3G_3+\alpha_4G_4+\alpha_5G_5+..-W')G_j=0 \tag{3}$$

obtaining:

$$\alpha_j \sum_{n=1}^{N} G_j^2(x_n, y_n) = \sum_{n=1}^{N} W'(x_n, y_n) G_j(x_n, y_n) \tag{4}$$

Thus, the coefficients α_j are:

$$\alpha_j = \frac{\sum_{n=1}^{N} W'(x_n, y_n) G_j(x_n, y_n)}{\sum_{n=1}^{N} G_j^2(x_n, y_n)} \tag{5}$$

To calculate these coefficients α_j we need to obtain the numerical values of the orthogonal polynomials $G_j(x_n, y_n)$ at all sampling points (x_n, y_n).

3. Gram-Schmidt Orthogonalization to Generate Orthogonal Polynomials $G_r(x,y)$

Gram-Schmidt orthogonalization, also called the Gram-Schmidt process, is a procedure which takes a nonorthogonal set of linearly independent functions and constructs an orthogonal basis over an arbitrary interval with respect to an arbitrary weighting function *w(x)*.

Applying the Gram-Schmidt process to the functions 1, x, x^2, ... on the interval [-1,1] with the usual L^2 inner product gives the Legendre polynomials [2]. In Figure 1 shown some calculations for an interferogram example

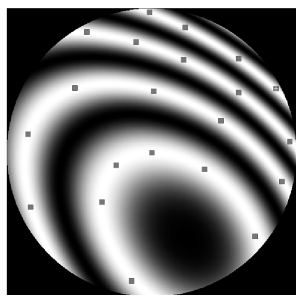

Figure 1. Aberration coefficients in fringe pattern (L=8)

	Un-Normalized	Normalized
β_1 =	0.00	0.00
β_2 =	1.0×10^{-5}	1.0×10^{-7}
β_3 =	0.00	0.00
β_4 =	1.0×10^{-7}	1.0×10^{-11}
β_5 =	5.0×10^{-8}	5.0×10^{-12}
β_6 =	0.00	0.00
β_7 =	0.00	0.00
β_8 =	2.0×10^{-10}	2.0×10^{-16}

Wavelength: 632.8 nm
Diameter: 200 mm

References

[1] Seidel Philipp L., "Ueber die Theorie der Fehler, mit welchen die durch optische Instrumente gesehenen Bilder, behaftet sind, und über die mathematischen Bedingungen ihrer Aufhebung.", Abhandlungen der naturwissenschaftlich-technischen Commission bei der Königl. Bayerischen Akademie der Wissenschaften in München, Nr. 1. (1857) 227-267
[2] Reed, M. and Simon, B. "Methods of Modern Mathematical Physics", Vol. 1: Functional Analysis. New York: Academic Press, pp. 46-47, 1972.

Extended Abstracts

Session
OPTICAL INSPECTION FOR INDUSTRY

Pg.

Three-dimensional shape measurement beyond diffraction limit for measurement of dynamic events 81
Yasuhiko Arai

3D electromagnetic surface wave transmission microscopy: thickness distribution of thin films over an extended area 83
F. Villa-Villa, Rodolfo Cortés, Cesar E. García-Ortiz, Víctor Coello, and B. Reyes-Ramírez

3D-profilometry for objects with surface discontinuities by the projection of two-frequency color-coded fringe patterns 85
Geliztle A. Parra, Jorge L. Flores, J. Matías Di Martino, Jose A. Ferrari

3D surface measurement using uni-axis image fiber system 87
Geliztle A. Parra Escamilla, David I. Serrano Garcia, Fumio Kobayashi, Nathan Hagen and Yukitoshi Otani

Projected fringes technique and penetrant liquid test to identification of the mechanical discontinuities 89
Mishraim Sánchez Torres, José Luis Javier Sánchez González, Amalia Martínez García, Juan Antonio Rayas, Víctor Ruiz Cortes, Víctor Manuel Juárez Luna

Refractive-Index Dispersion Curves by Radial-Shear Interference 91
G. Rodríguez-Zurita, G. Calderón-Hernández, A. Castillo-Cardoso,

Three-dimensional shape measurement beyond diffraction limit for measurement of dynamic events

Yasuhiko Arai
Kansai University 3-3-35 Yamate-cho Suita Osaka Japan
arai@kansai-u.ac.jp

Abstract: A three-dimensional (3-D) shape-measurement method is proposed for superfine structures beyond the diffraction limit of lens using the basic feature of speckle interferometry. Because the differential coefficient distribution of the shape of such an object can be detected by giving a known lateral shift to the measured object in speckle interferometry, the shape can be reconstructed by integrating the differential coefficient distribution. The influence of magnitude of lateral shift on measured shape and the method for measurement of dynamic events are discussed.

1. Introduction

Speckle interferometry, which has been conventionally treated as a deformation measurement method [1], was applied to the three-dimensional measurement of the shape using a lateral shift [2]. The influence of magnitude of lateral shift on measured shape and the method for measurement of dynamic events were discussed in this paper.
In experiments using diffraction gratings, the newly proposed optical system was constructed. The shape of a superfine structure can be measured by this method. The measured results were compared with results obtained using atomic force microscopy (AFM). It can be confirmed that the 3-D shape beyond the diffraction limit of a lens can be measured at high resolution using speckle interferometry.

2. Principle of three-dimensional shape measurement

The optical system used in this experiment was shown in Fig.1(a). The original system of the optical system can detect high-resolution deformation using only two sheets of speckle patterns before and after deformation of the measured object [1]. In addition, a piezo stage, which can provide a lateral shift (dx) to the measured object, was placed in the original system [2]. The lateral shift was provided in horizontal direction when performing 3-D shape measurements.
Now, the lateral shift of the measured object is given by dx. The cross-sectional shape of the measured object in the x-direction after shift becomes f(x + dx), and the cross-sectional shape before a shift is defined as f(x). When the two speckle patterns before and after the lateral shift are extracted and analyzed, the deformation value at the measured point becomes f(x) - f(x + dx). When the analyzed deformation value, f(x) - f(x + dx), is divided by the lateral shift (;dx), the resulting value can be assumed to be equivalent to an approximate-differential coefficient in the x-direction. Furthermore, when this differential coefficient is integrated over the x-direction, the 3-D shape f(x) in the x-direction can be obtained [2]. Because the differential coefficient is a finite difference value based on the limited finite value in the actual calculation, the calculated 3-D shape f(x) is a pseudo-integrated value in the integration calculation.

3. Production of artificial speckle pattern for one-shot 3-D shape measurement method

In this study, the speckle pattern obtained in one-shot was shifted as a virtual displacement in computer memory as shown in Fig.1 (b) and (c). Then, the second speckle pattern was produced artificially by shifting “k pixel”. By using both real and artificial speckle patterns, the 3-D shape measurement can be realized.

4. Confirmation of the validity of measurement principle

The measurement principle of the proposed method using only a one-shot speckle pattern image was tested by using a diffraction grating with relatively large pitch (1.67μm). The principle of the method is discussed using a grating where the 3-D shape is a unique shape (; saw shape).First, the 3-D shape was analyzed by two real speckle patterns using the conventional method. The results are shown in Figures 2 (a) and (b) as the slope and shape distributions, respectively. Second, 3-D shape analysis using the real speckle pattern and the artificial speckle pattern produced by using the real speckle pattern was performed. In this case, the artificial speckle pattern was produced by shifting five pixels (≅ 60nm) on the camera element in order tofulfil the same lateral shift as the real physical lateral shift. By considering lens magnification (200 times) and so on, the width of one pixel was set as corresponding to 12 nm in preparation of the measurement experiment.The results are shown in Figures 2 (c) and (d). It can be confirmed that the results in Figures 2 (a) and (b) using the physical lateral shift agree well with the results in Figures 2 (c) and (d). These results confirm the validity of the principle of the method using virtual shift.

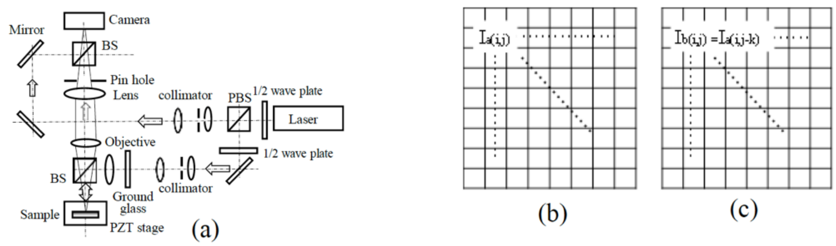

Fig.1 Optical system and data processing in computer

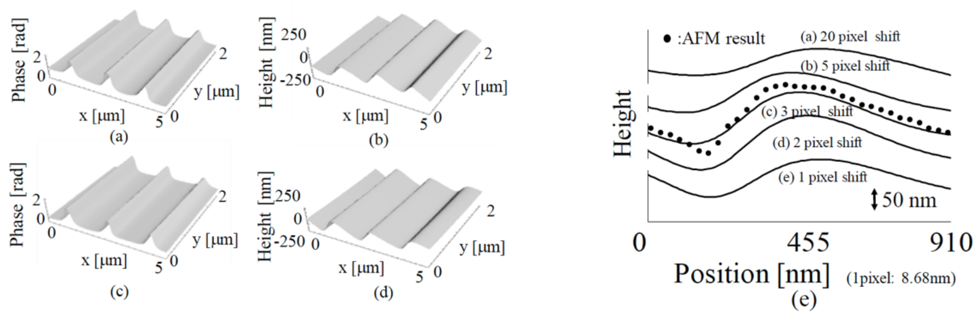

Fig.2 Slope and 3D shape distribution in experiment and influence of change of lateral shift in 3D shape

5. Influence of the magnitude of lateral shift

The influence of the magnitude of the lateral shift on the result was investigated. The height distribution is shown in Fig. 2 (e). In this case, the magnitude of the lateral shift was three pixels. After increasing or decreasing the magnitude of lateral shift, it is confirmed that the cross-section of the shape changed, as shown in Fig. 2 (e). The dotted line in Fig. 2 (e) is the measured result by atomic force microscope (AFM). It is confirmed that the optimum shift magnitude is about 3 pixels (≅26.0nm) in this case. It is confirmed that there would be the optimal lateral shift in this method.

6. Measurement beyond the diffraction limit of a lens

The proposed one-shot speckle pattern method was applied to measurement of superfine sizes beyond the diffraction limit of a lens. The results are shown in Figure 3. The dotted line in Fig. 3 (c) is the result from AFM. It is confirmed that the result (cross-section A-A) using new one-shot speckle interferometry agreed with the result by AFM well.

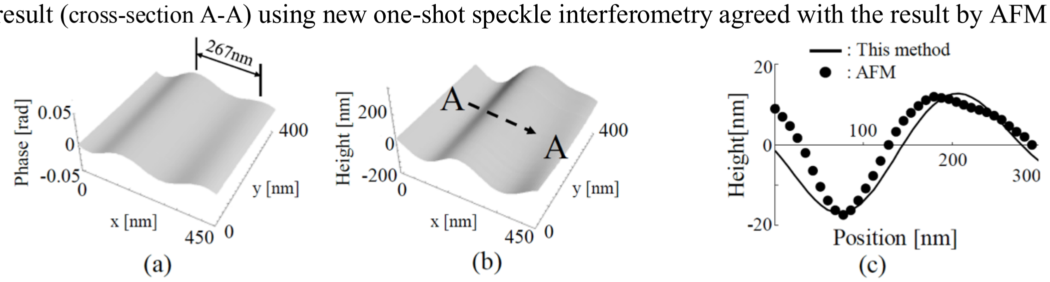

Fig. 3 Measurement results in the case of grating beyond limit of diffraction

7. Conclusion

In this paper, a basic method for measuring dynamic events using a one-shot speckle pattern was proposed. The validity of the proposed method was investigated with diffraction gratings and was confirmed from experimental results. Furthermore, the influence of the magnitude of lateral shift on the measured result was also discussed. Then, it was confirmed that there was an optimal lateral shift in this method. It was also confirmed that the new method could be used for superfine sizes beyond the diffraction limit of the lens.

References

[1] Y. Arai, Simultaneous in-plane and out-of-plane deformation measurement by speckle multi-recording method, Measurement, **91**, 582-589 (2016).
[2] Y. Arai, Three-dimensional shape measurement beyond the diffraction limit of lens using speckle interferometry, J. Modern Optics, doi.org/10.1080/09500340.2018.1470266 (2018).

3D electromagnetic surface wave transmission microscopy: thickness distribution of thin films over an extended area

F. Villa-Villa*, Rodolfo Cortés, Cesar E. García-Ortiz**, Víctor Coello**, and B. Reyes-Ramírez***
*Centro de Investigaciones en Optica, Loma del Bosque 115, Lomas del Campestre, León Gto. 37150 México.
**CICESE, Unidad Monterrey, Alianza Centro 504, PIIT Apodaca, N.L. 66629, México
e-mail: fvilla@cio.mx

Abstract: A measuring technique based on capturing the scattered light produced by a photonic crystal-bulk interface when an electromagnetic surface wave is present is proposed to characterize thin films along extended areas. Given the sensitivity of the method, this deserves the name of a microscopy, since it is possible to determine the thickness map distribution with precision up to a fraction of a nanometer.

1. Introduction

Surface electromagnetic waves (SW) that are highly confined fields around the interface between a truncated one-dimensional photonic crystal (1DPC) and a bulk (or vacuum) [1-3], can be used in sensing devices in a similar way to plasma surface waves (SPW) but with inherent advantages, since they involve the use of highly stable dielectric materials, and depending on the structure of the 1DPC, SW can exist at any frequency of the EM spectrum[1].These nonradiative waves propagate along the 1DPC-air interface with evanescent fields in the perpendicular direction away from the surface plane constituting a mechanism for energy loss [1-2], and can be excited by optical techniques identical to those used for excitation of SPW on metals by attenuated total reflectance [4].

If we consider a 1DPC-air system, in the context of photonic crystals language, SW can exist below the light line of vacuum and within a band gap [2-3]. In Fig. 1a we show the band structure under TE polarization of a 1DPC whose period is composed of three dielectric layers p/2-q-p/2 with refractive indices and thicknesses: $n_p = 2.44$ $d_p = 82.2$ nm, $n_q = 1.46$, and $d_q = 130.1$ nm respectively. In this dispersion diagram $\varpi = \omega\Lambda/2\pi c$, and $\bar{\beta} = \beta\Lambda/2\pi$ represent the reduced frequency, and the reduced parallel component of the wave vector respectively. The normalization constant is chosen to be $\Lambda = 2d_p + d_q$, and c is the speed of light in vacuum.

Within the first bang gap a SW is indicated by a dashed curve. In Fig. 1b the reflectance as a function of the wavelength in the region around the SW is graphed for a finite system with five periods. In order to observe the SW an absorption index $k_p = 0.01$ was considered.

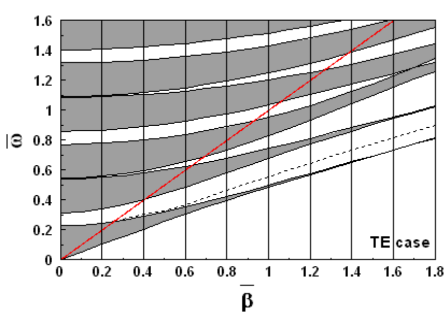

(a)

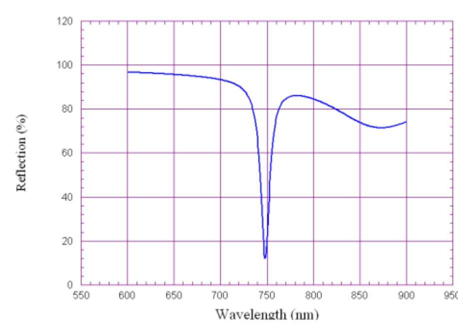

(b)

Fig. 1. a) Band structure of 1DPC under TE polarization. Allowed bands are indicated by shaded regions and band gaps with white color. The light line for vacuum is shown in red line b) Reflectance vs. wavelength in the region around the SW for $\bar{\beta} = 0.327$ and $\varpi = 0.281$, which correspond to $\theta = 50º$ with an incident medium of $n_0 = 1.52$.

2. Results

The experimental setup consists of a Kretschmann configuration with an imaging system installed on the same rotation stage as the prism (N-BK7), allowing us to take images with a charge-coupled device (CCD) camera of the same area of interest as the prism was rotated (Fig. 2a). In Fig. 2b the scattered measured signal is shown. The samples were positioned at the hypotenuse of a right angle prism, using refractive index-matching oil. In contrast to typical reflectivity measurements, we detected the scattered light produced by SW that are decoupled by the local roughness of the films. Each pixel of the CCD camera was intended to act as individual power detectors in order to determine the intensity at every excitation angle; nevertheless, the signal-to-noise ratio turned out to be too low if a single pixel was considered. We used the correlation coefficient R^2 of the fitting results as a figure of merit to determine the minimum amount of square pixels that would be necessary to average, in order to get a reliable experimental curve ($R^2 > 0.9$). The experimental data were fitted for arrays of 1×1, 2×2, and 3×3 pixels [Fig. 3(a)-(d)]. A full 3D reconstruction of the dielectric film thickness using the procedure as described in [4]. We our results we estimate a sensibility around 0.2 deg/nm for this technique. The dependence of the SW angle position with the outer thin film thickness shown that for films thicker than 60 nm, the SW angle surpasses 65°.

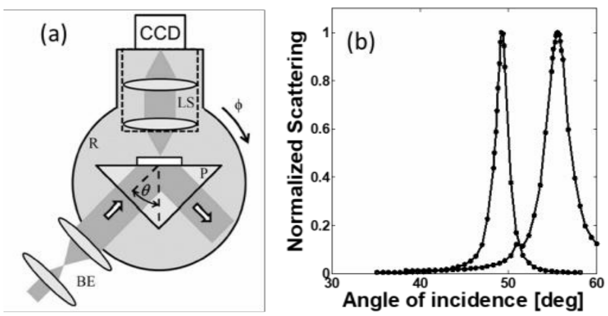

Figure 2. (a) Experimental setup which consists of a Kretschmann configuration where a CCD camera and a lens system (LS) have been attached to the same rotation stage (R) as the prism (P). The beam of the laser is expanded (∼1 cm) with a beam expander (BE) to illuminate the complete area of interest. (b) Scattering measurements (circles) obtained with the CCD camera).

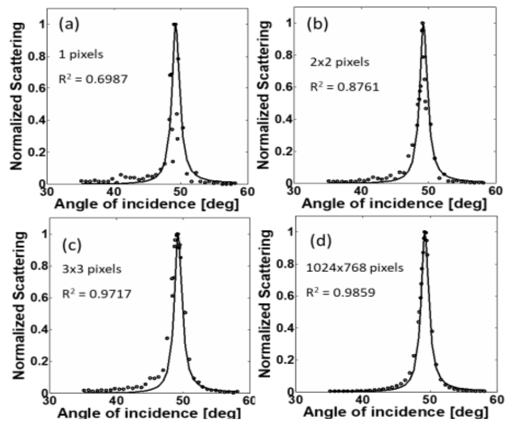

Figure 3. Intensity measurements obtained from pixels in the CCD camera for averaged arrays of (a) 1×1, (b) 2×2, (c) 3×3, and (d) 1024×768 pixels. The red solid curve corresponds to the best numerical fit, and the correlation coefficient R2 is labeled in each case. The wavelength considered was 760 nm.

3. Conclutions

Although not explicitly included here, with the presented technique is possible to reconstruct 3D thickness maps of dielectric thin films through the detection of scattered light from EM SW existing at a 1DPC-bulk interface by using a Kretschmann configuration. The high sensitivity of the SW due to changes in the geometrical parameters of a multilayer allows us to determine the local (point-by point) thicknesses of a thin film at a subnanometer scale. With our experimental set up, it is possible to determine the thickness distribution of a thin film along an extended area which is correlated to every pixel of the image associated to each point in the surface of the sample by using an automated post-processing algorithm based on numerical fitting.

References

[1] F. Villa, L. E. Regalado, F. Ramos-Mendieta, J. Gaspar-Armenta, and T. López-Ríos, "Photonic crystal sensor based on surface waves for thin film characterization", Opt. Lett. **27** 646-648 (2002).

[2] F. Villa, J. A. Gaspar-Armenta, and F. Ramos-Mendieta, "One-dimensional photonic crystals: equivalent systems to single layers with a classical oscillator like dielectric function", Opt. Comm. **216** 361-367 (2003).

[3] Jorge A. Gaspar-Armenta, Francisco Villa, "Band structure properties of one-dimensional photonic crystals under the formalism of equivalent systems," JOSA-B, 21 405-412 (2004).

[4] Cesar E. García-Ortiz,* Rodolfo Cortés, Robin Orejel, Raúl Hernández-Aranda, Israel Martínez-López, Félix Aguilar, and Víctor Coello, "3D thickness map reconstruction of dielectric thin films using scattering of surface plasmon polaritons," Opt. Lett,43(4) 691-694(2018).

3D-profilometry for objects with surface discontinuities by the projection of two-frequency color-coded fringe patterns

***Geliztle A. Parra[1], Jorge L. Flores[1], J. Matías Di Martino[2], Jose A. Ferrari[2]**
[1]Departamento de Electrónica, Universidad de Guadalajara, Av. Revolución 1500, 44840, Jalisco, México
[2] Instituto de Física, Facultad de Ingeniería, U de la R, J. Herrera y Reissig 565, 11300 Montevideo, Uruguay
E-mail: gparra82@hotmail.com

Abstract: 3D-profilometry of discontinuous solids by fringe projection is a difficult task due to the problem posed by the phase unwrapping at sharp borders. Our implementation is based on the acquisition of two frequency color-coded fringe patterns for reconstructing the discontinuous 3D surface. Experimental results are implemented showing the feasibility of the implementation.

1. Introduction

The algorithms focused to retrieve the phase in fringe projection techniques such as phase-shifting (PS) [1,2] or Fourier-based techniques [3], perform an arctangent calculation undertaken over the four quadrants of phasor space. For perfect experimental conditions, phase unwrapping is a straightforward and path-data-independent procedure. However, this is not the case when the sample presents abrupt discontinuities, complex irregular shapes resulting and several approaches have been proposed to overcome the problem of retrieving the profile with large discontinuities, for example, Servin et al. proposed a 2-step temporal phase unwrapping algorithm [4], which only needs the 2-extreme phase-maps to achieve the same results as the standard temporal unwrapping method; the phase map requires at least 3 fringe-shifted patterns, projected sequentially on a reference plane and on the object under test. The present work shows an implementation of this method considering the acquisition of two color-coded fringe patterns. The approach taken in this work have potential usage of in-line 3D profilometry acquisition systems [5] with the improvement of dynamic range on the reconstruction.

2. Profile unwrapping with color-coded patterns

Our implementation is based on a 2-sensitive fringe-pattern demodulation technique presented by Servin, et al at [4]. Servin et al. have demonstrated that by employing two frequency fringe pattern measurements, one at high-sensitive phase $\varphi_{w2}(x, y)$ and other with low-sensitivity phase estimation $\varphi_1(x, y)$, an efficient method for the reconstruction of surfaces with abrupt changes. The proposal is based on retrieve an estimation process considering the sensitivity gain G and the wrapping phase operator W as

$$\varphi_2(x, y) = G\varphi_1(x, y) + W[\varphi_{w2}(x, y) - G\varphi_1(x, y)] \quad (1)$$

The method is efficient for the reconstruction of surfaces with abrupt discontinuities, its drawback is the consideration of acquire at least six frames for the test object (three with a low-frequency carrier and other three frames with high-frequency carrier), and equivalently, other six frames for a reference plane. In our implementation, we employed a color-coded phase-shifting technique capable to acquire three phase-shifted patterns on single RGB-image [6], overcoming the time limitations of sequential PS fringe projection. The use of colored fringe patterns poses the issue of crosstalk between adjacent colors, which induces unevenly spaced phase delays between the different color patterns ($I_{R,G,B}$),

$$I_{R,G,B}(x, y) = a_{R,G,B} + b_{R,G,B} \cos[\varphi(x, y) + \delta_{R,G,B}] \quad (2)$$

where the sub-indices RGB indicate the color channels red, green and blue, respectively, $\varphi(x, y)$ is the phase to be determined, $a_{R,G,B}$ and $b_{R,G,B}$ are slowly varying functions of (x, y), and $\delta_{R,G,B}$ are unevenly spaced phase-step. The phase $\varphi(x, y)$ is retrieved by following Ayubi's algorithm [7], after removed the DC component $a_{R,G,B}$ [8] and compensated the color imbalance of the intensities $b_{R,G,B}$ [6].

$$\varphi(x,y) = \tan^{-1} \frac{(I_G - I_B)\cos(\delta_R) + (I_B - I_R)\cos(\delta_G) + (I_R - I_G)\cos(\delta_B)}{(I_G - I_B)\sin(\delta_R) + (I_B - I_R)\sin(\delta_G) + (I_R - I_G)\sin(\delta_B)} \quad (3)$$

3. Experimental Results

The images were acquired with an 8-bit digital color camera with 1280×1024 pixels. The fringe patterns were projected with a commercial LCD-projector with 1024×768 pixels under a viewing angle θ ≈ 13 deg. Figures 1(a) and 1(b) show the colored fringe patterns of low- and high-spatial frequency, respectively, projected on a reference plane. The frequency ratio is 10, i.e. $G = 10$. The patterns were projected over a static test object, a rectangular prism (4.2cm×6cm×8cm), Figs. 1(c) and 1(d). Figure 2(a) shows the phase profile $\varphi_2(x, y)$ unwrapped utilizing Eq. (1) and Fig. 2b) shows the unwrapped phase profile. The dark line shows the raw result modulated by spurious third-harmonics of the carrier frequency and the red line shows a high-quality result obtained after a median filter operation (size 5×5 pixels) applying the method of Pan [9].

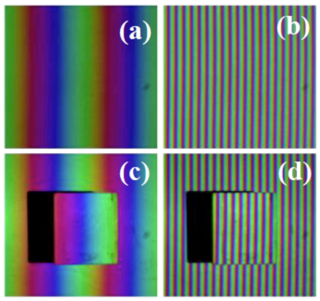

Fig.1. a and b) are the low- and high frequency colored fringe pattern projected over a reference plane. c) and d) are the low- and high frequency pattern projected over the test object.

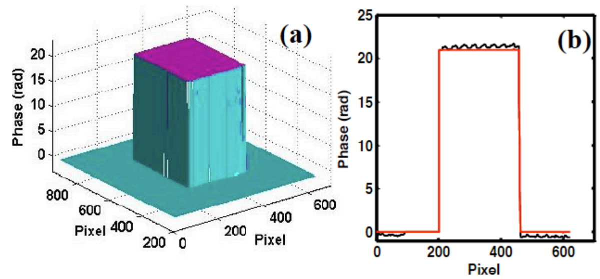

Fig. 2. a) Unwrapped profile $\varphi_2(x, y)$ in false color; b) Cut across the unwrapped phase profile. Dark line shows the raw result modulated by the spurious third harmonics of the carrier frequency and red line shows the result after a filtering operation.

4. Conclusions

We presented an improvement to the temporal unwrapping method reducing the number of necessary frames in a factor three by employing color-coded fringe patterns (i.e., RGB-images) for reconstructing the discontinuous 3D surface of the test object. The improvement proposed in the present work are potentially useful for automated profile reconstruction of moving or static objects with discontinuous surface, e.g. the proposed method can be used to produce high-resolution digital 3D models for reverse engineering and industrial metrology, also, it could be used as line profilers to surface or volumetric measurements at line production speed.

References

[1] J. L. Flores, B. Bravo-Medina, and J. A. Ferrari, “One-frame two-dimensional deflectometry for phase retrieval by addition of orthogonal fringe patterns,” Appl. Opt. 52, 6537–6542(2013).
[2] D. Malacara, Optical Shop Testing (Wiley, 2007), Chaps. 9 and 25.
[3] M. Takeda and K. Mutoh, “Fourier transform profilometry for the automatic measurement of 3D object shapes,” Appl. Opt. 22, 3977–3982 (1983).
[4] M. Servin, J.M. Padilla, A. Gonzalez, and G. Garnica, “Temporal phase-unwrapping of static surfaces with 2-sensitivity fringe-patterns,” Opt. Express 23(12) 15806-15815 (2015).
[5] Frankowski, G., & Hainich, R. (2009, February). DLP-based 3D metrology by structured light or projected fringe technology for life sciences and industrial metrology. In SPIE MOEMS-MEMS: Micro-and Nanofabrication (pp. 72100C-72100C).
[6] J.L. Flores, J.A. Ferrari, G García-Torales, R. Legarda-Saenz, and A. Silva, “Color-fringe pattern profilometry using a generalized phase-shifting algorithm,” Appl. Opt. 54(30) 8827-8833 (2015).
[7] G. A. Ayubi, C. D. Perciante, J. L. Flores, J. M. Di Martino, and J. A. Ferrari, “Generation of phase-shifting algorithms with N arbitrarily spaced phase-steps,” Appl. Opt. 53, 7168–7176 (2014).
[8] Y. Hu, J. Xi, J. Chicharo, and Z. Yang, “Blind color isolation for color channel-based fringe pattern profilometry using digital projection,” J. Opt. Soc. Am. A 24, 2372–2382 (2007).
[9] B. Pan, Q. Kemao, L. Huang, and A. Asundi, “Phase error analysis and compensation for nonsinusoidal waveforms in phase-shifting digital fringe projection profilometry,” Opt. Lett. 34(4) 416-418 (2009).

3D surface measurement using uni-axis image fiber system

***Geliztle A. Parra Escamilla[1], David I. Serrano Garcia[1], Fumio Kobayashi[2], Nathan Hagen[2, 3] and Yukitoshi Otani[2, 3]**

[1]Departamento de Electrónica, Universidad de Guadalajara, Av. Revolución 1500, 44840, Jalisco, México
[2]Utsunomiya University, Department of Optical Engineering,
[3]Center for Optical Research and Education, 7-1-2, Yoto, 321-8585 Utsunomiya-city, Tochigi, Japan
E-mail: gparra82@hotmail.com

Abstract: The surface variation of the samples is retrieved by using fringe contrast modulation and the technique considers the defocus change and the encoding information on the fringe contrast of the projected structured light pattern. We implement a 2D Fourier Transform filter for remove the baseline information for increasing the fringes contrast and also we improved the fitting function for better results in the 3D reconstruction. A comparison of the obtained results with a commercial microscope and different filters were implemented. The depth range of the system is 1.1 mm and a lateral range of 2 mm by 2 mm. We demonstrate the technique by showing the surface profile of a measured object.

1. Introduction

Applications of endoscopes range from medical, security purposes and industrial inspections due of the advantage of portability in small regions where the usage of common imaging systems encounters difficulties [1]. Uniaxial measurement techniques and imaging fiber-based systems presents a good matching due to the fiber property of carrying the illumination and imaging on the same axis, this combination offers a unique advantage, over the common triangulation based techniques, when objects have discontinuous of height steps, deep holes or the object is placed in confined space [2-8]. We have succeeded in combine the focus method with an imaging fiber, to acquire three-dimensional volume information of reflective samples in a uniaxial manner working as a 3D endoscopic system [9]. The implementation needs to consider noise generated from inner reflections (fiber bundle faces, lens surface) and the pixelated appearance of the images due to the fiber imaging bundle.

2. Theoretical background

The system is based on measuring the contrast variation $\gamma(x, y, z_i)$ at each pixel in the image (x, y) at different depth (z_i) by using a sinusoidal fringe pattern generated by a liquid crystal device. Contrast variation can be obtained by a combination of these intensities and a fitting process on a Gaussian function basis relates the contrast distribution, γ, with depth information, z_i, as:

$$\gamma = \gamma_0 \exp\left(-2\left(\frac{z_i - z_0}{A}\right)^2\right) \tag{1}$$

where γ_0, z_0,and A, represent the maximum contrast, location in depth of the maximum contrast and depth range were the 3D reconstruction can be obtained. By taking inverse of Eq.1, depth information can be retrieved.

3. Setup and experimental results

Figure 1 shows the optical setup for uniaxial depth measurement using a liquid crystal grating (LCG) for projecting grating patterns onto a sample. The grating image is focused onto an image fiber inlet and propagated to the image fiber outlet via the fiber bundle and transmitted back into the CCD camera.

Image data presents two features: a constant baseline signal due to the back reflection coming from the two fiber-surfaces removed by using a referenced non-reflective material. The second feature is a pixelated appearance of the images caused by the composition of the imaging fiber bundle (13,000 fibers) removed by using a frequency filtering process. A character of a one-yen Japanese coin (Fig. 2) was used as a sample to demonstrate three-dimensional reconstruction, Fig. 2a) and 2b) show the spatial distribution of the selected region measured with a commercial microscope and Fig. 2c) shows the profile of two region as a comparison of our result and the commercial microscope. Reconstruction of the sample is presented in Fig. 3.

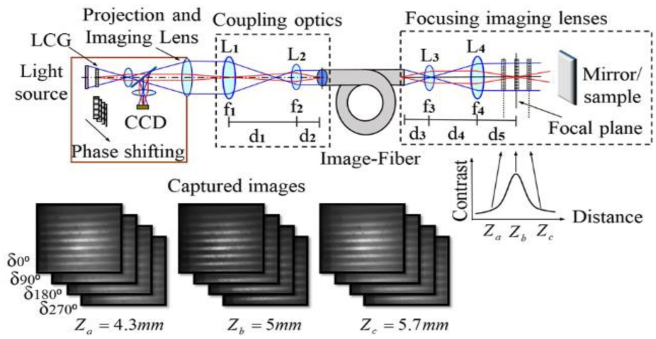

Fig. 1 Setup of the 3D profilometer using an imaging fiber in uniaxial configuration. z_a, z_b, z_c, represent the captured fringes at different depths.

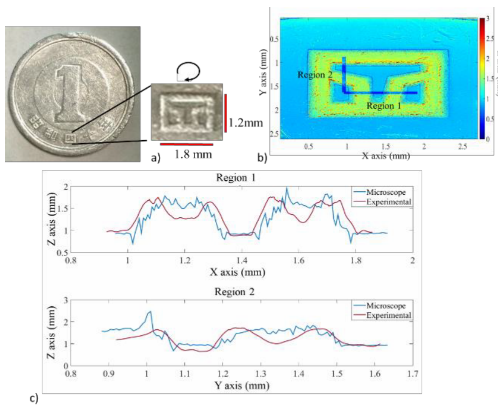

Fig. 2 a) Measurement symbol in a one-yen coin, b) 3D distribution of the symbol measured with a commercial microscope, and c) the graphs show the profile comparison of two regions: region 1 is the profile of the x axis and region 2 is the profile of the y axis.

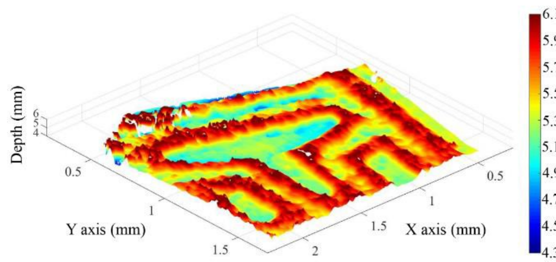

Fig. 3 Measured result of 3D surface distribution of a symbol in a one-yen coin after apply the frequency filter for remove the pixelated appearance.

4. Conclusion

We succeed to use the same imaging fiber as illumination and measurement medium. The depth range of the system is 1.1 mm and the lateral range of 2 mm by 2mm. The system offers the advantage of the transportability to the measurement to a confined space having potential application on medical or industrial endoscopes systems.

References

[1] J. Geng et al., "Review of 3-D endoscopic surface imaging techniques," IEEE Sens. J. 14 (4) (2014) 945-960.

[2] Y. Otani, F. Kobayashi, Y. Mizutani, S. Watanabe, M. Harada and T. Yoshizawa, "Uni-axial measurement of tree-dimensional Surface profile by liquid crystal digital shifter," Proc. SPIE 7790 (2010) 77900A-1.

[3] Y. Otani, F. Kobayashi, Y. Mizutani, and T. Yoshizawa, "Three-dimensional profilometry based on focus method by projecting LC grating pattern," Proc. SPIE 7432 (2009) 743210.

[4] Y. Mizutani, R. Kuwano, Y. Otani, N. Umeda and T. Yoshizawa, "Three-dimensional shape measurement using focus method by using liquid crystal grating and liquid varifocus lens," Proc. SPIE 60000J (2005).

[5] T. Yoshizawa, T. Shinoda and Y. Otani, "Uniaxis rangefinder using contrast detection of a projected pattern," Proc. SPIE 4190 (2001) 115-122.

[6] P. Birch, A. Buchanan, R. Young and C. Chatwin, "Depth from structured defocus that is independent of the object reflectivity function," Opt. Lett 36(12) (2011) 2194-2196.

[7] Y. Xu and S. Zhang, "Uniaxial three-dimensional shape measurement with projector defocusing," Opt. Eng. 51(2) (2012) 023604.

[8] M. Takeda, et al., "Absolute three-dimensional shape measurements using coaxial and co-image plane optical systems and Fourier fringe analysis for focus detection," Opt. Eng., 39(1) (2000).

[9] G. A. Parra Escamilla, F. Kobayashi and Y. Otani, "Three-dimensional surface measurement based on the projected defocused pattern technique using imaging fiber optics," Opt. Commun. 390 (2017) 57-60.

Projected fringes technique and penetrant liquid test to identification of the mechanical discontinuities

Mishraim Sánchez Torres[1], José Luis Javier Sánchez González[1], Amalia Martínez García[2], Juan Antonio Rayas[2], Víctor Ruiz Cortes[3], Víctor Manuel Juárez Luna[1]
[1]Universidad Autónoma de Baja California, Ensenada, Baja California, México
[2]Centro de Investigaciones en Óptica, A. C. León, Guanajuato, México
[3]Centro de Investigación Científica y de Educación Superior de Ensenada, Baja California, México
a356854@uabc.edu.mx

Abstract: The present work shows results of fracture measuring by projected fringes method. Square-shaped aluminum sheet sample was clamped along three corners while mechanically point loaded at fourth one. The mechanical stress leads to out-of-plane displacements. The mechanical fracture can be observed from displacements field measured. The non-fluorescent penetrating liquid test is applied to the same sample.

1. Introduction

The identification of the discontinuities represents an essential part for a complete analysis of quality in a metallic structure, in such a way that from these deformations it is possible to determine a correct valuation and continuity of operation of the same. Discontinuities can appear on the surface in the form of fractures or cracks. Non-destructive tests have been used to detect and quantify the quality of a piece. Some non-destructive techniques [1] have been based on recent technological developments such as electronic speckle pattern interferometry (ESPI), projected fringes technique, shearography, digital holography, etc. Many others have done so in traditional methods such as fluorescent fluids, magnetic inspection, ultrasound and x-rays [2,3]. In this work we analyzed the technique of projected fringes to locate mechanical fractures in comparison with non-fluorescent penetrating liquids test.

2. Experimental details

We used the optical setup shown in Fig. 1a. A projector (DELL model *109WX*, resolution *WXGA 1280* × *800*) was utilized for projecting gray-code fringes onto the surface of the specimen. $\boldsymbol{\alpha}$ was equal to $\mathbf{10^o}$. The illumination distance was selected adequately large, such that the CCD camera (Pixelink model *PL-B776*, QXGA resolution *2048* × *1536*, Pixel Pitch 3.2 × 3.2 $\boldsymbol{\mu m^2}$) in Fig. 1b captured, at the beginning of the test, nearly straight equally spaced fringes of period $\boldsymbol{p = 3.66\ mm}$. The out-of-plane deformation induced by the mechanical load application led to the departure of the viewed fringes from straight lines. The pulling direction was *z* and the stress of $\mathbf{14.8\ N}$. As the test progressed, we retrieved the whole-field phase map obtained from state 1 and 2, Fig. 1c.

If the in-plane displacement is adequately small, $\emptyset$ encodes information only on the out-of-plane displacement W (the departure of the surface from the initially surface) induced on the illuminated surface by the application of load. According to [4], the phase modulation $\emptyset$ is related to the corresponding out-of-plane displacement W by

$$W(x,y) = \frac{\phi(x,y)p}{2\pi \tan \alpha} \quad (1)$$

where α is the angle between the observation direction and the illumination direction.

Note that in general, $\emptyset$ stands for the phase modulation induced between any pair of load stages. When the phase stepping technique [5] is used to retrieve the phases at two load stages (Fig. 1c), the corresponding phase difference $\emptyset$ can be computed and then used (by applying Eq. 1) to evaluate the out-of-plane relative displacement W between these two load stages (Fig. 2a). The fringe projection technique has been successfully applied to monitor changes in the shape that involved out-of-plane deformations greater than $0.001\ mm$.

Later the sample was analyzed by penetrating liquids test, Fig. 2b. The stages are: immersion of the metallic material inside a nonfluorescent liquid (naphtha solvent red colorant), elimination of excess liquid, impregnation of dust layer that magnify the visualization of the fracture, inspection and evaluation of the sample and finally its cleaning. Fig. 3 exhibits some profiles from the graphic shown in Fig. 2a.

3. Conclusions

The present work shows results of fracture measuring by the technique of projected fringes to metallic plate. The sample was analyzed by the penetrating liquids test. One of disadvantage of this technique is that is a qualitative method in comparison with projected fringes technique.

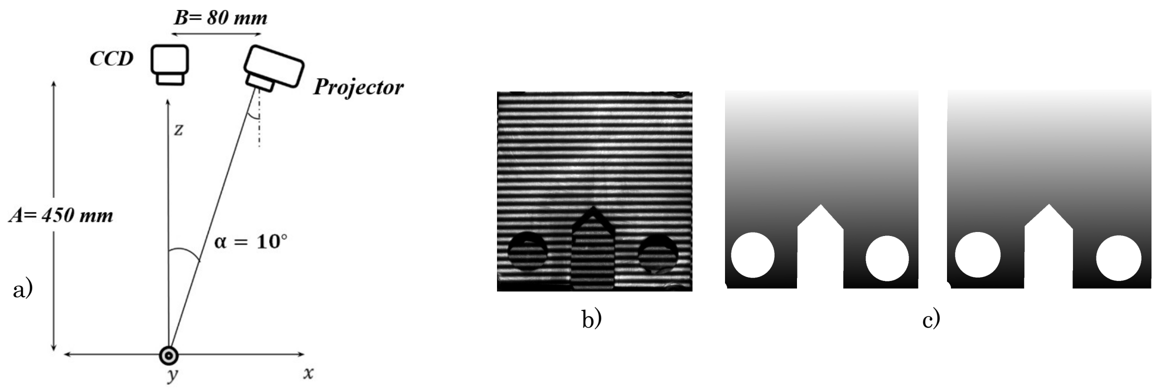

Fig. 1 a) Scheme of the fringe projection system, b) Projected fringes onto the sample, c) Unwrapped phase for the states 1 and 2.

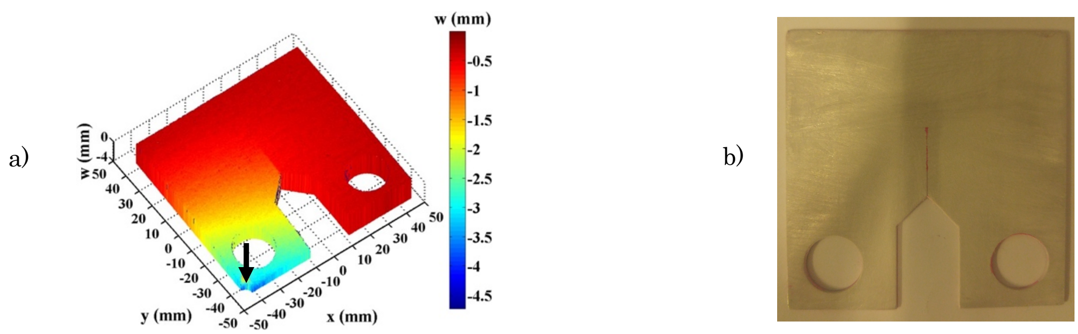

Fig. 2 a) Relative displacement W induced on the sample during the mechanical load applied. b) Visualization of the fracture by means of the test of penetrating liquids.

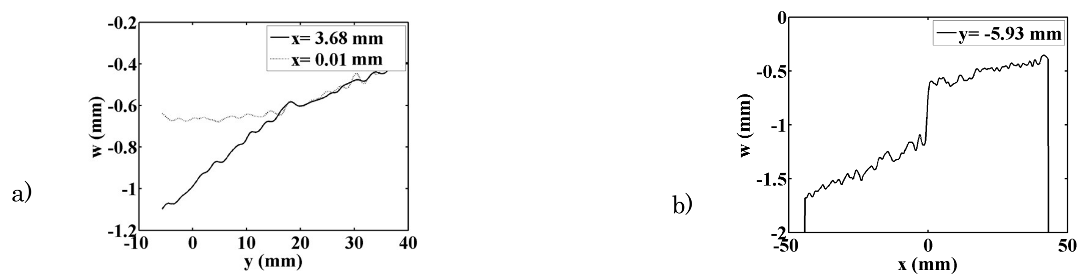

Fig. 3. a) One-dimensional plot of some columns from the graphic shown in Fig. 2a; b) plot to one row.

References

[1] Pramod Rastogi, "Optical measurement techniques – A push for digitization," Optics and Lasers in Engineering, **87,** 1-17 (2016).
[2] J. S. Epstein, *Experimental techniques in fracture* (VCH-SEM, New York, 1993).
[3] A. S. Kobayashi, *Handbook of experimental mechanics* (SEM, New York, 1994).
[4] Amalia Martínez, J. A. Rayas, R. R. Cordero, Daniela Baliero, Fernando Labbe, "Leaf cuticle topography retrieved by using fringe projection," Optics and Lasers in Engineering, **50**, 231-235 (2012).
[5] Cruz Santos W, L. López García, A. Redondo Galván, "Improving the accuracy of phase-shifting techniques," Optical Engineering, **54**, 112-20 (2015).

Refractive-Index Dispersion Curves by Radial-Shear Interference

G. Rodríguez-Zurita*, G. Calderón-Hernández, A. Castillo-Cardoso,
L. A. Rendón-Delgado, N. I. Toto-Arellano.[1]
Benemérita Universidad Autónoma de Puebla, Pue., 72570, México
[1]Universidad Tecnológica de Tulancingo, Tgo., México
gzurita@fcfm.buap.mx

Abstract: Refractive-index determination in thick parallel-plates made from homogeneous dielectric samples has been widely reported and a method of this type could serve for dispersion inspection. After trying several alternatives, a new simple method based on reflection of the first interface and transmission on the second interface under coherent illumination has proved to be useful for the task. Because the incident wave is a convergent one, both interfering waves form a non-compensated radial-shear interference pattern. For low numerical apertures and good parallelism in plate's faces, nearly compensation for aberrations is achieved and thus Newton rings are formed. An equivalent radius of curvature can be calculated from the resulting interferogram. From it, the refractive index can be calculated. Experimental results are shown applying this technique in some well-known glasses and liquids as well as photorefractive materials.

1. Introduction

For refractive-index dispersion measurements a simple and accurate method for refractive-index determination using several wavelengths is desirable. Refractive-index determination in parallel-plates made from homogeneous isotropic dielectric samples has been early described by M. Mantravadi as a two-stage technique [1] among other techniques. First, a collimated coherent beam is focused by a well-corrected lens on the sample plate's first interface. The reflection is returned to the focusing lens and pass through a beam splitter made of another plane plate acting as a lateral-shearing interferometer. The resulting pattern on an observing screen is expected to be made of parallel fringes having certain lowest frequency when perfectly focusing on that first interface because such condition allows the best collimation to achieve. Secondly, the plate is translated towards the focusing lens letting the convergent beam to enter the sample until the focusing perfectly reaches the second interface. This condition is similar to the first one and thus, parallel, low-frequency fringes on the viewing screen must also be formed. Within the paraxial approximation, the measurement of the difference of the two position is t/n', where t is the plate thickness and n' its refractive index.

We offered an alternative set-up to be used in flat plates as well but featuring no plate translation at all. It is based on focusing a collimated coherent beam on the first interface of the sample and collecting it for observation at a given screen. But the transmitted beam reflects itself in the second sample's interface before returning back to the first interface to leave the sample. Because this second beam superposes with the first one, an interference pattern appears on the observing screen. For a plate with perfect parallel plane faces, this situation acts as a non-compensated radial-shear interferometer suffering of spherical aberration as the second beam travels twice through the first interface. For an imperfect parallelism, a lateral shift is also induced, making its contribution to a relative complex pattern. However, for sufficiently low numerical apertures in the converging beam and with a plate with good parallelism, Newton rings can be observed. This basic pattern can be simply interpreted as one due to two spherical waves of different radius of curvature. From the equivalent radius of curvature and the observing distance, the refractive index $n'(\lambda)$ can be fitted for several used wavelengths. Moreover, the same technique can be used for liquids within a reservoir having a flat bottom reflective face, so as to form a parallel plate in the required region of the sample. When good alignment and levering is achieved, Newton rings also appear. This arrangement is an alternative to the known technique of immersing a lens within the sample with its curved face in contact with a flat reflecting surface (or only to filling the gap with some drops from the sample) to form Newton rings [2]. In this paper, a description of the method is presented in detail and examples of some obtained dispersion curves both with solid samples (soda lime, BK7), with distilled water and immersion oil type A and optically anisotropic solids as well are provided ($\lambda/2$ wave-plates made from birefringent quartz, $Bi_{12}GeO_{20}$, $LiNbO_3$).

2. Experimental setup

Fig. 1a depicts the geometric interpretation of the spherical waves giving rise to the relevant Newton rings which are observed. Under these conditions, Snell´s Law in paraxial approximation can be applied, resulting in $\Delta=\Delta_{par} = 2\ t/n'$, with t the sample's thickness and n' its refractive index (box in Fig.1.a). Standard procedure to calculate an equivalent radius from the pattern [3] enables the calculation of Δ by knowing one of both radius because Δ can be interpreted as the difference between them. The corresponding set-up is shown in Fig. 1.b.

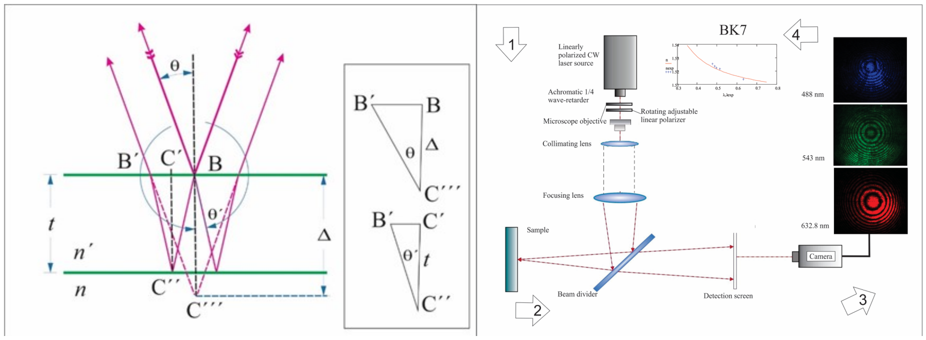

(a) **(b)**

Fig.1. (a) Basic geometric scheme to interpretation of Newton rings appearing as a radial-shear interference pattern. (b) Experimental set-up (labeled arrows from 1 to 3) and some examples of results (labeled arrows from 3 to 4).

3. Experimental Results

Fig. 2(a) show the exact position of C′′′ given by $\Delta(\theta)/t$ as a function of the incidence angle θ (deg). n = 1 and n' = 1.5, 1.6, 1.7. Up to 5 deg there is a negligible difference with Δ_{par}. The sample's refractive index can thus be determined by knowing t and Δ. Using several light sources of different wavelengths (476, 480, 496, 514.5, 632.8 nm) with appropriate coherence lengths, data for dispersion curves can be captured and Cauchy Coefficients can be calculated by appropriate fitting. Some results are presented in 2(b).

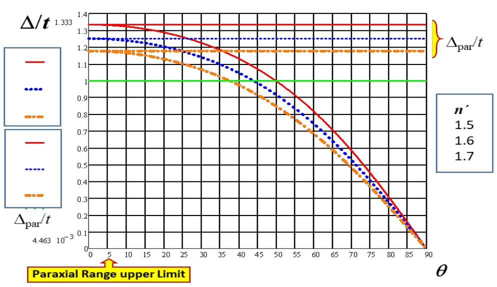

Sample	A, B [μm²]coefficients
Soda lime, t = 1.9 cm	1.512, 3.918x10^{-3}
BK7, t =1.9 cm	1.499, 5.853x10^{-3}
Distilled water (at 2200 MASL, 20ºC), t =1.1 cm	1.323, 3.234x10^{-3}
BGO (no applied electric field), t = 2 mm	2.294, 0.099

(a) **(b)**

Fig.2. (a) Exact position of C′′′ given by Δ(θ)/t as a function of the incidence angle θ (deg). n = 1 and n' = 1.5, 1.6,1.7. (b) Cauchy Coefficients **A** and **B** resulting from the described procedure for several samples.

4. Final Remarks

Δ must be of a value roughly between 2 mm and 4 cm for the patterns to be Newton rings and to be captured with no more than 10X amplification. Flatness in solid samples of λ/5 or better could be required as well as a good parallelism. Both conditions can be achieved in many samples, as in float glasses and also in liquids by proper levering. Birefringent samples with proper cuts could also be inspected with this technique for their principal refractive indexes to be measured just by adding polarization adjustments. Angular departures greater than about 3 mrads would render an additional lateral shift, thus giving rise to interferograms requiring of a more elaborate adjustment (based on the wave-front aberrations polynomial, for example). Non aberrations compensation must be also another feature to be consider in this same case.

References

[1] M. Mantravadi, "Shearing interferometry" Optical Shop Testing D. Malacara ed. (1997), Chap.5.
[2] vlab.amrita.edu,. (2013). Newton's Rings-Refractive index of liquid. Retrieved 18 January 2017, from vlab.amrita.edu/?sub=1&brch=189&sim=1520&cnt=1).
[3] R. S. Longhurst, sec.8-4 "Newton's rings" in Geometric and Physical Optics, 3rd ed., Longman (1973) London

Extended Abstracts

Session
OPTICAL MANIPULATION AND TWEEZERS AND THEIR APPLICATIONS

Pg.

Programable holographic materials based on semi-stable hydrogel composites 94
Yunuen Montelongo and Ali K. Yetisen

Programable holographic materials based on semi-stable hydrogel composites

Yunuen Montelongo and Ali K. Yetisen
Universidad De La Salle Bajío. Avenida Universidad 602, Lomas del Campestre, 37150. León, Guanajuato, México.
Author e-mail address: ymontelongo@delasalle.edu.mx

Abstract: On this research we propose a mechanism to produce a semi-static volumetric patterning of materials through standing waves of light. The composite proposed on this research consist of a hydrogel capable o maintaining nanoparticles in stable positions, but also, providing the flexibility to displace with a given optical pressure. We demonstrate multilayer active photonic crystals, hologram and lenses.

1. Introduction

Programable materials that change their physical properties in presence of light is a topic of interest in modern science. It is well stablished that highly intense light pulses are capable of ablating material. The process of ablation is non-reversible due the chemical decomposition of the involved materials. Nonetheless, materials whose chemical composition remain stable and are reversible still remind elusive. Techniques for non-reversible optical writing, such as silver halides and photoresist, are widely used in industry.

One of the most important observations of Maxwell was the association of light with the physical momentum. In the classical interpretation, light produces a momentum transfer to a material thanks to the electromagnetic Lorentz force. Maxwell described that a light beam hitting on a surface should produce a momentum transfer, either be the absorption or by the reflection of the beam. More recent observations conducted to the concept of optical tweezer[1], in which a particle scatters light producing a force, and therefore, a momentum transfer. The most typical application is the trapping of particles with dimension close to the wavelength of light. In this case, a focused beam shines on a particle whose refractive index is higher than that of the surrounding medium. The gradient of the focused beam creates a force, pushing the particle towards the center of the beam. This effect is considered as “optical trapping” or “optical tweezer” because it occurs in both directions of the beam: transversal and parallel, maintaining the particle at the highest intensity point of the beam, which is the focus. A more complex scenario occurs when the particle has metallic characteristics. In such case, the plasmonic resonance of the electromagnetic field can produce scattering in phase or out of phase, creating a respective positive or negative force[2].

2. Methods

In this research we propose the transfer motion in parallel of multiple particles, producing assembly through the interference of laser beams. The main difference with the traditional system of optical tweezers, is that the potential well for the particle trapping is produced with the standing waves of the interference of coherent light beams. The most basic application of this effect was demonstrated for the two-dimensional case[3]. This mechanism consisted in the assembly of multiple particle in parallel lines over a plane to form grooves over a surface. This mechanism was coined as ‘optical tractor’ because of the similarity with furrow patterns. A generalization of this phenomenon occurs in the three-dimensional space, where standing waves are formed in a volume rather than in a surface. Although this generalization can be applied straightforward, the physical demonstration requires a medium capable to maintain particles in stable positions in a volumetric space. This physical constrain is the most important challenge to produce configurable assemblies in the three-dimensional space. Once this challenge is overcome, it is possible to create arbitrary volumetric patterns with the interference of multiple beams[4].

In this work we have utilized hydrogels whose rheological characteristics allow particle to be displaced, but also, to be maintained in stable positions. We developed a composite consisting of silver nanoparticles of an average size of 50 nm suspended in a hydrogel of poly-HEMA. In this composite, the nanoparticle can be maintained in a stable position at room temperature and with no force applied to the material. Nevertheless, poly-HEMA is a soft material with shear-thinning characteristics. This implies that temperature and force reduce the stiffens of the material, softening the surroundings of the nanoparticles and allowing its displacement. Hence, a laser beam is capable of moving nanoparticles located in semi-static stages. Furthermore, this process is facilitated by the increment of temperature and by the reduction in stiffens because of the shear-thinning of the medium. Both effects are produced by the laser: the temperature increases because of the light absorption and the force because of the momentum transfer. In our mechanism, the displacement from an initial static stage to an assembled static stage occurs within an intermediate transition stage, where the nanoparticle increases its temperature (and therefore the temperature of the surrounding medium), but simultaneously, the nanoparticle is displaced with the applied optical pressure. In addition to the optical pressure, thermophoretic and acoustophoretic effects take place. Both effects have a negative force with respect to the intensity gradient[5]. According to our estimations, the contributions of these secondary physical mechanisms are minimal and can be neglected for our calculations.

3. Results and conclusions

To demonstrate the process of assembly, we exposed the material to a counterpropagating standing wave with a given tilting angle. The utilized laser was a pulsed Nd:YAG doubled to 532 nm. The beam consisted of a high intensity pulse of 10 mJ/cm^2 in 10 ns exposed in an area of about one square centimetre. This multilayer structure could create a diffraction spot when a white light beam was hitting the material. The diffraction spot had wavelength peak corresponding the band gap of the multilayer structure. Furthermore, it was observed that the diffraction efficiency increased with the number of exposures of the standing wave. Similarly, a further assembly could be stablished with new conditions (e.g. a new tilting angle). For instance, two consecutive standing waves with different tilting angle were capable of superposing two different diffraction spots. Interestingly, the second standing wave could make disappear the first diffraction spot. These erasing processes was investigated, and it was observed up to twelve writing-erasing cycles with minimal degradation.

Finally, different rewritable optical devices such as photonic crystal, lenses and holograms where fabricated. Rewritable photonic crystals were fabricated with the superposition of multiple counterpropagating standing waves of different tilting angles. Rewritable three-dimensional holograms were demonstrated with the interference of a reference planar beam with the reflection of a coin. Finally, a rewritable lens was fabricated with a methodology similar to the holographic recording. In this case, the reference beam was interfered with the reflection of a concave mirror. When the lens was recorded, it was possible to observe the reconstruction with a laser beam. The laser beam focused at a given distance from the material, that was the same distance of the focal point of the concave mirror.

It is envisioned that these new types of programable materials will open new possibilities in the fabrication of rewritable optical devices. These devices will have applications as active photonic crystals, metamaterials. holographic displays, optical elements, storage devices, among others.

References

[1] K. C. Neuman and S. M. Block, “Optical trapping,” *Rev. Sci. Instrum.*, vol. 75, no. 9, pp. 2787–2809, Sep. 2004.
[2] M. Šiler, L. Chvátal, and P. Zemánek, “Metallic nanoparticles in a standing wave: Optical force and heating,” *J. Quant. Spectrosc. Radiat. Transf.*, vol. 126, pp. 84–90, Sep. 2013.
[3] O. Brzobohatý, V. Karásek, M. Šiler, L. Chvátal, T. Čižmár, and P. Zemánek, “Experimental demonstration of optical transport, sorting and self-arrangement using a tractor beam,” *Nat. Photonics*, vol. 7, no. 2, pp. 123–127, Feb. 2013.
[4] Y. Montelongo, A. K. Yetisen, H. Butt, and S.-H. Yun, “Reconfigurable optical assembly of nanostructures,” *Nat. Commun.*, vol. 7, p. 12002, Jun. 2016.
[5] R. Klajn, K. J. M. Bishop, and B. A. Grzybowski, “Light-controlled self-assembly of reversible and irreversible nanoparticle suprastructures,” *Proc. Natl. Acad. Sci.*, vol. 104, no. 25, pp. 10305–10309, Jun. 2007.

Extended Abstracts

Session
OPTICAL METROLOGY

	Pg.
Application of photogrammetry for the dynamic characterization of 6DOF force and moment sensors Tutsch, Rainer; Nitsche, Jan; Kumme, Rolf	98
Compensation Model for Geometrical Error of Laser Tracer Huixu Song, Zhaoyao Shi and Hongfang Chen	100
Displacement measurement by means of speckle pattern interferometry with radial in-plane sensitivity Jorge R. Parra-Michel, David Asael Gutiérrez Hernández, Marco A. Escobar, Rafael Martínez-Peláez	102
Fundamental Study on Surface Topography Measurement with Wideband Spatial Frequency using Scattered Light Spectroscopy - Construction of Broadband Optical frequency Comb - Ippei Takahashi, Yasuhiro Takaya and Yasuhiro Mizutani	104
Deep neural network for fringe pattern filtering Alan Reyes and Mariano Rivera	106
Fringes Demodulation using Simulated Annealing with Independent Window Partition Iosvani Moré Quintero, Francisco J. Cuevas de la Rosa	108
Relative Error in Out-of-plane Measurement Due to the Object Illumination Type Gustavo A. Gómez-Méndez, Amalia Martínez-García, Ana Karen Reyes, Juan A. Rayas	110
Two-Step Shadow Moiré Fringe Analysis Chia-Cheng Lee, Terry Yuan-Fang Chen*, Fa-Yen Cheng	112
One-shot in slightly off-axis digital holographic microscopy based in a compact design Miguel León-Rodríguez, Juan A. Rayas, Amalia Martínez-García, Alejandro Barrientos-García, Orlando M. Medina-Cázares	114
3D Reconstruction System Based on Structured Light Projection and Artificial Neural Networks	116

J. V. Sosa-Balderas[1], F. J. Cuevas[1], J. Salazar-Medina[2], A. López-Martínez[1]

Simultaneous Measurement of Temperature and Velocity in a Synthetic Jet 118
B. Barrientos, C. Mares, D. Sarocchi, R. Valdivia, and A. Blanco

Evaluation of displacement fields using Digital Image Correlation 120
Zaira A. Morales-Espinoza and Víctor H. Flores-Muñoz

Internal defect identification using phase-sensitive optical coherence elastography 122
Bo Dong, Bing Pan

Real-Time 3D Measurement using Background-Modulated Modified Fourier Transform Profilometry 124
Xinran Liu, Jonathan Kofman

Multi-Ray Exponential Fringe-Pattern Projection for 3D Surface Measurement with Off-the-Shelf Hardware 126
Ali Babaei, Mohammad Saadatseresht, Jonathan Kofman

Optical Metrology for Alignment of Large Radio Telescopes 128
David M. Gale

Gates' interferometer configuration as a fringe projection unit 130
José Rubén Sánchez-Aguilar, J. A. Rayas, Amalia Martínez-García, Miguel León-Rodríguez

Application of photogrammetry for the dynamic characterization of 6DOF force and moment sensors

Tutsch, Rainer [1]; Nitsche, Jan[1,2]; Kumme, Rolf [2]
1) Institute of Production Metrology, Braunschweig University, Schleinitzstr. 20, 38106 Braunschweig, Germany
2.) Physikalisch-Technische Bundesanstalt PTB, Bundesallee 100, 38116 Braunschweig, Germany
r.tutsch@tu-bs.de

Abstract: Multi-axis sensors for force and moment are increasingly applied e.g. in automotive industry. Currently calibration is performed sequentially for the single axes. Crosstalk between the single axes cannot be detected. In this paper we present a technique for a multi-axis characterization of such devices. An electrodynamic shaker is used to introduce sinusoidal vibration with variable frequency. The sensor under test is loaded with a test mass that can be laterally adjusted to cause dynamic momentum. The absolute and relative movement of the shaker table and the load mass are measured optically, using a scanning laser vibrometer and a special photogrammetric setup. The dynamic sensitivity tensor of the sensor can be derived from these data.

1. Introduction

The international standard ISO 376 [1] and the national German standard DIN 51309 [2] describe the static calibration of uniaxial force sensors and moment sensors, respectively. There is no standard for multi-axial sensors and for dynamic loading conditions. It is, however, well known that the sensitivity is a function of the frequency of the force or moment [3, 4] and that crosstalk might occur, especially between force and moment channels. Investigations of the properties of multi-axis transducers have been performed using uniaxial excitation, but only with dynamic forces adjusted parallel to the axes of the sensor. Dynamic momentum was generated by attaching excentric load masses to the accelerated sensor [5]. In these experiments an acceleration sensor and a laser interferometer were used to measure the acceleration of the load mass. We have enhanced the setup by installing a photogrammetric camera system and are now able to measure all six degrees of freedom of the movement of the load mass.

2. Principle of measurement

According to Newton´s law a force F acting on a mass m causes it to move with an acceleration a = F/m. If we place a calibrated load mass on top of the sensor under test and put this arrangement on the platform of an electrodynamic shaker, then we can introduce dynamic forces that are directly proportional to the accelerations.

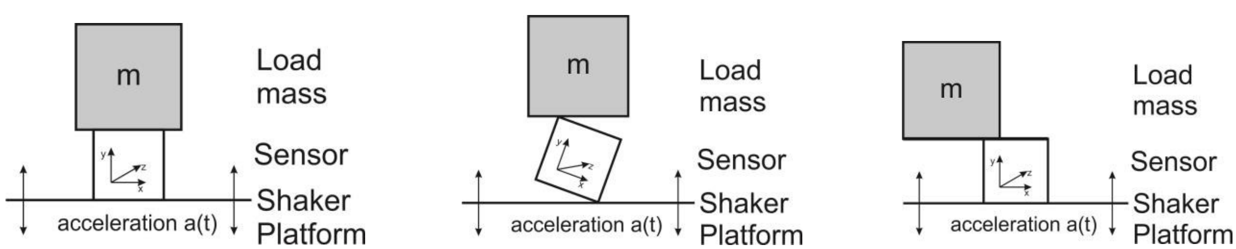

a) b) c)

Fig. 1: Basic principle of generating well defined dynamic forces and momenta.
a) Conventional arrangement, force direction parallel to sensor axes
b) Deliberately chosen force direction / c) Combination of force and momentum

Fig. 1 shows a simplified view of the measurement principle. If we measure the acceleration of the mass and we know the geometrical arrangement of sensor and mass we can calculate the acting force and momentum and we can compare these values to the output signals of the sensor. One difficult task was the design, manufacturing and evaluation of precision mechanical fixtures that allow an adjustable arrangement as shown in fig. 1 while being as stiff as possible to minimize measurement errors [6]. While in conventional experiments the sensor usually is being modelled as a system of two masses, a spring and a damper, we introduced a model with three orthogonal pairs of springs and dampers.

3. Experiments

We used a photogrammetric setup to measure the time-resolved movement of the load mass. The surface of the load mass was covered with a stochastic dot pattern and a pair of stereophotogrammetric cameras was used to track its movement (Fig. 2).

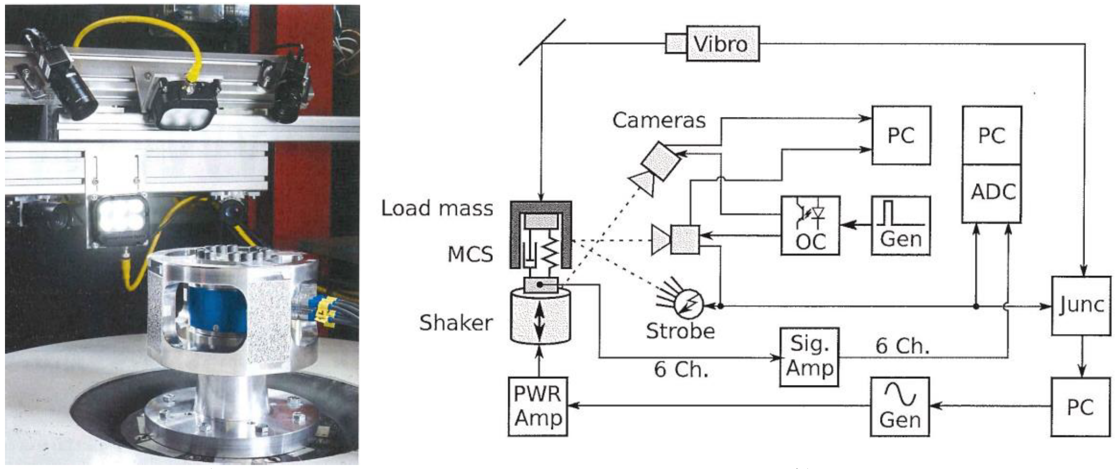

a) b)

Fig. 2: a) A pair of stereophotogrammetric cameras observing the load mass
b) Block diagram of the measurement setup

An identical pair of stereophotogrammetric cameras that was synchronized to the first one was tracking the platform of the shaker. The cameras were set to a maximum speed of 166 fps, but even this was not sufficient, because we investigated the frequency response up to 1000Hz. Therefore we applied a sub-Nyquist sampling technique, using the signal of the laser vibrometer as a reference. The frequency components of the vibration are calculated by an FFT analysis of the vibrometer signal. A sinusoidal fit to a set of harmonics of these frequencies is then applied to the photogrammetric data.

4. First results: A commercially available transducer with 6 DOF was measured in the frequency range up to 1000 Hz. For the sensitivity in z-direction a drop of about 5% compared to static calibration was observed at 1000Hz. The phase shift at that frequency was -0.25 rad. A rocking movement at a frequency of 376 Hz was observed from the 3D-evaluation of the photogrammetric sensor system.

5. Acknowledgement: The authors gratefully acknowledge the funding of this work by Deutsche Forschungsgemeinschaft (DFG) under grants Tu 135/24 and Ku 3367/1.

References

[1] N.N.: ISO 376: Metallic materials: Calibration of force-proving instruments used for the verification of uniaxial testing machines, International Standard, ISO, Geneva, 2011
[2] N.N.: DIN 51309: Werkstoffprüfmaschinen – Kalibrierung von Drehmomentmessgeräten für statische Drehmomente, National German Standard, DIN, 2005
[3] Schlegel, C.; Kieckenap, G.; Glöckner, B., Buß, A.; Kumme, R.: Traceable periodic force calibration. Metrologia, 49, 224-225, 2012.
[4] Vlajic, N.; Chijioke, A.: Traceable dynamic calibration of force transducers by primary means. Metrologia, 53, S136, 2016.
[5] Park, Y.-K.; Kumme, R.; Röske, D.; Kang, D.-I.: Column-type multi-component force transducers and their evaluation for dynamic measurement. Measurement Science and Technology, 19, 115205, 2008
[6] Nitsche, J.; Bruneniece, S.; Kumme, R.; Tutsch, R.: Design of a calibration setup for the dynamic analysis of multi-component force and moment sensors. Accepted as oral presentation at IMEKO World Conference, Belfast, Sep 3-6, 2018

Compensation Model for Geometrical Error of Laser Tracer

Huixu Song[1], Zhaoyao Shi[1] and Hongfang Chen[1]
1 Beijing Engineering Research Center of Precision Measurement Technology and Instruments, Beijing University of Technology, Beijing, 100124, China
huixu_song@outlook.com
shizhaoyao@bjut.edu.cn
hfchen@ bjut.edu.cn

Abstract: The use of high precision reference sphere, which serves as the reflection unit and is fixed on the base of Laser Tracer, can avoid the influence on measurement accuracy caused by the movements of rotatory axes and ensure large tracing angle, however, the geometrical errors of 2D gimbal mount axes can seriously affect the measurement accuracy of Laser Tracer. The nonlinear coupling relationship between the geometrical errors and the measurement accuracy of Laser Tracer is analyzed, which shows that the measurement error of Laser Tracer is certain and unique after the determination of the value and direction of all geometrical errors, no matter how large the measurement range is. Finally, a simple compensation model for geometrical error of Laser Tracer is given.

Key words: Laser Tracer; gimbal mount axes; geometrical error; compensation model.

1. Introduction

Traditional commercial laser tracker and Laser Tracer were developed on the basis of theodolite and total station. Deumlich analyzed the geometrical errors' sources which could affect the measurement accuracy of theodolite, and gave the relationship between the single geometrical error of rotatory axes and the measurement error of theodolite [1]. K. Lau et al. were the first to give a model of the squareness error for the laser tracker, a model of dead path error for laser interferometry and a model of alignment error for laser beam [2]. B. Muralikrishnan et al. intensively studied the influence of the angular measurement error for the laser tracker on the laser ranging measurement accuracy, and provided a geometrical model for calibrating the measurement error of the laser tracker [3, 4]. Hitherto, there was not any research on the geometrical error model for Laser Tracer.

2. Geometrical error model of rotatory axes in Laser Tracer

The schematic diagram of the Laser Tracer is shown in Fig. 1. The geometrical error model of rotatory axes is set as Fig. 2. On the premise of no geometrical errors, the laser ranging measurement value should be constant when the target is moving around the reference sphere with the radius of *L*. Therefore, the variation of laser ranging measurement value represents the measurement error of Laser Tracer in practice.

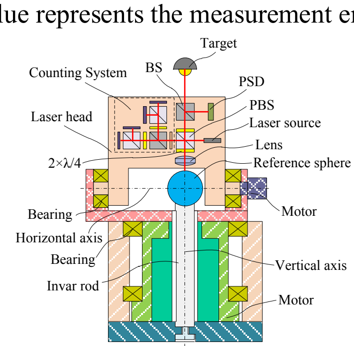

Fig. 1. Schematic diagram of Laser Tracer

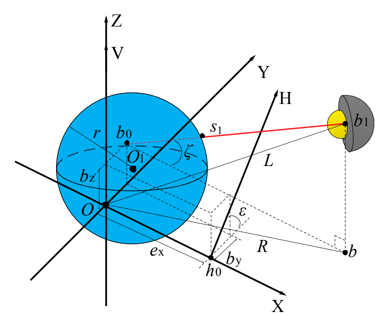

Fig. 2. Geometrical error model of rotatory axes

The initial intersection h_0 and direction vector $\mathbf{n}_{H0}$ are given as (1) and (2), and point b_0, b_1 and direction vector $\mathbf{n}_{B0}$ are given as (3) - (4).

$$\mathbf{h}_0 = \begin{bmatrix} e_x & 0 & 0 \end{bmatrix}^T \tag{1}$$

$$\mathbf{n}_{H0} = \begin{bmatrix} 1 & 0 & 0 \\ 0 & \cos\varepsilon & -\sin\varepsilon \\ 0 & \sin\varepsilon & \cos\varepsilon \end{bmatrix} \begin{bmatrix} 0 \\ 1 \\ 0 \end{bmatrix} \approx \begin{bmatrix} 0 \\ 1 \\ \varepsilon \end{bmatrix} \tag{2}$$

$$\mathbf{b}_0 = \begin{bmatrix} 0 & b_y & b_z \end{bmatrix}^T \tag{3}$$

$$\mathbf{b_1} = \begin{bmatrix} \sqrt{R^2 - b_y^2 - b_z^2} - e_x \\ b_y \\ b_z - \xi\sqrt{R^2 - b_y^2 - b_z^2} \end{bmatrix} \tag{4}$$

Point $b_0(\theta, \varphi)$, $b_1(\theta, \varphi)$ and direction vector $\mathbf{n_B}(\theta, \varphi)$ has changed after rotation (vertical axis – θ and horizontal axis -φ), and are given as (5) - (7).

$$\mathbf{b_0}(\theta,\varphi) = \begin{bmatrix} x_{b0} & y_{b0} & z_{b0} \end{bmatrix} = R_z(\theta)\mathbf{h_0} + R_z(\theta)R_x(\varepsilon)R_y(\varphi)R_x(-\varepsilon)\left[\mathbf{b_0} - \mathbf{h_0}\right] \tag{5}$$

$$\mathbf{b_1}(\theta,\varphi) = \begin{bmatrix} x_{b1} & y_{b1} & z_{b1} \end{bmatrix} = R_z(\theta)\mathbf{h_0} + R_z(\theta)R_x(\varepsilon)R_y(\varphi)R_x(-\varepsilon)\left[\mathbf{b_1} - \mathbf{h_0}\right] \tag{6}$$

$$\mathbf{n_B}(\theta,\varphi) = \begin{bmatrix} m & n & p \end{bmatrix} = R_z(\theta)R_x(\varepsilon)R_y(\varphi)R_x(-\varepsilon)\mathbf{n_{B0}} \tag{7}$$

The distance of $l_{s1b1}(\theta, \varphi)$ between s_1 and b_1 is given as (8).

$$l_{s1b1}(\theta,\varphi) = \sqrt{(x_{s1} - x_{b1})^2 + (y_{s1} - y_{b1})^2 + (z_{s1} - z_{b1})^2} \tag{8}$$

The dead path of laser interferometry system is set as $l_{s1b1}(0, 0)$. Therefore, Δl, the measurement error of the Laser Tracer, is given as (9). Moreover, the measurement range has nothing to do with the measurement accuracy of the Laser Tracer, shown as (10).

$$\Delta l = \frac{l_{s1b1}(\theta,\varphi) - l_{s1b1}(0,0)}{2} \tag{9}$$

$$\frac{d\Delta l}{dL} = 0 \tag{10}$$

3. Compensation model for geometrical error

In order to realize the movement of target with constant radius, a rotary table and a CMM are used. The 2-D linear guide is used to adjust Laser Tracer to be the same center with the rotary table, shown as Fig. 3. The calculation method of laser ranging measurement error is shown in Fig. 4.

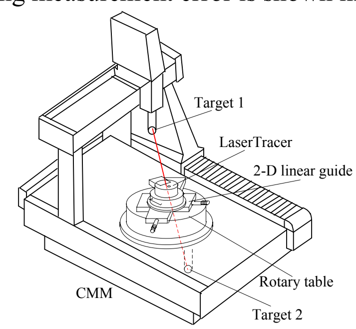

Fig. 3. Measurement scheme

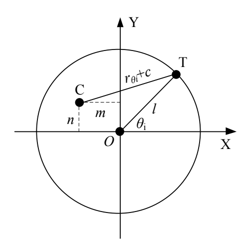

Fig. 4. Calculation method for laser ranging measurement error

By solving the least square equation (11), the eccentric coordinate of Laser Tracer (C) could be gotten, as well as the initial measurement displacement (c) of Laser Tracer.

$$f = (r_{\theta i} + c) - \sqrt{(l\cos\theta_i - m)^2 + (l\sin\theta_i - n)^2} \tag{11}$$

After adding the value of m, n, c and $r_{\theta i}$ to equation (12), $l_{\theta i}$ can be calculated when the rotary table is at any angle. Setting $l_{(\theta i=0)}$ as the initial value, $\Delta(\theta_i)=l_{\theta i} - l_{(\theta i=0)}$ represents the laser ranging measurement error which is also the compensation value for Laser Tracer when the horizontal axis is at a certain angle. Therefore, by moving the target along the axis Z, the error map of Laser Tracer in the whole measurement space could be drawn.

$$r_{\theta i} + c = \sqrt{(l_{\theta i}\cos\theta_i - m)^2 + (l_{\theta i}\sin\theta_i - n)^2} \tag{12}$$

References

[1] Deumlich F, *Surveying instruments* (Walter de Gruyter, 1982), Chap. 2.
[2] Lau K, Hocken R J, Haight W C, "Automatic laser tracking interferometer system for robot metrology", Precision Engineering, **1**, 3–8 (1986).
[3] Muralikrishnan B, Phillips S, Sawyer D, "Laser trackers for large-scale dimensional metrology: A review", Precision Engineering, **44**, 13-28 (2016).
[4] Muralikrishnan B, Ferrucci M, Sawyer D, et al., "Volumetric performance evaluation of a laser scanner based on geometric error model", Precision Engineering, **40**, 139-150 (2015).

Displacement measurement by means of speckle pattern interferometry with radial in-plane sensitivity

Jorge R. Parra-Michel[a], David Asael Gutiérrez Hernández[b], Marco A. Escobar[a], Rafael Martínez-Peláez[a].

[a] Universidad De La Salle Bajío, Av. Universidad 602, Col. Lomas del Campestre, León, Guanajuato, México.
[b] Tecnológico Nacional de México. Instituto Tecnológico de León. División de Estudios de Posgrado e Investigación. Avenida Tecnológico s/n, Industrial Julián de Obregón, 37290 León, Guanajuato, México.
jrparra@delasalle.edu.mx

Abstract: An in-plane radial sensitivity interferometer that uses the divergent illumination for the calculation of deformations in the radial direction is presented. The description and a mathematical model for calculating the sensitivity vector is also presented. The interferometer has two polarizing filters, a circular one and a linear one to implement the phase stepping technique. A measurement of the radial deformation by thermal expansion is performed over an aluminum plate in order to test the interferometer. The results indicate that the maximum contribution of the out-of-plane with respect to the radial in-plane sensitivity vector is less than 3% and decreases by less of 1% when measurements are performed near the optical axis.

1. Introduction

ESPI is an instrumental technique for full-field displacement and surface topography measuring when it is not possible the contact with the object. This technique has high accuracy on recording measurements, and its resolution can be adjusted in a wide range going from nanometers to micrometers [1]. ESPI is widely used as a non-destructive test in mechanical elements [2], dynamic deformation analysis [3] and surface topometric measurement [4]. Unfortunately, optical configurations in ESPI are limited to record displacement only in one direction, making necessary to employ an optical system for each direction of the displacement, preferably orthogonal and simultaneous ones, i.e. to measure the mechanical stresses around a crack it is necessary to determine the deformation in the radial direction in the edge of the crack tip. Since determining the direction in which a displacement occurs is essential to study deformations, several methods have been proposed to overcome this limitation; Hua Fan et al. [5], A.J. Moore et. al. [6] show distinct approaches to simultaneous and orthogonal deformation measurements based in ESPI and using different elements like polarizers, alternating measurements between optical systems, and simultaneous illumination with different wavelengths and interferometers.

On the other hand, Matías R. Viotti et al. and A. Albertazzi et al. introduced a device based on two conic mirrors and collimated illumination to measure residual stresses by interferometry with radial in-plane sensitivity [7,8]. The conic mirrors are interconnected with piezoelectric actuators, needed to implement the phase shift technique to find the deformation-associated optical phase. To diminish the measurement mistakes due to wavefront of illumination, it is necessary to keep constant the radial direction of the sensitivity vector using collimated illumination over the full conic mirror surface. This becomes increasingly expensive if the outer diameter of the conic mirror is big because it requires a collimating lens with the same diameter. In this work, we introduce a radial interferometer with divergent illumination that uses a linear polarizer and a ¼ wave retarder to perform the phase shift technique by polarization [9]. To verify the functionality of the radial interferometer with divergent illumination, we performed deformation measurements in a thin aluminum plate when it was punctually heated from the rear.

2. Optical arrangement

Figure 1 shows a diagram of the optical arrangement used for ESPI interferometry with radial in-plane sensitivity. A laser illumination beam strikes an optical fiber at one end emerging from the other end in such a way that it can be considered as a punctual source (spherical wavefront) which generates divergent illumination.

To implement our polarization phase shifting system, the illumination beam passes through a quarter-wave retarding plate. A ring-shaped film with linear polarization was used to polarize only the illumination beam reflected in the upper half of the conic mirror, while the illumination beam remains with the illumination passed through the ¼ wave retarder film.

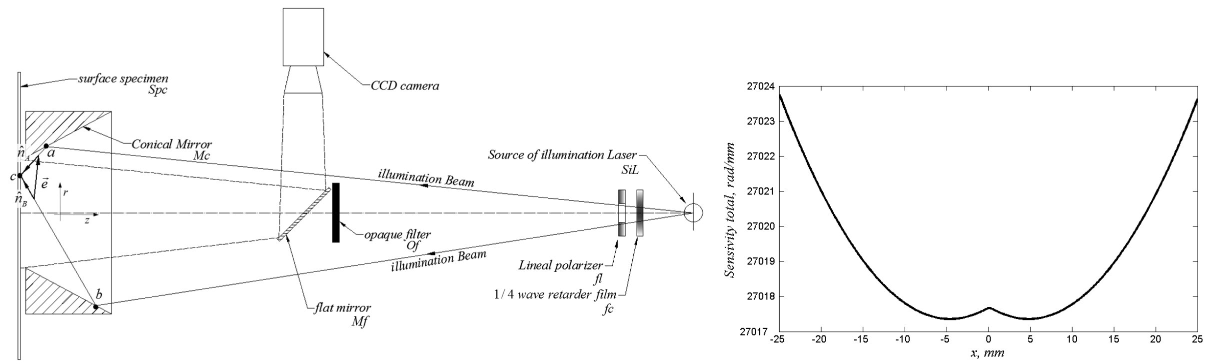

Fig. 1. Optical arrangement for ESPI interferometry with radial in-plane sensitivity and divergent illumination proposed and Total sensitivity in plane $y=0$.

3. simulation and Results

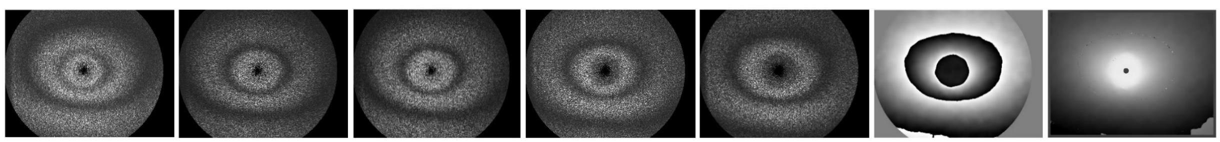

Fig. 3. Interferograms obtained in distinct relative angles of a the linear polarizer, (a) 0 rad, (b) $2\pi/5$ rad, (c) $4\pi/5$ rad, (d) $6\pi/5$ rad, (e) $8\pi/5$, (f) wrapped phase in module 2π terms, (g) $\Delta\phi$ optical phase in grey scale.

4. Conclusions

We showed a new configuration for the polarized interferometer with radial in-plane sensitivity using divergent illumination. We performed measurements of deformations due to the dilatation of an aluminum plate that was heated by the rear by contact with a small circular plate connected to an electric resistance. The implemented system allows measuring deformations mainly in the radial direction. The contribution of the sensitivity vector out-of-plane is less than 1% near to the center of the measurement and this increases in function of the radius of less than 3%. We can conclude than the contribution of the sensitivity vector out-of-plane increases proportionally to the radius.

References

[1] **Sirohi, R. S.,** *Speckle Interferometry,* Contemporary Physics, Vol. 43, No. 3, (2002), pp.161−180.

[2] **Ambu, R., Aymerich, F., Ginesu, F. and Priolo, O.,** *Assessment of NDT Interferometric Techniques for Impact Damage Detection in Composite Laminates*, Composites Science and Technology, Vol. 66, (2006), pp. 199-205.

[3] **Arikawa, S., Gaffney, J. A., Gomi, K., Ichinose, K., Ikeda, T., Mita, T., Rourks, R. L., Schneider, C. and Yoshida, S.,** *Application of Electronic Speckle Pattern Interferometry to High-speed Phenomena*, Journal of Material Testing Research Association of Japan, Vol. 52, No. 3, (2007), pp. 176−184.

[4] **Parra-Michel, J., Martínez, A., Anguiano-Morales, A. and Rayas, J. A.**, *Measuring Object Shape by Using In-plane Electronic Speckle Pattern Interferometry with Divergent Illumination*, Measurement Science and Technology, Vol. 21, (2010), pp. 1-8.

[5] **Hua Fan, Jun Wang, Yushan Tan**, *Simultaneous measurement of whole in-plane displacement using phase-shifting ESPI*, Optics and Lasers in Engineering (1997), Volume 28, Issue 4, , pp 249–257.

[6] **A. J. Moore and J. R. Tyrer**, *Two-dimensional strain measurement with ESPI*, Opt. Lasers Eng (1996), Vol. 24, pp. 381–402.

[7] **Matías R. Viotti, Armando Albertazzi Jr., Guillermo H. Kaufmann**, *Measurement of residual stresses using local heating and a radial in-plane speckle interferometer*, Optical Engineering (2005), Vol. 44 (9) 093606.

[8] **A. Albertazzi, M. R. Borges, and C. Kanda,** *"A radial in-plane interferometer for residual stresses measurement using ESPI",* in Proc. IX Int. Congress Exp. Mech., pp. 108–111, Society of Experimental Mechanics (2000).

[9] **G. Rodríguez-Zurita, A. García-Arellano, N. I. Toto-Arellano, V. H. Flores-Muñoz, R. Pastrana-Sánchez, C. Robledo-Sánchez, O. Martínez-Bravo, N. Vásquez-Pasmiño, and C. Costa-Vera.**, *One–shot phase stepping with a pulsed laser and modulation of polarization: application to speckle interferometry* Opt. Express (2015), Vol. 23, 23414-23427.

Fundamental Study on Surface Topography Measurement with Wideband Spatial Frequency using Scattered Light Spectroscopy
- Construction of Broadband Optical frequency Comb -

Ippei Takahashi[1], Yasuhiro Takaya[1] and Yasuhiro Mizutani[1]
Department of mechanical engineering, Osaka university, 2-1 Yamadaoka Suita-shi Osaka Japan
takahashi@optim.mech.eng.osaka-u.ac.jp

Abstract: An optical frequency comb (OFC) is regard as a multi-wavelength CW light source. We propose the improved laser inverse scattering method based on scattered light spectroscopy using an OFC that enables to evaluate a surface topography with wideband spatial frequency. In this paper, the broadband OFC is constructed by using a highly nonlinear fiber (HNLF). As a result, the spectrum with the width of several 100 nm could be obtained.

1. Introduction

A high precision freeform surface with the surface topography consisting of waviness of hundreds nanometer as well as surface roughness of less than 10 nm is demanded for a large optical component such as automotive parts with the size larger than 200 mm^2. To meet this demand, the development of the novel measurement technique which enables to evaluate a surface topography ranging from several micrometers to millimeter order in spatial frequency is required.

The previous research has suggested that the conventional laser inverse scattering method[1] has a disadvantage in wavelength dependence of the measurement range and resolution to measure a surface topography with wideband spatial frequency. To overcome this problem, we propose the improved laser inverse scattering method based on the scattered light spectroscopy. The optical property of an OFC, that is, a precise discrete frequency (wavelength) distribution in broader-band makes it possible to apply to surface topography measurement with wider-band spatial frequency as well as higher resolution. However, the frequency band of conventional OFC is not broad enough to achieve surface topography measurement with wideband spatial frequency. In this paper, the construction of broadband OFC is attempted to establish the improved laser inverse scattering method.

2. Principle of broadband OFC

Fig.1(a) shows the schematic diagram of a fiber laser, that is, an OFC generation device. In this fiber laser, mode-locking makes the phases of the lights with plural wavelengths uniform and oscillates as ultrashort pulse light. The Erbium-doped fiber (EDF: central wavelength 1550 nm) as a laser medium is excited with the semiconductor laser (wavelength of 980 nm). The isolator limits the propagation of the oscillated laser light only in one direction. The coupler takes out 30% of the laser light as an output, and returns 70% to the annular resonator. Mode-locking is performed by using nonlinear polarization rotation.

In order to broaden the band of the OFC, a method of generating supercontinuum (SC) light with nonlinear effect (four-wave mixing / stimulated Raman scattering) is applied by making the OFC incident to a highly nonlinear fiber (HNLF). It is known that the spectral width of the SC light depends on the strength of the nonlinear effect, namely it becomes stronger as the power of the incident light increases[2]. From this, it is necessary to enhance the power of the OFC in order to obtain SC light with a wider band. Here, as a method for increasing the power of the OFC, optical amplification using a EDFA (Erbium Doped Fiber Amplifier) is introduced[3].

Fig.1(b) shows the schematic of the broadband experimental system. The OFC incidents HNLF after amplified by the backward EDFA. Both four-wave mixing and the stimulated Raman scattering that make broadening of width of spectrum have polarization dependency. Therefore, the quarter-wave plate and the half-wave plate are inserted between the EDF and the isolator. While observing the SC light with the optical spectrum analyzer (OSA), the polarization state is adjusted using the quarter-wave plate and the half wave plate so that the spectral width of the SC light becomes the widest.

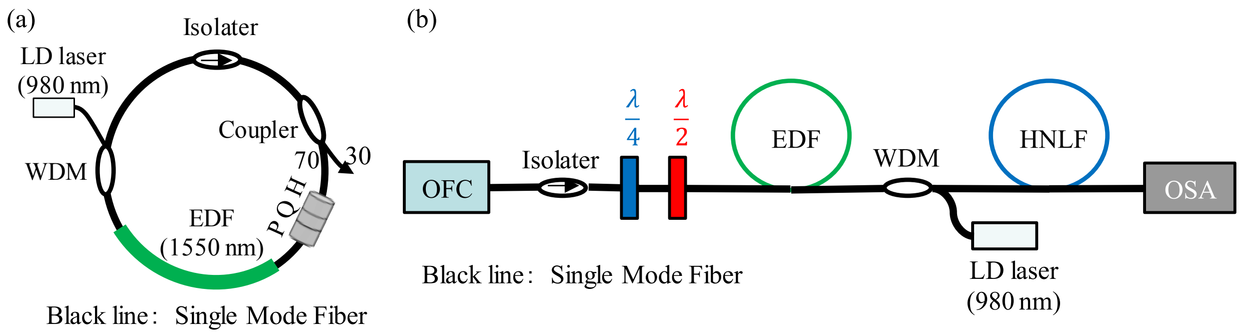

Fig.1 Schematic of (a) the OFC, (b) the broadband experimental system.

3. Verification of constructed broadband OFC

As shown in Fig.2(a), the spectrum of the OFC extends about 50 nm centering on 1560 nm. The band of the OFC was attempted to broaden using the broadband experimental system with a HNLF. As a result, we could obtain the SC light shown in Fig.2(b), where the measurement result shows up to just 1700 nm because of the measurement limit of the OSA. It is confirmed that the short wavelength side of the SC light is spreaded to about 1040 nm. The constructed broadband OFC light source is found to be useful for establishing the improved laser inverse scattering method based on the scattered light spectroscopy.

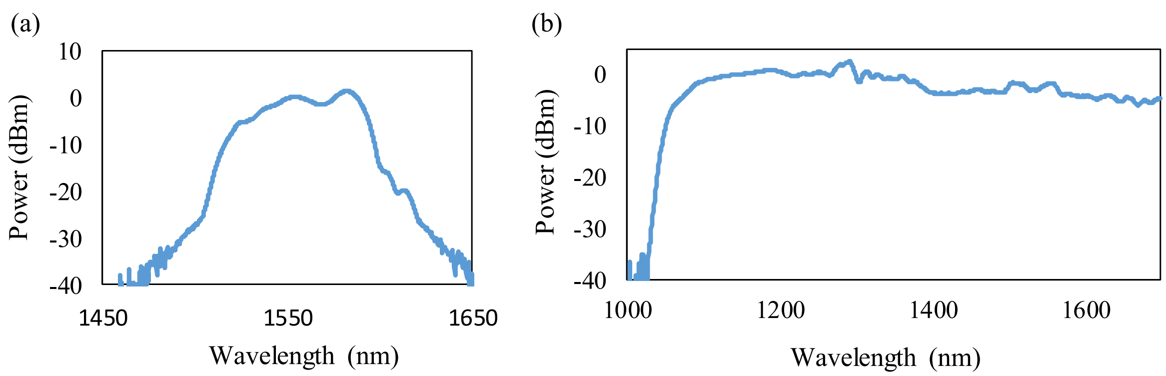

Fig.2 The spectrum of (a) the OFC, (b) SC light.

4. Conclusion

In this paper, we have constructed the broadband OFC to establish the improved laser inverse scattering method. We achieved to broaden the band of the OFC with the spectrum width of 50 nm by the constructed broadband experimental system consisting of the backward EDFA and the HNLF. As a result, the broadband OFC with the spectrum width of several 100 nm could be obtained.

References

[1] Atsushi Taguchi, et al., "Optical 3Dprofilometer for in-process measurement of microsurface based on phase retrieval technique," Precision Engineering. **28,** 152-163 (2004).

[2] Hiroyasu Sone, et al, "Condition for Generating Broadband and Flat Supercontinuum Spectrum Using a Dispersion-Flattened/Decreasing Fiber," Kogaku. **30**, 522-527 (2001).

[3] Yoshiaki Nakajima, et al, "Optimized amplification of femtosecond optical pulses by dispersion management for octave-spanning optical frequency comb generation," Optics Communications. **281**, 4484-4487 (2008).

Deep neural network for fringe pattern filtering

Alan Reyes and Mariano Rivera
Centro de Investigacion en Matematicas AC
mrivera@cimat.mx

Fringe Pattern (FP) denoising–normalization consists on removing background illumination variations, normalizing contrast and filtering noise of a FP modelled by

$$I(p) = a(p) + b(p)\cos(\phi(p)) + \eta(p) \tag{1}$$

---where p is the pixel position, a is the background illumination, b is the fringe contrast, ϕ is the phase map and η is additive noise. Then, the filtered—normalized FP can be represented by the simplified model:

$$I(p) = 1 + \cos(\phi(p)) \tag{2}$$

We propose to implement such a transformation with a Deep Neural Network (DNN). Image analysis techniques based on DNNs have demonstrated their capability to represent diverse transformation that maps an input image, x, into an output image, $\hat{x}$. Autoencoders are one kind of NNs that can map a tensor into another tensor. A tensor is a multidimensional array; thus, a scalar is a tensor of order zero and a vector a tensor of order one. Thus, we represent the FP (monochromatic images) with tensors of order two.

We build upon our DNN architecture on the UNet; which, in turns, generalize the basic autoencoder. An autoencoder has two main components: the encoder and the decoder. The *encoder* φ_1 that takes the data x in its original "spatial" dimension and produces a compressed vector y. Mathematically, the encoding can be expressed by

$$\hat{y} = \psi_1(x) \; = \; \sigma(W_1 x + b_1) \tag{3}$$

where W_1 is a weights matrix and b_1 is a bias. Then, the *decoder* φ_2 takes the coded data y and computes a reconstruction $\hat{x}$ of the original data x. This is expressed by

$$\hat{x} = \psi_2(y) \; = \; \sigma(W_2 y + b_2) \tag{4}$$

where W_2 is a weights matrix and b_2 is a bias. In this simplest case, given the training dataset X = {x1, x2, . . . , xm}, the autoencoder (coder and decoder) is trained by solving an optimization problem of the form:

$$argmin_{W1,W2,b1,b2} \; \sum_i \parallel x_i - (\psi_1 \circ \psi_2) x_i \parallel_M \tag{5}$$

where $\parallel \cdot \parallel_M$ represents a metric or divergence measure. The UNet is a Deep model, then the number of layers (coders and decoders) in the UNet model is substantially larger than the number of layers in the autoencoder. However, opposed in standard UNet, we reduce the number of filters and image features from as the layers are deeper on the encoder. Thus, the deeper layer produces the tensor with smallest dimension (spatial size and number of channels). Because of these characteristics that distinguish our architecture and provides it of an advantage for the regression task, we named VNet to our model (it uses tensors with few channels on deep layers, "sharp–tensors").

In order to train the VNet, we generate 46 pairs o random FPs (1024 × 1024 pixels): the corrupted FPs are generated according model Eq. (1) and the normalized FPs (ground–truth) according with model Eq. (2). Then, 25, 000 patches of 32 × 32 pixels are randomly sampled from 30 generated FPs used as training set; 2500 patches are used for validation. The normalized FPs (1024 × 1024 pixels) are computed using the trained convolutional VNet with a horizontal and vertical stride of 4 pixels and overlapped reconstructions are averaged. Fig. 1 resumes the experimental comparison of the UNet and VNet models in the FP restoration task. Fig. 2 shows an example of the computed results. Our experiments demonstrate that VNet improves the reconstruction when it is compared with respect to UNet.

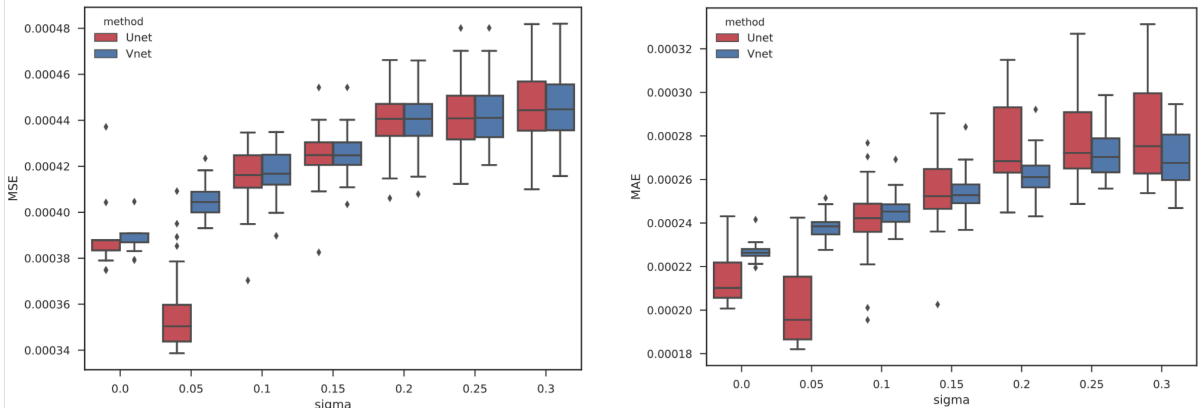

(a) (b)

Fig. 1 (a) Mean square error and (b) mean absolute error for reconstructed dataset: 46 FP corrupted with Gaussian noise with mean zero and standard deviation equals sigma. Since the reconstruction error are generally smaller than one, the MSE overestimate the performance of the UNet. MAE demonstrate the superior performance of the proposed VNet.

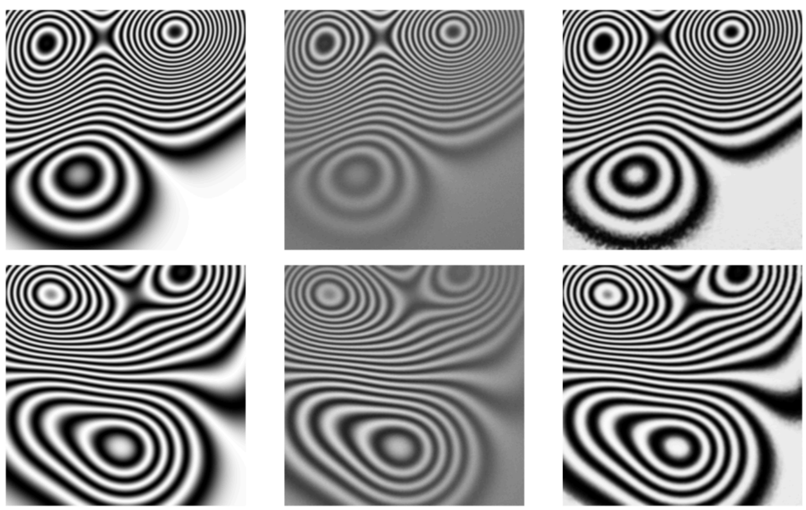

Fig. 2. First column: Ground truth. Second column: corrupted fringe FP. Third column: reconstructions using the proposed VNet.

References

[1] G. E. Hinton and R. R. Salakhutdinov, Reducing the Dimensionality of Data with Neural Networks, Science **313**, 504 (2006).

[2] O. Ronneberger, P. Fischer, and T. Brox, "U-net: Convolutional net- works for biomedical image segmentation," in MICCAI 2015, Springer Int. Pub. (Cham, 2015), pp. 234–241.

Fringes Demodulation using Simulated Annealing with Independent Window Partition

Iosvani Moré Quintero, Francisco J. Cuevas de la Rosa
Centro de Investigaciones en Óptica, A.C. Loma del Bosque 115, Colonia Lomas del Campestre
León, Guanajuato, CP: 37150
imore@cio.mx, fjcuevas@cio.mx

Abstract: A method for the partition of an interferogram used in the window fringes demodulation (WFPD) technique is presented. This algorithm can autonomously divide an interferogram based on the maximum number of fringes desired in each window. Basically, this consists in obtaining the minimum number of sub images consistent with the number of fringes allowed. To do this, a tree-type data structure was implemented, where each leaf of the tree represents a partition of the interferogram. Each sub-image will serve as an input to the Simulated Annealing algorithm, which estimates the phase map from a parametric function and its parameters are obtained by means of an optimization process. This technique achieves task independence, speeds up the demodulation process by simplifying the adjustment process and opens the possibility of analyzing interferograms of greater complexity.

1. Introduction

In Optical Metrology, a fringe pattern can be considered as a fluctuation of a sinusoidal signal in bidimensional space, which is related to the physical quantity being measured. The mathematical model that characterizes a pattern of fringes is given by the only measurable quantity, the intensity $I(x;\ y)$, which can be represented through its cosine profile as:

$$I(x,y) = a(x,y) + b(x,y)\cos\big(\phi(x,y) + n(x,y)\big) \qquad (1)$$

where $a(x,y)$ represents the background lighting, $b(x,y)$ the contrast or modulation of the signal, related to the reflectance of the object, $\phi(x,y)$ symbolizes the phase term, which is related to the physical amount to be quantified, and $n(x,y)$ represents the high-frequency noise.

Among the methods employed to calculate the phase term, the most popular is the phase shifting method (PSM) [1] and the Fourier method (FM) [2][3], which have been widely applied in interferogram demodulation. The main disadvantage of these techniques is that the obtained phase is wrapped, and thus requires a phase unwrapped algorithm.

The phase modulation problem has been treated with metaheuristics [4,5,6], which constitutes a new approach that couples Computer Science with Optical Metrology. Among the main artificial intelligence based methods for interferogram demodulation there is a new technique known as the Window fringe pattern demodulating (WFPD) [7].

This paper presents a method to divide a pattern of closed and under-sampled fringes into image windows or sub-images. The modulating phase in each sub-image is fitted by a parametric analytic function using the Simulated Annealing algorithm (SA) [8].

2. Algorithm for interferogram partition in independent windows (IPA).

In the proposed method, a fringe pattern is partitioned into a small window containing a defined number of fringes. This process consists of obtaining the minimum number of sub-images consistent with the number of allowed fringes. For this purpose, a tree-type data structure was implemented, where each leaf of the tree represents a partition of the interferogram.

The IPA is a recursive method that implements a post-order traversal and verifies that each sheet complies with the number of fringes restriction. The algorithm is based on the following steps:

1. A query is performed to verify if the node has a child and if so, the recursive method with all the children is called again.
2. Otherwise the node is a leaf and it is verified if it complies with the number of fringes restriction, if it completes the process for that window, otherwise the interferogram is partitioned into 4 sub-images.
3. The process is repeated until all sheets have a maximum number of required fringes.

3. Results

The algorithm is tested using a computer generated interferogram where the mathematical form of the original phase is given by:

$$f(x,y) = 0.0549778714378 21y^2 + 0.054977871437821x^2 - 2.199114857512860y - 2.199114857512860x + 0.219911485751286\,; \qquad x,y \in [0,40] \tag{2}$$

The result of applying the algorithm using a maximum number of fringes equal to 3 is shown in Figure 1.

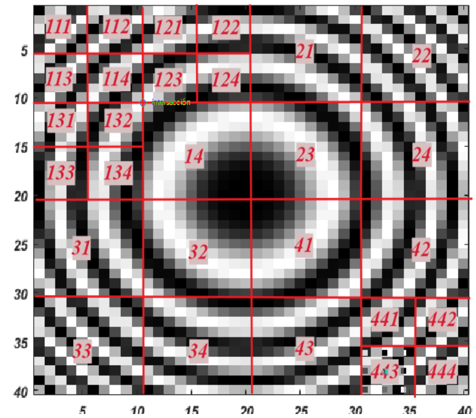

Figure 1: Result of algorithm window partitioning.

For each window, an instance of an RS algorithm was executed to demodulate each image segment. The results of the demodulation process are shown in the following figure.

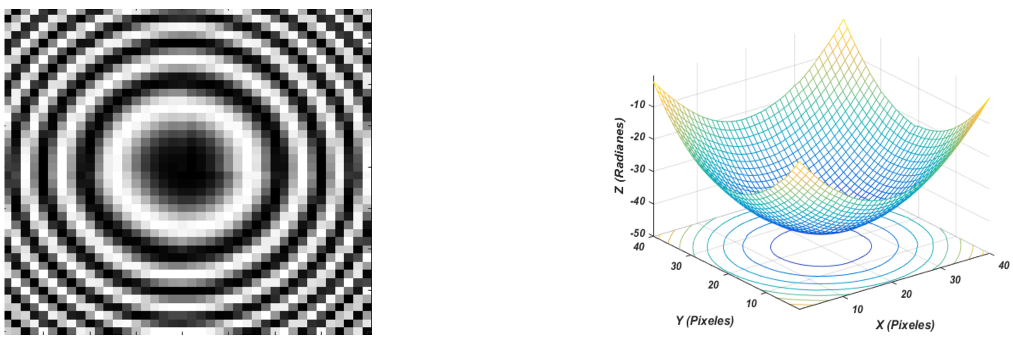

(a) (b)

Figure 2: a) Interferogram recovered by the algorithm (resolution 40x40 pixel). b) Recovered phase map.

4. Conclusions

Several tests were performed with different configurations of the parameters used during the optimization process and the best execution yielded an error between the original and the recovered phase maps of 0.3260%.

References

[1] D. Malacara, “Optical shop testing”, vol. 59. John Wiley & Sons, (2007).
[2] M. Takeda, H. Ina, and S. Kobayashi, “Fourier-transform method of fringe-pattern analysis for computer-based topography and interferometry,” Journal of the Optical Society of America, (1982) ,156–160.
[3] M. Takeda and K. Mutoh, “Fourier transform profilometry for the automatic measurement of 3-D object shapes,” Applied Optics, no. 22, (1983), 1–5.
[4] F. J. Cuevas, J. H. Sossa-Azuela, and M. Servin, “A parametric method applied to phase recovery from a fringe pattern based on a genetic algorithm,” Optics Communications, (2002),213–223.
[5] L. Espinosa and J. Valadez, “Demodulation of Interferograms of Closed Fringes by Zernike Polynomials using a technique of Soft Computing,” Engineering Letters, (2007).
[6] F. Cuevas and M. Servin, “Closed fringe demodulation by multi-polynomial fitting,” Proceedings of SPIE - The International Society for Optical Engineering, (2004) 405–412.
[7] F. J. Cuevas, F. Mendoza, M. Servin, and J. H. Sossa, “Window fringe pattern demodulation by multi-functional fitting using a genetic algorithm,” Optics Communications, (2006),231–239.[8] S. Kirkpatrick, C. D. Gelatt, and M. P. Vecchi, “Optimization by Simulated Annealing,” American Association for the Advancement of Science no. 4598, (1983), 671–680.

Relative Error in Out-of-plane Measurement Due to the Object Illumination Type

Gustavo A. Gómez-Méndez, Amalia Martínez-García, Ana Karen Reyes, Juan A. Rayas
Centro de Investigaciones en Óptica, Loma del Bosque 115, León, Gto. México
gustavogomez@cio.mx

Abstract: In this work the sensitivity vector is analyzed for collimated and divergent illumination for an out-of-plane arrangement. The geometry of the optical setup that we used allowed us to find sensitivity mostly along the pulling direction; the other two components of the sensitivity vector were relatively small. We measured the displacement induced only along the pulling direction. Experimental and theoretical results are presented for the out-of-plane electronic speckle pattern interferometer. The analyzed object was an aluminum plate.

1. Introduction

Out-of-plane arrangements based on electronic speckle pattern interferometry (ESPI) allow investigating the mechanical behavior of an object subjected to stress. The technique comprises obtaining a phase map which is correlated with the sensitivity vector in pursuit of knowing the displacement map. According the setup, the sensitivity *vector* depends on both its geometry and of the type object illumination [1-3]. In this work it is presented an analysis of sensitivity vector when divergent or collimated light is used to illuminate the surface target.

2. Theory

Electronic speckle pattern interferometry (ESPI) is well established method for measuring 3D deformations and thus 3D strains. First, a laser is split into two illuminating beams (an object beam and a reference beam). The object beam is then directed to the surface of the sample and its reflecting beam is combined with the reference beam. The phase difference between the reflecting beam and the reference beam is indirectly recorded through intensity of an interference pattern named as a speckle interferogram. Alteration in the phase difference, $\Delta\phi$, before and after a mechanical loading is determined by the scalar product of the displacement vector, $\vec{d}$, and the sensitivity vector $\vec{e}$:

$$\Delta\emptyset = \vec{d}(P) \cdot \vec{e}(P), \quad (1)$$

where $\vec{e}$ is given by:

$$\vec{e}(P) = \frac{2\pi}{\lambda}\left[\hat{b}(P) - \hat{s}(P)\right], \quad (2)$$

and $\hat{b}$ and $\hat{s}$ are observation and illumination unit vectors respectively.

Because usually the influence of the transversal sensitivity vector components (e_x and e_y) on Eq. (1) is small, the displacement is evaluated by expression

$$\Delta\phi = \frac{2\pi}{\lambda} e_z w. \quad (3)$$

Commonly, interferometric optical arrangements use collimated wavefronts for object surface illumination. In other cases, divergent illumination is used. For simplicity in both cases, it is considered that the interest component of the sensitivity vector is constant. In our case, it means that the e_z component is considered as constant. This approach introduces an error in the calculation of the displacement field.

In the case of out-of-plane interferometers, both kind of illumination produce a sensitivity vector varying with the position. Then, errors in the measurements are introduced when considering collimated illumination [1], especially, in order to characterize extended target objects.

During the design stage of an interferometer should be useful to know the components of sensitivity vector in order to minimize the un–required sensitivity vector components. To build up only an out-of-plane sensitive interferometer, the condition $\theta \approx 0$ is imposed experimentally.

Fig. 1 shows the error maps associated to out-of-plane displacement field $w(x,y)$ due to use of divergent illumination and collimated, and the assumption that sensitivity vector component e_z in Eq. (3) is constant, respectively.

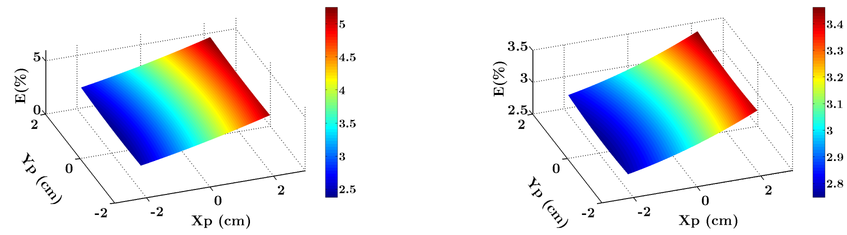

a) b)

Fig. 1. Error map due to the assumption of that sensitivity vector component e_z is constant when is used: a) divergent illumination (E_{max}: 5.24%); b) collimated light (E_{max}: 3.46%).

3. Experimental results

The optical system is shown in Fig. 2a. He-Ne laser (*LB*) with $\lambda = 632.5\ nm$ is used. The divergent source (*SF*) is placed at $28.63\ cm$ radial distance from object (*O*), and at 20º respect to optical axis. The distance between the object (O, aluminum plate: $4 \times 3.6 \times 1\ cm^3$) and observer (CCD) is $45\ cm$. Fig. 2b and 2c show the w displacement fields associated to divergent and collimated illumination, respectively.

Since the errors in the e_z components of sensitivity vector associated to divergent light (E_{max}: 5.24%) and collimated light (E_{max}: 3.46%) are known, it is possible to compute the error for the respective w-displacements by using Eq. (3).

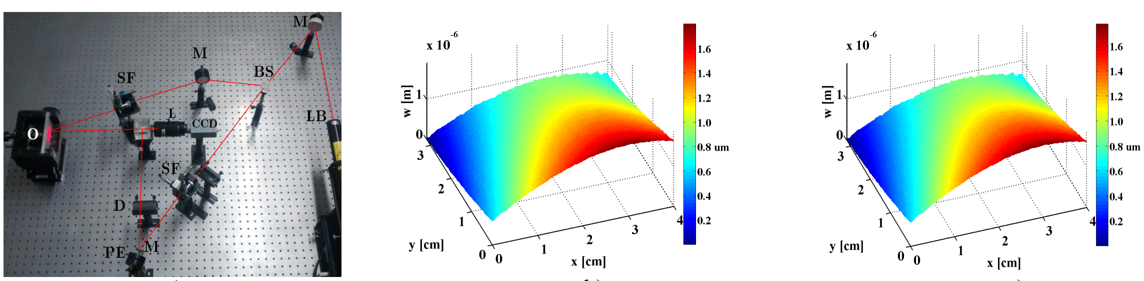

a) b) c)

Fig. 2. a) Experimental setup used. Out-of-plane displacement calculated when the experiment was accomplished with b) divergent illumination ($w_{max} = 1.799\ nm$ and c) collimated illuminated is considered ($w_{max} = 1.774\ nm$).

4. Conclusions

We have analyzed the use of object divergent and collimated illumination in out-of-plane speckle interferometry. The displacement field $w(x, y)$ and associated error to its measurement were evaluated when divergent illuminated was used in the experiment and it is supposed that the sensitivity vector component e_z is constant. The analysis of the sensitivity vector variation due to spherical illumination is important in the stage of planning an interferometric measurement experiment to minimize the required displacement component error.

References

[1] H. J. Puga, R. Rodríguez-Vera, and A. Martínez, "General model to predict and correct errors in phase map interpretation and measurement for out-of-plane ESPI interferometers," Optics & Laser Technology, **34**, 81-92, (2002).

[2] Thomas Kreis, *Holographic Interferometry, Principles and Methods*, Ed. Akademie Verlag, VCH Publishers (Germany, 1996).

[3] Amalia Martínez, Juan A. Rayas, Ramón Rodríguez-Vera, and Héctor J. Puga, "Three-dimensional deformation measurement from the combination of in-plane and out-of-plane electronic speckle pattern interferometers," Applied Optics, 4652-4658, (2004).

Two-Step Shadow Moiré Fringe Analysis

Chia-Cheng Lee, Terry Yuan-Fang Chen*, Fa-Yen Cheng
Department of Mechanical Engineering, Nation Cheng Kung University Tainan, Taiwan 701
*ctyf@mail.ncku.edu.tw

Abstract: For accurate measurement, phase-shifting technique is usually adopted to the shadow moiré measurement system. Accurately introducing the amount of phase shift is required in order to extract the phase properly. However, the specimen or system may be moved during the time of image capture, and not suitable for in-line measurement. In order to overcome this drawback and make an in-line measurement, a shadow moiré system consisted of two light sources of different color (red and green), and a color CCD camera is proposed. The phase shift is introduced by using two light sources illuminate the grating from different position simultaneously. The two moiré fringe patterns are captured by the color CCD camera, and are processed by a fringe analysis scheme using spiral phase transform (SPT) and optical flow techniques. The proposed fringe analysis scheme was applied to simulated surface profiles and real specimen. The test results are reported, and the validity of the scheme is investigated.

1. Introduction

Shadow moiré method is an effective optical technique for surface profile measurement of diffusely reflecting objects. Due to cheap and easy to implement in industry environment, the method has been widely used in the semiconductor industry for distortion/warpage evaluation under thermal and/or mechanical loading. For accurate measurement, phase-shifting technique is usually adopted to improve the sensitivity of shadow moiré measurement system. However, accurately introducing the amount of phase shift is required in order to extract the phase properly. Moreover, the specimen or system may be moved during the time of image capture, and not suitable for in-line measurement. In order to overcome this drawback and make an in-line measurement, a two-step shadow moiré system consisted of two light source of different color (red and green), and a color CCD camera was proposed to analyze the fringe patterns using spiral phase transform (SPT) and optical flow techniques.

In our set-up, the phase shift is introduced by using two light sources illuminate the grating from different position simultaneously. The two moiré fringe patterns are captured by the color CCD camera simultaneously, and separated into three monochromatic (red, green and blue) fringe patterns for fringe phase analysis. The proposed fringe analysis procedure first adjusts the intensity range of the two images to be equal, then removes the DC term of the images. Thereafter spiral phase transform (SPT) and optical flow techniques are employed to determine the wrapped phase of one image. Finally, the surface profile can be calculated from the unwrapped phase. The proposed fringe analysis scheme was examined through simulated surface profiles and real specimen. Figure 1 shows the schematic of proposed experimental setup. The simulated two original Cos and transformed Sin fringe patterns is shown in Fig. 2. A comparison of the grey level distribution along a 45 degree line of transformed and theoretical Sin fringe patterns is given in Fig. 3. It can be seen that the two patterns agree well with each other. The mean error of the points on the line is about 3μm.

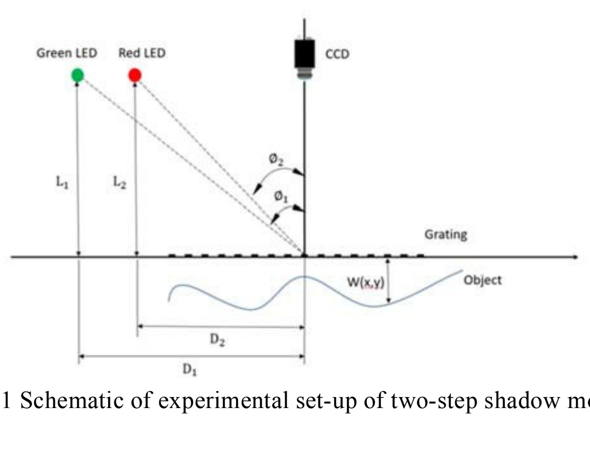

Fig.1 Schematic of experimental set-up of two-step shadow moiré

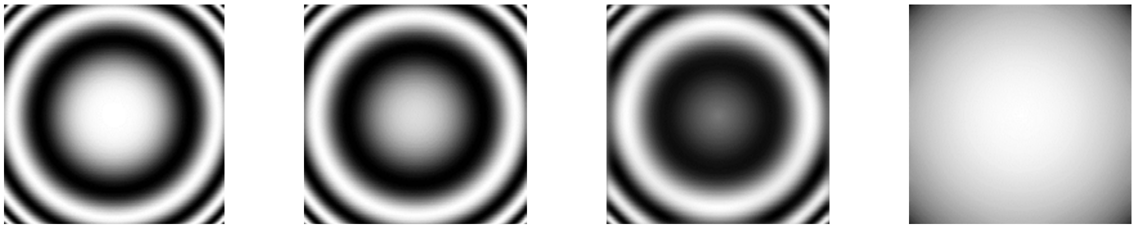

(a) (b) (c) (d)

Fig. 2 Simulated (a)-(b) two original Cos fringe patterns, (c) transformed Sin fringe pattern, and (d) unwrpaaed phase.

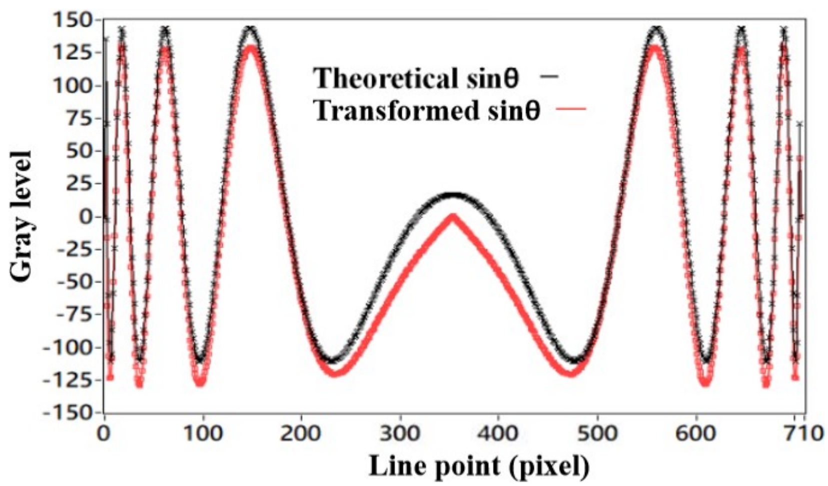

Fig. 3 Comparison of the grey level distribution along a 45 degree line of transformed and theoretical Sin fringe patterns

References

[1] Gómez-Pedrero, J.A., Quiroga, Juan A., José Terrón-López, M., Crespo, Daniel., "Measurement of surface topography by RGB Shadow-Moiré with direct phase demodulation", Optics and Lasers in Engineering, (2006), 44(12): p. 1297-1310.

[2] Du, H., H. Zhao, and B. Li.," Fast phase shifting shadow moiré by utilizing multiple light sources," Proc. of SPIE Vol. 8681 (2013) 86812A-6.

[3] Vargas, J., Quiroga, J. Antonio., Sorzano, C. O. S., Estrada, J. C. Carazo, J. M.," Two-step interferometry by a regularized optical flow algorithm", Optics Letters, 2011. 36(17): p. 3485-3487.

One-shot in slightly off-axis digital holographic microscopy based in a compact design

Miguel León-Rodríguez[1], Juan A. Rayas[2], Amalia Martínez-García[2], Alejandro Barrientos-García, Orlando M. Medina-Cázares
[1]Universidad Politécnica de Guanajuato, Av. Universidad sur 1001, C.P. 38496 Cortazar, Guanajuato, Mexico
[2]Centro de Investigaciones en Óptica, A.C. Loma del Bosque 115, C.P. 37150 León, Guanajuato, Mexico
Author e-mail address: y_migue@hotmail.com

Abstract: Here we present a compact optical design to implement in digital holographic microscopy. The proposal shows that it can be perform in off-axis, in-line and slightly off-axis digital holographic microscopy configurations. This optical setup not only is insensitive to vibrations but also is compact due to minimum elements used in it. We present simulation and experimental results. This proposal permits us to use a LED as illuminating source to avoid parasitic interference and it can be use in biological applications.

1. Summary

Digital holographic microscopy (DHM) is a novel tool in the study of samples that mainly yield quantitative information of the transmitted-or-reflected wavefront through three-dimensional (3D) objects. Many studies with DHM have been reported in biological applications [1]. DHM can be performed in three different scheme, these are on-line, off-axis and slightly off-axis. In the first one schema we normally use the phase-sifting technique (PS) to get the wavefront object [2], while the second and the third scheme we use Fourier filtering method (FF) [1,3]. Here we present a compact optical design to implement in digital holographic microscopy that it can be perform in off-axis, in-line and slightly off-axis digital holographic microscopy configurations. This optical setup not only is insensitive to vibrations but also is compact due to minimum elements used in it. We present simulation and experimental results. Figure 1 shows a photograph of the digital holographic microscope implemented in lab. An expanded laser beam is coming from a laser of 632.8 nm of wavelength.

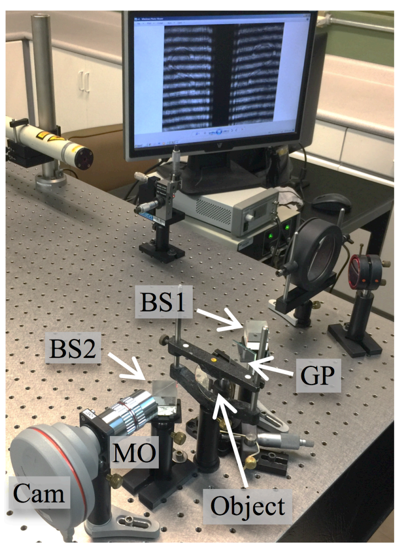

Figure 1. Digital holographic microscope

The beam is divided in two identical beams by the beam splitter 1 (BS1), one is the wavefront named object (O) because it goes trough the object and the other one is named the reference wavefront (R). A glass plate (GP) attached on a gyratory stage is used to implement the PS technique. A second beam splitter (BS2) interferes R with O and the hologram is magnified by the 10X microscope objective (MO) and registered by the Pixelink CCD camera of 4.4 x 4.4 microns of pixel size. Only two shots are required to implement the four-frame PS algorithm with the proposal. Figure 2 shows the four $\pi/2$ shifted holograms. To perform the slightly off-axis method a pair of these holograms are required. Only one hologram is required to perform off-axis method.

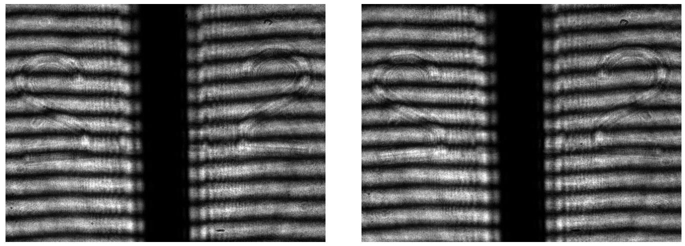

Figure 2. Four $\pi/2$ shifted holograms

2. Experimental results

We carried out a numerical simulation to validate the experimental results when a low coherence source is used in the proposal. The principal limitation is the low fringe density when a low coherence is used. In simulation we use low fringe density to perform the three schemes mentioned above. Figure 3 presents the simulation result. Figure 3 a) presents the amplitude and phase distributions when the PS technique is applied. Figure 3 b) presents the amplitude and phase distributions when we applied the slightly off-axis scheme and Figure 3 c) presents the reconstructed amplitude and phase distributions when the configurations correspond to the off-axis scheme. Figure 4 shows the experimental results for a 100 nm stepwise specimen made of TiO2 thin film, with a refraction index of 1.82 for a wavelength of 632.8 nm, was used as a phase calibrating gauge. The sample was made at home using a Balzer B-510 vapor deposition machine. Figure 4 a) shows the amplitude and wrapped phase distributions when slightly off-axis scheme is performed. Figure 4 b) shows the amplitude and wrapped phase distributions when off-axis scheme is implemented. Finally, Figure 4 c) shows the amplitude and wrapped phase distributions when PS technique is implemented. Due to the results we can conclude that PS technique is the best method to get the best lateral resolution but it need almost three holograms. Off-axis scheme permits to apply the DHM in dynamical events but is the worst method related to the lateral resolution. Slightly off-axis scheme can be used in in dynamical events as off-axis scheme with this proposal and it can only lost 50% of the lateral resolution compared with its counterpart PS technique.

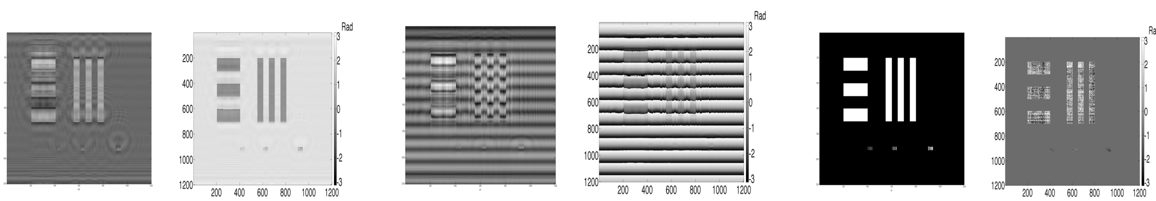

a) b) c)

Figure 3. Simulation results of amplitude and phase distribution for: a) PS technique, b) slightly of-axis scheme, and c) off-axis scheme.

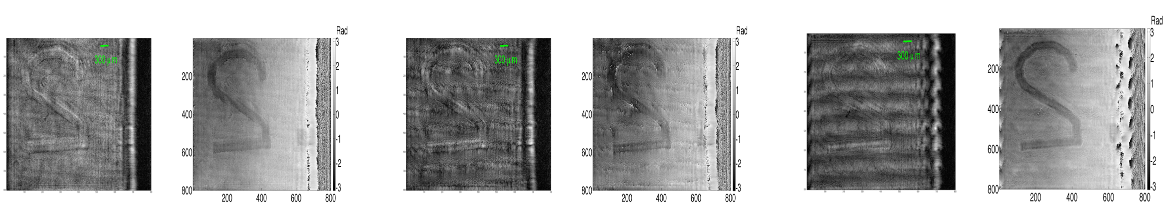

a) b) c)

Figure 4. Experimental results

References

[1] Peng Gao, Baoli Yao, Junwei Min, “Parallel two-step phase-shifting point-diffraction interferometry for microscopy based on a pair of cube beamsplitters”, Opt. Express **19**(3), (2011).

[2] A. Asundi, *Digital Holography for MEMS and Microsystem Metrology*, John Wiley Ltd., (2011).

[3] F. Dubois, “Border processing in digital holography by extension of the digital hologram and reduction of the higher spatial frequencies,” Appl. Opt, 41, 2621-2626(2002).

3D Reconstruction System Based on Structured Light Projection and Artificial Neural Networks

J. V. Sosa-Balderas[1], F. J. Cuevas[1], J. Salazar-Medina[2], A. López-Martínez[1]
[1] Centro de Investigaciones en Óptica, A.C., Lomas del Bosque 115, Lomas del Campestre, León, Gto, México.
[2] Universidad Tecnológica de León, Blvd. Universidad Tecnológica 225, San Carlos la Roncha, León, Gto, México.
{vicentesosa, fjcuevas, alan.lopez}@cio.mx

Abstract: In this work, we introduce a 3D reconstruction system that only requires a single image. To this end, structured light projection and Artificial Neural Networks (ANN) are used. To calibrate the system, *n* images are captured. Then, these images are processed to extract characteristic points. These characteristic points are the inputs to train the ANN. The topology of the ANN is: input layer, 4 neurons; hidden layer, 20 neurons; and output layer, 3 neurons. The learning rate, on the other hand, was fixed at 0.01. To evaluate our proposed approach, experiments were carried out. The relative learn error was 0.019%, and the relative reconstruction error was 3.47 %.

1. Introduction

For industrial measurements, optical techniques have many advantages. For instance, optical methods can be non-destructive, non-contact, and easy to adapt for different industrial environments. Typically, industrial measurement systems seek fast image processing at low price. However, optical techniques can be expensive, since they commonly precise good illumination, different lenses, among others. Our system, on the contrary, only uses a camera, a projector, and a processing unit.

Structured Light Projection (SLP) is a technique classified as 3D Optical Metrology [1]. This technique is now well-established for the rapid gathering of 3D coordinate details of an object under test. SLP is completely non-contact, thus it can be used for Automated Optical Inspection (AOI) of manufactured parts for in-line assembly processes and small molded parts. In such applications, the whole surface distribution of the Device Under Test (DUT) can be calculated and compared with a reference surface within seconds.

In this work, the use of SLP it is proposed to obtain the surface from a variety of objects by using one single image. For the system calibration, an Artificial Neural Network (ANN) is trained by using multiple images.

2. System Calibration

In order to calibrate the proposed system, many captured images are required, which are obtained by using the mechatronic system shown in the Figure 1 a). The projector emits a light pattern (clouds points) onto the reference plane and then the camera captures the projected pattern. The Reference Plane is moved some steps (eah of ΔZ) from Z_0 to Z_n. Where

$$\Delta Z = cte. \quad (1)$$

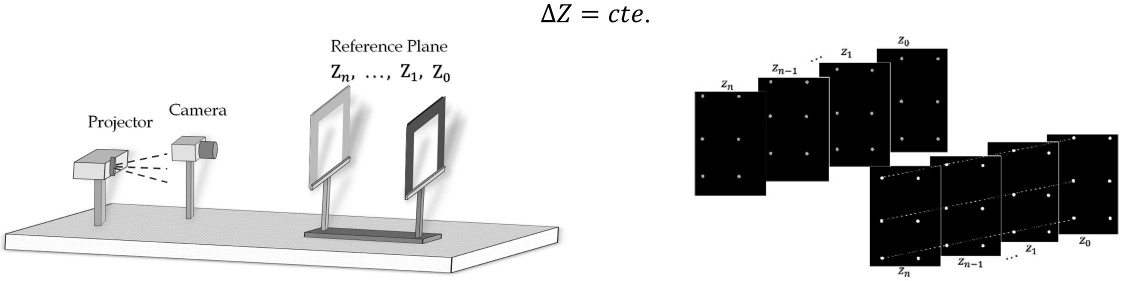

a) b)

Figure 1. Setup of the calibration system to capture images. (a) The mechatronic system is used to move the reference plane. (b) Captured images at different displacements of the reference plane (left top); a function is adjusted through the points in the Z axis (right lower).

The *i-th* captured image corresponds to Z_i and is processed. Since the image captures are points, it is necessary to label every point within the image (see Fig. 1b). Figure 2, on its part, shows the pseudo-code for point labeling in a binary image as obtained in [2]. This code reads the image in gray-scale and write a new matrix with the binary values. To tag points, we use the method named flood-fill. While the point is being tagged, the counters XT, YT and

AT increment. The centroid of point (rows and columns) are the values to train to ANN [3]. At the output layer, the expected values are X, Y and Z, where X and Y are automatically obtained with a calibration grid, at the plane Z_0.

```
Begin
    read Img_gray[,]
    initialize Img_binary[,] = graytobinary(Img_gray)
    initialize   XY_centroids[points_expected, 2]
    int i, j, number_label=0,
    int points_expected,   int x, y
        for (i=0; i<image(rows); i++)
            for(j=0; j<image(columns); j++)
                XT = 0; YT = 0; AT = 0
                    if(Img_binary [j,i] = = point_not_label)
                        number_label +=1
                        XT++; YT++; AT++;
                        //Label the point with flood-fill
                        and obtain the centroid
                    endif
            end for
        end for
    return XY_centroids
End
```

Figure 2. Pseudo-code for obtain the centroids of the points in an image.

3. Experiments

The Fig. 3 a) and b) show the designed surface, and its 3D printed surface with Polylactic Acid (PLA). The Fig. 3 c) shows the projected points onto the printed surface. On the other hand, the topology of the ANN is of 4 neurons at the input layer, 20 neurons in the hidden layer and 3 in the output layer. The ANN was trained by using a 12×12 matrix of the projected points (Fig 3 c) and 9 planes Z_{1-9} being separated $\Delta Z = 5mm$. Furthermore, the learn rate was 0.01, the number of epochs was 100,000. We obtained a percent relative error of 0.019 % at the end of the training.

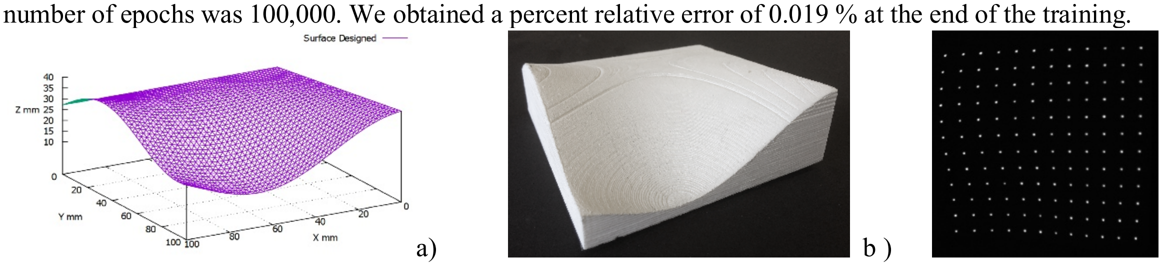

Figure 3. Methodology to obtain the shape reconstruction of a calibration object. a) Designed surface for calibration, b) Printed surface with PLA, c) Projected points onto the object.

Figure 4 a) illustrates the retrieved surface using our proposal. The Figure 4 b) shows the error map between the designed and the reconstructed surfaces, where we can see that the relative error was of 3.47%.

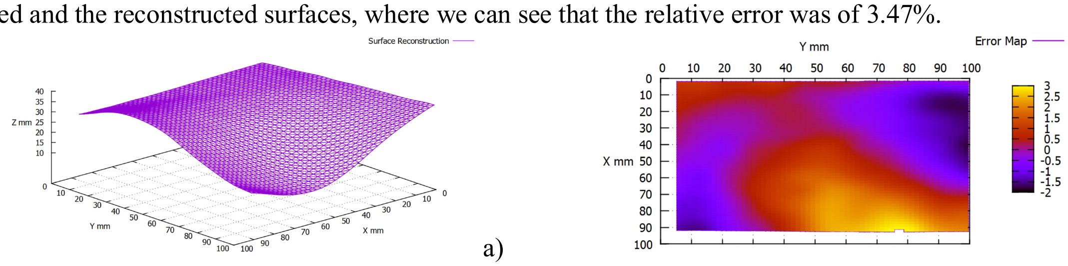

Figure 4. Retrieved surface and Error Map. (a) Reconstructed surface of the test object. (b) Error map between designed and reconstructed surfaces.

4. Conclusions

The use of SLP along with an ANN was satisfactory for 3D-shape reconstruction using only one image. The reconstruction error was of 3.47%. By using the closest point algorithm, the error is reduced. The proposed approach does not depend on the camera parameters or triangulation between reference plane-camera-projector. On the other hand, Phase-Shifting technique requires at least of three images of the object. Conversely, the proposed method only uses a single image to obtain the 3D surface.

References

[1] Jin, Hong. Wu, Fupei. Yang, Chun. Chen, Lian and Li, Shengping,"A Review of 3-D Reconstruction Based on Machine Vision", Intelligent Robotics and Applications, Springer International Publishing, 195-203(2014).
[2] N. Otsu, “A threshold selection method from gray-level histograms,” IEEE Transactions on Systems, Man, and Cybernetics, vol. 9, no. 1, pp. 62-66, Jan 1979.
[3] P. Viñuela and I. León, *Redes de neuronas artificiales: un enfoque práctico*. Editorial Alhambra S.A. (SP), 2004.

Simultaneous Measurement of Temperature and Velocity in a Synthetic Jet

B. Barrientos[1], C. Mares[2], D. Sarocchi[2], R. Valdivia[1], and A. Blanco[3]
Centro de Investigaciones en Óptica
Universidad Autónoma de San Luis Potosí
Universidad Tecnológica de León
bb@cio.mx

Abstract: We present results that show the feasibility to measure simultaneously temperature and velocity in a pulsed synthetic jet produced by a Helmholtz resonator. Two optical techniques, background-oriented schlieren (BOS) and particle image velocimetry (PIV), are employed. Simultaneity of the measurements has been achieved by the use of two synchronized frame-straddling cameras and two different light sources (a LED and a laser). For the realization of PIV, the jet is seeded with smoke, which initially fills the Helmhotz cavity; this type of seeding guarantees minimum disturbance of the jet. Results related with the dynamics of the jet, from the moment it exits the cavity until interaction with a hot plate, are presented.

1. Introduction

Two optical techniques, BOS [1] and PIV [2], are used for the simultaneous measurement of temperature and velocity in a phase object. BOS is an optical technique capable of measuring the gradient of the refractive index distribution in a region of interest. The object under analysis is placed between a background and a camera. Complementarily, PIV allows us to obtain velocity fields by imaging a planar cross-section of a fluid flow. In both techniques, two images are captured (reference and displaced images): in BOS, with and without object, and in PIV, two consecutive object states.

In BOS, as the phase object is introduced, the phase of the fringe pattern is modulated by the changes in refractive index. These phase changes can be recovered by the Fourier method. On the other hand, by cross-correlating the reference and displaced PIV images, velocity maps can be calculated.

When using BOS and PIV simultaneously we need to consider differences in their requirements for imaging. In BOS, the camera is focused on the background, and in PIV, on the object plane defined by an illuminating sheet. Besides, since in BOS quasi-collimated light is preferred, the use of long focal distances is necessary. In PIV, a restriction of the distance between object and imaging lens arises from the finite energy of the light source (pulsed laser); therefore, the imaging lens is placed as close as possible to the object.

The phase object that is analyzed by the two techniques corresponds to a synthetic jet produced by a Helmholtz resonator, which interacts with the plume generated by a hot plate. The dimensions of the jet are about 1 cm long and 2 mm wide. The images are captured by a pair of synchronized frame-straddling cameras.

There have been previous works where the dynamics of this type of objects have been studied [3-4], but temperature and velocity have been assessed in a separate way.

2. Theory

In BOS, the optical phase difference $\Delta\phi$ between a reference and a displaced image is obtained via the Fourier transform phase extraction method, where double application of the Fourier transform is carried out. Then, the derivative of the refractive index n can be computed by $\partial n / \partial x = n_0 T \Delta\phi / (2\pi D L)$ [5], where T is the period of the grating, and n_0, D, L, and x stand for the reference index of refraction of the region of interest, the distance between the object and the background, the thickness of the object, and the spatial coordinate in the direction the rays are deflected, respectively. Finally, the temperature field T is given by $T = T_0 (n_0 - 1)/(n - 1)$, where T_0 is the reference temperature. In the case of PIV, the images are divided into subimages and the displacement vector for a certain subimage can be obtained by computing their correlation, $c(\Delta x, \Delta y) = \mathcal{F}^{-1}\left\{ \mathcal{F}\{I_R(x,y)\}\, \mathcal{F}\{I_D(x,y)\}^* \right\}$, where the Fourier transform operator is indicated by $\mathcal{F}\{\ \}$ and the reference and displaced images by I_R and I_D.

3. Results

In Fig. 1(a) we show the setup for implementing the technique. A beam splitter, BS, is used to access simultaneously to BOS and PIV images. For BOS, a Ronchi grating B of 150 lpi is illuminated by a 3-W white LED, E (a red filter R is positioned in front of the LED). The grating is imaged by a lens L1 of focal distance 300-mm (before the lens, another red filter R is used). For the PIV part, a double-pulsed Nd:YAG is used to illuminate the object O (via a cylindrical lens). In this case, a lens L2 of focal distance 45 mm is used for imaging (a green filter G is used before the lens). A couple of straddling-frame cameras (Sharp-Vision 1400-DE, IDT, 1280x1024 pix) C1 and C2 detect the images for BOS and PIV, respectively. The Helmholtz cavity has an internal diameter of 8.3 cm, wall thickness of 6.3 mm, and contains a hole of diameter 3 mm (resonant neck), see Fig. 1(b). The cavity is driven by a speaker at 120 Hz. The hot plate has dimensions of 10x10 cm^2 (EchoTherm IC30, Torrey Pines Scientific), and is set to a temperature of 80 ºC. A synchronizer (MotionPro Timing Hub, IDT) is employed to synchronize the light sources (LED and laser), the cameras and the speaker. Only the first fully-developed jet is analyzed. Before firing the system, smoke is injected into the Helmholtz. In Fig. 1(c) we show the resulting temperature field related to the hot plate (in this case, the reference image corresponds to the ambient and the displaced image, to an image with the hot plate). This temperature field is then used as the reference temperature for the analysis of the dynamics of the jet. When firing the system, first a reference BOS image is recorded (LED is on, laser is off), and 20 μs later the speaker is started. After a variable delay time (around 20 μs), each camera registers a pair of images. For the BOS camera, only one of the images is used as the displaced image, but for the PIV camera, the two images are utilized and correspond to the reference and displaced object states (time separation on the order of 10 μs). In Fig. 1(d)-(e) we present two BOS-PIV results corresponding to time delays of 0.33 and 1.30 ms after the exit of the pulsed jet from the cavity (each result corresponds to different measurements since continuous sampling of the development of the jet is not feasible).

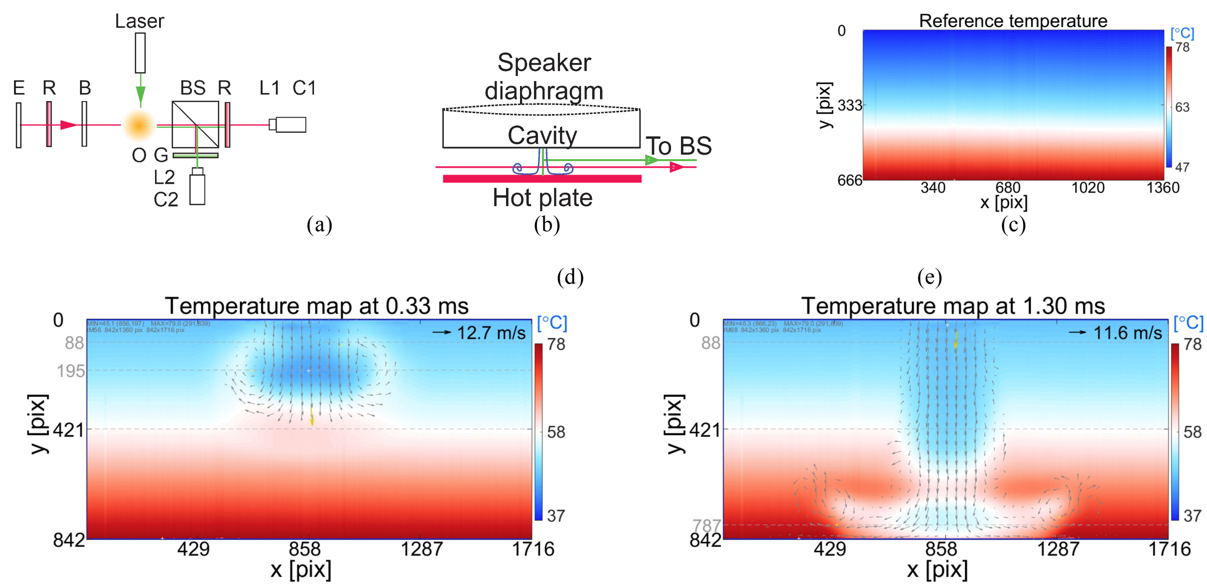

Fig. 1. (a) Setup (top view). (b) Phase object (side view). (c) Reference temperature map. Temperature maps of jet at time delays of (d) 0.33 ms and (e) 1.3 ms.

References

[1] B. S. Dalziel, G. O. Hughes, and B. R. Sutherland, "Whole-field density measurements by synthetic schlieren," Exp. Fluids 28, 322-335 (2000).

[2] M. Raffel, C. Willert, and J. Kompenhans, *Particle image velocimetry, a practical guide* (Springer, 1998).

[3] B. L. Smith and G. W. Swift, "A comparison between synthetic jets and continuous jets," Exp. Fluids 34, 467-472 (2003).

[4] L. Venkatakrishnan, A. Wiley, R. Kumar, and F. Alvi, "Density field measurements of a supersonic impinging jet with microjet control," AIAA J **49**(2), 432-438 (2011).

[5] A. Blanco, B. Barrientos, and C. Mares, "Performance comparison of background-oriented schlieren and fringe deflection in temperature measurement: part I. Numerical evaluation," Opt. Eng. **55**(5), 054102 (2016).

Evaluation of displacement fields using Digital Image Correlation

Zaira A. Morales-Espinoza [1,*] and Víctor H. Flores-Muñoz [1,2]
[1] Universidad Politécnica del Bicentenario, Silao, Gto, México
[2] Centro de Investigación en Matemáticas A.C., Guanajuato, Gto, México
Author e-mail address: 16030399@upbicentenario.edu.mx

Abstract: In this work we use the technique of Digital Image Correlation (DIC) for the evaluation of the *in-plane* displacements. The Direct Linear Transformation (DLT 11) calibration method is applied to the conversion of the units of length. Experimental results are presented for a latex sample.

1. Introduction

In 3-D machine vision, it necessary to know the relationship between the 3-D object coordinates and the image coordinates. This transformation is determined in geometric camera calibration by solving the unknown parameters of the camera model. Initially, camera calibration techniques were developed in the field of photogrammetry for aerial imaging and surveying. First, photographic cameras were used, but recently video cameras have replaced them almost completely. Also new application areas, like robot vision and industrial metrology, have appeared, where camera calibration plays an important role.

Calibration is a necessary step in 3D computer vision to create a metric relationship between the captured 2D image and the 3D scene by using the extrinsic and the intrinsic parameters of the camera [1]. Our attention is focused on method of Direct Linear Transformation (DLT).

On the other hand, the digital correlation of images, better known as DIC (acronym in English), is a technique of artificial vision that is based on finding a correspondence between two images. It allows experimental analysis based on the treatment of digital images, in which the technique consists in the maximization of a correlation coefficient that is determined from the analysis of a subset of pixels between the two images [2]. For our application, we use this technique to evaluate the displacement fields of a latex sample.

2. Methodology

DIC offers characterization of material parameters far into the range of plastic deformation. Its powerful data analysis tools allow the determination of the location and amplitude of maximum strain, which are important functions in material testing. We will present experimental results of elastic deformation for a target sample.

Figure 1 shows the arrangement for DIC. The first step is the calibration of the system by using a calibration target and using the DLT method.
The steps involved in obtaining 2D displacements data using DIC are:

- The process starts with the camera parameter calibration to identify the relative position and orientation of camera.
- Two images are recorded to view same object area before and after the mechanical stress is applied.
- 2D image correlation is performed to identify matching regions in different views.
- Thereby, the displacement vector *(u,v)* is obtained for all points.

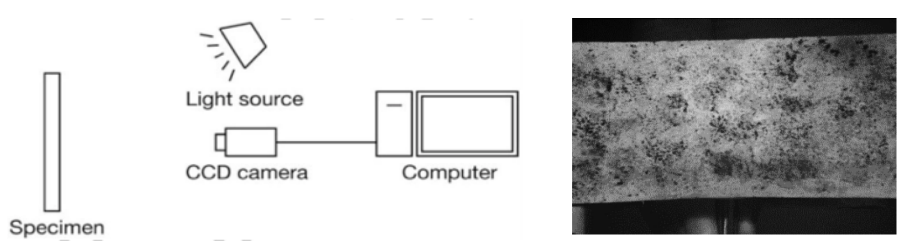

(a) (b)

Fig. 1. (a) Scheme of the technique DIC, (b) Latex sample.

3. Results

The graphs shown in figure 2 represent the displacement fields in *x* and *y* directions, obtained by the DIC algorithm.

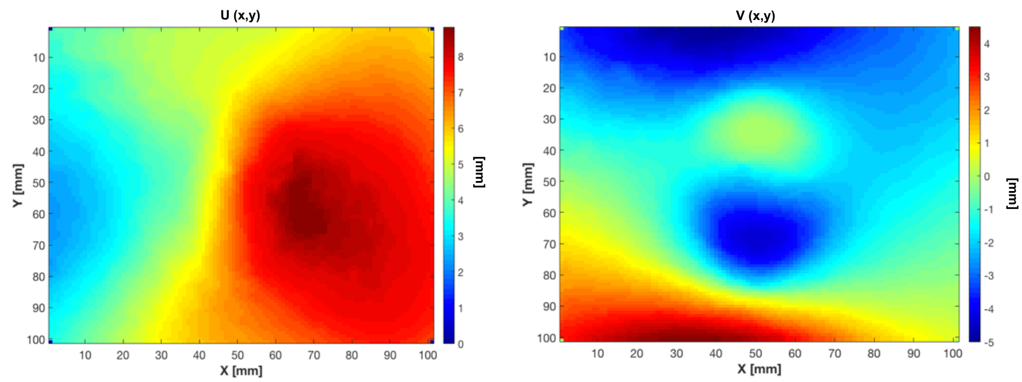

(a) (b)

Fig 2. Displacement fields: a) *U(x,y)* and (b) *V(x,y)*.

The maximum displacement in *U(x,y)* is *8.72 mm*. The range of displacement in *V(x,y)* is between *-5 mm* to *4 mm*. The conversion from pixels to metric units was done by using the *L* parameters from the calibration [1].

The total *in-plane* displacement field of the latex sample is evaluated as the norm of the *u* and *v* displacement vector that is showed in Figure 3. The maximum displacement was *9.3 mm*.

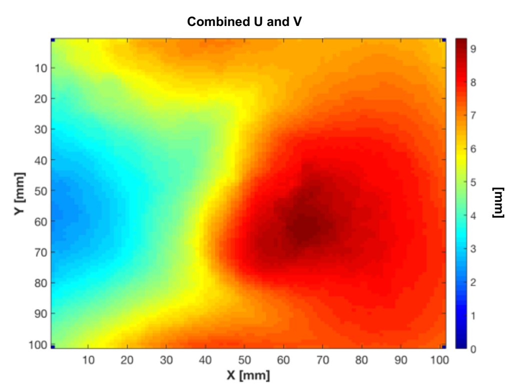

Fig 3. Plot of combined *u(x,y)* and *v(x,y)*.

4. Conclusions

Digital Image Correlation was used for 2D displacements measurement of latex sample. Geometric camera calibration is needed to describe the mapping between 3-D world coordinates and 2-D image coordinates. In our case, the Direct Linear Transformation (DLT 11) calibration method was used.

DIC has several advantages over conventional Non-Destructive Test methods and some of the other optical techniques such as laser shearography and speckle interferometry, which are generally more expensive and more difficult to use outside the laboratory as they require precise setup and low vibrational environments, also the equipment is not always suitable for use outdoors.

References

[1] Abdel-Aziz, Y. I. (1971). Direct linear transformation from comparator coordinates into object space in close-range photogrammetry. In *Proceedings of the ASP Symposium on Close-Range Photogrammetry, 1971* (pp. 1-18). American Society of Photogrammetry.
[2] Flores Muñoz, Víctor H. (2015). New optical setups focused on the measurement of the shape and displacement fields (Tesis doctoral). Centro de Investigaciones en Óptica, León, Gto., Mexico.

Internal defect identification using phase-sensitive optical coherence elastography

Bo Dong, Bing Pan*
Institute of Solid Mechanics, Beihang University, Beijing, 100191, China
Author e-mail address: b.dong@foxmail.com

Abstract: Phase-sensitive optical coherence elastography (PhS-OCE) is a highly sensitive method for measuring depth-resolved displacement field distribution inside tissues and semi-transparent materials. In addition to characterizing mechanical properties, we found the method is also effective in identification of defects inside tissues and materials. By mapping phase-difference map before and after specimen deformation, defects can be discovered from the phase-difference distribution anomalies. Samples, including polymer films and human tooth, with internal defects were measured using an established PhS-OCE system. The results show that some micro defects, which could not be observed from the cross-sectional images, were able to be detected from the measured phase-difference maps.

1. Introduction

Optical coherence elastography OCE is a method for measuring depth-resolved displacement field inside scattering mediums [1]. By taking advantage of phase-sensitive detection, even sub-nanometer displacement can be measured [2]. Recently, this novel method has been employed for characterizing mechanical properties inside tissues and semi-transparent materials and achieves good results [3, 4].

In addition to mechanical characterization, we found the method is also effective in micro-defect identification [5]. In this work, a phase-sensitive OCE (PhS-OCE) system was established to identify micro defects inside polymer films and human tooth.

2. Methodology

The schematic of a line-field PhS-OCE system is shown in Fig. 1(a). The system is composed of a light source, an interferometry, and a spectrometer. A cross-section of the sample is firstly illuminated by the light source, and then the scattered light from the sample interferes with the reference and forms an interference spectrum imaged on the CCD camera. As shown in Fig. 1(b), the cross-sectional image (b3) and phase-difference map (b4) are firstly evaluated by using the spectrum captured before and after the sample deformation (b1 and b2), and then the displacement field distribution (b5) of the tested section is acquired according to the relationship

$$w(y,z) = \frac{\lambda_c}{4\pi n} \Delta\varphi(y,z), \tag{1}$$

where w is the out-of-plane (z-directional) displacement, λ_c is the center wavelength of the light source, n is the refractive index of the specimen, and $\Delta\varphi$ is the phase-difference. Because the defects inside sample will induce anomalies in displacement field and phase-difference map, it can be used as a method for defect identification.

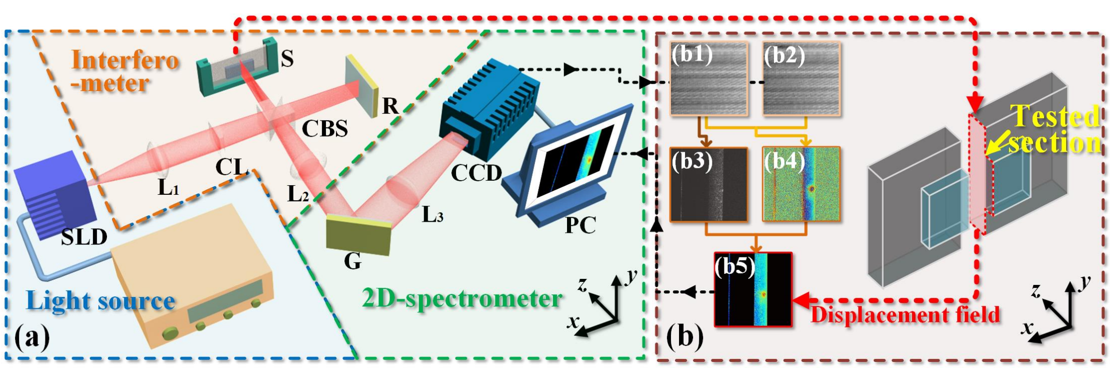

Fig. 1 The schematic of (a) configuration of a PhS-OCE system (b) displacement field evaluation procedure. SLD: Super-luminescent laser diode; L1-L3: lens; CL: cylindrical lens; S: sample; CBS: cube beam splitter; R: reference plane; G: diffraction grating; CCD: CCD camera; PC: personal computer.

3. Experiment

After establishing a PhS-OCE system according to Fig. 1, polymer films and human tooth with internal defects were measured to validate the effectiveness of the proposed method. During polymer films curing, the cross-sectional image and the phase-difference maps were measured as shown in Fig. 2(a) and (b). In Fig. 2(a1) and (a2), a relatively large defect was observed from both cross-sectional image and phase difference map. In Fig. 2(b1) and (b2), a relatively small internal defect can only be observed from phase-difference maps. During temperature decreasing, the phase-difference maps of the tooth were measured as shown in Fig. 2(c), where (c1) is the photograph of the sample, (c2) - (c4) are the phase-difference maps when the tooth temperature decreased from 45°C to 42°C, 41°C, 40°C respectively. From the phase difference discontinuity, the internal crack of the tooth can be clearly observed. From the experiments above, it is noticed that some micro defects, which could not be observed from the cross-sectional images, were able to be detected from the measured phase-difference maps.

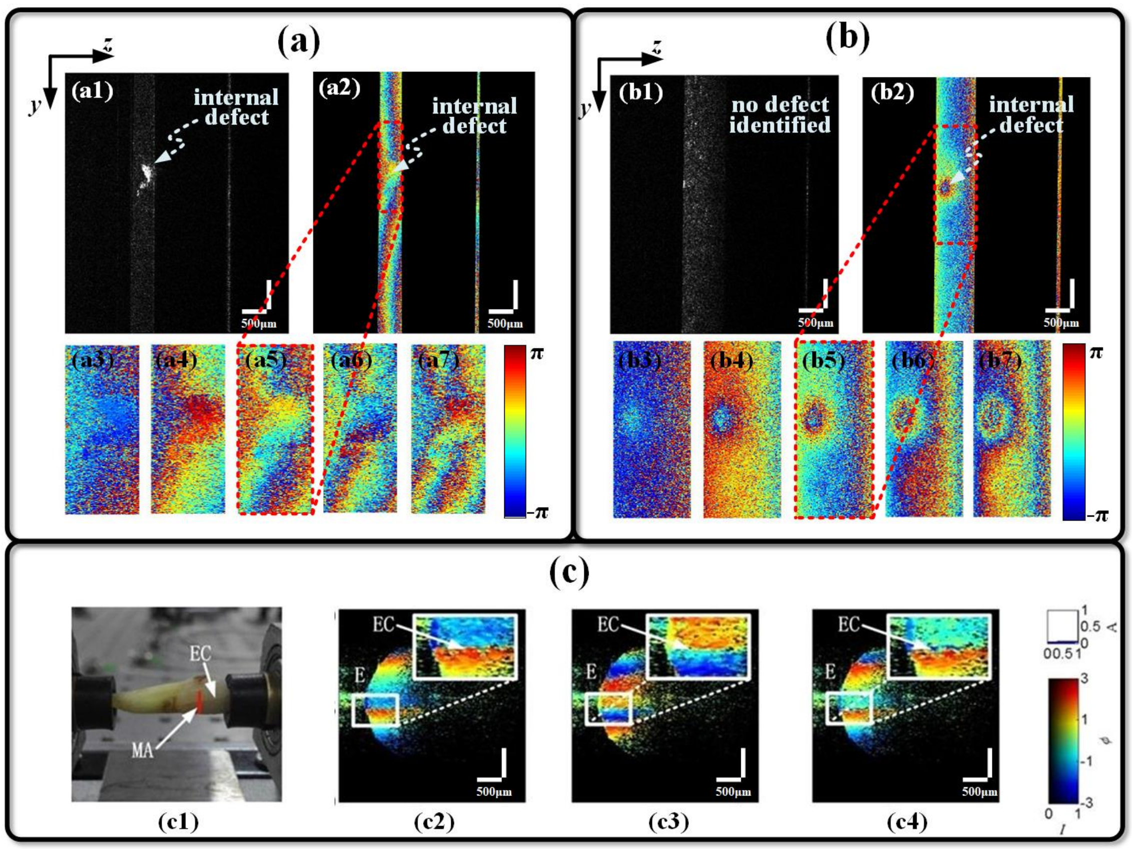

Fig. 2 Experimental results (a) a polymer film with large internal defect; (b) a polymer sample with small internal defect; (c) a human tooth with enamel crack. MA: measured area, EC: enamel crack, E: enamel.

References

[1] Kennedy B F, Wijesinghe P, and Sampson D D, "The emergence of optical elastography in biomedicine," Nat. Photonics **11**, 215-221 (2017).
[2] Zaitsev V Y, Matveyev A L, Matveev L A, Gelikonov G V, Gubarkova E V, Gladkova N D, and Vitkin A, "Hybrid method of strain estimation in optical coherence elastography using combined sub-wavelength phase measurements and supra-pixel displacement tracking," J. Biophotonics, **9**, 499 (2016).
[3] Zhang Y, Dong B, Bai Y, Ye S, Lei Z, and Zhou Y, "Measurement of depth-resolved thermal deformation distribution using phase-contrast spectral optical coherence tomography," Opt. Express, **23**, 28067 (2015).
[4] Leartprapun N, Iyer R R, Untracht G R, Mulligan J A, Adie S G, "Photonic force optical coherence elastography for three-dimensional mechanical microscopy," Nat. Commun., **9**, 2079 (2018).
[5] Dong B, Pan B, Zhang Y, and Bai Y, "Microdefect identification in polymers by mapping depth-resolved phase-difference distributions using optical coherence tomography," Polym. Test. **68**, 233-237 (2018).

Real-Time 3D Measurement using Background-Modulated Modified Fourier Transform Profilometry

Xinran Liu, Jonathan Kofman
Department of Systems Design Engineering, University of Waterloo, 200 University Avenue West, Waterloo, ON N2L 3G1, Canada xinran.liu@uwaterloo.ca, jkofman@uwaterloo.ca

Abstract: A method for real-time 3D measurement was developed using background-modulated modified Fourier transform profilometry fringe patterns and geometry constraints. GPU processing permits real-time 3D surface reconstruction in parallel with image acquisition with only two high-frequency fringe patterns required for the 3D reconstruction from phase maps. The new method achieved high measurement accuracy in static measurement, and in dynamic measurement of a moving object.

1. Introduction

In full-field fringe projection methods for three-dimensional (3D) surface-shape measurement, fringe patterns are projected onto an object surface, and captured images of the deformed patterns are used to compute a phase map by fringe analysis techniques. While Fourier transform profilometry (FTP) is one fringe analysis technique used to compute the phase map [1], a modified FTP method using two fringe patterns with a π phase shift difference permits removal of the unwanted image background and improved measurement range [2]. However, a wrapped phase map with 2π discontinuities is generated, and phase unwrapping is necessary.

Recently, geometry-constraint based techniques were developed to permit object surface reconstruction directly from wrapped phase maps, and pixel-wise determination of point correspondences between camera and projector images. High-frequency fringe patterns embedded with statistical patterns, triangular patterns, or binary stripe patterns have been used to reduce the number of candidate points in camera-projector point-matching, while achieving high measurement accuracy. The relationship between fringe pattern frequency, number of candidate points in the measurement volume, and system geometric constraints has been modelled in [3]. This paper presents a method for real-time 3D measurement that uses new background-modulated modified FTP fringe patterns and geometry constraints, and requires only two high frequency fringe patterns for 3D surface reconstruction.

2. Method

Modified FTP uses the following pair of fringe patterns:

$$I_1(x,y) = B(x,y) + A(x,y)\cos\varphi(x,y)$$
$$I_2(x,y) = B(x,y) + A(x,y)\cos[\varphi(x,y) - \pi] \quad (1)$$

where $B(x, y)$ and $A(x, y)$ represent the background intensity and amplitude of modulation, respectively, and $\varphi(x, y)$ is the phase map. Background removal can be achieved by subtraction. The background-modulated modified FTP uses an additional pair of fringe patterns that include a background offset B_0:

$$I_1'(x,y) = B(x,y) + A(x,y)\cos\varphi(x,y) + B_0(x,y)$$
$$I_2(x,y) = B(x,y) + A(x,y)\cos[\varphi(x,y) - \pi] + B_0(x,y) \quad (2)$$

Continuous real-time measurement is achieved by projection of the two pairs of patterns (1) and (2) alternately, and capturing the corresponding images from two cameras. The background offset B_0 is set to cB when the phase period is odd, and $-cB$ when the phase period is even, where $0 < c < 1$ is a background offset scale factor. The background offset is determined from two sequential pairs of fringe images (1) and (2), and then binarized using a threshold zero:

$$B_0(x,y) = [I_1'(x,y) + I_2'(x,y) - I_1(x,y) - I_2(x,y)]/2 \quad (3)$$

With the measurement system calibrated earlier, 3D reconstruction is achieved from only a single image pair. For each pair, either background-modulated modified FTP (2) or modified FTP (1), the left-camera phase map and computed binary pattern are used to determine left-camera to projector correspondence; the right-camera phase map is used to refine selected corresponding points; and stereovision 3D reconstruction is used to compute a 3D point cloud. Only one fringe image pair is required for surface reconstruction during continuous real-time 3D measurement. Geometry-constraint based techniques utilize a pre-defined measurement volume to limit the number of candidate surface points for a given camera pixel. There would be several candidate positions for each left-camera pixel; however, only one candidate position is correct and located on the object surface. The relation between the number of candidate positions, camera-projector baseline and other calibration parameters, measurement volume depth, and fringe pattern wavelength, has been mathematically modelled in [3]. In order to minimize the number of candidate surface points, while avoiding restrictions on the measurement volume size and fringe pattern wavelength, the left-camera-projector baseline is minimized in the measurement system design. This results in only two candidate neighboring 3D positions in the measurement volume, one corresponding-point candidate in an odd phase period, one in an even phase period. The correct corresponding-point is selected using the binarized background offset B_0. After selection of the correct corresponding-point in the projector image, the corresponding-point in the right-camera image is computed and refined. After following the same procedure for all points, the 3D coordinates for all surface points can be calculated using stereovision 3D reconstruction techniques.

3. Experiments and Results

The background-modulated modified-FTP method was demonstrated using an optical measurement system with two monochrome cameras (720×540 images) and a DLP projector (912×1140), with left-camera projector baseline 57 mm, left-camera right-camera baseline 164 mm, and approximate working distance 700 mm. Measurement was performed on a double hemisphere object with radii 50.8 mm and centre-to-centre distance 120.0 mm. In measurement of the static object, RMS errors were: 0.12, 0.11, 0.11, and 0.11 mm with centre-to-centre error 0.10 mm. In dynamic measurements of the object moving at approximately 25 cm/s, RMS errors were 0.13 and 0.12 mm for the two spheres, with centre-to-centre error 0.13 mm.

Real-time performance of the measurement system using the background-modulated modified-FTP method was demonstrated in measurement of a moving and deforming hand. The 3D point cloud object-surface reconstruction and display (Fig. 1) were performed in real-time with 2D image capture. (The approximate mean number of points per surface reconstruction was 100K). The mean GPU runtime of a single 3D reconstruction including memory transfer between host and device was approximately 10 ms.

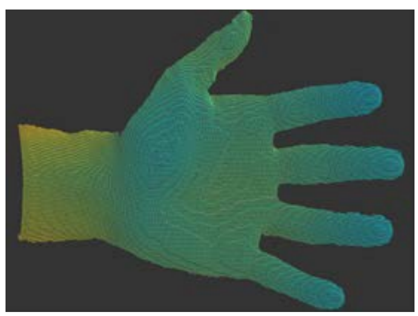

Fig. 1 Measurement result of a moving and deforming hand.

4. Conclusion

A real-time 3D surface measurement method, developed based on background-modulated modified FTP fringe patterns and geometry-constraint techniques, achieved high accuracy in measurement of static and moving objects. GPU processing permitted real-time 3D surface reconstruction in parallel with image acquisition with only two high-frequency fringe patterns required for the 3D reconstruction from phase maps.

References

[1] M. Takeda and K. Mutoh, “Fourier transform profilometry for the automatic measurement of 3-D object shapes,” Appl. Opt. **22**, 3977–3982 (1983).

[2] J. Li, X. Su, and L. Guo, “Improved Fourier transform profilometry for the automatic measurement of three-dimensional object shapes,” Opt. Eng. **29**, 1439–1444 (1990).

[3] X. Liu and J. Kofman, “High-frequency background modulation fringe patterns based on a fringe-wavelength geometry-constraint model for 3D surface-shape measurement,” Opt. Express **25**, 16618–16628 (2017).

Acknowledgement

This research was supported by the Natural Sciences and Engineering Research Council of Canada (NSERC); University of Waterloo; and China Scholarship Council (CSC).

Multi-Ray Exponential Fringe-Pattern Projection for 3D Surface Measurement with Off-the-Shelf Hardware

Ali Babaei[1], Mohammad Saadatseresht[1], Jonathan Kofman[2]
[1]University of Tehran, College of Engineering, School of Surveying and Geospatial Engineering, Tehran, Iran
[2]University of Waterloo, Dept. of Systems Design Engineering, 200 University Ave. W., Waterloo ON, Canada
babaei.a@ut.ac.ir, msaadat@ut.ac.ir (corresponding author), jkofman@uwaterloo.ca

Abstract: Multi-ray exponential fringe-pattern projection was developed for 3D measurement with low-cost off-the-shelf hardware. System self-calibration for exponential-pattern projection from multiple projector positions permits simultaneous gamma nonlinearity correction, system parameter determination, and 3D measurement with higher accuracy than conventional methods.

1. Introduction

Use of off-the-shelf low cost components in 3D optical metrology presents three main challenges: the radiometric or gamma-nonlinearity distortion of projector input to output, which leads to error in phase and 3D measurement [1]; unstable and unknown lens parameters (intrinsic geometry) of the camera and projector; and uncertainty of 3D reconstruction due to limited number of ray intersections. In this paper, exponential fringe-patterns generate a gamma-corrected phase map, additional parameters correct for lens distortion, and self-calibration using multiple projector poses lead to high-accuracy measurement with a low-cost off-the-shelf camera and projector.

2. Method

Projector-input fringe patterns are generated by an exponential cosine function, with $\delta_n = 2\pi n/N$ phase shift, $n = 0, 1,..., N-1$ fringe pattern index, N number of phase shifts, f spatial frequency, $A(i, j)$ intensity bias, $B(i, j)$ intensity modulation (amplitude), and (i, j) pattern coordinates (column, row):

$$I_n(i,j) = A(i,j) + B(i,j)\exp\left[\frac{1}{2}+\frac{1}{2}\cos(\phi(i,j)+\delta_n)\right], \tag{1}$$

where a gamma-corrected wrapped phase map $\phi(i, j)$ is calculated using four-step phase shifting (N=4):

$$\varphi(i,j) = \tan^{-1}\left[\ln\left(s(i,j)\right)/\ln\left(t(i,j)\right)\right] \tag{2}$$

$$s(i,j) = \frac{\left[I_4'(i,j)-I_1'(i,j)\right]\left[I_4'(i,j)-I_3'(i,j)\right]}{\left[I_1'(i,j)-I_2'(i,j)\right]\left[I_3'(i,j)-I_2'(i,j)\right]}, \quad t(i,j) = \frac{\left[I_4'(i,j)-I_1'(i,j)\right]\left[I_1'(i,j)-I_2'(i,j)\right]}{\left[I_4'(i,j)-I_3'(i,j)\right]\left[I_3'(i,j)-I_2'(i,j)\right]}, \tag{3}$$

where $I_n'(i,j)$ is the intensity value at pixel (i, j) in the nth camera-captured fringe pattern [2]. Six wrapped phase maps are generated using six different pattern pitches, and multiple-wavelength phase unwrapping generates a single unwrapped phase map. By self-calibration, a calibration object with known targets locations is not needed; the object being measured is used for system calibration. Collinearity equations are solved to simultaneously obtain unknown object coordinates and system parameters. Self-calibration in digital fringe projection permits redundant observations to increase 3D reconstruction accuracy. While this has achieved high accuracy using industry-grade components [3], in this paper, exponential fringe patterns to obtain gamma-corrected phase maps, and redundant multiple rays from multiple projector locations, compensate for inaccuracy of off-the-shelf components.

Using a fixed camera, horizontal and vertical fringe patterns are projected onto the surface from different positions (Fig. 1). For each projector position, vertical and horizontal phase values are computed at each pixel in the camera image $\varphi_H(i,j), \varphi_V(i,j)$ are the replacements of image coordinates in photogrammetry collinearity equations [4]; the phase indicates the point position in the projector image plane. Using $\xi_{ij}^k, \eta_{ij}^k = \left(\varphi_H^k(i,j), \varphi_V^k(i,j)\right)$ to denote the vertical and horizontal phase values of the k^{th} projector position at camera pixel (i,j), $[X\ Y\ Z]$ object coordinates, ξ_0^k, η_0^k phase values at projector principal point for k^{th} position, the modified collinearity equation is:

$$\begin{aligned}\xi_{ij}^k - \xi_0^k + \Delta\xi_{ij} &= (-c_k\frac{2\pi}{\lambda})\frac{r_{11}^k(X-X_0^k)+r_{21}^k(Y-Y_0^k)+r_{31}^k(Z-Z_0^k)}{r_{13}^k(X-X_0^k)+r_{23}^k(Y-Y_0^k)+r_{33}^k(Z-Z_0^k)},\\ \eta_{ij}^k - \eta_0^k + \Delta\eta_{ij} &= (-c_k\frac{2\pi}{\lambda})\frac{r_{12}^k(X-X_0^k)+r_{22}^k(Y-Y_0^k)+r_{32}^k(Z-Z_0^k)}{r_{13}^k(X-X_0^k)+r_{23}^k(Y-Y_0^k)+r_{33}^k(Z-Z_0^k)}\end{aligned} \tag{4}$$

where $\Delta\xi_{ii}$ is distortion (symmetric-radial, decentering, in-plane image [4]), c_k projector focal length, $[r_{11}, r_{12}, r_{13},$

$r_{21}, r_{22}, r_{23}, r_{31}, r_{32}, r_{33}]^k$ projector rotation matrix elements, and $[X_0\ Y_0\ Z_0]^k$ projector perspective center coordinates.

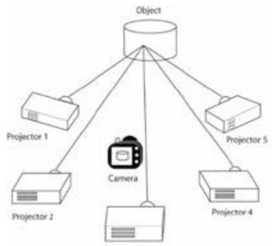

Fig. 1. Mulı-ray fringe projection.

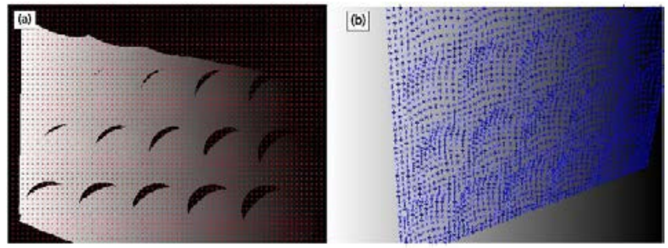

Fig. 2. Camera-projector phase-map correspondence: a) Phase map from camera images for one projector position and selected sparse grid pixels, b) projector phase map, and projector image-plane points corresponding to camera-image grid points.

The camera image plane is used as an intermediate reference to determine correspondences between projector images at different projector positions. For each projector position, correspondences between the projector and camera image-planes are determined by searching for $\varphi_H(i, j)$, $\varphi_V(i, j)$ in the projector phase maps (Fig. 2), for each camera pixel. Correspondences between all projector planes are established. Self-calibration uses correspondences of a sparse grid (Fig. 2a) to minimize computation and 3D reconstruction is based on multi-ray intersection for all valid camera pixels. A visibility map shows the number of projector rays (positions) for every camera pixel (Fig. 3a).

3. Experiments and Results

The multi-ray digital fringe-projection method was used with a fixed camera and 12 projector positions. The minimum number of projector rays to define a valid point was set to three. Points illuminated by fewer projector rays (outer margins, top) (Fig. 3a) had higher error (Fig. 3b) than points illuminated by many projector rays (center). Points illuminated by less than three projector rays were not computed (black) in Fig. 3b.

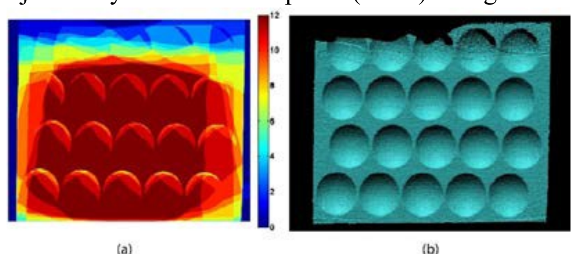

Fig. 3. Test object: a) visibility map showing number of projector rays for every pixel, b) surface mesh from point cloud.

In measurement of a double hemisphere object with known geometry, the multi-ray exponential fringe-projection method had higher accuracy than the conventional camera-projector method with gamma-corrected phase. The radius of a hemisphere fitted to the computed point cloud was 50.752 mm with RMSE 0.252 mm (new method) compared to 51.309 mm and RMSE 0.648 mm (conventional), for a true hemisphere radius 50.8 mm.

4. Conclusion

Multi-ray exponential fringe projection permits 3D surface measurement with high accuracy using low-cost off-the-shelf hardware. Self-calibration for multiple projector poses with exponential-pattern-projection gamma correction permits higher accuracy than the conventional single projector-camera configuration with gamma correction. Self-calibration with exponential-pattern projection permits simultaneous gamma correction, system-parameter determination, and 3D measurement, without requiring gamma or geometric calibration procedures separate from measurement. Knowledge of camera geometric and optical parameters are not required.

References

[1] Dhillon, D.S., Govindu, V.M., "Geometric and radiometric estimation in a structured-light 3D scanner," Mach. Vis. Appl. **26**(2), 339-352 (2015).

[2] Babaei, A., Saadatseresht, M., Kofman, J., "Exponential fringe pattern projection approach to gamma-independent phase computation without calibration for gamma nonlinearity in 3D optical metrology," Opt. Express **25**, 24927-24938 (2017).

[3] Schreiber, W., Notni, G. "Theory and arrangements of self-calibrating whole-body three-dimensional measurement systems using fringe projection technique," Opt. Eng. **39**(1), 159-169 (2000).

[4] Fraser, C.S., "Digital camera self-calibration," ISPRS J. Photogramm. Remote Sens. **52**(4), 149-159 (1997).

Optical Metrology for Alignment of Large Radio Telescopes

David M. Gale
Large Millimeter Telescope Alfonso Serrano
Instituto Nacional de Astrofísica, Óptica y Electrónica (INAOE), Luis Enrique Erro No.1, Santa Maria Tonantzintla, San Andrés Cholula, Puebla 72840, Mexico.
dgale@inaoep.mx

Abstract: Single-dish radio telescopes have probably reached the upper limit of collecting area for steerable antenna, given the engineering challenges and high costs involved in constructing large precision reflector surfaces. In this presentation we summarize the traditional methods for antenna reflector alignment, taking as an example the Large Millimeter Telescope in Mexico, and present two new techniques being developed for radio astronomy using state-of-the-art optical metrology.

1. Reflector surface accuracy considerations for radio astronomy

The error budget for reflector components of a single-dish radio telescope typically adheres to the 1/10 or 1/20 wavelength requirement for acceptable image quality. In radio astronomy the observing wavelength extends from several meters down to the sub-millimeter, hence reflector surface error budgets may be measured in tens of millimeters, down to tens of microns for the highest frequency antenna. The Large Millimeter Telescope (LMT) located in central Mexico operates in the frequency range 75-350 GHz, or wavelengths from 4 mm to 0.85 mm. The design error budget for the LMT is 75 microns rms under good site conditions.

The error budget usually considers the combined error from both the primary and secondary reflectors, and additional system optics where fitted. Due to it's large size and resulting mechanical complexity, the primary reflector accounts for most of the budget. Key elements of surface accuracy include reflector panel manufacturing error, assembly and alignment error, and adjuster or actuator error, depending on whether the surface is of fixed shape or features active compensation. The error budget may also include gravitational and thermal distortions, and environmental conditions such as wind and solar, since many radio telescopes are operational during the day time.

2. Traditional reflector alignment methods

Smaller reflectors for lower-frequency use are designed to be assembled and aligned using theodolite equipment. Indeed this manual technique was used on large (30-meter) antenna in the late sixties and seventies for surface precision of the order of one millimeter. The theodolite or total station is still widely used for initial placement of higher-precision reflector surfaces. The advent of portable coordinate measurement technology in recent decades allows a factor of ten improvement in measurement accuracy for large surfaces. Laser trackers are used routinely at the LMT for reflector subpanel alignment off-antenna, and have provided moderate success for global primary surface alignment. Since the tracker requires manual scans of the surface with a retro-reflector, see fig. 1 (left), data collection for large surfaces is slow and tedious. Measurements may also be degraded by air turbulence.

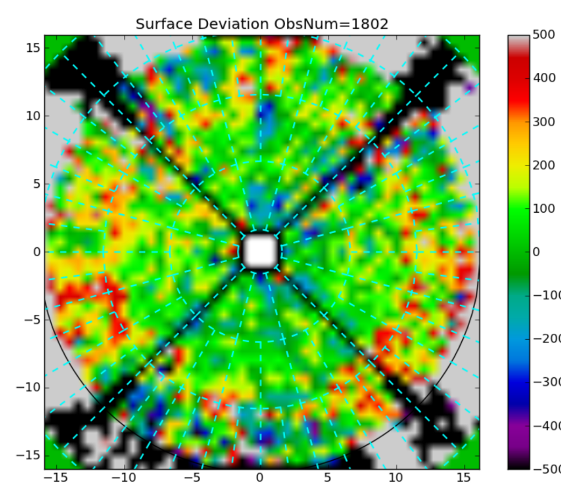

Fig 1. Left: LMT primary surface measurement using a laser tracker. Right: holography map of the inner 32.5-meter surface.

Phased holography provides faster surface mapping for reflector alignment, and has been used successfully on several radio telescopes. A dual-horn holography receiver is mounted at the telescope focus and views an artificial satellite X-band source both directly and after traversing the telescope optics. Reflector elevation during measurement is determined by the available sources. The telescope is scanned across the source to obtain a full map, which may take an hour or longer. Fig. 1 (right) shows a holography map of the LMT primary. Drawbacks for the LMT are relatively low spatial resolution, and shadowing produced by the tetrapod legs of the secondary reflector.

Photogrammetry is used extensively for antenna surface measurement, and is currently the main technique for setting the full 50-meter LMT primary. The surface requires targeting (fig.2. left), and the distribution of camera stations necessitates the use of a mobile platform or crane. Measurement accuracy is similar to that of the laser tracker and holography, but mapping times of an hour or less provide more useful "snapshots" of the antenna's thermal behavior. Fig. 2 (right) shows an early error map of the LMT primary during initial alignment. Comparisons of tracker, holography and photogrammetry techniques on the LMT have been reported previously [1].

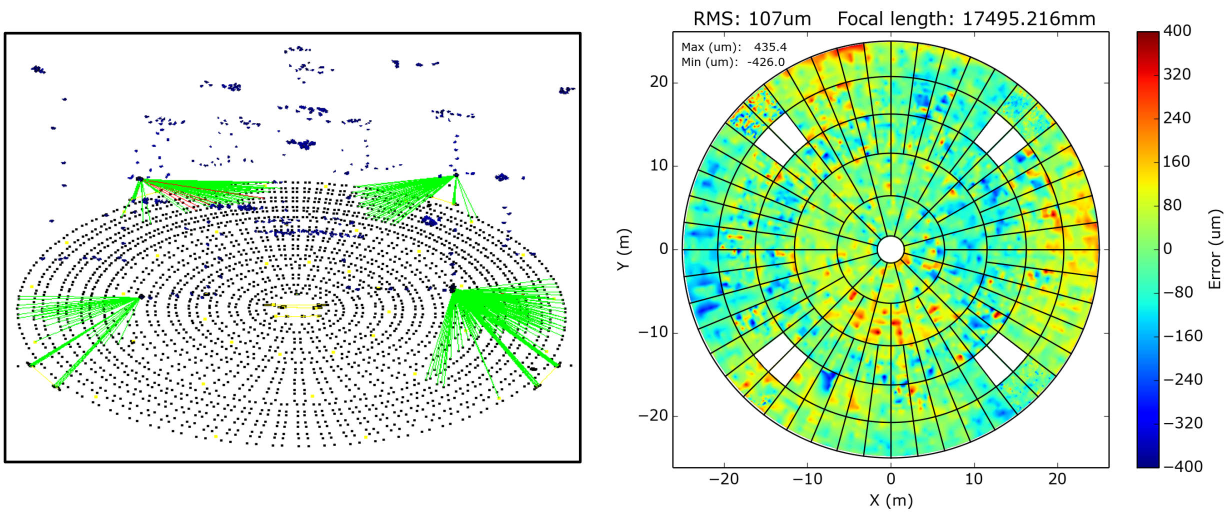

Fig. 2. Left: 50-meter primary target layout (black) and camera stations (blue) for an LMT primary surface photogrammetry map. Surface coverage for four camera stations is shown in green. Right: early photogrammetry map of the full 50-meter surface.

3. Recent developments in commercial optical metrology

The aforementioned systems are usually employed at night, when antenna surfaces are stable. To minimize telescope downtime, mapping and adjustment forms part of the maintenance schedule. Next-generation metrology will feature active monitoring of reflectors, allowing better control of thermal distortions for both night and daytime observing.

Multi-channel interferometers based on frequency-scanning interferometry (FSI) are now commercially available. Linear distance measurement is achieved with higher accuracy than conventional interferometers and without beam interruption issues. FSI is being developed for structural monitoring on the future Giant Magellan Telescope (GMT) [2], and could also be employed for fixed-beam surface monitoring on sub-millimeter antennas.

Terrestrial Laser Scanning (TLS) is a LiDAR technique that requires no fixed targets or beam lines. Inherent accuracy is of the order of millimeters, however the collection of several million data points allows accuracy improvements using bundle adjustment and other methods to reduce measurement uncertainty. Commercial TLS systems are currently under evaluation on several radio telescopes [3]. While traditional metrology techniques will continue to be widely used, especially for initial construction and alignment, both FSI and TLS promise major enhancements for radio astronomy operations and image quality.

References

[1] D. Gale et al, "Mapping the LMT primary reflector using photogrammetry; a first comparison with 12 GHz holography", in SPIE Vol. 9912 Astronomical Telescopes and Instrumentation (Edinburgh, UK, 2016), paper 151.

[2] A. Rakich et al, "A 3-D metrology system for the GMT", in SPIE Vol. 9906 Astronomical Telescopes and Instrumentation (Edinburgh, UK, 2016), paper 112.

[3] C. Holst et al, "Terrestrial Laser Scanner Two-Face Measurements for Analyzing the Elevation-Dependent Deformation of the Onsala Space Observatory 20-m Radio Telescope´s Main Reflector in a Bundle Adjustment", in Sensors 17(8), 1833 (2017).

Gates' interferometer configuration as a fringe projection unit

José Rubén Sánchez-Aguilar[1,*], J. A. Rayas[1], Amalia Martínez-García[1], Miguel León-Rodríguez[2]
[1]Centro de Investigaciones en Óptica A. C., León, Guanajuato, México
[2]Universidad Politécnica de Guanajuato, Cortazar, Guanajuato, México
*jrsanchez@cio.mx

Abstract: In this paper we present the use of a Gates's interferometer configuration to the generation of a fringe pattern used as *fringe projection profilometry system*. The proposed interferometer consists of only a single beam splitter cube with one wedged entrance face and is insensitive to environmental vibration due to its common path configuration. The generated fringes are not localized which is one of advantages of this interferometer.

1. Introduction

Among the optical techniques used for the generating three-dimensional (3D) surfaces of complex objects, the use of *fringe projection profilometry system* have developed great interest in the metrology field [1], it is widely used in application such as medicine [2], 3D machine vision [3], industry[4], etc.
A typical *fringe projection profilometry system* consists of a camera as the image acquisition unit, an object to be measured and a fringes projection unit [5], commonly a digital projector. The used of the projector unit as a digital projector limited the resolution of the measurement, spatially in small object or surfaces details. In this work we substituted the use of a digital projector as a projector unit, instead, we used the Gates's interferometer configuration [6] that consist of a splitter cube 50/50 to generate a fringe pattern by means of interference of the light.

2. Methodology and experimental results

Based on a typical *fringe projection profilometry system*, the arrangement shown in Fig. 1 was mounted, with the modification of the conventional system on the use of the Gates's Interferometer configuration as subsystem/unit of fringes projection. The Gates's Interferometer configuration consists of a laser beam and a nonpolarizing cube beam splitter 50T-50R, as shown in Fig. 2. The collimated laser beam hits on the edge of the cube, parallel to the prism's junction, with this configuration we produce fringe not localized with a period that depend on the tilt of the cube.

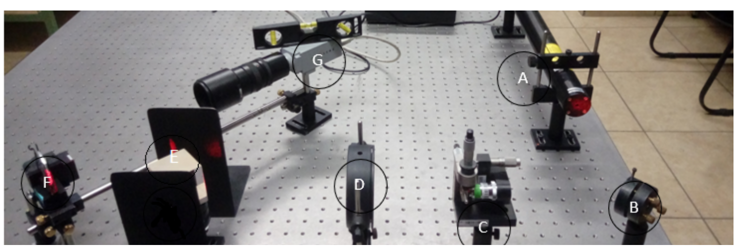

Fig. 1. Photo of the used optical array: A) He-Ne laser with $\lambda = 632\ nm$, B) mirror, C) spatial filter, D) collimator lens, E) beam splitter cube 50-50, F) sample G) CCD.

The fringes pattern was projected with a period of $0.5\ mm$ on the object, the splitter cube had a tilt of $8°$ and an angle of $65°$ between the CCD camera and the projection axis of the pattern.

Through the technique of Fourier transform for demodulation of fringes proposed by Takeda [7] the phase wrapped was obtained and using an unwrapping algorithm [8] we obtained the unwrapped phase. Finally, by triangulation, we performed the conversion of phase map to height map [1].

In Fig. 3 the results of the experiment are shown, from left to right we present the wrapped phase obtained by using the technique of Fourier transform [7], the unwrapped phase and the height map (reconstruction of the object).

a)

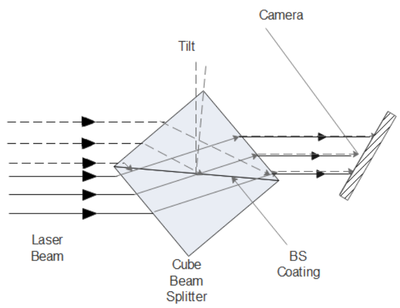

b)

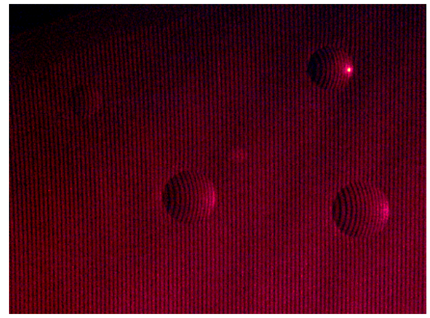

Fig. 3. a) The Gates's Interferometer configuration that consists in a cube beam splitter and a laser beam. b) Pattern of fringes projected onto the object (camera view).

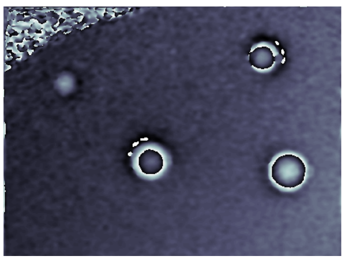

a)

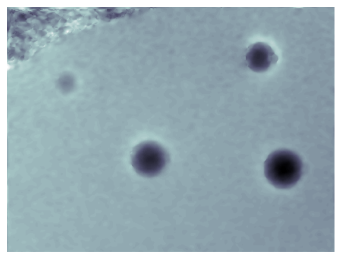

b)

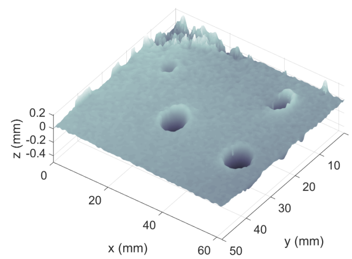

c)

Fig. 4 a) Wrapped phase, b) Unwrapped phase, c) Height map.

3. Conclusions

In this work, the Gates´s interferometer configuration was implemented as a subsystem of projection to generate non-localized fringes. Some advantages are: allow to have shorter period than the obtained with conventional projector, nonlocalized fringes exist everywhere within an extended (three-dimensional) region of space which allows to place the object without problem. One disadvantage of this configuration is that the period is limited mainly by the size of the speckle and the resolution of the camera.

As a future work, a low coherence laser will be used to reduce noise in the fringes.

References

[1] S. S. Gorthi and P. Rastogi, "Fringe projection techniques: Whither we are," Opt. Lasers Eng. **2,** 133–140 (2010).

[2] F. Berryman, P. Pynsent, J. Fairbank, and S. Disney, "A new system for measuring three-dimensional back shape in scoliosis," Int. J. Optomecha. **5,** 663–672 (2008).

[3] C. Chen and A. Kak, "Modeling and calibration of a structured light scanner for 3-D robot vision," 1987 IEEE Int. Conf. Robot. Autom **4,** 807–815 (1987).

[4] H. N. Yen, D. M. Tsai, and J. Y. Yang, "Full-field 3-D measurement of solder pastes using LCD-based phase shifting techniques," IEEE Trans. Electron. Packag. Manuf. **1,** 50–57 (2006).

[5] J. Geng, "Structured-light 3D surface imaging: a tutorial," Int. J. Optomec Adv. Opt. Photonics. **3,** 128–160 (2011).

[6] J. A. Rayas, M. León-Rodríguez, A. Martínez et. al., "Using a single-cube beam-splitter as a fringe pattern generator within a structured-light projection system for surface metrology," Opt. Eng. **56(4)**, 1-8, (2017).

[7] M. Takeda and K. Mutoh, "Fourier transform profilometry for the automatic measurement of 3-D object shapes," Appl. Opt. **24,** 3977-3982 (1983).

[8] D.Ghiglia and L. Romero, "Robust two-dimensional weighted and unweighted phase unwrapping that uses fast transforms and iterative methods," Appl. Opt. Soc. Am. A **11,** 107-117 (1994).

Extended Abstracts

Session
OPTICAL SENSORS ON ROBOTICS AUTONOMOUS VEHICLES AND OTHER APPLICATIONS

Pg.

Classification of Electromagnetic Spectrum in the Visible Range Using Machine Learning 133
Gonzalo Vargas, José Antonio González, Mauricio Ortiz

Visual Memory Construction for Autonomous Humanoid Robot Navigation 135
A. López-Martínez, F.J. Cuevas, and J.V. Sosa-Balderas

Adaptive 3D Object Pose Estimation through Particle Swarm Optimization 137
Akbar Assa, Farrokh Janabi-Sharifi

A Nonlinear Adaptive Model-Predictive Approach for Visual Servoing of Unmanned Aerial Vehicles 139
Sina Sajjadi, Mehran Mehrandezh, and Farrokh Janabi-Sharifi

Projection of Depth Fringe Pattern for Measurement of Shape and Out-of-Plane Deformation 141
Yuta Goto, Kohhei Kawahara and Motoharu Fujigaki

Classification of Electromagnetic Spectrum in the Visible Range Using Machine Learning

Gonzalo Vargas[1,*], José Antonio González[1], Mauricio Ortiz[2]
[1]Insituto de Física y Matemáticas, Universidad Michoacana de San Nicolás de Hidalgo
[2]Facultad de Ciencias Físico-Matemáticas, Universidad Michoacana de San Nicolás de Hidalgo
*gvargas@ifm.umich.mx

Abstract: Spectrophotometers are instruments that measure parameters of samples as a function of wavelength and are composed of a source of broad spectrum light, a diffractive element and a detector. Those instruments are widely used in chemistry, physics materials and medicine labs among others. The design of a spectrophotometer in the visible range of the electromagnetic spectrum is presented is this work and is composed of a white LED, a holographic grating and the Samsung camera as a detector; the spectrum generated by placing a liquid sample in the spectrophotometer is analyzed by three artificial intelligence algorithms that are artificial neural networks, convolutional neural networks and support vector machines. These type of algorithms take part of machine learning which is currently used to solve classification and regression problems, for example facial recognition, speech recognition, search engine and medical diagnostic, among others. In this thesis, these algorithms were implemented to determinate which one is the best to classify the samples, considering the accuracy and execution time.

Introduction

The UV-Vis spectrophotometer uses UV radiation from 80 to 400 nm, mainly from 200 to 400 nm (near UV) and visible light from 400 to 800 nm, so it is very useful to characterize the solutions in the region of the ultraviolet-visible spectrum. It is governed by a very important law which is expressed with the Beer-Lambert equation [1]. A holographic diffraction grating will help to obtain the spectrum of the substance to be analyzed. An effective way to find the relationship between the spectra and their concentration can be using machine learning methods.

Machine learning is part of the artificial intelligence that focuses on developing techniques that allow computers to "learn" [2], this learning process occurs through programs capable of generalizing behaviors from information provided in the form of examples. Therefore, it is an induction process of knowledge. There are different algorithms within machine learning such as decision trees, genetic algorithms, artificial neural networks, convolutional, support vector machines, among others.

Conventional computing is characterized by development of a mathematical formation of the problem, development of an algorithm to implement a solution, coding an algorithm for a specific problem and finally the execution of that code. As it has been observed, this type of processing is very successful to solve and simulate complex mathematical models and they are also successful to perform repetitive, fast and well-defined tasks. On the other hand, computation based on machine learning is characterized by being massively parallel, adaptive, highly interconnected and tolerant to noise. In recent publications and conferences, neural networks and support vector machines have had applications in the area of image processing and computational vision [3], specifically in pattern recognition analysis. This work implements neural networks (convolutional and artificial) and support vector machines in order to compare them and determine which of these is the best algorithm to classify the concentration of the samples with the best accuracy and in the least execution time.

Electromagnetic spectrum

The substances to be analyzed are water with green vegetable dyes at 1.78%, blue at 2% and red at 2% of the McCormick brand. For these samples, we needed to dilute the original dyes in water since they were quite concentrated, this was done in relation to 1.25 mL of dye per 500mL of water. After that, the variation in concentration was as follows; the highest concentration is only the diluted dye with a total volume of 3000µL, the next sample consists of removing 20µL of the vegetable dye and replacing it with the same amount in water, every ten samples the amount of dye replaced was 50µL instead 20µL. 50 samples were taken per color giving a total of 150 samples with different concentrations. For future references the highest concentration of dye will be sample number 50 while the lowest concentration will be number 1.

Conventional spectrophotometers focus the polychromatic light of the source in a monochromator. The monochromator has as main components an input slot, an element to scatter light in its composition by wavelengths and an output slot which allows to select the desired wavelength. That monochromatic light goes through the sample and reaches the detector. Photometric measurements are made based on the relationship between the intensity of the light reaching the detector when the sample is interposed and when it is not. Based on the basic design of a spectrophotometer, an optical array shown in Fig. 1(a). It was designed to obtain the spectrum for each sample, which consists of an LED extracted from a Philips model 92900II237, a holographic grid of 930 lines / mm located at 58° respect to the LED (this angle was selected by the characteristics of the grid [4]) and a Samsung camera of 14 MP. One of the spectrums obtained with this arrangement is shown in Fig. 1(b).

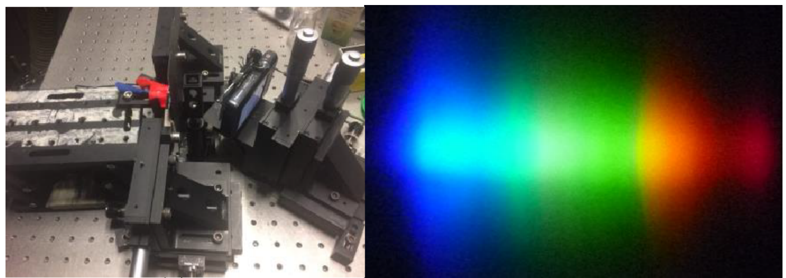

(a) (b)

Fig. 1. (a) Shows the experimental arrangement to obtain electromagnetic spectrum and (b) shows the spectrum obtained

Classification

To classify the electromagnetic spectrum based on the color and concentration of the samples, three different algorithms were used: artificial neural networks (ANN) [5], convolutional neural networks (CNN) [6] and support vector machines (SVM) [7]. These algorithms will be compared when performing the classification to select the best of them in terms of efficiency and execution time. Two classifications were made on the samples; the first one is to separate them by color, the second is the classification by the variation of dye concentration. The algorithms for the neural networks were developed using the library provided by Google called TensorFlow and for the support vector machines the LIBSVM library [8] was used. The method called cross-validation [5] was used to determine the best configuration on the free parameters in the classification algorithms, such as the number of neurons per hidden layer in artificial neural networks, the number of filters and their respective size for convolutional neural networks and constants C and gamma in the RFB Kernel [8] used in vector support machines. All the algorithms successfully classified the samples by their colors having an efficiency of 100% while the results for the classification by their concentration are shown in Tab. 1.

	EFFICIENCY (%)		
COLOR	ANN	CNN	SVM
BLUE	100	100	100
GREEN	90	90	90
RED	80	100	100

Tab. 1

References

[1] Litter, M. I.; Armienta, M. A.; Farías, S. S. “Metodologías analíticas para la determinación y especiación de arsénico en aguas y suelos”. IBEROARSEN, CYTED, Buenos Aires, Spanish, 2009.
[2] Bishop, Christopher. “Pattern Recognition and Machine Learning”. 2007.
[3] Schalkoff, Robert J. “Artificial neural networks”. McGraw-Hill Higher Education, 1997.
[4] Palmer, Christopher A.; Loewen, Erwin G. “Diffraction grating handbook”. Springfield, Ohio, USA: Newport Corporation, 2005.
[5] Michie, Donald; Spiegelhalter, David J.; Taylor, Charles C. “Machine learning, neural and statistical classification”. 1994.
[6] Matsugu, M., Mori, K., Mitari, Y., & Kaneda, Y. “Subject independent facial expression recognition with robust face detection using a convolutional neural network”. Neural Networks, 2003, vol. 16, no 5-6, p. 555-559.
[7] Smola, Alex J.; Schölkopf, Bernhard. “A tutorial on support vector regression”. Statistics and computing, 2004, vol. 14, no 3, p. 199-222.
[8] Chang, Chih-Chung and Lin, Chih-Jen LIBSVM : “A library for support vector machines”. ACM Transactions on Intelligent Systems and Technology, 2011, vol. 2, no 3, p. 27:1–27:27.

Visual Memory Construction for Autonomous Humanoid Robot Navigation

A. López-Martínez[1], F.J. Cuevas[1], and J.V. Sosa-Balderas[1]
[1]Centro de Investigaciones en Óptica, A.C., Lomas del Bosque 115, Lomas del Campestre, León, Gto, México.
{alan.lopez, fjcuevas, vicentesosa}@cio.mx

Abstract: A Visual Memory (VM) is a topological map that represents an environment as a graph of key-images. Thus, visual information acquired from cameras onboard the robot are the only data to construct the VM. This work presents the construction of a VM for humanoid robot navigation. Additionally, a Genetic Algorithm (GA) is proposed to tackle the problem of image matching used within the VM construction process. To validate the efficacy of the proposed approach, experimental results using a humanoid robot dataset are presented. Further, the solution for image matching based on the proposed GA was compared with RANSAC.

1. Introduction

Mapping the environment is an important step for autonomous robot navigation. Topological maps, oppositely from metric maps, relieve the computational burden of extracting and storing metric and 3D information. A visual memory (VM) is a topological map that represents an environment by a connected graph [1]. The nodes of the VM are key-images that represent relevant positions within the world. The edges, on the other hand, describe the relationships between nodes. The motivation behind the VM framework is to imitate the human behavior of memorizing key scenes the first time an environment is explored, in order to facilitate a subsequent navigation in the same environment.

Given the advantages of using a VM for autonomous navigation, different strategies using this approach have been proposed using visual servoing to control robot displacements [1, 2]. Different approaches for the VM construction have been presented mostly for mobile robots. Unfortunately, less effort has been done in order to construct a VM for humanoid robot navigation. A particular problem related to this type of robots involves images with blur effects, due to the inherent jerk of humanoid walks.

2. Visual memory construction

The proposed approach tackles the task of constructing an accurate and efficient representation for the navigation environment. An efficient representation is the one that permits a fast and easy localization, and allows a simple, yet robust path planning. The whole framework for the VM construction as proposed in this work is shown in Fig. 1. First, the robot is operated manually to capture a training video of the environment. Then, an off-line process consisting in different steps is carried out: (i) Frame extraction. From the training video, a set $V = \{I_1, I_2, \cdots, I_n\}$ containing all frames is obtained. (ii) Key-image selection. From the set V, a smaller set $V_k = \{I_{k1}, I_{k2}, \cdots, I_{km}\}$ that contains only key-images is obtained. (iii) Graph construction. The set V_k is manually organized into a graph that is the final VM. These steps are now described in detail.

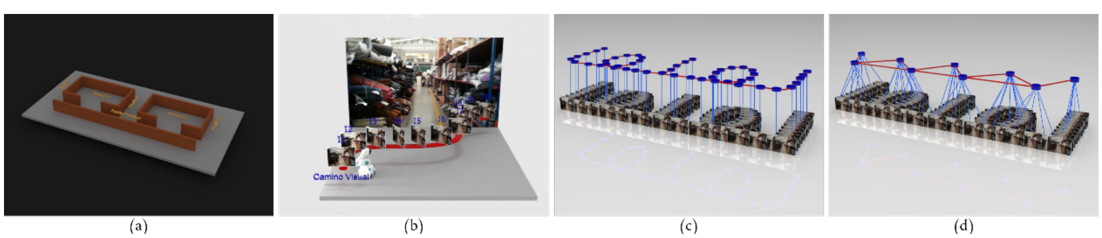

Fig 1. Visual memory construction. (a) Environment to map. (b) The robot is operated manually to obtain the set of training images. (c) A reduced number of key-images are selected from this set. (d) Finally, the key-images are grouped together to form a connected graph, i.e. the visual memory.

Frame extraction is the first off-line process. The aim of this step is to extract the whole set of frames within the training video. It is noted that, since the training video is acquired manually, the quality of the VM depends on the expertise of the user. The better the training video (i.e. the more the environment is explored), the better the VM.

The aim of key-image selection step is to extract key-images. This step is the core of the proposed approach. First, to tackle the problem of images with high motion blur due to humanoid movements, we remove the images for which the variance of the Laplacian of Gaussian (LoG) is bellow a threshold, commonly $\sigma^2(LoG) = 10$ [3]. This also allow us to discard images with low textures.

Two conditions must be optimized for key-image selection: 1. The overlap between key-image $I_{k1}$and I_{k1+1} must be maximum; and 2, the number of frames between key-image $I_{k1}$and I_{k1+1} must be maximum. Additionally, two hypotheses must be considered for key-image selection: 1. Two key-images $I_{k1}$and I_{k1+1} must contain a set P_i of matched key-points. The cardinality of the set must be enough to compute a control law for navigation; and 2, there must be a possible path between the position of capture of image I_{k1} to the image I_{k1+1}.

To compute image overlap, image matching using a GA is performed. First, we extract and describe key points. To this end, the SURF extractor and descriptor was selected because its complexity is O(log(N)), and the method is invariant to illumination, scale, and rotation. After matching descriptors, we authenticate the matches with the epipolar constraint using a GA that estimates the Essential (E) matrix. Since the E matrix encodes the displacement and rotation between frames, each individual is represented with a fixed length binary string as: $chromosome = [\Phi, \theta, \psi, t_x, t_y]$. Where each variable is allowed within a specific range: $\Phi, \theta, \psi \in [0,2\pi]$, and $t_{x,}t_y \in [-5,5]$. The parameters for the GA are as follows: Population size, 100; Crossover rate 0.95; Mutation rate, 0.01; Elite size, 15. A Boltzmann fitness scale was used to control pressure selection. To score solutions, a fitness function *F* was proposed as follows. We first extract the epipolar lines from the E matrix encoded by the chromosome. Then, the value of *F* is the sum of points that deviate less than a predefined threshold *T = 1 pixels* from its corresponding epipolar line.

The final step involves the grouping of nodes that share a common location, like a corridor or a room. We make this step manually in order to finally construct the VM.

3. Experiments and results

The proposed approach was carried out using the *CIMAT-NAO-A* dataset, which was acquired with a NAO humanoid robot, and is available in http://personal.cimat.mx:8181/~hmbecerra/CimatDatasets.zip. The dataset contains 399 different images with blur effects and low textures. Fig. 2 shows sample images from the dataset, and the key-images selected by our algorithm.

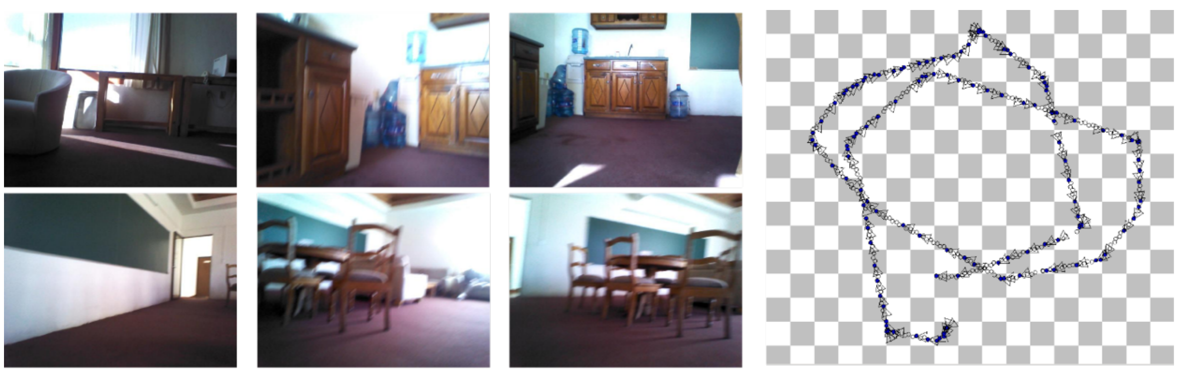

(a) (b)

Fig. 2 Topological map for the data set *CIMAT-NAO-A*. (a) Sample images from the dataset. (b) Key-images are highlighted In blue.

The image matching solution based on a GA was compared with an heuristic method call RANdom SAmple Consensus (RANSAC). Both methods were compared with the odometry of the robot, and the results demonstrate that the GA obtains a lower error than the RANSAC method.

4. Conclusions

In this work, an environment representation was presented using only visual information. Further, a GA was proposed to tackle the problem of image matching. Results obtained with a humanoid walk dataset show that the proposed approach efficiently describe the environment. Consequently, an adequate VM is constructed.

References

[1] Courbon, J., Mezouar, Y., and Martinet P., "Autonomous navigation of vehicles from a visual memory using a generic camera model", Tans, on Intelligent Transportation Systems. **10,** 392-402 (2009).
[2] Delfin, J., Becerra, H. M., and Arechavaleta, G., "Humanoid localization and navigation using a visual memory", 16th International Conference on Humanoid Robots (Humanoids), (Cancún, México, 2016), pp. 725-731.
[3] Ovalle E., "Generación de una memoria visual para la navegación autónoma de un robot humanoide", (2016).

Adaptive 3D Object Pose Estimation through Particle Swarm Optimization

Akbar Assa[a], Farrokh Janabi-Sharifi[b]
a) University of Toronto, b) Ryerson University
a) akbar.assa@utoronto.ca, b) fsharifi@ryerson.ca

Abstract: Estimating the pose of objects is an important problem in vision-based robotics. Kalman filters are commonly used for such a purpose. However, the performance of these filters deteriorates if system's noise statistics is not known a priori. This work proposes an adaptive scheme based on particle swarm optimization (PSO) to adjust the measurement noise covariance of the filter. The experimental results confirm the effectiveness of the proposed method.

1. Introduction

Acquiring the pose of the observed objects is a crucial requirement in many vision-based robotic and computer vision applications such as visual servoing [1] and augmented reality [2]. Numerous methods were proposed to accurately estimate the pose of the objects exploiting the features extracted from images [3-5]. However, most of these methods approximate the relative pose of the objects without considering the measurement noise, induced by the camera and the image processing algorithms. By contrast, Kalman filters provide accurate estimations despite the uncertainties of the visual measurements and therefore have gained popularity in robotic applications.

While Kalman-based pose estimation algorithms perform well under known noise statistics, their performance diminishes in the absence of such knowledge. Traditionally, adaptive methods such as multiple model-based schemes [6] and innovation-based methods [7] are employed to simultaneously adjust the noise parameters of the filter using the observed measurements. However, the former methods combine the estimations of multiple filters each tuned with a set of parameters and do not adjust the noise parameters, while the latter schemes estimate the noise parameters from the innovation sequence, assuming the system to be linear. In another group of works, optimization-based methods, and in particular PSO [8], were employed to estimate the noise parameters. These works were focused on adaptation of the process noise, assuming the measurement noise to be known. However, the measurement noise statistics is the most important parameter of the filter and its estimation is usually non-trivial.

This work proposes an adaptive extended Kalman filter (AEKF) for camera pose estimation. The PSO algorithm is adopted to estimate the measurement noise covariance. This PSO method allows multiple samples of the noise covariance to evolve towards the correct value for the measurement noise covariance. The closeness of the particles to the true value is measured exploiting the measurement likelihood function. The experimental results confirm the effectiveness of the proposed AEKF method for object pose estimation in a robotic scenario.

2. Pose Estimation and Extended Kalman Filter

To estimate the pose of the object of interest with respect to the camera, the state of the system is formed as follows,

$$X^c_{o,k} = \begin{bmatrix} x^c_{o,k} & y^c_{o,k} & z^c_{o,k} & \varphi^c_{o,k} & \theta^c_{o,k} & \psi^c_{o,k} & \dot{x}^c_{o,k} & \dot{y}^c_{o,k} & \dot{z}^c_{o,k} & \dot{\varphi}^c_{o,k} & \dot{\theta}^c_{o,k} & \dot{\psi}^c_{o,k} \end{bmatrix}, \tag{1}$$

which includes the position and orientation (in Euler angles) of the object with respect to the camera and their time derivatives. The filter is initialized by setting the initial noise covariance matrices, the state and its error covariance. Then at each time step, first the state is predicted and then adjusted using the measurement vector as follows,

$$X^c_{o,k+1} = FX^c_{o,k} + K_k\left(Y_k - h(FX^c_{o,k})\right) \tag{3}$$

where F is the transition matrix, h is the measurement function, Y_k is the vector of image features and K_k is the Kalman gain. In order to calculate the correct value of the Kalman gain, the measurement noise covariance (i.e. R) should be known. In this work, a proper value for R is sought through PSO as it is explained in the sequel.

3. Particle Swarm Optimization

Particle swarm optimization offers an interesting solution towards finding a proper value for R. In PSO, multiple particles are used. Each particle has a position and a velocity, which are initialized first, and then evolved through a constant velocity approach. The velocity of each particle is updated iteratively as follows,

$$v^m_{i+1} = av^m_i + b_1 r_1 (p - x^m_{i-1}) + b_2 r_2 (g - x^m_{i-1}) \tag{4}$$

where $x_i^m = x_{i-1}^m + v_i^m$ is the position of particle m at iteration i, p is the best particle position in iteration i, g is the absolute best particle position, a, b_1, b_2, r_1, and r_2 are model parameters. Each particle contains diagonal parameters of the measurement noise (i.e., $R_k^i = diag(x_k^i)$)The particle fitness is measured using the measurement likelihood,

$$\text{FIT}=P(Y_K \mid R_k^i, X_{o,k-1}^c) = \frac{\exp(-\frac{1}{2}(Y_K - FX_{o,k-1}^c)^T (H_k P_{k|k-1} H_k^T + R_k^i)^{-1} (Y_K - FX_{o,k-1}^c))}{\det(2\pi(H_k P_{k|k-1} H_k^T + R_k^i))} \tag{5}$$

At each iteration, p and g are found through the FIT function [8] and then the particles velocities and positions are updated. The updating continues till satisfactory FIT value for the global particle position is obtained.

4. Experimental Results

The proposed AEKF is used on data collected from a robotic cell, where a robot mounted camera is maneuvered around an object with four circular features. The center of these features are extracted and used as measurements of the filter. The pose estimation error is depicted in Fig. 1. As it can be seen the proposed adaptive method could adjust the value of the measurement noise covariance correctly to enhance the accuracy of the estimations.

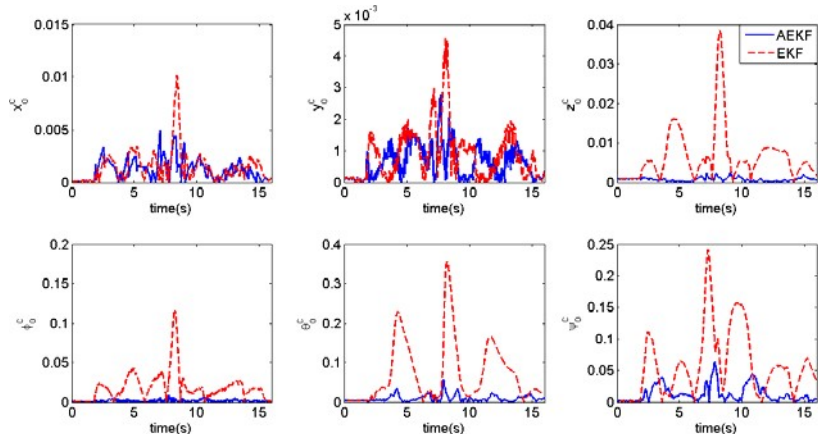

Fig. 1. Pose estimation errors using the proposed AEKF as compared to non-adaptive EKF

5. Conclusion

An AEKF was proposed in this work for pose estimation. The measurement noise covariance was updated using the PSO algorithm, which resulted in satisfactory results in the experiment. The work is expected to be extended by including a more general form of the measurement noise as well as the other filter noise parameters.

References

[1] K. Fathian, J. Jin, S.G., Wee, D.H. Lee, Y.G. Kim, N.R. Gans, "Camera relative pose estimation for visual servoing using quaternions," *Robotics and Autonomous Systems*, 2018.

[2] E. Marchand, H. Uchiyama, and F. Spindler, "Pose estimation for augmented reality: a hands-on survey," *IEEE Transactions on Visualization and Computer Graphics*, vol. 22, no. 12, pp. 2633-2651, 2016.

[3] A. Assa, and F. Janabi-Sharifi, "Virtual visual servoing for multicamera pose estimation," *IEEE/ASME Transactions on Mechatronics*, vol. 20, no. 2, pp.789-798, 2015.

[4] A. Tejani, R. Kouskouridas, A. Doumanoglou, D. Tang, and T.K. Kim, "Latent-class Hough forests for 6 DoF object pose estimation," *IEEE Transactions on Pattern Analysis and Machine Intelligence*, vol. 40, no. 1, pp. 119-132, 2018.

[5] T.N. Tan, G.D. Sullivan, and K.D. Baker, "Linear algorithms for object pose estimation," in *BMVC92*, Springer, London, pp. 600-609, 1992.

[6] P.D. Hanlon, and P.S. Maybeck, "Multiple-model adaptive estimation using a residual correlation Kalman filter bank," *IEEE Transactions on Aerospace and Electronic Systems*, vol. 36, no. 2, pp.393-406, 2000.

[7] A.H. Mohamed, and K.P. Schwarz, "Adaptive Kalman filtering for INS/GPS," *Journal of geodesy*, vol. 73, no. 4, pp.193-203, 1999.

[8] D.J. Jwo, and S.C. Chang, "Particle swarm optimization for GPS navigation Kalman filter adaptation," *Aircraft Engineering and Aerospace Technology*, vol. 81, no. 4, pp.343-352, 2009.

A Nonlinear Adaptive Model-Predictive Approach for Visual Servoing of Unmanned Aerial Vehicles

Sina Sajjadi*, Mehran Mehrandezh*, and Farrokh Janabi-Sharifi°
* Faculty of Engineering & Applied Science, University of Regina, Canada.
° Department of Mechanical and Industrial Engineering, Ryerson University, Toronto, Canada.
e-mail address: (Mehran.Mehrandezh@uregina.ca)

Abstract: Aerial vehicles, due to the very nature of their operation, are subject to many uncertainties. The problem is aggravated in GPS-denied environments. As a result, vision-based control (or visual servoing) solutions are sought to address such issues. In this work, visual servoing is formulated as a nonlinear optimization problem in the image plane. The proposed approach is based on a class of nonlinear model predictive control that takes constraints into consideration. A 2-DOF model helicopter is considered for initial formulations and verification of the approach. The model helicopter has a coupled nonlinear pitch/yaw dynamics. It is also capable of a pitch over (i.e., hover at a non-zero pitch angle) around its pivotal axis of rotation due to the offset between the Center of Mass (CoM) of its fuselage and the rotation axis. This further, makes the linearized model (calculated around any pitch angle) a Linear Parameter Varying (LPV) system, for an adaptive control is formulated within the model predictive visual sevroing framework. In this paper, a design guideline is provided under model predictive visual servoing paradigm that considers Filed of View (FOV) constraints, the constraint on the pitch angle, and also the maximum voltages that can be applied to independently-controlled pitch/yaw motors. The control space is parameterized via Laguerre basis network functions that makes the optimization scheme computationally less expensive, thus, suitable for real time applications. The proposed servoing strategy is validated via simulations and experiments, and the results are compared with those obtained from commonly-utilized infinite-horizon LQR.

1. Problem Definition

An adaptive model-predictive visual servoing in presence of task, sensor, and control-space constraints is designed and developed. The control algorithm is implemented in simulation and via experiments on a 2-DOF model helicopter from Quanser, [1]. Problem formulation is carried out for the case that a perspective camera is being mounted in front of the 2-DOF model helicopter. A pinhole projection model, without any lens distortion, is considered. Figure 1 shows a picture of the 2-DOF model helicopter. As can be seen from Figure 1, the helicopter can turn around a pivot point (aka, axis of rotation) via two axes, namely yaw (or pan motion) and pitch (tilt motion). The CoM of the helicopter is located in front of the rotation axis, therefore, a constant pitching torque would be required to compensate for gravitation forces. This additional pitching torque can make the 2-DOF model helicopter hover at any pitch angle.

Figure 1: The 2-DOF model helicopter, [1].

This model helicopter was chosen as a testbench due to its coupled and nonlinear pitch/yaw dynamics. Furthermore, the linearization of the dynamic model around any pitch angle would lead to a Linear Parameter Varying (LPV) system, whose state interaction matrix will have time/state-variant elements. A local adaptive model-predictive visual servoing is formulated to account for time/state-variant parameters in system's dynamics via successive linearization, that outperforms a global nonlinear optimization in terms of time complexity and convergence rate. Furthermore, a Laguerre network function is used for parametrizing the control space under an infinite-horizon control framework. Reducing the size of the control space via proposed parametrization makes it suitable for real time applications, without compromising the stability.

Performance of the proposed visual servoing strategy is depicted via simulations and experiments with the case study of tracking/servoing a colored ball. The center point of the ball in the image is taken as the only image feature to track or servo to. While the distance between the camera and the ball can be estimated from the size of the ball in the image, however, this calculation is not critical to our control algorithm, since only pan and tilt motions of the 2- DOF model helicopter are controlled.

2. Problem Formulation

The state vector of the model helicopter consists of pitch angle, θ, and the yaw angle, φ. The control space consists of the input voltages applied to the independently-controlled pitch and yaw motors, u_θ , and u_φ . Due to gyroscopic effects, the pitch and yaw motions will be coupled. The dynamics of the system, and constraints on motion control inputs can be presented in a compact form as follows:

$$\begin{gathered} \dot{x} = f(\,x(t), u(t)) \\ g_l \ll g(x(t), u(t)) \leq g_u \\ x(0) = x_0 \end{gathered} \tag{1}$$

A point feature is defined in the image that corresponds to the center point of a ball-shape object to track or servo to. The optical flow associated with this proposed image feature, $\dot{s}$ is related to the rate of change in pitch and yaw motions, $\dot{x}$ via image Jacobian, L_s, as in Eqn. (2), considering the state and also image constraints, [2]:

$$\begin{gathered} \dot{s} \;\; = L_s(s)\dot{x} \\ h_l \quad \ll h(s(t), x(t)) \quad \ll \quad h_u \\ s = [u, v]^T, x = [\theta, \varphi]^T, and\ L_s = \begin{bmatrix} \frac{-1}{z}\ 0\ \frac{u}{z}\ uv\ -(1+u^2)\ v \\ 0\ \frac{-1}{z}\frac{v}{z}\ (1+v^2) - uv\ -u \end{bmatrix} \end{gathered} \tag{2}$$

Combining Eqns. (1) and (2) leads to Eqn. (3) in which the full dynamics of the coupled system is given:

$$\begin{gathered} \dot{s} \;\; = \;\; L_s\, f(x(t), u(t)) \\ I_l \ll I(s(t), x(t), u(t)) \ll I_u \\ x(0) = x_0, s(0) = \;\; s_0 \end{gathered} \tag{3}$$

The control objective is to bring the point feature, associated with the center point of the ball (i.e., the candidate image moment representing the ball), to the center point of the image while minimizing the motion and also the energy consumption based on a quadratic performance index. A control-space parametrization was also carried out to conduct the optimization over an infinite horizon in real time by using an exponentially-decaying basis function based on orthonormal *Laguerre* functions, [3]. It is note worthy that this parametrization will guarantee an asymptotic stability via successive linearization of the nonlinear system, [4].

3. Results

Figures 2a and 2b show a representative of the results on tracking a ball in the image. The ball was located at the center point of the image initially, then moved diagonally towards the image's right-bottom corner, and finally came to rest. The 2-DOF model helicopter tracks the ball attempting to bring the image of the ball to the center point of the image plane.

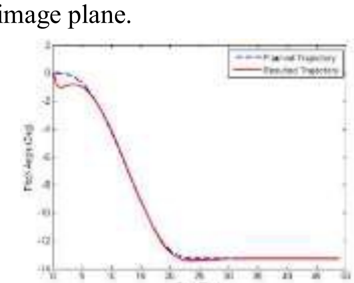

Figure 2a: Pitch angle vs. time when tracking a ball.

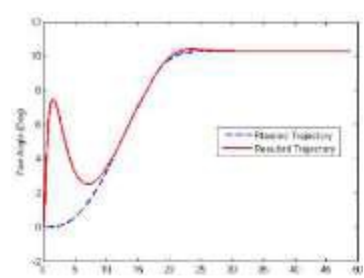

Figure 2b: Yaw angle vs. time when tracking a ball.

References

[1] www.quanser.com (last viewed on: August 6, 2018).

[2] G. Allibert, E. Courtial, and F. Chaumette, "*Visual Servoing via Advanced Numerical Methods*", Springer Publishing, 2010, Chapter 20, pp. 375-393.

[3] L. Wang, "*Model Predictive Control System Design and Implementation using MATLAB*" Springer, 2009.

[4] M. Muehlebach, et. al., "Implementation of a Parametrized Infinite-Horizon Model Predictive Control Scheme with Stability Guarantees", *IEEE Int. Conf. on Robotics and Automation* (ICRA), Singapore, 2017, pp. 6189-6196.

Projection of Depth Fringe Pattern for Measurement of Shape and Out-of-Plane Deformation

Yuta Goto, Kohhei Kawahara and Motoharu Fujigaki
Graduate School of Engineering, University of Fukui, Fukui 910-8571, Japan y-goto@u-fukui.ac.jp

Abstract: For measuring the shape and out-of-plane deformation of an object located at long far distance with spatial resolution of sub-millimeter, we proposed the fringe projection method based on three-beam interference. In this paper, we demonstrate the measurement of the depth interference fringe projected on an object that located at 600 mm distance from the camera.

1. Introduction

Fringe projection is the method that the shape and displacement of an object can be measured non-destructively and non-contactly by irradiating the spatially intensity-modulated light or interference fringes [1, 2]. However, the imaging with the camera, which is significantly tilted respect to the optical axis of the light source, is required to obtain information along the out-of-plane direction. Thereby, it is difficult to keep the size of the measurement system. When interference fringes are used, the resolution with sub-micrometer order can be obtained, and then it is not suitable for measurement of large structures.

To solve these problems, we proposed a shape and out-of-plane deformation measurement using fringe projection based on three-beam interference. In this method, a fringe pattern, which has an intensity variation along the optical axis direction, can be obtained by the three-beam interference. Since the shape of the object in the out-of-plane direction appears as a contour as shown in Fig. 1, it can be directly measured by the camera. In addition, it is possible to measure a distant object while keeping the approximately coaxial arrangement between the light source and the camera. In the paper, to confirm the basic principle, we demonstrate the measurement of the depth fringe pattern projected on an object that located at 600 mm distance from the camera.

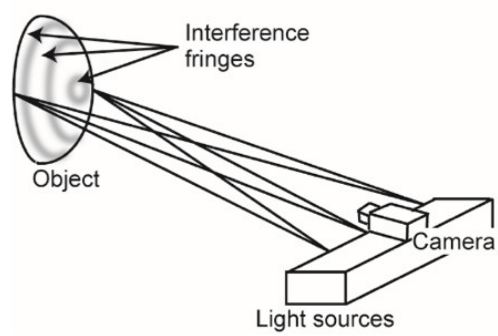

Fig. 1. Conceptual image of our method.

2. Fringe Projection Based on Three-Beam Interference

When superimposing two collimated beams E_0 and E_1, the interference fringe, which has the intensity variation along the orthogonal direction with the axial-direction, is appeared. The pitch of this interference fringe d_s is expressed as

$$d_s = \frac{\lambda}{\tan\theta_1}, \tag{1}$$

where, λ is wavelength of the light source and θ_1 is the angle between E_0 and E_1. When $\theta_1 \approx 0$, Eq. 1 can be transformed as

$$d_s = \frac{\lambda}{\theta_1}. \tag{2}$$

As shown in Fig. 2, the case of the three-beam interferometry involving third beam E_2, the interference fringe with intensity distribution along the axial-direction because two interference fringes by E_0, E_1 and E_2 are superimposed. Here, the angle between E_0 and E_2 is θ_2 and then $\theta_1 = \theta_2$. In Fig. 3, the pitch of depth fringe pattern d_L is expressed as

$$d_L = \frac{d_s}{\tan\theta_2}. \tag{3}$$

In addition, when $\theta_1 \approx 0$, similar to Eq. (2), Eq. (1) can be transformed as below.

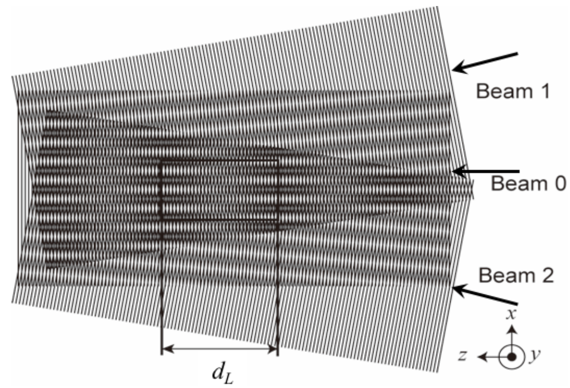

Fig. 2. Conceptual image for three-beam interference.

$$d_L = \frac{d_s}{\theta_2}. \tag{4}$$

In this method, the interference fringe, which has the intensity variation along the optical axis, can be generated using the three-beam interference. By projecting this fringe pattern onto the object, it is possible to directly obtain the shape and out-of-plane deformation without the interpolation and the coordinate transform by inclining the camera.

The depth fringe pattern is appeared by the difference in contrast of fringes of the two-beam interference. It is possible to extract only this contrast difference by calculating the amplitude distribution of fringes using the sampling Moiré method [3].

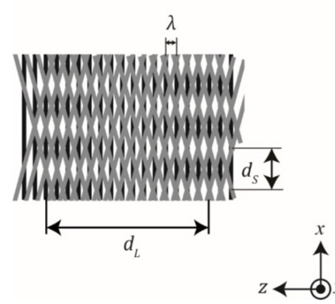

Fig. 3. Relation between d_s and d_L

3. Experiment

We performed an experiment for confirming the principle of three-beam interference. The optical setup is shown in Fig. 4(a). A collimated laser beam (wavelength is 532 nm) is divided by three mirrors into three parts. Mirror1 and mirror2 are slightly tilted so that divided beams interfere on the object. Then, the interference fringes on the object is captured by the camera. Here, a rough-surface object, which has the plane tilted by 40° on x-axis respect to the optical axis of E_0, is used as shown in Fig. 4(b).

Figure 5(a) shows the interference fringe captured by the camera. In Fig. 5(a), small pitch fringes by two-beam interference were appeared in area W, whereas these fringes were almost not appeared in area B. In addition, Fig. 5(b) shows an amplitude distribution of depth fringe pattern obtained by the sampling Moiré method. By calculating the amplitude distribution, W area became the bright and B area became the dark, respectively. Thereby, we can see the depth fringe by three-beam interference. Here, the obtained pitch of the depth fringe was approximately 7.00 mm. Considering that the object's surface tilted by 40°, the resulting pitch of the depth direction was calculated using Eq. (4) to be 6.94 mm. Therefore, the value of the experimental result agreed with the calculation result of Eq. (4). From the result, we confirmed that the depth direction interference fringes were caused by the interference of the three beams.

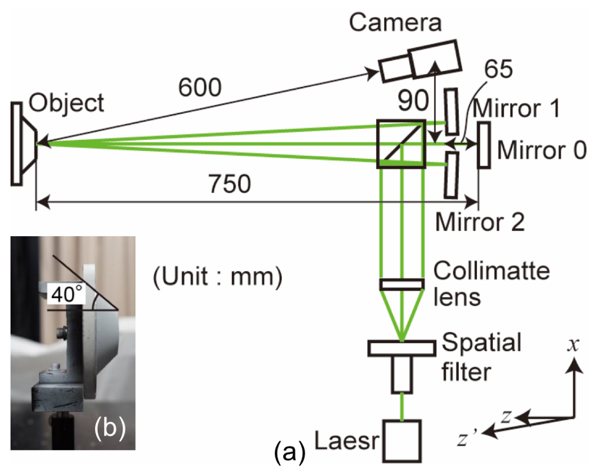

Fig. 4. Experimental setup, (a) schematic illustration, (b) picture of object.

4. Conclusion

We demonstrated the measurement of the depth interference fringe projected on an object that located at 600 mm distance from the camera. From the results, the depth fringe by the three-beam interference was confirmed. In the future, we perform the measurement for the out-of-plane shape and displacement of an object by performing the phase analysis to the obtained depth fringe.

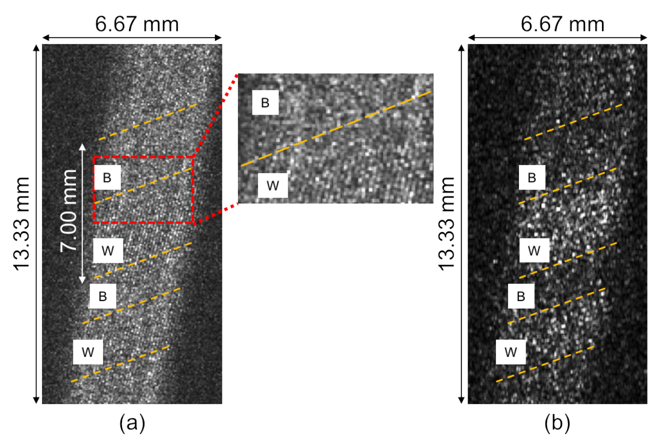

Fig. 5. Obtained images, (a) captured interference fringe, (b) calculated amplitude image.

[1] C. Quan, *et al.*, "Shape measurement of small objects using LCD fringe projection with phase shifting," Opt. Commun. **189**, 21–29 (2001).
[2] M. Schaffer, *et al.*, "Coherent two-beam interference fringe projection for highspeed three-dimensional shape measurements," Appl. Opt. **52**, 2306–2311 (2013)
[3] S. Ri, *et al.*, "Sampling Moiré method for accurate small deformation distribution measurement," Exp. Mech. **50**, 501–508 (2010).

Extended Abstracts

Session
OPTOMECHATRONICS FOR SENSING AND IMAGING

	Pg.
Optomechatronic system for measuring optical fibers parameters F. Chávez-Gutiérrez, J. A. Guerrero-Viramontes, A. Martínez-Ríos, D. Toral-Acosta, and D. Torres-Armenta	144
Calculation of optimal trajectory of mobile robots using PSO and shape descriptors for mobile robots Víctor H. Flores-Muñoz, Hugo A. Mendez-Guzmán, Cesar P. Carrillo-Delgado	146
Towards the development of a low-cost high precision instrumented mini solar sensor Arturo Díaz Ponce, Rubén A. Garrido Moctezuma, Manuel I. Peña-Cruz, Luis V. Coronado, Iván Salgado Transito, Fernando Martell, Samantha A. Cajero Roodriguez	148
Smart Emergency Response Interface for Fire Detection Takawira J. Mumanga, Rodolfo M. Martinez, Michael F. Grobler	150
Investigation of Oversampling for Amplitude Multi-Level Two-Dimensional Data Array in Holographic Memory Tetsuhiko Muroi, Yutaro Katano, Nobuhiro Kinoshita, and Norihiko Ishii	152
Single-pixel spectral imaging with hole-array coding masks Yoshio Hayasaki and Ryo Sato	154
Optical Design for Camera Calibration-free 3D Shape Measurement Using Feature Quantity Type Whole-Space Tabulation Method Motoharu Fujigaki, Yoshiyuki Kusunoki, Yuta Goto, and Daishi Takata	156

Optomechatronic system for measuring optical fibers parameters

F. Chávez-Gutiérrez[1], J. A. Guerrero-Viramontes[1], A. Martínez-Ríos[2], D. Toral-Acosta[2], and D. Torres-Armenta[2]
1 TecNM/Instituto Tecnológico de Aguascalientes, Adolfo López Mateos 1801, Aguascalientes Ags. 20256, México
2 Centro de Investigaciones en Óptica A. C., Lomas del Bosque 115., León Gto. 37150, México
Author e-mail address: fchavez.ita@gmail.com

Abstract: An optomechatronic measurer of optical fibers parameters of single (SMFs) and multi-mode fibers (MMFs) based on digital image processing is reported. With this system, it is possible extract the intensity profile from the output light of the fiber output end projected into a screen. A mechanical position system moves the screen at long an axis with millimetric precision, and with a commercial smartphone camera which is sensitive to near-infrared (NIR) the transverse intensity of the light over screen is captured in images. The processing of the image lets to extract the information necessary for the simultaneous measurement of the numerical aperture (NA) and mode field diameter (MFD) on several commercial fibers. Measurements from different fiber optical validate the performance of this system. NA and MFD measurements are compared to the values of the certificate of compliance from manufactures with a ±10% error.

1. Introduction

Numerical aperture (NA) and mode field diameter (MFD) are two of the most important optical fiber parameters in single-mode fibers (SMFs). Both parameters give information about how the light diverges from the output fiber end and the beam size, so that they let estimate the coupling efficiency with other fibers or optical devices. They are an indication of the beam quality. The NA denotes the maximum angle of incidence, with which any incident light beam is propagated through the fiber core without refraction at the core-cladding interface [1]. On the other hand, the MFD specifies a measure of the transverse extent of the electromagnetic field intensity of a mode of light in an optical fiber cross-section [2]. NA and MFD are used to predict launching efficiency, joint loss at splices, micro/macro bending performance, estimate joint losses between fibers, coupling efficiency, the effective cross-section area, backscattering characteristics, and even waveguide dispersion [3]. There are techniques used for measuring these parameters, the detection systems directly receive the output power from the fiber [4], either in the near field (NF) or the far field (FF) [5] by using visible and near-infrared (NIR) laser sources [5]. But the detection systems (photodetectors, cameras or CCDs) often may limit the allowable power that can be measured. Despite this, there are commercial systems that measuring one or the other parameter, but the manufacturers do not provide any detail about the processing methods are used for this purpose [6].

2. Experimental Methodology

In this work, we demonstrate an optomechatronic system that is based on the intensity profile extraction from images, for the simultaneous measurement of the NA and MFD by means of digital image processing of the output light projected into a screen [7]. The camera used in this work consists of a low-cost smartphone camera in front to the screen and reduces significantly the cost of the whole measurement equipment to a few hundred of dollars. The digital image processing is applied to images in different distances between the fiber output end and a screen. The rectification of perspective distortion from the images is made using homography transform [8]. In Fig. 1. is presented the conceptual design schematic diagram of measuring system principle. According to [1], given the geometry of the system, the NA can be calculated by:

$$NA = sin\theta_a = \sin(tan^{-1}(D/2z)) \tag{1}$$

where z is the distance between the emitting end of the fiber and the screen, D is the position corresponding to the v point where intensity drops to $1/e^2$ SMFs and 5% MMFs of the maximum light intensity measured by the camera. The MFD is the diameter where the optical power drops to $1/e^2$ from its peak level in a SMFs output end. In accordance with the TIA/EIA FOTP-191, in Ref. [9] the MFD is calculated using the Petermann II method:

$$MFD = \frac{2z}{k}\left[\int_0^{Xmax}\left[1-\frac{P(x)}{P_{max}}\right]xdx\right]^{-1/2} \tag{2}$$

where $P(x)$ is, the normalized power acquired from the image, k is the wave number, $Xmax$ is the maximum half-width of the D position corresponding to the v point where intensity drops to $1/e^2$ and z is the distance between the fiber output facet and the screen, in the setup. The fiber output end is mounted onto a xyz – positioner. It is moved and controlled with micrometric precision from the PC.

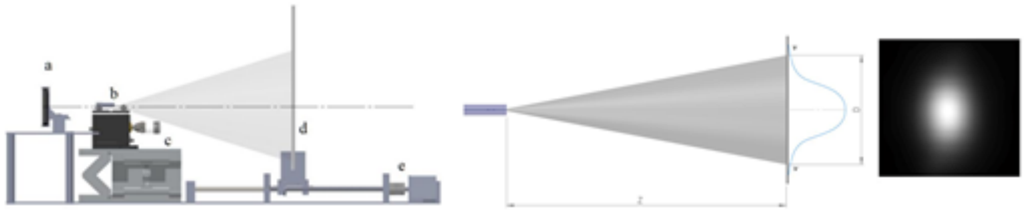

"Fig. 1. Conceptual design of the Optomechatronic instrument: (a) smartphone camera; (b) fiber holder; (c) xyz – positioner; (d) screen; and (e) mechanical positioning system drive."

3. Results

Once the system is calibrated, the images are acquired and analyzed. The value of spot size D is determinate with the information vector, that is extracted from the intensity profiles. The measured data is used to compute the NA and the MFD using Eq. (1) and Eq. (2), respectively. In order to test the system performance, several commercial fibers were used for the measurement of their NA and MFD. An ytterbium fiber laser (PYL-10-LP, 1060 nm, 10W, IPG Photonics Corporation) and a wavelength-stabilized fiber-coupled diode laser (K976AA2RN, 976 nm, 18W, BWT Beijing) are used as the pump sources for the SMF and MMF, respectively. Table 1 show that the instrument has a good and reliable performance, with a ±10% error.

Table 1. NA and MFD measurements compared to the data from manufactures

Fiber	Type	λ (nm)	NA Meas.	NA data	% Error	MFD Meas. (μm)	MFD (μm) data	% Error	Manufacturer
1060xp			0.14 ±0.003	0.14	4.68	6.17 ±0.37	6.5	5.67	Nufern
UHNA3	SMF	1060	0.37 ±0.013	0.35	6.29	2.17 ±0.14	2.4	9.36	Nufern
PS980			0.14 ±0.011	0.14	6.78	6.02 ±0.81	5.8	3.92	Fibercore
HCF-250-27			0.45 ±0.029	0.46	1.90				Coractive
MM-S200 /220-22A	MMF	976	0.22 ±0.008	0.217	5.94				Nufern

4. Conclusions

An instrument for the simultaneous measuring of the NA and MFD of SMFs based on acquisition and processing of the output light projected into a screen was demonstrated. This instrument is a great advantage of being able to measure the NA and MFD simultaneously, and can be very useful for other processes, for example thermal core diffusion, estimate joint losses between fibers, and so on. The advantages of this measurer are (1) it is possible to measure higher powers without risking the integrity of the photo-detection system since in certain sense is an indirect measurement; (2) it is simple to operate; (3) it is low cost, robust, portable and reliable measurement system.

References

[1] A. K. Ghatak and K. Thyagarajan, *Introduction of Fiber Optics,* (Cambridge University, 1998).
[2] TIA, "Measurement of mode field diameter of single-mode optical fiber," TIA/EIA FOTP-191 (1998).
[3] R. Hui and S. O´sullivan, *Fiber Optic Measurement Techniques,* (Elsevier, 2009).
[4] S. Q. Mawlud and N. Q. Muhamad, "Theorical and experimental study of a numerical aperture for multimode PCS fiber optics using an image technique," Chin. Phys. Lett. 29, 114217 (2012).
[5] D. C. Che, "Research of the measuring technique of numerical aperture of optical fiber using near infrared light," Microw. Opt. Technol. Lett. 50, 582-584 (2008).
[6] Large Beam Profiling System, http://www.dataray.com/large-beamprofiling-system.html.
[7] F. Chavez-Gutierrez, A. Martinez-Rios, D. Toral-Acosta, D. Torres-Armenta, and J. A. Guerrero-Viramontes, "Measurement of optical fiber parameters and thermal core diffusion characteristics by digital image processing," Appl. Opt. 57, 4331-4336 (2018)
[8] G. A. Kiran and S. Murali, "Automatic rectification of perspective distortion from a single image using plane homography," Int. J. Comput. Sci. Appl. 3, 47-58 (2013).
[9] M. Artiglia, G. Coppa, P. Di Vita, M. Potenza, and A. Sharma, "Mode field diameter measurements in single mode optical fibers," J. Lightwave Technol. 7, 1139–1152 (1989).

Calculation of optimal trajectory of mobile robots using PSO and shape descriptors for mobile robots

Víctor H. Flores-Muñoz [1,2,*], Hugo A. Mendez-Guzmán [2], Cesar P. Carrillo-Delgado [2]
[1] Centro de Investigación en Matemáticas A.C., Guanajuato, Gto, México
[2] Universidad Politécnica del Bicentenario, Silao, Gto, México
Author e-mail address: viktorhfm@gmail.com

Abstract: In this work we present the behavior of the *Particle Swarm Optimization* (PSO) algorithm modeling the environment of a mobile robot with the presence of virtual obstacles of regular and non-regular geometries. The image is acquired by a webcam and processed with OpenCV to obtain the start/end points of the trajectory plus modeling the scene and the cost function depending of the chosen shape descriptor. The intermediate points of the trajectory are generated by the PSO algorithm and used by a differential mobile robot, decomposing the movement in rotative and linear displacements. As a result, we present the comparative of the optimum trajectories generated with conical descriptors, region descriptors and Y-axis using the same random trajectory.

1. Introduction

Obstacle evasion in mobile robotics is one the common tasks that are required to do a specific job such as material transportation, environment recognition, object search, etc.

An alternative for the mobile robots to execute their tasks is under the supervision of their environment using surveillance cameras. In these conditions, it is possible to calculate a precise and fast movement considering obstacle evasion and environmental hazards. To do so, there are several techniques for searching the optimal solution in dynamic and lineal programming but the computing cost is high. Another approach is the use of heuristic algorithms which speed of convergence to an optimal solution is higher [1].

The Particle Swarm Optimization (PSO) is a heuristic algorithm based on the social behavior where the evaluation to the best solution to a problem is based on the individual and collective experience of a group of agents [2].

In this work we present the optimum solutions generated by the PSO algorithm with different perspectives of scene modeling. Once the layout is generated, the optimal solution is calculated avoiding the obstacles, covering the less possible distance with the less curvature. The trajectory is used to control a differential mobile robot.

2. Methodology

Considering a scenery supervised by an aerial camera as shown in Figure 1a, where the mobile robot has to navigate from a start point to an end point using the shortest trajectory while avoiding obstacles. The solution to this problem comprehends the acquisition of an image and the extraction of the characteristics that describe the environment (Figure 1b), until the calculation of the optimal trajectory and it decomposition into simple movements of the robot.

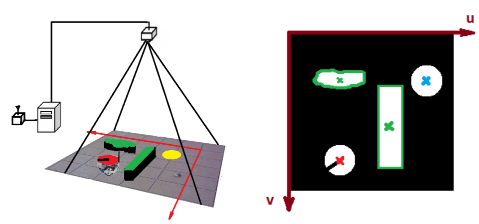

(a) (b)

Fig. 1. Representative scheme of the problem: (a) Scene supervised by a camera, (b) Description of the scene using DIP (red: start point, blue: end point, green: obstacles).

Once the image is captured and processed using RGB segmentation to identify the objects (obstacles), their shape is detected in order to calculate the trajectory. The shape of an object can be detected using their contour and characterized using algorithms such as convex hull, polygonal approximation, invariant moments, etc. [3]. Our work presents the use of descriptors such as centroids, smallest enclosing circle [4], area, bounding rectangle and convex hull.

For the generation of the optimal trajectory we apply the Particle Swarm Optimization (PSO) algorithm [5,6] which consists that *n* particles, which each particle is a vector that represents the solution to the problem, are ruled by 3 principles:

1. Keep their inertia when they memorize the last flight direction.
2. Change their condition according to the best optimal solution.
3. Change their condition according to the best optimal solution of the hive.

The best solution given represents the spatial function of the trajectory that the mobile robot has to follow considering the starting point as *(0,0)*. Finally, the optimal trajectory, which is the shortest one with the lesser curvature, is decomposed into lineal a rotational movement of the differential robot, as shown in figure 2.

3. Results

For the modeling of the scene we considered 2 situations, the first is only taking the shortest trajectory and the second is considering also the curvature. For these simulations we applied the PSO with different shape descriptors such as conical descriptor, region descriptor and Y-axis. Results of the optimal trajectory is shown in figure 2.

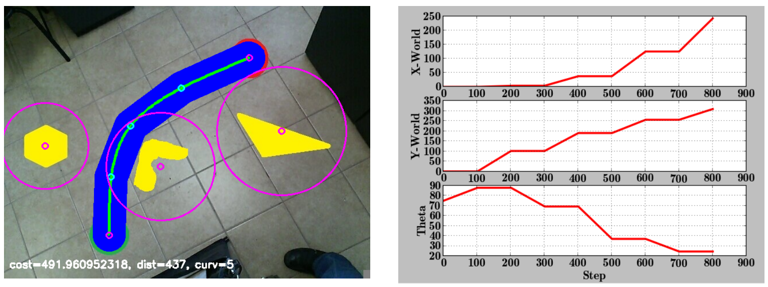

(a) (b)

Fig. 2. Execution of the optimal trajectory. (a) Evolution of the movement of the robot. (b) Decomposition of the trajectory into rotational and lineal ones

The optimal trajectory with les computational cost was obtained using Y-axis codification for the shape detection of the obstacles (figure 2a). The different movements done by the differential robot during the execution of the trajectory are shown as X, Y, θ displacements (figure 2b).

4. Conclusions

In this work we presented the behavior of the PSO algorithm applied for trajectory calculation of a mobile robot. The algorithm was tested with different shape descriptors as scene models, the ones we used were Y-axis, region descriptor and conical descriptor, being Y-axis the one that presented the smallest computational cost. The optimal trajectory obtained by the PSO was decomposed into discrete points in order to send different displacements for the control of a differential mobile robot. Finally, we made the comparison of the different optimal trajectories generated by modifying different shape descriptors.

References

[1] Madic M., Markovik D., Radovanovic M. “Comparison of Meta-Heuristic Algorithms for Solving Machining Optimization Problems”, FACTA Universitatis, Mechanical Engineering, Vol. 11, N° 1, 2013, pp. 29-44.

[2] Kokash N. “An introduction to heuristic algorithms”, Department of Informatics and Telecommunications, University of Trento, Italy.

[3] Morse B. “Shape Description (Contours)”, Brigham Young University, 2000. http://homepages.inf.ed.ac.uk/rbf/CVonline/LOCAL_COPIES/MORSE/boundary-rep-desc.pdf

[4] Sven Skyum’s Algorithm for Computing the Smallest Enclosing Circle, Department of Computer Science, Aarhus University, 2014.

[5] Bai Q. “Analysis of Particle Swarm Optimization Algorithm”, College of Computer Science and Technology Inner Mongolia University for Nationalities, China, 2010.

[6] Malathi M., Ramar K., Paramasivam C. “Optimal Path Planning for Mobile Robots Using Particle Swarm Optimization and Dijkstra Algorithm with Performance Comparison”, Middle-East Journal of Scientific Research 24, pp: 312-320, 2016.

Towards the development of a low-cost high precision instrumented mini solar sensor

Arturo Díaz Ponce[1], Rubén A. Garrido Moctezuma[2], Manuel I. Peña-Cruz[1], Luis V. Coronado[1], Iván Salgado Transito[1], Fernando Martell[1], Samantha A. Cajero Roodriguez[1]

[1]CONACYT - Centro de Investigaciones en Óptica, A.C. Unidad Aguascalientes - Prol. Constitución 607, 10 Fracc. Reserva Loma Bonita, 20200, Aguascalientes, Aguascalientes, Mexico.

[2]CINVESTAV-IPN, Departamento de Control Automático. Av. IPN 2508 San Pedro Zacatenco, Mexico City 07360, *MEXICO.*

adiaz@cio.mx, garrido@ctrl.cinvestav.mx, mipec@cio.mx, luismvc@cio.mx, isalgadotr@cio.mx, fmartell@cio.mx sam.cajero019@gmail.com

Abstract: In this work the development of a low-cost solar sensor capable of locating the position of the sun through photo-sensors is presented. In addition, the sensor is integrated with the instrumentation to provide the information of a solar position algorithm. As preliminary results, we present the methodology followed for the development of the sensor as well as the theoretical characterization carried out through the Tonatiuh software.

1. Introduction

Having a good solar tracking module for Concentration Photovoltaics (CPV) systems or Concentrating Solar Power (CSP) systems is fundamental to achieve maximum efficiency. In practice, there are two ways of locating the position of the sun with respect to an observer on earth: i) Solar location in open loop and ii) Solar location in closed loop. In the first case the estimation of the position is made through the solar coordinates, which requires some input parameters such as the observer's geographical position, date, time, altitude and orientation, among others. Solar tracking systems in open loop have the advantage of not being affected by cloudiness. However, it is essential to provide the system with the necessary instrumentation to obtain the input parameters in real time. On the other hand, closed-loop solar location generally employs photosensors and, although these systems are more complex, they have the ability to achieve a high solar tracking precision, so they are used in systems where accuracy is fundamental, for instance in CPV and CSP systems. In recent years, hybrid solar tracking systems have been presented where an algorithm based on the solar coordinates provides rough tracking photodiode-based sensor allows for fine tracking in closed loop. In this paper we present the development of a solar sensor integrated by a quadrant of photodiodes, an accelerometer, a magnetometer, an altimeter, a barometer and a temperature sensor which provide the necessary data to carry out hybrid tracking without using external instrumentation.

2. Methodology

The development of the proposed sensor is divided into two parts. The first one consists of the location of the apparent position of the sun using the commercial quadrant of photodiodes QP5.8-6 TO (5.8 mm² Quadrant PIN detector) shown in Figure 1, which produces a current proportional to the incoming sun radiation. These quadrant of photodiodes consists of four separate P on N silicon photosensitive surfaces. They are chosen because of their high sensitivity, small gap and low dark current. In order to detect only direct radiation from the sun, a plastic cover with a 1mm hole was designed as shown in Figure 2. The photodiode F_i produces the current I_{Fi} according to the incident radiation. This current is linearly converted into a voltage V_{Fi} by a transimpedance quad amplifier SLG88104 [1]. With the configuration shown in Figure 2 and equations (1) and (2), the ideal position occurs when the tracking system places the sensor perpendicular to the sun's rays, then the following equalities hold $V_{F1} = V_{F2} = V_{F3} = V_{F4}$; i.e. $x = 0$ and $y = 0$. On the contrary, when the sensor is not perpendicular to the sun, a voltage difference between the photodiodes is generated, which is detected by a controller that activates the tracking system until the solar sensor is placed in its ideal position

$$x = \frac{(V_{F1} + V_{F3}) - (V_{F2} + V_{F4})}{V_{F1} + V_{F2} + V_{F3} + V_{F4}} \tag{1}$$

$$y = \frac{(V_{F1} + V_{F2}) - (V_{F3} + V_{F4})}{V_{F1} + V_{F2} + V_{F3} + V_{F4}} \tag{2}$$

Figure 1. Four Quadrant Photo detector QP5.8-6 TO

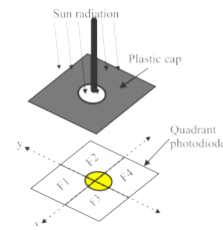

Figure 2. Sketch of the proposed sun sensor

The second part of the mini solar sensor consists of a microcontroller (μC) PIC18f2550 that processes the signals p from all the elements that are part of the sensor: an MPU9250 module to obtain the acceleration in two axes, temperature, atmospheric pressure and altitude with respect to the sea level, and the module QMC5883l that indicates the direction of the magnetic north with the objective of referencing the tracking structure. The communication between the microcontroller and the modules is done through the communication protocol I^2C. With the information of all the elements installed in the sensor, it is planned to use one of the state of the art high precision solar tracking algorithms [2] to perform hybrid solar tracking without the use of other external sensors. It is important to mention that the total cost of the proposed sensor is less than 130 USD, which is a lot cheaper than the cost of high precision commercial solar sensors [3].

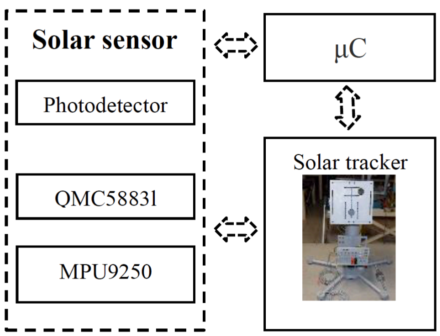

Figure 3. General configuration of the solar sensor with the tracking system.

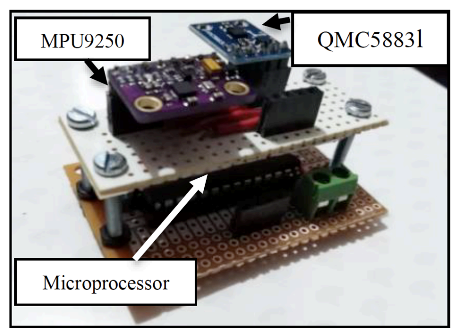

Figure 4. Proposed sensor

3. Results

Until now we have developed the first solar sensor prototype. The theoretical characterization of the sensor was carried out using the Tonatiuh ray tracing software. As a result of the analysis we found that it is possible to locate the position of the sun at an angle maximum deviation between the normal of the sensor and the sun's rays of 30°. It is important to mention that a wide opening angle decreases the accuracy of the sensor, thus, it is initially necessary to pre-orient the solar sensor until the sun is within its opening angle. The pre-orientation will be carried out through a solar position algorithm running on the microprocessor.

4. Conclusion

This work presents preliminary results obtained in the development of a low-cost solar sensor capable of tracking the sun through a quadrant of photosensors and with the ability to feed the required data for a hybrid tracking algorithm. We also have implemented a tracking algorithm using a microprocessor. We believe that the development of this sensor will improve the performance of hybrid tracking systems reaching the level of precision required in high solar concentration systems at a low cost.

References

1.SILEGO SLG88103/4. 2017.
2. Reda, I. and A. Andreas, Solar position algorithm for solar radiation applications. Solar energy, 2004. 76(5): p. 577-589.
3. Solar-Technologies, Sun sensor ISS-DX: technical specifications. Tecnoincubadora Marie Curie, Leonardo da Vinci 18, C.P. 41092, Seville, Spain.

Smart Emergency Response Interface for Fire Detection

Takawira J. Mumanga[1], Rodolfo M. Martinez[2], Michael F. Grobler[3]
[1]Centro de Investigaciones en Óptica, A.C. Lomas del Bosque 115, Lomas del Campestre, León, 37150, Guanajuato, México; [2]Centro de Investigaciones en Óptica, A.C. Prol. Constitución 607, Fracc. Reserva Loma Bonita Aguascalientes, 20200, México; [3]Electrical and Electronic Engineering Science Department, University of Johannesburg, Auckland Park 2006, Republic of South Africa.
takah@cio.mx

Abstract: The safety of people and their assets against fires is of paramount importance for all large building complexes. The conventional smoke detector has a 50% success rate in preventing fire outbreaks within buildings. In the case of a fire outbreak requiring immediate but ordered evacuation, the conventional procedure requires the detection of smoke, then the recognition of the fire alarm sound and an instinctive evacuation response often aided by exit route signs. This project introduces a real-time multipoint temperature monitoring system with an audio-visual emergency response interface aimed at enhancing fire detection and the evacuation procedure so as to reduce the likelihood of harm and damage from interior fire outbreaks.

1. Introduction.

It is necessary for every facility to have interior safety measures and an emergency response plan in place to protect people and their assets during occurrences of danger. These include fires, bomb threats, gas leaks, earthquakes, tornados, hazmat spill and violence. The most common and still the worst danger to occur within a building is an accidental fire. Accidental fires are one of the most deadly and costly natural disasters in existence today. They occur anywhere and anytime, mostly when we least expect them; damaging billions worth of property in the process.

Though flames can cause serious burns, most injuries and deaths in fires are related to smoke inhalation and a lack of oxygen. Smoke and toxic gasses from fires are much more dangerous than the flames themselves [1]. In addition, heat is even more dangerous. The high heat in a burning room can cause additional injuries. The air at eye-level in a burning building can reach up to 300 degrees Celsius, causing serious burn injuries without ever coming into contact with the flame. It is important therefore to have a well-planned, continuous, unobstructed exit route so that everyone in the building may escape unharmed in the event of a fire [1].

2. Our project.

The objective is to design and operate a heat detector, as an effective reinforcement solution to counter the disadvantages of smoke detectors and establish a smart interface for fire emergency alerts and evacuation purposes. There needs to be a way of reinforcing the present function of smoke detectors by using advanced heat detectors so that fire detection may be more effective and reliable.

There are certain fire-protection applications where smoke detectors are not suitable nor adequate. These include non-life-safety installations where the environment has too many airborne particulates. These may be due to excessive steam, moisture, dust, humidity or temperature. These include attics, kitchens, garages, warehouses, storage facilities, elevator machine rooms and electrical closets.

High ceiling buildings make the installation of smoke detectors difficult and less effective. Fires that start due to overheating or intense flames cannot be detected until smoke is released during combustion. This occurs after some form of damage has already been done. Smoke detectors applied in these environments and conditions are useless and cost prohibitive from a maintenance standpoint [2]. This work proposes the use of semiconductor, fiber optic and zero-contact photoluminescence heat detectors.

In addition, in most premises, the evacuation in case of fire will simply be by means of a warning signal produced when a fire is discovered. People then make their way out of the building by the means of exit signs. They however are never certainly sure that they are moving in the right direction and not towards the fire.

In some larger complex premises, it may be more appropriate to start the evacuation by initially evacuating only the area closest to the fire and warning other people to stand by. This is called a phased evacuation [3]. It reduces panic, avoids congestion at the escape routes and lowers the risks of injury. A Labview algorithm that interfaces multiple computers is reported as the tested solution.

Fig. 1. Project objective equation

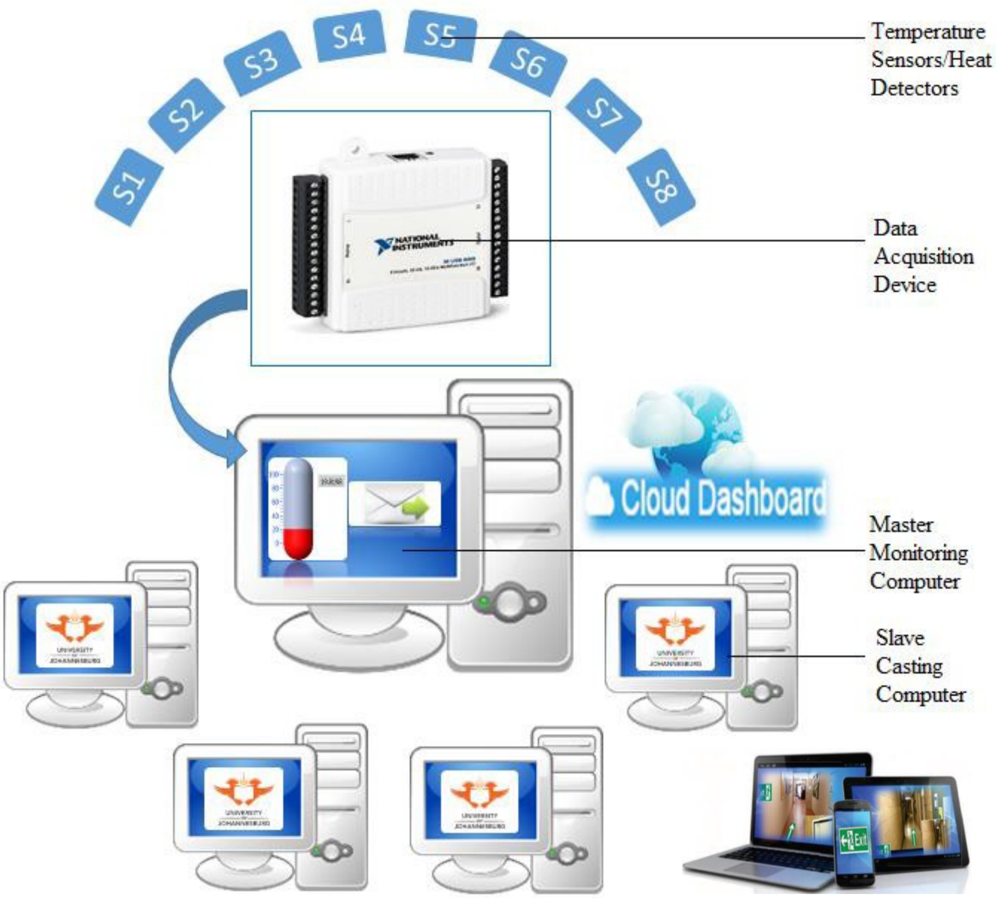

Fig. 2. Overview of the Specified Tools and their interaction and the evacuation interface [4-5]

References

[1] "Ace Fire Equipment," [Online]. Available: http://www.acefireequipment.com/articles/. [Accessed 18 06 2014].
[2] L. S. Magazine, "Guidelines: Top Five Things to Know about Heat Detectors," no. 11, 2009.
[3] F. S. A. Center, "Fire Emergency Evacuation Plan and the Fire Procedure," Safelincs Ltd, Lincolnshire, 2011.
[4] C. Ford, "Design for ECE Engineers," ECE 404 Scott Umbaugh.
[5] R. Devdas Shetty, "Mechatronics System Design," 2nd ed., Stamford, Cengage Learning, 2011, pp. 132-133.

Investigation of Oversampling for Amplitude Multi-Level Two-Dimensional Data Array in Holographic Memory

Tetsuhiko Muroi, Yutaro Katano, Nobuhiro Kinoshita, and Norihiko Ishii
Japan Broadcasting Corporation (NHK), 1-10-11 Kinuta, Setagaya-ku, Tokyo 157-8510, Japan
Author e-mail address: muroi.t-hc@nhk.or.jp

Abstract: Multi-level two-dimensional data arrays were investigated as a way of increasing the capacity and data transfer rate of holographic memory. We investigated sampling of a four-amplitude-level data array and found that sampling rate required for decreasing the symbol error rate with the multilevel array was higher than with a two-amplitude-level data array. We then devised a data array with black areas between symbols and confirmed that symbol error rate for it could be reduced when the sampling rate was 2.

1. Introduction

Holographic memory has been investigated as a recording system with a large capacity and a high data transfer rate. The digital data to be recorded and reproduced are arranged two dimensionally into "data pages". A spatial light modulator (SLM) is used for recording the data, and a two-dimensional sensor is used for reproducing the data. By changing the incident angle of the beam entering the medium through a galvanometer mirror (GM), different data pages can be stored at the same position in the medium, thereby making a large capacity memory possible. The data transfer is fast when the sampling rate, which is defined as the data page symbol pitch divided by the sensor pixel pitch, is low, because the required number of pixels in the sensor is small, but the signal to noise ratio (SNR) of the reproduced data deteriorates. In a conventional holographic memory, the amplitude level of symbols in the data pages is two and the sampling rate is less than 2 [1]. Multi-level symbols have recently been investigated as a way to increase the capacity and data transfer rate [2,3]. However, noise caused by sampling, interference and scatter in the optical setup and medium affect multi-level symbols more than they do two-level symbols. In this study, we investigated sampling of data pages with four-amplitude-level symbols, devised a data page structure that can reduce the error of the reproduced data page at a sampling rate of 2, and confirmed its effectiveness experimentally.

2. Principle of holographic memory and investigation of sampling rate

Figure 1 shows a schematic image of the optical setup in a holographic memory. The signal beam is amplitude modulated by the SLM displaying the page data in the path of the signal beam. Figure 2(a) shows an enlarged image of the data page to be recorded. Symbols in the data page have one of four levels: 0, 85, 192, or 255. The signal beam is focused on the medium. The reference beam arrives at the medium after going through a GM, which controls the beam's direction. By changing the incident angle of the beam on the medium by using the GM, another data page can be stored at the same position. When reproducing the data, only the reference beam enters the hologram medium. The reconstructed beam with the data page is obtained from the hologram, and data is reproduced by capturing the beam with the sensor.

We simulated sampling of data pages by a sensor to investigate the degradation of the reproduced data when a four-amplitude-level data page is captured. The simulation considered only noise due to sampling. Figure 3 shows the

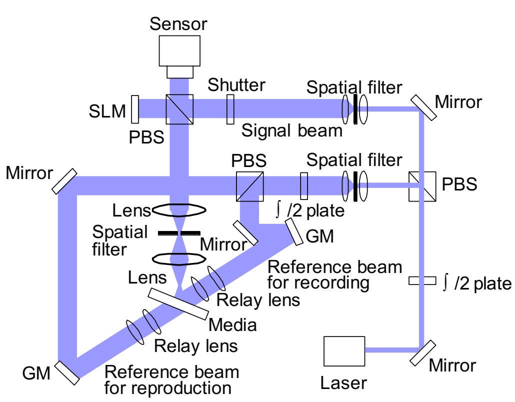

Fig. 1 Optical setup of holographic memory

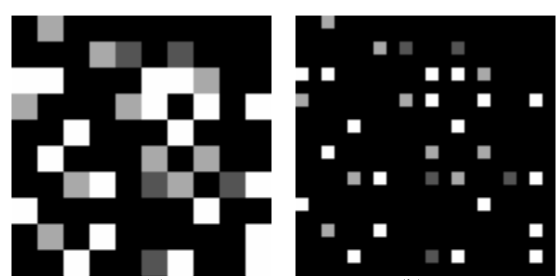

(a) (b)

Fig. 2 Enlarged image of four-amplitude-level data page: (a) conventional and (b) proposed.

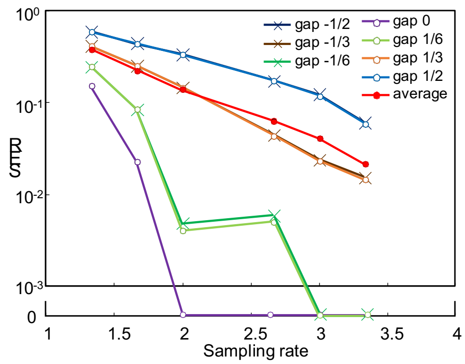

Fig. 3 Symbol error rate as a function of sampling rate in four-amplitude-level data page shown in Fig. 2(a)

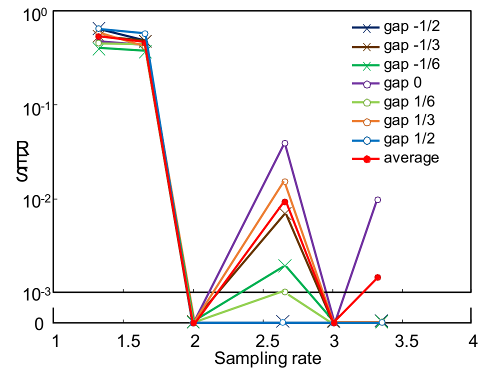

Fig. 4 symbol error rate as a function of sampling rate with black area in data page shown in Fig. 2(b)

symbol error rates (SER; error rate of brightness symbols) depending on the sampling rate of the sensor. Since it is difficult to make the relative positions of the sensor pixels and symbols completely correspond over the entire data page due to distortion caused by the lens, we determined the SERs at various relative positional gaps and averaged them. When the sensor pixel's position completely corresponds to the symbol's position in the data page, the relative positional gap is 0 and this position is set as the reference point. Positional gaps of ±1/6, ±1/3, and ±1/2 hence correspond to sensor positions that are ±1/6, ±1/3, and ±1/2 of a pixel pitch away from the reference point. The SERs decrease in accordance with an increasing sampling rate in each condition. When the sampling rate is 2 and relative positional gap is 0, the SER of the reproduced data becomes zero. But when the relative positional gap is not zero, and especially is ±1/2, the reproduced data deteriorates and the SERs increase. However, if we can find a condition where the degradation does not occur even if the relative positions do not correspond, we can reduce the SER without having to increase the sampling rate.

3. Data page structure for reducing the error rate

To reproduce data with a low SER in the case where the relative positions do not correspond, we devised a data page structure in which black areas are inserted between the symbols, as shown in Fig. 2(b). The symbol pitch is the same as that of the conventional data page structure in Fig. 2(a), but the bright area decreases to 1/4; namely, the fill factor is 1/4. Figure 4 shows the SER in accordance with sampling rate for the proposed data page. Even if the relative positions do not correspond, the SERs are zero at a sampling rate of 2.

Next, we experimentally recorded and reproduced the proposed data pages using the optical setup shown in Fig. 1. The symbol size was 16 μm, and the sensor pixel size was 8.35 μm; accordingly, the sampling rate was 1.9. By changing the incident angle of the reference beam by using the GM, we recorded five data pages with angle multiplexing and reproduced them. We confirmed that reproduced data were error-free after error correction for all data pages.

4. Conclusions

To increase the capacity and data transfer rate of holographic memory, we investigated the relation between the sampling rate of the sensor versus the data pages and the SER of the data pages with four-amplitude-level symbols. We found that the sampling rate in the case of two-amplitude-level symbols is not enough to reduce the SER when using four-amplitude-level symbols. Upon noting that the SER becomes zero at a sampling rate of 2 when the relative positions of the symbol and sensor pixel correspond, we devised a data page structure that does not increase the SER even if the relative positions do not correspond. The proposed data page includes black areas between the symbols, and we found that the SER becomes zero at a sampling rate of 2 even when the relative positions of the symbol and pixel do not correspond. In addition, we experimentally confirmed that the reproduced data was error-free after decoding the proposed data pages. This method is effective for multi-level recording in holographic memory.

[1] T. Hoshizawa, K. Shimada, K. Fujita, and Y. Tada, "Practical angular-multiplexing holographic data storage system with 2 terabyte capacity and 1 gigabit transfer rate," Jpn. J. Appl. Phys., **55,** 09SA06 (2016).
[2] G. W. Burr, G. Barking, H. Coufal, J. A. Hoffnagle, C. M. Jefferson, and M. A. Neifeld, "Gray-scale data pages for digital holographic data storage," Opt. Lett., **23**, 1218-1220 (1998).
[3] T. Utsugi, "Spatial Differential Encoding and Wavefront Estimation for Phase Multi-level Holographic Data Storage," ISOM'17 Tech. Dig., 2017, Tu-G-2 (2017).

Single-pixel spectral imaging with hole-array coding masks

Yoshio Hayasaki and Ryo Sato
Center for Optical Research and Education, Utsunomiya University
Author e-mail address: hayasaki@cc.utsunomiya-u.ac.jp

Abstract: A single-pixel camera composed of optical coding masks, a photo detector, and a decoding computation has an important feature of no image sensor for imaging, therefore it has very simple optical and electrical architectures. The optical coding masks whose implementation is a novelty of our research are composed of holes on a substrate, and arranged on the circumference of a disk enables us to switch the masks with its rotation. The main features are small wavelength dependence other than air for wideband spectral imaging, and the simple structure. The spectral imaging for a sample composed of three color films is demonstrated, and the accuracy of the proposed system is evaluated.

1. Introduction

Spectral imaging [1,2] is very effective in various fields of biology, food science, health science, medicine, remote sensing, and astronomy. It acquires the wavelength information in addition to a two-dimensional (2D) light intensity distribution that is an image. There are four types of optical configurations for the spectral imaging. The optical configurations are decided by the way that the three-dimensional (3D) spectral image data cube (x, y, λ) are obtained by a one-dimensional (1D) sensor or a 2D array sensor. The most straightforward configuration has a spectrometer composed of a dispersive device and a 1Darraysensor, anda2Dscanneralongtwolateral direction (x and y) by either moving the sample or steering the beam.

The single-pixel imaging architecture [3-5] is composed of optical coding masks, a photodetector, and a decoding calculation. The biggest feature is simple optics and simple electronics because it can perform an imaging without an image sensor. The implementation with a simple photodetector for the light detection gives wide opportunity for developing a new imaging system. Especially, it is very effective when an image sensor with a sufficient performance cannot be available for a given budget or in a frequency region that an image sensor is not existed at present. The spectral imaging can be performed without a special technique only by replacing from the photodetector to a spectrometer. The coding masks are mostly implemented by a liquid crystal spatial light modulator (LCSLM) and a digital micromirror device (DMD). The spectral property of these devices gives a limit in the spectral imaging. The key idea of this study is that the coding mask is made of hole arrays drilled in a plate. It has no wavelength dependence except for an optical absorption of air. The hole arrays are placed on a disk that is rotated to change the cording mask. Itis also possible to operate the rotation with a hand. The coding masks are made of holes arrays drilled in a plate, which is the key idea in this research. The most important feature of the light modulation using holes is no wavelength dependence except for an optical absorption of air. In addition, it has an easy and low-cost fabrication. The hole arrays are placed on the circumference of a disk that is rotated to change the cording masks.

2. Experimental setup

Figure 1 shows an experimental setup for the single-pixel spectral imaging. The experimental setup was composed of an illumination light source, coding masks on a rotational disk, a spectrometer, a set of relay lenses, a laser, and a computer. A transmissive object was illuminated with white light generated by a halogen lamp (MHAB-150W-100V , Moritex). The light passing through the object was imaged on a coding mask and spatially encoded by the coding mask. The disk was rotated with a motorized rotation stage to evaluate the system performance. The arrangements of the holes were the pseudo-Hadamard matrix that the value of -1 was changed to the value of 0. Therefore, the first pixel had a lot of noises. The disk had another hole at the symmetric position of each mask for indicating the position of the light detection (a position indicator) illuminated by a He-Ne laser. The encoded image was detected by a fiber-based spectroscope (C7473, Hamamatsu) through the relay lenses. The spectral range was from 200 nm to 950 nm with the resolution of < 2 nm. The spectrum was continuously detected at the minimum sampling period of 19 ms while the disk was rotating, and the intensity for each mask was extracted by referring the position indicator signal. Finally, the inverse matrix calculations were performed at each wavelength.

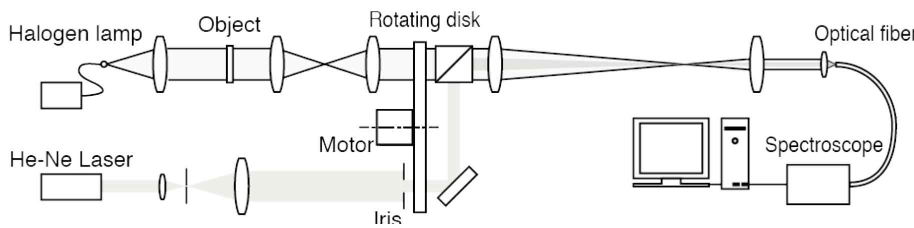

Fig. 1 Experimental setup.

Figure 4 shows an object and the reconstructed spectral images. The object shown in Fig. 4(a) was made of plastic color films with different spectral transparencies, which were put on the frame. The spectral images fat 500, 600, and 700 nm are shown in Fig. 4(b). Figure 5 shows the spectrum of the red film from 300 nm to 750 nm. The red curve was obtained by an ordinary spectroscopy. The dots were obtained by the single pixel spectral camera. They were well agreed. The measurement RMS errors were 2.82% on the red film, 5.12% on the blue film, and 2.28% on the blue film.

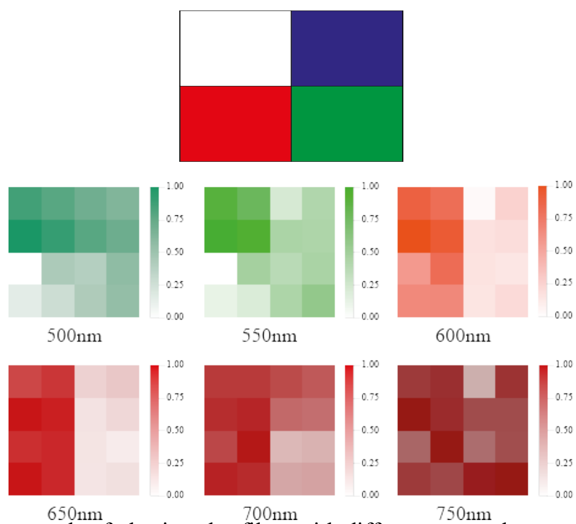

Figure 2 (a) Object made of plastic color films with different spectral transparencies. (b) The spectral images at 500, 600, and 700 nm.

We developed a new implementation method of a single-pixel camera for spectral imaging. The optical coding masks were composed of holes on a substrate, and arranged on the circumference of a disk enables us to switch with a rotation of the disk. The main features are small wavelength dependence other than air for wideband spectral imaging, and the simple structure. The spectral imaging for a sample composed of three color films was demonstrated, and the measurement accuracy of the present system was less than 3% at red channels. The spectral range from 300 to 750nm depended on the performance of the spectrometer we used. The next subjects of our single-pixel spectral camera will be to improve the detections speed and the spatial resolution.

References

1. Y. Garini, I. T. Young, and G. McNamara, "Spectral imaging: principles and applications," Cytometry Part A **69A**,735– 747 (2006).
2. Q. Li, X. He, Y. Wang, H. Liu, D. Xu, and F. Guo, "Review of spectral imaging technology in biomedical engineering: achievements and challenges," J. Biomed. Opt. **18**, 100901 (2013).
3. M. F. Duarte, M. A. Davenport, D. Takhar, J. N. Laska, T. Sun, K. F. Kelly, and R. G. Baraniuk, "Single-pixel imaging via compressive sampling," IEEE Signal Process. Mag. **25**, 83–91 (2008).
4. D. L. Donoho, "Compressed sensing," IEEE Trans. Inf. Theory **52**, 1289–1306 (2006).
5. W. L. Chan, K. Charan, D. Takhar, K. F. Kelly, R. G. Baraniuk, and D. M. Mittleman, "A single-pixel terahertz imaging system based on compressed sensing," Appl. Phys. Lett. **93**, 121105 (2008)

Optical Design for Camera Calibration-free 3D Shape Measurement Using Feature Quantity Type Whole-Space Tabulation Method

Motoharu Fujigaki, Yoshiyuki Kusunoki, Yuta Goto, and Daishi Takata
Graduate School of Engineering, University of Fukui, Fukui 910-8571, Japan
fujigaki@u-fukui.ac.jp

Abstract: A feature quantity type whole-space tabulation method (F-WSTM) was proposed by authors to make 3D shape measurement devices robust for vibrating. This method makes possible a camera calibration-free 3D shape measurement. Three phase information obtained with three projectors are used to obtain 3D coordinates without any camera parameters. That is, change of lens position does not cause the systematic error. In this method, focusing, zooming, pan and tilt are available anytime. In this paper, the optical design to produce the 3D shape measurement device using the F-WSTM and the prototype of the 3D shape measurement device are shown.

1. Introduction

3D shape measurement using fringe projection method is useful for many fields [1]. In the case of almost all of conventional methods, camera parameters are used to obtain 3D coordinates on the object surface. The method is, however, not robust for vibrating of the measurement device. Especially, the positions of an imaging sensor and lenses are changed easily owing to vibration. It causes some systematic errors.

Authors proposed a feature quantity type whole-space tabulation method (F-WSTM) to overcome this problem. This method makes possible a camera calibration-free 3D shape measurement. Three projectors are used to perform 3D shape measurement. 3D coordinates at a point on the object can be obtained from only three phases projected at the point. Any camera parameters are not necessary to measure 3D shape. That is, change of lens position does not cause the systematic error. In this method, focusing, zooming, pan and tilt are available anytime.

In this method, the arrangement of three projectors is important. All sets of three projected phases should be obtained as an independent vector at each position in the measurement region. In this paper, the optical design to produce the 3D shape measurement device using the F-WSTM and the prototype of the 3D shape measurement device are shown.

2. Principle and Optical design of F-WSTM

In general, 3D coordinates (x, y, z) can be obtained from an independent set of three values mathematically. Figure 1 shows the principle of the F-WSTM. Three projectors P_A, P_B, and P_C are fixed in a 3D shape measurement device. Each projector is projecting grating pattern onto an object. Projectors P_A, P_B, and P_C give phases ϕ_A, ϕ_B, and ϕ_C at point P, respectively. The phases ϕ_A, ϕ_B, and ϕ_C are obtained by a camera. A set of 3D coordinates (x, y, z) is obtained immediately from a table of feature quantities to 3D coordinates. The table is prepared in advance using reference planes on a calibration process.

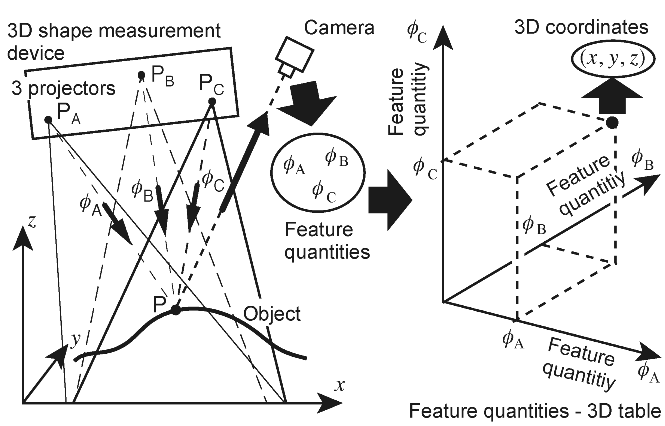

Fig. 1 Principle of F-WSTM

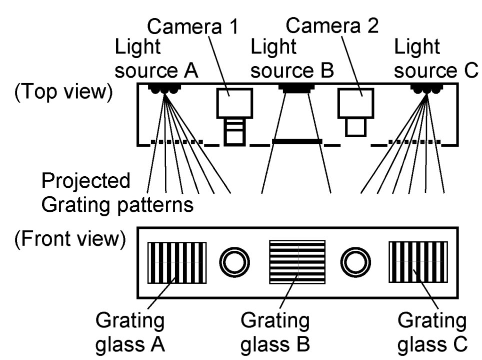

Fig. 2 Example of optical design of 3D shape measurement device using F-WSTM

Three stable projectors are required for this method. Recently, authors developed a leaner LED device for 3D shape measurement [2]. A compact and stable grating projector can be produced using this device. A high-speed phase-shift is also available [3, 4]. Figure 2 shows an example of optical design of 3D shape measurement device using F-WSTM. If any sets of three projected phases are independent in the measurement area, 3D coordinates (x, y, z) can be obtained from the three projected phases.

3. Experiment

A prototype for confirming the principle of the F-WSTM was constructed as shown in Fig. 3(a). Figure 3(a) shows a measurement setup including a reference plane and a linear stage for calibration. Figure 4(a) shows a specimen with a 10.0 mm step. An area measured by the prototype is shown as the area surrounding with broken lines. Figure 4(b) shows the measured result. The 3D shape of the specimen was reconstructed as shown in Fig. 4(b). The measured step distance was 9.0 mm. In this case, the error was 1.0 mm and it was not small. The reason is presumed that the intervals of reference planes movement for the z-direction in the calibration process was 1.0 mm.

4. Conclusion

Authors proposed a F-WSTM as a robust 3D shape measurement. The optical design to produce the 3D shape measurement using the F-WSTM are introduced in this paper. We will evaluate the robustness of a prototype using this method as a future work.

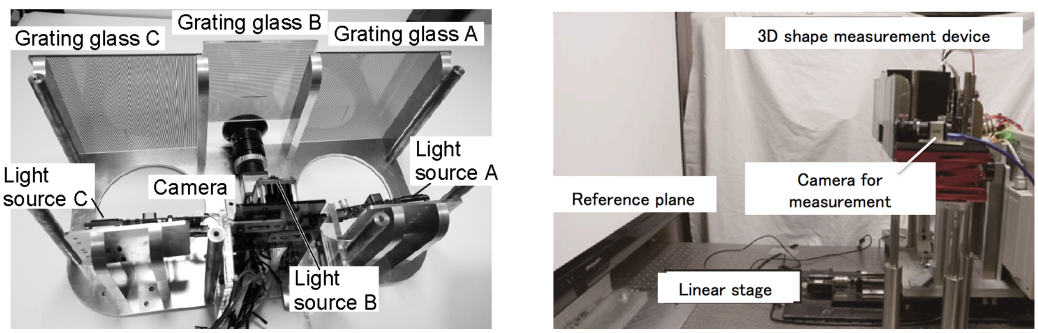

(a) Photograph (b) Measurement setup

Fig. 3 Prototype of 3D shape measurement device

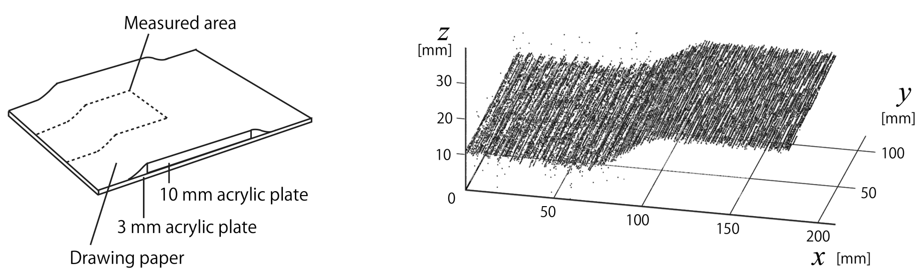

(a) Specimen (b) Measured result

Fig. 4 Result of 3D shape measurement using F-WSTM

References

[1] S. S. Gorthi, P. Rastogi, "Fringe projection techniques: whither we are?" Optics and Lasers in Engineering, **48**(2), 133-140 (2010).

[2] M. Fujigaki, Y. Oura, D. Asai and Y. Murata, "High-speed height measurement by a light-source-stepping method using a linear LED array," Optics Express, **21**(20), 23169-23180 (2013).

[3] M. Fujigaki, T. Sakaguchi, Y. Murata, "Development of a compact 3D shape measurement unit using the light-source-stepping method," Optics and Lasers in Engineering, **85**, 9-17 (2016).

[4] Y. Akatsuka, M. Fujigaki, T. Matui, "Three-dimensional shape measurement using optimal number of phase-shifting steps based on light-source-stepping method," Advanced Experimental Mechanics, **2**, 105-111 (2017).

Extended Abstracts

Session
SOLAR CELL

Pg.

Hole transport layer in OSC based on fluorinated reduced graphene oxide 159
Juan Nicasio-Collazo, Julio Salinas, Denisse Barreiro-Argüelles, Daniel Romero-Borja, José-Luis Maldonado

Multilayer reduced graphene oxide films as a hole transport layer for organic photovoltaic devices. 161
P. G. Otal, Juan Nicasio-Collazo, Daniel Romero-Borja, J. L. Maldonado and R. Castro-Beltrán

Hole transport layer in OSC based on fluorinated reduced graphene oxide

Juan Nicasio-Collazo*, Julio Salinas, Denisse Barreiro-Argüelles, Daniel Romero-Borja, José-Luis Maldonado*

Research Group of Optical Properties of Materials (GPOM), Centro de investigaciones en Óptica, A.P. 1-948, 37150 León, Guanajuato, México

* *E. Mail:* nicasio.collazo@cio.mx, jlmr@cio.mx

Abstract: Here is reported the photovoltaic performance of organic solar cells (OSCs) by using a graphene oxide derivative in (OSCs), as hole transport layer (HTL). OSCs were based on PTB7:PC_{71}BM blend as active layer and the alternative metal top electrode Field´s metal (FM, Bi/In/Sn: 32.5% 51% 16.5%), which can be easily deposited thought a vacuum-free process at regular atmosphere and low temperature (90 °C). To form the HTL, graphene oxide was chemically reduced with pentafluorophenylhydrazine, the fluorinated reduced graphene oxide (F5-rGO) was used to create a thin film by spin-deposition. Likewise, a bilayer of F_5-rGO/PEDOT:PSS was also used as HTL. The best photon conversion efficiency (PCE) achieved from the fabricated OSCs for a single layer of F_5-rGO was 5.82%. An increment in PCE (7.67%) for OSCs with a bilayer F_5-rGO/PEDOT:PSS as HTL was found.

Organic solar cells (OSCs) have been widely investigated in recent years due to excellent advantages such as flexibility, lightweight, semi transparency in visible region and low-cost manufacture [1,2]. To date, the power conversion efficiency (PCE) of single cells has reached over 14% [3,4]. In addition, the highest solar cell efficiencies that has been achieved using two or more subcells (tandem cell), is 15%; they combine a solution-processed non-fullerene-acceptor-based infrared absorption subcell and a visible-absorbing fullerene-based subcell grow by vacuum thermal evaporation [5].

On the other hand, graphene has a high electrical conductivity, transparency, and high carrier mobility [6,7], these excellent properties makes it a great potential candidate for optoelectronic applications. Graphene derivatives can be used as different components in OSCs to serve a diverse range of functions, as transparent electrode, in the active layer and have been used as both hole and electron transport layers (HTL and ETL) in OSCs [8-9].

Recently, we have reported the use of thermal reduced graphene oxide (T-rGO) as HTL, the T-rGO was deposited onto ITO glass substrates by reiterative spin-cast and thermal reduction processes in ITO/T-rGO//PTB7:PC_{71}BM/PFN/FM [11]. A PCE of 5.5% was reached with the 6-layer deposition of T-rGO; it suggested a good electronic alignment of 6-T-rGO films between ITO and the active layer.

OSCs under the architecture ITO/HTL/PTB7:PC_{71}BM/PFN/FM fabricated for this work are schematized in figure 1, where HTL could be F_5-rGO or PEDOT:PSS (reference), or F_5-rGO/PEDOT. The bulk heterojunction (BHJ) OSCs were based on the fullerene derivative (PC_{71}BM) as electron-acceptor and the polymer poly[[4,8-bis(2-ethylhexyl)oxy]benzo[1,2-b:4,5-b´]dithiophene-2,6-diyl][3-fluoro-2-[(2-ethylhexyl)carbonyl]thieno[3,4-b]thiophenediyl]] (PTB7, as electron-donor).

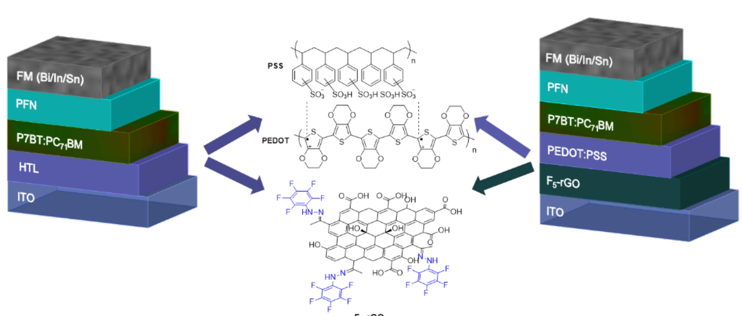

Figure 1. Architecture of the OSC fabricated and tested in this work

Layers of F_5-rGO were compared with the common reported PEDOT:PSS as hole transport layer in ITO/HTL/PTB7:PC_{71}BM/PFN/FM devices. Under our studied conditions the best performance was reached in OSCs, tested under normal room conditions, with F_5-rGO for a single layer, having a PCE = 5.82%, slightly less efficient than control device (PCE = 7.29%), achieved with PEDOT:PSS. On the other hand, a bilayer F_5-rGO/PEDOT:PSS was used as HTL in ITO/HTL/PTB7:PC_{71}BM/PFN/FM devices. OSCs showed a J_{SC} of -15.65 mA/cm^2, V_{OC} of 0.79 V, FF = 0.62 to give a PCE of 7.62%, an increase of 5% with respect to the PEDOT:PSS control device. This photovoltaic performance is compared with that of previously reported OSCs with Field´s metal by our group [11,12]. In addition, devices with F_5-rGO/PEDOT:PSS showed the best stability and photovoltaic performance, it could be attributed to synergistic effects on the charge-transporting ability when simultaneously used as composite interfacial layers [13,14].

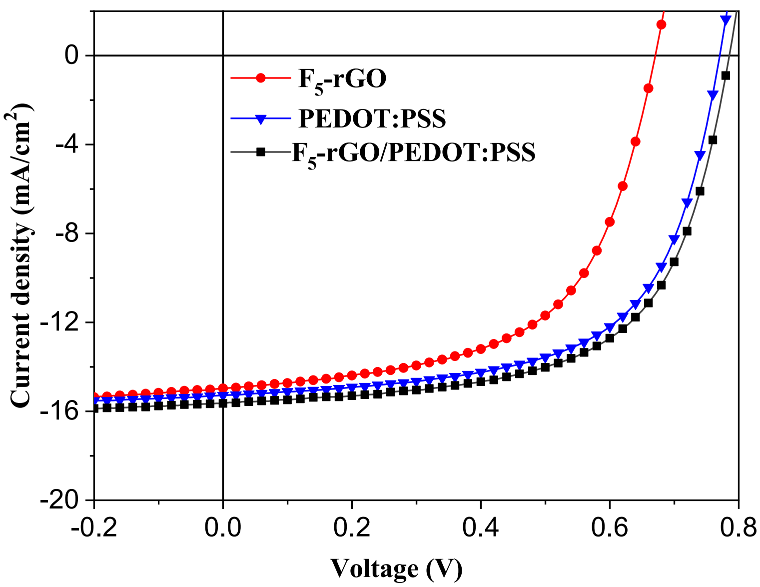

Figure 2. *J-V* curves of OSC with F_5-rGO and PEDOT:PSS as HTL and FM as top electrode. OSCs were fabricated and tested under room atmosphere conditions. Used architecture: ITO/HTL/PTB7:PC_{71}BM/PFN/FM

Acknowledgements: Ce-MIIE-Sol 207450/27, CONACyT-SENER 329449 (México) and CONACyT 281164 (LNMG) México.

Keywords: OSCs, hole transport layer, fluorinated reduced graphene oxide, bilayer.

References

[1] Hengevoss, D., *et al.*, *Sol. Energy,* **137**, 317, (2016)
[2] Song, Y., *et al.*, *Adv. Energy Mater.,* **6** (20), 1600847, (2016)
[3] Li, S., *et al.*, *J. Am. Chem. Soc.,* **140** (23), 7159, (2018)
[4] Zhang, H., *et al.*, *Adv. Mater.*, 1800613, (2018)
[5] Che, X., *et al.*, *Nat. Energy,* **3** (5), 422, (2018)
[6] Bolotin, K. I., *et al.*, *Solid State Commun.,* **146** (9-10), 351, (2008)
[7] Mahmoudi, T., *et al.*, *Chem. Commun.,* **50** (63), 8705, (2014)
[8] Mahmoudi, T., *et al.*, *Nano Energy,* **47**, 51, (2018)
[9] Stylianakis, M. M., *et al.*, *Carbon,* **50** (15), 5554, (2012)
[10] Sygellou, L., *et al.*, *J. Phys. Chem. C,* **120** (1), 281, (2016)
[11] Romero-Borja, D., *et al.*, *Carbon,* **134**, 301, (2018)
[12] Barreiro-Arguelles, D., *et al.*, *IEEE J. Photovoltaics,* **7** (1), 191, (2017)
[13] Yu, J.-H., *et al.*, *Nanoscale,* **9** (44), 17167, (2017)
[14] Lee, D.-Y., *et al.*, *Nanoscale,* **8** (3), 1513, (2016)

Multilayer reduced graphene oxide films as a hole transport layer for organic photovoltaic devices.

P. G. Otal [1,2]*, Juan Nicasio-Collazo [2], Daniel Romero-Borja [2], J. L. Maldonado [2] and R. Castro-Beltrán [1].

[1] División de Ciencias e Ingenierías, Universidad de Guanajuato, Loma del Bosque #103, Lomas del Campestre, C.P. 37150. León Gto., México.

[2] Research Group of Optical Properties of Materials (GPOM), Centro de Investigaciones en Óptica, A.C., Loma del Bosque #115, Lomas del Campestre, C.P. 37150. León Gto., México.

*pg.olveraotal@ugto.mx

Abstract: In this work is reported the analysis of the number of deposited layers of reduced Graphene Oxide (rGO) functionalized with phenylhidrazine (PHrGO), as a hole transport layer (HTL) [1], in organic photovoltaic (OPV) devices. OPVs cells were fabricated under the bulk heterojunction architecture with the configuration glass/ITO/PHrGO/P3HT:PC61BM/FM. Field's metal (FM) is a eutectic alloy, composed by 32.5% Bi, 51% In and 16.5% Sn, that melt at 65°C and is easily deposited on top of the electron transport layer (ETL) at low temperature (~ 90 °C) [2]. PEDOT:PSS film as a HTL is used as a control device, an improved power conversion efficiency (PCE) was observed, from 1% to 1.4%, by depositing a second PHrGO film, this PV performance achieved with this alternative HTL is promising and could be a replacement option of PEDOT:PSS that degrades the OPVs devices.

Introduction.

In photonics and organic electronics, poly (3,4-ethylenedioxythiophene):poly(styrene sulfonate) (PEDOT:PSS) is the material used as a hole transport layer due to its high optical transparency, solution processability, good work function , and high electrical conductivity. However, there is a drawback in its use due to its acid and hygroscopic nature that can damage a transparent electrode such as indium tin oxide (ITO), and decomposes the active layer materials such as P3HT:PCBM [3, 4]. These characteristics can drastically reduce the useful life of organic solar cells.

To overcome these challenges, researchers are trying to replace the PEDOT: PSS film with alternative compounds that also could be processable materials in solution such as reduced graphene oxide (rGO) as a hole transport layer [5]. The r-GO is a suitable material for use in organic solar cells due to its easy processability of the solution, high Young's modulus, high electrical, thermal and optical properties; low weight and large surface area [6].

To further investigate the device, atomic force microscopy (AFM) analysis was carried out. Moreover, the proposed device´s electrical properties, such a current-voltage (J-V), power conversion efficiency (PCE), fill factor (FF), short-circuit current density (Jsc), and open circuit voltage (Voc), were also studied.

Experimental procedure.

Figura 1 (a -d) shows the chemical structure of the organic compounds used in this study. ITO-coated glass was used as a substrate, initially was washed and agitated in a bath sonicator with chlorobenzene, acetone, ethanol for 10 min each. The HTL made of PEDOT:PSS was deposited by spin coating dispersion at 4500 rpm for 60 s onto an ITO-coated glass substrate and annealed at 80°C for 20 min under atmospheric conditions. The HTL made of PHrGO was deposited by spin coating dispersion at 3000 rpm for 60 s and annealed at 150°C for 30 min, and the same condition for the other layers. To fabricate the active layer, P3HT:PC61BM (1:0.8 wt ratio) were dissolved at 20 mg/ml in chlorobenzene and then stirred for 16 h. Then, the active layer was spin coated at 1800 rpm for 60 s onto de HTL, and annealed at 80°C for 20 min. The specific area of OPV device was 0.07 cm^2, finally the Field´s metal was deposited on top at 90°C. The J-V characteristics were measured under illuminated conditions of 100 mW/cm^2. The surface morphology was investigated by using AFM-Nanosurf static mode.

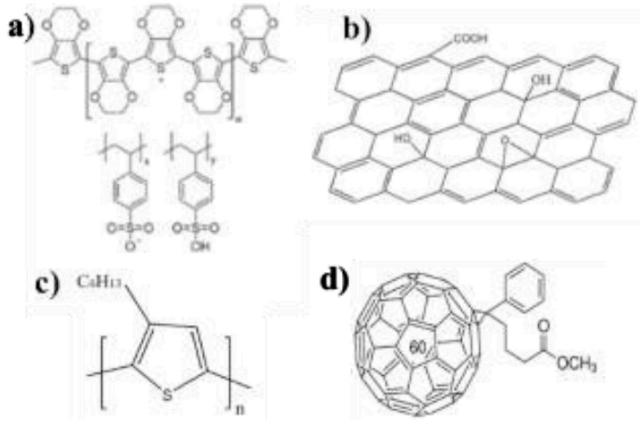

Figura 1. Molecular structures of a) PEDOT:PSS, b) rGO, c)P3HT and d) PC61BM.

Results and discussion

The J-V characteristics curves are shown in Figura 2, an improved PCE was observed, from 1% to 1.4%, by depositing a second PHrGO film and consequently the short-circuit current density (Jsc) increases from 4.8 mA/cm^2 to 6.2 mA/cm^2 because of the increase in charge carrier collection. In comparison with the values of the control device, where a PCE of 1.7% and Jsc of 7.3 mA/cm^2 were obtained.

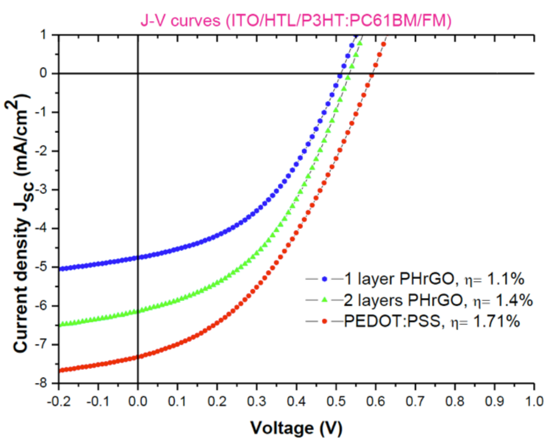

Figura 2. J-V curves for OPVs devices.

Acknowledgements: Ce-MIE-Sol 207450/27, CONACyT-SENER 245754 and CONACyT 293371 (LNMG) Mexico.

References

[1] D. Romero Borja, J. L. Maldonado, et al., «Organic solar cells based on graphene derivatives and eutectic alloys vacuum-free deposited as top electrodes,» Carbon, **134**, 301-309, (2018).
[2] D. Barreiro Argüelles, G. Ramos Ortiz, . J. L. Maldonado y E. Pérez Gutiérrez, «Stability study in organic solar cells based on PTB7:PC71BM and the scaling effect of the active layer,» Solar Energy, **163**, 510-528, (2018).
[3] B. Ecker, et al., «Degradation effects related to the hole transport layer in organic solar cells,» Adv. Funct. Mater., **21**, 2705-2711, (2011).
[4] Z. Zhao, et al., «Improving the conductivity of PEDOT:PSS hole transport layer in polymer solar cells via copper (II) bromide salt doping.,» ACS Appl. Mater, Interfaces, **7**, 1439-1448, (2015).
[5] E. Jokar, et al., «Anomalous charge-extraction behavior for graphene-oxide (GO) and reduced graphene-oxide (rGO) films as efficient p-contact layers for high-performance perovskite solar cells.,» Adv. Energy Mater, **8**, 1-10, (2018).
[6] D. Yu, et al., «Fullerene-grafted graphene for efficient bulk heterojunction polymer photovoltaic devices,» J. Phys. Chem. Lett., **2**, 1113-1118, (2011).

Extended Abstracts

Session
THIN FLIM TECHNOLOGY

Pg.

Luminescent properties of SRO thin films grown by RF sputtering 164
B. Reyes-Ramirez, Jorge Molina-González, J. Briones and A. Benitez-Lara

Luminescent properties of SRO thin films grown by RF sputtering

B. Reyes-Ramirez, Jorge Molina-González, J. Briones and A. Benitez-Lara*
Centro de Investigaciones en Óptica, Loma del Bosque 115, Colonia Lomas del Campestre León, Guanajuato, México. Código Postal 37150.
*alfredbl@cio.mx

Abstract: In this work, luminescent properties of silicon rich oxide (SRO) thin films obtained by sputtering is presented. The conditions of deposition of the films are the novelty of this work which consists on use targets of Si and SiO_2 where the grown of SiO_2 is constant and the Si is deposited around one minute in periods of time. The samples were characterized with photoluminescence (PL) and scanning electron microscope (SEM). The SRO films exhibit wide band photoluminescence (PL) spectra with the main components at 650 nm, 692 nm, 766 nm and 826 nm. In general, the silicon nanocristals (nc-Si) and interface defects nc-Si/SiO_2 are the two accepted process to produce the PL which corresponds to the range emission shown in the results. The micrographs of SEM reveal thickness from 103 to 130 nm.

1. Introduction

In the last years, many nanometric materials made of Si have been studied since the phenomenon of PL in range of visible of silicon porous [1 ,2]. Other material based on silicon is the silicon nanowire (nw-Si), where the nw-Si offer good properties for conductivity and PL [3]. In this work, the material based on Si is the SRO which it have been scoop from the scientific community due to silicon nanocristals embedded in a SiO_2 matrix implies on low dimension and a good source of emission light in room temperature [4, 5]. However, absorption and emission are correlated with nc-Si quantum effects also to interface defects between to nanocristals and the matix [6]. The SRO could be deposit by many methods like low pressure chemical vapor deposition (LPCVD), hot filament chemical vapor deposition (HFCVD), plasma enhanced chemical vapor deposition (PECVD), sol-gel, ionic implantation and sputtering [7-12]. Furthermore, the methods mentioned are compatible with the fabrication technology of microelectronic and a lot of application such as no volatile memories, sensors and emission devices [8-10].

2. Experiment setup

An Armstrong sputtering model Amod 230 with two RF sputter sources was used for the deposition of SRO. For this work, two reactive radio frequency magnetrons were employed at 13.6 MHz one with a Si target and the other with SiO_2 target both of two inches of diameter. The sputter pressure for the Si target was 1.5 mTorrs and 3.5 mTorrs for SiO_2 and 75 and 180 W, respectively. Then, the Ar flow was 200 sccm. Conversely, the substrate used in this work were p-type Si(100) with low resistivity wafer. In this method, SiO_2 deposition was constant during 30 min, however Si deposition were activated every three minutes for sample A and every nine minutes for sample B for one minute. The PL spectra were measured with a 2300i spectrograph from Acton Research with a R955 Hamamatsu photomultipliler tube and a wavelength excitation of 254 nm. Then, the micrographs of the samples were obtained with Jeol JSM7800F. On the other hand, transmittance was measure using an Agilent UV-VIS model Cary 5000.

3. Results

The results of PL are shown in figure 1 and reveal wide range spectra in visible region with main peaks around 652, 692, 713, 767 and 827 nm for sample A and B. Understanding the PL emission is necessary to explain the emission mechanism that gives the PL in the SRO. Two emission mechanisms are accepted for the PL and they are the quantum confinement (QC) due the nc-Si and interface defects between the nc-Si and SiO_2 matrix. The QC is related to band to band transitions of electron-holes pairs confined in the nc-Si with emission range of 700 to 900 nm. The second mechanism is due to radiative centers in the interface nc-Si/SiO_2 due to double Si-O bound which has a emission range of between 600 to 700 nm related to oxygen vacancies with neutral charge (NOV), no-bridging oxygen hole charge (NBOHC), oxygen vacancies with positive charge and oxygen interstitial. Therefore, the emission of the depositions exhibits both mechanisms. Nevertheless, the mechanism due the interface nc-Si/SiO_2 prevails over the nc-Si emission which is shown in the deconvolution peaks from figure 1b. Then, the PL results reveal a decrement in the peak of 652 nm but an increment on 692, 767 and 827 in sample B. Hence, this difference could be associated to the concentration of Si in the deposits. According to the QC, the emission peaks of 713, 767 and 827 belongs to nc-Si of 3.6, 4.2 and 5.1 nm of diameter, respectively.

The micrographs reveal that the thicknesses from the samples were 130 nm for sample A and 105 nm for sample B. The differences between the thicknesses could be explained by the deposit conditions, where the Si/SiO_2 rate codeposition is around 9 nm per minute compare with the SiO_2 rate deposition at 3 nm per minute.

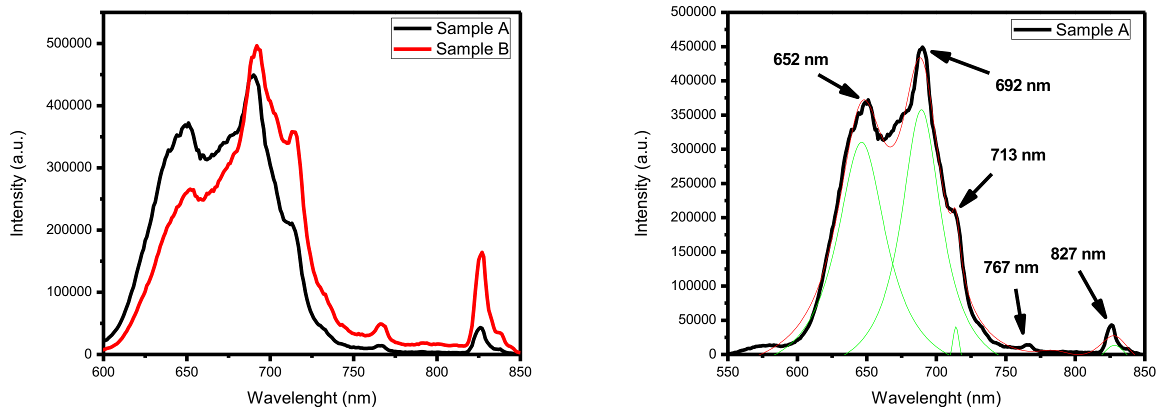

Figure 1 a) PL spectra for sample A and B. b) Deconvolution from sample A showing the principal emission peaks at 652, 692, 713, 767 and 827 nm.

References

[1] L. T. Canham, Silicon quantum wire array fabrication by electrochemical and chemical dissolution of wafers, Applied Physics Letters, vol. 57, no. 10, p. 1046, 1990.
[2] H.S. Nalwa, “Handbook of Nanostructured Materials and Nanotechnology: Porous Silicon”, Vol. 4, Academic Press, pp. 160-229.
[3] K. Sattler, “Encyclopedia of Nanoscience and Nanotechnology: Silicon Nanowires”, American Scientific Publishers, Vol. 9, 2004, pp. 815-835.
[4] E. A. Irene, Preparation and Some Properties of Chemically Vapor-Deposited Si-Rich SiO2 and Si3 N 4 Films, J.Electrochem. Soc. 125 819-823, (1978).
[5] Y. C. Fang, W. Q. Li, L. J. Qi, L. Y. Li, Y. Y. Zhao, Z. J. Zhang, and M. Lu, Photoluminescence from SiO*x* thin films: effects of film thickness and annealing temperature**,** Nanotechnology, 15, 495-500 (2004).
[6] A. Luna-López, M. Aceves-Mijares, O. Malik, J. Pedraza and C. Falcony, Proc. ICO20, 20th congress of the International Commission for Optics, Changchun, China, Vol. 6029, (2005).
[7] Z. Yu, M. Aceves, J. Carrillo y F. Flores, “Single electron charging in Si nanocrystals embedded in silicon-rich oxide”, Nanotechnology, 14, 2003, pp. 959-964.
[8] M. Aceves, A. Malik, and R. Murphy, *Sensors and Chemometrics,* In: Maria Teresa Ramirez–Silva *et al.,* Eds. Research Signpost, p1-25, (2001).

Extended Abstracts

Session
VISUAL MOTION TRACKING AND CONTROL VISION BASED MONITORING AND CONTROL

Pg.

6D Object Pose Estimation for Robot Programming by Demonstration 167
Mohammad Ghahramani, Alexander Vakanski and Farrokh Janabi-Sharifi

Satellite Image Processing for Retrieving Historical Solar Irradiance Data within the Mexican Territory 169
Juan M. Callejas-Cornejo, Manuel I. Peña-Cruz, Luis M. Valentín-Coronado.

SDH Technique Applied to Range Images in Order to Detect Keypoints in a Scene 171
Alejandra Cruz-Bernal Diana-Guadalupe Gutiérrez-León

Micro-scale surface contouring via microscope vision system based on micro laser line projection 173
J. Apolinar Muñoz Rodríguez, Francisco Carlos Mejía Alanís and Francisco Chávez Gutiérrez

Feature extraction of a soccer field for humanoid robot localization 175
Daniel Silva Medina, Juan Humberto Sossa Azuela, José Luis Vázquez Ávila, Alberto Elías Petrilli Barceló

Phase sensitive CT measurement using a pixelated polarizing shearing interferometer 177
David I. Serrano-García and Yukitoshi Otani

6D Object Pose Estimation for Robot Programming by Demonstration

Mohammad Ghahramani*, Alexander Vakanski# and Farrokh Janabi-Sharifi*
* Ryerson University, Eric Palin Hall, 87 Gerrard Street East, Toronto, Ontario, Canada, M5B 2K3
# University of Idaho, 1776 Science Center Drive, Idaho Falls, ID 83402
mgh@ryerson.ca, vakanski@uidaho.edu, fsharifi@ryerson.ca

Abstract: Estimating the position and orientation (6D pose) of objects in images is a crucial step toward successful robot programming by demonstration using visual learning. Currently, many algorithms including conventional image processing methods and the state-of-the-art methods based on deep leaning architectures are able to detect and track objects in images accurately. However, the problem of accurate estimation of 6D pose of objects in a sequence of video frames still poses challenges. In this paper, we present a novel deep learning regression method for pose estimation based. For training purposed, thousands of images from different poses of an object are generated based on the generated 3D model of the object. The proposed trained network can estimate the object orientation accurately and in real-time. Using the object position coordinates obtained from Kinect v 2.0 and the orientation of the object we have its 6D pose at each time frame is calculated and employed for trajectory learning. Robot inverse kinematics is applied to program the robot for task execution.

1. Introduction and literature review

We as humans learn to perform new tasks by learning skills from visual observation of teachers or parents demonstrating skill examples. The term robot Programming by Demonstration (PbD) is motivated from this learning approach and refers to transferring the required skill information from a human teacher to a robot by demonstrating examples of skill trajectories. Robot perception of human demonstrations encompasses detection, tracking and estimating the position and orientation of relevant objects for accomplishing desired task goals. Vakanski et al. proposed a trajectory learning approach by using Hidden Markov Models for modeling a set of demonstrated trajectories, and subsequently multidimensional dynamic time warping algorithm is employed to align the extracted trajectories features from multiple demonstrations in the time domain [1]. Afterwards, cubic-spline regression is applied to produce a generalized trajectory for task reproduction by a robot learner [1, 2]. The initial step of trajectory learning involves object detection and tracking, and has been investigated by both conventional [3] and deep network architectures [4]. These models are currently available in open source libraries in MATLAB or Tensorflow. Once the object is detected and tracked along the keypoints in the trajectory, its location can be accurately obtained from the point cloud information recorded from Kinect v2.0. The tracking algorithms generate object position coordinates in the RGB plane, and the relative points in the Depth plane indicate object coordinates in the 3D space.

Estimating object orientation in images is more challenging aspect of past perception in robotic learning. There have been numerous research works using conventional image processing algorithms to calculate object pose using artificial markers/labels attached to the object [5] or employing deep architectures to map the image captured from a particular view of the object to a database containing manually labeled images for different orientations [6]. However, such approaches suffer from **intrusive markers/sensors**, **required CAD models** and **limited orientations,** where the generated database of the object should contain acceptable subclasses of orientations to cover various poses of the object along the trajectory. Next, we propose a method to introduce a general framework for object pose estimation.

2. Proposed method

Our team developed an alpha version prototype of a robot programming by visual learning from demonstrations [7]. It was tested for multiple industrial applications, such as programming by demonstration for a painting task, where the paint spray gun is the object of interested and the goal is to learn the trajectory of the paint spray gun. First, we build a database of images of the object. Autodesk Recap® [8] was used as a powerful yet simple tool (i.e., free academic license) to generate an accurate 3D model of an object by just using photos of the object captured from different viewpoints on a simple background. Next, we employ MATLAB Java Robot library to control Autodesk 3D MAX® (free academic license) to synthesize images from various angle of the object by entering all possible Yaw, Pitch and Role values in increments of 10 degrees. The resulting set of images are then augmented by introducing different scales at 75% and 50% and illumination variation at 85% and 75%. We employed a pre-trained VGG16 neural network model and performed transfer learning [9], to calculate the orientation of the object based on a trained regression model of the dataset consisting of pairs of image and orientation angles. As shown in Fig. 1 the approach accurately estimated the object orientation in Yaw, Pitch and Roll, respectively, on 1,000 randomly selected images of the object. However, based on the geometry of the object, the overall accuracy of the Yaw angle was less accurate, whereas the Root Mean Squared Error (RMSE) of the yaw, pitch, and roll are 11, 2 and 7 degrees respectively.

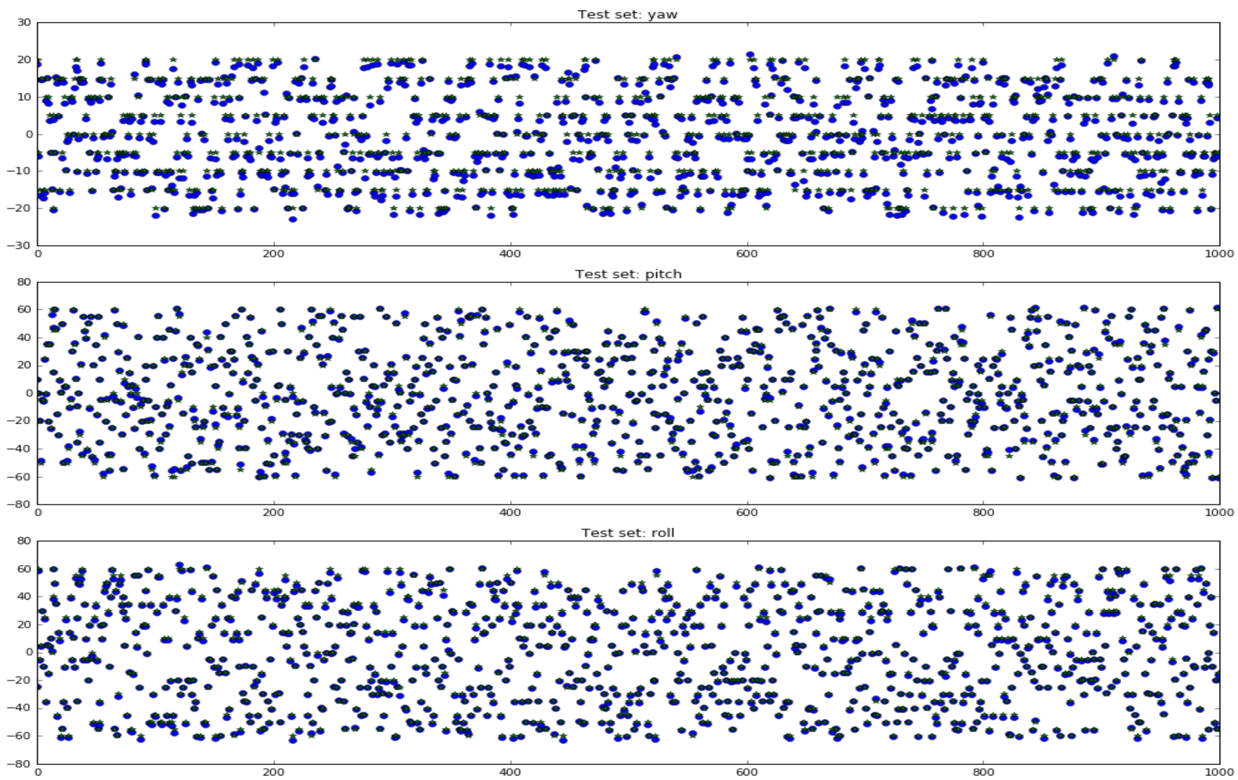

Fig. 1. From top to bottom estimating Yaw, Pitch and Roll on 1000 random samples. The blue dots denote the true values of the orientation angles, while the green star marks denote the prediction values of the orientation angles by the neural network.

3. Acknowledgment

This work was supported by NSERC, Innovation to Idea (I2I) grant (I2I PJ 486866-15). We would like to thank Miss. Kaiqi Cheng for validating experiments.

References

[1] A. Vakanski, I. Mantegh, A. Irish, and F. Janabi-Sharifi, "Trajectory learning for robot programming by demonstration using hidden Markov model and dynamic time warping," IEEE Trans. Sys. Man, Cybern.: Part B, vol. 41, no. 4, Aug. 2012, pp. 1039–1052.
[2] C. M. Bishop, *Pattern Recognition and Machine Learning*. NewYork: Springer-Verlag, 2006.
[3] X. Jia, H. Lu and M. Yang, "Visual tracking via adaptive structural local sparse appearance model," *2012 IEEE Conference on Computer Vision and Pattern Recognition*, Providence, RI, 2012, pp. 1822-1829.
[4] D. Li and W. Chen, "Object tracking with convolutional neural networks and kernelized correlation filters," *2017 29th Chinese Control And Decision Conference (CCDC)*, Chongqing, 2017, pp. 1039-1044.
[5] A. Vakanski, F. Janabi-Sharifi, and I. Mantegh, "An image-based trajectory planning approach for robust robot programming by demonstration," *Journal Robotics and Autonomous Systems,* vol. 98, pp. 241-257, 2017.
[6] P. Wohlhart and V. Lepetit, "Learning descriptors for object recognition and 3D pose estimation," *2015 IEEE Conference on Computer Vision and Pattern Recognition (CVPR)*, Boston, MA, 2015, pp. 3109-3118.
[7] Demos available at https://youtu.be/G09J57jMzmg
[8] available at https://www.autodesk.com/products/recap/overview
[9] S. Karen, and A. Zisserman. "Very deep convolutional networks for large-scale image recognition." *arXiv preprint* arXiv:1409.1556 (2014).

Satellite Image Processing for Retrieving Historical Solar Irradiance Data within the Mexican Territory

Juan M. Callejas–Cornejo[1], **Manuel I. Peña–Cruz**[2]*, **Luis M. Valentín–Coronado**[2]
[1]PICYT - Centro de Investigaciones en Optica A.C. Unidad Aguascalientes, Prol. Constitución 607, Fracc. Reserva Loma Bonita, C.P. 20200, Aguascalientes, Ags, México. Phone: +52 01 (449) 442 8124,
[2]CONACYT - Centro de Investigaciones en Optica A.C. Unidad Aguascalientes, Prol. Constitución 607, Fracc. Reserva Loma Bonita, C.P. 20200, Aguascalientes, Ags, México. Phone: +52 01 (449) 442 8124,
*email: mipec@cio.mx.

Abstract: Solar resource assessment is a key subject for the viability and implementation of solar power plants. Solar sensors measure irradiance locally, but high cost of these specialized sensors difficult its implementation trough all the Mexican territory. Satellite images provide a valuable tool for the determination of solar irradiance trough image processing. In this work, an algorithm for estimation of global solar irradiance based on determining cloud index trough pixel analysis from a particular region of Mexico is implemented.

1. Introduction

The solar radiation that reaches the top of the atmosphere and reaches the surface of the Earth depends on different variables, i.e. the factor of atmospheric transmission, available albedo and atmospheric pollution. Solar sensors (radiometers) measure components from the solar radiation reaching the Earth. Direct solar irradiance (DNI) is the component that comes directly from the sun without any deviation from the atmosphere (pyrheliometers). Diffuse solar irradiance (DHI) is what reaches the Earth's surface due to the deviation or scattering of direct solar rays from the sun; commonly, caused by clouds, gases and particles in the atmosphere (pyranometers). Both components comprise the global solar irradiance (GHI). However, these sensors measure solar irradiance locally and its implementation trough all the Mexican territory has been a difficult task historically due to cost and maintenance. Due to this, satellite imaging provides a valuable tool for the analysis of cloud behavior and solar irradiance assessment by replacing traditional radiometers with pixel information from the satellite camera, providing higher resolution maps for the Mexican region (See Fig. 1) [1].

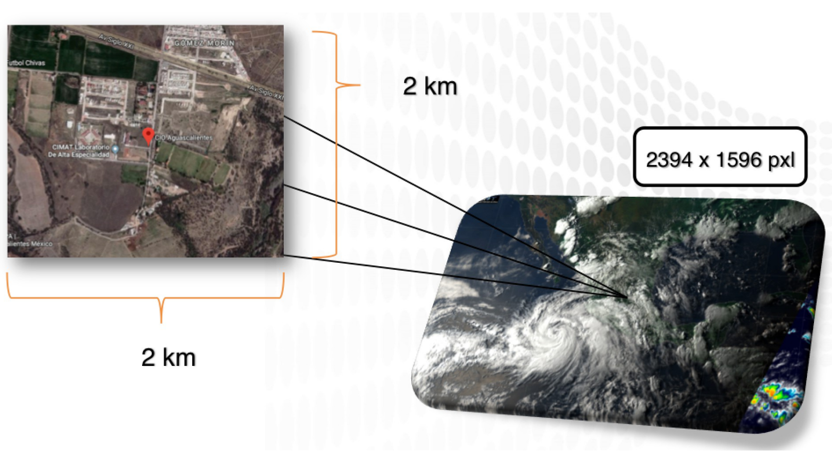

Figure 1. Satellite image and pixel equivalence of the zone of interest. Aguascalientes, Ags., Mexico.

2. Methodology

GOES is a satellite sent to the exosphere by the US National Weather Service (NWS) program in 2016. The objective of the satellite is to provide information flows in the form of images for weather forecast, storm tracking and meteorological research.

Taking advantage of the geostationary satellite capabilities requires careful analysis of the information provided by the camera [2]. Pixel information contains intensity values in the RGB channels. This has to be related accordingly depending on whether there is cloudiness present in the region of interest or not. Water vapor affects directly solar irradiance passing through the atmosphere, so greater accumulation of water vapor in the atmosphere reduces the irradiance reaching the ground sensor. This is also observed in the pixel intensity level of the image in the region of interest. The value of each pixel depends on its brightness, intensity, noise and color/gray level that the cloud is scattering back to the camera [3]. By this relationship, an irradiance measurement can be inferred accordingly to Equation 1:

$$GHI_{SAT} = [0.02 + 0.98\,(1 - Ci)] * GCH_{sky} \quad \text{... Ec. 1}$$

Where:

$$Ci = \frac{\alpha - \alpha_{min}}{\alpha_{max} - \alpha_{min}} \quad \text{... Ec. 2}$$

And

GHI_{SAT} = global horizontal irradiance calculated by the model (Wm^{-2}). Ci = Cloud Index. GHC_{sky} = global horizontal irradiance from clear sky (Wm^{-2}) and α is the pixel channel intensity of the camera for a particular region of interest.

3. Results

The results presented below are based on June 04, 2018 in the State of Aguascalientes, coordinates 21 ° 50'40.4 "N - 102 ° 20 ' 34.8 "W.

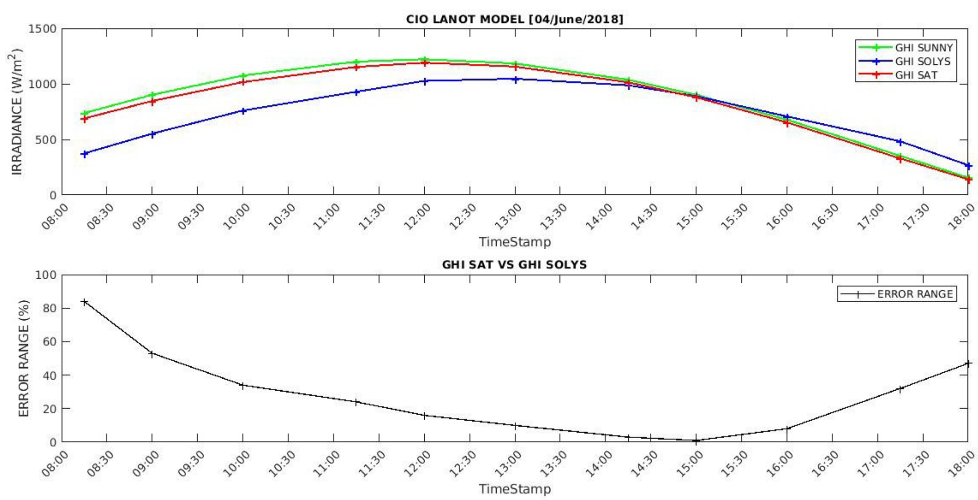

Figure 2. Comparison between solar irradiance numerical models vs. data from a solarimetric station.

4. Conclusions

Although, there is still some margin of error due to solar luminance during the sunrise and sunset hours, it can be notices that there is a good correlation between the irradiance values provided by the model (GHI SAT) and the data provided by the solarimetric station (GHI SOLYS), making this a valuable tool to study for generating solar irradiance maps for the Mexican territory and providing certainty for the solar power industry.

References

[1] http://www.lanot.unam.mx

[2] Description of an operational tool for determining global solar radiation at ground using geostationary satellite images. Solar Energy, 42 (1989), pp. 201-207

[3] Perez R., (2002): Time Specific Irradiances Derived from Geostationary Satellite Images. Journal of Solar Energy Engineering, February 2002 issue.

SDH Technique Applied to Range Images in Order to Detect Keypoints in a Scene

Alejandra Cruz-Bernal Diana-Guadalupe Gutiérrez-León
Universidad Politécnica de Guanajuato acruz@upgto.edu.mx

Abstract: This proposal presents how through SDH technique is possible to detect interest points. Therefore, sum and difference histograms are introduced as an alternative to the usual co-occurrence matrices used for texture analysis. The interesting of this proposal consist in the application of the technique in range images. The obtained results make evident that, these images can be processed as textured images where, the blurring generated by SDH technique is an advantage. That, we can used to our favor because, this singularity allows us to find a homogeneity surface to carry out a process to select the interesting points, that aim to describe the scene by means of its contour. Additionally, the proposed method over other methods of the-state-of-art shows the decrease in computation time as well as, a major number of found interesting points. We demonstrate the capabilities of our approach through several tests realized with a generic dataset.

1. Introduction

Identifying robust features from geometric objects is of crucial importance in many areas of computer vision. In this sense, the depth sensing technology of Kinect could be extended far beyond gaming, such as presented by [1] and at a much lower cost than traditional 3-D cameras (as reference, see survey [2]). Particularly, the geometric information is robust to variants to scale, rotation and illumination, as it presents in [3].

2. Methodology

The interesting point detection is an essential phase to develop a local feature extractor [4], recently investigations present the performance results of these descriptors when combined with different 3D keypoint detection methods such as in [5, 6]. In this phase, the information (for instance, texture for intensity images) is obtained in order to carry out the characterize the interest points. Therefore, if we consider that, the texture is a property of neighborhood, then in accordance with [7], it is possible to characterize the surface of the range images through density probability functions.

Unser in [8] proposed the SDH technique (Sum and Difference Histogram technique), with which through estimates of the first order probability functions to aim to identify textures into region. We adapt the SDH technique applied to range images through a set of second-order statistics. Here, the grey levels that represent the geometric information are processed as texture. This is, a pair of pixels (y_1, y_2) in a relative position fixed by (d_r, θ) in polar coordinates where, $d_r = [d_1, d_2]$, and θ is the angle. It is defined $y_1 = y_{k,l}$ and $y_2 = y_{k+d1,l+d2}$ such that, the histograms for the differences and sums of whole those valid pixels that are at that distance and angle, it is expressed as,

$$\begin{cases} S_{k,l} = y_{k,l} + y_{k+d1,l+d2} \\ d_{k,l} = y_{k,l} + y_{k+d1,l+d2} \end{cases} \tag{1}$$

It is important to note that, if d_r rises, the blurring effect is proportional to this increase (see, first and second columns Fig. 1). This effect is desirable due that, when to compute the homogeneous surface [10], the regions are split. This result allows us to describe the picture by means of lines of iso-elevations, which give volume to contained objects in the scene.

3. Results

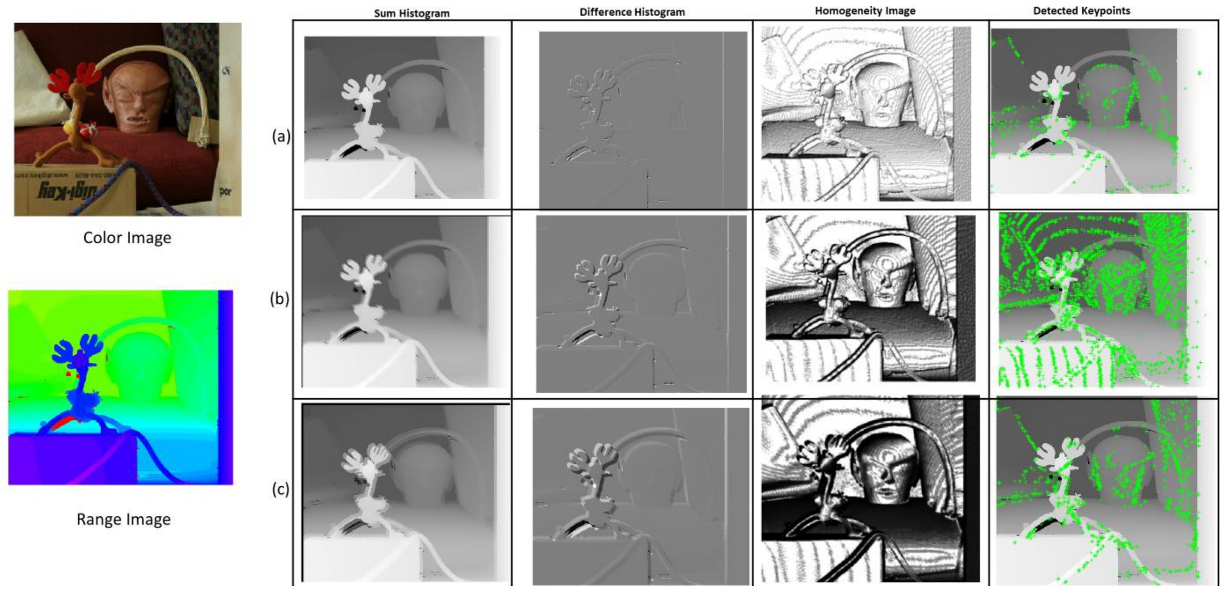

Fig. 1. The obtained results are presented with respect to Reinder of Middlebury dataset [10]. a) $d_r = [1, 1]$; b) $d_r = [3, 3]$; c) $d_r = [6, 6]$. In all cases $\theta = 0^0$. Qualitatively, it can be observed as the blurring effect is increasing from (a) to (c) in the first column (sum histogram). While, in the second column (difference histogram) is formed several regions as consequence of the blur generated by d_r. Third column shows the homogeneity image from homogenous surface. Finally, fourth column presents the detected interest points accordance with the characterization of homogenous surface by means of analysis of mass probability function [8, 10].

References

[1] Han, Jungong, et al. "Enhanced computer vision with microsoft kinect sensor: A review." IEEE transactions on cybernetics (**43**) **5**, 1318-1334 (2013).
[2] Smisek, Jan, Michal Jancosek, and Tomas Pajdla. "3D with Kinect." *Consumer depth cameras for computer vision*. (Springer, London, 2013).
[3] Pears, N. C., Austin, J. "A Machine-Learning Approach to Keypoint Detection and Landmarking on3D Meshes". International Journal of Computer Vision. **102**, 146-179 (2013).
[4] Tombari F., Salti S., Di Stefano L.: "Performance Evaluation of 3D Keypoint Detectors". International Journal of Computer Vision. **102**,128-220 (2013).
[5] Guo, Yulan, et al. "A comprehensive performance evaluation of 3D local feature descriptors." International Journal of Computer Vision (**116**)**1**, 66-89 (2016).
[6] Mukherjee, Dibyendu, QM Jonathan Wu, and Guanghui Wang. "A comparative experimental study ofimage feature detectors and descriptors." Machine Vision and Applications (**26**) **4**, 443-466 (2015).
[7] Lategahn, Henning, et al. "Texture classification by modeling joint distributions of local patterns withGaussian mixtures." IEEE Transactions on Image Processing (**19**) **6**, 1548-1557 (2010).
[8] Unser, Michael. "Sum and difference histograms for texture classification." IEEE transactions onpattern analysis and machine intelligence **1** 118-125 (1986).
[9] Haralick, Robert M. "Statistical and structural approaches to texture." Proceedings of the IEEE (**67**) **5**. (1979). pp.786-804
[10] Hirschmuller, Heiko, and Daniel Scharstein. "Evaluation of cost functions for stereo matching." Computer Vision and Pattern Recognition, 2007. CVPR'07. IEEE Conference on. IEEE, (2007).
[10] Cruz-Bernal, Alejandra, Dora-Luz Almanza-Ojeda, and Mario-Alberto Ibarra-Manzano. "Contour Detection at Range Images Using Sparse Normal Detector." Mexican Conference on Pattern Recognition. Springer, (2016).

Micro-scale surface contouring via microscope vision system based on micro laser line projection

J. Apolinar Muñoz Rodríguez, Francisco Carlos Mejía Alanís and Francisco Chávez Gutiérrez[1]
Centro de Investigaciones en Óptica A.C.
Apartado Postal 1- 948, León, GTO, 37150, México
[1]Instituto Tecnológico de Aguascalientes
Apartado Postal 20256, Aguascalientes, Ags., México

Abstract: A microscope vision system to retrieve micro scale surface via micro laser line projection is presented. In this technique, a 36 μm laser line is projected on the target surface. The surface topography is computed by triangulation by means of the line position and microscope vision parameters. The calibration of the microscope vision parameters is carried out by means of an adaptive genetic algorithm. This procedure avoids errors produced by the missing of references and physical measurements. The contribution of the proposed system is corroborated by an evaluation via accuracy of the traditional microscope imaging systems.

1. Introduction

Nowadays, microscope imaging systems play an important role to retrieve micro-scale surface measurements in areas such as: micro surface inspection, micro texture characterization, micro positioning and so on. The proposed microscope vision system is performed via micro laser line scanning. This technique computes the micro-scale surface through the laser line position and the microscope vision parameters, which are calibrated by an evolutionary algorithm. In the microscope system, the micro laser line is projected perpendicularly to the surface and the microscope is aligned at an angle. The line scanning is carried out by moving the microscope vision system by means of a slider device. During the scanning, a CCD camera captures the laser line and its position is detected via Bezier curves [1]. The calibration of microscope vision parameters is carried out by an evolutionary algorithm based on the microscope geometry. This leads to improve the accuracy of the traditional microscope vision systems. It is because errors of external references are not added to the microscope calibration. The contribution of the proposed microscope vision system is corroborated by an evaluation via accuracy and speed of traditional microscope vision systems.

2. Surface contouring via Microscope vision system

The microscope vision system to retrieve micro-scale surface is shown in Fig. 1(a). In this arrangement, the *x*-axis and *y*-axis are located on the surface plane, which is situated perpendicularly to *z*-axis. The micro laser line is projected perpendicularly on the surface and the optical microscope is aligned at an angle. The CCD camera is attached to the microscope to capture the micro laser line. The symbol θ indicates the angle between the laser line and the optical axis. The distance between the objective lens and the surface is defined by D. The objective focal length and the objective focus are represented by f_{ob} and F_{ob}, respectively. The distance between the image plane of the objective lens and the ocular lens is depicted by L_t. The ocular focal length in indicted by f_{oc} and the ocular focus is represented by F_{oc}y. The laser line coordinates in the CCD array in *x*-axis are denoted by $x_{i,j}$, where x_c is the image center and η is the pixel size. The line coordinates in the CCD array in *y*-axis are indicated by $y_{i,j}$, and y_c is the image center. The surface coordinates $h_{i,j}$ in *z*-axis are computed by means of the expressions

$$h_{i,j} = \frac{\eta(\mathrm{x}_c - \mathrm{x}_{i,j}) L_t F_{ob}}{\sin(\theta)(f_{ob} - F_{ob}) f_{oc}} \quad , \tag{1}$$

$$y_{i,j} = \frac{\eta(\mathrm{y}_{i,j} - \mathrm{y}_c) L_t D}{f_{oc} f_{ob}} . \tag{2}$$

The surface coordinates in x-axis is defined by the position where the laser line is projected. This coordinate is provided by the slider device. Based on the vision parameters (x_c, y_c, η, θ, D, L_t, f_{ob}, F_{ob}, F_{oc}, f_{oc}) and the line position $x_{i,j}$, the surface topography $h_{i,j}$ is computed via Eq.(1). The line position is determined through the maximum intensity via Bezier curves [2]. The proposed technique is applied to retrieve the metallic surface shown in Fig.1(b), which is represented in *mm* in x-axis. The micro laser line projected on this surface is shown in Fig. 1(c). To retrieve se surface, the microscope system is moved by the slider device in x-axis to scan the whole surface. During the scanning, the micro laser line is captured by the CCD camera. In each image, the line position $x_{i,j}$ is computed along y-axis. Then, the line position is substituted in Eq.(1) to calculate the surface topography $h_{i,j}$. Thus, the surface coordinate in z-axis is represented by $z_{i,j}=h_{i,j}$. By processing one laser line, a transverse secction of the metalic surface is contoured. By processing all images during the scanning the wholes surface is retrieved.
Thus, the proposed microscope vision system performs micro-scale measurements with an error minor than *rms*=0.35 μm, which leads to achieve a relative error minor than 1.0 % [3]. This error is produced by the line position error, slider position error, and the calibration error. Also, this method reduces the consumed time to obtain the micro-scale measurements. These results lead to achieve a contribution in microscope vision systems to perform micro-scale surface contouring.

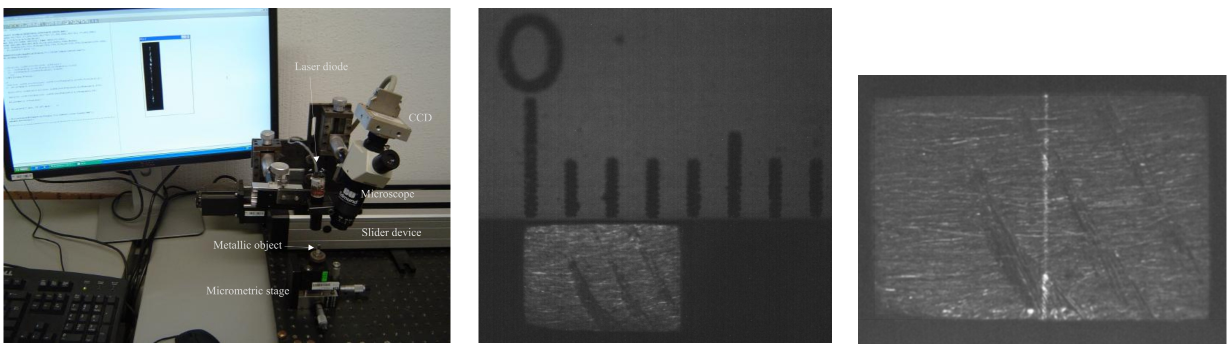

(a) (b) (c)

Figure 1. (a) Microscope vision system. (b) Metallic surface to be contoured. (c) Micro laser line projected on the surface target.

References

[1] J. A. Muñoz Rodriguez, “Microscope self-calibration based on micro laser line imaging and soft computing algorithms”, Optics and Lasers in Engineering, Vol. 105, p. 75-85 (2018)..

[2] J. A. Muñoz Rodríguez, “Calibration modeling for mobile vision based laser imaging and approximation networks”, Journal of Modern Optics, Vo. 57 No.17, 1583-1597, (2010).

[3] J. A. Muñoz Rodriguez, Three-dimensional microscope vision system based on micro laser line scanning and adaptive genetic algorithms, Opt. Commun., Vol. 385, p. 1–8, (2017).

Feature extraction of a soccer field for humanoid robot localization

Daniel Silva Medina [1], Juan Humberto Sossa Azuela [2], José Luis Vázquez Ávila [1], Alberto Elías Petrilli Barceló [3]

[1]*Universidad Autónoma del Carmen.*
[2] *Centro de Investigación en Computación del Instituto Politécnico Nacional.*
[3]*Universidad Tecnológica de la Mixteca.*

Abstract: The present work shows a set of artificial vision techniques combined with projective geometry to help us make decisions on a known environment.

Over the years humanoid robots have made a great leap in terms of structural development, solving most of the problems that arise by mechanical design, this time we will address a problem referred to decision making in a known environment. Therefore, it is proposed to use a set of segmentation techniques and image rectification in order to obtain Euclidean properties through visual information. The information will be compiled from a football field with the dimensions of the international competition Humanoid Soccer Standard Platform League belonging to RoboCup. In this competition two teams consisting of five nao humanoids robots must play football soccer autonomously.

In order to a robot can play soccer, it is necessary first instance, to be able to extract the set of characteristics that make up the environment to navigate, which that determine the limits of the soccer field. The feature extraction must be done in the computer on board the robot, so it is important that the feature extraction algorithms are efficient. In the present work, computer vision algorithms are presented for feature extraction, these algorithm can be able to operate within the real time limits on a Nao V4 robot.

To start obtaining features, it is known that the soccer field is green, which is delimited with white lines, a central circle, and it is at ground level. With this information it is possible to define a search region then the line to the horizon is calculated that comes from the intersection of a plane parallel to the floor and that passes through the center of the robot's camera with the plane of the image[1], to this is used a camera model called pinhole. To be able to use this model is required to estimate the focus of the camera, the size of the sensor of the camera and the main point of the camera.

(a) View of the plane parallel to the floor and that passes through the center of the robot's camera

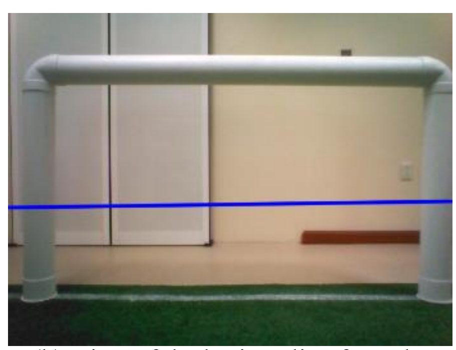

(b) View of the horizon line from the robot, represented with a blue line.

Fig. 1 Representation of horizon line.

This guarantees that what is being processed is the football field, avoids processing areas that are not of interest, avoid wasting computing time and making the segmentation algorithm more efficient. For segmentation, images were taken inside a soccer field. This was done throughout the field, to get the variations of color and lighting that exist within it.

Later with these images a pre-processing was carried out in which it consisted in calculating purity of the green color with (1) where G is the value of color green, R the value of red and B the value for color blue [2].

$$Gr = \frac{G}{R+G+B} \qquad (1)$$

With this it is build a histogram to get a density function of the color that it´s being sensed, with this information of the purity of the color the density function was calculated of the results this we can create a filter defined by the thresholds given by the calculated density function. We proceed to look for the features of the field.to do this, a discrete derivative is applied on the x-axis joint whit the technique of Scan Lines [3] this to extract color discontinuities by establishing a decision system, if in the calculation of the derivative a negative value is obtained it is counted as a discontinuity and therefore belongs to a of the lines or circle.

The points cloud obtained from these discontinuities are rectified using a technique called IPM (inverse perspective mapping) which consists of creating a matrix using the model of the camera combined with the matrix that define the rotational movements of the camera to create a matrix H of homography (2), in case it has degrees of freedom, this to avoid the projective deformation that is caused at the time of 3D mapping of the real world to the 2D plane that are generated in the camera and thus recover the properties of parallelism and angles that it causes us.

$$H = \begin{bmatrix} h_{11} & h_{12} & h_{13} \\ h_{21} & h_{22} & h_{23} \\ h_{31} & h_{32} & h_{33} \end{bmatrix} \qquad (2)$$

For the search of lines the Hough transform is used, this consists in forming a vote counting system through the cloud of points that are obtained from the extraction of characteristics, to create said system the points in Hough space creating an accumulator, then a threshold is proposed which delimits us how many votes are allowed to proceed to make the decision if what is being analyzed is a line or some other object, the selection of the line is made depending on of the votes, once the lines are obtained, proceed to make the change to coordinates to define the lines found. RANSAC is a robust algorithm that fits a set of outliers to find a specific mathematical model[4], in this case resemble a model that describes a circumference by n iterations taking three random points with which fits a circumference model, if these points belong to this circumference can be taken as a consensus set and so for the n iterations, at the end the sets with more votes are selected to define where the circumference was found.

(a) Image with the homography (b) Results of the algorithms for line and circle.

Fig. 2 Perception of the robot with the technics applied.

This information about the lines and circles can be used to feed other filters, such as the Kalman filter or the particle filter.

References

[1] Qian, Y., & Lee, D. D. (2016, June). Adaptive field detection and localization in robot soccer. In *Robot World Cup* (pp. 218-229). Springer, Cham.
[2] Jüngel, M., Hoffmann, J., & Lötzsch, M. (2003, July). A real-time auto-adjusting vision system for robotic soccer. In *Robot Soccer World Cup* (pp. 214-225). Springer, Berlin, Heidelberg.
[3] Álvarez, R., Millán, E., & Swain-Oropeza, R. (2005, November). Multilevel seed region growth segmentation. In *Mexican International Conference on Artificial Intelligence* (pp. 359-368). Springer, Berlin, Heidelberg.
[4] J. B. Pablo Flores, «Algoritmo RANSAC: fundamento teorico,» 2011.

Phase sensitive CT measurement using a pixelated polarizing shearing interferometer

David I. Serrano-García[1] and Yukitoshi Otani [2,3]

[1]Electronic Engineering Department, University of Guadalajara, Av. Revolución No. 1500, CP. 44430 Guadalajara, Jalisco, México

[2]Utsunomiya University, Center of Optical Research and Education, 7-1-2 Yoto, Utsunomiya, Tochigi, 321-8585, Japan

[3]Utsunomiya University, Department of Optical Engineering

david.serrano@academicos.udg.mx

Abstract: We implemented a phase sensitive computed tomography (CT) measurement by using a lateral shear interferometer with a pixelated polarizing camera to retrieve phase in a single shot manner. Inner information of the sample was retrieved by rotating the sample and using inverse Radon transform procedures. A polymer bead immersed in water at refractive index matching condition was used to emulate a 3D phase distribution to be measured.

1. Introduction

Interferometry provides information about the light passing through it due to inner refractive index variations of a transparent sample in the propagation direction. If the sample presents non-uniformities or non-symmetric variations, computed tomography algorithms can be implemented to obtain information about its inner distributions. This process has been successfully implemented in medical x-rays imaging by considering the beam properties of the beam (attenuation, deflection, etc.) passing through a patient from different directions. The purpose of this research is to combine a stable interferometric system with computed tomography techniques to retrieve volumetric information of a transparent sample.

2. Lateral Shear Interferometer Employing Pixelated Polarization Camera

The interferometric system used is based on a triangular path configuration that introduces a controllable lateral shear by moving one of the mirrors on optical axis direction, figure 1. The sample is placed at the entrance of the interferometer and interference pattern will be obtained due of the interference of the sheared image copy of the input wavefront [1, 2]. Single shot phase measurement condition is obtained by the usage of the polarizing beam splitter (PBS), quarter wave plate at 45º (QWP45º) and the pixelated polarizing camera. Due of the usage of the polarization camera, imaging and speckle reduction system were selected to properly image the sample information on the CCD sensor after passing the micro-polarizer array.

Sample were rotated 180 degrees for implement inverse radon procedures, Figure 2 shows the data arrangement for reconstruction were each unwrapped differential phase is stacked in a cube of data for the CT reconstruction. This cube of data represents the 3D sinogram information that will be processed to retrieve the 3D phase localization of the sample.

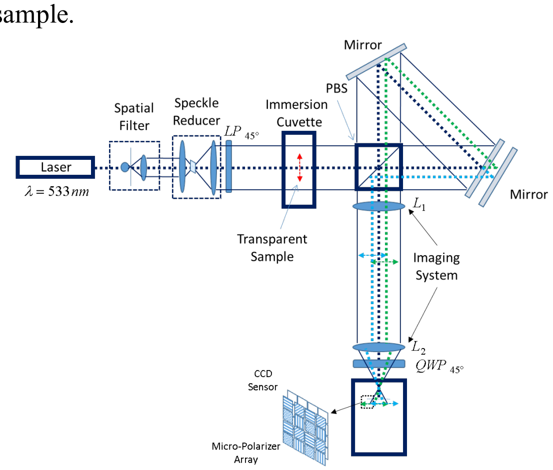

Figure 1. Lateral shear interferometer based on a triangular Sagnac configuration using pixelated polarizing camera.

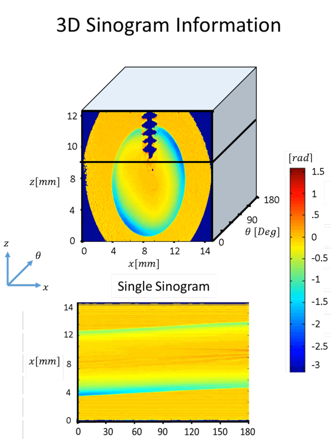

Figure 2. Phase information is arranged for retrieve slice sinograms for reconstruction by using inverse Radon transform.

2. 3D Phase Data Reconstruction

After measuring the differential phase information, at different angles of rotation, an inverse Radon transform algorithm is used for the 3D reconstruction [3]. Figure 3 shows two side views of the reconstruction obtained. The information represents locations were phase changes occurred on the light passing through the sample due of refractive index changes inside the sample. The current stage of the project is based on identify those regions, for retrieve the refractive index distribution an integration process needs to be done on the current reconstruction in direction of the shear.

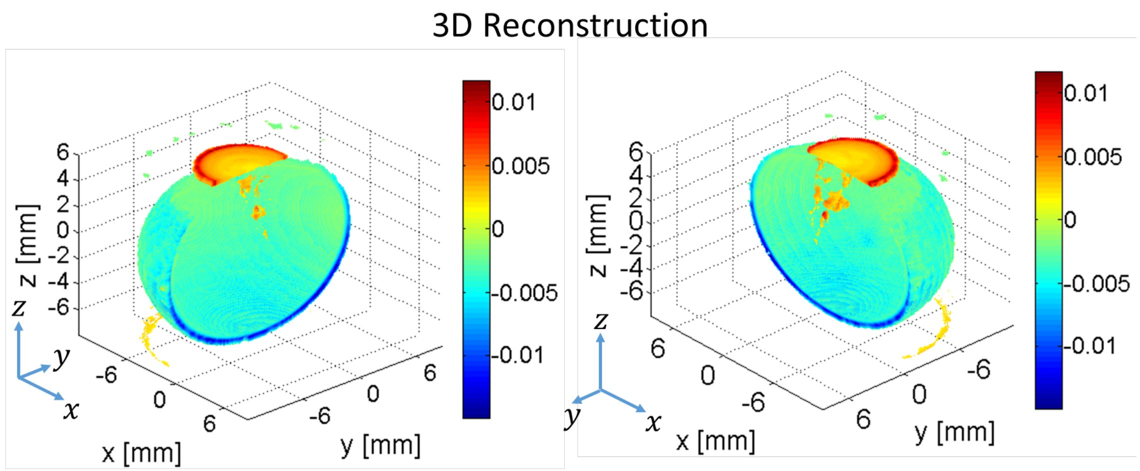

Figure 3. Two views of the 3D Reconstruction of a polymer bead immersed in water showing inner distribution.

3. Conclusions

By the implemented system inner distribution of the sample can be retrieved. The information represents phase changes obtained on the light passing trough of the sample due of inner refractive index changes. By the CT procedure, 3D localization of the phase variation can be obtained.

Acknowledgements

The authors acknowledge the funding support provided under The Project for Bio-Imaging and Sensing at Utsunomiya University. D.I. Serrano-García is currently occupying a post doc position at Utsunomiya University in the Center for Optical Research and Education under the same project.

References

[1] Hariharan P. and D. Sen, “Cyclic Shearing Interferometer,” J. Sci. Instrum., 37, 374-376 (1960).
[2] Y. P. Kumar and S. Chatterjee, "Measurement of longitudinal displacement using lateral shearing cyclic path optical configuration setup and phase shifting interferometry," Appl. Opt. 50, 1350-1355 (2011).
[3] K. Iwata et al., "Measurement of Dynamic Flow Field by Optical Computed Tomography with Shearing Interferometers", Opt. Rev., 7, 5, 415-419 (2000).

Extended Abstracts

Session
SPECIAL SESSION 1: POLARIZATION TECHNOLOGY

Pg.

Determination of the optical phase by using coupled interferometric systems 180
German Reséndiz-Lopez, Luis Antonio Bonilla-Jiménez, Areli Montes-Pérez, Jaime Garnica-González, Juan M. Islas-Islas, David Serrano-García, and Noel I. Toto-Arellano

Study of the response of the NOLM experimental scheme to polarization in mode-locking and continuous-wave 182
J R Martinez-Angulo, J C Hernandez-García, J H Barron-Zambrano, J M Estudillo-Ayala, C M Carrillo-Delgado, J A Martin-Vela and R Rojas-Laguna

Phase Retardation Parameters Measurement by a Dual Rotating Polarizer Polarimeter 184
David I. Serrano-García, Humberto Macías-Mendoza, Jorge L. Flores, Guillermo García-Torales, Geliztle A. Parra-Escamilla and Antonio Muñoz

Differential interference contrast video microscope using pixelated polarization camera 186
Yukitoshi Otani, Wataru Takano, Shuhei Shibta, Nathan Hagen

Limits on experimental Mueller-polarimeter errors including the eigenvalue calibration method 188
N.C. Bruce, O.G. Rodríguez-Herrera, J.M. Lopez-Tellez, O. Rodríguez-Nuñez,

Characterization of the optical behavior of an electro-optic modulator as a function of the temperature 190
Joel Cervantes-L, Shunya Masaki, Yuki Shimamoto, Yoshio Hayasaki

Determination of the optical phase by using coupled interferometric systems

German Reséndiz-Lopez,[1,4] Luis Antonio Bonilla-Jiménez,[2] Areli Montes-Pérez,[3] Jaime Garnica-González,[4] Juan M. Islas-Islas,[1] David Serrano-García,[5] and Noel I. Toto-Arellano.[1]

[1]Cuerpo Académico de Ingeniería Ciencias e Innovación Tecnológica. Centro de Tecnologías Ópticas y Fotónicas, Universidad Tecnológica de Tulancingo, 43642, Hgo., México.
[2]Universidad Tecnológica de Xicotepec de Juarez, 73080 Xicotepec de Juárez, Pue., México.
[3]Laboratorio de Óptica Física de la Benemérita Universidad Autónoma de Puebla, 72592, Puebla, Pue., México.
[4]Universidad Autónoma del Estado de Hidalgo, 42000, Pachuca, Hgo., México.
[5]Centro Universitario de Ciencias Exactas e Ingenierías, Universidad de Guadalajara, 44430, Guadalajara, México.
noel.toto@utectulancingo.edu.mx

Abstract: We developed a simultaneous phase shifting interferometric system based in coupled interferometers. The system is capable to obtain four simultaneous interferograms in a single capture, the phase shifts are controlled by placing a linear polarizer in each replica obtained. The system retrieves four interferograms with a relative phase shift of π/2 and the optical phase map is calculated using the four-step algorithm. To show the advantage of the technique, experimental results are presented for static and dynamic transparent samples.

1. Introduction

Currently Phase Shifting Interferometry (PSI) techniques have been developed allowing the study of static and dynamic events by employing polarization techniques and precision optics, such as pixelated masks, holographic elements or diffractive elements, these systems allow the capture of several interferograms simultaneously retrieving optical phase variation instantaneously [1-3]. However, some of these components are expensive, or they must perform specialized alignment procedures. For these reasons, the implementation of a simultaneous phase shift technique is proposed. Our proposal is composed by the combinations of three systems: A polarizer interferometer allowing generating two beams at its output with orthogonally linearly polarization states, and two Michelson interferometers which generates four replicas, as a result, eight beams are generated at its output and by alignment procedures, four interference patterns are obtained. The system is based on polarization a phase shifting technique which introduces a controllable phase shift on each of the replica controlled by a polarizer [3].

2. Experimental Set-up

The setup is presented in Fig.1. A 630 nm laser with 30mW output is used as light source. A spatial filter system (SFS) and a collimating lens L0 generates a plane wave front which passes through a linear polarizer (P45) with fast axis orientation at 45°. The output of the MZI generates two beams with orthogonal linear polarization states. After the output of the MZI, two replication systems are used: 1) a Michelson configuration composed by a beam splitter and mirrors [M3, M4], Fig 1-MI and 2) a beam splitter system (BSS) composed by a beam splitter, Fig 1-BSS. Mirror M3 to M5 are aligned according to each replica obtained. The interference pattern is obtained and can be depicted as the common interferogram equation with a phase difference $\boldsymbol{\phi(x,y)}$ between both beams and a controllable phase shift twice the fast axis orientation,$\boldsymbol{\psi}$, of the polarizer as

$$I(x,y) = A^2 + B^2 + AB\cos\left[2\psi - \phi(x,y)\right] \tag{1}$$

where A^2+B^2 corresponds to the bias term and AB the amplitude modulation. Considering the four patterns generated by the system, each replica obtained will need its polarizer (at the polarizer array) at the following angles $\psi_1 = 0$ $\psi_2 = \pi/4$ $\psi_3 = \pi/2$ $\psi_4 = 3\pi/4$ with a respective phase shifts of $0,\ \pi/2,\ \pi,\ 3\pi/2$; the phase at each point is [4]:

$$\phi(x,y) = tan^{-1}\left[\frac{I_2 - I_4}{I_1 - I_3}\right] \tag{2}$$

The phase variations are converted to OPD variations by using, $\boldsymbol{OPD = [\lambda\phi(x,y)]/2\pi}$, each interferogram was low pass filtered and we employed the Quality-Guided Path Following Method [5] for unwrapping the phase.

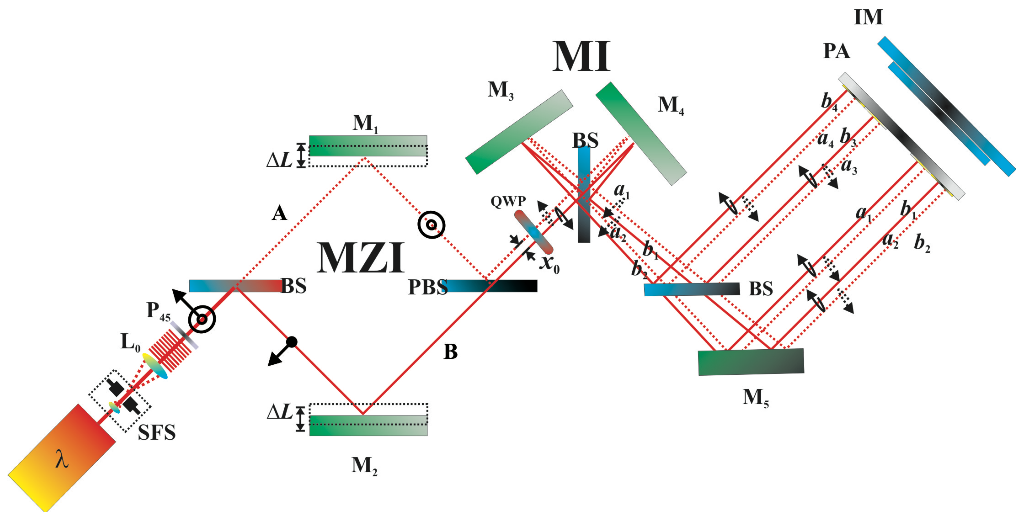

Figure 1. Single shot Mach-Zehnder Interferometer (MZI) composed by two replication systems.

3. Experimental Results

The setup is presented in Fig.1. The optical system uses a He-Ne laser (635 nm) and a CMOS camera with a resolution of 2048 x 1536 pixels. Figure 2(a) shows the interferograms generated for the wavefront and Fig. 2(b), the resulting OPD.

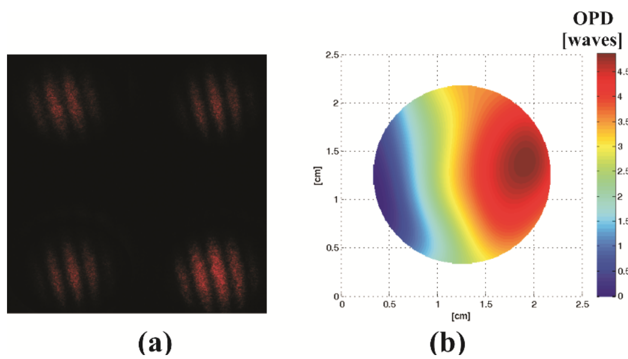

Figure 2. Wavefront. (a) Four simultaneous interference patterns. (b) OPD in waves. Scale: 2.5 cm × 2.5 cm

4. Final remarks

We report a simultaneous phase shifting technique based in a MZ interferometer and coupled systems (a Michelson interferometer and cube beam splitter), the complete implementation can generate four interference patterns with independent phase shifts.

References

[1]. P. Carré, “Installation et utilisation du comparateurphotoélectrique es interferétiel du Bureau International des Poids et Measures,” Bureau International des Poids et Measures 2, 13-23 (1966)
[2]. Wyant, J.C., “Use of an ac Heterodyne Lateral Shear Interferometer with Real-Time Wavefront Correction Systems,” Appl. Opt., 14, 2622(1975).
[3]. Toto-Arellano N. I., Serrano-García D. I., Martínez-García A., Rodríguez Zurita G., and Montes-Pérez A., “4D profile of phase objects through the use of a simultaneous phase shifting quasi-common path interferometer,” Journal of Optics, 13(11), 2011, pp. 115502.
[4]. Malacara D., Servin M., Malacara Z., “Phase Detection Algorithms in interferomgram Analysis for Optical Testing,” Wiley, New York, 2005.
[5]. Ghiglia C. and Pritt M. D., Chapter .4 in “Two-Dimensional Phase Unwrapping: Theory, Algorithms, and Software” (New York: John Wiley and Sons, 1998).

Study of the response of the NOLM experimental scheme to polarization in mode-locking and continuous-wave

J R Martinez-Angulo[1], J C Hernandez-García[1,2], J H Barron-Zambrano[3], J M Estudillo-Ayala[1], C M Carrillo-Delgado[1], J A Martin-Vela[1] and R Rojas-Laguna[1]

[1]Departamento de Electrónica, División de Ingenierías DICIS, Universidad de Guanajuato, Carr. Salamanca-Valle de Santiago Km 3.5 + 1.8, Comunidad de Palo Blanco, Salamanca, Gto. 36885, México
[2]Consejo Nacional de Ciencia y Tecnología, Insurgentes Sur 1582, Del. Benito Juárez, 03940, México
[3]Universidad Autónoma de Tamaulipas, Matamoros S/N, Zona Centro, CP 87000, Cd. Victoria, Tamaulipas, Mexico
Author e-mail address: jchernandez@ugto.mx

Abstract: In this work, an experimental analysis of light transmission is shown for both continuous and pulsed operation; for a low power Nonlinear Optical Loop Mirror (NOLM) scheme. The NOLM configuration is composed of $39\ m$ of low birefringence and highly twisted standard SMF-28 fiber (5 turns/m) and a QWR. The results obtained show that the transmission can be adjusted by rotating the QWR and varying the birefringence, as well as the torque in the NOLM output arms.

1. Introduction

The NOLM [1], consisting of a symmetrical coupler and low birefringence fiber with torsion and Quarter Wave Retarder (QWR), is still an excellent device for use in applications such as: ultra-fast switching [2], demultiplexing [3], pulse amplitude regulation on passive mode mooring fiber optic lasers as a saturable absorber [4], among others. The operation of the NOLM is basically based on Nonlinear Polarization Rotation (NPR) as is mentioned in [5], where a study of the changes in the intensity dependent polarization state due to Self-Phase Modulation and Cross-Phase Modulation (XPM) is shown, when orthogonally polarized single pulse components propagate within the optical fiber. In this work, an experimental analysis of the light transmission is shown, both for the continuous and pulsed regime, taking care of the polarization at the input of the NOLM; the scheme has a QWR to generate an asymmetry, and thus obtain a phase difference as a result of the XPM.

2. NOLM operation

The retarder device allows changing the polarization of the input, so that the transmission characteristic of the device is achieved due to the different intensity of the non-linear effects affecting each type of beam polarization [6].

$$T_L = \frac{1}{2} - \frac{1}{2}\cos(2\alpha) cos\left(\frac{1}{2}\beta L P_{in} + 2\alpha\right) \tag{1}$$

$$T_c = \frac{1}{2} - \frac{1}{2}\cos\left(\frac{1}{4}(sen(2\psi)\beta L P_{in}\right) \tag{2}$$

Where α is the angle of the plate, $\gamma, \beta = 1\, W^{-1}km^{-1}$ (typical value for a standard fiber (SMF-28), as nonlinear coefficient, P_{in} Input power, L is the fiber length and ψ is the input angle for a linear polarization input. The equations for linear transmission are the parameter of $\alpha = 0$.

3. Description of the scheme

The figure 1, shows the scheme used, where for change in CW and pulse mode for NOLM input, is used as an optical power supply the output of the Figure-eight fiber Laser (F8L) scheme, the pulses are generated with repetition rate at $f_r = 939$ Khz (Period $T = 1.0650$ μs), $P_{out} = 5.92\, mW$.

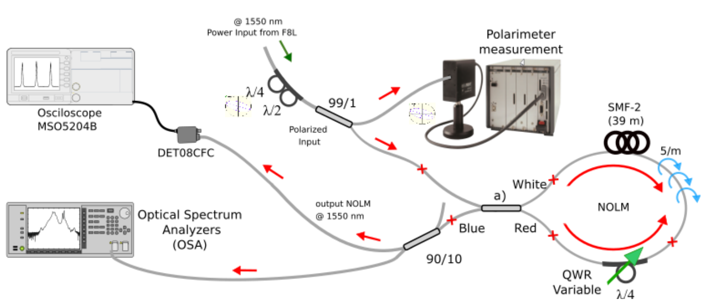

Fig. 1. Experimental NOLM scheme

4. Experimental results

Figure 2a and 2b, shows the transmission behavior of the NOLM when using noise like pulses (NLPs) [7] and a linear input. Where an oscillating signal is observed in the transmission as the angle of the QWR plate varies. The transmitted power starts from 0 and increases to 0.01 when the QWR plate is set to $40°$, then decreases the power at $0.6234x10^{-3}$ to an angle of $85°$. As the QWR plate continues to be set, the power increases to 0.04832; this value is due to a maximum transmission with an angle of 155°. The figure 2c and 2d shows the the behaviour for an circular polarization at the NOLM input.

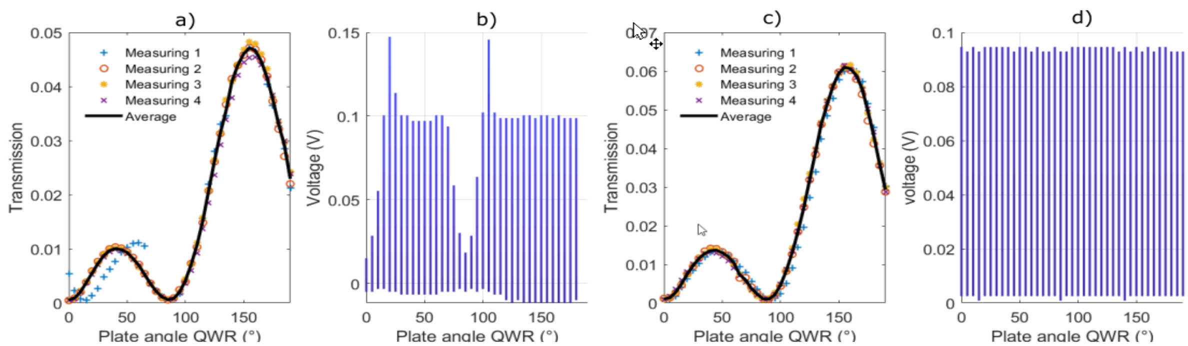

Fig. 2. a) Transmission NOLM response with mode-locking (linear polarization) and b) evolution of voltage to the output, c) Transmission NOLM response with continuous-wave (circular polarization) and d) evolution of voltage to the output.

5. Conclusions

In the proposed laser scheme, polarization evolves differently by including a non-linear device in the NOLM array such as the highly twisted fiber for polarization change. This evolution of the transmission was observed as a function of the variation of the QWR rotation angle, and a low birefringence fiber of 5 turns / m. which caused a change in the polarization and therefore a change in the behavior of the transmittance at the output at a low power at the NOLM input.

Acknowledgements

This work was supported by the Catedras CONACyT project No. 3155, CONACyT 'Ciencia Básica' projects No. 257691, Universidad de Guanajuato with the " Convocatoria Institucional de Investigación Científica 2018" CIIC 89/2018 and by the Universidad Autónoma de Tamaulipas with fellowship No. 511-6/17-6886.

References

[1] N. J. Doran and D. Wood, "Nonlinear-optical loop mirror," *Optics Letters,* vol. 13, pp. 56-58, 1988/01/01 1988.
[2] V. Vali and R. W. Shorthill, "Fiber Laser Gyroscopes," in *1976 SPIE/SPSE Technical Symposium East*, 1976, p. 6.
[3] A. Bogoni, P. Ghelfi, M. Scaffardi, and L. Poti, "All-optical regeneration and demultiplexing for 160-gb/s transmission systems using a NOLM-based three-stage scheme," *IEEE Journal of Selected Topics in Quantum Electronics,* vol. 10, pp. 192-196, 2004.
[4] I. N. Duling, "All-fiber ring soliton laser mode locked with a nonlinear mirror," *Optics Letters,* vol. 16, pp. 539-541, 1991/04/15 1991.
[5] B. Ibarra-Escamilla, E. A. Kuzin, O. Pottiez, J. W. Haus, F. Gutierrez-Zainos, R. Grajales-Coutiño, *et al.*, "Fiber optical loop mirror with a symmetrical coupler and a quarter-wave retarder plate in the loop," *Optics Communications,* vol. 242, pp. 191-197, 2004/11/26/ 2004.
[6] O. Pottiez, E. A. Kuzin, B. Ibarra-Escamilla, and F. Méndez-Martínez, "Theoretical investigation of the NOLM with highly twisted fibre and a λ/4 birefringence bias," *Optics Communications,* vol. 254, pp. 152-167, 2005/10/01/ 2005.
[7] O. Pottiez, H. E. Ibarra-Villalon, Y. Bracamontes-Rodriguez, J. A. Minguela-Gallardo, E. Garcia-Sanchez, J. P. Lauterio-Cruz*, et al.*, "Soliton formation from a noise-like pulse during extreme events in a fibre ring laser," *Laser Physics Letters,* vol. 14, p. 105101, 2017.

Phase Retardation Parameters Measurement by a Dual Rotating Polarizer Polarimeter

David I. Serrano-García[1], Humberto Macías-Mendoza[1], Jorge L. Flores[1], Guillermo García-Torales[1], Geliztle A. Parra-Escamilla[1] and Antonio Muñoz[2]
[1]Electronic Engineering Department, University of Guadalajara, Av. Revolución No. 1500, CP. 44430 Guadalajara, Jalisco, México
[2]Engineering Department, Universidad de Guadalajara, Av. Independencia Nacional 151, C.P. 48900 Autlán, Jalisco, México
david.serrano@academicos.udg.mx

Abstract: We present a polarimetric system dedicated to retrieving elliptical phase retardation properties by rotating two linear polarizers. We proposed a demodulation algorithm based on the modulation intensity obtained. The polarimetry setup employs a monochrome camera as detection system and a HeNe laser as light source. Simulation and experimental results in transparent samples are presented showing the feasibility of the proposal.

1. Introduction

Polarimetry is an experimental technique to determine optical properties of a sample by measuring the polarization variation of light reflected or transmitted by the sample providing extra measurement metrics. Polarimetric measurements have been applied in atmospheric sensing for characterizing the pollution particles on the environment [1,2] and climate variations [3] to mention some. Several polarimeter designs to determine the Mueller matrix information can be found in the literature, for example, based on dual rotating retarder configuration [4], phase modulators [5] and the use of liquid crystal retarders [6]. The Mueller matrix information is arranged in a 4×4 matrix and it can be decomposed in three polarimetric properties known as diattenuation, retardance, and depolarization. These properties describe the polarization dependence of attenuation, retardance and its possibility to maintain the polarization properties of the light that pass through it [17]. We propose a technique for retardance polarization measurement based on a dual rotating polarizer arrangement.

2. Dual Rotating Polarizer Polarimeter Sensitive to Elliptical Retardation Parameter

The optical setup consists of a laser illumination source of $\lambda = 632.8nm$, spatial filter and beam expander lens, three linear polarizers $[LP(0°), LP(\theta), LP(4\theta)]$ and a monochrome camera for capture the two-dimensional distribution of the intensity, figure 1. The first polarizer, $LP(0°)$, acts as an orientation reference of the measurement and the other ones, $[LP(\theta), LP(4\theta)]$, rotate at an angular velocity ratio 1:4 employing an electronic controlled mechanical rotation stage. The transparent sample is treated as an elliptical retarder, $ER(\theta_s, \delta_s, \varphi_s)$ and it is placed between the last two polarizers. Our approach is based on the usage of three linear polarizers [LP_0, LP_1, LP_2], and the sample is depicted as an elliptical retarder [ER] described in [8]. By following the polarization states after each component and retrieve the theoretical detected intensity we could successfully retrieve the ellipticity parameter of the retarder sample distributed in three parameters: fast axis orientation θ_s, total retardance δ_s and an ellipticity related parameter φ_s.

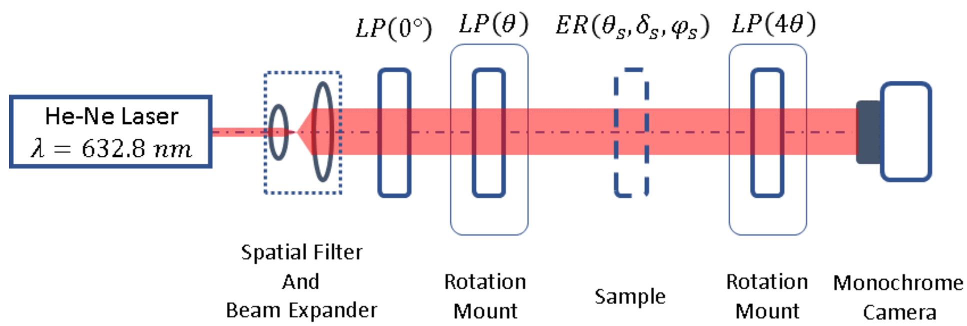

Figure 1: Dual rotating polarimeter sensitive to elliptical retardance parameters.

3. Numerical Simulations and Experimental Results

We conducted a series of computer simulations to test the performance of our approach. Figure 2.a) shows the retardance variation, δ_s, following a radial distribution laying in a $25 \pm 5°$ range; Fig. 2.b) shows the angular variation, θ_s, laying in a range of $45 \pm 25°$ and Fig. 2.c) the ellipticity phase parameter, φ_s, of $10°$ equally distributed in space. Simulations were performed in a grid of 200x200 pixels. Uniform distributable noise was added in the input stokes vector with $S_0 = .9875 \pm .012$ with non-polarized light. The noise emulates variations on the illumination source during the measurement. Figure 2 d) to f) shows the output results obtained through the simulation. We made a retardance variance phantom by stacking several layers of transparent scotch tapes as it is commonly used in photoelasticity experiments due to the induced birefringence. Figure 3 depicts preliminary experimental results with the phantom showing 6 regions. The first region corresponds to the response in the air, region 2 corresponds to the response obtained with the glass slide, region 3 corresponds to one layer of the scotch tape, region 4 with 2 layers, region 5 with 3 layers and region 6 with 4 layers. Figure 3 a) shows one intensity frame, θ=0°, b) the arrangement of the scotch tape layers on the glass slide, c) retardance $\delta_s(x, y)$, d) the angular orientation $\theta_s(x, y)$ and e) the ellipticity related parameter $\varphi_s(x, y)$.

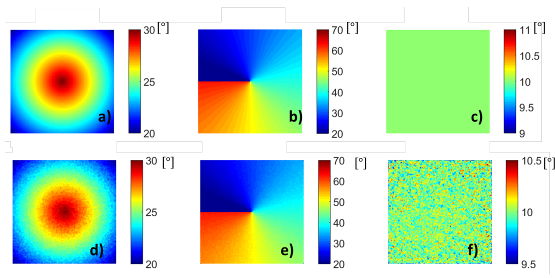

Figure 2.- Simulation results obtained by emulating variation variations at the input light.

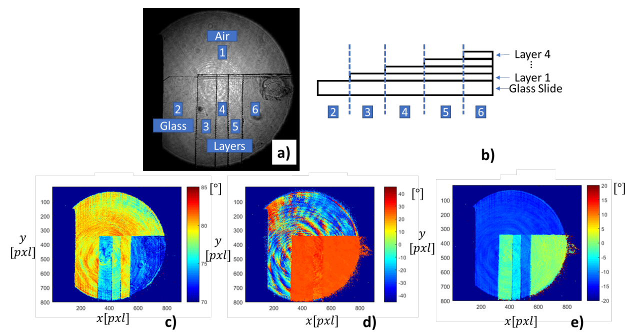

Figure. 3. Stacked layers of scotch tape emulating a retardance variation sample. Six regions are identified, 1) Air, 2) Glass slide and 3) to 6) corresponds from 1 to 3 stacked layers.

4. Conclusion and Final Remarks

We developed a retardance dependent polarimeter based on a dual rotating polarizer configuration. Through the Mueller matrix approach, a demodulation algorithm was developed by obtaining the frequency response due of the rotating polarizer used on the detection.

References

[1] J. C. Roger, R. Santer, M. Herman and J. L. Deuzé, "Polarization of the solar light scattered by the earth-atmosphere system as observed from the U.S. shuttle," Remote Sensing of Environment, Vol. 48 (3) pp. 275-290. (1994).
[2] G. van Harten, J. de Boer, J. H. H. Rietjens, A. Di Noia, F. Snik, H. Volten, J. M. Smit, O. P. Hasekamp, J. S. Henzing, and C. U. Keller, "Atmospheric aerosol characterization with a ground-based SPEX spectropolarimetric instrument," Atmospheric Measurement Technology, Vol. 7, pp 4341–4351, (2014).
[3] D. Li, N. Zeng, D. Zhan, Y. Chen, M. Zeng and H. Ma, "Differentiation of soot particulates in air using polarized light scattering method," Applied Optics, Vol. 56 (14), pp. 4123-4129. (2017)
[4] D. H. Goldstein, "Mueller matrix dual-rotating retarder polarimeter," App. Opt. 31(31) pp. 6676–6683, (1992).
[5] E. Compain, B. Drevillon, "Complete high-frequency measurement of Mueller matrices based on a new coupled-phase modulator," Review of Scientific Instruments, Vol. 68 (7), pp. 2671–2680 (1997).
[6] B. L. Boulesteix, A.D. Martino, B. Drévillon, L. Schwartz, "Mueller polarimetric imaging system with liquid crystals, Applied Optics, Vol. 43 (14), pp. 2824–2832, (2004).
[7] S. Y. Lu, R.A. Chipman, Interpretation of Mueller matrices based on polar decomposition", Journal of the Optical Society of America A, Vol. 13 (5), pp. 1106–1113 (1996).
[8] D. Kliger and J. Lewis, Polarized Light in Optics and Spectroscopy (Academic, 2012).

Differential interference contrast video microscope using pixelated polarization camera

Yukitoshi Otani, Wataru Takano, Shuhei Shibta, Nathan Hagen
Department of optical Engineering / Center for Optical Research and Education (CORE)
Utsunomiya University, Tochigi, Japan
Author e-mail address: otani@cc.utsunomiya-u.ac.jp

Abstract: We propose a differential interference contrast (DIC) microscope for phase distribution analysis of a small sample. Its phase and amplitude are analyzed by phase shifting technique by a polarization camera. We succeeded to measure phase distribution of an alive fish and its egg as bio-samples. It is also demonstrated to show a 3D structure analysis by optical sectioning whose sensitivity reaches to as same as for an optical coherence microscopy (OCT).

1. Introduction

In the field of biology, it is important to analyze inside structures of a living bio-sample. The most common method is to observe it y a microscope after staining a specific tissue for fluorescence. There are some advantages, such as visualization of living cell and simultaneous cell recognition by multiple staining. However, disadvantages show requirement for staining and damaging by fluorescent dye. To overcome these problems, a differential interferometric contrast (DIC) microscope has been proposed for analyzing detailed structures, observing small step height on the surfaces, and high sensitivity of optical sectioning [1-3]. However, previous reposts for the DIC microscopes had a difficulty to be extended to a quantitative 3D reconstruction of microstructures of specimen. Ishiwata succeeded analyze it using a liquid crystal modulator but it is difficult to analyze real-time phenomena [4]. In this report, we propose a snapshot measurement of 3D reconstruction of inside structure by differential interference contrast (DIC) microscope using pixelated polarization camera. We also focus to reconstruct 3D structure by optical sectioning whose sensitivity reaches to as same as for an optical coherence microscopy (OCT).

2. Principle of differential interference contrast video microscopy

Figure 1 shows a differential interference contrast (DIC) microscopy as same as a shearing interferometer between two orthogonal polarized beams that pass through slightly different areas with amount of the shear as Δ of a transparent sample. It visualizes the optical path difference between two beams of light. After passing through a sample, phase of two wave fronts change independently according to thickness of sample as as same as optical path. They combine two wave frons again in the Nomarski prism. We can observe interferogram after analyzer and its structure information includes phase and amplitude data. It is not so easy to analyze quantitative phase data from interferogram. We can detect them using phase shifting technique by polarization camera. Two DIC images with different retardations makes phase difference as $\pm\delta$. By using polarization camera, we capture two images with $\pm 45^{o}$ of azimuthal angle of polarizer and after applying deconvolution algorism, such as FFT decopose MTF and inverse FFT, we can obtain real phase data.

An optical sectioning of DIC microscope is achieved as same as confocal microscope. It is possible to determine a 3D reconstruction when we moved a sample along to z-direction by z motor stage.

3. Experimental results of Principle of differential interference contrast video microscopy

Figure 2 shows a blood flow in an egg of Medaka fish with 10msec per flame. We can observe artery and chorda. Figure 3 shows a 3D sectioning of a head of transparent Medaka. In conclusions, a DIC microscope with polarization camera is proposed to analyze a dynamic measurement without staining method. It is also possible to detect with snapshot. A 3D reconstruction is demonstrated by optical sectioning.

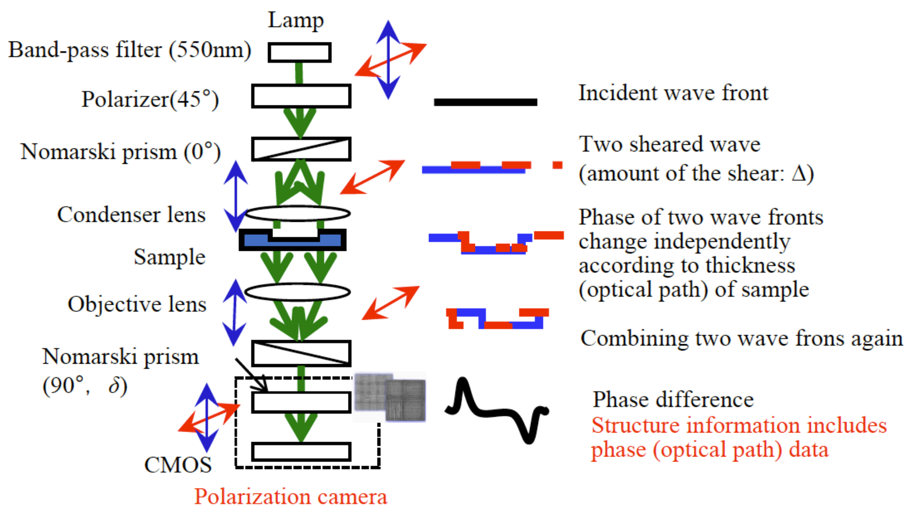

Fig. 1. Differential interference contrast (DIC) microscopy by polarization camera

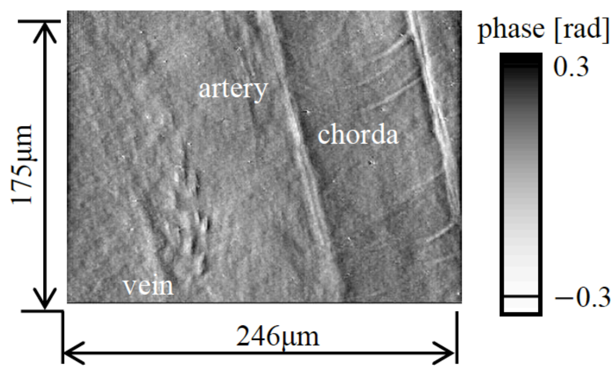

Fig.2 Sectioning of blood flow in an egg of Medaka.

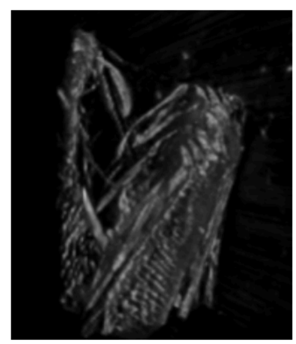

Fig.3 3D reconstruction of a head of transparent Medaka.

4. Conclusion

We proposed a snapshot measurement of 3D reconstruction of inside structure by differential interference contrast (DIC) microscope using pixelated polarization camera. It is succeeded to reconstruct a 3D structure by an optical sectioning whose sensitivity reaches to as same as for an optical coherence microscopy (OCT).

Acknowledgements

The authors acknowledge the funding support provided under The Project for Bio-Imaging and Sensing at Utsunomiya University and useful discussion with Dr. H.Ishiwata at Olympus corporation.

References

[1] D. L. Lessor, et.al. : J.Pot.Soc.Am., 69 (1979) pp.357-366.
[2] J. S. Hartman, et.al.: Appl. Opt., 19 (1980) pp.2998-3009.
[3] J. S. Hartman, et.al.: Appl. Opt., 20 (1981) pp.2665-2669.
[4] H Ishiwata,et.al. : Opt. Comm, 282 (2009) pp.117-126.

Limits on experimental Mueller-polarimeter errors including the eigenvalue calibration method

N.C. Bruce, O.G. Rodríguez-Herrera, J.M. Lopez-Tellez*, O. Rodríguez-Nuñez,
Instituto de Ciencias Aplicadas y Tecnología, Universidad Nacional Autónoma de México, CDMX, México
*College of Optical Sciences, University of Arizona, 1630 E. University Blvd., Tucson, AZ 85721, USA
neil.bruce@icat.unam.mx

Abstract: An optimized Mueller-matrix polarimeter is simulated and optimized by finding the configurations of the polarization state generator and polarization state analyzer that give the minimum condition number. The eigenvalue calibration procedure is used to reduce the errors in the final calculated Mueller matrix. Then, noise is included in the measurement of the polarimeter intensities, and controlled errors are introduced to the polarimeter configuration to simulate more realistic experimental conditions. The error in the final measured Mueller matrix is calculated as a function of these configuration errors. It is found that the alignment of the retarder axes in the polarimeter is much more important than the use of the ideal, optimized retardance values. In particular, the misalignment of the retarders farthest from the sample is the error source with highest impact in the precision of the polarimeter. The limiting error values for which the eigenvalue calibration procedure works are also found.

1. Introduction

Polarimetry is being used in many applications, such as remote sensing, imaging, microscopy and metrology. Traditional polarimeters can use rotating fixed retarders but rotating polarization components can cause vibrations in optical systems and have speeds limited by mechanical restrictions. Non-rotating polarization components, such as electro-optic cells or liquid crystals, which have changes in retardance with changes in applied voltage are now being used more in polarimetry. Liquid crystal cells have some advantages over other methods: small size and weight, fast response and small controlling voltages (typically in the range of 0-10V). However, there are still experimental errors which affect results, so calibration techniques have been developed, using known samples, to calculate and remove the effect of these errors. We have worked with Mueller polarimeters and we have found that the eiegenvalue calibration scheme is robust and reliable for correcting many of the errors in the polarimeter. However, it is clear that any calibration method will not work if the random measurement errors and/or the systematic polarimeter errors are too large.   In this work a numerical study is carried out to find the experimental conditions necessary in a Mueller-matrix polarimeter.

2. Theory

The complete polarization characterization of a sample is its Mueller matrix M, defined by the relationship between a Stokes vector incident on the sample, S^{inc}, and the corresponding Stokes vector leaving the sample, S^{det} ; $S^{det} = M\, S^{inc}$ [1]. A typical Mueller matrix polarimeter, measures the Mueller matrix of the sample by constructing a minimum of 16 different and independent combinations of incident and detected Stokes vectors and detecting the intensity in the first element of S^{det} [2,3]. For the general case of N incident polarization states and N detected polarization states, the characteristic matrices of the polarimeter can be constructed [2]

$$\boldsymbol{P^{inc}} = (\boldsymbol{S^{inc1}} \quad \boldsymbol{S^{inc2}} \ \dots \ \boldsymbol{S^{incN}}) \qquad \boldsymbol{P^{det}} = (\boldsymbol{S^{det1}} \quad \boldsymbol{S^{det2}} \ \dots \ \boldsymbol{S^{detN}}) \tag{1}$$

Tyo [11] showed that the propagation of the experimental errors from the measured intensity values for each of the PSG and PSA combinations is determined by the condition numbers of these matrices. For a measurement configuration to be optimized, both of these condition numbers must be as small as possible, and Tyo showed that, for $N=4$, the minimum condition number is 1.7321. The polarimeter was optimized following the procedure discussed by DeMartino [4]. This process involves numerically sampling the polarimeter parameters, retardance values and retarder fast-axes positions, over the full range of their possible values, and calculating the condition number for each configuration. The cases with the minimum value of condition number are stored, to be used as the base values in the error-analysis simulation. The values of the optimized polarimeter for the retarder fast-axes positions were chosen to be [4]

$$\theta_1 = \theta_4 = 27.4° \qquad \theta_2 = \theta_3 = 72.4° \tag{2}$$

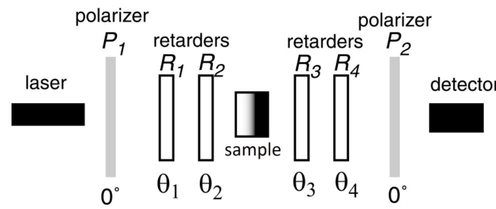

Fig. 1: Experimental setup of a Mueller matrix polarimeter

where the subindex indicates which retarder the axis position refers to, and the retardance values used in the PSG and the PSA are given by the sequence

$$\begin{aligned}(\boldsymbol{\delta_1}, \boldsymbol{\delta_2}, \boldsymbol{\delta_3}, \boldsymbol{\delta_4}) = {} & (\Delta_1,\Delta_1,\Delta_1,\Delta_1),(\Delta_1,\Delta_1,\Delta_1,\Delta_2),(\Delta_1,\Delta_1,\Delta_2,\Delta_1),(\Delta_1,\Delta_1,\Delta_2,\Delta_2),(\Delta_1,\Delta_2,\Delta_1,\Delta_1),(\Delta_1,\Delta_2,\Delta_1,\Delta_2),\\ & (\Delta_1,\Delta_2,\Delta_2,\Delta_1),(\Delta_1,\Delta_2,\Delta_2,\Delta_2),(\Delta_2,\Delta_1,\Delta_1,\Delta_1),(\Delta_2,\Delta_1,\Delta_1,\Delta_2),(\Delta_2,\Delta_1,\Delta_2,\Delta_1),(\Delta_2,\Delta_1,\Delta_2,\Delta_2),\\ & (\Delta_2,\Delta_2,\Delta_1,\Delta_1),(\Delta_2,\Delta_2,\Delta_1,\Delta_2),(\Delta_2,\Delta_2,\Delta_2,\Delta_1),(\Delta_2,\Delta_2,\Delta_2,\Delta_2) \qquad (3)\end{aligned}$$

with $\Delta_1 = \mathbf{135°}$ and $\Delta_2 = \mathbf{315°}$. In the simulation there was one error associated with each of the values of the angle of the retarder axes, Ec. (2), and one error for each of the retardance values, Ec. (3).

3. Results

For the results shown here the total rms error in the known calibration sample is given by the rms of the difference between the ideal Mueller matrices and the calculated Mueller matrices. From Figs. 2 and 3 it can be seen that the permitted condition number is much closer to the optimized system when the intensity measurement noise is higher, and that the angles of the retarder axes have much tighter tolerances than the retardance values. This means that the retarder axes values must be set more precisely in any polarimeter experiment [5,6].

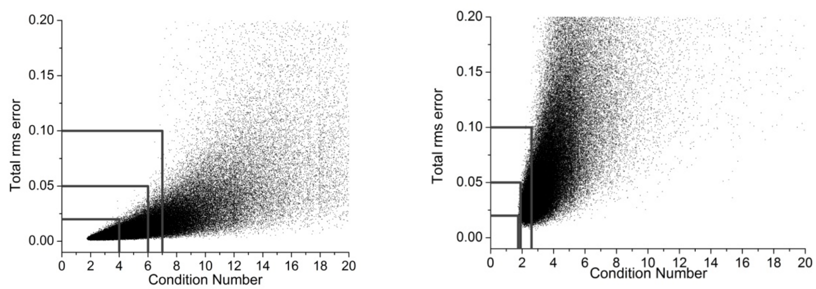

Fig. 2: Total rms error versus condition number for a intensity noise of 0.5% (left) and 5.0% (right).

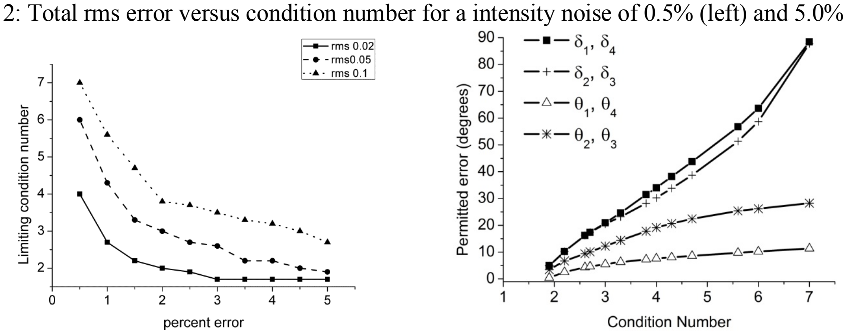

Fig.3: Limiting condition number versus intensity noise for different final rms error values (left), and the permitted parameter errors as a function of condition number (right).

References

1. D. Goldstein, *Polarized Light, Second Edition,* (CRC, Boca Raton 2003).
2. R.A. Chipman, "Polarimetry", in *Handbook of Optics*, M. Bass ed. (McGraw-Hill, Columbus, 1995), Chap. 22
3. D.H. Goldstein, "Mueller matrix dual-rotating-retarder polarimeter," Applied Optics, **31**, 6676-6683 (1992)
4. A. de Martino, Y.-K. Kim, E. García-Caurel, B. Laude and B. Drévillon, "Optimized Mueller polarimeter with liquid crystals," Optics Letters, **28**, 616-618 (2006)
5. N.C. Bruce, J.M. López-Téllez, O. Rodríguez-Nuñez, O.G. Rodríguez-Herrera, "Permitted experimental errors for optimized variable-retarder Mueller-matrix polarimeters", Optics Express, **26**, 13693-13704 (2018)
6. N.C. Bruce, O.G. Rodríguez-Herrera, J.M. López-Téllez, O. Rodríguez-Nuñez, "Experimental limits for eigenvalue calibration in liquid-crystal Mueller-matrix polarimeters", Optics Letters, **43**, 2712-2715 (2018)

Characterization of the optical behavior of an electro-optic modulator as a function of the temperature

Joel Cervantes-L[1,2], Shunya Masaki[1], Yuki Shimamoto[1], Yoshio Hayasaki[1]
[1]Electronic Engineering Department, University of Guadalajara, Av. Revolución No. 1500, CP. 44430 Guadalajara, Jalisco, México
[2]Center for Optical Research and Education (CORE), Utsunomiya University, 7-1-2 Yoto, Utsunomiya, Tochigi, 321-8585, Japan
joel@opt.utsunomiya-u.ac.jp, drjoelcervantes@gmail.com

Abstract: The Muller matrix calculation is performed to calculate the ellipticity of an electro-optic modulator as a function of the temperature. The modulator was built with two MgO:LiNbO3 crystals. The behavior of the modulator is a function of the static retardance, elliptical retardance and relative orientation between the crystals. Simulations and experimental results are presented.

1. Introduction

Electro-optic crystals modulators (EOMs) has been acquired great importance due to they can control the phase, polarization and amplitude of the light. EOMs have found many applications in different fields as can be under wireless optical communications (UWOC) [1,2] where the crystals are used to generate an optical signal for underwater blue-green laser communication. The EOMs are usually used to increases the measurements of the Stokes vectors of the light reflective from the tissues [3,4], or EOMs are used to reduce the noise in the signal in quantum cryptography [5] among others applications. $LiNbO_3$ is a common material to build these devices which are sensitive to temperature variations and also it would induce a temperature-dependent phase shift in the light [6]. An important property of the crystal as the ellipticity can be described by the Muller matrix approach and also it can be affected by temperature changes. In this report we analyze changes in the ellipticity parameter as a function o temperature by means of the Mueller Matrix approach.

2. Optical setup and mathematical model

The optical setup is shown in Fig. 1, consists of a broadband light source with a center wavelength of 840 nm and a FWHM of 50 nm. The light coming from the source was coupled and then collimated, an isolator was used whose function was acted as a linear polarizer. Then the light passes through of an electro-optic modulator built with two MgO:LiNbO3 crystals oriented at ±45º with respect to the horizontal. Finally, a linear polarizer acted as an analyzer and a photodetector was used to detect the signal. The analyzer was rotated different angles θ_A =0º, 30º, 90º and 120º.

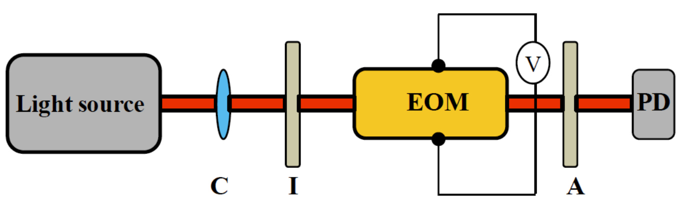

Figure 1 Schematic representation of the setup. The light coming from the light source is collimated by C, then the light passes through isolator which has a function of a linear polarizer (I). After the polarizer, the light passes through the EOM and the light is analyzed by means of a linear polarizer with θ_A orientation with respect to the axis polarization

The output Stokes vector of the signal is represented by Eq. 1 [7]. The analyzer was set an angle θ_A and the polarizer was oriented 90º. S_{in} =[1 0 0 0]^T represents non-polarized light, induced retardance is represented by δ_i and δ_s is the static retardance, w is the elliptical retardance, and the $\Delta_{\theta 1}$ and $\Delta_{\theta 2}$ represents a common and relative orientation difference between the crystals

$$S_{out}\left[w, \Delta_{\theta_1}, \Delta_{\theta_2}, \delta_s, \delta_i\right] = A\left[\theta_A\right] \cdot M_{EOM}\left[w, \Delta_{\theta_1}, \Delta_{\theta_2}, \delta_s, \delta_i\right] \cdot P\left[90^{\circ}\right] \cdot S_{in}. \quad (1)$$

Eq. 2 described the intensity [7] as a function of ellipticity w, the induced voltage V and the analyzer orientation θ_A, intrinsic parameters of the EOM.

$$I\left(\theta_A,\Delta_{\theta_1},\Delta_{\theta_2},\delta_s,\delta,w\right)=\frac{1}{4}\Big[1+\cos 2\theta_A\cos 2\delta_i+2\sin 2\theta_A\left(\Delta_{\theta 1}+\Delta_{\theta 2}+\Delta_{\theta 1}\cos 2\delta_i+4w\cos\left(\delta_i+\delta_s\right)-2w\sin 2\delta_s+4\Delta_{\theta 1}\sin\left(\delta_i+\delta_s\right)\right)\Big]. \quad (2)$$

By selecting the correct voltages and settings we will be able to retrieve the parameters of the crystals.

3. Experimental Results

We conducted an experiment by changing the orientation of the analyzer θ_A for 0º, 30º, 90º and 120º when the temperature of the room varied in a range of 24 to 29 Cº. Figure 2 shown the signal obtained for different rotations of the analyzer. For each measurement we performed a fitting of the experimental data obtained the ellipticity value w. Figure 3 shown the values of the ellipticity as a function of the temperature.

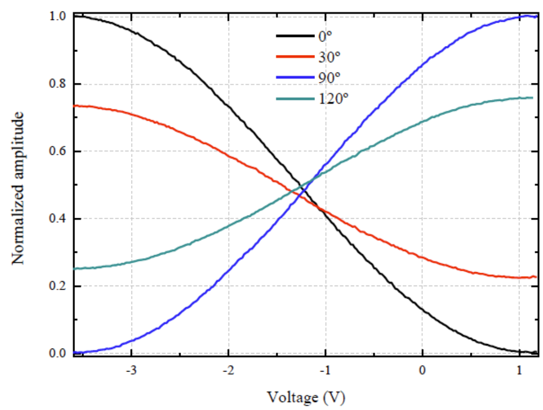

Figure 2.- Normalized amplitude by means of Eq. 2 for 0º, 30º, 90º and 120º orientations angles of the analyzer.

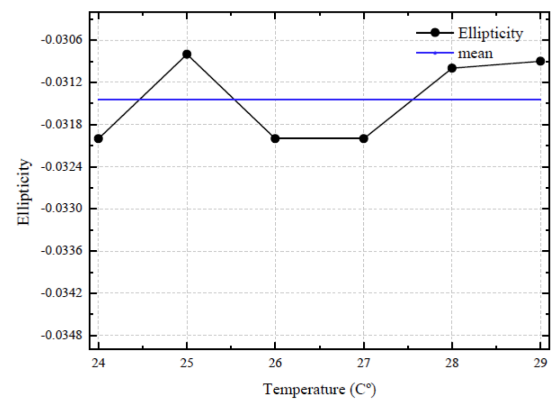

Figure. 3. Measurement of the w value as function of the temperature

4. Conclusions

We Reported the ellipticity parameters as a function of the temperature. The Mueller matrix approach was used in order to extract the w parameter by means of a fitting. Parameters as static retardance, elliptical retardance and relative orientation between the crystals were used in order to perform the measurements.

References

[1] H. Kaushal, and G. Kaddoum, "Underwater optical wireless communication", IEEE Access 4, 1518–1547 (2016).

[2] Z. Zeng, S. Fu, H. Zhang, Y. Dong, and J. Cheng, "A survey of underwater optical wireless communication", IEEE Commun. Surv. Tut. 19, 204-238 (2017).

[3] H. Song, Y. Zhao, X. Qi, Y. T. Chui, and S. A. Burns, "Stokes vector analysis of adaptive optics images of the retina," Opt. Lett. 33(2), 137–139 (2008).

[4] H. Song, X. Qi, W. Zou, Z. Zhong, and S. A. Burns, "Dual electro-optical modulator polarimeter based on adaptive optics scanning laser ophthalmoscope," Opt. Express 18(21), 21892–21904 (2010).

[5] J. Lodewyck, M. Bloch, R. García-Patrón, S. Fossier, E. Karpov, E. Diamanti, T. Debuisschert, N. J. Cerf, R. Tualle-Brouri, S. W. McLaughlin, and P. Grangier, "Quantum key distribution over 25 km with an all-fiber continuous-variable system," Phys. Rev. A 76(4), 042305 (2007).

[6] T. A. Maldonado, "Electro-optic modulators," in Handbook of Optics, M. Bass, ed. (McGraw Hill, 1995). [7] S. Y. Lu, R.A. Chipman, Interpretation of Mueller matrices based on polar decomposition", Journal of the Optical Society of America A, Vol. 13 (5), pp. 1106–1113 (1996).

[7] Joel Cervantes-L, David I. Serrano-Garcia, Yukitoshi Otani, and Barry Cense, "Mueller-matrix modeling and characterization of a dual-crystal electro-optic modulator," Opt. Express 24, 24213-24224 (2016)

Extended Abstracts

Session
SPECIAL SESSION 2: SENSORS BASED ON THE USE OF LASERS AND FIBER OPTICS

	Pg.
CURVATURE SENSOR BASED ON AN ERBIUM DOPED FIBER LASER Guzman-Chavez A. D., Vargas-Rodriguez E., Cervantes-Meza H. J., Perez-Lopez R	194
SASP: Self-adaptive speckle pattern for 3D measurement systems Danish Khan and Min Young Kim	196
Stimulated Raman scattering in visible spectrum for sensing applications O. X. Vera-Duarte, J. D. Filoteo-Razo, J. M. Estudillo-Ayala, J. C. Hernández-García, D. Jauregui-Vazquez, J. M. Sierra-Hernandez, J. R. Martinez-Angulo, R. Rojas-Laguna	198
Ring Fiber Laser Based on a Modified Mach-Zehnder Interferometer J. A. Martin-Vela, E. Gallegos-Arellano, J. M. Sierra-Hernández, D. Jauregui- Vazquez, J. C. Hernandez-Garcia, J. M. Estudillo-Ayala, E. C. Silva-Alvarado and R. Rojas-Laguna	200
Modal Fiber Interferometer with YDF-Coreless Fiber Structure Tania Lozano-Hernandez, Daniel Jauregui-Vazquez, Julian M. Estudillo-Ayala, Juan C. Hernandez Garcia, Juan M. Sierra-Hernandez and Roberto Rojas-Laguna	202
Angular deflection laser sensor K.E. Contreras-Vallejo, J.M. Estudillo Ayala, R. Rojas-Laguna, D. Jauregui-Vazquez, J.C. Hernandez-Garcia, J.M. Sierra-Hernandez, J.A.Martin-Vela	204
Experimental Study for Supercontinuum Generation with Special Optical Fibers D. Torres-González, J. M. Sierra-Hernández, D. Jáuregui-Vázquez, J. C. Hernández-García, J. M. Estudillo-Ayala and R. Rojas-Laguna	206
Semiautomatic platform for the construction of Fabry-Perot microcavities Carmen E. Domínguez-Flores, Josué I. Basulto, Daniel López-Cortés, David Monzón-Hernández	208
Suppression of Kelly sidebands on the soliton spectrum pulse using a Non-Linear Loop Mirror Mahrokh Avazpour, Georgina Beltrán Pérez, Evgeny Kuzin	210

Optimal Visual Servoing using Laser-Optic-based Structured Light with Applications in Robotic Pipe Inspection 212
Juan Echavarria, Ivan Perez, Mehran Mehrandezh, and Raman Paranjape

Temperature sensor based on a structured optical fiber 214
M. C. Alonso-Murias, I. Hernández-Romano, D. A. May-Arrioja, D. Monzón-Hernández and M. Torres-Cisneros

Automated System for Characterizing a Laser Diode Applied to the Development of Optical Fiber Laser 216
C M Carrillo-Delgado, J C Hernandez-Garcia, J M Estudillo-Ayala, J D Filoteo-Razo, O Pottiez, J P Lauterio-Cruz, R Rojas-Laguna, D Jauregui-Vazquez

Optical fiber Surface Plasmon Resonance-based temperature sensor 218
Monserrat Alonso Murias, Josué I. Basulto, J. Salvador Velázquez González, S. Marquez, and David Monzón-Hernández

CURVATURE SENSOR BASED ON AN ERBIUM DOPED FIBER LASER

Guzman-Chavez A. D.[1], Vargas-Rodriguez E.[1], Cervantes-Meza H. J.[2], Perez-Lopez R[1].
[1]Departamento de Estudios Multidisciplinarios, Universidad de Guanajuato, Col. Yacatitas, Av. Universidad S/N, zip 38940, Yuriria, Guanajuato.
[2]Facultad de Ingeniería Electrónica, Corporación Politécnico de la Costa Atlántica, Av. Los Estudiantes-Carrera 38 # 79A-167, Barranquilla, Colombia.
ad.guzman@ugto.mx

Abstract: in this work a curvature optical sensor based on an erbium doped fiber laser is presented. Here, the laser has a Fabry-Perot cavity which is formed by a Faraday rotator mirror and an interferometric system. Besides, a standard fiber optic was spliced inside the cavity and curvature was applied to it with the purpose to increase cavity losses and to induce a change in the laser transient parameters such as the time delay. It is shown that by monitoring this parameter it was possible to measure curvature with a nonlinear sensitivity of 326 ms/cm^{-1} within a curvature range from 0.76 to 2.22 cm^{-1}.

1. Introduction

Fiber optic sensors (FOS) have won special interest because of their flexibility to be used in different potential applications. Particularly FOS for measuring curvature have been used for instance in robot arms and monitoring structural deformations of buildings [1]. Nowadays, a great variety of configurations of curvature FOS, where their response is measured in the frequency domain, have been proposed. For example, multiple fiber optic arrangements for bend sensing can be found in literature which are based on different optical devices [2-5]. The disadvantages of these type of sensor is that it is needed high cost equipment to interpret the value of the measured physical variable.

In counterpart, configurations of FOS that use techniques translating the measurement to the time domain have been propounded. For instance, those based on erbium doped fiber lasers (EDFLs) to measure gases and refractive index [6] were reported. Some of these FOS based on EDFLs rely on power emission changes caused by cavity loss variations. The advantages of these kind of FOS is that it is possible to acquire and process the information easily and accurately using reliable and low cost electronics.

In this work the experimental study of a FOS based on an EDFL for measuring curvature is presented. The EDFL has a Fabry-Perot cavity which is formed by a Faraday rotator mirror (FRM) and an interferometric system (IS) of two silicon (Si) wafers which act as Fabry-Perot interferometers (FPIs). Besides, a standard fiber optic was spliced inside the cavity and in such a way that cavity losses increase as curvature is applied. These losses, affect the time delay (τ_d) that is one of the laser transient parameters. Hence, we were able to determine curvature by monitoring the τ_d with a nonlinear sensitivity of 326 ms/cm^{-1} for the curvature range from 0.76 to 2.22 cm^{-1}.

2. Experimental setup and operation principle

The sensor arrangement based on an EDFL for measuring curvature is shown in Fig. 1a. Here a piece of erbium doped fiber (EDF Liekki Er80-8/125) of 98 cm was pumped with a diode laser with λ= 976 nm. The Fabry-Perot cavity is formed by a FRM and an IS, which was formed by two Si wafers with thicknesses of 90.5 and 376 µm. The laser emission is governed by one of the maximum peaks of the interference spectrum of the IS. Due to the thermo-optic properties of the Si, the spectrum can be shifted with temperature (see Fig. 1b), so it was necessary to maintain the IS temperature at 17.7 ºC in order to keep stable the laser emission wavelength at 1562.3 nm. Inside the cavity a piece of SMF was spliced and it was bended to induce cavity losses and therefore to modify the laser transient.

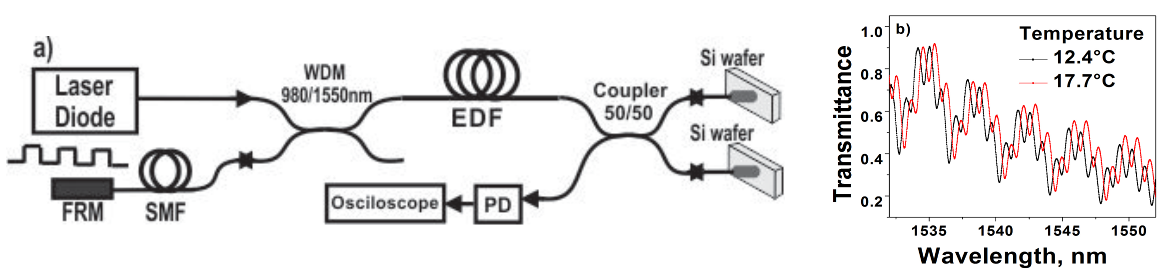

Fig. 1. a) Experimental setup of the FOS for measuring curvature. b) Interference spectrum of the IS at different temperatures.

Once the mechanism to induce cavity losses is determined, the pump power was modulated with a pulse train waveform at 20 Hz to obtain the laser transient behavior. In particular, we focused on the time delay (τ_d) that is a characteristic of the laser transient behavior. It is defined as the time from the moment when the pump is switched on and until the laser emission reaches the mid-amplitude of the level when it is stabilized (Fig. 2a). In our experimental work the laser transient behavior was measured by using a fast photodiode and recorded with an oscilloscope.

3. Experimental results

In figure 2a the measured laser transient response for different curvatures is shown. Here, it can be observed that τ_d gets longer as the curvature increases. It is because as higher the bend applied to the SMF larger are the cavity losses. Consequently, as the cavity losses increases a longer time is needed to reach the laser threshold condition [7].

In figure 2b, a detailed experimental evolution of the time delay as a function of the curvature and its exponential fit are presented. Here, the modulated pump power had a low level of 0 mW and high level of 230 mW. Besides, from this figure, it is evident the nonlinear behavior of the τ_d as the curvature increases. This behavior is due to the nonlinearity of the laser dynamics itself and the nonlinear increment of losses as a function of the curvature. Therefore, the nonlinear curvature sensitivity achieved was 326 ms/cm^{-1} for the curvature range from 0.76 to 2.22 cm^{-1}.

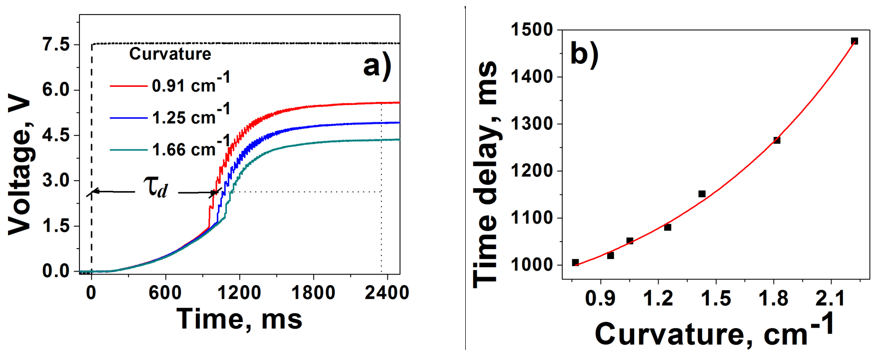

Fig. 2. a) Laser transient behavior for different curvatures. The upper trance correspond to the pump switching on. b) Laser rime delay as a function of curvature applied to the SMF.

4. Conclusions

In this work, we report a curvature optical sensor in which a piece of SMF to be bended is inserted into the cavity of an erbium doped fiber laser based on two silicon wafers. By taking advantages of the thermo-optic properties of the silicon, it was possible to maintain a stable laser emission at 1562.3 nm with a temperature of 17.7 ºC. The curvature applied to the SMF can be determined from the time delay parameter of the laser transient response. The nonlinear sensitivity achieved for the curvature range from 0.76 to 2.22 cm^{-1} was 326 ms/cm^{-1}. Finally this sensor arrangement can be used for quasi real time applications.

References

[1] H.J. Patrick, C.c. Chang, and S.T. Vohra, "Long period fibre gratings for structural bend sensing," Electron. Lett. **34**, 1773-1775 (1998).

[2] M. Cano-Contreras, A.D. Guzman-Chavez, R.I. Mata-Chavez, E. Vargas-Rodriguez, D. Jauregui-Vazquez, D. Claudio-Gonzalez, and J. M. Estudillo-Ayala, "All-fiber curvature sensor based on an abrupt tapered fiber and a Fabry-Perot interferometer," IEEE Photon. Technol. Lett. **26**, 2213-2216 (2014).

[3] Y.G. Han, G. Kim, K. Lee, S.B. Lee, C.H. Jeong, C.H. Oh, and H.J. Kang, "Bending sensitivity of long-period fiber gratings inscribed in holey fibers depending on an axial rotation angle," Opt. Exp. **15**, 12866-12871 (2007).

[4]Y.G. Han, B.H. Lee, W.-T. Han, U.-C. Paek, and Y. Chung, "Fibre-optic sensing applications of a pair of long-period fibre gratings," Meas. Sci. Technol. **12**, 778-781 (2001).

[5] K. Ni, T. Li, L. Hu, W. Qian, Q. Zhang, and S. Jin, "Temperature-independent curvature sensor based on tapered photonic crystal fiber interferometer," Opt. Commun. **285**, 5148-5150 (2012).

[6] H. Arellano-Sotelo, Yu.O. Barmenkov, and A.V. Kir'yanov, "The use of erbium fiber laser relaxation frequency for sensing refractive index and solute concentration of aqueous solutions," Laser Phys. Lett. **5**, 825-829 (2008).

[7] H.K. Hisham, G.A. Mahdiraji, and A.F. Abas, "Characterization of Transient Response in Fiber Grating Fabry-Perot Lasers," IEEE Photon. J. **4**, 2353-2371 (2012).

SASP: Self-adaptive speckle pattern for 3D measurement systems

Danish Khan[1] and Min Young Kim[1, 2 *]
[1] School of Electronics Engineering, IT College, Kyungpook National University, 1370 Sankyuk-dong, Buk-gu, Daegu, 702-701 Korea
[2] Research Center for Neurosurgical Robotic System, Kyungpook National University, 1370 Sankyuk-dong, Buk-gu, Daegu, 702-701 Korea
Author e-mail address: mykim@ee.knu.ac.kr

Abstract:
Like an autofocus system in modern digital cameras adjust the camera lens to obtain focus on the subject, the proposed system adapts itself to achieve the desired speckle size when the measuring distance or type of object is changed. This can increase the measurement range, improve the density of the 3D reconstruction and robustness to object change in any laser speckle based 3D measurement system.

1. Introduction

The use of speckle pattern for three-dimensional (3D) shape acquisition is justified and well-proven. A number of commercial 3D sensors such as Microsoft Kinect, Prime Sense, and Intel Real Sense exploit some kind of speckle pattern to retrieve the geometrical 3D information. Among different types of speckle patterns, the speckles generated by a coherent laser light are widely adopted in stereo photogrammetric systems [1-3]. The laser light reflected from a surface with variation in thickness (rough surface) produces a grainy pattern due to the interference of the scattered waves. This pattern is known as laser speckle pattern and assists in establishing the correspondence between the stereo pairs. Speckle size is an important factor to change the appearance of pattern and determines the range and resolution of the 3D measurement systems [3, 4]. Depending on the employed algorithm, an optimal speckle size is required for the accurate and dense 3D reconstructions. A number of factors depend on the speckle size, such as radius of the focal laser spot, roughness of the diffuser, aperture and focal length of the imaging system. These conditions can be optimized to achieve the required speckle size at a certain distance. But the speckle size also depends on the distance at which it is imaged by a camera. When the object goes out of a specified range the spatial resolution has to be compromised or else manually changing the speckle size is required. Furthermore, the object with different reflectance property exhibit different results on the speckle size estimation. Even at the same distance, the adjustment of speckle size is required when different objects are measured. A typical approach to change the speckle size is to change the distance between the rough surface and the observation plane. In real time systems when the objects are dynamic or continuously moving, maintaining the speckle size is a strenuous task and often disturbs the hardware setup prompting to recalibration of the system.

To cope with aforementioned issue in speckle based 3D acquisition system, we present the concept of self-adaptive speckle pattern (SASP). The pattern maintains the optimal speckle size (defined by the user) when the size changes during the measurement due to any reason.

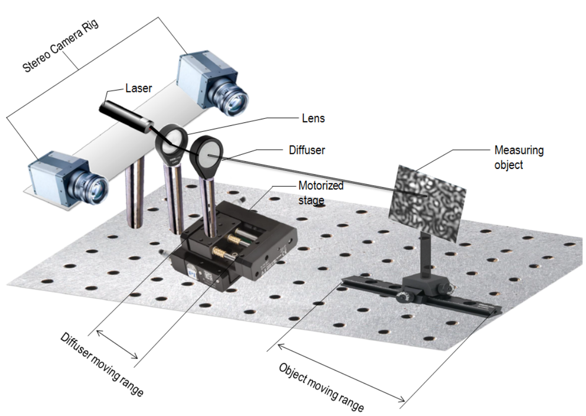

(a)

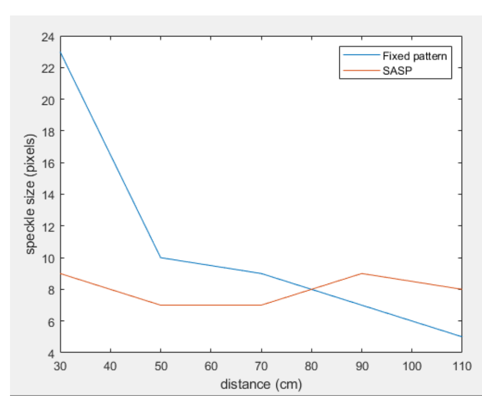

(b)

Fig. 1. (a) Hardware setup for the proposed system (b) comparison of fixed pattern vs SASP

2. Proposed system for SASP

Fig.1 depicts the optical configuration of the proposed SASP in conjunction with a stereo vision system. The laser beam is focused on a ground glass diffuser using a lens to generate the speckle pattern on the measuring object. The diffuser is fixed on a mini motorized precision linear stage (PI-M-111) connected to a DC motor controller. The stage can be moved in the backward and forward direction within the range of 25 mm. Any one of the image from the stereo pair can be used to calculate the speckle size. On the basis of the calculated speckle size, the stage can be moved to the position where the optimal speckle size can be achieved. After achieving the optimal speckle size the 3D coordinates of the object can be extracted by the stereo camera system. This paper only deals with adjusting the speckle size for 3D measurement. The process of 3D measurement is not the scope of this paper.

3. Real time speckle size calculation

The average speckle size can be estimated by calculating the autocovariance function of the digitized intensity speckle pattern[5]. The full width at half maximum (FHWM) of the Gaussian fit to the sum of the normalized autocorrelation function provides the average size of a speckle. This method works best when the entire image is full of speckles with no dark background. If the large part of image is without the speckles, it will have a needle like peak in the center with little fluctuation elsewhere. The average speckle size cannot be estimated in such case. The raw images acquired from the cameras in laser speckle based systems contain substantial amount of dark long range background as the object containing the speckles covers only some part of the image. Hence, to calculate the speckle size in real time, the part of the image containing only the speckle pattern is desired. For this purpose a framework is developed which includes following major steps:

1. Binarize the grayscale image by the following condition
$$I_B(i,j) = \begin{cases} 1\ for\ I(i,j) \geq t \\ 0\ for\ I(i,j) < t \end{cases} \tag{1}$$
Where $I_B(i,j)$ is the pixel value at the (i,j) position after binarization, $I(i,j)$ is the pixel value at the (i,j) position before binarization and t is the threshold.
2. Extract the largest blob in the binarized image using the connected components.
3. Calculate the centroid of the largest blob.
4. By using the centroid location of the binarized image, extract the 200 * 200 or 300 * 300 patch from the original greyscale image around the centroid.

The above method works on the assumption that the speckle pattern covers only the object to be measured without any additional object present in the scene. A reasonable estimate of the speckle size can be achieved using the image patch extracted from the above image processing technique as it contains some part of the object which is completely covered the speckles.

4. Results

To verify the workability of the SASP, first the speckle size is calculated at five different distances with the fixed diffuser. As can be seen in the fig.2, the speckle size is decreasing as the distance is increasing. This is due to the fact that that the speckles has low brightness and contrast with the increasing distance. To maintain the brightness of the speckle at different distance, the aperture has to be changed. In contrast, the SASP pattern maintains the optimal speckle size which is defined to be 7 to 9 pixels in this case. SASP can increase the measurement range and improve the density of the laser speckle based 3D acquisition. This system can also be used in single camera systems to maintain the speckle size at it used single image to calculate the speckle size in real time.

References

[1] M. Schaffer, M. Grosse, and R. Kowarschik, "High-speed pattern projection for three-dimensional shape measurement using laser speckles," *Applied optics,* vol. 49, pp. 3622-3629, 2010.
[2] S. Heist, P. Lutzke, P. Dietrich, P. Kühmstedt, and G. Notni, "Experimental comparison of laser speckle projection and array projection for high-speed 3D measurements," in *Optical Measurement Systems for Industrial Inspection IX*, 2015, p. 952515.
[3] D. Khan, M. A. Shirazi, and M. Y. Kim, "Single shot laser speckle based 3D acquisition system for medical applications," *Optics and Lasers in Engineering,* vol. 105, pp. 43-53, 2018/06/01/ 2018.
[4] G. Crammond, S. Boyd, and J. Dulieu-Barton, "Speckle pattern quality assessment for digital image correlation," *Optics and Lasers in Engineering,* vol. 51, pp. 1368-1378, 2013.
[5] H. Lin, "Speckle mechanism in holographic optical coherence imaging," University of Missouri--Columbia, 2009.

Stimulated Raman scattering in visible spectrum for sensing applications

O. X. Vera-Duarte[1], J. D. Filoteo-Razo[1], J. M. Estudillo-Ayala[1,*], J. C. Hernández-García[2], D. Jauregui-Vazquez[1], J. M. Sierra-Hernandez[1], J. R. Martinez-Angulo[1], R. Rojas-Laguna[1]

[1]División de Ingenierías Campus Irapuato-Salamanca, Universidad de Guanajuato, Carr. Salamanca-Valle de Santiago km 3.5+1.8 km, Comunidad de Palo Blanco, Salamanca, Gto. 36885, México
[2]CONACYT. Catedrático CONACYT, Av. Insurgentes Sur No. 1582, Crédito Constructor, Benito Juárez, 03940, México
[*]Author e-mail address: julian@ugto.mx

Abstract: In this work, we present a study of the interaction stimulated Raman scattering (SRS) of a broadband visible spectrum in thin-core fiber (TCF) for optical sensing applications by means of an end-of-fiber tip. The fiber tip is formed by a conventional optical fiber with a diameter of 10 µm and a length of 5 cm. Besides, bending deformation study for the fiber tip with the visible spectrum results are discussed.

1. Introduction

Supercontinuum (SC) generation is a nonlinear process produced by the interaction of multiple phenomena such as self-phase modulation (SPM), cross-phase modulation (XPM), stimulated Raman scattering (SRS), four-wave mixing (FWM), the formation of high order solitons, modulational instability (MI) and parametric mix [1]. SC generation in optical fibers has attracted considerable research interest in the last years, basically thanks to the development of special optical fibers, for instance, single-mode fiber (SMF), high-nonlinearity fiber (HNLF) or photonic crystal fiber (PCF) with a high nonlinear coefficient and dispersion properties. Besides, presents applications in diverse fields such as optical communication, metrology, and sensors [3]. We propose a sensor fiber tip and SC visible light source based on SRS interaction as the pump source. Hence, we study the light distribution at the spectrum changes in the visible light source. The wavelength changes are generated by bending deformation of the fiber tip.

2. Experiments and discussion

Fig. 1 shows the experimental setup for the visible light source; here a microchip passively Q-switched laser is used as a pumping source. This laser emitted at 532 nm, with 5 kHz repetition rate, 3 µJ pulse energy, and 0.75 ns pulse duration. The laser beam was coupled into a TCF with a length around 30 m by using a 10X microscope objective mounted in an XYZ translation stage; at the end of TCF was coupled conventional optical fiber tip with a diameter of about 10 µm and a 5 cm-long. The spectrum was registered with an optical spectrum analyzer Ocean Optics USB2000.

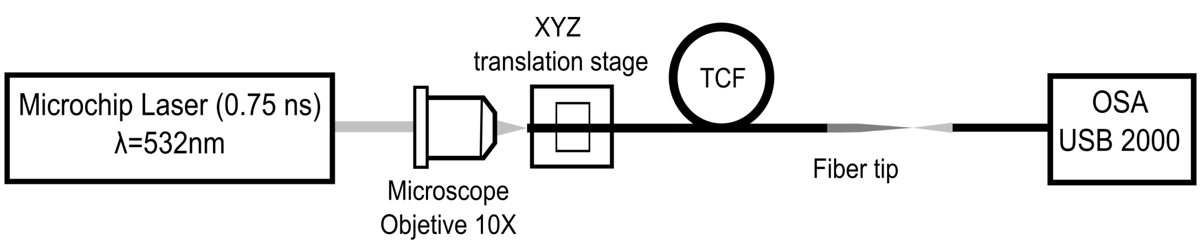

Fig. 1. Experimental setup.

Fig. 2 a) present the spectrum of SC visible light source. Where we observe the appearance of new spectrum peaks. This indicates the order Stokes spectrum emitted from the TCF. The Stokes frequency is

$$\omega_s = \omega_p - \omega_v \tag{1}$$

where ω_v represent the frequency difference between the pump and Stokes waves. In the case of pure silica, Raman gain g_R is about 13. 2 THz [3]. Six frequencies appear centered at 543.4 nm, 557 nm, 571.5 nm, 586 nm, 602 nm and 618.7 nm, respectively. Given the above result, appear sixth-order Stokes in Fig 2 a). In Fig. 2 b) present the spectra evolution gradually bending the fiber tip in fourth-order Stokes. Stokes frequency and anti-Stokes frequency are incident light beam photons are dispersed by silica molecules, by that suffer a frequency shifting [4]. These are obtained by the SBS.

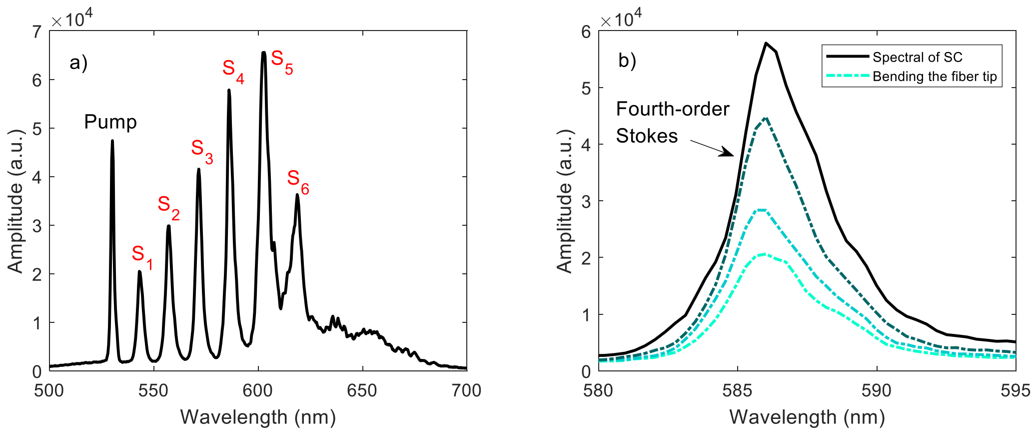

Fig. 2. a) generation of sixth-order Stokes in spectrum of SC visible light source in 30 m of TCF pumped by microchip laser. b) Spectra evolution gradually bending the fiber tip in fourth-order Stokes.

3. Conclusion

We studied experimentally the interaction SRS of a broadband visible spectrum by mean a microchip laser at 532 nm, in a length of 30 m of TCF. We observed the appearance of the sixth-order Stokes in the visible spectrum. We show the wavelength changes in the spectra gradually bending the fiber tip. This fiber tip can propose in future experiments with other measurable physical variables such as curvature and torsion.

4. Acknowledgments

J. D. Filoteo-Razo was supported by the CONACYT grant #477506. and Cátedras-CONACYT #3155; and by the University of Guanajuato *"Convocatoria Institucional de Investigación Científica 2018"* CIIC 89/2018, DAIP108/2018.

References

[1] Agrawal G, *Nonlinear Fiber Optics* (Academic Press, 2001), Chap. 13.
[2] Genty, G., Coen, S. & Dudley, J. M. "*Fiber supercontinuum sources*", J. Opt. Soc. Am. B **24**(8), 1771–1785 (2007).
[3] R. H. Stolen and E. P. Ippen. "Raman gain in glass optical waveguides", Appl. Phys. Lett. 22, 276-2278 (1973).
[4] M. A. González-Reyna, J. M. Estudillo-Ayala, R. Rojas-Laguna and E. Vargas-Rodríguez, "Experimental analysis of the interaction between modulation instability and stimulated Raman scattering in short lengths of optical fibers," 2014 International Conference on Electronics, Communications and Computers ,160-165 (2014).

Ring Fiber Laser Based on a Modified Mach-Zehnder Interferometer

J. A. Martin-Vela[1], E. Gallegos-Arellano[2], J. M. Sierra-Hernández[1]*, D. Jauregui-Vazquez[1], J. C. Hernandez-Garcia[1], J. M. Estudillo-Ayala[1], E. C. Silva-Alvarado[1] and R. Rojas-Laguna[1]

1 Departamento de Ingeniería Electrónica, División de Ingenierías, Campus Irapuato-Salamanca, Universidad de Guanajuato, Carretera Salamanca-Valle de Santiago km 3.5+1.8, Comunidad de Palo Blanco, Salamanca, Gto., C.P. 36885, México.
2 Departamento de Mecatronica, Universidad Tecnologica de Salamanca, Av. Universidad #200, Colonia Ciudad Bajio, Salamanca, Gto., C.P. 36766, México.
*jm.sierrahernandez@ugto.mx

Abstract: A laser temperature sensor based on a core-offset aluminum coated Mach-Zehnder interferometer is presented. The experimental results shown a temperature sensitivity of 28 pm/°C and a signal to noise ratio of 45 dB.

1. Introduction

In recent years, the use of fiber temperature sensors has been increased since these offers different advantages such as durability in harsh environment, high sensitivity and immunity to electromagnetic interference [1]. Moreover, these sensors can be implemented to measure different applications among them heat treatments for food, health monitoring and aeronautics [2]. In this present paper all-fiber ring cavity laser sensor based on a core-offset aluminum coated Mach-Zehnder interferometer (MZI) is proposed for temperature sensing. Here, the MZI is fabricated by core-offset fusion splicing 5 cm of single mode fiber (SMF) between two segments of SMFs and the central section is coated with aluminum by using the thermal evaporation technique [3]. The experimental results that, the laser emission wavelength is shifted when the temperature effect is applied over the aluminum coated MZI in a range from 0 to 90 ºC at 1557 nm and linewidth of 0.07 nm can be obtained.

2. Principle of Operation of the Core-Offset Aluminum Coated Mach-Zehnder Interferometer

Temperature sensor based on a fiber ring laser has previously been reported in other setup [4]. However, in this work the MZI was used as wavelength selective filter (WSF) and not as head sensing. For this reason, the authors of this work coated the core-offset MZI with aluminum in order to use both as WSF and head sensing. For the purpose of implementing the core-offset MZI three sections of conventional single-mode fiber (SMF-28) were used. The segments were fusion splicing with an electrical discharger machine (Fitel S175), the central piece of fiber was spliced with a displaced downward of 30 µm. Furthermore, the coating process was carry out in a PVD chamber equipped with a thermal evaporation system. The fiber was mounted in a simple holder and it was exposed to the vapor for several minutes until the aluminum cover all the MZI. Hence, the principle operation of this coated aluminum MZI can be explained as follows: in the first core-offset splice, a part of the energy traveling as fundamental core mode is transmitted through the core of the next section of SMF, and another part of the energy couples both as cladding-aluminum section of the next SMF. Due, to the effective refractive index difference among core and cladding-aluminum, a phase difference can be produced through the same physical length. Thus, the core, and cladding-aluminum modes travel throughout coated aluminum SMF. Here, it is important to point out, that the aluminum acts as a mirror in the cladding-metal interface and recovers some of the energy that was lost before, increasing the quantity of modes participating in the interference pattern [5]. At the second core-offset splice, part of the energy traveling through the cladding couples back into the core and interfere with the fundamental core mode, causing an interference pattern. Finally, core cladding and aluminum metal sections of the central SMF act as the MZI arms and core-offset sections act as an optical coupler.

3. Results and discussion

The experimental setup for laser temperature sensor is shown in Fig. 1a. Here, a laser diode was used as pumping source. As an active medium, 5m segment of erbium-doped fiber was used. The polarization state inside of the cavity was adjusted by using of polarization controller. Moreover, to ensure unidirectional light propagation an optical isolator was used. Furthermore, the laser output was extracted from the ring cavity by a 99/1 fiber coupler. The output was recorded with an optical spectrum analyzer (OSA, Yokogawa AQ6370B). We used a MZI both as WSF as head sensing in the setup. For this reason, in order to measure the response of the sensor, the aluminum coated MZI was fixed over a Peltier cell heated by using of a proportional-integral-derivative controller (PID) (See Fig. 1b). This temperature control device allows increase the range from 0 to 90 ºC in steps of 10 ºC. In this way, fiber laser output spectra for different temperature values are shown in Fig. 2. Here, can be observed, that the laser emission is tuned from 1557 to 1560 nm. This can be explained by the fact that the thermal coefficient for aluminum is higher than the one for silica. Therefore, by coating a silica with a metal, the enhanced volume change in the device can contribute to the fringe shift in temperature changes. Furthermore, the signal to noise ratio of the laser output was ~45 dB, which does not change significantly with the applied temperature (See, Fig. 2). In Fig. 3 a laser emission (at 1557 nm) behavior is seen, which shows a linear relationship between the wavelength spectra shifting and temperature applied. Finally, the maximum sensitivity of our sensor was of 28 pm/ºC and R^2= 0.9723 was reached.

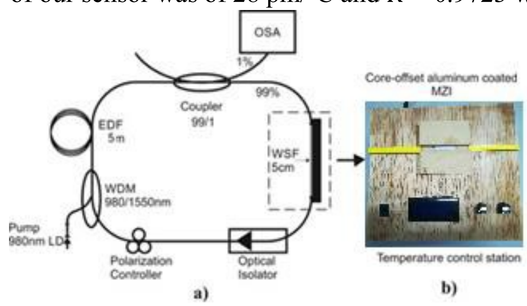

Fig. 1. a) Experimental setup of the laser temperature sensing and b) Schematic diagram of the control to change the temperature

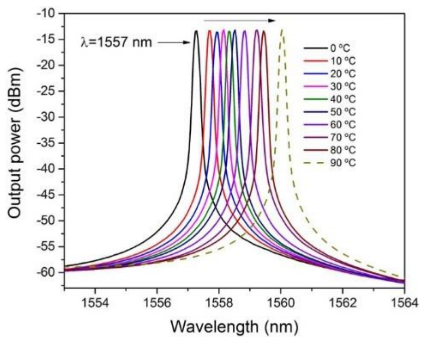

Fig. 2. Laser emission spectra for different temperatures values.

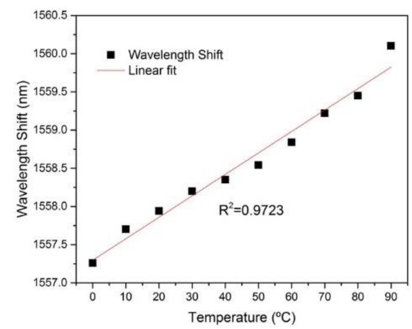

Fig. 3 Wavelength shifting as a function of the temperature.

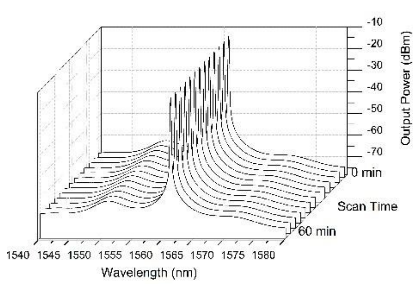

Fig. 4. Measured output spectra recorded every 5 min.

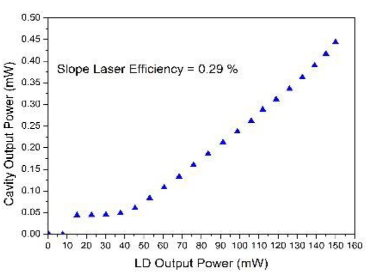

Fig. 5 Slope Laser Efficiency.

4. Acknowledgements

This work was partially funded by APOYO A LA INCORPORACION DE NUEVOS PTC DEL PRODEP (project UGTO-PTC-568), 2016.

References

[1] B. Q. Kieu, "Biconical fiber taper sensors," IEEE Photon. Technol. Lett., vol. 18, pp. 2239-2241 (2006).
[2] M.E. Sosa-Morales,"Optical fiber temperature sensors: Applications in heat treatments for foods," Proc. SPIE, vol. 7839, pp. 78391L (2010).
[3] E. Huerta-Mascotte, "A core-offset Mach-Zehnder interferometer based on a non-zero dispersion-shifted fiber and its torsion sensing application," Sensors, vol. 16, pp. 856, (2016).
[4] M. A. Gonzalez-Reyna. "Laser temperature sensor based on a fiber Bragg grating," IEEE Photon. Technol. Lett.,. vol. 27, pp. 1141-1144 (2015).
[5] D. Lopez-Torres, "Photonic crystal fiber interforemeter coated with PAH/PAA nanolayer as humidity sensor," Sensors and Actuators B, vol. 242, pp. 1065-1072 (2016).

Modal Fiber Interferometer with YDF-Coreless Fiber Structure

Tania Lozano-Hernandez, Daniel Jauregui-Vazquez, Julian M. Estudillo-Ayala, Juan C. Hernandez Garcia, Juan M. Sierra-Hernandez and Roberto Rojas-Laguna
Departamento de Ingeniería Electrónica, Campus Irapuato-Salamanca, Universidad de Guanajuato, Carretera Salamanca-Valle de Santiago Km 3.511.8, Comunidad Palo Blanco, Salamanca, Gto., 36885 México
jaureguid@ugto.mx

Abstract: In this letter, a modal fiber interferometer structure is proposed experimentally. The interferometer is simply fabricated by splicing a section of ytterbium-doped fiber (YDF) to a coreless fiber between two segments of single mode fiber (SMF). The fringe contrast can reach as high as ~5.124 dBm and exhibits a wavelength nonperiodical transmission sprectrum with a maximum free spectral range (FSR) of 6.016 nm.
Key words: Optical fiber, modal fiber interferometer, ytterbium-doped fiber (YDF), coreless fiber, interferometer fabrication

1. Introduction

Interferometers, since its emergence to recent times, have been widely used due to their advantages of immunity to electromagnetic interference, high resolution and sensitivity, compact size, cost-effective, and so on [1- 3]. Optical fiber sensors, based on interferometers, play an important role in fields such as biomedicine, biomechanics, environmental monitoring, food engineering, seismic and sonar applications, oil industry, navigation and other fields [1, 4]. The interferometric sensors, have also been used for the measurement of refractive index (RI) [1, 5, 6]. In recent years, many interferometers based RI sensors have been commercialized successfully [1].

To date, several structures of in-fiber interferometers have been implemented based on different optical fibers. Optical fibers doped with rare earths have been investigated to develop a new technology of temperature sensors because their emission and absorption properties depend on this parameter [7-9].

In this paper, a simple modal fiber interferometer based on a compact structure is presented, which was formed by fusion splicing a section of ytterbium-doped fiber with another segment of coreless fiber between two SMFs.

2. Modal Fiber Interferometer Fabrication Process

The modal fiber interferometer structure proposed is illustrated in Fig. 1. The fabrication process only involved fiber cleaving and fusion splicing. A section of end cleaved single mode YDF (Yb1200-4/125, Ytterbium Doped Fiber, Liekki), the choice of YDF was due to its smaller core diameter than that of SMF, the core and cladding diameter were ~4.4 µm and 125 µm, respectively, this piece was spliced to a standard communication SMF (SMF-28e, Corning) by a commercial fusion splicer (FSM-100M, Fujikura), in the manual mode, then the other end of the YDF was achieved another splicing joint to a segment of coreless fiber (Thorlabs) with a certain length, the cladding diameter of coreless fiber employed in experiment were 125 µm. And finally, the other end of the coreless fiber was spliced to SMF piece. The YDF has exceptionally high doped concentration, which makes the refractive index of its core slightly larger than the SMF.

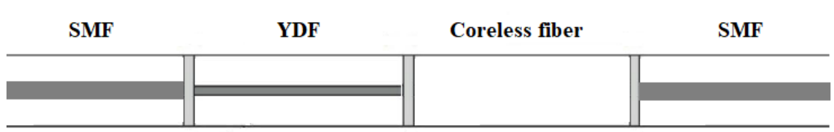

Fig 1. Schematic diagram of the modal fiber interferometer

3. Experimental Setup

The schema based on the use of a YDF-coreless fiber interferometer is shown in Fig. 2. The experimental setup includes 0.26 m of YDF used as a gain medium. The YDF is pumped by a laser diode with maximal power of 250 mW at 980 nm through a 980/1060 nm wavelength division multiplexer (WDM). The output spectrum is measured by using an optical spectrum analyzer (OSA) with resolution 0.5 nm.

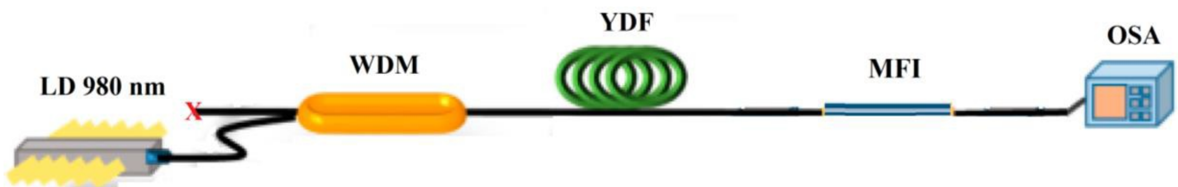

Fig 2. Experimental setup

4. Results and Discussion

When the light passes through SMF into the YDF, more power is injected into the cladding of YDF due to its smaller diameter of fiber core. At the YDF/coreless fiber interface, the fundamental mode of YDF will begin to diffract, now, the power is coupled into the coreless fiber, which structure works as a core of 125 µm. And then, at the spliced point of coreless fiber/SMF, light will be coupled back to SMF core. Three similar structures were fabricated under the same characteristics, were obtained their spectral response and spatial frequency spectrum for each structure in two forms, YDF-coreless fiber and coreless fiber-YDF.

4. Conclusions

The interference phenomenon, was tested experimentally in three similar structures, which measurements were about a maximum FSR of 6.01 nm, minimum FSR of 1.11 nm, and a maximum and minimum fringe contrast of 5.12 dBm and 0.22 dBm, respectively. In addition, the proposed structure is easy to fabricate and is formed by a section of optical fiber doped with a rare earth (Yb), these advantages make it suitable for sensing applications.

References

[1] Md. Rajibul Islam, Muhammad Mahmood Ali, Man-Hong Lai, Kok-Sing Lim, and Harith Ahmad. "Chronology of Fabry-Perot Interferometer Fiber-Optic Sensors and Their Applications: A Review". *Sensors*, (2014).

[2] Han J., Neikirk D.P. "Deflection behavior of Fabry-Perot pressure sensors having planar and corrugated membrane". Proceedings of the SPIE 2882, Micromachined Devices and Components II; Austin, TX, USA, pp. 79–90, (1996).

[3] L. Li, Q. Ma, M. Cao, G. Zhang, Y. Zhang, L. Jiang, C. Gao, J. Yao, S. Gong, W. Li, "High stability Michelson refractometer based on an in-fiber interferometer followed with a Faraday rotator mirror", *Sens. Actuators*, B 234 (2016) 674–679.

[4] Lee C.E., Taylor H.F. "Fiber-optic Fabry-Pérot temperature sensor using a low-coherence source". *J. Light. Technol*, 9:129–134, (1991).

[5] Y. López-Diéguez, J. M. Estudillo-Ayala, D. Jauregui-Vazquez, L. A. Herrera-Piad, J. M. Sierra-Hernandez, J. C. Hernandez-Garcia, M. Bienchetti, J. R. Reyes-Ayona, R. Rojas-Laguna. "Tip Fiber-Optic Intermodal Interferometer for Refractive Index Sensing". *IEEE Photon. Tech. Lett.* Vol. 30, pg. 15 – 18, (2018).

[6] Lee C.-L., Hsu J.-M., Horng J.-S., Sung W.-Y., Li C.-M. "Microcavity Fiber Fabry-Pérot interferometer with an embedded golden thin film". *IEEE Photon. Tech. Lett.* 25:833–836, (2013).

[7] Berthou, H. & Jorgensen, C. K. (1990). "Optical-fiber temperature sensor based on upconversion-excited state fluorescence". *Optics Letters*, Vol. 15, No. 19, pg. 1100–1102, ISSN 0146-9592, (1990).

[8] Farries, M. C. Fernmann, M. E. Laming, R. I. Poole, S. B. Payne, D. N. & Leach, A.P. (1986). "Distributed temperature sensor using Nd3+-doped optical fibre". *Electronics Letters*, Vol. 22, No.8, pp. 418-419, ISSN 0013-5194, (1986).

[9] Krug, P.A. Sceats, M.G. Atkins, G.R. Guy, S.C. & Poole, S.B. (1991). "Intermediate excited state absorption in erbium-doped fiber strongly pumped at 980 nm". *Optics Letters*, Vol. 16, No. 24, pp. 1976-1978, ISSN 0146-9592, (1991).

Angular deflection laser sensor

K.E. Contreras-Vallejo[1], J.M. Estudillo Ayala[1], R. Rojas-Laguna[1], D. Jauregui-Vazquez[1], J.C. Hernandez-Garcia[1], J.M. Sierra-Hernandez[1], J.A.Martin-Vela[1]
[1]División de Ingenierías, Campus Irapuato-Salamanca, Universidad de Guanajuato,
Comunidad de Palo Blanco, Salamanca, Gto., C.P. 36885, México.
Author e-mail address: julian@ugto.mx

Abstract: An angular deflection laser sensor in ring configuration is presented, based on a wavelength selective filter (WSF), which was manufactured by splicing a segment of thin core fiber (Thin-Core Fiber, TCF) between two segments of single-mode fiber SMF-28 (Single-Mode Fiber). A spectral shift of the thin core fiber modal interferometer TCFMI (Thin-Core Fiber Modal Interferometer) was obtained at different angles of deflection in steps of 17.86 µrad. Also, a single-line laser emission was obtained, which was uniformly displaced to the left side in a range of 1534.7 nm to 1531.5 nm by means of the angular deflection in the interferometer section. Finally, the experimental results showed a sensitivity of 0.87498 nm/µrad for angular deflection on the interferometer section.

OCIS codes: (280.3420) Laser sensors (060.0060) Fiber optics and optical communications.

1. Introduction

In recent years, tunable fiber optic lasers have been studied. Tuning can be achieved using different techniques, which are based on Bragg gratings, long period gratings (LPG) and wavelength selective filters (WSF) such as Mach Zehnder and Fabry-Perot interferometers [1,2]. Also, filters based on long-period gratings connected with thin-core fiber (TCF) have been implemented to simultaneously measure the refractive index of a liquid and its temperature [3]. On the other hand, intensity demodulated torsion sensors have also been implemented based on selective filters of thin-core fiber (Thin-Core Fiber, TCF) [4]. In the previously described research work, some techniques to achieve the tuning of a fiber laser are studied, and some sensors based on selective filters of thin core fiber (Thin-Core Fiber, TCF) are studied. This work focuses on the implementation of an angular deflection laser sensor, which is based on a thin-core fiber modal interferometer (Thin-Core Fiber Modal Interferometer) to which deflection angles of less than 1 rad are applied to achieve the tuning of the laser.

2. Experimental setup and Results

The experimental configuration of the tunable laser is presented (figure 1 (a)), in which a semiconductor diode with a wavelength of 980 nm was used as a pump source (Thorlabs, model QFBGLD-980-350) and as a means of tuning and sensing a modal interferometer was used which was built with a thin core fiber segment (Thin-Core Fiber, TCF) between two communications fiber segments SMF28 (Single-Mode Fiber, SMF). The designed TCFMI (Thin-Core Fiber Modal Interferometer) interferometer was implemented with a 2 cm segment of commercial thin-core optical fiber (460-HP, Nufern) whose core diameter is 2.5 µm with a cut-off wavelength of 430 ± 20 nm. The pigtail fiber was configured at 104 mW and the tuning of the fiber laser was achieved by means of the angular deflection of the TCFMI interferometer in steps of 17.86 µrad. A section of the spectral response of the implemented interferometer shows a shift towards the left side in a range of 1549 nm to 1552 nm (figure 1(b)), the TCFMI follows the principle of a Mach Zehnder type interferometer, in which the separation $\Delta\lambda$ between consecutive crests is given by the equation $\Delta\lambda = \lambda^2/(\Delta n_e L)$ where Δn_e is the effective refractive index difference between the core and cladding regions of the thin core fiber TCF, λ is the wavelength and L is the length of the interferometer. Also, a sensitivity of 0.87498 nm was obtained (figure 1(c)). On the other hand, a tuning range of 1534.7 nm to 1531.5 nm nm was obtained (figure 1(d)).

3. Conclusion

An angular deflection laser sensor was implemented, a tuning range of 1534.7 nm to 1531.5 nm nm was obtained by the method of angular deflection in the TCFMI interferometer section. Also, the angular deflection laser sensor had a good linearity in the dynamic range between 0 to 89.3 µrad and a sensitivity of 0.87498 nm/µrad.

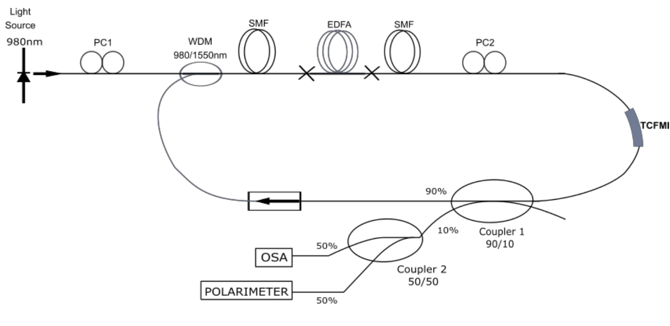

(a)

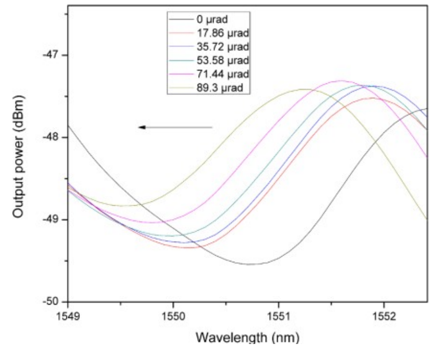

(b)

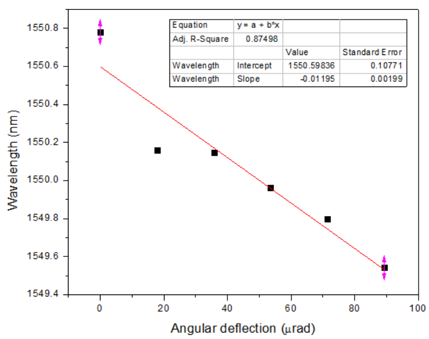

(c)

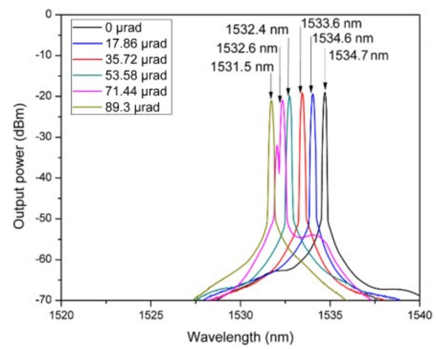

(d)

Figure 1. (a) Tunable laser experimental setup. (b) Section of the spectral response of the TCFMI interferometer. (c) Sensitivity response for TCFMI. (d) Tuning of a single laser emission.

Acknowledgements

K.E. Contreras-Vallejo is grateful to CONACYT for the research grant No. 616051. This work was supported by DAIP Project “108/Investigación de los efectos de luz polarizada en los sistemas láseres de fibra óptica sintonizables” and CONACyT project CB2016-286916.

References

[1] Huerta-Mascotte, E., Sierra-Hernandez, J. M., Mata-Chavez, R. I., Jauregui-Vazquez, D., Castillo-Guzman, A., Estudillo-Ayala, J. M, Rojas-Laguna, R., “A core-offset Mach Zehnder interferometer based on a non-zero dispersion-shifted fiber and its torsion sensing application”, Sensors, 16, 856 (2016).
[2] Estudillo-Ayala, J. M., Jauregui-Vazquez, D., Haus, J. W., Perez-Maciel, M., Sierra-Hernandez, J. M., Avila-Garcia, M. S., Rojas-Laguna, R., Lopez-Dieguez, Y., Hernandez-Garcia, J. C., “Multi-wavelength fiber laser based on a fiber Fabry-Perot interferometer”, Applied Physics B: Lasers and Optics, 121, 407–412 (2015).
[3] Jiang, M., Wang, Z. M., Zhao, Z. Z., Li, K., & Yang, F., “Long-period fiber grating cascaded to thin-core fiber for simultaneous measurement of liquid refractive-index and temperature”, Sensor Review, 38, 79-83 (2018).
[4] Kang, X., Zhang, W., Zhang, Y., Yang, J., Chen, L., Kong, L., Zhang, Y., Yu, L., Yan, T., Geng, P., “Intensity-demodulated torsion sensor based on thin-core polarization-maintaining fiber”, Appl. Opt., 57, 3474–3478 (2018).

Experimental Study for Supercontinuum Generation with Special Optical Fibers

D. Torres-González, J. M. Sierra-Hernández, D. Jáuregui-Vázquez, J. C. Hernández-García, J. M. Estudillo-Ayala and R. Rojas-Laguna*

Departamento de Ingeniería Electrónica, División de Ingeniería, Campus Irapuato-Salamanca, Universidad de Guanajuato, Carretera Salamanca-Valle de Santiago km 3.5+1.8, Comunidad de Palo Blanco, 36885. Salamanca, Guanajuato, México.

* rlaguna@ugto.mx, d.torres.gonzalez@ugto.mx

Abstract: In this work, we present an experimental study of supercontinuum generation using a high-power sub-nanosecond microchip laser and special optical fibers, such as high-numerical aperture and dispersion shifted fiber, with the addition of 100 m of single mode fiber (SMF-28) wrapped around different diameters. Furthermore, the change of order where these fibers were spliced produced an output spectrum width of 950 nm or power variation of 1.5 dB for the best conditions.

1. Introduction

Supercontinuum generation (SG) is a nonlinear phenomenon, observed by first time in 1970 [1]. SG received more attention in the middle of 90's with the invention of microstructured optical fibers and the development of commercially available high-power pulsed lasers. SG is the spectral broadening of light caused by the interplay of linear and nonlinear effects, such as Stimulated Raman Scattering (SRS), Self-Phase Modulation (SPM), Cross-Phase Modulation (XPM), and Modulation Instability (MI). The involved nonlinear effects depend on the pump wavelength and the zero-dispersion wavelength of the optical fiber [2-4]. There are two main parameters to obtain a nonlinear phenomenon: a high-power pump and a nonlinear media. The objective of this study was to obtain SG, as flat as possible, by induction of bending loss, employing different optical fibers.

2. Experimental setup

A sub-nanosecond microchip pulsed laser was used as pump with an operating wavelength of 1064 nm, repetition rate of 5 kHz, output energy of 8μJ, and output peak and average power of 8 kW and 100 mW, respectively. Light emitted from the microchip laser was coupled into the optical fiber by means of a microscope objective. The first special optical fiber placed was a 5 m high-numerical aperture (High-NA) fiber (Fiberlogix) or a 20 m High-NA fiber (Thorlabs). Next, we spliced two other optical fibers, 5 m of dispersion shifted fiber (DSF) (Corning) and 100 m of single mode fiber (SMF-28), whose order were exchanged to observe the differences in the output spectrum. From past works, we know that supercontinuum spectrum can be modified by inducing bending losses to the fiber [5]. For this reason, we wrapped around the SMF-28 in three different objects with different diameters: a 14 cm cylinder, a 5.4 cm cylindrical tube and a cone. These three configurations were exchanged with the DSF to get numerous measurements given by diverse setups of optical fibers.

3. Results and Discussion

Figures 1 and 2 show the best results obtained using first 5 m of High-NA and 20 m of High-NA, respectively. Additionally, the configurations used may be seen in the legend. High-NA fiber spliced with DSF were added to show the evolution of the output spectrum. First and second Stokes were visible in 1115 nm and 1174 nm, which means that Stimulated Raman Scattering (SRS) is involved in the broadening process. The addition of SMF increased notably the spectral width to a maximum of 950 nm, from 750 to 1700 nm, limited by the OSA span (from 600 to 1700 nm). Two important flatness sections for Figure 1 are from 750 to 1064 nm and from 1350 to 1700 nm. In the blue line, a 6-dB variation is observed in the first region, while a larger variation of 10 dB happened for the second region. This is the same for the green line with a considerable power loss in the first region. There was an inverse relationship with spectral width and flatness in the second region: while spectral width increased, flatness decreased; and while spectral width increased, power variation increased as well.

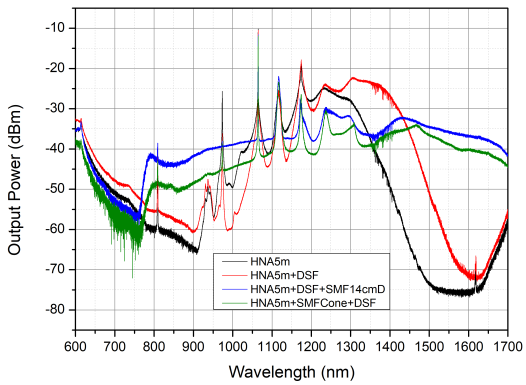

Figure 1. SC output spectrum with 5 m of High-NA fiber.

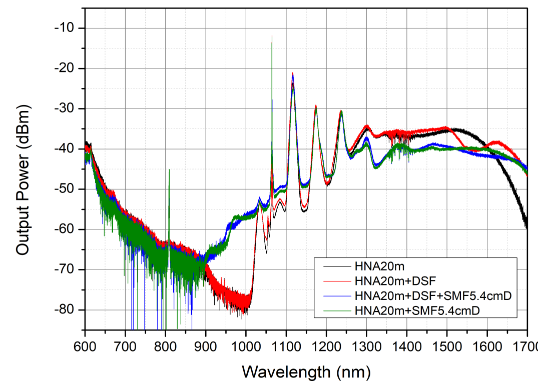

Figure 2. SC output spectrum with 20 m of High-NA fiber.

However, if high-flatness is pursued, the configurations in Figure 2 are recommended. First, there is a totally different output spectrum for High-NA fiber in comparison with Figure 1, which immediately has high-flatness. Nevertheless, there is a lower spectral width since there is a lack of broadening below the pump wavelength, due to the properties of the optical fiber. Moreover, a remarkable 1.5-dB power variation within the range from 1400 to 1600 nm was achieved, as well as a third Stokes at 1237 nm.

4. Conclusion

Supercontinuum generation was achieved by means of a high-power microchip pulsed laser, standard and special optical fibers, such as High-NA fiber and DSF. Furthermore, a maximum spectral width of 950 nm and a high-flatness of 1.5 dB power variation was achieved with two different configurations. With the correct design and elements available, the broadband spectrum could be used as active medium for a fiber laser.

Acknowledgement

This work has been carried out with the support of the CONACyT (Consejo Nacional de Ciencia y Tecnología) under Project CB2016-286916.

References

[1] Alfano, R. R., and Shapiro, S. L. "Emission in the region 4000 to 7000 A via four-photon coupling in glass," in Phys. Rev. Lett. **24**, 584-587 (1970).
[2] Guttierrez-Gutierrez, J., Vargas-Treviño, M., Romero-Salazar, C., Hernandez-Flores, O. A., Kuzin, E. A., Ibarra-Escamilla, B., Grajales-Coutiño, R., Rojas-Laguna, R., Estudillo-Ayala, J. M., Vargas-Rodriguez, E., and Gutierrez-Zainos, F. "Influencia de la inestabilidad modulacional en la generación de un espectro continuo en fibras ópticas con pulsos de nanosegundos," in Revista Mexicana de Física **55**(5), 359-366 (2009).
[3] Alexander, V. V., Kulkarni, O. P., Kumar, M., Xia, C., Islam, M. N., Terry, F. L., Welsh, M. J., Ke, K. Freeman, M. J., Neelakandan, M., and Chan, A. "Modulation instability initiated high power all-fiber supercontinuum lasers and their applications," in Optical Fiber Technology **18**, 349-374 (2012).
[4] Dudley, J. M., Genty, G., and Coen, S. "Supercontinuum generation in photonic crystal fiber," in Reviews of Modern Physics **78**, 1135-1184 (2006).
[5] Rojas-Laguna, R., Hernandez-Garcia, J. C., Estudillo-Ayala, J. M., Ibarra-Escamilla, B., Pottiez, O., Vargas-Rodriguez, E., and Barrientos-Garcia, A. "Analysis of a low-cost technique for the generation of broadband spectra with adjustable spectral width in optical fibers" in Proc. SPIE, **9347**, 934713-1-934713-5 (2015).

Semiautomatic platform for the construction of Fabry-Perot microcavities

Carmen E. Domínguez-Flores, Josué I. Basulto, Daniel López-Cortés, David Monzón-Hernández
Centro de Investigaciones en Óptica A. C. Loma del Bosque 115, León GTO. 37150, México
carmendmz@cio.mx

Abstract: A semi-automatic and reconfigurable mechatronic stage was designed and constructed to precisely control the fiber cleaving process to obtain Fabry-Perot (FP) cavities of small size. It was possible to fabricate FP interferometers with cavity length as small as 5 µm. The theoretical reflectance of the fiber FP cavities was studied by means of the simulation of the interference phenomenon. This simulation also allowed to calculate the length FP cavities fabricated by comparing the experimental and theoretical reflection spectra. The FP cavities fabricated can be used to develop optical fiber sensors to measure physical variables as strain.

1. Introduction

Fiber optic interferometers have important advantages for sensing including high resolution, good electromagnetic interference immunity, and fast response. The simplest configuration is the Fiber-optic Fabry–Perot Interferometers (FFPI) also known for its high sensitivity and its impact in harsh environment sensing [1]. The most common fabrication process of the FFPIs consists of three steps: wet chemical etching, fusion splicing, and cleave. FFPI structure is simple, in contrast to fiber Mach–Zehnder and Michelson interferometers where couplers can potentially obscure sensor operation and data analysis [2]. In this work, a semiautomatic platform for the construction of micrometric FFPI is proposed. Several FFPIs with cavity lengths of 5 to 300 µm were fabricated in order to characterize the performance of the process; length of the cavities were calculated through the simulation of the interference phenomenon [3].

2. Fundamentals of the Fiber-optic Fabry–Perot Interferometers FFPI

A typical FFPI sensor consists of fiber section (cavity) sandwiched between two semi-reflecting surfaces with reflectivity R_0 and R_1, respectively, as seen in Fig. 1. The cavity acts as the sensing element of the device, it has been shown that sensitivity increases as the FP cavity length (L_1) decreases.

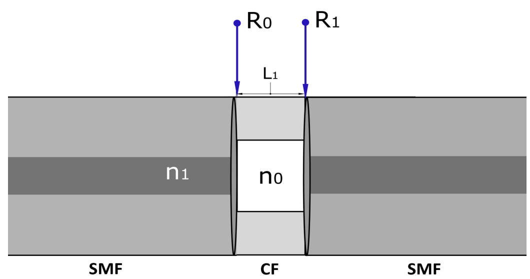

Fig. 1. Basic scheme of the FFPI

The reflectivity of the FFPI structure shown in Fig. 1 is described by the equation (1), where φ is the initial phase.

$$R = R_0 + (1-R_0)^2 R_1 + 2(1-R_0)\sqrt{R_0 R_1}\cos(2kn_0L_1 + \varphi) \tag{1}$$

3. Platform design and fabrication

In order to construct an FFPI with a specific cavity length, the alignment of the optical fiber is very important. In Fig. 2 a representation of the portable platform is shown, this included two double scissor platforms, two bases for the motorized translation stage, two fiber optic fasteners, a scissor platform for the cleaver that were designed and constructed in the center facilities. Two compact motorized translation stages MTS50-Z8E, THORLABS were used to control the fiber movement. A fiber cleaver FC-6, SUMITOMO ELECTRIC, an EDMUND OPTICS microscope and a charge-coupled device (CCD) with a resolution of 640x480 pixels where installed to control the fiber cleaving process. With this platform it is possible to construct FFPI easily and repeatable.

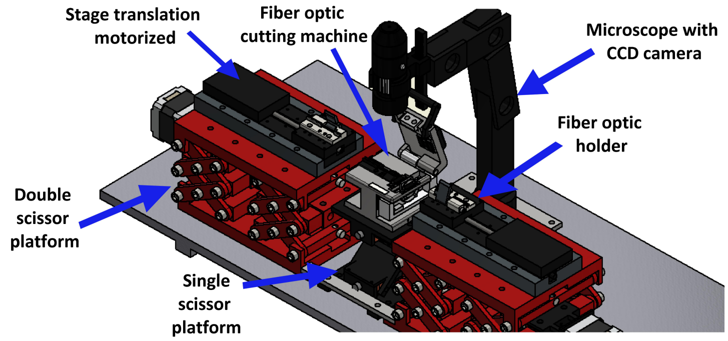

Fig. 2. Scheme of the semiautomatic platform designed and constructed.

4. Fabrication and characterization of Fabry-Perot cavities

Once the platform was assembled FP cavities were fabricated following the same procedure. The first step was to stablish the real capabilities of the platform by finding the smallest cavity that can be fabricated. The calculated lengths of the smallest cavities fabricated are shown in Table 1. This shows that it is possible to build small FP cavities serially with a standard deviation in the cavity length L_1 of 0.97μm. The experimental reflectance of some of these cavities are shown in Fig. 3, the simulated reflectance was obtained using Eq. (1). The lengths of the cavities was calculated by means comparing the experimental and simulated spectra. Figure 3 shows the measured reflection spectra of three different FFPIs and their theoretical approximation.

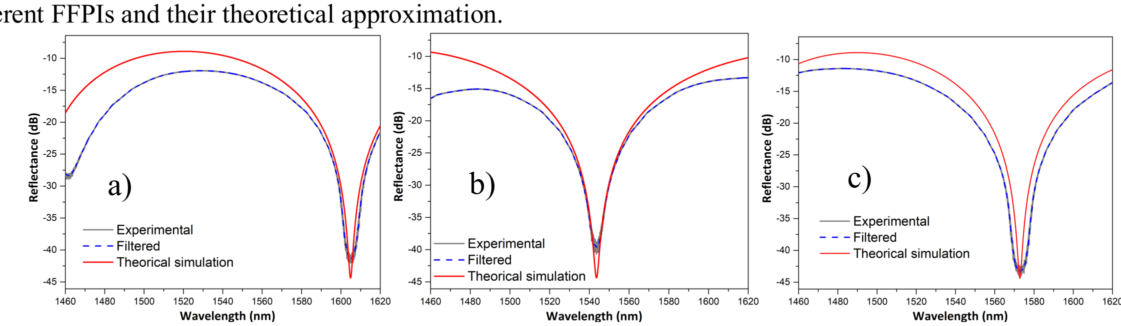

Fig. 3. Optical spectra of the FFPI reflectance assuming a cavity length of a) 7.22μm, b) 5.401μm and c) 7.0755μm.

Table 1. Calculated lengths of the cavities FP constructed.

No.	L_1 [μm]	No.	L_1 [μm]	No.	L_1 [μm]
1	4.92	5	5.401	9	7.0755
2	5	6	5.429	10	7.22
3	5.1	7	6.452	11	7.396
4	5.178	8	6.483	12	7.455

5. Conclusion

A semi-automatic platform was designed and built to manufacture FP cavities in a simple and repeatable way. FFPI were fabricated and the experimental spectra were compared with the simulated spectra calculated from the interference model. It was shown that it is possible to build FP cavities up to 4.92μm. The final cavity length was estimated comparing the simulated and experimental spectra. This platform allowed to fabricate FFPI with potential applications to develop high sensitivity strain sensors and other physical variables.

References

[1] T. Yoshino, T. Ose, K. Kurosawa, K. Itoh, Fiber-Optic Fabry–Perot Interferometer and Its Sensor Applications, IEEE Trans. Microw. Theory Tech. 30 (1982) 1612–1621. doi:10.1109/TMTT.1982.1131298.
[2] L.H. Chen, C.C. Chan, R. Menon, P. Balamurali, W.C. Wong, X.M. Ang, P.B. Hu, M. Shaillender, B. Neu, P. Zu, Z.Q. Tou, C.L. Poh, K.C. Leong, Fabry-Perot fiber-optic immunosensor based on suspended layer-by-layer (chitosan/polystyrene sulfonate) membrane, Sensors Actuators, B Chem. 188 (2013) 185–192. doi:10.1016/j.snb.2013.06.093.
[3] Domínguez-Flores Carmen E., "Diseño, fabricación y caracterización de interferómetros Fabry-Perot de fibra óptica extrínsecos y su aplicación en sistemas de sensado de variables físicas" Tesis de maestría, Centro de Investigaciones en Óptica. 2018.

Suppression of Kelly sidebands on the soliton spectrum pulse using a Non-Linear Loop Mirror

Mahrokh Avazpour[1], Georgina Beltrán Pérez[1], Evgeny Kuzin[2]

[1]Facultad de Ciencias Físico Matemáticas, Benemérita Universidad Autónoma de Puebla, Avenida San Claudio y 18 Sur, Colonia San Manuel, Ciudad Universitaria C.P. 72570 Puebla, México.

[2]INAOE, Enrique Erro 1, Tonantzintla, CP 72840 Puebla, México Mahrokh.avazpour@gmail.com

Abstract

Cleaning and compressing soliton spectrum plays important role in the all-optical process. In the present work, we report the suppression of Kelly sideband as well as compressing the soliton spectrum through a polarization-imbalanced NOLM. As an input source we used a mode-locked fiber ring laser with 0.6 ps time duration and 1550 nm central wavelength. The results show more than 95% suppression of Kelley sidebands and two times compression of bandwidth. The maximum transmission of NOLM was 20%. The cleanup of soliton spectrum is possible using a NOLM as intensity filter without dependence of wavelength.

1. Introduction

In the passive mode-locked fiber laser, the soliton pulses are often accompanied with dispersive waves that can form of spectral sidebands due to spatial in homogeneities in the cavity, these spectral sidebands called Kelly sidebands [1]. Spectrum soliton without sidebands is important for many applications such as optical sensors, processing, optical communication, and pulse generation [2-3]. Non-linear loop mirror (NOLM) with soliton input pulses founds a good technique for cleaning of Kelly sidebands. The NOLM can be imbalanced in different ways, as power, dispersion and polarization. Polarization imbalance non-linear loop mirror indicates fantastic results [4-5], due to its possibility to obtain from lowest to highest transmission. The soliton pulses with 0.6 ρs time duration used as input source, which generated by a fiber optical ring laser. The result shows applying 1.7 mW of input power is sufficient to get very good suppression of sidebands in different wavelengths. In the other hand for 0.9 mW of input power more than two times compressing of spectrum was observed at the output of NOLM, and only the 5% of Kelly sidebands remained.

2. Experimental setup

The experimental setup used for suppression and compression of the spectrum is shown in Fig. 1. Soliton pulses generated by a mode-locked fiber ring laser with 0.6 ps time duration and 1550 nm central wavelength as an input signal source. The pulses were amplified by an EDFA. It passed through an isolator to avoid the reflection of light inside the laser source. Then, the light goes toward the polarization controller (PC1) to adjust circular polarization. The pulses split by a 90/10 coupler, 10% for monitor the polarization and power and 90% goes to the NOLM but before there is PC2 to obtained circular polarization in the input of NOLM. The NOLM consist of two 50 m pieces of fibers twisted in opposite directions; for cancelling the birefringence. A quarter wave retarder (QWR) used to break-up the symmetry of loop and achieve different nonlinear phase shift for counter-propagating pulses. A 50/50 coupler placed to have very low transmission at low power. The spectrum was measured at input and output of the NOLM using optical spectrum analyzer.

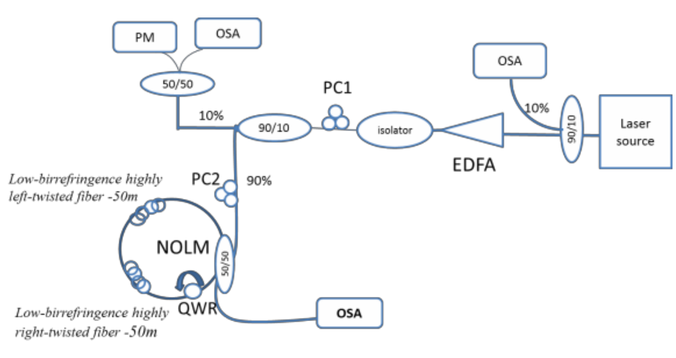

Fig.1. Experimental setup

3. Results

Figure 2 (a) shows the input spectrum of NOLM with power of 0.9 mW with Full Width High Maximum (FWHM) 5.5 nm. From the figure the maximum Kelly sidebands appeared in 1559 nm. The others are in 1555 nm and 1570 nm. Figure 2 (b) indicate the result of output of NOLM. From the output it is clear that there is two times compression of bandwidth. In the 1559 nm there is 95% suppression of the Kelly sideband. In this case the transmission of NOLM is 1.5%. Furthermore, for wavelength of 1555 nm and 1570 nm there are 55% and 85% suppression of Kelly sidebands, respectively. Figure 3 (a) shows input spectrum of NOLM with power of 1.7 mW and FWHM=4.23 nm. It is showing in this power the number of Kelly sidebands increased. The maximum pedestal is for 1559 nm. Figure 3 (b) indicates the result of NOLM output with two times compression and 83% subtracting of sidebands for 1559 nm. The transmission of NOLM in this case is 20%.

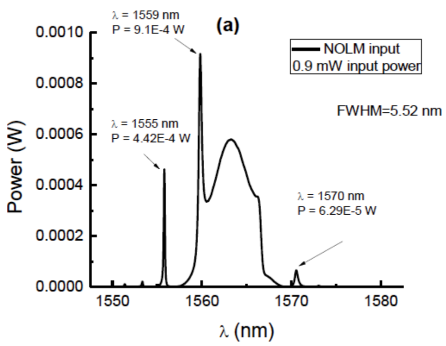

Fig. 2 (a). Input spectrum of NOLM with power of 0.9 mW with FWHM = 5.5 nm.

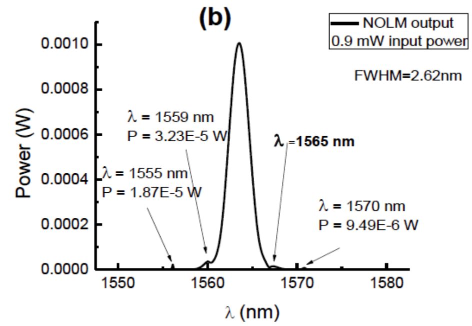

Fig. 2 (b). Output spectrum of NOLM with power of 0.9 mW with FWHM = 2.62 nm.

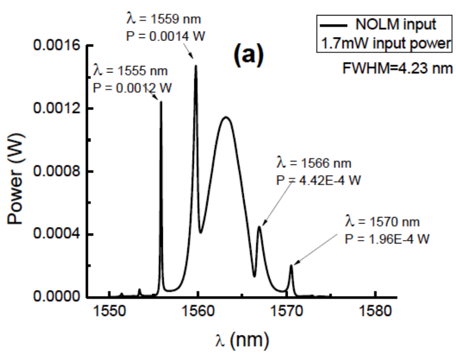

Fig. **3 (a)**. Input spectrum of NOLM with power of 1.7 mW with FWHM = 4.23 nm.

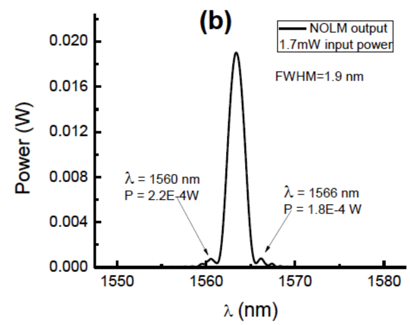

Fig. **3 (b)**. Output spectrum of NOLM with power of 1.7 mW with FWHM = 1.9 nm.

4. Conclusion

In summary, an experimental study of the use of the polarization-imbalanced NOLM to clean and compress solitons was presented. In the input power with 0.9 mW and 1.7 mW, we observed the compression of the spectrum more than two times. The strong side bands present at the input were suppressed more than 95% for 0.9 mW input power. Moreover, for 1.7 mW of input power we observed 85% suppression for 1570 nm.

References

[1] R. Weill, A. Bekker, V. Smulakovsky, B. Fischer, and O. Gat, “Spectral sidebands and multipulse formation in passively mode-locked lasers,” *Phys. Rev. A*, vol. 83, no. 4, p. 43831, 2011.

[2] T. chao et al., “Adiabatic pulse propagation in a dispersion-increasing fiber for spectral compression exceeding the fiber dispersion ratio limitation,” J. Opt. Lett. 39(4), 853–856 (2014

[3] O. Pottiez, E. A. Kuzin, “Theoretical investigation of the NOLM with highly twisted fibre and a λ/4 birefringence bias,” Opt. Commun. 254, 152-167 (2005)

[4] I. Armas-Rivera, E.A.Kuzin, “Experimental study of the polarization symmetrical NOLM with adjustable switch power”, Opt. Commun, 350, 165-169, (2015)

[5] L A Rodríguez-Morales, E.A.Kuzin “Experimental investigation of polarization imbalanced nonlinear loop mirror with double-sense twisted fiber as a filter to cleanup solitons” J. Opt. 20 (2018).

Optimal Visual Servoing using Laser-Optic-based Structured Light with Applications in Robotic Pipe Inspection

Juan Echavarria, Ivan Perez, Mehran Mehrandezh, and Raman Paranjape
[*] Faculty of Engineering & Applied Science, University of Regina, Canada. e-mail address:
(Mehran.Mehrandezh@uregina.ca)

Abstract: Automated inspection of pipes using robotic systems is of great importance to the pipe manufacturing sector. While conducting visual inspection of larger pipes by humans is practiced in industry, extending this to smaller pipes would not be a possible solution. Robotic systems, instead, are gaining attention for being used for conduction pipe inspection either as an alternative or a complementary method to that by subjecting pipes to high hydrostatic pressure for testing (pipe bursting test). Structured light, such as that in collimated laser patterns, can be very effective in highlighting defects seen by the imaging sensors. In order to achieve the highest spatial resolution, keeping the relative pose between the imaging sensor and pipe's surface at constant plays a crucial role. In this paper, we propose a visual servoing technique based on laser-optics structured light and perspective imaging using two collimate parallel laser lines projected onto the pipe's inner surface, for positioning the imaging sensor right on the center line of the pipe. The proposed visual servoing technique guarantees that the distance and orientation between the imaging sensor and the pipe's surface will remain the same through a 360-degree radial rotation, leading to the highest spatial resolution that the system can provide. A model-based optimal control strategy is used that minimizes the deviation from the image set point while keeping the energy consumption, due to the camera motion, at minimum without violating the constraints associated with the imaging sensor's FOV, and the voltage applied to the joint motors.

1. Problem Definition

The research problem is: Servo control all degrees of motions of a laser-optics sensor mounted on a wheeled- based robot moving inside a pipe for doing pipe inspection. A CAD model of the system and also a picture of the experimental setup can be seen in Figures (1a) and (1b), respectively.

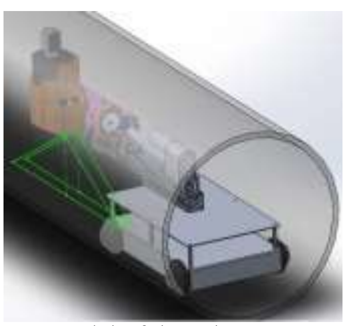

Figure 1a: CAD model of the robot.

Figure 1 b: The experimental setup.

As can be seen from Figure (1a/b), a laser-projecting device, that shines two collimated parallel laser lines onto the pipe's surface, along with a perspective camera, with its projection center right on the bisection of these laser lines, are mounted on a platform that can move vertically. The sensor platform, namely the laser line projector and the camera, can also rotate 360 degrees along the longitudinal axis of the pipe. The sensor platform is also mounted on a wheeled-based robot that can provide forward/backward motion inside the pipe, which facilitates pipe inspection segment by segment. The inspection process is carried out in a stop-scan-go fashion for each segment.

In this paper, we assume that any sway motion in the mobile base is compensated by a separate controller, which is not addressed in this paper. It is noteworthy that this sway in motion is kept at minimum given that the mobile base will move at a slow speed (i.e., 5 cm/s) and that it is equipped with wheels with trapezoidal profiles, which tend to bring the robot back to the middle of the pipe passively.

Precise and fast servoing of the imaging platform towards its goal configuration, while inspecting the pipe is of great importance for achieving the highest accuracy and resolution. Defect detection, sizing, and classification would be required for inspecting pipes. These will be affected by the relative pose between the imaging sensor and pipe's surface, therefore, maintaining the pose of the camera at its desired value, despite external disturbance, is critical.

An optimal control strategy based on Model Predictive Control (MPC) paradigm is proposed for fast and energy-optimal control of the sensor's motion while not violating constrains that the system is subjected to. Examples are: Constraints on the camera's FOV, kinematic and range-of-motion (i.e., reachability) constraints on the linkages used in the sensor platform, and constraints on motor's dynamics (i.e., how fast they can move and what their permissible acceleration/deceleration are).

2. Problem Formulation

The dynamics of the linear actuator and the parallel platform attached to that holding the imaging sensor can be written in the compact form as:

$$\begin{aligned} \dot{x} &= f(\,x(t), u(t)) \\ g_l &\ll g(x(t), u(t)) \leq g_u \\ x(0) &= x_0 \end{aligned} \tag{1}$$

The image feature, s is defined as the distance between the two collimated laser lines in the image, d, and the position of the vertical bisection line between these two lines in pixels, o. The optical flow associated with this proposed image feature, $\dot{s}$ is related to the rate of change in the parallel platform's vertical motion, $\dot{z}$ via image Jacobian, L_s, as in Eqn. (2), considering the state and image constraints, [2]:

$$\begin{aligned} \dot{s} &= L_s(s)\dot{x} \\ h_l &\ll h(s(t), x(t)) \ll h_u \\ s &= [d, o]^T, \quad x = [z]^T \end{aligned} \tag{2}$$

Combining Eqns. (1) and (2) leads to Eqn. (3) in which the full dynamics of the coupled system is given:

$$\begin{aligned} \dot{s} &= L_s\, f(x(t), u(t)) \\ I_l &\ll I(s(t), x(t), u(t)) \ll I_u \\ x(0) &= x_0, s(0) = s_0 \end{aligned} \tag{3}$$

The control objective is to bring the image feature, e.g., the distance between laser lines in the image and the location of its center point, to their desired value and location within the image, respectively, while minimizing the motion and also the energy consumption based on a quadratic performance index.

A control-space parametrization is also carried out to conduct the optimization over an infinite horizon in real time by using an exponentially-decaying basis function based on orthonormal Laguerre functions, [4].

3. Results

The proposed servoing algorithm was implemented on the experimental setup. Figure 2 shows a representative set of results. As can be seen, the controller performs well in terms of servoing the imaging sensor towards its desird position inside the pipe using the information obtained from the images of the two collimated parallel laser lines. Servoing was conducted with a reasonable response time and without violating neither sensor nor control input constraints.

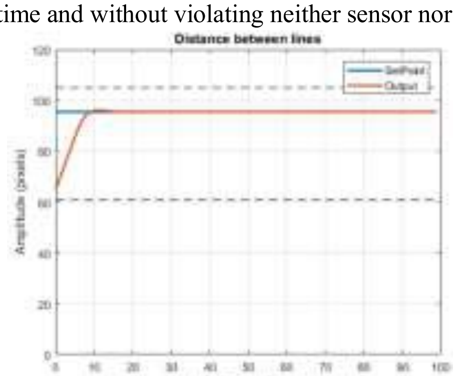

Figure 2: Servoing the imaging sensor to its desired pose.

References

[1] A. Kaehler et. al., *"Learning OpernCV 3 : Computer Vision in C++ With OpenCV Library"*, O'reilly 2016.

[2] G. Allibert, E. Courtial, and F. Chaumette, "*Visual Servoing via Advanced Numerical Methods*", Springer Publishing, 2010, Chapter 20, pp. 375-393.

[3] L. Wang, "*Model Predictive Control System Design and Implementation using MATLAB* " Springer, 2009.

[4] M. Muehlebach, et. al., "Implementation of a Parametrized Infinite-Horizon MPC Scheme with Stability Guarantees", *IEEE International Conf. on Robotics and Automation* (ICRA), Singapore, 2017, pp. 6189-6196.

Temperature sensor based on a structured optical fiber

M. C. Alonso-Murias[1], I. Hernández-Romano[2], D. A. May-Arrioja[3], D. Monzón-Hernández[3] and M. Torres-Cisneros[4]

[1] Instituto Tecnológico de Tuxtla Gutiérrez, Carretera Panamericana Km. 1080, Tuxtla, Chiapas.
[2] CONACYT Research Fellow, Electronics Department, División de Ingenierías CIS, University of Guanajuato Salamanca, Guanajuato 36885, México.
[3] Centro de Investigaciones en Óptica A.C., León, Guanajuato 37150, México.
[4] Electronics Department, División de Ingenierías CIS, University of Guanajuato, Salamanca, Gto. 36885, México

Abstract: A temperature sensor consisting of two three-core-fiber segments is demonstrated. Ratiometric measurements of the signals provide a sensitivity of 0.036/ºC which is two orders of magnitude higher than their individual signals.

1. Introduction

Up to now, plenty of fiber optic sensors have been implementing to measure temperature by using Mach-Zenhder interferometer [1], photonic crystal fibers (PCF) [2], and Fabry-Perot cavities [3], just to mention few. The output of these sensors is an interference pattern that undergoes a spectral shift when the temperature is modified. Most of them take advantage of the thermo-optic coefficient (TOC) of the silica which has a low value (6.3x10-6/ºC) [4], allowing the measurement of high temperatures with these fiber sensors. Materials with high TOC are added to such sensors in order to increase their sensitivity and then it is feasible monitoring with high precision temperatures below 60 ºC [5]. The disadvantages of these sensors are not only their complex fabrication process but also expensive equipment to interrogate them, such as an optical spectrum analyzer (OSA).

Here we report a fiber optic sensor based on a multicore fiber (MCF) in a ratiometric power scheme. This configuration provides a simple fabrication process, which is also cost-effective since an OSA is not required for monitoring the output.

2. Fabrication process and experimental results

The MCF that was used to fabricate this sensor consists of three coupled germanium-doped cores whose diameters and pitch are 9 µm and 11 µm, respectively. This TCF does not require a special technique to be spliced with a single mode fiber (SMF) since one of its cores is at the center of the fiber. A FITEL splicer (Model S178) was used to splice the TCF with the SMF using a program that aligned the fibers by the cladding. Two sensors were fabricated by cutting two segments of TCF, whose length was 3 cm, and by splicing them between two SMF. In order to test each sensor an experimental setup was built consisting of a superluminescent diode (SLD) to launch light (from 1450 nm to 1650 nm) into a directional coupler (50/50), which is transmitted through a polarization controller before it reaches the TCF. The output signal from the sensing elements can be detected either by an OSA or individual identical photodetectors, as shown in Fig. 1 (a).

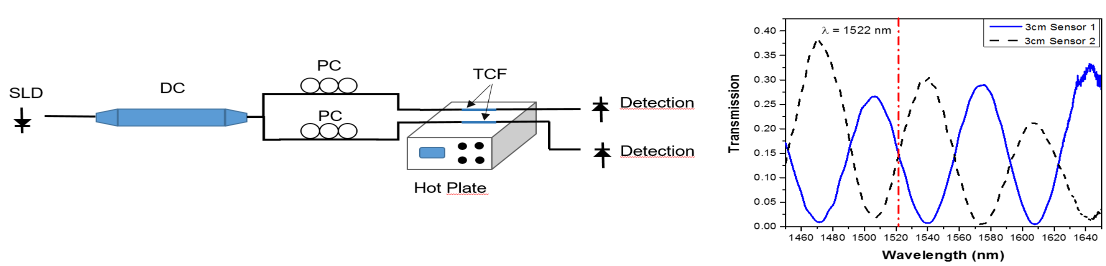

(a) (b)

Fig. 1. (a) Schematic diagram of the measuring setup. SLD: Superliminicent Diode, DC: Directional coupler (50/50), PC: polarization controller. TCF: Three-core-fiber. (b) Experimental interference patterns out of phase by tuning the polarization observed with 3 cm-long TCF.

The fundamental mode from the SMF that is coupled to the central core of the TCF excites supermodes, and the interference between them as they propagate along the TCF produce a sinusoidal signal that was detected by the OSA.

We adjusted the polarization controllers to obtain that the transmission of the sensor 1 is out of phase (π radians) with respect to the signal of the sensor 2, see Fig. 1 (b). When the temperature is increased both transmission function of the sensors underwent a redshift. In this situation the sensor 1 increased its power whereas the sensor 2 decreased its power, see Fig. 2 (a). The sensitivity of sensor 1 and sensor 2 are 3.5×10^{-4}/ºC and 2.5×10^{-4}/ºC, respectively. In spite of the low sensitivities, the sensors were capable to measure the changes in the temperature. Nevertheless, taking advantage of the opposite amplitude response of the sensing elements, we can take the ratio of both signals in order to enhance the sensitivity of the system. A higher sensitivity was achieved by making a comparison between the outputs of the two sensors (rate between sensor 1/ sensor 2). The sensitivity of this ratiometric device was 0.036/ºC, as shown in Fig, 2 (b), which is two orders of magnitude higher as compared to each sensing element. This new scheme not only achieves a higher sensitivity (two orders of magnitude higher) but also provides a more reliable sensor.

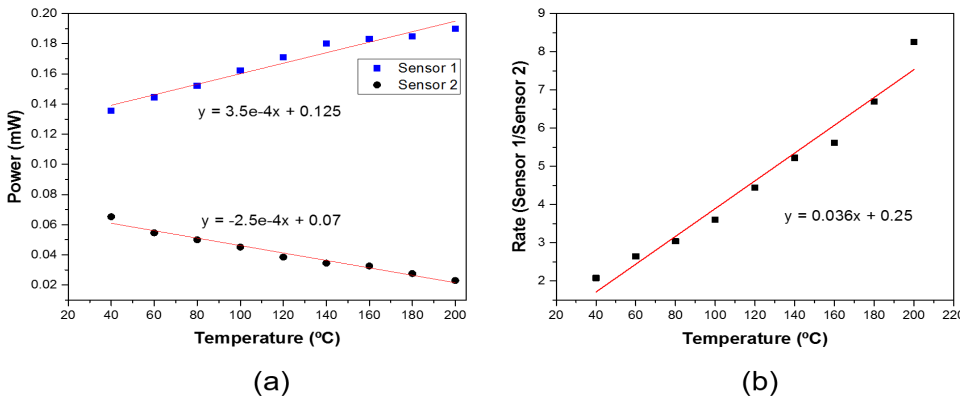

Fig. 2. (a) Variation of the optical power at difference temperatures, for sensor 1 and sensor 2. (b) Variation of the rate between sensor 1 and sensor 2 at different power.

3. Conclusions

In summary, a new temperature sensor based on TCF in a ratiometric power scheme was proposed and demonstrated. The sensor is simple to fabricate and capable of measuring a range of temperature from 22 ºC to 200 ºC. A higher sensitivity was accomplished with the ratiometric power scheme by using TCF, and the interrogation system of this device is simple to implement and is relatively inexpensive. Such advantages make them a good candidate for real industrial applications.

4. Acknowledgments

We are very grateful to the Microstructured Fibers and Devices Group, CREOL, The college of Optics and Photonics, for providing the TCF used in this work. Also, DAMA and MTC would like to acknowledge to CONACYT for the partial support through the CB 2016 projects; 286368 and 286629.

References

[1] P. Lu, L. Men, K. Sooley, and Q. Chen, "Tapered fiber Mach–Zehnder interferometer for simultaneous measurement of refractive index and temperature," Appl. Phys. Lett. 94, 131110-1–131110-3 (2009).
[2] D. Monzon-Hernandez, V. P. Minkovich, and J. Villatoro, "High-temperature sensing with tapers made of microstructured optical fiber," IEEE Photon. Technol. Lett. 18, 511 (2006).
[3] H. Y. Choi, K. S. Park, S. J. Park, U. C. Paek, B. H. Lee, and E. S. Choi, "Miniature fiber-optic high temperature sensor based on a hybrid structured Fabry-Perot interferometer," Opt. Lett. 33(21), 2455–2457 (2008).
[4] Z. L. Ran, Y. J. Rao, W. J. Liu, X. Liao, and K. S. Chiang, "Laser-micromachined Fabry-Perot optical fiber tip sensor for high-resolution temperature-independent measurement of refractive index," Opt. Express 16(3), 2252–2263 (2008).
[5] I. Hernández-Romano, M. A. Cruz-Garcia, C. Moreno-Hernández, D. Monzón-Hernández, E. O. López-Figueroa, O. E. Paredes-Gallardo, M. Torres-Cisneros, and J. Villatoro, "Optical fiber temperature sensor based on a microcavity with polymer overlay," Opt. Express 24, 5654-5661 (2016).

Automated System for Characterizing a Laser Diode Applied to the Development of Optical Fiber Laser

C M Carrillo-Delgado[1], J C Hernandez-Garcia[1,2], J M Estudillo-Ayala[1], J D Filoteo-Razo[1], O Pottiez[3], J P Lauterio-Cruz[1], R Rojas-Laguna[1], D Jauregui-Vazquez[1]

[1]DICIS, Universidad de Guanajuato, Carr. Salamanca-Valle de Santiago Km 3.5+1.8, Comunidad de Palo Blanco, Salamanca, Gto. 36885, México

[2]CONACyT, Av. Insurgentes Sur 1582, Col. Crédito Constructor, Del. Benito Juárez, 03940, México

[3]CIO, Loma del Bosque 115, Col. Lomas del Campestre, León Gto., 37150, México.

Corresponding author e-mail address: jchernandez@ugto.mx

Abstract: It is presented a system for automating the current and temperature in the controller ITC4020, necessary to characterize and handle until 20 A of current of a laser diode (LD) which is applied in the development of pulsed fiber lasers.

1. Introduction

The laser diode (LD) is an electronic device, which transforms electricity into light. Its principle of operation is like other laser, constituted by: source of pumping, a gain medium and a resonant cavity [1]. Even though a LD is designed to operate for more than 100,000 hrs. At the laboratory it is common to find several damaged devices, with symptoms ranging from: loss of brightness, shift in the threshold current of the diode, change in the divergence of the beam, difficulty to focus the beam spot, until finally the lack of lase [2].

We use high power LD for developing pulsed optical fibers lasers [3], and is mandatory the well-functioning on the LD. Thus, it is recommended to make a small investment of time and effort to choose or develop the best equipment, that adapts to the needs of the LD to be implemented. However, most of the equipment has connectivity systems, designed to operate through general purpose computer or PC.

2. Development of the system proposal

In this section is described the basis and first steps for controlling a LD instrument, the current and temperature controller, the Thorlabs ITC4020. The protocol is known as standard commands for programmable instruments (SCPI) [4]. The idea is stablishing a connection with the instrument via general-purpose instrumentation bus (GPIB) or more recently the universal serial bus (USB), see Fig. 1 (b). Mechatronics plays an important role automating the experiments; all you need to know is programing in a common language like C++, C#, or Visual Basic (VB), an example on Fig. 1 (a) for VB.

(a)

```
Sub Main()
    'Create TL4000 object
    'You can find the device resource name in the ITC4000 Remote Control menu
    'Eqivalent serial numbers are listed in the method description
    Dim itc = New TL4000("USB::4883::32842::M00300050::INSTR", True, False)
```

(b)

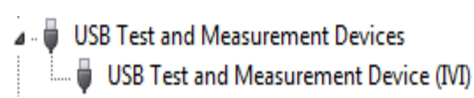

Fig. 1. (a) Extract of code for include the instrument, (b) Instrument recognized by a PC.

Next steps include download drivers, firmware, utilities and programming references. Once the device is identified it can be manipulated, controlling parameters like the on/off, voltage/current of operation, time delay on, the proportional-integral-derivative constants. Taking control on the full functionalities of the instrument. Including in some cases the manipulation of levels not reachable in the manually mode.

There are in the market various boards, working with microcontrollers or microprocessors, some popular, like Arduino, or the pic32, but there are also new ideas, in this case the eight-core propeller microcontroller, besides we find the well-known raspberry-pi or the beagle bone black (that needs for operate an operative system).

3. Results and discussion

The advantages are automatization in the laboratory, it means you can turn on/off devices even when you have not arrived the lab, or protect it when a variable jump up, in a program adequate for your needs. The system helps us to automate a high-power LD fiber pigtailed. That we need to increase the current automatically while we ensure the coupling into an optical fiber. In the experiment we vary the current that is supplied to the LD, covering an interval from 700 [mA] to almost 5500 [mA], with increments of 50mA. Fig. 2 (a) shows the instrument, the LD and the system for automating the current change. At Fig. 2 (b) depicts the current-optical power (I-P) graph. Finally, at Fig. 2 (c) is presented an example on how the automated LD is applied for pumping and characterizing an ytterbium doped fiber (YDF), necessary for our high-power pulsed fiber lasers.

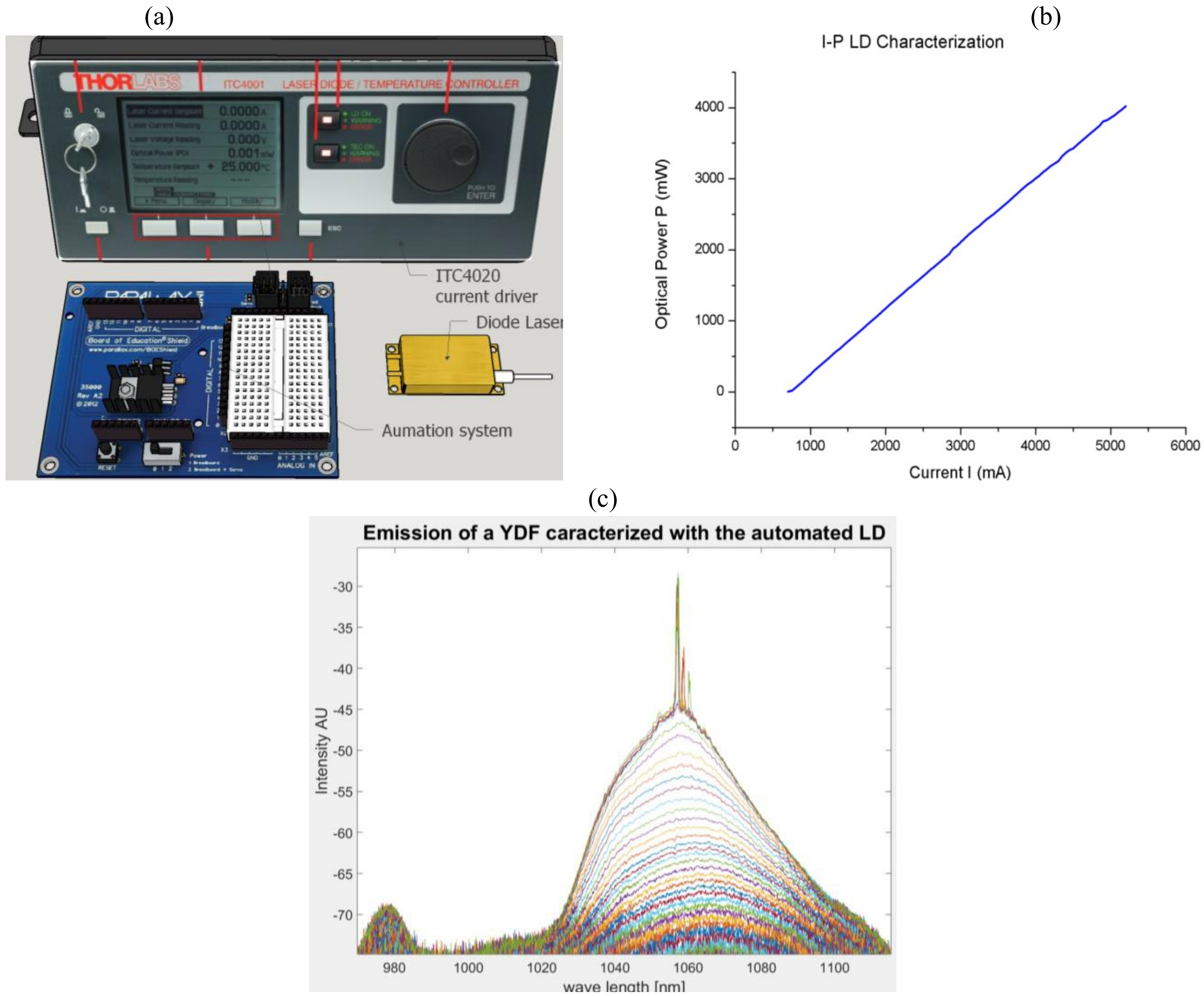

Fig. 2. (a) Automated system scheme, (b) I-P LD characterization, and (c) several measurements on a YDF pumped by the automated LD.

4. Conclusions

The implementation of this system is useful for the automation of the instrument. Because the control allows us to have better operating resolutions, in terms of current and temperature; with increments than are not possible manually. Those advantages allow us to work accurately on the experimentation of high power pulsed fiber lasers, where a power variation makes appears undesired nonlinear phenomena.

This work was supported by CONACyT on the doctoral student 245146, the Cátedra project No. 3155, and the projects CB 257691 and CB 2016-286916.

References

[1] R. Paschotta. (2018-08-15). *laser diodes*. Available: https://www.rp-photonics.com/laser_diodes.html

[2] D. Hodgson and B. Olsen, "Protecting your laser diode," *Newport Corporation Application Note,* p. 9, 2003.

[3] A. Braglia, A. Califano, Y. Liu, and G. Perrone, "Architectures and components for high power CW fiber lasers," *International Journal of Modern Physics B,* vol. 28, p. 1442001, 2014.

[4] S. Houlihan and A. Kalman, "Applying Standard Commands for Programmable Instruments (SCPI) to CubeSats," 2014.

Optical fiber Surface Plasmon Resonance-based temperature sensor

Monserrat Alonso Murias, Josué I. Basulto, J. Salvador Velázquez González, S. Marquez, and David Monzón-Hernández
Centro de Investigaciones en Óptica A. C. Loma del Bosque 115, León GTO. 37150, México
monsealo@cio.mx, dmonzon@cio.mx

Abstract: An accurate optical fiber thermometer based on Surface Plasmon Resonance (SPR) phenomenon is proposed and experimentally demonstrated. The fiber device consist of a single-mode fiber (SMF) spliced between two multimode fibers (MMF), the SMF section was coated with a thin Cr/Au film. The evanescent wave of the modes propagating through the SMF cladding interacts with the gold layer producing the plasmon excitation. Gold-coated fiber was covered with Polydimethylsiloxane (PDMS), due to its high thermo-optic coefficient, which acts as temperature transducer. Tracking the wavelength of the SPR dip allowed to measure the temperature with a sensitivity of 3066 pm/°C.

1. Introduction

Optical fiber sensors technology have been continuously evolving to satisfy the growing demand of sensors with improved sensitivity, resolution, accuracy or dynamic range. This demand is mainly motivated by the unique properties that fiber optics offer (electromagnetic immunity, low chemical and biological reactivity, small size and low weight, multiplexing capabilities), highly appreciate in a wide range of industrial applications. Optical fiber temperature sensors are the most representative example of the successful expansion of this technology to practically all strategic industries. Fiber Bragg gratings (FBGs) and fiber interferometers (FI) are intrinsically sensitive to temperature, condition that has been successfully exploited to propose a myriad of schemes to sense temperature. However, the temperature sensitivity of FBGs is modest (10 pm/°C), besides they are highly sensitive to stress (2 pm/με) [1]. By contrast, the temperature sensitivity of some interferometric sensors is high (1000 pm/°C) but the sensor schemes and the interrogation methods are in general complicated [2]. Here we propose a temperature sensor that takes advantage of the high refractive index sensitivity of the fiber SPR sensors. In this scheme the condition for plasmon excitation is tuned by the external temperature that changes the refractive index of a material with a high thermo-optic coefficient bonded to the fiber. We demonstrate that this temperature sensor is highly accurate and stable, with a temperature sensitivity of 3066 pm/°C, is biocompatible and can be easily integrated in schemes for biosensing applications.

2. Optical fiber Surface Plasmon Resonance sensor fabrication

The structure of the fiber used is shown in Fig. 1(a), which consists of a piece of SMF (10 mm) inserted between two MMF. Light injected into the core of the lead-in MMF is partially coupled to the core of the SMF and the rest is coupled to cladding modes. A small portion of the energy of the cladding modes is propagated as evanescent wave at the interface of cladding-external medium. Finally, part of the energy of the SMF cladding modes is coupled to the MMF core. When SMF cladding is coated with a gold thin film the plasmon excitation is possible. The evanescent wave is coupled to plasmon when phase-matching condition between the light and plasmon wave-vector is satisfied. Using the multilayer method described in [3], assuming a SMF length of 10 mm, and a MMF and SMF core diameter of 62.5 and 4.5 μm, respectively, it was found that the most suitable thin gold film thickness for this application was 30 nm. A chromium and gold thin film of 3 and 30 nm were successively deposited over one side of the SMF section by thermal and electron beam evaporation, respectively. Then fiber was rotated 180 degrees and the same thin films were evaporated. A white-light source and an optical spectrum analyzer were connected to each end of the gold-coated fiber device, as can be seen in the diagram shown in Fig. 1(b). The gold-coated fiber was mounted inside a rectangular container (35x10x10 mm, WxDxH) made with a stereolithography 3D printer (Form2, Formlabs), and the transmission spectrum was recorded. Then Polydimethylsiloxane (mixing ratio 1:15, PDMS Sylgard 184) was poured into the container to cover the fiber, the transmission spectrum was recorded and normalized to that measured in air. The resulted spectrum exhibits a characteristic SPR dip at 786.72 nm, see Fig. 2(a). PDMS was cured by heating it at 40 °C for 6 h using a Peltier plate, after curing the transmission spectrum (blue line) was shifted to a new position at 808.32 nm. The overall power level of the dip also increases, we believe this change is due to the thermal expansion coefficient of the resin used to fabricate the container that causes a slight strain of the fiber. Finally, the refractive index change of PDMS before and after curing was 1.4192 and 1.4246, these values were taken from the refractive index characterization curve of the gold-coated fiber obtained by immersing the fiber into water-glycerol solutions with different concentrations whose refractive indexes were measured with an Abbe refractometer.

3. Optical fiber temperature sensor characterization

When fiber sensor is heated (cooled) the refractive index of PDMS decreases (increases), due to the high thermo-optic coefficient $\left(\left[\frac{dn}{dt}\right] = -4.66\,x\,10^{-4}\,/\,°\mathrm{C}\right)$, and the resonance dip of the SPR curve shifts toward shorter (longer) wavelengths as can be seen in Fig. 2(b). By tracking the wavelength of the dip it is possible to stablish a one to one calibration curve between temperature and resonance wavelength. The sensor calibration curve exhibits a linear behavior in the range from 10 to 40°C as can be seen in Fig. 2(c).

4. Conclusions

A fiber thermometer based on an optical fiber SPR sensor was proposed and demonstrated. A multimode – single-mode – multimode fiber structure was used as a coupler to excite plasmon at the interface of thin gold film deposited over the SMF section and the external medium. The fiber SPR sensor is highly sensitive to the external medium refractive index changes. Embedding the fiber in PDMS that has a high thermo-optic coefficient, allowed to measure ambient temperature by tracking the shift of the SPR dip produced by the refractive index changes of the PDMS. The sensor exhibited a linear response in the range of 10 to 40 °C with a temperature sensitivity of 3066 pm/°C and a resolution of 0.5 °C. The structure of the thermometer is robust and compact, besides the response is highly stable, these features makes this sensor highly attractive for biosensing applications.

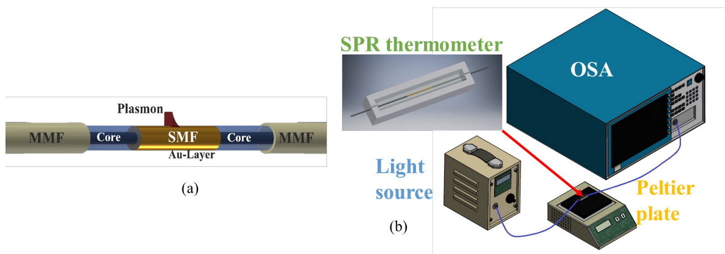

Fig. 1 (a) Representation of the optical fiber device. (b) Experimental setup for fiber transmission measurement.

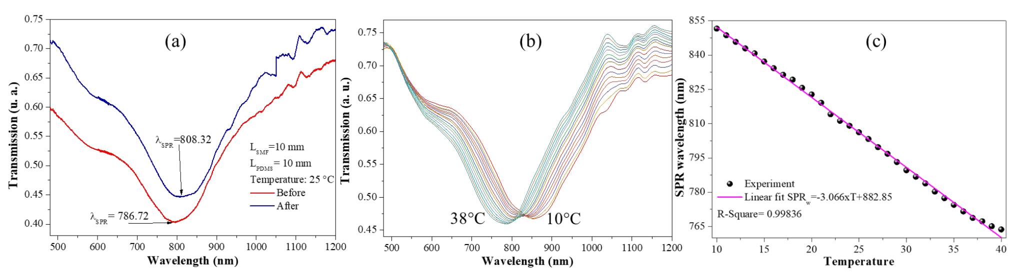

Fig. 2. (a) Experimental transmission spectra of fiber SPR when is covered with PDMS, before and after curing. (b) Experimental transmission spectra of fiber sensor when external temperature changes. (c) Temperature sensor calibration curve and linear approximation.

References

[1] A. Othonos and K. Kalli, "Strain and temperature sensitivity of Bragg gratings," in book *Fiber Bragg Gratings*, Ed. (Artech House, Norwood, MA. 1999).
[2] A. N. Starodumov, L. A. Zenteno, D. Monzon, and E. De La Rosa, "Fiber Sagnac interferometer temperature sensor," Appl. Phys. Lett. 70, 19-21, (1997).
[3] Y. Yuan, L. Ding, Z. Gou, "Numerical investigation for SPR-based optical fiber sensor," Sens. Actuators B, Chem, 101, 240-245, (2011).

Acknowledgement

Authors are grateful to CONACYT for financial support through the projects CB 257046 and 293442. We also want to thanks CONACYT for scholarships conceded to M. Alonso Murias, J. I Basulto, and J. S. Velázquez-González. This work was successfully carried out with the unconditional technical support of CIO´s mechanical and optical workshop.

Extended Abstracts

Session
OTHERS

	Pg.
Numerical investigation of a dual-channel prism-based Surface Plasmon Resonance sensor J. S. Velázquez-González, D. Monzón-Hernández, M. Torres-Cisneros, S. Marrujo-García, and I. Hernández-Romano	222
Effects of the roughness in the optical response of a 2DPhC that have dielectric or dispersive LHM cylindrical inclusions: The triangular lattice V Castillo-Gallardo, L Puente-Díaz, E Lozano-Trejo, H Pérez-Aguilar, and A Mendoza-Suárez	224
Disordered field patterns in a photonic crystal waveguide H. Alva Medrano, A. Mendoza Suárez, H. Pérez Aguilar	226
Optical response of two-dimensional square lattices with smooth and rough surfaces that include dispersive left-handed materials L. E. Puente-Díaz, V. Castillo-Gallardo, E. Lozano-Trejo, H. Pérez-Aguilar, A. Mendoza-Suárez	228
Electromagnetic surface modes in Photonic Crystal Waveguides that include rough surfaces of dispersive metamaterial J. E. Medina-Magallón, H. E. Alva-Medrano, H. Pérez-Aguilar, Petr Zhevandrov, A. Mendoza-Suárez	230
Acousto-optic dispersion applicability to plastic auto-part characterization Cesar Isaza, Ely Karina Anaya Rivera, Jonny Paul Zavala De Paz, Jose Amilcar Rizzo Sierra, and Julio Mosquera	232
Electromagnetic surface waves at the interface of a semi-infinite one-dimensional photonic crystal: an overview F. Villa-Villa, J. A. Gaspar-Armenta	234
Design and development of a dynamic images system for plantar pressure distribution monitoring Rodolfo Martínez-Manuel, Daniel A. Martínez-Barba, Leonel Daza-Benítez, Agustín Vidal-Lesso, R.M. Camarillo-Escobedo	236
Modelling and control of a two-axis solar tracking system	238

Yves J. Pérez D., Rubén Garrido, Arturo Díaz Ponce

Location of the highest intensity autocorrelation amplitude in the focusing of femtosecond pulses 240
J.A. Moreno-Larios, M. Rosete-Aguilar, O.G. Rodríguez-Herrera, J. Garduño-Mejía, and N.C. Bruce

Numerical investigation of a dual-channel prism-based Surface Plasmon Resonance sensor

J. S. Velázquez-González[1], D. Monzón-Hernández[1], M. Torres-Cisneros[2], S. Marrujo-García[2], and I. Hernández-Romano[3*]

[1]Grupo de sensores ópticos y microdispositivos (*GSOM*), Centro de Investigaciones en Óptica A. C., Loma del Bosque 115, C.P. 37150, León, Gto., México, [2]Electronics Department, DICIS, University of Guanajuato, Gto. 36885, México, [3]CONACYT-Electronics Department, University of Guanajuato, Gto. 36885, México.
*hromano@ugto.mx

Abstract: A numerical study of a dual-channel prism-based Surface Plasmon Resonance (SPR) sensor is accomplished considering a three-layer structure (prism/metal/polymer). Two different materials for each layer are taking into account to optimize the performance of the sensor.

1. Introduction

Refractive index (RI) sensors based on SPR using a prism have been shown high sensitivity, precision, and reproducibility. These characteristics have made them appeal for application in different areas such as biology, chemistry, and pharmaceutical industry. One drawback of the RI sensors is that any environmental temperature variations cause a RI value fluctuation, which means that an error is introducing in the measurement. It has been proposed devices that measure these two parameters at the same time to overcome this issue [1, 2].

Here, we report a numerical analysis of a SPR sensor based on a prism, in Kretschmann configuration, for measuring RI and temperature simultaneously. The sensor structure comprises a semi-cylindrical prism whose base is coated with a metal layer; then, a thick polymer layer is covering half of this film generating two sections for sensing. Laser beam is aligned to hit at the interface of these two sections, in the angle rotation scheme the reflected signal exhibits two well defined dips. The metal-bare section and the polymer-pad can be used for sensing RI and temperature changes, respectively. In the numerical simulations the following material were used SF10 and NSK16 (glass of the prism), Au and Ag (metals), and polydimethylsiloxane (PDMS) and poly (methyl methacrylate) (PMMA) (polymers).

2. Simulation results and discussion

The setup that is used for simulating the experiment is shown in Fig. 1 (a). Using the multi-layer (N-layer) model [3], it was simulated the reflectance of a prism made of NSK16 coated with 50 nm-thick film of silver (gold) and half of this films was covered with PDMS (PMMA), sea Fig. 1 (b) and (c). It was assumed that metal layer in the bare section is in direct contact with water (n = 1.3328) but in the section covered with the polymer does not interact with the liquid due to polymer thickness (5 mm). Silver-coated prims shows two well behaved dips for both polymers, but in the case of gold layer and PMMA dip generated is thicker and deformed due to high RI of the polymer (this configuration is not good for multi-parameter sensing). Using a prism made of SF10, the simulation was repeated, see Fig 1 (d) and (e). Two well behaved dips were observed for each polymer. Sharper SPR valleys are generated by using a silver film since the dielectric constant of the silver (real and imaginary part) is smaller than that of the gold.

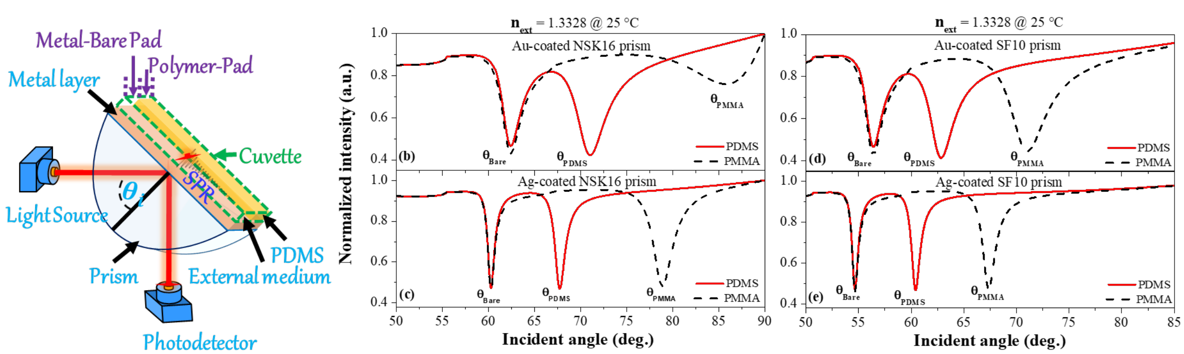

Fig. 1 (a) Setup used for the simulating experiment. Simulated reflectance using NSK16 prism coated with (b) gold, and (c) silver. Simulated reflectance using SF10 prism coated with (d) gold, and (e) silver.

RI sensibility was analyzed by simulating the reflectance of the prisms made of NSK16 and SF10 coated with silver and gold, respectively, and half covered with PMMA, see Fig. 2 (a) and (b). The temperature was fix at 25 ºC meanwhile the RI of the liquid that was in contact with the bare section was varied. The sensitivity of the NSK16/silver/PMMA is larger than that of SF10/gold/PMMA. Although silver gets sharper dips and better sensibility, gold does not oxidize as fast as silver when it gets in contact to liquids. Since PDMS thermo-optic coefficient (-4.66×10^{-4}/°C [4]) is higher than PMMA coefficient (-1.3×10^{-4}/°C [5]), PDMS is better for temperature sensing. Then, we decided to use NSK16, gold, and PDMS for simulating the following experiment. The reflectance of this device is numerical simulated using a prism made of NSK16 coated with 50 nm-thick film of gold and half of this films covered with PDMS. Fig. 2 (c) shows how the PDMS dip moves as the temperature increase, in a similar way the resonance angle θ_{Bare} of the dip moves as the RI varies, see Fig. 2 (d). The temperature sensitivity of the polymer pad and the RI sensitivity of the bare section were -0.0596 deg/ºC and 96.6797deg/RIU, respectively, see Fig 2 (e).

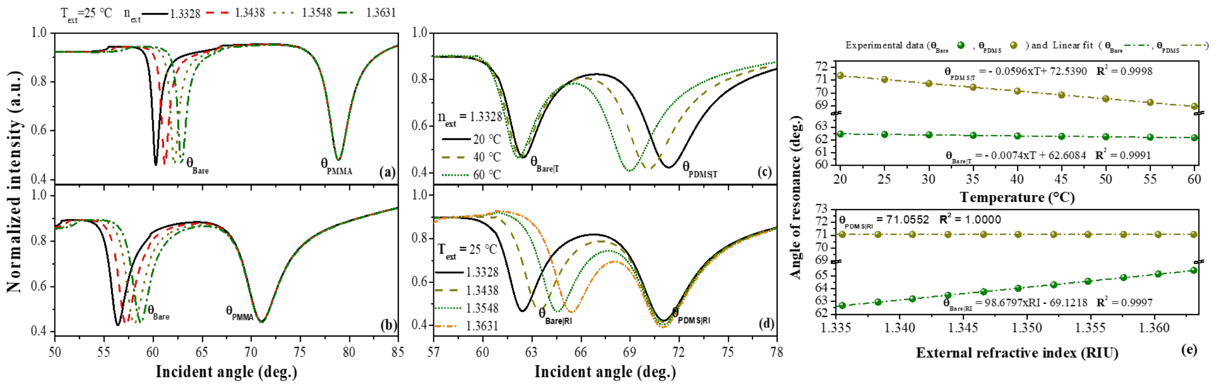

Fig. 2 (a) Simulated reflectance using NSK16 prism coated with silver. (b) Simulated reflectance using SF10 prism coated with gold. Simulated reflectance using NSK16 prism coated with gold (c) at three different temperatures and (d) four different RI at 25 ºC. (e) Temperature and RI sensitivities of the sensor.

3. Conclusions

In summary, a dual-channel prism-based SPR sensor was proposed and numerical analyzed. In this study, we found out that structure that presented a better performance was NSK16/gold/PDMS. The temperature sensitivity of the polymer pad and the RI sensitivity of the bare section were -0.0596 deg/ºC and 96.6797deg/RIU, respectively.

Acknowledgements

This research was supported through the CONACyT project CB 257046. J. Salvador Velázquez-González acknowledge CONACyT for financial support through postdoctoral scholarship. I. Hernández-Romano and M. Torres-Cisneros acknowledge the founding through the projects UG-DAIP-CIIC 2018: 71 and 72. Also S. Marrujo-García and M. Torres-Cisneros are in debt to CONACyT for the Ph.D. scholarship and for the project CB2016:#286629, respectively.

References

[1] W. Luo, S. Chen, L. Chen, H. Li, P. Miao, H. Gao, Z. Hu, M. Li, "Dual-angle technique for simultaneous measurement of refractive index and temperature based on a surface plasmon resonance sensor," Opt. Express, **25**, 2733-42 (2017).
[2] J. S. Velázquez-González, D. Monzón-Hernández, D. Moreno-Hernández, F. Martínez-Piñón, and I. Hernández-Romano, "Simultaneous measurement of refractive index and temperature using a SPR-based fiber optic sensor," *Sens. Actuators B, Chem.,* **242**, 912–920 (2017.)
[3] Y. Yuan, L. Ding, and Z. Guo, "Numerical investigation for SPR-based optical fiber sensor," Sens. Actuators B, Chem., **157**, 240–245 (2011).
[4] C. Moreno-Hernández, D. Monzón-Hernández, I. Hernández-Romano, and J. Villatoro, "Single tapered fiber tip for simultaneous measurements of thickness, refractive index and distance to a sample," Opt. Exp., **23**, 22141–22148, (2015.)
[5] Z. Zhang, P. Zhao, P. Lin, and F. Sun, "Thermo-optic coefficients of polymers for optical waveguide applications," Polymer, **47**, 4893–4896 (2006).

Effects of the roughness in the optical response of a 2DPhC that have dielectric or dispersive LHM cylindrical inclusions: The triangular lattice

V Castillo-Gallardo, L Puente-Díaz, E Lozano-Trejo, H Pérez-Aguilar*, and A Mendoza-Suárez
Facultad de Ciencias Físico-Matemáticas, UMSNH. Avenida Francisco J. Múgica S/N, C.P. 58030, Morelia, Michoacán, México.
E-mail: hiperezag@yahoo.com

Abstract: In this work, a numerical technique known as Integral Equation Method (IEM) was used to model the optical response of two-dimensional photonic structures of hexagonal lattice with rods that have smooth and rough surfaces, under TM polarization. Photonic structures were modeled by different materials. One of them was formed with dielectric – dielectric media and the other with dielectric – dispersive LHM media. We found that the optical response was modulated by the roughness of the surface of the inclusions. We also found that scattering patterns depend on the type of photonic structure and the incidence angle. Additionally, when we consider the two-dimensional photonic structure with rough surfaces, we approach a real physical system and this causes changes in the reflective optical properties.

1. Introduction

Photonic Crystals (PCs) are periodic arrays of different materials in one- (1DPC), two- (2DPC), and three- dimensions (3DPC) whit unit cells whose magnitude is on the order of the wavelength of the light [1]. PCs properties have been the subject of much research in last years because of its potential to development completely optical integrated circuits [2], or optical sensors [3]. In 2DPCs periodicity occurs in two directions, while in the other it is invariant. One of the purposes of this type of material is to control the reflection and/or transmission of light through its structure by the diffraction phenomenon. The reflective optical properties of the 2DPhC depend on the type of periodicity, geometry of the inclusions, the refractive index contrast and the filling fraction of the photonic structure [4].

When proposing a PC it is necessary to study the optical response of the system. In this work, the IEM [5] is used to calculate the optical response of 2DPC of the hexagonal periodicity with cylindrical inclusions with smooth and rough surfaces, under TM polarization. The results show that the roughness of the surfaces modulates the optical response. The IEM is based on the two-dimensional Green's second integral theorem applied to the Helmholtz's equation, in which integral equations obtained form a set of unknowns that are the field and its normal derivative evaluated in the contours that separate the regions of the system. In order to have a finite sampling of points, the contours are divided into small regions, Δs, so the coupled equations are approximated by sums that result in an inhomogeneous matrix system, whose solution determines the source functions. With these source functions, the optical response is obtained.

2. Results

The optical response of a two-dimensional photonic structure that consisting of a periodic array of parallel dielectric rods of circular cross section embedded in background dielectric material ($\varepsilon = 1$), whose intersections with a perpendicular plane form a triangular lattice is presented in Fig. 1. The rough surface profile on the inclusion wall of circular cross section is obtained by means of a realization of a Gaussian correlated random process that obeys a negative exponential probability-density function (PDF). Reflectance and scattering patterns for a photonic structure with 500 (5×100) dielectric circular cylinders are shown in Figs. 1(a)-(c), and a photonic structure with 720 (6×120) dispersive LHM circular cylinders in Figs. 1(d)-(f). The dashed curves shown correspond to an independent realization of the roughness with a correlation length $l_c = 0.05\lambda$ and a standard deviation of heights $\sigma = 0.01\lambda$ and the solid curves for a smooth profile of the inclusions cross section. In both cases, the filling fraction $f = 0.10$ was used. Photonic structures were illuminated with a Gaussian beam. The $1/e$ half-width of the modulus of the incident Gaussian beam projected on the center of the structures was $g = 12$ µm with TM polarization.

For these cases, the optical reflectance and transmittance are modulated due to the roughness of the surface of the inclusions, as shown in Fig. 1(a) and Fig. 1(d). However, the scattering patterns remain unchanged. Thus, scattering patterns depend on the type of photonic structure and the incidence angle.

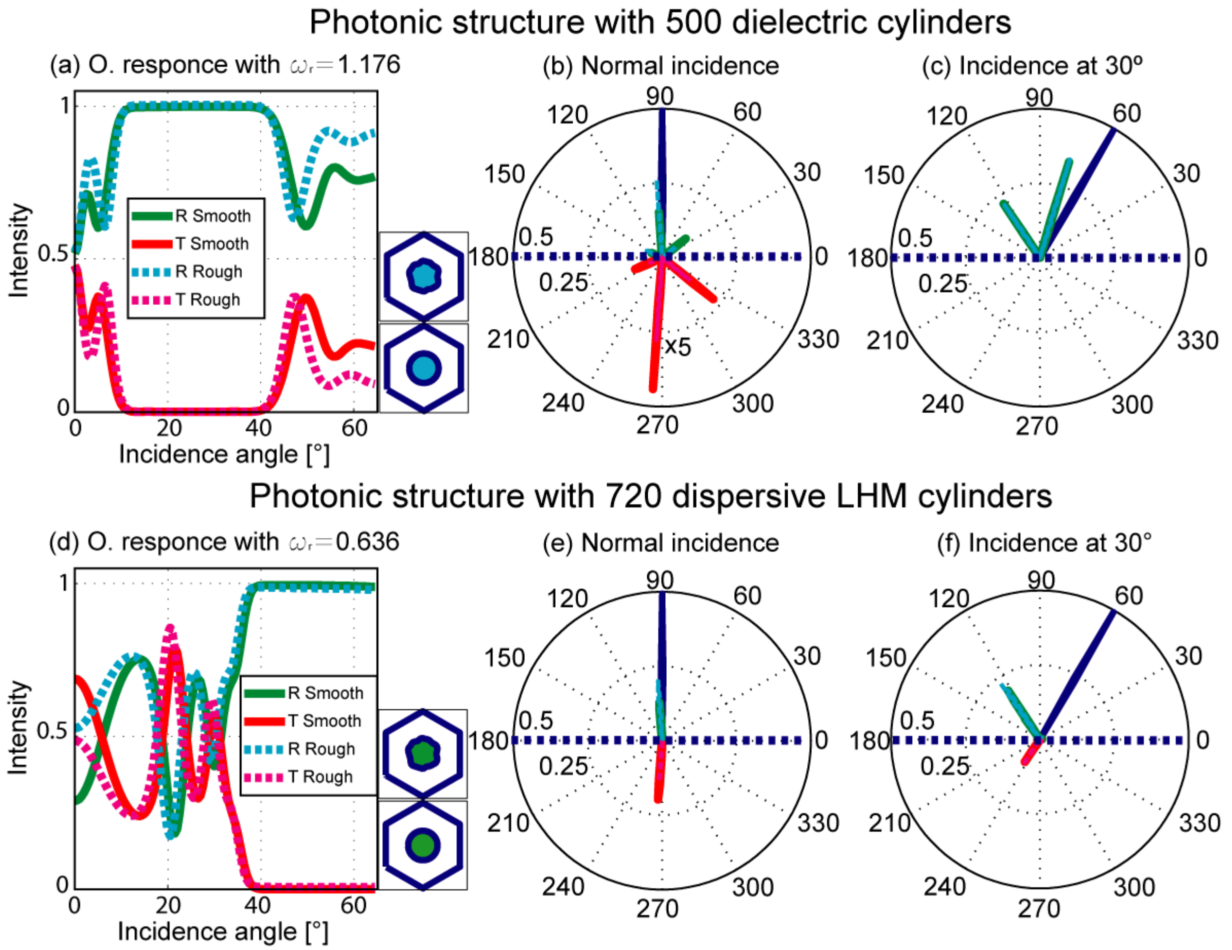

3. Conclusions

Using the integral method, it was possible to study the propagation of electromagnetic waves through truncated periodic photonic structures. This provided the opportunity to model the reflectance and scattering patterns of a couple of two-dimensional photonic structure that consisting of a periodic array of parallel dielectric rods of circular cross section embedded in background dielectric material. We found that the optical response was modulated by the roughness of the surface of the inclusions. We also found that scattering patterns depend on the type of photonic structure and the incidence angle.

[1] J D Joannopoulos, S G Johnson, J N Winn, and R D Meade, *Photonic Crystals: Molding the Flow of Light* (Princeton University Press, 2008), Chaps. 4-6.
[2] Anupam Mukherjee, *et al*, "Controlling the optical properties of composite multilayered photonic structures: effect of superposition," Opt. Express, **21**, 17324-17339 (2013).
[3] T V K Karthik, *et al*, "Porous silicon ZnO/SnO2 structures for CO2 detection," Journal of Alloys and Compounds **731** 853-863 (2017).
[4] Krauss T F and De La Rue R M, "Photonic crystals in the optical regime: past, present and future," Prog. Quant. Electron **23**, 51-96 (1999).
[5] A Mendoza-Suárez, *et al*, "Numerical method based on the solution of integral equations for the calculation of the band structure and reflectance of one- and two-dimensional photonic crystals," J. Opt. Soc. Am. B **23**, 2249 - 2256 (2006).

Disordered field patterns in a photonic crystal waveguide

H. Alva Medrano[1], A. Mendoza Suárez[1], H. Pérez Aguilar[1,*]
[1]Facultad de Ciencias Físico-Matemáticas, Universidad Michoacana de San Nicolás de Hidalgo, Av. Francisco J. Mujica S/N 58030, Morelia, Michoacán, México.
(*) E-mail: hiperezag@yahoo.com

Abstract: In this work we consider an electromagnetic system composed of two flat perfectly conductor surfaces and a periodic array of circular cylindrical inclusions forming a photonic crystal waveguide. This periodic system has a band structure given by a dispersion relation that allows us characterize eigenmodes of the system. We consider an integral numerical method to calculate field intensities corresponding to eigenmodes over a wide frequency range. Under certain conditions, the system presents disordered patterns of field intensities. We believe that the explanation of disordered patterns is the phenomenon of electromagnetic chaos. Since it is well known that the surfaces of materials always have a certain degree of roughness, it can be concluded that chaos contributes to the presence of disordered field patterns.

1. Introduction

It is now recognized that the basic random interference phenomenon underlying disordered patterns has close parallels in many other branches of physics and engineering [1]. It is also well known that, as a result of the interference among the distinct random contributions from the scattering centers, on scale of the optical wavelength, the scattered field pattern appears disordered, with certain granularity. This irregular pattern is best described by methods of probability theory and statistics.

The study of the statistical properties of disordered systems is of fundamental importance because it leads to phenomena such as weak (enhanced backscattering) [2] and strong (Anderson) [3] localization, intensity correlations [4], and universal conductance fluctuations [5]. The study of the transport properties of random systems has considered that the disorder in the system is usually represented by impurities that are randomly distributed throughout the sample. However, it is worth mentioning that our system of a waveguide with smooth rippled surfaces can present disordered field patterns; under certain conditions, of course. This kind of systems has been the subject of several studies in recent years due to their importance in waveguides that are related to photonic crystals, as per Ref. [6]. These systems, which constitute periodic arrays of different materials with a unit cell of dimensions of the order of the wavelength, have the potential to develop new technologies of integrated optical circuits [7]. The geometry of waveguides with inclusions has been considered to constitute some billiard systems in order to study their quantum and classical transport properties [8].

This paper examines an electromagnetic waveguide composed of two flat perfectly conductor (PEC) surfaces and a periodic array of circular cylindrical inclusions [See Fig. 1]. We used an integral numerical method to calculate field intensities corresponding to eigenmodes over a wide frequency range. Thus, this paper completes the study of the system introduced in Ref. [9]. The results of this study show that the system has many interesting properties.

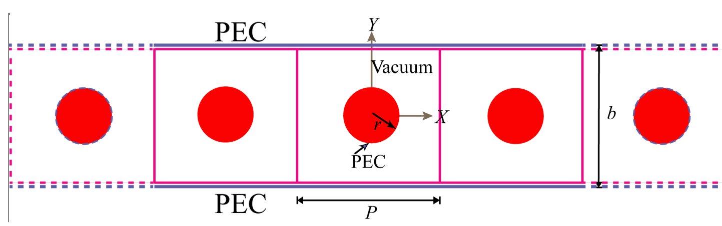

Fig. 1. Waveguide composed of two flat perfectly conductor surfaces and a periodic array of circular cylindrical inclusions.

2. Results

For this work, a waveguide formed by two flat perfectly conductor surfaces (without inclusions) was considered, with $b = 1.5,\ P = 2\pi,\ r = 0.$ In these calculations it is common to introduce dimensionless quantities, so our results will be expressed in terms of a reduced frequency given by $\omega_r = P/2\pi\,\omega$ and a reduced Bloch vector given by $k_r = P/2\pi\,k$. We obtained the field normalized intensity for both the low reduced frequency $\omega_r = 2.2400$ [Fig. 2(a)], and the high frequency $\omega_r = 70.0122$ [Fig. 2(b)]. In the case of a waveguide with flat walls, no chaos phenomenon appears.

In order to make reliable calculations in the case of high frequencies, it is necessary to use small discretization intervals. Due to numerical approximations involved, $\Delta S = (P/\omega_{rmax})/20$ was used. This value produced a good resolution in our calculations, which was then verified by comparing the numerical results with the corresponding analytical results for the flat waveguide.

Finally we consider a waveguide formed by two flat perfectly conductor surfaces and a periodic array of circular cylindrical inclusions forming a photonic crystal waveguide. The parameters considered are: $b = 1.5,\ P = 2\pi,\ r = 0.3b$. In this case we obtained the normalized field normalized for the reduced frequency $\omega_r = 1.2100$ [Fig. 2(c)] and $\omega_r = 70.0224$. For all cases we use the Bloch vector $k_r = 0$ and TE polarization.

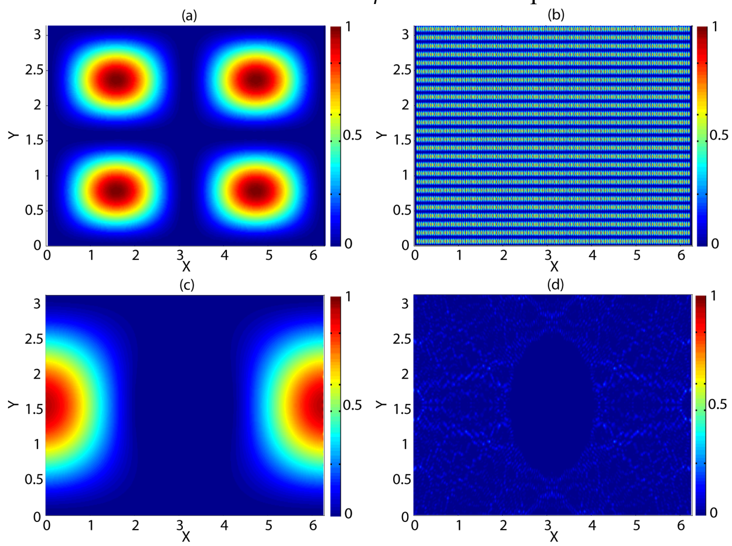

Fig. 2. Field intensities in a photonic crystal waveguide with $b = 1.5$, and $P = 2\pi$, for $r = 0$ with (a) $\omega_r = 2.2400$ and (b) $\omega_r = 70.0122$, and for $r = 0.3b$ with (c) $\omega_r = 1.2100$ and $\omega_r = 70.0224$.

Upon comparing the normalized field intensities obtained, the last case [Fig. 2(d)] shows a distribution of the field with greater disorder. We believe this is a manifestation of electromagnetic wave chaos, since in this regime led us to think that the intensity of the eigenmode is an uncorrelated random variable as a function of a point (x, y) in the unit cell. The field intensity shown in Fig 2(d) is not enough to ensure the presence of chaos; nevertheless, some systems classical with similar geometry, such as the Sinai billiard, presents chaos behavior, and this is our main argument.

3. Conclusions

An integral numerical method was applied to study a photonic crystal waveguide composed of two flat perfectly conductor surfaces and a periodic array of circular cylindrical inclusions. It is important to note that for certain conditions, disordered patterns of field intensities in our system were obtained. Some classical systems with similar geometry, such as the Sinai billiard, presents chaos behavior. This is our main argument in terms of interpreting some of our results as manifestations of electromagnetic wave chaos in the analyzed system.

References

[1] Shen, J.-T. and S. Fan, “Strongly correlated two-electron transport in a quantum waveguide having a single Anderson impurity,” New J. Phys. **11**, 113024 (2009)

[2] Sheng, P., Scattering and Localization of Classical Waves in Random Media, (World Scientific Publishing, 1990).

[3] Anderson, P. W., “Absence of diffusion in certain random lattices,” Phys. Rev. B. **109**, 1492–1505 (1958).

[4] Michel, T. R. and K. A. O’Donnell, “Angular correlation functions of amplitudes scattered from a one-dimensional, perfectly conducting rough surface,” J. Opt. Soc. Am. A, **9**, 1374–1384 (1992).

[5] Webb, R. A., S. Washburn, C. P. Umbach, and R. B. Laibowitz, “Observation of h/e Aharonov-Bohm oscillations in normal-metal rings,” Phys. Rev. Lett. **54**, 2696–2699 (1985).

[6] Mendoza-Suárez, A., H. Pérez-Aguilar, and F. Villa-Villa, “Optical response of a perfect conductor waveguide that behaves as a photonic crystal,” Progress In Electromagnetics Research. **121**, 433–452 (2011).

[7] Inoue, K. and K. Ohkata, Photonic Crystals, (Springer, 2004).

[8] Deng, Jiawen, et al. “Merits and qualms of work fluctuations in classical fluctuation theorems.” Physical Review E. **95**, 012106 (2017).

[9] Pérez-Aguilar, H., and A. Mendoza-Suárez. "Numerical study on a photonic crystal waveguide that includes a dispersive metamaterial." J. Opt. Soc. Am. B. **23,** 2249-2256 (2006).

Optical response of two-dimensional square lattices with smooth and rough surfaces that include dispersive left-handed materials

L. E. Puente-Díaz[1], V. Castillo-Gallardo[1], E. Lozano-Trejo[1], H. Pérez-Aguilar[1*], A. Mendoza-Suárez[1]

1. Facultad de Ciencias Físico-Matemáticas, Universidad Michoacana de San Nicolás de Hidalgo. Avenida Francisco J. Múgica S/N, C.P. 58030, Morelia, Michoacán, México.
(*) e-mail: hiperezag@yahoo.com

Abstract: In the present work, we show a numerical study of the electromagnetic response of two-dimensional square lattices such as finite photonic structures formed by cylinders embedded in air and holes in a drilled in a metamaterial matrix. We applied a numerical technique known as Integral Equation Method (IEM) to calculate the optical response of the proposed finite systems by calculating reflectance and transmittance as a function of the angle of incidence. The calculations were performed by varying the filling fractions and introducing a roughness on the surfaces of the cylindrical inclusions under TE polarization. The results obtained show that the roughness on the surfaces of the cylindrical inclusions affects their reflective and transmissive properties of two-dimensional square lattices.

1. Introduction

Metamaterials, also known as Left-Handed Materials (LHMs), have attracted great research interest among researchers in different fields. This enthusiasm can be attributed mainly to its unique electromagnetic characteristics, due to the fact that the light vectors (**E**, **H**, **k**) form a triad of orthogonal vectors with left orientation for a wave propagating through these media [1]. An important quality of these materials is that they have a negative refractive index within a given range of the electromagnetic spectrum.

The study of the propagation of light in finite photonic structures is based on numerical methods. In this work, we applied the numerical IEM [2, 3] which presents some advantages in comparison with other methods, since it has the capacity to study different aspects of these systems that have complicated geometries and very novel physical properties, such as those corresponding to the LHMs.

2. Theoretical approach

The present work aims to make a theoretical and numerical study of the electromagnetic response of finite systems such as photonic structures formed by cylinders embedded in air and holes in a drilled in a metamaterial matrix, considering a roughness on the surfaces of the cylindrical inclusions. The IEM employed is based on the Green's second identity to solve the Helmholtz equation. The description of the Integral Equation Method can be found in Ref. [3], as well as the dielectric function and magnetic permeability, as a function of frequency, used to numerically model the optical properties of the LHMs.

3. Optical response of finite two-dimensional square lattices composed of cylindrical inclusions with smooth and rough surfaces

As examples of applications, we consider different systems of finite two-dimensional square lattices such as photonic structures formed by cylinders embedded in air and holes in a drilled in a metamaterial matrix, considering a roughness on the surfaces of the cylindrical inclusions that form our proposed systems. Finite photonic structures are composed of 500 inclusions (125 inclusions in the X-direction and 4 inclusions in direction of the Y-direction). In Figs. 1(a) and (c) show the results obtained from the optical response by calculating the reflectance and transmittance as a function of the incident angle that is illuminated by a Gaussian beam and filling fractions $f = 0.04$ and $f = 0.06$, respectively for the TE polarization. To study the effects of roughness in these systems, we considered a profile that has a roughness with a correlation length $\delta = 0.05\lambda$ and a standard deviation of heights of $\sigma = 0.02\lambda$ on the surfaces. This profile is defined by a realization of a Gaussian-correlated random process that obeys a negative exponential probability-density function (PDF) [4]. In Figs. 1(b) and (d), we show the results of the equivalent system formed by cylinders embedded in air that include LHM.

In these systems, the optical properties given by the refractive indexes $n = -1.87$ and $n = -1.25$ correspond to medium containing inclusions in the case of finite photonic structures formed by air holes in an finite plate and the medium contained in the cylindrical inclusions embedded in air, respectively. The parameters used for these systems were: a length of interfaces $l = 125$ μm, a distance between interfaces $d = 5$ μm and a half-width of the Gaussian beam of $g = 2.12$ μm for $\lambda = 1.33$ μm ($\omega_r = 0.75$) and of $g = 1.99$ μm for $\lambda = 1.25$ μm ($\omega_r = 0.80$).

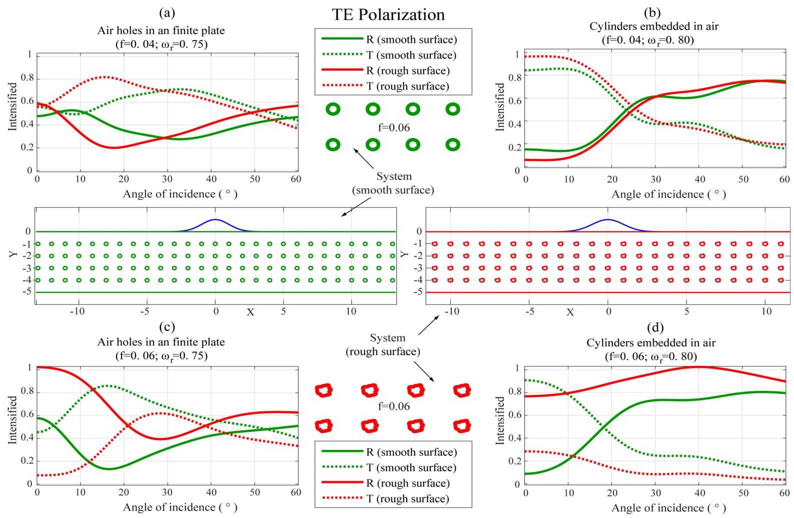

Fig. 1. Reflectance (solid curves) and Transmittance (dotted curves) for finite two-dimensional square lattices formed by periodic arrays of cylindrical inclusions of smooth or rough surfaces (with parameters $\boldsymbol{\delta = 0.05\lambda}$ and $\boldsymbol{\sigma = 0.02\lambda}$) with filling fractions of ((a) and (b)) $\boldsymbol{f = 0.04}$ and ((c) and (d)) $\boldsymbol{f = 0.06}$ for the TE polarization.

When comparing the results of the different systems of finite two-dimensional square lattices with cylindrical inclusions of smooth surface with their corresponding rough surface systems, we can observe that the reflective and transmissive properties are affected for the polarization TE by including a roughness on the surface of the cylindrical inclusion.

4. Conclusions

A numerical method, known as the IEM, was used to calculate the electromagnetic response of two-dimensional square lattices. By comparing the results of the optical response, of the different proposed systems, we conclude that the roughness on the surfaces of the cylindrical inclusions affects the reflective and transmissive properties. These results are very important because they indicate that this aspect is important to take into account in the process of manufacturing of a finite two-dimensional square lattice.

References

[1] V. G. Veselago, "The Electrodynamics of Substances with Simultaneously Negative Values of ε and μ," Sov. Phys. Usp. **10**, 509-514 (1968).
[2] A. Mendoza-Suárez, F. Villa-Villa, and J. A. Gaspar-Armenta, "Numerical method based on the solution of integral equations for the calculation of the band structure and reflectance of one- and two- dimensional photonic crystals," J. Opt. Soc. Am. B. **23**, 2249-2256 (2006).
[3] A. Mendoza-Suárez, F. Villa-Villa, and J. A. Gaspar-Armenta, "Band structure of two-dimensional photonic crystals that include dispersive lefthanded materials and dielectrics in the unit cell," J. Opt. Soc. Am. B. **24**, 3091-3098 (2007).
[4] A. A. Maradudin, T. Michel, A. R. McGurn and E. R. Méndez, "Enhanced backscattering of light from a random grating," Ann. Phys. (N.Y.). **203**, 255-307 (1990).

Electromagnetic surface modes in Photonic Crystal Waveguides that include rough surfaces of dispersive metamaterial

J. E. Medina-Magallón[1], H. E. Alva-Medrano[1], H. Pérez-Aguilar[1,*], Petr Zhevandrov[1], A. Mendoza-Suárez[1]

1. Facultad de Ciencias Físico-Matemáticas, Universidad Michoacana de San Nicolás de Hidalgo. Avenida Francisco J. Múgica S/N, C.P. 58030, Morelia, Michoacán, México
(*)E-mail: hiperezag@yahoo.com

Abstract: In this work we present a numerical study of the electromagnetic response of a Photonic Crystal Waveguide (PCW) formed by two flat conductive plates containing inclusions with smooth and rough surfaces of dispersive metamaterial (LHM). The numerical technique we have used to perform the calculations is known as the "Integral Equation Method" (IEM). The numerical results the PCW that contains dispersive metamaterial (LHM) inclusions with arbitrary geometries, present an electromagnetic surface mode at frequency $\omega_r = 0.7503$. This mode is a surface-plasmon mode with a frequency very close to ω_r^{psw}, whose corresponding intensity distribution is highly-localized in the vicinity of the vacuum–LHM interface.

1. Introduction

In recent decades, many researchers have done various theoretical studies on how to control the electromagnetic properties of materials and the behavior of light through them. The interest of this work is to the study of surface plasmon polariton (SPPs) excitation in PCWs that contain LHM because the behavior of light when interacting with these have interesting properties in since electric field **E**, magnetic field **H** and wave vector **k** form a system of orthogonal vectors with a left orientation for a wave propagating through these media [1]. This property is useful in the development of new integrated optical circuits having novel features [2].

2. Theoretical approach

Assuming the time dependence $e^{-i\omega t}$ for the electromagnetic fields, the wave equation can be transformed to the equation of Helmholtz

$$\nabla^2\Psi_j(\mathbf{r}) + k^2\Psi_j(\mathbf{r}) = 0, \tag{1}$$

where the index j = 1 or 2 indicates the j-th medium with dielectric constant ε_j forming the system under study, as shown in Fig. 1. The function $\Psi_j(\mathbf{r})$ represents the field E_z in the case of TE polarization being considered in this work. It is considered that the electromagnetic field $\Psi_j(\mathbf{r})$ satisfies the boundary conditions and periodicity conditions of the PCW in the horizontal direction by means of the Bloch theorem. Now we introduce a function of Green $\mathrm{G}(\mathbf{r},\mathbf{r}') = i\pi H_0^{(1)}(\omega|\mathbf{r}-\mathbf{r}'|/c)$ where $H_0^{(1)}(z)$ is the Hankel function of the first kind and zero order. Taking into consideration the geometry of the system shown in Fig. 1, and applying the two-dimensional Green's second identity for the functions Ψ and G, we obtain

$$\frac{1}{4\pi}\oint_C \left[\frac{\partial\Psi(\mathbf{r}')}{\partial \mathrm{n}}\mathrm{G}(\mathbf{r},\mathbf{r}') - \frac{\partial \mathrm{G}(\mathbf{r},\mathbf{r}')}{\partial \mathrm{n}}\Psi(\mathbf{r}')\right] ds' = \theta(\mathbf{r})\Psi(\mathbf{r}), \tag{2}$$

being $\theta(\mathbf{r}) = 1$ if **r** is inside the unit cell and $\theta(\mathbf{r}) = 0$ otherwise. ds' is the differential arc's length, $\hat{\mathbf{n}}$ is the outward normal vector to C, and the observation point **r** is infinitesimally separated of contour C outer to the unit cell.

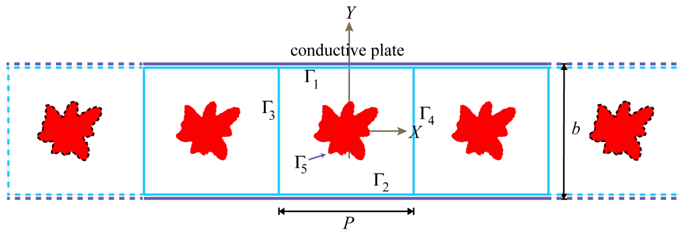

Fig.1. Graphic description of the PCW of flat conductive surfaces and a periodic array of inclusions with arbitrary geometry of different materials. The Γ contours define the unit cell or the system with periodicity in the x-direction.

By doing a discretization of the contours Γ_j, we can numerically represent Eq. (4) through an algebraic linear system $M(\omega)F(\omega) = 0$ which has an associated representative matrix, M, whose a nontrivial solution is if the determinant function $D(k,\omega) = \ln(|\det(M)|)$ is zero. More details on the method are given in Ref. [3].

The properties of LHM given by $\varepsilon(\omega)$ and $\mu(\omega)$ are expressed in the form [4]

$$\varepsilon(\omega) = 1 - \frac{\omega_p^2}{\omega^2} \text{ y } \mu(\omega) = 1 - \frac{F\omega^2}{\omega^2 - \omega_0^2}, \tag{3}$$

with the plasma frequency ω_p and the resonance frequency ω_0. These functions allow us to determine the region where the LHM has a negative refraction index within the frequency range $\omega_0 < \omega < \omega_{LM}$ with the parameters $\omega_p = 10/2\pi$, $\omega_0 = 4/2\pi$, $F = 0.56$ and $\omega_{LM} = \frac{\omega_0}{\sqrt{1-f}} = 0.9597$ [3].

3. Results

In Fig. 2, we show the functions $D(k = 0, \omega_r)$. The geometric values of the unit cell were: $b = 4\pi$, $P = 2\pi$ and the filling fraction $f = 0.005$ (Figs. 2(a) and (c)). Firsly, we illustrate the case with smooth surfaces (Fig. (a)). Subsequently, the surface roughness with standard deviation of heights $\sigma = 0.17\lambda$ and correlation length $\delta = 0.001\lambda$ (Fig. 2(c)). Showing the position of the extreme minimum is identified as the frequency of the mode with the value $\omega_r = 0.7503$, in both cases. Which corresponds to a surface plasmon mode with a frequency of $\omega_r^{psw} = \omega_0\sqrt{2/(2-F)} = 0.7502$ in the LHM–vacuum interface [3]. Moreover, the intensity of the electric field within of the unit cell is shown in Fig. 2(b) and (d), respectively.

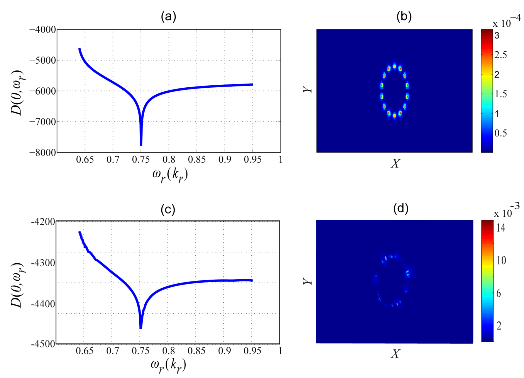

Fig. 2. Functions $D(k = 0, \omega_r)$ for PCWs formed with two perfectly conducting flat surfaces and a periodic arrangement of cylindrical inclusions of dispersive LHM. The parameters used were: $b = 4\pi$, $P = 2\pi$ and $f = 0.005$ of cylindrical inclusions with (a) smooth and (c) rough surfaces with $\sigma = 0.17$, $\delta = 0.001$. (b) and (d) electric field distribution at the frequency $\omega_r = 0.7503$ corresponding to the cases shown in (a) and (c).

It should be noted that due to the computational challenge we face when calculating the electric field intensity, we are still improving the calculation of it with a larger roughness. However, these results give evidence of the surface-plasmon mode in the vicinity of the vacuum-LHM interface.

4. Conclusions

For the specific LHM considered, we found surface-plasmon modes on the vacuum-LHM interface of cylindrical inclusions with smooth and rough surfaces. Which allow us to conclude that the roughness does not affect the position of the mode, even varying the size and shape of the LHM inclusion. These surface modes can be used as another alternative in the development of applications in different fields of science and technology ranging from biomedicine to telecommunications.

References

[1] V. G. Veselago, "The Elecctrodynamics of Substances with Simultaneously Negative Values of ε and μ," Sov. Phys. Usp. **10** 509-514 (1968).
[2] J. M. J. Santillán, F. A. Videla, L. B. Scaffardi, "Plasmon Spectroscopy for Subnanometric Copper Particles: Dielectric Function and Core–Shell Sizing," Plasmonics **8** 341-348 (2013).
[3] H. Pérez-Aguilar, y A. Mendoza-Suárez, "Numerical study on a photonic crystal waveguide that include a dispersive metamaterial," Opt. Pura Apl. **49** (3) 115-123 (2016).
[4] J. B. Pendry, A. J. Holden, D. J. Robbins, and W. J. Stewart, "Low frequency plasmons in thin-wire structures," Journal of Physics: Condensed Matter **10**, 4785-4809 (1998).

Acousto-optic dispersion applicability to plastic auto-part characterization

Cesar Isaza[a], Ely Karina Anaya Rivera[a], Jonny Paul Zavala De Paz[a], Jose Amilcar Rizzo Sierra[a], and Julio Mosquera[b].
(a) Universidad Politécnica de Querétaro. El Marqués, Querétaro, México.
(b) Universidad del Quindío. Quindío, Colombia.
amilcar.rizzo@gmail.com

Abstract: Acoustic-optic (or acousto-optics) dispersion is a phenomenon that occurs when light as an electromagnetic field interacts with a translucent material in which a sound-induced spatial distribution of its refractive index is present. That is, light from a source of interest gets diffracted by a crystal lattice in which sound-provoked photo-elasticity occurs. That diffracted light can then be analyzed for different properties of the source. The experimental and theoretical basis of the phenomena were proposed in early 20th century, mainly by Brillouin and Raman, respectively. Since the progressive development in optics and electronics over the last century, acousto-optics as a field in its own right has strongly transited towards applied technology such as image processing in military applications. We propose the conformation and setup of an acoustic-optic system in order to capitalize on its capability to provide hyper-spectral images of objects to explore the possibility of conducting plastic auto-parts characterization in terms of color. Current methodologies regarding the same subject use mainly Colorimeters, which by default can not provide the same amount of spectral information than an acousto-optic system could gather. Yet still, some of the current methodologies keep relying on naked eye subjective observations for certain stages of their data gathering. In this context, a distinctive potential of acousto-optic technology lies within the subject of plastic auto-parts cosmetic corrosion (PACC) characterization, term which would refer to the study of undesirable changes in color (in plastic auto-parts) due to time and exposure.

1. Introduction.

Auto-parts industry is clearly one of the most important industrial sectors in Mexico. In 2016 figures it represented 2.8\% of its gross domestic product and 16.9\% of its total manufacture activity, and the country consolidated itself as the 7th world's largest auto-parts producer in 2017. The industry has shown an overall growth of more than 40\% from 2008 to 2016. That represented an approximate growth from 9.5\% to 16.9\% of the manufacture sector GDP in that time frame [1, 2]. That dynamic has brought intense accompanying research and development activity in Mexico related to the sector as well, both in private and public institutions in a much needed and developing supporting role to the industry.

One of the current concerns that more technology and economy-savvy customers have been expressing to automotive industry relates to undesirable cosmetic or aesthetic changes due to time and exposure of all kinds of plastic auto-parts used for both interior and exterior application in motor vehicles. It is understood that this represents one of the most important factors upon which buying decisions are made by actual customers, complementing usual factors such as vehicle performance, security, communication, and technology integration features, along with a numerous list of others. Facing that, the automotive industry have had to develop standards and protocols to ensure its processes can come up with products with sufficient quality to meet these and others consumer's criteria. For example: research, development, and testing of plastic materials which retain its cosmetic properties in terms of color for at least a period of time equivalent to the engine/chassis warranty is one of the goals within this subject.

Besides being one of the customers main concerns regarding automotive aesthetics perceptions and requirements, the subject has in itself great importance as well, since the industrial treatment to the plastic materials which happens to prove itself to fulfill cosmetic requirements could affect other material properties as well, such as mechanical ones. Additionally, the standards that currently are typically used to validate a new material before sending it to plastic injection processes present a lack of proper technical measurement for the optical aspects defining important properties in the context of plastic auto-parts cosmetics, such as color. One key aspect to consider is that all current tests employed in the industry are, in one stage or another, based on human naked eye observations, prone to different types of methodological subjectivity.

Thus, we propose in this paper a new methodology to study changes in automotive plastic components by using acousto-optic filtering of the light coming from them. This technology has the ability to analyze the reflection of objects for a wide range of the spectrum; from the near infrared to the ultraviolet [3-10]. The images are acquired at a high spectral resolution that gives details about the hyper-spectral information of a particular material, greatly complementing the information that can be gathered by means of Colorimeters, which are the main current data gathering technology employed in the subject.

References

[1] Retos de la Industria Automotriz ante los cambios en los bloques comerciales. Boletín: Sector Externo. Centro de Estudios de las Finanzas Públicas (2018), http://www.cefp.gob.mx/publicaciones/boleco/2018/becefp0172018.pdf Accesed on 05/08/2018.
[2] INE with data from INEGI & IHS MARKIT, (2018).
[3] Berg, Norman J., and John N. Lee. "Acousto-optic signal processing: theory and implementation." New York, Marcel Dekker, Inc. (Optical Engineering. Volume 2), 1983, 496 p. No individual items are abstracted in this volume. Vol. 2. 1983.
[4] Rhodes, William T. "Acousto-optic signal processing: convolution and correlation." Proceedings of the IEEE 69.1 (1981): 65-79.
[5] Gat, Nahum. "Imaging spectroscopy using tunable filters: a review." Proc. Spie. Vol. 4056. No. 1. 2000.
Denes, Louis J., Milton S. Gottlieb, and Boris Kaminsky. "Acousto-optic tunable filters in imaging applications." Optical Engineering 37.4 (1998): 1262-1267.
[6] Bei, Ling, et al. "Acousto-optic tunable filters: fundamentals and applications as applied to chemical analysis techniques." Progress in Quantum Electronics 28.2 (2004): 67-87.
[7] Tran, Chieu D. "Principles and analytical applications of acousto-optic tunable filters, an overview." Talanta 45.2 (1997): 237-248.
[8] Voloshinov, V. B., V. Ya Molchanov, and J. C. Mosquera. "Spectral and polarization analysis of optical images by means of acousto-optics." Optics & Laser Technology 28.2 (1996): 119-127.
[9] Korpel, Adrianus. "Acousto-optics¿a review of fundamentals." Proceedings of the IEEE 69.1 (1981): 48-53.
[10] Chang, I. C. "Tunable acousto-optic filters: an overview." Opt. Eng 16.5 (1977): 455-460.

Electromagnetic surface waves at the interface of a semi-infinite one-dimensional photonic crystal: an overview

F. Villa-Villa*, J. A. Gaspar-Armenta**
*Centro de Investigaciones en Optica, Loma del Bosque 115, Lomas del Campestre, León Gto. 37150 México.
**Departamento de Investigación en Física, Universidad de Sonora, A.P. 5-088, Hermosillo, Sonora, México, 83190
e-mail: fvilla@cio.mx

Abstract: The progress achieved in the application of EM surface modes as sensing devices in systems composed of one-dimensional photonic crystals-bulk materials is reviewed, and some features not considered in the existing literature are analyzed. In particular the decaying length beyond the transverse section of a Gaussian beam is determined when considering that composing materials are real dielectrics with a small extinction coefficient.

1. Introduction

Some years after the invention of photonic crystals (PC) [1], surface electromagnetic waves (SW) that can exist at the interface between a semi-infinite one-dimensional photonic crystal (1DPC) and a bulk material [1-3] have been applied in a sensing device based on the attenuated total reflectance in a similar way to surface plasma waves (SPW) on metals to determine optical properties of thin films and liquid substances [4].

Important advantages of SW against SPW as a sensing device are that PC surface modes are built from highly stable dielectric materials. The 1DPC-bulk system can be constructed to present SW at any frequency of the electromagnetic spectrum and its sensitivity can be manipulated depending on many factors, as the truncation of the layer in contact with the bulk material, the extinction coefficient of composing dielectric layers, and the number of periods of the finite 1DPC. These factors will affect the penetration depth of the EM waves within the PC and the decaying length along the surface and as a consequence the sensitivity of the system.

It has been demonstrated elsewere [1-2] that a SW which is a highly localized mode long a PC-bulk interface is located in regions of the dispersion diagram below the light line of air or vacuum and within a band gap [2-3]. In Fig. 1a we show the band structure under TE polarization of a 1DPC whose period is composed of symmetric period of three dielectric layers p/2-q-p/2 with refractive indices and thicknesses: $n_p = 2.44$ $d_p = 48.4 nm$, $n_q = 1.46$, and $d_q = 157\ nm$ respectively. In this dispersion diagram $\bar{\omega} = \omega\Lambda / 2\pi c$, and $\bar{\beta} = \beta\Lambda / 2\pi$ represent the reduced frequency, and the reduced parallel component of the wave vector respectively. The normalization constant $\Lambda = 2d_p + d_q$ and *c* is the speed of light in vacuum.

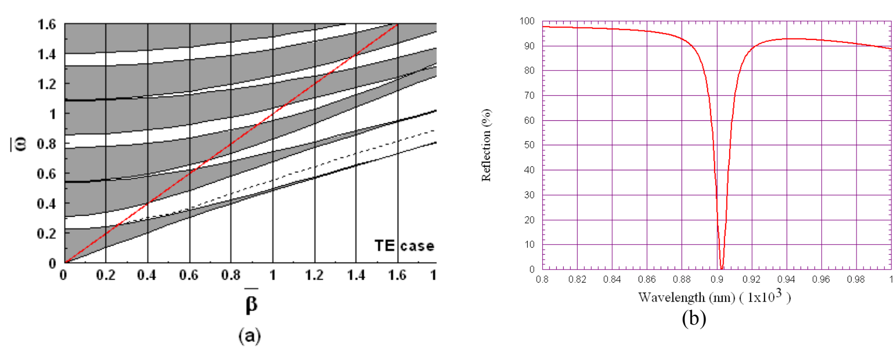

Fig. 1. a) Band structure of 1DPC under TE polarization. Allowed bands are indicated by shaded regions and band gaps with white color. The light line for vacuum is shown in red line b) Reflectance vs. wavelength in the region around the SW for $\bar{\beta} = 0.327$ and

$\varpi = 0.281$, which correspond to $\theta = 50^{\circ}$ with an incident medium of $n_0 = 1.52$.

Within the first bang gap an SW is indicated by a dashed curve. In Fig. 1b the reflectance as a function of the wavelength in the region around the SW is graphed for a finite system with five periods. In order to observe the SW a five period PC was considered assuming an absorption index $k_p = 0.01$.

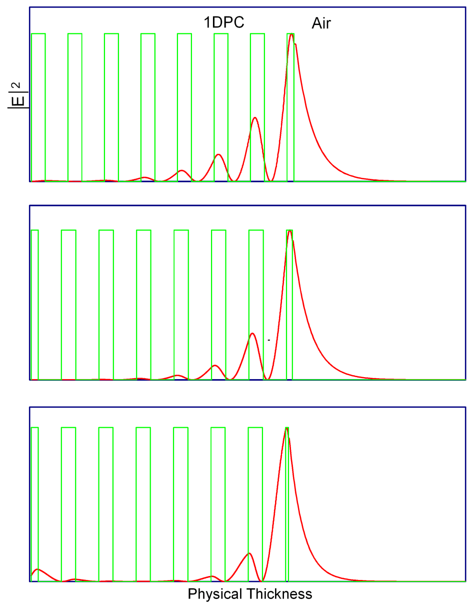

Fig. 2. Profile of the electric field intensity for different truncations of the layer in contact with the bulk. a) upper graphic SW at $\lambda = 902.7$ *nm* last layer $d = 48.4$ *nm*. Middle SW at $\lambda = 859.2$ *nm* $d = 40$ *nm*. Lower SW at $\lambda = 859.2$ *nm* $d = 20$ *nm*.

References

[1] F. Villa, L. E. Regalado, F. Ramos-Mendieta, J. Gaspar-Armenta, and T. López-Ríos, “Photonic crystal sensor based on surface waves for thin film characterization”, Opt. Lett. **27** 646-648 (2002).

[2] F. Villa, J. A. Gaspar-Armenta, and F. Ramos-Mendieta, “One-dimensional photonic crystals: equivalent systems to single layers with a classical oscillator like dielectric function”, Opt. Comm. **216** 361-367 (2003).

[3] Jorge A. Gaspar-Armenta, Francisco Villa, “Band structure properties of one-dimensional photonic crystals under the formalism of equivalent systems,” JOSA-B, 21 405-412 (2004).

[4] A. Sinibaldi, N. Danz, E. Descrovi et al., “Direct comparison of the performance of Bloch surface wave and surface plasmon polariton sensors,” Sensors. and actuators B-Chemical **174,** 292-298 (2012).

Design and development of a dynamic images system for plantar pressure distribution monitoring

Rodolfo Martínez-Manuel[1*], Daniel A. Martínez-Barba[1,2], Leonel Daza-Benítez[3], Agustín Vidal-Lesso[4], R.M. Camarillo-Escobedo[2]

[1]Centro de Investigaciones en Óptica, A.C., CIO, Aguascalientes, 20200, México.
[2]Instituto Tecnológico de la Laguna, Blvd. Revolución y Calz. Cuauhtémoc, 27000 Torreón, Coahuila, México.
[3]Hospital Ángeles León, Servicio Reumatología, Av. Cerro gordo, 37150, León, Gto. México.
[4]Universidad de Guanajuato, Departamento de Ingeniería Mecánica, 36885, Salamanca, Guanajuato, México.
*rodolfom@cio.mx

Abstract: In this work, we report an autonomous system for real-time monitoring of the plantar pressure distribution. The system is developed using standard components which add versatility to the system. Sensors are integrated in insoles that are incorporated to the footwear. Wireless transmitters are used to transmit the information from sensors to the computer, where the developed graphical interface shows the dynamic images representing the plantar pressure distribution. Hardware and algorithms are presented.

1. Introduction.

Osteoarthritis (OA) is considered a health problem worldwide, the prevalence of the OA increases with the time, being almost permanent on people over 75 years old [1]. OA is a chronic-degenerative disease characterized by the progressive loss of the cartilage that covers the joint surface; it affects knees, hip, shoulders and hands [2]. OA is the most common degenerative disease of the knee, being one of the main causes of pain and incapacity on the elder adult; affecting their economic situation and lifestyle [3]. OA is a multifactorial disease mainly caused by age, gender, obesity, joint misalignment, among others [4].

Although some of the risk factors cannot be controlled like age or gender, factors as joint misalignment, overweight and lifestyle can be moderated to preserve the articular cartilage of the knee. The knee joint misalignment can be originated by anomalies on the plantar pressure distribution [5]. These anomalies are caused mainly by deformities on the foot or bad gait habits. For this reason, the need arises to detect these anomalies on the plantar pressure distribution on an early stage to have a proper treatment for it; avoiding joint misalignment and decelerate the cartilage degeneration in the knee joint. In this work, the design and development of a dynamic images system for plantar pressure distribution is presented.

2. Experimental methodology and results.

The dynamic image monitoring of the plantar pressure distribution is performed using a pair of sensing insoles integrated on footwear. The sensing insoles were constructed with standard components, decreasing the cost 90% compared to other existing systems in the market. Each insole has eleven sensors distributed on specific supporting points of the foot. Acquisition signal, signal conditioning and wireless transmission of sensing data are performed by the control circuit which can be found inside of a pocket sewed on the upper part of the footwear; making the monitoring system an autonomous device.

Fig. 1. Sensing footwear

The sensing data is transmitted through radio frequency modules to a computer, where the graphical interface processes and displays in real-time the plantar pressure distribution. The graphical interface was programmed on LabVIEW. The interface has other features as well, like customization, organization and storage of the plantar pressure distribution files. In Figure 2, the main screen of the LabVIEW´s graphical interface developed is shown.

Fig. 2. Main screen of LabVIEW´s interface

The graphical interface generates real time images from the plantar pressure distribution. These images can be an important source of information for a specialist to determine a treatment for the adjustment of the plantar pressure distribution of a patient. Also the real-time monitoring system can be implemented for following up the evolution of plantar pressure distribution in patients before, during and after the treatment.

Fig. 3. Images of plantar pressure distribution

The adjustment of the plantar pressure distribution will help to prevent joint misalignment and, at the same time, to decelerate the degeneration of the knee joint cartilage; improving the quality of life of patients with risk of suffering knee osteoarthritis.

The presented system makes use of standard components, pressure sensors, multiplexors, microcontrollers and radio frequency modules. This makes the system versatile as any change needed can be immediately applied. Also the system allows remote access to the sensing data which opens the possibility for image processing algorithms to identify pathologies on the knee joint.

References

[1] Molinero Rodriguez C, P. H. “Impacto laboral por enfermedades reumáticas en el municipio 10 de octubre,”(2003).. Revista Cubana de Reumatología , 3.
[2] Figueroa, R. M., Figueroa, C. M., Rodriguez, R. C., & Poblete, D. F. (2015). Osteoartritis (artrosis) de rodilla. Revista Chilena De Ortopedia Y Traumatología, 56(3), 45-51. doi:10.1016/j.rchot.2015.10.005
[3] Altman R, A. E. (1986). Development of criteria for the classification and reporting of osteoarthritis: classification of osteoarthritis of the knee. Arthritis & Rheumatism , 1039-49.
[4] Rolando Espinosa Morales, et al. “Reunión multidisciplinaria de expertos endiagnóstico y tratamiento de pacientes con osteoartritis. Actualización basada en evidencias”. Med. Int. Mex. 2013; Vol. 29(1): p. 67-92.
[5] C. Salazar Gómez. “Flat foot, as the origin of biomechanic alterations in progression”

Modelling and control of a two-axis solar tracking system

Yves J. Pérez D.[1], Rubén Garrido[2], Arturo Díaz Ponce[3]
Departamento de Control Automático, CINVESTAV-IPN, Av. IPN 2508 San Pedro Zacatenco, Mexico City[1,2].
CONACYT—Centro de Investigaciones en Óptica, A.C. Unidad Aguascalientes—Prol. Constitución 607, Fracc. Reserva Loma Bonita, Aguascalientes 20200, Aguascalientes, Mexico[3]
yperez@ctrl.cinvestav.mx[1], garrido@ctrl.cinvestav.mx[2], adiaz@cio.mx[3]

Abstract: The present work focuses on the analysis of a two-axis solar tracking system controlled in open- loop by a Proportional-Integral-Derivative control plus feedforward and a solar position algorithm in order to calculate the trajectories.

1. Introduction

One of the main sources of renewable energy is the Sun, which produces energy in its inner core in a process called nuclear fusion, this energy is radiated and is known as solar energy. The solar tracking systems seek to take advantage of the largest amount of solar energy with the correct position, this condition requires that the collector surface is as perpendicular as possible to the sun's rays, therefore, the optimal collection can only be reached by making the system follow the Sun. By providing tracking to the system, the total energy received on a clear day can be 35% to 40% greater than the same system in a static state.

The two most common systems for tracking the sun's trajectory to achieve the highest possible performance are: with one axis, this is employed to follow the sun from east to west, and with two axes, which guarantees to follow the sun directly and thus to take full advantage of the solar radiation. To determine the Sun's position relative to any point on the surface of the Earth, two angles are enough, the angle of elevation and the azimuth angle, or the zenith angle and the azimuth angle. These angles vary throughout the day, they also depend on the geographic coordinates of the place and the day of the year [1].

2. Methodology

The trajectories are computed in Matlab / Simulink ® software using the solar position algorithm described in [2], on March 15, 2018, in the interval between 6:00 a.m. to 7:00 p.m., with a step of 1 second between each calculation of the position; located in the CINVESTAV-Unidad Zacatenco, time zone is -6hrs, coordinates longitude -99.13047°, latitude 19.50991° and altitude 2224m. Assuming an annual average temperature of 16.6 °C and atmospheric pressure of 781 mbar. It is proposed the use of polynomials of third order and fifth order to smooth the beginning of the trajectories and for the restoration of initial conditions. The trajectories are entered into a trajectory generation block to have access to the estimation of the first two derivatives.

The kinematic and dynamic modelling of the solar tracking system of two degrees of freedom composed of revolute joints is performed, obtaining the Euler-Lagrange equations in their matrix form showed in Eq. 1, following the methodology described in [3], the solar tracker joints that coincide with the azimuth angle and elevation angle are taken as generalized coordinates.

$$M(q)\ddot{q} + C(q,\dot{q})\dot{q} + G(q) = \tau \tag{1}$$

The dynamic model of the solar tracker is obtained with DC gearmotors. It is determined that for very small speeds and large reduction ratios, the torques due to the dynamics of the solar tracking mechanism are considered as disturbances in the model of the DC motor. Therefore, the simplified model for each servomotor is showed in Eq. 2.

$$\ddot{q}_k + a_k\dot{q}_k = b_k u_k + d_k \tag{2}$$

Where:

$$a_k = \frac{B_{mk}}{J_{mk}}, \quad b_k = \frac{k_k}{J_{mk}R_k}, \quad d_k = \frac{h_{mk}}{J_{mk}R_k} - \frac{g_k(q)}{J_{mk}R_k^2}$$

With B_{mk} viscous friction, J_{mk} inertia, k_k gain, h_{mk} disturbances, R_k reduction y g_k gravity terms.

A PID plus feedforward control is proposed for tracking trajectories, let the tracking error $e_k = r_k - q_k$, with the first two derivatives continuous, r_k is the desired trajectory and q_k the actual trajectory. The control law is: $u_k = u_{pk} + u_{rk}$ where $u_{pk} = \frac{1}{b_k}[a_k\dot{r}_k + \ddot{r}_k]$ is the feedforward and $u_{rk} = \frac{1}{b_k}\left[k_{pk}e_k + K_{dk}\dot{e}_k + K_{ik}\int_0^t e_k(\tau)d\tau\right]$ is the feedback. K_{pk}, K_{ik} and K_{dk} are the Proportional-Integral-Derivative gains for each servomotor.

3. Results

The real-time experiments were implemented with the solar tracking mechanism (Fig. 1). The servomotor model RH-14D6002-E100AL brand Harmonic Drive is used for both axes, the estimated parameters are $a = a_1 = a_2 = 10.2250$ and $b = b_1 = b_2 = 1275.8$, determined by the least squares method. An LQR optimal control is proposed to tune the gains of the PID controller, achieving a weighting of the total energy consumption. The system in state space without disturbances is represented as:

$$\dot{X} = AX + Bu_r = \begin{bmatrix} 0 & 1 & 0 \\ 0 & a & 0 \\ 1 & 0 & 0 \end{bmatrix} X + \begin{bmatrix} 0 \\ -b \\ 0 \end{bmatrix} u_r, \quad \text{with} \quad X = \left[e, \ \ \dot{e}, \ \ \int_0^t e(\tau)d\tau \right]^T$$

Solution of the algebraic Riccati equation Eq. 3 allows to calculate the optimal gains for the PID control [4].

$$A^T S + SA - SBQ_1 B^T S + Q_2 = 0, \quad \text{where} \quad Q_1 > 0, Q_2 > 0 \quad \text{and} \quad S > 0 \tag{3}$$

The optimal gains for the PID control are calculated as $[K_p, K_d, K_i]^T = bQ_2^{-1}B^T S$. We obtain the total energy consumption W in Joules and the Integral Square Error (ISE) is used as a performance criterion. The results are show in the Table 1, using the matrix $Q_1 = \text{diag}(500,1,600)$.

Table 1. Results for different values of the weight parameter Q_2

Q_2	K_p	K_d	K_i	W_1	W_2	ISE_1	ISE_2
800	1078.01	55.312	1104.8	39.182	17.944	60.396	28.204
1700	745.19	40.296	757.94	35.806	16.779	124.277	56.790

Fig. 2 shows trajectory tracking, where r_1 is the desired trajectory of the azimuth axis and q_1 the actual trajectory, while r_2 is the desired trajectory of the elevation axis and q_2 the actual trajectory. The time is compressed by a factor of 1000 to be able to perform the experiments of a full day in a time of 86.4 s.

Fig 1. Two-axis solar tracking system

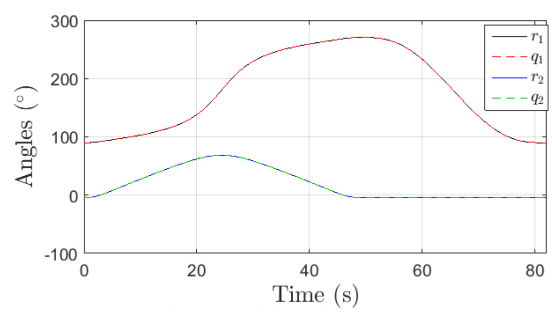

Fig 2. Tracking with $Q_2 = 800$

4. Conclusion

The trajectories of the azimuthal and elevation angles were obtained with the solar position algorithm and it was verified that the PID plus feedforward control makes a good trajectory tracking of both axes, the use of the LQR allows to tune the control and the increase of the value Q_2 from 800 to 1700, causes the decrease of the total energy consumption, from 39.182 Joules to 35.806 Joules for azimuth axis and from 17.944 Joules to 16.779 Joules for elevation axis, with the disadvantage of the ISE increment from 60.396 a 124.277 for azimuth axis and from 28.204 a 56.790 for elevation axis.

References

[1] Gopal Nath Tiwari.Solar energy: fundamentals, design, modelling and applications.Alpha Science Int'l Ltd., 2002.
[2] Reda, Ibrahim, and Afshin Andreas. "Solar position algorithm for solar radiation applications." Solar energy 76.5 (2004): 577-589.
[3] Mark W Spong, Seth Hutchinson y Mathukumalli Vidyasagar. Robot modeling and control. Vol. 3. Wiley New York, 2006.
[4] Rubén Garrido y Roger Miranda. "Autotuning of a DC servomechanism using closed loop identification". In: IEEE Industrial Electronics, IECON 2006-32nd Annual Conference on. IEEE. 2006, pags. 258-263

Location of the highest intensity autocorrelation amplitude in the focusing of femtosecond pulses

J.A. Moreno-Larios, M. Rosete-Aguilar, O.G. Rodríguez-Herrera, J. Garduño-Mejía, and N.C. Bruce
Instituto de Ciencias Aplicadas y Tecnología, Universidad Nacional Autónoma de México, Av. Universidad 3000, Coyoacán, Ciudad de México, 04510, México
Author martha.rosete@icat.unam.mx

Abstract: In nonlinear microscopy using femtosecond pulses to illuminate the sample can degrade the resolution of the system if aberrations are not corrected. These aberrations can also couple in time stretching the pulses beyond their minimum transform-limited durations. In this work we present a theoretical model, based on the scalar diffraction theory, to analyze the coupling through aberration and time at the focal region of an optical system that introduces no dispersion or the dispersion has been pre-compensated. The analysis for locating the shortest pulse duration, the smallest spot size and the highest intensity autocorrelation amplitude are performed with the same techniques used in the laboratory.

1. Introduction

In nonlinear microscopy applications, the light from a femtosecond laser source has to be expanded to fill the full aperture of the focusing system, normally a microscope objective [1,2]. Additionally to expanding the beam, other optical instrumentation is required to manipulate and/or to measure the pulse in time. For example, a pulse compressor is necessary to correct for the group velocity dispersion (GVD) of the complete system, in order to achieve the minimum transform-limited duration of the pulse at the sample [3]. A two-photon-absorption (TPA) intensity autocorrelation (IA) has to be introduced into the system for temporal characterization [4]. Not only these instrumentation introduce wavefront aberrations into the illuminating beam but also the sample itself introduces aberration. The coupling through aberrations and time into femtosecond pulses will reduce the nonlinear effect generated by the TPA which requires a very high peak amplitude of the intensity autocorrelation. In this work we present the modelling of femtosecond pulses at the focal region of an optical system by using the scalar diffraction theory [5]. We assumed that any dispersion effect has been corrected so only the aberration and diffraction (for a few-optical-cycle pulses) couple through time modifying the response of the TPA intensity autocorrelation signal.

To measure the pulse in time, we use two methods: (a) by fitting a Gaussian to the intensity autocorrelation and (b) by measuring the mean square deviation (MSQ) of the temporal distribution as proposed in reference [6]. The spatial distribution of the pulse is also measured by two methods: (a) by modelling the knife-edge test and fitting a Gaussian to the beam spatial-profile and (b) by measuring the MSQ of the spatial distribution. We will show that the two methods give different information for the position of the shortest pulse duration and the smallest spot size. The location for the highest IA amplitude is, however, independent of the method used to measure time or space.

2. Results and Discussion.

The results for the location of the smallest spot size, shortest pulse duration and the highest IA amplitude measured with respect to the paraxial focal point of an ideal and spherical mirror with a focal length of 50mm, diameter of 12.7mm and numerical aperture NA=0.127 for initial pulse durations of 5fs, 20fs and 200fs@810nm are presented for the Gaussian Fit to the IA for temporal distribution and the knife-edge test for the spatial distribution in table 1 and for the MSQ in table 2. We can see how the position for the shortest pulse duration and the smallest spot size depends on the method used to estimate them but the position for the highest IA signal is independent of the method. For 200fs the pulse duration does not change in the sweep interval so it is omitted in both tables.

In the laboratory the temporal estimation of the pulse is calculated from the IA signal obtained from the experiment and by using the knife-edge test to measure the spot size. So, we can conclude that the MSQ method proposed in reference [6] does not necessarily give the same information as the one obtained from the experiment for the location of the smallest spot size and shortest pulse duration. Notice that the highest IA amplitude for the ideal system is not located at zero for very short pulse, we attribute this shift to the spatial chirp introduced by diffraction [7].

Table 1. Gaussian Fit to the IA (time profile) and the knife-edge test.

Initial FWHM pulse duration [fs]	Analysis type	Min spot on x-axis pos [μm]	Shortest pulse duration pos [μm]	IA max pos [μm]
5	Ideal	0	0	-5
5	Aberrated	-55	-115	-120
20	Ideal	0	0	-10
20	Aberrated	-55	-135	-190
200	Ideal	0	-.-	0
200	Aberrated	-55	-.-	-60

Table 2. MSQ for measuring temporal and spatial distributions.

Initial FWHM pulse duration [fs]	Analysis type	MSQ in space x-axis [μm]	MSQ in time pos [μm]	IA max pos [μm]
5	Ideal	0	0	-5
5	Aberrated	-65	-115	-120
20	Ideal	0	0	-10
20	Aberrated	-65	-110	-190
200	Ideal	0	-.-	0
200	Aberrated	-65	-.-	-60

Acknowledgments.

Dirección General de Asuntos del Personal Académico, Universidad Nacional Autónoma de México (DGAPA, UNAM), (PAPIIT- IN107018 and PAPIIT-IN111818). José Agustín Moreno-Larios acknowledges grants from Consejo Nacional de Ciencia Y Tecnología (CONACyT), México and from the Programa de Maestría y Doctorado de Ingeniería, UNAM.

References

[1] Rui Li, Xinxin Wang, Yi Zhou, Huan Zong, Maodu Chen, Mengtao Sun, “Advances in nonlinear optical microscopy for biophotonics,” J. Nanophoton. **12,** 033007 (2018).
[2] M. Rutkauskas, D.T. Reid, J. Garduño-Mejía, M. Rosete-Aguilar, “Time-domain measurements reveal spatial aberrations in a sub-surface two-photon microscope, Appl. Opt. 56, 5047-5053 (2017).
[3] P. Castro-Marín, G. Castro-Olvera, J. Garduño-Mejía, M. Rosete-Aguilar, N.C. Bruce, D.T. Reid, and O.G. Rodríguez-Herrera, “Autocorrelation z-scan technique for measuring the spatial and temporal distribution of femtosecond pulses in the focal region of lenses,” Opt. Express 25, 14473-14482 (2017).
[4] D.T. Reid, W. Sibbett, J.M. Dudley, L.P. Barry, B. Thomsen, and J.D. Harvey, “Commercial semiconductor devices for two photon absorption autocorrelation of ultrashort light pulses,” Appl. Opt. **37**, 8142-8144 (1998).
[5] S. Anaya-Vera, L. García-Martínez, M. Rosete-Aguilar, N.C. Bruce, and J. Garduño-Mejía, “Temporal spreading generated by diffraction in the focusing of ultrashort light pulses with perfectly conducting spherical mirrors,” J. Opt. Soc. Am. A 30, 1620-1626 (2013).
[6] J.C. Diels and W. Rudolph, “Femtosecond optics,” in *Ultrashort Laser Pulse Phenomena*, 2nd ed. (Elsevier, 2006).
[7] N. C. Bruce, M. Rosete-Aguilar, O. G. Rodríguez-Herrera, J. Garduño-Mejía, and R. Ortega-Martínez, “Spatial chirp in the focusing of few-optical-cycle pulses by a mirror,” J. Mod. Opt. **60**(13), 1037–1044 (2013).

Local Information

CANCÚN, MÉXICO

Located on the state of Quintana Roo, México, in the Yucatán Peninsula, the City of Cancún is bordered by the Caribbean Sea and is one of the most important and modern touristic resorts in the country.
The natural beauty of Cancún, with wonderful beaches characterized by the white sand and clear water with many shades of blue, a great hotel infrastructure, nightclubs, shops, restaurants and world-class services, have made a city of choice for tourists and to organize, weddings, conventions, musical concerts, and of course conferences and symposiums.
This great venue is conveniently situated near the Mayan city of Chichen Itza and other important sites of this great civilization that can make a pleasant cultural visit.

Chichen Itza archeological site

Tulum

The cenotes

The Cancun underwater museum

Isla Mujeres

Spend a day at Xcaret Park

Author Index

Alonso Murias Monserrat	218
Alonso-Murias M.C.	214
Alva Medrano Hugo	226, 230
Álvarez-Valtierra Leonardo	26
Anaya Rivera Ely Karina	232
Arai Yasuhiko	81
Arriaga Rodríguez J. Jesús	46
Assa Akbar	137
Avazpour Mahrokh	210, 46
Babaei Ali	126
Barreiro-Argüelles Denisse	159
Barrientos Bernardino	118
Barrientos-Gracia Alejendro	68, 114
Barron-Zambrano Jose H.	182
Basulto Josué I.	208, 218
Beltrán Pérez Georgina	210
Benitez-Lara Alfredo	164
Bhattacharya Indrani	60
Blanco Alan	118
Bonilla-Jimenez Luis-A.	180
Bravo-Medina Beethoven	76
Briones Joel	164
Bruce Neil Charles	240, 188
Bruno Binal P.	57
Cajero Rodriguez Sammantha	148
Calderón-Hernández G.	91
Callejas-Cornejo Juan M.	169
Camarena-Chávez Victor	26
Camarillo-Escobedo Rosa M.	236
Carrillo Cesar	146
Carrillo-Delgado Carlos M.	182, 216
Castañeda-Priego Ramon	28
Castillo Gallardo Victor	224, 228
Castillo-Cardoso A.	91
Castro-Beltrán Rigoberto	26, 28, 161
Cervantes Meza Hernando J.	194
Cervantes-L Joel	190
Chávez Gutiérrez Francisco	144, 173
Chen Cheng	37
Chen Hongfang	100
Chen Terry Yuan-Fang	112
Cheng Fa-Yen	112
Clévy Cédric	53
Coello Victor	83
Contreras Medina Luis M.	41
Contreras Vallejo Karla E.	204
Coronado Luis Valentín	169, 148
Cortés Rodolfo	83
Courjal Nadège	51, 53
Cruz-Bernal Alejandra	171
Cuevas de la Rosa Francisco	116, 135, 108
Cywiak Moisés	43
Daza-Benítez Leonel	236
De Coss-Gómez Maritza	34
Di Martino J. Matías	85
Díaz Ponce Arturo	238, 148
Domínguez-Flores Carmen E.	208
Dong Bo	122
Echavarría Juan	212
Escobar Marco A	102
Estudillo-Ayala Julian Moises	41, 200, 198, 204, 182, 206, 216
Fernandez Jaramillo Arturo A	41
Ferrari Jose A.	85
Filoteo-RazoJose D.	198, 216
Flores Jorge L.	184, 85
Flores Moreno Jorge M.	66
Flores Víctor	146, 120
Franco Juan Manuel	43
Fujigaki Motoharu	156, 141
Gale David M.	128
Gallegos Arellano Eloísa	200
Gantes Nuñez Francisco J.	78
Garcia Cesar E.	83
Garcia Torales Guillermo	184
Garduño-Mejía Jesus	240
Garnica-Gonzalez Jaime	180
Garrido Moctezuma Rubén	148
Garrido Rubén	238
Gaspar Jorge A.	234
Ghahramani Mohammad	167
Gómez-Méndez Gustavo A.	110
González Ávila José Luis	175
González José Antonio	133
Goto Yuta	156, 141
Grobler Michael F.	150
Grunwald Ruediger	57
Guel-Tapia Juan	68
Guerrero-Viramontes J. Ascención	144, 48
Gutiérrez Hernández David	102
Gutierréz Juárez Gerardo	26
Gutiérrez-León Diana-G.	171
Guzman Chavez Ana Dinora	194

Hagen Nathan	186, 87
Hashimoto Manabu	24
Hayasaki Yoshio	190, 154
Hazra Lakshminarayan	60
Hernández-García Juan C.	41, 200, 198, 204, 182, 206, 216
Hernández-Romano Ivan	222, 214
Hesami Majid	46
Huang Hong-Yu	64
Hwang Chi Hung	74
Isaza Cesar	232
Ishii Norihiko	152
Islas-Islas Juan Manuel	180
Iturbe Castillo Marcelo David	46
Jan Nitsche	98
Janabi-Sharifi Farrokh	167, 137, 139
Jáuregui-Vázquez Daniel	206
Javier González Francisco	66
Juarez Luna Victor Manuel	89
Katano Yutaro	152
Kawahara Kohhei	141
Khan Danish	196
Kim Min Young	196
Kinoshita Nobuhiro	152
Kobayashi Fumio	87
Kofman Jonathan	126, 124
Korneev Nikolai	39
Kumme Rolf	98
Kusunoki Yoshiyuki	156
Kuzin Evgeny	210
Laurati Marco	28
Lauterio-Cruz Jesus Pablo	216
Le Trong-Nhan	30
Lee Chia-Cheng	112
Lemke Florian	55
León-Rodríguez Miguel	68, 114, 70, 130
Lin Jing-Yao	62
Lin Po-Chen	64
Lin Shyh-Tsong	62, 64
Lin Yu-Hsin	64
Liu Xin-Yu	62
Liu Xinran	124
Lo Yu-Lung	30
López Téllez Juan Manuel	188
López-Cortés Daniel	208
López-Martínez Alan	135
Lozano Tania	202
Lozano Trejo Eliezer	224, 228
Lugo-Jiménez Jorge	34
Luis Noriega Daniel	66
Lutz Philippe	51, 53
Ma Chao-Ting	64
Macías-Mendoza Humberto	184
Malacara Hernandez Daniel	78
Malacara-Doblado Daniel	78
Maldonado Rivera José Luis	159, 161
Mares Carlos	118
Marquez Salomon	32, 218
Marrujo-García Sigifredo	222
Martell Fernando	148
Martin-Vela Javier A.	200, 204, 182
Martínez Ramírez Laura G.	41
Martínez Ríos Alejandro	48
Martinez Rodolfo M.	150
Martinez-Angulo Jose R.	198, 182
Martínez-Barba Daniel A.	236
Martínez-García Amalia	114, 70, 110, 89, 130
Martinez-Manuel Rodolfo	236
Martínez-Peláez Rafael	102
Martínez-Ríos A.	144
Masaki Shunya	190
May-Arrioja D.A.	214
Medina Magallón José Eduardo	230
Medina-Cazares Orlando	68, 114
Mehrandezh Mehran	139, 212
Mejía Alanís Francisco Carlos	173
Méndez Otero Marcela M.	46
Méndez-Dzul Hector	34
Mendez-Guzmán Hugo A.	146
Méndez-Lozoya Javier	66
Mendoza Santoyo Fernando	66
Mendoza Suárez Alberto	224, 226, 228, 230
Meng Fanchao	37
Mizutani Yasuhiro	104, 72
Molina-González Jorge	164
Montelongo Yunuen	139
Montes Perez Areli	180
Monzón-Hernández David	222, 208, 214, 218
Morales Espinoza Zaira	144
Moré Quintero Iosvani	108
Moreno-Larios José Agustín	240
Mosquera Julio	232
Mumanga Takawira J.	150
Muñoz Antonio	184
Muñoz Rodríguez J. Apolinar	173
Muroi Tetsuhiko	152
Nagata Noriko	24
Nicasio-Collazo Juan	159, 161
Ortiz Mauricio	133

Otal Penélope Gisel	161
Otani Yukitoshi	186, 177, 87
Pan Bing	122
Paranjape Raman	212
Parra Escamilla Geliztle A	184, 85, 87
Parra-Michel Jorge R.	102
Peña-Cruz Manuel I.	169, 148
Pérez Aguilar Héctor	226, 228, 230
Perez Delgado Yves Jesus	238
Perez Ivan	212
Perez Lopez Ricardo	194
Petrilli Barceló Alberto Elías	175
Piazza Valeria	32
Pottiez Olivier	216
Puente Díaz Luis Eduardo	224, 230
Ramos-Ortiz Gabriel	26
Rayas Juan	114, 70, 110, 89, 130
Rendón-Delgado L. A.	91
Reséndiz-Lopez German	180
Reyes Alan	106
Reyes Ana Karen	110
Reyes-Ramirez Bartolomé	83, 164
Rivera Meraz Mariano	106
Rizzo Sierra Jose Amilcar	232
Rodríguez Herrera Oscar G.	188, 240
Rodríguez Nuñez Omar	188
Rodríguez-Zurita G.	91
Rojas-Laguna Roberto	41, 200, 198, 202, 204, 182, 206, 216
Romero-Borja Daniel	159, 161
Ruiz Cortes Victor	89
Saadatseresht Mohammad	126
Sajjadi Sina	139
Salgado Tránsito Ivan	148
Salinas Julio	159
Sanchez Gonzalez Jose L. J.	89
Sánchez José	130
Sarocchi Damiano	118
Sato Ryo	154
Septien Eduardo	48
Serrano Garcia David I.	184, 177, 87. 180
Shi Zhaoyao	100
Shibta Shuhei	186
Shimamoto Yuki	190
Sierra-Hernandez Juan M.	41, 198, 202, 204, 206
Silva Medina Daniel	175
Song Huixu	100
Sosa-Balderas Juan Vicente	116, 135
Sossa Azuela Juan Humberto	175
Soto Maria	28
Strojnik Marija	76
Sun Cuiru	37
Taguchi Hiroki	72
Taguchi Koichi	24
Takano Wataru	186
Takata Daishi	156
Takaya Yasuhiro	104, 72
Tobitani Kensuke	24
Toral Daniel	48
Toral-Acosta Daniel	144
Torres-Armenta Diego	144
Torres-Cisneros Miguel	222, 214
Torres-González Daniel	206
Toto-Arellano Noel-Ivan	91, 180
Tran Hong-Chuong	30
Tutsch Rainer	98
Vakanski Alexander	167
Valdivia Ricardo	118
Vargas Rodriguez Everardo	194
Velázquez J. Salvador	222, 218
Vera-Duarte Oscar X.	198
Vidal-Lesso Agustín	236
Villa Francisco	234, 83
Vinajera-Reyna Carlos	34
Wallrabe Ulrike	55, 57
Wang Wei-Chung	74
Wapler Matthias C	55
Weber Pascal M	55
Yáñez Etna	43
Yetisen Ali K.	94
Zavala de Paz Jonny Paul	232
Zhevandrov Petr	230


20 th
ISOT
International Symposium on Optomechatronic Technology
GOA . 2019 . INDIA
NOVEMBER 5 to 8
ISOM
International Society for Optomechatronics
KEY DATES :
Deadline for Submission of Extended Abstracts : August 15, 2019
Acceptance Notification : September 15, 2019
Deadline for Early Bird Registration : October 7, 2019
UNIVERSITY OF CALCUTTA · ADVANCEMENT OF LEARNING
ESTD. 1857
Topics included but not limited to :
Optical Metrology
Optical Interferometry
Optical Imaging
Optical Sensors
Polarization Optics
Diffractive optics
Optical waveguides
Optical Tweezers
Optical Micromanipulation
Nano photonics
Superresolution microscopy
Nonlinear optics applications
Astronomical Optics
Biomedical Optics
Organized by:
Department of Applied Optics and Photonics
University of Calcutta, INDIA
Contact: isotindia2019@gmail.com

· SPONSORS ·

CENTRO DE INVESTIGACIONES EN OPTICA, A.C.

ISOM International Society for Optomechatronics

SPIE.

OSA The Optical Society | 100 Since 1916

Coordinación de la Investigación Científica

BENEMÉRITA UNIVERSIDAD AUTÓNOMA DE PUEBLA 1578

ACADEMIA MEXICANA DE ÓPTICA, A.C.

ICAT Instituto de Ciencias Aplicadas y Tecnología

UNIVERSIDAD DeLaSalle BAJIO

SATEL sa

UPG UNIVERSIDAD POLITÉCNICA DE GUANAJUATO

Edmund optics | worldwide

DITEK